frontiers | Research Topics

Nonlinear dynamics and complex patterns in the human musculoskeletal system and movement

Edited by
Yih-Kuen Jan, Cheng-Feng Lin, Fuyuan Liao and Navrag B. Singh

Coordinated by
Ben-Yi Liau and Chi-Wen Lung

Published in
Frontiers in Bioengineering and Biotechnology

ISSN 1664-8714
ISBN 978-2-8325-4222-4
DOI 10.3389/978-2-8325-4222-4

About Frontiers

Frontiers is more than just an open access publisher of scholarly articles: it is a pioneering approach to the world of academia, radically improving the way scholarly research is managed. The grand vision of Frontiers is a world where all people have an equal opportunity to seek, share and generate knowledge. Frontiers provides immediate and permanent online open access to all its publications, but this alone is not enough to realize our grand goals.

Frontiers journal series

The Frontiers journal series is a multi-tier and interdisciplinary set of open-access, online journals, promising a paradigm shift from the current review, selection and dissemination processes in academic publishing. All Frontiers journals are driven by researchers for researchers; therefore, they constitute a service to the scholarly community. At the same time, the *Frontiers journal series* operates on a revolutionary invention, the tiered publishing system, initially addressing specific communities of scholars, and gradually climbing up to broader public understanding, thus serving the interests of the lay society, too.

Dedication to quality

Each Frontiers article is a landmark of the highest quality, thanks to genuinely collaborative interactions between authors and review editors, who include some of the world's best academicians. Research must be certified by peers before entering a stream of knowledge that may eventually reach the public - and shape society; therefore, Frontiers only applies the most rigorous and unbiased reviews. Frontiers revolutionizes research publishing by freely delivering the most outstanding research, evaluated with no bias from both the academic and social point of view. By applying the most advanced information technologies, Frontiers is catapulting scholarly publishing into a new generation.

What are Frontiers Research Topics?

Frontiers Research Topics are very popular trademarks of the *Frontiers journals series*: they are collections of at least ten articles, all centered on a particular subject. With their unique mix of varied contributions from Original Research to Review Articles, Frontiers Research Topics unify the most influential researchers, the latest key findings and historical advances in a hot research area.

Find out more on how to host your own Frontiers Research Topic or contribute to one as an author by contacting the Frontiers editorial office: frontiersin.org/about/contact

Nonlinear dynamics and complex patterns in the human musculoskeletal system and movement

Topic editors

Yih-Kuen Jan — University of Illinois at Urbana-Champaign, United States
Cheng-Feng Lin — National Cheng Kung University, Taiwan
Fuyuan Liao — Xi'an Technological University, China
Navrag B. Singh — Department of Health Sciences and Technology, ETH Zürich, Switzerland

Topic Coordinators

Ben-Yi Liau — Feng Chia University, Taiwan
Chi-Wen Lung — University of Illinois at Urbana-Champaign, United States

Citation

Jan, Y.-K., Lin, C.-F., Liao, F., Singh, N. B., Liau, B.-Y., Lung, C.-W., eds. (2024). *Nonlinear dynamics and complex patterns in the human musculoskeletal system and movement*. Lausanne: Frontiers Media SA. doi: 10.3389/978-2-8325-4222-4

Table of contents

frontiers | Frontiers in Bioengineering and Biotechnology

TYPE Editorial
PUBLISHED 14 December 2023
DOI 10.3389/fbioe.2023.1339376

OPEN ACCESS

EDITED AND REVIEWED BY
Markus O. Heller,
University of Southampton,
United Kingdom

*CORRESPONDENCE
Yih-Kuen Jan,
yjan@illinois.edu

RECEIVED 16 November 2023
ACCEPTED 08 December 2023
PUBLISHED 14 December 2023

CITATION
Jan Y-K, Lin C-F, Liao F and Singh NB (2023), Editorial: Nonlinear dynamics and complex patterns in the human musculoskeletal system and movement. *Front. Bioeng. Biotechnol.* 11:1339376. doi: 10.3389/fbioe.2023.1339376

Editorial: Nonlinear dynamics and complex patterns in the human musculoskeletal system and movement

Yih-Kuen Jan[1]*, Cheng-Feng Lin[2], Fuyuan Liao[3] and Navrag B. Singh[4,5]

[1]Rehabilitation Engineering Lab, Department of Kinesiology and Community Health, University of Illinois at Urbana-Champaign, Champaign, IL, United States, [2]Department of Physical Therapy, National Cheng Kung University, Tainan, Taiwan, [3]Department of Biomedical Engineering, Xi'an Technological University, Xi'an, China, [4]Department of Health Sciences and Technology, ETH Zurich, Zurich, Switzerland, [5]Singapore-ETH Centre, Future Health Technologies Program, CREATE Campus, Singapore, Singapore

KEYWORDS

complexity, dynamics, modeling, movement, nonlinearity, tissue

Editorial on the Research Topic
Nonlinear dynamics and complex patterns in the human musculoskeletal system and movement

The human body consists of interacting systems, such as musculoskeletal, nervous, and cardiovascular systems, that work together to perform complex body functions and movements (Shiogai et al., 2010; Stergiou and Decker, 2011). In the past decades, researchers have focused on the study of individual systems using biomechanical approaches to better understand the structure and function of the human system and how pathological diseases affect the human musculoskeletal system function and movement (Jan et al., 2013; Liao and Jan, 2017; Liau et al., 2019). Although the concepts of non-linear dynamics and complex patterns have been recognized as emerging methods to better understand the human musculoskeletal system and movement, the non-linear dynamics and complex patterns of human musculoskeletal system and movement remain largely unexplored (Shiogai et al., 2010; Stergiou and Decker, 2011; Orter et al., 2019). This Research Topic aims to highlight novel applications of non-linear dynamic and complexity methods to understand the human musculoskeletal system and its interactive systems (e.g., nervous, cardiovascular, and integumentary systems) and movement in healthy and pathological populations.

Concepts of non-linear dynamics and complex interactions in the human musculoskeletal system and movement refer to variability, adaptability, and pattern formation. Wang et al. investigated the interaction between changes in muscle activation and cortical network dynamics during isometric elbow contraction using surface electromyography (sEMG) and functional near-infrared spectroscopy (fNIRS). Fuzzy approximate entropy was used to evaluate signal complexity in various motor tasks. Their results demonstrated that connectivity between brain regions assessed through fNIRS in motor tasks on the dominant side was significantly higher and that there was a significant positive correlation between entropy and hemodynamic values in the contralateral brain regions in both dominant and non-dominant sides. These findings provide evidence of the interaction between the brain and the musculoskeletal system.

Wolff et al. explored the effects of age, body dimension, and handgrip strength on the plantar pressure trajectory. Their results indicate that age, body weight, body height, and body mass index can explain up to 46% of the variability in plantar pressure trajectories. They conclude that age and body dimension should be used to adjust plantar pressure data. Burdack et al. intended to detect cross-movement commonalities of individual walking, running, and handwriting patterns using data augmentation. They used the conditional cycle-consistent generative adversarial network (CycleGAN). The model was trained by data obtained from 17 healthy adults and was then used to artificially generate other movement data. The classification F1-score ranged from 46.8% for handwriting data and 98.9% for walking data. Their model supports the existence of inter-individual differences while performing various activities, with handwriting being more personalized than walking or running.

In this Research Topic, studies explored the interactions between components of the musculoskeletal system and their effect on movement performance. Bai et al. explored the use of non-negative matrix factorization (NNMF) to extract mechanical characteristics of foot functional units during walking and running. Their results demonstrate that walking and running can be decomposed into two foot functional units, namely, buffering and push-off. The forefoot occupies a certain weight in both buffering and push-off functions indicating that there may be a complex foot function transformation mechanism in the transverse arch of the foot. Their study suggests that NNMF is feasible for analyzing foot mechanical characteristics. Moon et al. used a musculoskeletal modeling approach to investigate the effect of an increase in sprinting velocity on the load of the anterior cruciate ligament and knee joint. Their results indicate that factors such as knee joint shear force, extended landing posture with increasing sprinting velocity, internal rotation moment, and femoral muscle activity imbalance influence the increase of anterior cruciate ligament load during a sidestep cutting maneuver. He et al. used a musculoskeletal modeling approach to investigate the differences in lumbar and pelvis movements between cross-court and long-line topspin forehand strokes in table tennis. They found that the lumbar and pelvis embody greater weight transfer and greater energy production mechanisms in cross-court compared to long-line topspin forehand. Xi et al. intended to address soft tissue artifacts when quantifying the motion of the spine using optical motion capture with retroreflective markers. They found that anatomical direction, marker location, and anatomical segment depend on soft tissue artifacts. These findings could help develop location- and direction-specific weighting factors for use in global optimization algorithms aimed at minimizing the effects of soft tissue artifacts on the calculation of lumbar joint kinematics.

Because human systems are complex, the use of linear and non-complex methods might not allow a comprehensive understanding of how pathological diseases, as well as aging and growth, affect the performance of the human musculoskeletal system and movement. In this Research Topic, finite element modeling has been used to quantify these interactions. Wang et al. evaluated the effectiveness of an innovative hourglass-shaped graft *versus* a traditional columnar graft for restoring joint stability and avoiding notch impingement following anterior cruciate ligament reconstruction. Using finite element modeling, the authors found that with a knee flexion angle of 30°, an hourglass-shaped graft was better able to restore joint stability compared to columnar grafts. Another finite element simulation was conducted by Wan et al. to investigate the cause of polyethylene liner dissociation after reverse shoulder arthroplasty. Their results demonstrate that humeral adduction impingement could lead to the deformation of the claw-shaped liner fixation structure, which might be one of the reasons for the linear dissociation, and the increased stiffness of the liner material helps to reduce the deformation of the fixation structure. Hsieh et al. proposed a non-articulating, additively manufactured hybrid total disc replacement (TDR) with an ultra-high molecular weight polyethylene core and polycarbonate urethane fiber jacket to mimic the motion of normal discs. A finite element study was conducted to optimize the lattice structure and assess the biomechanical performance of the proposed TDR. Their finding suggests the feasibility of implanting an additively manufactured multi-material artificial disc that allows for better physiological motion than the current ball-and-socket design. Wei et al. investigated the mechanical properties of tibial plateau fractures after internal fixation and bone using a finite element model. Their results indicate that the internal fixation system tolerates some of the body's typical actions and may sustain all or part of the weight early in the postoperative period.

This Research Topic also highlights novel applications of non-linear dynamic and complexity methods in assessing the musculoskeletal system and movement in various pathophysiological conditions. Xv et al. used the common chimpanzee to elucidate the evolution mechanisms of hominin bipedality by exploring the effect of skeletal architecture and muscle properties on bipedal standing. The authors proposed a musculoskeletal model with the mechanical relationships of the Hill-type muscle-tendon units. Their finding bridges the gap between skeletal architecture, along with muscle properties, and the biomechanical performance of the common chimpanzee during bipedal standing, which advances the understanding of bipedal evolution in humans. Luis et al. compared estimated muscle excitation and muscle fiber lengths among model selection, and performance criteria to solve muscle redundancy and approaches for scaling muscle-tendon properties at various walking speeds. They found that there were discrepancies in estimating fiber lengths and muscle excitations among the models and no single model combination estimated the most accurate muscle excitations for all muscles.

It is evident from the articles in this Research Topic that non-linear and complex properties and their interactions exist in the human movement and musculoskeletal system. The Research Topic of articles available within this Research Topic provides the foundation for further communication between clinical and non-linear dynamics and complexity researchers to advance our understanding of complex human musculoskeletal systems and related systems and movement for making better clinical decisions on assessments and treatments. Our Research Topic

provides novel insights into the effects of various pathophysiological mechanisms, aging, and growth as well as rehabilitative interventions on the musculoskeletal system and movement, and thereby opens up new avenues for improved diagnosis and treatment of conditions of the musculoskeletal system.

Author contributions

Y-KJ: Writing–original draft, Writing–review and editing. C-FL: Writing–review and editing. FL: Writing–review and editing. NS: Writing–review and editing.

Acknowledgments

The authors thank Dr. Markus Heller for his valuable suggestions on developing this Research Topic.

Conflict of interest

The authors declare that the research was conducted in the absence of any commercial or financial relationships that could be construed as a potential conflict of interest.

The author(s) declared that they were an editorial board member of Frontiers, at the time of submission. This had no impact on the peer review process and the final decision.

Publisher's note

References

Jan, Y. K., Lung, C. W., Cuaderes, E., Rong, D. Q., and Boyce, K. (2013). Effect of viscoelastic properties of plantar soft tissues on plantar pressures at the first metatarsal head in diabetics with peripheral neuropathy. *Physiol. Meas.* 34, 53–66. doi:10.1088/0967-3334/34/1/53

Liao, F. Y., and Jan, Y. K. (2017). Nonlinear dynamics of skin blood flow response to mechanical and thermal stresses in the plantar foot of diabetics with peripheral neuropathy. *Clin. Hemorheol. Microcirc.* 66, 197–210. doi:10.3233/ch-160239

Liau, B. Y., Wu, F. L., Lung, C. W., Zhang, X., Wang, X., and Jan, Y. K. (2019). Complexity-based measures of postural sway during walking at different speeds and durations using multiscale entropy. *Entropy* 21, 1128. doi:10.3390/e21111128

Orter, S., Ravi, D. K., Singh, N. B., Vogl, F., Taylor, W. R., and Konig Ignasiak, N. (2019). A method to concatenate multiple short time series for evaluating dynamic behaviour during walking. *PLoS One* 14, e0218594. doi:10.1371/journal.pone.0218594

Shiogai, Y., Stefanovska, A., and Mcclintock, P. V. (2010). Nonlinear dynamics of cardiovascular ageing. *Phys. Rep.* 488, 51–110. doi:10.1016/j.physrep.2009.12.003

Stergiou, N., and Decker, L. M. (2011). Human movement variability, nonlinear dynamics, and pathology: is there a connection? *Hum. Mov. Sci.* 30, 869–888. doi:10.1016/j.humov.2011.06.002

frontiers | Frontiers in Bioengineering and Biotechnology

TYPE Original Research
PUBLISHED 17 August 2022
DOI 10.3389/fbioe.2022.960063

OPEN ACCESS

EDITED BY
Cheng-Feng Lin,
National Cheng Kung University, Taiwan

REVIEWED BY
Alexander Breen,
Bournemouth University,
United Kingdom
Alex Kernkamp,
Leiden University Medical Center,
Netherlands

*CORRESPONDENCE
Tsung-Yuan Tsai,
tytsai@sjtu.edu.cn
Yan Yu,
yyu15@tongji.edu.cn

†These authors share first authorship

SPECIALTY SECTION
This article was submitted to Biomechanics,
a section of the journal
Frontiers in Bioengineering and Biotechnology

RECEIVED 02 June 2022
ACCEPTED 18 July 2022
PUBLISHED 17 August 2022

CITATION
Xi X, Ling Z, Wang C, Gu C, Zhan X, Yu H, Lu S, Tsai T-Y, Yu Y and Cheng L (2022), Lumbar segment-dependent soft tissue artifacts of skin markers during in vivo weight-bearing forward–Backward bending.
Front. Bioeng. Biotechnol. 10:960063.
doi: 10.3389/fbioe.2022.960063

Lumbar segment-dependent soft tissue artifacts of skin markers during *in vivo* weight-bearing forward–Backward bending

Xin Xi[1,2†], Zhi Ling[3†], Cong Wang[3], Chunya Gu[4], Xuqiang Zhan[1,2], Haixin Yu[5], Siqi Lu[1,2], Tsung-Yuan Tsai[3,6*], Yan Yu[1,2*] and Liming Cheng[1,2]

[1]Department of Spine Surgery, Tongji Hospital, School of Medicine, Tongji University, Shanghai, China, [2]Key Laboratory of Spine and Spinal Cord Injury Repair and Regeneration, Ministry of Education, Department of Spine Surgery, Tongji Hospital, School of Medicine, Tongji University, Shanghai, China, [3]School of Biomedical Engineering, Shanghai Jiao Tong University, Shanghai, China, [4]Department of Spinal Rehabilitation, Tongji Hospital, School of Medicine, Tongji University, Shanghai, China, [5]Department of Orthopedic Surgery, Yangpu Hospital, School of Medicine, Tongji University, Shanghai, China, [6]TAOiMAGE Medical Technologies Corporation, Shanghai, China

Traditional optical motion capture (OMC) with retroreflective markers is commonly used to measure joint kinematics but was also reported with unavoidable soft tissue artifacts (STAs) when quantifying the motion of the spine. Additionally, the patterns of the STA on the lumbar spine remain unclear. This study aimed to 1) quantify the *in vivo* STAs of the human lower back in three-dimensional directions during weight-bearing forward–backward bending and 2) determine the effects of the STAs on the calculated flexion angles between the upper and lower lumbar spines and adjacent vertebrae by comparing the skin marker (SM)- and virtual bone marker (VM)-based measurements. Six healthy volunteers were imaged using a biplanar radiographic system, and thirteen skin markers were mounted on every volunteer's lower back while performing weight-bearing forward–backward bending. The STAs in the anterior/posterior (AP), medial/lateral (ML), and proximal/distal (PD) directions were investigated. The flexion angles between the upper and lower lumbar segments and adjacent intervertebral segments (L2–L5) throughout the cycle were calculated. For all the participants, STAs continuously increased in the AP direction and exhibited a reciprocal trend in the PD direction. During flexion, the STA at the lower lumbar region (L4–L5: 13.5 $\pm$ 6.5 mm) was significantly higher than that at the upper lumbar (L1–L3: 4.0 $\pm$ 1.5 mm) in the PD direction ($p < 0.01$). During extension, the lower lumbar (L4–L5: 2.7 $\pm$ 0.7 mm) exhibited significantly less STAs than that exhibited by the upper lumbar region (L1–L3: 6.1 $\pm$ 3.3 mm) ($p < 0.05$). The STA at the spinous process was significantly lower than that on both sides in the AP direction ($p < 0.05$). The present results on STAs, based on dual fluoroscopic measurements in healthy adult subjects, presented an anatomical direction, marker location, and anatomic segment dependency, which might help describe and quantify STAs for the lumbar spine kinematics and thus help develop location- and direction-specific weighting factors for use in global optimization algorithms aimed at

minimizing the effects of STAs on the calculation of lumbar joint kinematics in the future.

KEYWORDS

lumbar spine, forward–backward bending, *in vivo* kinematics, soft tissue artifacts, dual fluoroscopy

1 Introduction

Low back pain (LBP) is one of the most common musculoskeletal disorders and a leading cause of disability, globally creating a substantial personal, community, and financial burden (Airaksinen et al., 2006; Delitto et al., 2012; Itz et al., 2013; Maher et al., 2017). Approximately 85%–95% of LBP cases have no identifiable cause or pathology and are, therefore, classified as non-specific LBP (NS-LBP). Hoy et al. (2012), Maher et al. (2017), and Wallbott (1989) characterized the way patients with NS-LBP perform daily activities and defined movement quality (MQ) as "the way in which human movement is executed with respect to the dimensions of time and space." Observation, analysis, and the influence of whole-body movements on the MQ are the key elements of LBP management (Laird et al., 2012; Hodges et al., 2013).

The common final manifestation of LBP is a change in spine kinematics (Liguori and ACSM, 2021). Accurately quantifying three-dimensional (3D) joint kinematics during *in vivo* lumbar motion is essential for a detailed understanding of joint function, investigating pathologies, and assessing the success of therapies (Aiyangar et al., 2014). 3D motion analysis, such as optical motion capture (OMC), using skin markers is the most common method for measuring spine joint kinematics *in vivo* (Wang et al., 2016; Huang et al., 2021). Unfortunately, when skin-marker trajectories are used in human motion analysis, the skin-mounted markers move over the underlying bone, generating the so-called soft tissue artifact (STA), which makes the estimation of the instantaneous skeletal pose difficult (Leardini et al., 2005). Motions of soft tissue covering the spine may cause large errors (Mo¨rl and Blickhan, 2006). STA represents one of the main limitations in obtaining accurate and reliable skeletal kinematics from motion capture (Cereatti et al., 2017).

Many previous studies have demonstrated that the extent of STAs, caused by a combination of skin stretching and sliding, muscle contraction, gravity, and inertia, is unique to each specific body segment (Akbarshahi et al., 2010), the physical characteristics of individuals (Holden et al., 1997), marker locations (Schwartz et al., 2004), and the nature of the performed movement task (Fuller et al., 1997). Several studies have validated the STAs of skin markers on different body regions (Wang et al., 2016; Camomilla and Bonci, 2020; Metcalf et al., 2020). However, validation studies for lumbar spine segments are rare (Zemp et al., 2014, Mo¨rl and Blickhan, 2006). Moreover, most studies investigated lumbar STAs in a seated upright position (Mo¨rl and Blickhan, 2006) or static sitting position (Zemp et al., 2014), and a few have been validated against global spinal shape.

It is also important to quantify the propagation of STAs to estimate lumbar joint kinematics. Various studies have used intrusive techniques to quantify STAs; for example, intra-cortical pins (Fuller et al., 1997; Benoit et al., 2006; Dal Maso et al., 2016), external fixators (Cappozzo et al., 1996), and percutaneous skeletal trackers (Manal et al., 2000) have been used to quantify joint motion *in vivo*. Unfortunately, these devices restrict the movement of the participant and alter the normal, unimpeded sliding of the soft tissues relative to the underlying bone. Moreover, these techniques are invasive; therefore, their use is limited. To overcome these problems, non-invasive methods, such as magnetic resonance imaging (MRI) (Sangeux et al., 2006; Zemp et al., 2014) and X-ray fluoroscopy (Garling et al., 2007), have been used to quantify joint motion *in vivo*. However, the methods proposed in these studies have several limitations: 1) they capture several terminal static poses in different directions rather than measuring a continuous dynamic motion; 2) they use a skin marker set and compare the measurements collected from 2D images to quantify STAs at the lower back; and 3) they investigate only a single motor task (Garling et al., 2007; Zemp et al., 2014). The dual fluoroscopy imaging system (DFIS) has been recognized as an accurate and validated *in vivo* evaluation technique for determining vertebra translations and orientations with the accuracy of 0.3 mm and 0.70° (Wang et al., 2008). Recent studies have demonstrated that the motion tracking technique based on dual fluoroscopic imaging is a reliable method for determining intervertebral motion and adjacent segment kinematics in various functional spine motions (Wawrose et al., 2020; Zhou et al., 2020). Therefore, in this study, we used a DFIS combined with a validated 3D-to-2D registration technique (Wang et al., 2020; Zhou et al., 2021) to quantify *in vivo* intervertebral and upper-lower lumbar segment kinematics in asymptomatic subjects during forward–backward bending.

The present study aimed to describe patterns and magnitudes of STAs *in vivo* in three different directions on the full region of the human lumbar spine during weight-bearing forward–backward bending. Vertebral movement through the cycle was measured using the DFIS. It also aimed to determine the effects of STAs on the calculated flexion angles between the upper and lower lumbar spine and adjacent intervertebral levels for L2–L5 by comparing the skin marker (SM)- and virtual bone marker (VM)-based measurements. We hypothesized that the *in*

vivo patterns of skin markers in the lumbar region would be direction- and segment-dependent patterns and that STAs would significantly affect the kinematic variables in human spinal motion investigation.

2 Materials and methods

2.1 Participant preparation

The present study was conducted with the approval of the institutional review board at Tongji Hospital, Shanghai, China (Protocol Number: 2021-011-SK), and followed the guidelines of the Helsinki Declaration (2013) (World Medical Association, 2013). The recruitment was conducted in the personal and workplace environment of the investigators. Ten asymptomatic adults without prior diagnosed spinal disorders were recruited. All the participants provided written informed consent before any personal or health-related data were collected. The inclusion criteria were as follows: age between 18 and 75 years, ability to perform the required functional tasks, and sufficient understanding of Chinese. Individuals were excluded in the case of any history of LBP in the past 6 months; injuries or operations on the spine, hip, knee, or ankle; and any comorbidities or circumstances (e.g., pregnancy) that could limit the forward–backward bending capabilities. Additionally, yoga practitioners, dancers, gymnasts, and those who had physical therapy within the last three months were ineligible owing to potential bias toward bending activities.

All the participants underwent a lumbar spine computed tomography (CT) scan (United Imaging, uCT760, voltage 120 kV, resolution 512 × 512, layer spacing 1.0 mm) in a supine, relaxed position. The CT images were imported into the 3D visualization and modeling software, Amira 6.7 (Thermo Fisher Scientific, Rockford, IL, United States), to reconstruct 3D bone models of the lumbar spine. All images were processed using Digital Imaging and Communications in Medicine (DICOM) and bitmap file formats. Four participants were excluded because of poor biplane image quality of the lumbar spine due to abdominal obesity and difficulties in later registration. Eventually, six pain-free female adults (age: 26.17 ± 3.55 years, body mass index (BMI): 19.76 ± 1.36 kg/m^2) were included in this study.

2.2 Experiment procedure

A trained physiotherapist (7 years of experience in motion analysis) equipped all the participants through manual palpation with the subject standing upright. Based on our lumbar marker set (Gombatto et al., 2017; Papi et al., 2019), 13 custom reflective spherical markers (diameter: 14 mm) with a lead core (diameter: 3 mm) were used. The central marker was always positioned on the L1, L3, and L5 spinous processes (Markers 1, 3, and 5), which were identified following the palpation guidelines (Field and Hutchinson, 2012). Six lateral markers were placed 5 cm on either side from the spinous process of the first (Markers L1 and R1), third (Markers L3 and R3), and fifth (Markers L5 and R5) lumbar vertebrae separately. Four markers were attached 2.5 cm to each side of the spinous process of the second (Markers L2 and R2) and fourth (Markers L4 and R4) lumbar vertebrae (Papi et al., 2019). The primary goal of this marker set (Table1) was to constrain the lumbar segment (L1–L5) so that the flexion angles between the upper and lower lumbar spine and adjacent vertebrae could be obtained *via* kinematic calculation (Figure 1).

TABLE 1 Marker placement and abbreviations.

Abbreviations	Marker placement description
L5	5.0 cm left lateral back on the fifth lumbar vertebrae
5	Spinous processes of the fifth lumbar process
R5	5.0 cm right lateral back on the fifth lumbar vertebrae
L4	2.5 cm left lateral back on the fourth lumbar vertebrae
R4	2.5 cm right lateral back on the fourth lumbar vertebrae
L3	5.0 cm left lateral back on the third lumbar vertebrae
3	Spinous processes of the third lumbar process
R3	5.0 cm right lateral back on the third lumbar vertebrae
L2	2.5 cm left lateral back on the second lumbar vertebrae
R2	2.5 cm right lateral back on the second lumbar vertebrae
L1	5.0 cm left lateral back on the first lumbar vertebrae
1	Spinous processes of the first lumbar process
R1	5.0 cm right lateral back on the first lumbar vertebrae

Quasi-static dual-digital radiography (DR) images (TAOiMAGE, Shanghai, China; image resolution 2804 × 2804 pixels) were initially captured during a static standing trial with the subject's feet shoulder-width apart for two seconds. Next, each participant performed weight-bearing forward–backward bending from maximum extension to approximately 45° of flexion (measured using a protractor) to keep the participants within view of the system (Figure 2). In order to reduce the overlapping of skin markers and various internal bony structures in dual fluoroscopic lumbar spine images and enhance the efficiency and accuracy of registration and recognition, the participants stood in an oblique position of 45°. Before the formal collection, we pasted marked lines at different heights of the participants' lower limbs, instructed the participants to place their palms in front of their lower limbs, and moved down to the designated marking line in an orderly manner. While reaching the designated marked position, they were asked to cross their hands behind their heads and keep still. Participants were

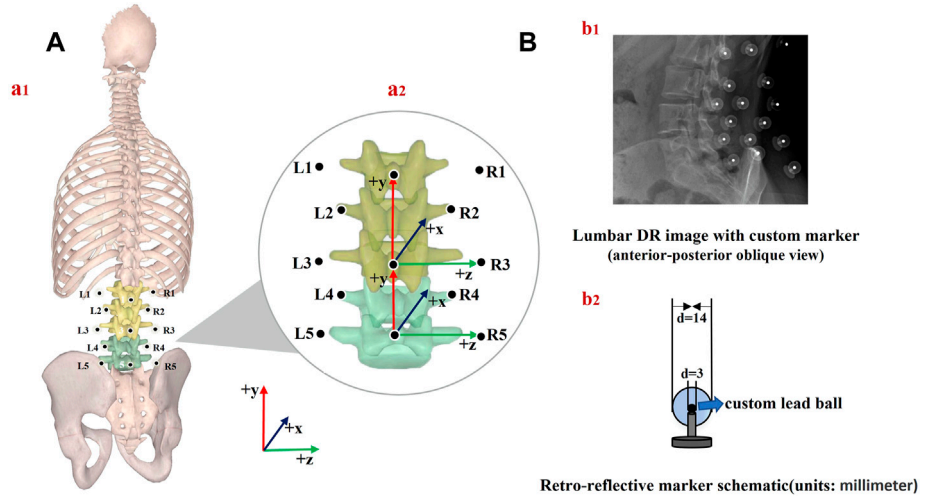

FIGURE 1
(A) Schematic of marker placement and spine anatomical frames of reference (a1); joint coordinate system axes of rotation for the upper and lower lumbar segment considered (a2), **(B)** lumbar DR image (b1) and retroreflective marker schematic (b2).

trained to keep both knees straight throughout the process. After the preparation above, anteroposterior and lateral biplanar images of the lumbar vertebrae were recorded synchronously at different bending angles. Participants practiced the activities before the actual testing to get familiar with the tasks. The testing was repeated if the participants violated the task instructions, resulting in non-valid trials. During the experiment, all the participants were required to wear lead protective clothing in non-collection areas to reduce unnecessary radiation. During testing, the participant was exposed to approximately seven pairs of fluoroscopic projections. The entire image collection process took around 10 min to complete. According to the product manual provided by the manufacturer, the effective dose under our typical testing conditions (78 Kv, 40 mA) is 0.16 mSv for each paired image of the lumbar or less than 1.20 mSv per test, approximately 6% of the average dose limit for occupational exposure in a year.

2.3 *In vivo* kinematics measurements

Two multi-segmental kinematic models of the lumbar spine were used to derive lumbar spine kinematics based on virtual bone and skin markers. At each vertebral level and lumbar segment, anatomical coordinate systems were defined based on the recommendations of the International Society of Biomechanics (Wu et al., 2002).

1) At each vertebral level, the origin was in the middle of the upper and lower endplates. The *y*-axis (proximal/distal, PD) was defined as the line passing through the centers of the upper and lower vertebral endplates. The *z*-axis (medial/lateral, ML) was defined as the line parallel to a line joining similar landmarks on the bases of the right and left pedicles, pointing to the right. The *x*-axis (anterior/posterior, AP) was perpendicular to the *y*- and *z*-axes and pointed anteriorly.
2) The upper lumbar segment was defined by its origin at L3, a vertical axis from the spinous process of L3 to L1 (PD, +y), an AP axis (+x) orthogonal to the plane formed by the PD axis, the line connecting the left and right transverse processes of L3, and a horizontal axis (ML, +z) cross-product of AP and PD axes. The lower lumbar segment was defined by its origin at L5, a vertical axis from L5 to L3 (PD, +y), an AP axis orthogonal to the plane formed by the PD axis, the line connecting the left and right transverse processes of L5, and a horizontal axis cross-product of the AP and PD axes (Gombatto et al., 2017) [Figure 1A (a2)].

2.4 Data processing and analysis

The STA-free trajectories of the markers (i.e., "virtual bone markers") were derived from the kinematics of the bones. 2D DR images and 3D models were imported into a registration program (MATLAB, R2018a MathWorks, Natick, MA, United States). The 3D positions of each lumbar vertebra and marker were adjusted until they matched the corresponding outlines on the DR images. The 3D positions of the skin markers relative to the underlying vertebra in each frame were defined. This technique was validated by the roentgen stereophotogrammetric analysis technique as the gold

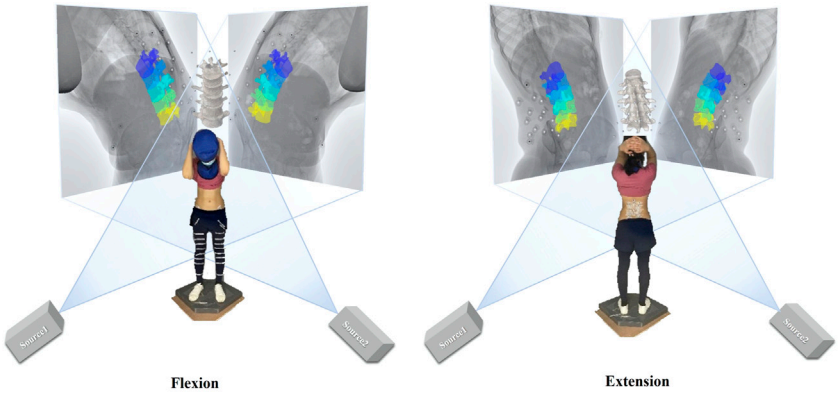

FIGURE 2
Experimental setup of the dual fluoroscopic system for capturing lumbar spine and marker positions *in vivo*; virtual reproduction of the dual fluoroscopic system and vertebral positions.

standard for achieving submillimeter accuracy in our preliminary study (Li et al., 2009). Bone landmark positions from CT measurements were transformed into the biplanar DR coordinate system and combined with a skin marker to determine the flexion angles of the upper lumbar relative to the lower lumbar segment. In order to evaluate the higher derivatives of the motion parameter based on the two systems, flexion angles between the adjacent lumbar vertebra (L2–L3, L3–L4, and L4–L5) were also examined. Lumbar joint angles were calculated using the relevant segment poses following a z-x-y cardanic rotation sequence (Robertson et al., 2004; Lees et al., 2010), which corresponded to flexion+/extension−, right bend+/left bend−, and right twist+/left twist−. The effects of STAs on lumbar kinematics were quantified throughout the motion using the differences between the SM-determined and VM-determined kinematics.

Each local coordinate system was located at the center of gravity of the respective vertebral bodies. The global coordinates of the markers were converted into the corresponding local vertebral coordinate system. STA was calculated by subtracting the displacement of the skin marker under the coordinate system of each vertebra from the corresponding marker in the static standing position. The overall flexion angle of the lumbar spine was described as the angle between the fitting line through the center of all vertebrae in each frame and the static standing position. The STA at each tested flexion angle of each subject was normalized to one bending cycle, from full extension (0% of normalized cycle) to maximal flexion (100% of normalized cycle), through data interpolation. The flexion angle ranged from −15° to 45° with an interval of 7.5°. The mean values and range of the STAs in the AP, ML, and PD directions among all the participants were investigated. The mean STAs at the lower lumbar (Markers R5, 5, L5, R4, and L4) and upper lumbar regions (Markers L3, 3, R3, L2, R2, L1, 1, and R1) among all the participants during extension and flexion were calculated. Meanwhile, the STAs at the spinous processes (Markers 1, 3, and 5) and both sides (Markers L1, R1, L2, R2, L3, R3, L4, R4, L5, and R5) were calculated.

2.5 Statistical analysis

Continuous variables are presented as means and standard errors. Normal distribution was verified using the Shapiro Wilk test and Q-Q-plot inspection for discrete parameters. A paired *t*-test with a significance level of 0.05 was used to compare 1) the STAs at the lower and upper lumbar regions, 2) the STAs at the spinous processes and both sides, and 3) the SM- and VM-determined flexion angles among all the participants at each tested frame. The correlation between the flexion angles based on the two measurements throughout the entire cycle was estimated using the Spearman correlation coefficient.

3 Results

3.1 Lumbar soft tissue artifact patterns and magnitudes in three directions during forward–backward bending

3.1.1 Anterior–posterior direction

The quantitative plots of STAs during the bending cycle demonstrated that the amount of movement of skin markers relative to the underlying bi-planar DR-measured bone STAs at each lumbar level showed a similar increasing trend from full extension to flexion in the AP direction (Figure 3). All the markers were anteriorly shifted during the entire cycle. The smallest STA through the bending cycle occurred at marker

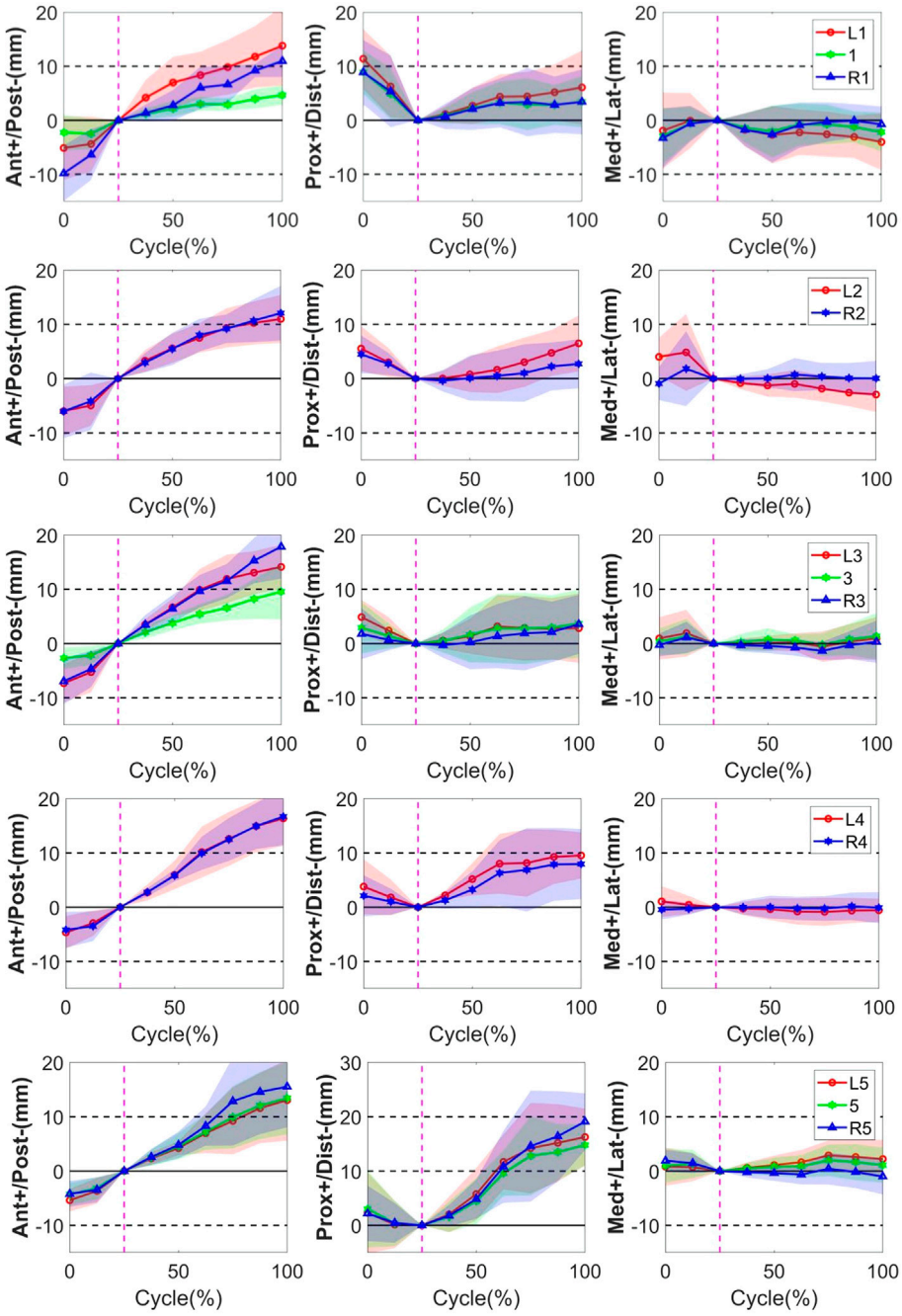

FIGURE 3
STA of the thirteen skin markers from L1 to L5 level during the bending cycle (0%, 25%, and 100% represent extension, neutral, and flexion, respectively). The solid line represents the mean STA for all the subjects, and the shaded-area error bands represent the standard deviation of the STA. The vertical dotted line represents the neutral position.

spinous processes of L1, ranging from −2.3 ± 3.3 mm at full extension to 4.7 ± 1.9 mm at maximal flexion. The largest STAs occurred at the marker right side of the spinous process of L3, ranging from −6.9 ± 4.2 mm to 17.8 ± 5.9 mm (Table 2).

3.1.2 Proximal–distal direction

In the PD direction, the STA exhibited an approximately reciprocal pattern during the lumbar extension and flexion (Figure 3). The STA underwent a sharp increase during

flexion at the L5 level (Markers L5, 5, and R5 shifted 16.3 ± 5.2 mm, 14.8 ± 3.8 mm, and 19.1 ± 5.2 mm proximal from the static position to maximal flexion, respectively), followed by the L4 level (Markers L4 and R4 shifted 9.5 ± 4.3 mm and 8.0 ± 6.5 mm proximal from the static position to maximal flexion, respectively), and slightly increased at the L1-L3 level (maximal STA < 6.5 mm). At the extension phase, the STA in the PD direction slightly decreased at the L3–L5 level (maximal STA < 4.9 mm), and the greatest decrease occurred at the L1 level (Markers L1, 1, and R1 shifted 11.4 ± 5.6 mm, 8.9 ± 4.0 mm, and 8.9 ± 6.0 mm distal from full extension to the static position, respectively), followed by L2 (Markers L2 and R2 shifted 5.5 ± 4.1 mm and 4.5 ± 3.5 mm distal from full extension to the static position, respectively) (Table 2). The positions of the markers did not move either to the right or left during the bending motion.

3.1.3 Medial–lateral direction

Throughout the bending cycle, the changing trend of the STA in the ML direction was stable relative to the AP and PD. In the extension phase, the largest STA occurred at Marker R1 (−3.3 ± 5.5 mm), and the smallest STA occurred at Marker R3 (−0.3 ± 2.1 mm). During flexion, the smallest STA occurred at Marker R4 (0.1 ± 2.9 mm), and the largest STA occurred at Marker L1 (−4.0 ± 5.3 mm) (Table 2).

In conclusion, as the gross spinal angle increased, the STA became prominent in the AP and PD directions. Specifically, the skin markers moved from posterior to anterior with respect to the underlying vertebra through the bending cycle in AP, whereas, in the PD direction, it shifted from proximal to distal during extension and from distal to proximal during flexion (Figure 3).

3.2 Quantification and characteristics of lumbar soft tissue artifact in upper and lower lumbar regions during forward–backward bending

The results showed that the range of STAs during flexion was 13.0 ± 3.4, 7.7 ± 5.6, and −0.8 ± 1.8 mm in the AP, PD, and ML directions, respectively, and −5.2 ± 2.0, 4.8 ± 3.1, and −0.7 ± 2.0 mm in the AP, PD, ML directions, respectively, during extension. During flexion, the STA at the lower lumbar (L4, L5: 13.5 ± 6.5 mm) was significantly higher than that at the upper lumbar regions (L1–L3: 4.0 ± 1.5 mm) in the PD direction ($p < 0.01$). During extension, the STA at the lower lumbar (L4–L5: 2.7 ± 0.7 mm) was significantly less than that at the upper lumbar region (L1–L3: 6.1 ± 3.3 mm) in the PD direction ($p < 0.05$). The STA at the spinous process was significantly lower than that on both sides in the AP direction during extension and flexion ($p = 0.02$) (Table 3).

3.3 Effects of soft tissue artifact on the calculation of flexion angles between the upper and lower lumbar spine and adjacent intervertebral levels

Significant effects of STAs on the calculated vertebral flexion angles were observed. VM measurement demonstrated a consistent increase in intervertebral flexion with overall body flexion, with an intervertebral range of motion (ROM) of 2.70 ± 4.23°, 2.30 ± 2.74°, and 3.06 ± 3.95° during extension and 8.62 ±

TABLE 2 Direction-related (AP, PD, and ML) mean marker artifact (mean) with their standard deviations (SDs) of all the lumbar skin markers in the flexed and extended positions.

Marker	AP (mm)		PD (mm)		ML (mm)	
	Ext. (mean ± SD)	Flex. (mean ± SD)	Ext. (mean ± SD)	Flex. (mean ± SD)	Ext. (mean ± SD)	Flex. (mean ± SD)
L5	−5.4 ± 2.1	13.0 ± 7.5	2.3 ± 7.5	16.3 ± 5.2	0.8 ± 3.5	2.2 ± 3.5
5	−4.3 ± 2.0	13.4 ± 6.7	3.0 ± 7.1	14.8 ± 3.8	1.0 ± 3.1	1.1 ± 3.2
R5	−4.2 ± 2.4	15.5 ± 7.5	2.2 ± 5.1	19.1 ± 5.2	1.9 ± 2.0	−1.0 ± 3.3
L4	−4.7 ± 3.0	16.4 ± 5.1	3.8 ± 5.1	9.5 ± 4.3	1.1 ± 2.9	−0.6 ± 2.1
R4	−4.2 ± 3.3	16.7 ± 5.2	2.1 ± 3.8	8.0 ± 6.5	−0.4 ± 1.8	−0.1 ± 2.9
L3	−7.3 ± 3.5	14.1 ± 4.1	4.9 ± 3.2	2.8 ± 6.4	0.9 ± 3.9	0.9 ± 3.9
3	−2.7 ± 2.0	9.6 ± 5.1	2.9 ± 4.7	3.7 ± 6.3	0.4 ± 2.4	1.3 ± 4.3
R3	−6.9 ± 4.2	17.8 ± 5.9	1.8 ± 4.7	3.6 ± 5.4	−0.3 ± 2.1	0.3 ± 3.9
L2	−6.0 ± 4.5	11.0 ± 4.4	5.5 ± 4.1	6.5 ± 5.2	4.0 ± 3.6	−2.9 ± 3.2
R2	−6.0 ± 4.9	12.1 ± 5.0	4.5 ± 3.5	2.7 ± 4.5	−0.9 ± 3.0	0.6 ± 3.2
L1	−5.1 ± 5.9	13.8 ± 7.3	11.4 ± 5.6	6.1 ± 6.9	−1.9 ± 7.1	−4.0 ± 5.3
1	−2.3 ± 3.3	4.7 ± 1.9	8.9 ± 4.0	3.4 ± 4.7	−2.9 ± 5.2	−2.2 ± 3.6
R1	−9.8 ± 5.2	11.0 ± 2.9	8.9 ± 6.0	3.4 ± 6.0	−3.3 ± 5.5	−0.8 ± 3.4

AP, anterior/posterior; ML, medial/lateral; PD, proximal/distal; Flex., flexion; Ext., extension.

TABLE 3 Segment-related (upper lumbar, lower lumbar) mean marker artifact (mean) with their standard deviations (SD) of the lumbar skin markers in the flexed and extended positions and the 95% confidence interval (95% CI) of difference.

Segment	Flex. (mm)			Ext. (mm)		
	AP (mean ± SD)	PD (mean ± SD)	ML (mean ± SD)	AP (mean ± SD)	PD (mean ± SD)	ML (mean ± SD)
Upper lumbar	11.8 ± 3.8	4.0 ± 1.5	−0.9 ± 2.0	−5.8 ± 2.5	6.1 ± 3.3	−0.5 ± 2.4
Low lumbar	15.0 ± 1.7	13.5 ± 6.5*	0.3 ± 1.3	−4.6 ± 0.5	2.7 ± 0.7*	0.9 ± 0.8
p-value	0.105	0.009*	0.268	0.309	0.023*	0.239
95%CI of difference	(−7.3,0.8)	(−15.2,3.8)	(−3.4,1.0)	(−3.7,1.3)	(0.6,6.2)	(−3.8,1.1)

AP, anterior/posterior; ML, medial/lateral; PD, proximal/distal; Flex., flexion; Ext., extension.
*Significant differences with upper lumbar ($p < 0.05$).

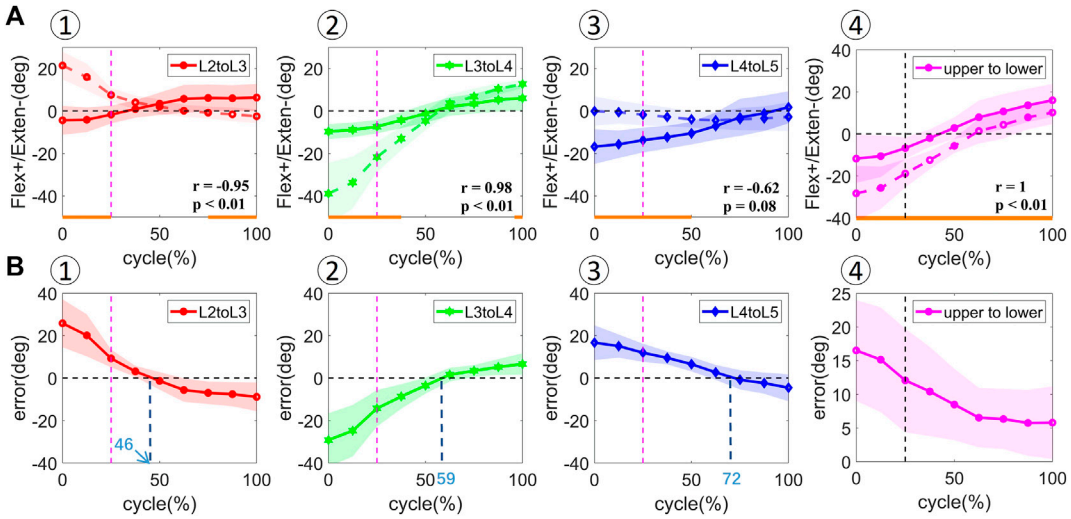

FIGURE 4
[**(A)** ①–④] *In vivo* kinematics measured by two measurements at adjacent vertebral levels (L2–L3, L3–L4, L4–L5) and upper and lower lumbar levels (upper to lower). The solid line represents the mean values for all the subjects measured by DR. The dotted line represents the mean values for all the subjects measured by skin markers. Statistical significance between the two measurements is marked by the solid orange line along the *x*-axis of top-row graphs. [**(B)** ①–④] Rotational error at adjacent vertebral levels (L2–L3, L3–L4, L4–L5) and upper and lower lumbar levels (upper to lower). The shaded area represents the standard deviation of the values.

5.78°, 13.57 ± 3.36°, and 15.39 ± 2.61° during flexion for L2–L3, L3–L4, and L4–L5 levels, respectively. The overall patterns of joint angles measured by SM over the bending cycle were opposite to VM for the L2–L3 ($r = -0.95$, $p < 0.01$) and L4–L5 levels ($r = -0.62$, $p = 0.08$), but similar for the L3–L4 level ($r = 0.98$, $p < 0.01$) (Figure 4). However, the amplitude of variation of the flexion angle at the L3–L4 level was overestimated by SM measurements, with L3 more extended during the 0%–50% cycle and more flexed during the 50%–100% cycle. Significant differences in the joint angles among all the participants occurred during the 0%–25%, 75%–100%; 0%–37.5%, 100%, and 0%–50% cycles for L2–L3, L3–L4, and L4–L5 levels, respectively ($p < 0.05$). The zero kinematic errors of L2/L3, L3/L4, and L4/L5 under the two measurement methods are at 46%, 59%, and 72%, respectively (Figure 4), indicating that the skin movement characteristics of the upper and lower lumbar segments were different. These discrepancies can be explained by the skin deformation mechanism caused by complex lumbar muscle deformation. Second, it is speculated that the kinematic error of zero for the two measurements at 50% of the bending cycle occurs near the L3 level, which may be related to its anatomical and biomechanical characteristics because L3 is the apex of lumbar lordosis and the center of lumbar motion.

The flexion angles between the upper and lower lumbar levels from full extension to maximal flexion demonstrated a similar increasing trend in SM and VM measurements (Figure 4). The VM- and SM-derived flexion angles were 4.99 ± 6.57° and 9.44 ± 11.84° during extension and 23.53 ± 4.66° and 29.00 ± 7.87° during flexion, respectively. A significant difference in the flexion angle was observed among all the participants during the entire cycle ($p < 0.05$). A linear relationship was found between the flexion angles during the bending cycle and both measurements ($r = 1$, $p < 0.01$). The error in the measured flexion angle decreased from the extension to the flexion phase.

4 Discussion

The most important finding of the present study is that the extent of STAs in the lumbar spine differed by anatomical direction, marker location, lumbar segment, and bending phases when the participants performed forward–backward bending under the weight-bearing condition. Specifically, the STA was prominent in the AP and PD directions. As the flexion angle increased, the STA continuously increased in the AP direction and exhibited a reciprocal trend in the PD direction during extension and flexion. The STA in the lower lumbar region was significantly smaller than that in the upper lumbar region during extension and larger during flexion in the PD direction. The STA at the spinous process was significantly smaller than that on either side. These findings were consistent with those of the previous studies that described the factors that influence the STA extent (Fuller et al., 1997; Holden et al., 1997; Schwartz et al., 2004). These specific patterns and magnitudes of STAs in the lumbar spine might help clinicians and physical therapists assess kinematic errors and devise methods to minimize its effects on the calculation of lumbar joint kinematics.

STA is particularly evident in the analysis of the lumbar spine because the markers are close to each other, and small relative movements among them may lead to large errors in the assessment of vertebral position and orientation (Ciavarro et al., 2006). Previous studies showed that some general features might be identified. For instance, for tasks performed by non-obese volunteers and motor tasks that do not involve high accelerations or impacts, the largest proportion of the STA-affecting markers located on a given body segment is closely correlated to the relevant joint movement (Cappozzo et al., 1996; Bonci et al., 2014; Camomilla et al., 2015). Evidence showed that forward bending (Corkery et al., 2014; van Wingerden et al., 2008), lifting (Hemming et al., 2018; Pranata et al., 2018), and walking (Henchoz et al., 2015; Lamoth et al., 2006) are key activities in assessing subjects with NS-LBP, also corresponding to the most frequently reported treatment goals of patients with LBP on the Patient-Specific Functional Scale (Stratford, 1995). In this study, we chose forward–backward bending, which is relatively simple in execution and acquisition, as the daily activity for evaluating MQ in healthy participants. To ensure the accuracy and validity of the registration and final quantification data, we finally selected six participants with a relatively low BMI and good image quality.

To the best of our knowledge, only a few studies have reported STA results in the spinous process (Mo¨rl and Blickhan, 2006; Zemp et al., 2014). They showed that the largest STA was 27.4 mm for marker spinous process L5 in the flexed position, and the largest absolute value of STA was 18.3 mm for marker spinous process L3 in the extended position (Zemp et al., 2014). It is higher than our results for the corresponding marker location and task position (L3: 7.6 mm, L5: 20.1 mm). This may be because our experiment was performed under the weight-bearing condition, which is different from those in previous studies using magnetic resonance imaging MRI or CT machines, which limit the positions of the subject to only passive posture (Mo¨rl and Blickhan, 2006; Zemp et al., 2014). In fact, increasing the load significantly affects the movement of the lumbar joints (Wen et al., 2022), and flexion of the spine under active conditions is the most common mechanical cause of lumbar injuries (Shahbazi Moheb Seraj et al., 2018). During extension, the STA in the lower lumbar region was significantly smaller than that in the upper lumbar region in the PD direction, whereas, in the flexion phase, the STA gradually increased from proximal to distal. The maximum STA reached approximately 20 mm at the L5 level, followed by approximately 10 mm at the L4 level, and fell below 10 mm from L1–L3. A high degree of lumbar STA variability was observed during lumbar extension and flexion. The characteristics of STAs at each specific lumbar level may help quantitatively describe the lumbar segment-related kinematic errors caused by STAs, thus providing a better understanding of the normal and pathological biomechanics of the lumbar spine during functional activities.

Various marker placement methods have already been used to track the movement of the human lumbar spine, which is mainly separated into upper and lower segments, to study the kinematic characteristics of LBP (Gombatto et al., 2015; Hemming et al., 2018; Papi et al., 2019). Our study is the first to investigate the *in vivo* 3D STA of markers on either side of the spinous process. The overall direction of the marker shift was similar to that reported in a previous study (Zemp et al., 2014). We demonstrated that the 3D STA at the spinous process was significantly smaller than that on either side, which means that markers at anatomical landmarks would be least affected by lumbar motion. This is consistent with not only the STA's markers' location-related characteristics but also the theoretical conjecture. Because the marker at the spinous process is the closest to the osseous structure of the internal spinous process, there are relatively few soft tissues, such as muscle and fat, between the two, which ultimately results in the

least amount of surface-skin deformation caused by internal-muscle deformation.

The present study demonstrated a linear correlation between the flexion angle measured using skin markers and dual DR focused on the upper and lower lumbar segments. This result supports previous findings that the marker set is reliable in assessing lumbar kinematics regardless of the STAs (Seerden et al., 2016). On the contrary, intervertebral rotations measured by the skin markers in our study were far from the intrinsic values measured by fluoroscopy for the L2–L3 and L4–L5 levels. Although a high correlation between the flexion angles at the L3–L4 level ($r = 0.98$, $p < 0.01$) derived by the two methods was found, the irregular STA of markers on different lumbar levels in the AP direction together led to a significant overestimation of the flexion angles. The consistency of marker positions and vertebral motion at the L3–L4 level was aligned with some previous studies (Mo¨rl and Blickhan, 2006; Hashemirad et al., 2013); however, the errors should be considered when performing marker-based motion tracking on the lumbar spine. Moreover, given that the overall distribution of the STAs in the lumbar area is lacking, the effectiveness of our markers in estimating the joint angles needs further verification.

This study had several limitations. First, only young women with relatively low BMI were included in the experiment. This experiment was designed to maintain high image quality for accurate *in vivo* vertebral-motion tracking with thinner fat on the back of the participants. However, large individual differences still exist because of the heterogeneity of each person. While the STA and its effects on spinal kinematics may be affected by the subject's BMI, age, and sex (Tsai et al., 2011), participants of a larger age and male sex could be involved in the future. Second, to improve the accuracy of STAs and reduce unnecessary radiation, we focused on the flexion-extension direction for acquisition and analysis; therefore, the distribution characteristics and quantitative results of lumbar spine STAs in other degrees of freedom were lacking. However, learning the displacement of the marker set in the full region of the lumbar forward–backward bending could provide a useful reference for estimating 6DOF lumbar motions using SMs. Third, the quasi-static images captured in the current study presented the STA during different bending phases but still could not represent the instantaneous dynamic positions of the marker relative to the vertebra. However, "quasi-static" indicates a dynamic effect, and quasi-static load indicates that the load is applied slowly such that the structure deforms significantly slowly (at a considerably low strain rate); therefore, the inertial force is significantly small and can be ignored. Last but not least, the experimental collection was carried out asynchronously under the motion capture and DFIS, and the errors in OMC measurement differ from the SM measured radiographically, which might limit the utility of this study in future research. However, the quantitative results and patterns of STAs on the lumbar spine might help develop factors for use in global optimization algorithms aimed at minimizing the effects of STAs on the building of specific lumbar kinematic models and calculation of lumbar joint kinematics in the future.

In summary, the extent of STAs in the lumbar spine differed with respect to anatomical direction, marker location, lumbar segment, and flexion phases when the participants performed forward–backward bending under the weight-bearing condition. The STA was prominent in the AP and PD directions during the forward–backward bending motion. As the flexion angle increased, the STA continuously increased in the AP direction and exhibited a reciprocal trend in the PD direction during extension and flexion. The STA in the lower lumbar region was significantly smaller than that in the upper lumbar region during extension and larger during flexion in the PD direction. Skin markers at the spinous process were least affected by the motion of the lumbar spine. The STA characteristics at different lumbar vertebral levels may help clinicians and physical therapists assess kinematic errors and devise methods to minimize its effects on the calculation of lumbar joint kinematics. Credible and valid lumbar spine kinematic results are important for future studies aiming to provide personalized clinical management for LBP.

Data availability statement

The raw data supporting the conclusions of this article will be made available by the authors without undue reservation.

Ethics statement

The studies involving human participants were reviewed and approved by the institutional review board at Tongji Hospital, Shanghai, China. The patients/participants provided their written informed consent to participate in this study.

Author contributions

XX designed the research methods, performed the experiments, analyzed the data, and drafted the manuscript. ZL contributed to acquisition, interpretation of data, and critical review of the manuscript. CW contributed to critical review of the manuscript. CG performed the experiments. XZ, HY, and SL participated in the experiments. T-YT and YY designed the research, interpreted data, and revised the manuscript. LC revised the manuscript. All authors meet the International Committee of Medical Journal Editors (ICMJE) criteria for authorship for this article and are

responsible for the integrity of the work as a whole. All authors have read and approved the final submitted manuscript.

Funding

This study was funded by the Clinical Research Plan of SHDC (SHDC2020CR 2035B). The funder had no involvement in the study design, data analysis, and interpretation of the results.

Conflict of interest

Author T-YT was employed by TaoImage Medical Technologies Corporation.

The remaining authors declare that the research was conducted in the absence of any commercial or financial relationships that could be construed as a potential conflict of interest.

Publisher's note

All claims expressed in this article are solely those of the authors and do not necessarily represent those of their affiliated organizations or those of the publisher, the editors, and the reviewers. Any product that may be evaluated in this article, or claim that may be made by its manufacturer, is not guaranteed or endorsed by the publisher.

References

Airaksinen, O., Brox, J. I., Cedraschi, C., Hildebrandt, J., Klaber-Moffett, J., Kovacs, F., et al. (2006). Chapter 4. European guidelines for the management of chronic nonspecific low back pain. *Eur. Spine J.* 15 (2), S192–S300. doi:10.1007/s00586-006-1072-1

Aiyangar, A. K., Zheng, L., Tashman, S., Anderst, W. J., and Zhang, X. (2014). Capturing three-dimensional *in vivo* lumbar intervertebral joint kinematics using dynamic stereo-X-ray imaging. *J. Biomech. Eng.* 136, 011004. doi:10.1115/1.4025793

Akbarshahi, M., Schache, A. G., Fernandez, J. W., Baker, R., Banks, S., and Pandy, M. G. (2010). Non-invasive assessment of soft-tissue artifact and its effect on knee joint kinematics during functional activity. *J. Biomech.* 43, 1292–1301. doi:10.1016/j.jbiomech.2010.01.002

Benoit, D. L., Ramsey, D. K., Lamontagne, M., Xu, L., Wretenberg, P., and Renström, P. (2006). Effect of skin movement artifact on knee kinematics during gait and cutting motions measured *in vivo*. *Gait Posture* 24, 152–164. doi:10.1016/j.gaitpost.2005.04.012

Bonci, T., Camomilla, V., Dumas, R., Chèze, L., and Cappozzo, A. (2014). A soft tissue artefact model driven by proximal and distal joint kinematics. *J. Biomech.* 47, 2354–2361. doi:10.1016/j.jbiomech.2014.04.029

Camomilla, V., and Bonci, T. (2020). A joint kinematics driven model of the pelvic soft tissue artefact. *J. Biomech.* 111, 109998. doi:10.1016/j.jbiomech.2020.109998

Camomilla, V., Bonci, T., Dumas, R., Chèze, L., and Cappozzo, A. (2015). A model of the soft tissue artefact rigid component. *J. Biomech.* 48, 1752–1759. doi:10.1016/j.jbiomech.2015.05.007

Cappozzo, A., Catani, F., Leardini, A., Benedetti, M. G., and Croce, U. D. (1996). Position and orientation in space of bones during movement: Experimental artefacts. *Clin. Biomech. (Bristol, Avon)* 11, 90–100. doi:10.1016/0268-0033(95)00046-1

Cereatti, A., Bonci, T., Akbarshahi, M., Aminian, K., Barré, A., Begon, M., et al. (2017). Standardization proposal of soft tissue artefact description for data sharing in human motion measurements. *J. Biomech.* 62, 5–13. doi:10.1016/j.jbiomech.2017.02.004

Ciavarro, G. L., Santambrogio, G. C., and Andreoni, G. (2006). Assessment of soft tissue artifacts for flexion/extension movements of the lumbar spine. *J. Biomech.* 39, S172–S173. doi:10.1016/s0021-9290(06)83605-5

Corkery, M. B., O'Rourke, B., Viola, S., Yen, S.-C., Rigby, J., Singer, K., et al. (2014). An exploratory examination of the association between altered lumbar motor control, joint mobility and low back pain in athletes. *Asian J. Sports Med.* 5, e24283. doi:10.5812/asjsm.24283

Dal Maso, F., Blache, Y., Raison, M., Lundberg, A., and Begon, M. (2016). Glenohumeral joint kinematics measured by intracortical pins, reflective markers, and computed tomography: A novel technique to assess acromiohumeral distance. *J. Electromyogr. Kinesiol.* 29, 4–11. doi:10.1016/j.jelekin.2015.07.008

Delitto, A., George, S. Z., Van Dillen, L., Whitman, J. M., Sowa, G., Shekelle, P., et al. (2012). Low back pain. *J. Orthop. Sports Phys. Ther.* 42, A1–A57. doi:10.2519/jospt.2012.42.4.A1

Field, D., and Hutchinson, J. O. (2012). *Field's anatomy, palpation & surface markings*. 5th ed. London, England: Churchill Livingstone.

Fuller, J., Liu, L.-J., Murphy, M. C., and Mann, R. W. (1997). A comparison of lower-extremity skeletal kinematics measured using skin- and pin-mounted markers. *Hum. Mov. Sci.* 16, 219–242. doi:10.1016/s0167-9457(96)00053-x

Garling, E. H., Kaptein, B. L., Mertens, B., Barendregt, W., Veeger, H. E. J., Nelissen, R. G. H. H., et al. (2007). Soft-tissue artefact assessment during step-up using fluoroscopy and skin-mounted markers. *J. Biomech.* 40 (1), S18–S24. doi:10.1016/j.jbiomech.2007.03.003

Gombatto, S. P., Brock, T., DeLork, A., Jones, G., Madden, E., and Rinere, C. (2015). Lumbar spine kinematics during walking in people with and people without low back pain. *Gait Posture* 42, 539–544. doi:10.1016/j.gaitpost.2015.08.010

Gombatto, S. P., D'Arpa, N., Landerholm, S., Mateo, C., O'Connor, R., Tokunaga, J., et al. (2017). Differences in kinematics of the lumbar spine and lower extremities between people with and without low back pain during the down phase of a pick-up task, an observational study. *Musculoskelet. Sci. Pract.* 28, 25–31. doi:10.1016/j.msksp.2016.12.017

Hashemirad, F., Hatef, B., Jaberzadeh, S., and Ale Agha, N. (2013). Validity and reliability of skin markers for measurement of intersegmental mobility at L2-3 and L3-4 during lateral bending in healthy individuals: A fluoroscopy study. *J. Bodyw. Mov. Ther.* 17, 46–52. doi:10.1016/j.jbmt.2012.04.010

Hemming, R., Sheeran, L., van Deursen, R., and Sparkes, V. (2018). Non-specific chronic low back pain: Differences in spinal kinematics in subgroups during functional tasks. *Eur. spine J.* 27 (1), 163–170. doi:10.1007/s00586-017-5217-1

Henchoz, Y., Soldini, N., Peyrot, N., and Malatesta, D. (2015). Energetics and mechanics of walking in patients with chronic low back pain and healthy matched controls. *Eur. J. Appl. Physiol.* 115, 2433–2443. doi:10.1007/s00421-015-3227-4

Hodges, P. W., Van Dillen, L. R., Mcgill, S., Brumange, S., and Hides, J. A. (2013). "State-of-the-art approach to clinical rehabilitation of low back and pelvic pain," in *The rehabilitation of back pain: State of the art and science*. Editors P. W. Hodges, J. Cholewicki, and J. H. Van Dieën (Edinburgh: Elsevier).

Holden, J. P., Orsini, J. A., Siegel, K. L., Kepple, T. M., Gerber, L. H., and Stanhope, S. J. (1997). Surface movement errors in shank kinematics and knee kinetics during gait. *Gait Posture* 5, 217–227. doi:10.1016/s0966-6362(96)01088-0

Hoy, D., Bain, C., Williams, G., March, L., Brooks, P., Blyth, F., et al. (2012). A systematic review of the global prevalence of low back pain. *Arthritis Rheum.* 64, 2028–2037. doi:10.1002/art.34347

Huang, X., Lin, D., Liang, Z., Deng, Y., He, Z., Wang, M., et al. (2021). Mechanical parameters and trajectory of two Chinese cervical manipulations compared by a motion capture system. *Front. Bioeng. Biotechnol.* 9, 714292. doi:10.3389/fbioe.2021.714292

Itz, C. J., Geurts, J. W., van Kleef, M., and Nelemans, P. (2013). Clinical course of non-specific low back pain: A systematic review of prospective cohort studies set in primary care: Clinical course of non-specific low back pain. *Eur. J. Pain* 17, 5–15. doi:10.1002/j.1532-2149.2012.00170.x

Laird, R. A., Kent, P., and Keating, J. L. (2012). Modifying patterns of movement in people with low back pain -does it help? A systematic review. *BMC Musculoskelet. Disord.* 13, 169. doi:10.1186/1471-2474-13-169

Lamoth, C. J. C., Meijer, O. G., Daffertshofer, A., Wuisman, P. I. J. M., and Beek, P. J. (2006). Effects of chronic low back pain on trunk coordination and back muscle activity during walking: Changes in motor control. *Eur. Spine J.* 15, 23–40. doi:10.1007/s00586-004-0825-y

Leardini, A., Chiari, L., Della Croce, U., and Cappozzo, A. (2005). Human movement analysis using stereophotogrammetry. *Gait Posture* 21, 212–225. doi:10.1016/j.gaitpost.2004.05.002

Lees, A., Barton, G., and Robinson, M. (2010). The influence of Cardan rotation sequence on angular orientation data for the lower limb in the soccer kick. *J. Sports Sci.* 28, 445–450. doi:10.1080/02640410903540352

Li, G., Wang, S., Passias, P., Xia, Q., Li, G., and Wood, K. (2009). Segmental *in vivo* vertebral motion during functional human lumbar spine activities. *Eur. Spine J.* 18, 1013–1021. doi:10.1007/s00586-009-0936-6

Liguori, G.American College of Sports Medicine (ACSM) (2021). *ACSM's guidelines for exercise testing and prescription*. 11th ed. Baltimore, MD: Wolters Kluwer Health.

Maher, C., Underwood, M., and Buchbinder, R. (2017). Non-specific low back pain. *Lancet* 389, 736–747. doi:10.1016/s0140-6736(16)30970-9

Manal, K., McClay, I., Stanhope, S., Richards, J., and Galinat, B. (2000). Comparison of surface mounted markers and attachment methods in estimating tibial rotations during walking: An *in vivo* study. *Gait Posture* 11, 38–45. doi:10.1016/s0966-6362(99)00042-9

Metcalf, C. D., Phillips, C., Forrester, A., Glodowski, J., Simpson, K., Everitt, C., et al. (2020). Quantifying soft tissue artefacts and imaging variability in motion capture of the fingers. *Ann. Biomed. Eng.* 48, 1551–1561. doi:10.1007/s10439-020-02476-2

Mörl, F., and Blickhan, R. (2006). Three-dimensional relation of skin markers to lumbar vertebrae of healthy subjects in different postures measured by open MRI. *Eur. Spine J.* 15, 742–751. doi:10.1007/s00586-005-0960-0

Papi, E., Bull, A. M. J., and McGregor, A. H. (2019). Spinal segments do not move together predictably during daily activities. *Gait Posture* 67, 277–283. doi:10.1016/j.gaitpost.2018.10.031

Pranata, A., Perraton, L., El-Ansary, D., Clark, R., Mentiplay, B., Fortin, K., et al. (2018). Trunk and lower limb coordination during lifting in people with and without chronic low back pain. *J. Biomech.* 71, 257–263. doi:10.1016/j.jbiomech.2018.02.016

Robertson, D. G. E., Hamill, J., Caldwell, G. E., Kamen, G., and Whittlesey, S. (2004). *Research methods in biomechanics*. Champaign, IL: Human Kinetics.

Sangeux, M., Marin, F., Charleux, F., Dürselen, L., and Ho Ba Tho, M. C. (2006). Quantification of the 3D relative movement of external marker sets vs. bones based on magnetic resonance imaging. *Clin. Biomech. (Bristol, Avon)* 21, 984–991. doi:10.1016/j.clinbiomech.2006.05.006

Schwartz, M. H., Trost, J. P., and Wervey, R. A. (2004). Measurement and management of errors in quantitative gait data. *Gait Posture* 20, 196–203. doi:10.1016/j.gaitpost.2003.09.011

Seerden, Stefan, Dankaerts, Wim, and Vanwanseele, Benedicte (2016). Reliability of a multi-segmental kinematic model to analyse 3D movement in the lumbar spine. *Gait Posture*. 49 53. doi:10.1016/j.gaitpost.2016.07.117

Shahbazi Moheb Seraj, M., Sarrafzadeh, J., Maroufi, N., Ebrahimi Takamjani, I., Ahmadi, A., and Negahban, H. (2018). The ratio of lumbar to hip motion during the trunk flexion in patients with mechanical chronic low back pain according to O'sullivan classification system: A cross-sectional study. *Arch. Bone Jt. Surg.* 6, 560–569.

Stratford, P. (1995). Assessing disability and change on individual patients: A report of a patient specific measure. *Physiother. Can.* 47, 258–263. doi:10.3138/ptc.47.4.258

Tsai, T.-Y., Lu, T.-W., Kuo, M.-Y., and Lin, C.-C. (2011). Effects of soft tissue artifacts on the calculated kinematics and kinetics of the knee during stair-ascent. *J. Biomech.* 44 (6), 1182–1188. doi:10.1016/j.jbiomech.2011.01.009

van Wingerden, J.-P., Vleeming, A., and Ronchetti, I. (2008). Differences in standing and forward bending in women with chronic low back or pelvic girdle pain: Indications for physical compensation strategies. *Spine* 33, E334–E341. doi:10.1097/brs.0b013e318170fcf6

Wallbott, H. G. (1989). "Movement quality changes in psychopathological disorders," in *Normalities and abnormalities in human movement*. Editor B. Kirkcaldy (Basel: Karger), 128–146. doi:10.1159/000416532

Wang, H., Zhou, C., Yu, Y., Wang, C., Tsai, T. Y., Han, C., et al. (2020). Quantifying the ranges of relative motions of the intervertebral discs and facet joints in the normal cervical spine. *J. Biomech.* 112, 110023. doi:10.1016/j.jbiomech.2020.110023

Wang, J., Lui, Z., Qian, Z., and Ren, L. (2016). Soft tissue artifact evaluation of the cervical spine in motion patterns of flexion and lateral bending: A preliminary study. *PeerJ* 4, e1893. doi:10.7717/peerj.1893

Wang, S., Passias, P., Li, G., Li, G., and Wood, K. (2008). Measurement of vertebral kinematics using noninvasive image matching method-validation and application. *Spine* 33, E355–E361. doi:10.1097/brs.0b013e3181715295

Wawrose, R. A., LeVasseur, C. M., Byrapogu, V. K., Dombrowski, M. E., Donaldson, W. F., Shaw, J. D., et al. (2020). *In vivo* changes in adjacent segment kinematics after lumbar decompression and fusion. *J. Biomechanics* 26, 109515. doi:10.1016/j.jbiomech.2019.109515

Wen, W., Xu, H., Zhang, Z., Kou, B., Sun, Q., and Miao, J. (2022). The effect of various weight-bearing activities on the motion of lumbar facet joints *in vivo*. *J. Orthop. Surg. Res.* 17, 114. doi:10.1186/s13018-022-03016-5

World Medical Association (2013). World medical association declaration of Helsinki: Ethical principles for medical research involving human subjects: Ethical principles for medical research involving human subjects. *JAMA*.310, 2191–2194. doi:10.1001/jama.2013.281053

Wu, G., Siegler, S., Allard, P., Kirtley, C., Leardini, A., Rosenbaum, D., et al. (2002). ISB recommendation on definitions of joint coordinate system of various joints for the reporting of human joint motion—part I: Ankle, hip, and spine. *J. Biomech.* 35, 543–548. doi:10.1016/s0021-9290(01)00222-6

Zemp, R., List, R., Gülay, T., Elsig, J. P., Naxera, J., Taylor, W. R., et al. (2014). Soft tissue artefacts of the human back: Comparison of the sagittal curvature of the spine measured using skin markers and an open upright MRI. *PLoS ONE* 9, e95426. doi:10.1371/journal.pone.0095426

Zhou, C., Li, G., Wang, C., Wang, H., Yu, Y., Tsai, T. Y., et al. (2021). *In vivo* intervertebral kinematics and disc deformations of the human cervical spine during walking. *Med. Eng. Phys.* 87, 63–72. doi:10.1016/j.medengphy.2020.11.010

Zhou, C., Wang, H., Wang, C., Tsai, T. Y., Yu, Y., Ostergaard, P., et al. (2020). Intervertebral range of motion characteristics of normal cervical spinal segments (C0-T1) during *in vivo* neck motions. *J. Biomech.* 98, 109418. doi:10.1016/j.jbiomech.2019.109418

frontiers | Frontiers in Bioengineering and Biotechnology

TYPE Original Research
PUBLISHED 06 October 2022
DOI 10.3389/fbioe.2022.1002731

OPEN ACCESS

EDITED BY
Navrag B. Singh,
Department of Health Sciences and Technology, ETH Zürich, Switzerland

REVIEWED BY
Emanuel Andrada,
Friedrich Schiller University Jena, Germany
Georgios Giarmatzis,
Democritus University of Thrace, Greece

*CORRESPONDENCE
Elena M. Gutierrez-Farewik,
lanie@kth.se

SPECIALTY SECTION
This article was submitted to Biomechanics, a section of the journal Frontiers in Bioengineering and Biotechnology

RECEIVED 25 July 2022
ACCEPTED 20 September 2022
PUBLISHED 06 October 2022

CITATION
Luis I, Afschrift M, De Groote F and Gutierrez-Farewik EM (2022), Evaluation of musculoskeletal models, scaling methods, and performance criteria for estimating muscle excitations and fiber lengths across walking speeds.
Front. Bioeng. Biotechnol. 10:1002731.
doi: 10.3389/fbioe.2022.1002731

Evaluation of musculoskeletal models, scaling methods, and performance criteria for estimating muscle excitations and fiber lengths across walking speeds

Israel Luis[1], Maarten Afschrift[2], Friedl De Groote[2] and Elena M. Gutierrez-Farewik[1,3]*

[1]KTH MoveAbility Lab, Department of Engineering Mechanics, KTH Royal Institute of Technology, Stockholm, Sweden, [2]Department of Movement Sciences, KU Leuven, Leuven, Belgium, [3]Department of Women's and Children's Health, Karolinska Institutet, Stockholm, Sweden

Muscle-driven simulations have been widely adopted to study muscle-tendon behavior; several generic musculoskeletal models have been developed, and their biofidelity improved based on available experimental data and computational feasibility. It is, however, not clear which, if any, of these models accurately estimate muscle-tendon dynamics over a range of walking speeds. In addition, the interaction between model selection, performance criteria to solve muscle redundancy, and approaches for scaling muscle-tendon properties remain unclear. This study aims to compare estimated muscle excitations and muscle fiber lengths, qualitatively and quantitatively, from several model combinations to experimental observations. We tested three generic models proposed by Hamner et al., Rajagopal et al., and Lai-Arnold et al. in combination with performance criteria based on minimization of muscle effort to the power of 2, 3, 5, and 10, and four approaches to scale the muscle-tendon unit properties of maximum isometric force, optimal fiber length, and tendon slack length. We collected motion analysis and electromyography data in eight able-bodied subjects walking at seven speeds and compared agreement between estimated/modelled muscle excitations and observed muscle excitations from electromyography and computed normalized fiber lengths to values reported in the literature. We found that best agreement in on/off timing in vastus lateralis, vastus medialis, tibialis anterior, gastrocnemius lateralis, gastrocnemius medialis, and soleus was estimated with minimum squared muscle effort than to higher exponents, regardless of model and scaling approach. Also, minimum squared or cubed muscle effort with only a subset of muscle-tendon unit scaling approaches produced the best time-series agreement and best estimates of the increment of muscle excitation magnitude across walking speeds. There were discrepancies in estimated fiber lengths and muscle excitations among the models, with the largest discrepancy in the Hamner et al. model. The model proposed by Lai-Arnold et al. best estimated muscle excitation estimates

overall, but failed to estimate realistic muscle fiber lengths, which were better estimated with the model proposed by Rajagopal et al. No single model combination estimated the most accurate muscle excitations for all muscles; commonly observed disagreements include onset delay, underestimated co-activation, and failure to estimate muscle excitation increments across walking speeds.

KEYWORDS

musculoskeletal modeling, optimal control, muscle-tendon parameter, performance criteria, EMG, fiber length

Introduction

Neuromusculoskeletal modeling enables the study of individual muscle-tendon unit (MTU) behavior, joint kinematics, dynamics, and neuromuscular control strategies by non-invasive means. Simulation studies have provided insights into the MTU mechanics in able-bodied individuals (Heintz and Gutierrez-Farewik, 2007; Hamner et al., 2010; Arnold et al., 2013; Swinnen et al., 2019; Delabastita et al., 2020), and in individuals with disabilities in unassisted motions (Krogt et al., 2016) and with the support of assistive devices (Lotti et al., 2020). A realistic representation of MTU behavior depends on adequately modeling skeletal anatomy and muscle architecture and decoding neuromuscular control. The most challenging aspect is to perform *in vivo* measurements, i.e., muscle and ligaments properties (Charles et al., 2019a), anatomical degrees of freedom (Zandbergen et al., 2020), or muscle dynamics, and to validate them with experimental observations (Hicks et al., 2015). As such, simplifications of the neuromusculoskeletal system are necessary. Consequently, it is critical to review and refine these methods to gain confidence in their use.

Neuromusculoskeletal modeling integrates musculoskeletal modeling, which describes the mechanics of the human biological system, and neuromuscular control, which synthesizes the principles for controlling such a system. Musculoskeletal models incorporate a description of the bone geometry, degrees of freedom, and body-segment physical properties: mass, inertia, and center of mass, and muscle geometry, architecture, and dynamics. Muscle dynamics is subdivided into activation and contraction dynamics (Zajac, 1989). Activation dynamics describes the relationship between the motor unit discharges from the nerve to the muscle, muscle excitation, and the concentration of calcium ions within the intracellular space, muscle activation. Contraction dynamics describes the force-generating capacity of the muscle and the behavior of connective tissue: tendon and aponeurosis and is commonly represented by a Hill-type model. This model includes parameters such as maximum isometric force (MIF), maximum contraction velocity (MCV), optimal fiber length (OFL), pennation angle (PA) at OFL, and tendon slack length (TSL). Muscles' contractions are mainly responsible for the development of skeletal motion. However, their coordination pattern is not trivial as human movement is highly redundant; there are more muscles than degrees of freedom. To address this redundancy in neuromuscular control, it is typically assumed that human movement control is governed through optimizing some performance criterion. Therefore, muscle controls are estimated by solving an optimization problem. Different performance criteria, e.g., minimal muscle activation, joint force, metabolic demand, etc., have been proposed to solve for individual muscle forces (Heintz and Gutierrez-Farewik, 2007). The combination of musculoskeletal models and optimal control provides a framework for investigating MTU behavior underlying an observed movement pattern.

A series of generic musculoskeletal models have been proposed in previous decades, but a comprehensive comparison of how model choice influences the estimation of underlying muscle excitations involved in movement is lacking. Musculoskeletal models have progressively increased their physiological fidelity, initially developed from cadaveric databases, and currently integrating *in vivo* observation of MTU characteristics through biomedical imaging and computational optimization techniques. Several generic musculoskeletal models have been revised, updated, and implemented in biomechanical modeling and simulation software, such as OpenSim. Frequently used models include those by Delp et al. (Delp et al., 1990), Hamner et al. (Hamner et al., 2010), Arnold et al. (Arnold et al., 2010), Rajagopal et al. (Rajagopal et al., 2016), and Lai et al. (Lai et al., 2018). In pioneering work, Delp et al. (Delp et al., 1990) formulated a lower limb model with MTU parameter values mainly obtained from five cadavers and TSL estimation from the model itself. Hamner et al. (Hamner et al., 2010) incorporated torso and arm segments in the Delp et al. model to study muscle contributions during running. Arnold et al. (Arnold et al., 2010) further developed the model by updating bone geometry (Arnold et al., 2000) and by implementing muscle architecture from a more comprehensive dataset from 21 cadavers (Ward et al., 2009). This model allowed a detailed description of the operating range of multiple muscles (Arnold et al., 2013), for instance, the soleus, which was aligned with experimental findings (Rubenson et al., 2012). Rajagopal et al. (Rajagopal et al., 2016) further updated the model of Arnold et al. by incorporating the relationship between individual muscle

volume and leg volume in able-bodied young adults (Handsfield et al., 2014) and included torso and arm segments. Rajagopal et al. reported that this model overestimated fiber length change and passive fiber force due to the limitation of modeling the MTU with only a one-dimensional path, and that the excessive passive forces led to anomalous compensatory muscle excitations at the knee (Rajagopal et al., 2016) and hip extensors (Lai et al., 2018). Lai et al. refined the Rajagopal model by increasing knee range of motion and updating the tibiofemoral kinematics, as well as attachment points, wrapping surfaces, and TSL and OFL of gastrocnemius lateralis, gastrocnemius medialis, gluteus maximus, rectus femoris, semimembranosus, soleus, vastus intermedius, vastus medialis, and vastus lateralis. Lai et al. reported that their model estimated lower muscle co-activation and muscle excitations that overall agreed better with recorded EMGs in walking, running, and pedalling (Lai et al., 2018) than the model by Rajagopal et al. This succession of models has incorporated more information about MTU geometry and parameters that are likely to estimate with increasing accuracy MTU time-dependent behavior, such as muscle excitation. However, validation has only been performed in a few physical activities. To the best of our knowledge, a quantitative evaluation and comparison of their biofidelity over a range of walking speeds, compared with experimental data, has not been performed.

A generic musculoskeletal model must be scaled to a subject's anthropometry to be suitable for analyzing muscle behavior during measured movement patterns, though how to scale MTU parameters is not fully known. In OpenSim, scaling is performed based on a calibration trial, wherein dimensions of model segments are modified to fit the subject's anthropometry. Muscle-tendon attachment points are scaled linearly, proportionally to generic and scaled model segment lengths, as are OFL and TSL, by maintaining the same OFL/TSL ratio. However, this procedure has questionable validity, as OFL has been reported to not correlate linearly to leg length (Charles et al., 2020). In addition, MIF is generally not scaled, which is also questionable as muscle volume (and indirectly physiological cross-sectional area) has been reported to vary with height and weight (Handsfield et al., 2014; Charles et al., 2019b), age, gender, among other factors (Thelen et al., 2003). Computational methods have been proposed to scale MTU parameters (Winby et al., 2008; Krogt et al., 2016; Modenese et al., 2016). Modenese et al. implemented an algorithm to estimate OFL and TSL based on mapping a muscle's operating range of a generic model onto a scaled model (Modenese et al., 2016). Rajagopal et al. scaled the MIF based on individual muscle volume, which was in turn estimated based on a regression equation from a study using magnetic resonance imaging (Rajagopal et al., 2016), and van der Krogt et al. scaled MIF by taking into account the generic and scaled models' mass ratio (Krogt et al., 2016). Despite the introduction of numerous scaling methods, studies that evaluate their effect in the estimation of the muscle-tendon dynamics are scarce. Recently Charles et al. reported a better estimation of joint torque during maximum voluntary contraction trials in a model that scaled MIF as per van der Krogt et al. and OFL/TSL as per Modenese et al., compared to generic MTU parameters (Charles et al., 2020). This finding provided evidence that supports MTU parameter scaling. However, it is unknown whether scaling methods can improve estimation of MTU mechanics in different musculoskeletal models.

Simulation studies examining performance criteria are also numerous. Ackermann and van den Bogert simulated motion pattern and foot-ground contact forces with a two-dimensional musculoskeletal model walking at 1.1 m/s and solved the redundancy using performance criteria of minimum sum of muscle activations to the powers of 1, 2, 3, and 10, and with or without scaling muscle volume, with an aim to identify which combination provide the best estimation of muscle excitation, joint kinematics, and ground reaction force (Ackermann and van den Bogert, 2010). The best agreement was obtained using minimum sum of muscle activation to the power of 10. Zargham et al. investigated the effect of multiple performance criteria on estimated muscle excitation in simulation with prescribed kinematics and dynamics obtained from subjects with instrumented knee prostheses at a self-selected speed (1 m/s) (Zargham et al., 2019). They found that performance criteria of minimum sum of muscle activations to a power of 3 or 4, with and without scaled muscle volumes, resulted in better agreement with experimental EMGs than other criteria such as minimizing muscle force or contact force. In addition, both studies were only performed at one walking speed, so it is unclear whereas performance criteria based on minimal muscle effort allow to estimate muscle activation trends across walking speed and which power better performs.

In summary, although multiple generic musculoskeletal have been developed, they have not been quantitatively examined to determine which most accurately estimates underlying muscle excitation in observed movements. It is also unclear how muscle model parameter scaling, and different performance criteria based on muscle effort influence MTU mechanics estimations. As such, the goals of this study were to compute muscle excitations with three different generic open-source models, using four different performance criteria based on muscle effort, and four different methods to scale MIF, OFL, and TSL, of walking at 7 different speeds, and to qualitatively and quantitively evaluate which combination(s) of model, scaling method, and performance criterion yields muscle excitations that agree best with experimentally observed EMGs in eight muscles. Another goal was to evaluate indicators of validity of prescribed musculoskeletal simulations by studying whether MTU actuators were capable of reproducing the inverse dynamic joint torques (Hicks et al., 2015). Subsequent goals were to compare estimated fiber lengths of vastus lateralis, tibialis anterior, gastrocnemius

medialis and lateralis, and soleus with those reported in literature.

Materials and methods

Musculoskeletal models, MTU-scaled parameters, and performance criteria

Three generic models available on the SimTK website were examined, referred to as Hamner (Hamner et al., 2010), Rajagopal (Rajagopal et al., 2016), and Lai-Arnold (Lai et al., 2018) models. Each model was anisotropically scaled: muscle attachments, skeletal geometry, and segment inertial properties were scaled to anthropometric dimensions obtained from a static calibration trial from 3D motion capture. Model segments were scaled using the marker positions based on the Conventional Gait Model with the extended foot model (CGM 2.4).

MTU parameters of the Hill-type muscle models were scaled in 4 different ways. OFL and TSL were scaled in two ways - linearly by the ratio between MTU lengths in the scaled and generic model (anatomic position, OpenSim's Scale Tool) or non-linearly to preserve the operating range of the muscles (Modenese et al. (Modenese et al., 2016)). For each of these, MIF was either unscaled (generic MIF) or scaled based on muscle volumes derived from a regression equation that relates MRI-based muscle volumes to the subject's height and weight (Handsfield et al., 2014). Thus, for each individual, each of the 3 models was scaled in 4 scaling variants:

S1: Linear scaling of OFL and TSL, generic MIF.

S2: Non-linear scaling of OFL and TSL, generic MIF.

S3: Linear scaling of OFL and TSL, scaled MIF.

S4: Non-linear scaling of OFL and TSL, scaled MIF.

Scaled MIFs were computed based on the assumption that MIF is proportional to the physiological cross-sectional area (PCSA) and specific tension, as shown in Eq. 1

$$F^0_{Mi} = A_i\sigma = \frac{V_{M_i}V_T}{l^0_{Mi}}\sigma \tag{1}$$

Where F^0_{Mi} is the maximum isometric force, A_i is the physiological cross-sectional area, l^0_{Mi} is the optimal fiber length, V_T is the total leg volume, and V_{M_i} is the percentage of muscle volume with respect to the total leg volume of the muscle i, both estimated from Handsfield et al. (Handsfield et al., 2014), and σ is the specific tension, which has a value of 60 N/cm^2 for each muscle (Rajagopal et al., 2016). All models assume the same MCV (10 OFL/s), activation time constant (10 ms), and deactivation time constant (40 ms) for all muscles, and PA was as per the original models. In addition, the non-linear tendon stiffness of gastrocnemius medialis, gastrocnemius lateralis, and soleus were set to 15 (nondimensionalized), according to ultrasound studies (Swinnen et al., 2019; Delabastita et al., 2020) that describe the Achilles tendon as highly compliant. Similarly, the non-linear tendon stiffness of vastus lateralis, vastus medialis, vastus intermedius, and rectus femoris was set to 20 (nondimensionalized), according to findings that modelling the Patellar tendon as highly compliant agrees better with experimental observations (Chleboun et al., 2007; Bohm et al., 2018), including muscle fiber operating range (Son et al., 2018).

In addition, for each model and scaling variant, 4 performance criteria based on minimum muscle effort, defined as the sum of muscle activations and excitations to powers (p) of 2, 3, 5, and 10, were examined as shown in Eq. 2

$$J_p = \int_{t_i}^{t_f}\left(\sum_{i=1}^{N}\frac{(e_i^p(t) + a_i^p(t))}{2}\right)dt \tag{2}$$

Where t_i is the initial time of the gait cycle, t_f is the final time of the gait cycle, e_i is muscle excitation of the muscle i, a_i is muscle activation of the muscle i, and N the total number of muscles in one leg of each model. These performance criteria are referred to as J2, J3, J5, and J10

Subjects

Eight able-bodied adults (5 males, 3 females, mean [SD] age: 37.8 [9.6] years, height: 1.76 [0.10] m, mass: 76.6 [14.4] kg) participated in this experiment as part of a more comprehensive study to characterize energetics in locomotion.

Experimental setup and protocols

Subjects walked at different speeds based on the expected preferred walking speed (PWS), based on each subject's gender, age, and height (Bohannon, 1997). The subjects walked on a treadmill at 55%, 70%, 85%, 100%, 115%, 130%, and 145% of the PWS in randomized order, and each subject's cadence at each speed was recorded. Then, for overground walking along a walkway, each of the 7 walking speeds was estimated by matching the cadence of treadmill walking. Reflective marker positions (100 Hz) and ground reaction forces (1,000 Hz) were measured during overground walking using optical motion capture (Vicon V16, Oxford, United Kingdom) and strain gauge force platforms (AMTI, Watertown, MA, United States). Full-body marker placement was implemented based on the Conventional Gait Model with the extended foot model (CGM 2.4). EMGs from eight muscles in one leg were recorded (1,000 Hz): biceps femoris long head (BF), semitendinosus (ST), vastus lateralis (VL), vastus medialis (VM), tibialis anterior (TA), gastrocnemius lateralis (GL), gastrocnemius medialis (GM) and soleus (SO), using bipolar surface wireless electrodes (Myon aktos/Cometa systems, Milan, Italy). The selection of the leg side for each

subject was randomized. Skin preparation and electrode placement followed Electromyography for the Non-Invasive Assessment of Muscles guidelines (SENIAM) (Hermens et al., 2000). Subjects were asked to perform functional tests, such as standing heel raise, standing toe raises, squat, knee flexion, and hip flexion/extension, to corroborate the placement of the EMGs.

Data and statistical analysis

Generic models were scaled to each subject's dimensions as described above. Marker trajectories and ground reaction forces during 21 gait cycles per subject (3 gait cycles at each of 7 walking speeds) were used in 3D inverse kinematics (IK) and inverse dynamics (ID) using OpenSim 4.1. IK tracking weights were selected to minimize the error between experimental markers and virtual markers placed on the model. For each subject, the same weights were used for each model, scaling variant and performance criteria. Subtalar and metatarsal joints were fixed at anatomically neutral positions. Muscle excitations and corresponding fiber lengths were estimated using a direct collocation dynamic optimization algorithm that incorporates activation and contraction dynamics (De Groote et al., 2016). IK and ID solutions were prescribed, and the objective function consisted of three terms: the first term refers to the muscle effort, as described above, the second term to the torque produced by reserve actuators, i.e., ideal actuators at each joint that served to generate the joint torques that the MTU actuators are not able to reproduce, and the third term, to the fiber velocity to improve the numerical computation. The mathematical expression of the objective function is shown in Eq. 3

$$J = w_e J_p + w_r \int_{t_i}^{t_f} \left(\sum_{j=1}^{J} e_{Rj}^2(t) \right) dt + w_v \int_{t_i}^{t_f} \left(\sum_{i=1}^{N} v_i^2(t) \right) dt \quad (3)$$

Where e_{Rj} is the reserve actuator of the joint j, v_i is the muscle velocity of the muscle i, J the total number of joints in one leg of each model, and w_e, w_r, and w_v are the weight of the terms related to muscle effort, reserve actuators, and fiber velocities, respectively. The value of w_e is 1, the value of w_r is 1,000, and w_v is 0.01. As such, the use of the reserve actuators was highly penalized in the objective function, and the influence of the fiber velocity was relatively small. MTU parameters MIF, OFL, TSL, and tendon compliance, defined as OFL/TFL, as well as muscle excitations were computed for each gait cycle for each of the 3 musculoskeletal models, the 4 scaling variants (S1, S2, S3, and S4), and the 4 performance criteria (J2, J3, J5, and J10), which resulted in 48 estimates per gait cycle.

Recorded EMGs were processed using a fourth order zero-lag Butterworth band-pass filter (20–400 Hz), full-wave rectification, and a fourth order zero-lag Butterworth low-pass filter (6 Hz). Experimental muscle excitations were processed throughout the same 21 gait cycles per subject described above.

Scaled values of OFL, and TSL of each model and scaling variant were compared to experimental values reported by Ward et al. (Ward et al., 2009). Also, excessive reliance on reserve actuators to reproduce inverse dynamic joint torque was reported for each model combination.

Qualitative evaluation of estimated muscle excitation was performed by examining on/off timing agreement, defined as the period during which muscles are active, i.e., when EMGs or computed muscle excitations exceed a threshold, in this case 50% of the maximum value during each gait cycle.

Quantitative evaluation was performed by examining the agreement between excitation patterns and average excitation increments across walking speeds between EMGs and estimated muscle excitations. Time-series agreement was evaluated by computing correlation coefficients (r) and root-mean-squared error (RMSE) between normalized EMGs and estimated muscle excitations. Both EMGs and estimated excitations were normalized to the maximum value during that gait cycle. As such, we only evaluated correspondence of the pattern (Zargham et al., 2019) but not of the magnitude.

We also computed excitation/speed increment rate m as the rate at which the average muscle excitation increased with walking speed *via* a linear regression between the average excitation magnitude and walking speed. Thus, m was computed from average EMG values (m_{exp}) and from the simulations (m_{sim}) for each model combination. Both observed and estimated muscle excitations were normalized to their average value observed during walking at PWS; thus $m_{exp} \approx 1$ and $m_{sim} \approx 1$ at PWS. Increment rate disagreement m_d between m_{exp} and m_{sim} was evaluated as their difference, proportional to m_{exp} and as a percent, shown in Eq. 4

$$m_d = \left(\frac{m_{sim} - m_{exp}}{m_{exp}} \right) \cdot 100\,[\%] \quad (4)$$

Therefore, $m_d > 0$ indicates that the model overestimated excitation/speed increments, $m_d = 0$ indicates that the model's excitation/speed increments were identical to those from EMGs, and $m_d < 0$ indicates that the underestimated excitation/speed increments.

Finally, the fiber lengths were estimated for each model combination and compared to reported values; estimated normalized fiber lengths of VL, TA, and GL at PWS, as well as GM and SO at low, normal, and fast walking speeds, were compared to experimental values reported available in the literature. To facilitate the comparison, the normalized fiber length was divided into four categories based on muscle fiber

TABLE 1 Average and SD of MIF [N], OFL [cm], TSL [cm], and MTU compliance, defined as TSL/OFL, among all subjects scaling variants: linear scaling of OFL and TSL and generic MIF (S1), non-linear scaling of OFL and TSL and generic MIF (S2), linear scaling of OFL and TSL and scaled MIF (S3), and non-linear scaling of OFL and TSL and scaled MIF (S4), in Hamner (H), Rajagopal (R), and Lai-Arnold (L) models in 8 muscles.

		S1				S2				S3				S4			
		MIF	OFL	TSL	TSL/OFL	MIF	OFL	TSL	TSL/OFL	MIF	OFL	TSL	TSL/OFL	MIF	OFL	TSL	TSL/OFL
BF	H	896.0 [0.0]	10.6 [0.6]	31.7 [1.9]	3.0 [0.0]	896.0 [0.0]	11.6 [0.8]	30.6 [1.8]	2.6 [0.2]	1,207.7 [212.3]	10.6 [0.6]	31.7 [1.9]	3.0 [0.0]	1,096.9 [146.6]	11.6 [0.8]	30.6 [1.8]	2.6 [0.2]
	R	1,313.2 [0.0]	9.4 [0.4]	31.4 [1.4]	3.3 [0.0]	1,313.2 [0.0]	10.0 [0.7]	31.0 [1.3]	3.1 [0.2]	1,357.6 [251.3]	9.4 [0.4]	31.4 [1.4]	3.3 [0.0]	1,274.5 [174.4]	10.0 [0.7]	31.0 [1.3]	3.1 [0.2]
	L	1,313.2 [0.0]	9.4 [0.4]	32.2 [1.4]	3.4 [0.0]	1,313.2 [0.0]	10.0 [0.7]	31.7 [1.3]	3.2 [0.2]	1,356.4 [250.1]	9.4 [0.4]	32.2 [1.4]	3.4 [0.0]	1,273.7 [173.6]	10.0 [0.7]	31.7 [1.3]	3.2 [0.2]
ST	H	410.0 [0.0]	19.7 [1.2]	25.0 [1.5]	1.3 [0.0]	410.0 [0.0]	21.2 [1.6]	23.2 [1.5]	1.1 [0.1]	579.2 [101.1]	19.7 [1.2]	25.0 [1.5]	1.3 [0.0]	535.2 [71.2]	21.2 [1.6]	23.2 [1.5]	1.1 [0.1]
	R	591.3 [0.0]	18.8 [0.9]	24.1 [1.1]	1.3 [0.0]	591.3 [0.0]	19.8 [1.4]	23.1 [1.2]	1.2 [0.1]	607.4 [111.3]	18.8 [0.9]	24.1 [1.1]	1.3 [0.0]	574.7 [79.1]	19.8 [1.4]	23.1 [1.2]	1.2 [0.1]
	L	591.3 [0.0]	18.8 [0.9]	24.0 [1.1]	1.3 [0.0]	591.3 [0.0]	19.8 [1.4]	23.0 [1.2]	1.2 [0.1]	607.6 [111.3]	18.8 [0.9]	24.0 [1.1]	1.3 [0.0]	574.1 [78.4]	19.8 [1.4]	23.0 [1.2]	1.2 [0.1]
VL	H	1871.0 [0.0]	8.2 [0.4]	15.4 [0.8]	1.9 [0.0]	1871.0 [0.0]	8.1 [0.5]	15.5 [0.8]	1.9 [0.0]	6,217.2 [1,089.6]	8.2 [0.4]	15.4 [0.8]	1.9 [0.0]	6,319.3 [1,072.8]	8.1 [0.5]	15.5 [0.8]	1.9 [0.0]
	R	5,148.8 [0.0]	9.8 [0.4]	21.7 [0.9]	2.2 [0.0]	5,148.8 [0.0]	9.5 [0.3]	21.8 [1.1]	2.3 [0.1]	5,235.3 [923.8]	9.8 [0.4]	21.7 [0.9]	2.2 [0.0]	5,387.7 [1,034.2]	9.5 [0.3]	21.8 [1.1]	2.3 [0.1]
	L	5,148.8 [0.0]	11.5 [0.5]	21.7 [0.9]	1.9 [0.0]	5,148.8 [0.0]	11.6 [0.3]	21.6 [1.1]	1.8 [0.1]	4,446.5 [783.0]	11.5 [0.5]	21.7 [0.9]	1.9 [0.0]	4,392.6 [823.4]	11.6 [0.3]	21.6 [1.1]	1.8 [0.1]
VM	H	1,294.0 [0.0]	8.6 [0.5]	12.2 [0.6]	1.4 [0.0]	1,294.0 [0.0]	8.8 [0.5]	12.1 [0.7]	1.4 [0.0]	3,089.2 [540.7]	8.6 [0.5]	12.2 [0.6]	1.4 [0.0]	3,006.2 [514.5]	8.8 [0.5]	12.1 [0.7]	1.4 [0.0]
	R	2,747.8 [0.0]	9.5 [0.4]	19.5 [0.9]	2.1 [0.0]	2,747.8 [0.0]	9.4 [0.3]	19.6 [1.0]	2.1 [0.1]	2,808.4 [496.6]	9.5 [0.4]	19.5 [0.9]	2.1 [0.0]	2,835.1 [531.8]	9.4 [0.3]	19.6 [1.0]	2.1 [0.1]
	L	2,747.8 [0.0]	10.8 [0.5]	20.3 [0.9]	1.9 [0.0]	2,747.8 [0.0]	11.1 [0.3]	20.1 [1.0]	1.8 [0.0]	2,470.2 [436.0]	10.8 [0.5]	20.3 [0.9]	1.9 [0.0]	2,390.4 [437.8]	11.1 [0.3]	20.1 [1.0]	1.8 [0.0]
TA	H	905.0 [0.0]	10.1 [0.7]	23.1 [1.7]	2.3 [0.0]	905.0 [0.0]	10.0 [0.8]	23.2 [1.6]	2.3 [0.1]	824.5 [126.9]	10.1 [0.7]	23.1 [1.7]	2.3 [0.0]	839.6 [125.7]	10.0 [0.8]	23.2 [1.6]	2.3 [0.1]
	R	1,227.5 [0.0]	7.0 [0.5]	24.7 [1.7]	3.5 [0.0]	1,227.5 [0.0]	6.9 [0.5]	24.7 [1.6]	3.6 [0.1]	1,193.9 [189.4]	7.0 [0.5]	24.7 [1.7]	3.5 [0.0]	1,203.0 [181.2]	6.9 [0.5]	24.7 [1.6]	3.6 [0.1]
	L	1,227.5 [0.0]	7.0 [0.5]	24.6 [1.6]	3.5 [0.0]	1,227.5 [0.0]	6.9 [0.5]	24.7 [1.6]	3.6 [0.1]	1,195.4 [190.0]	7.0 [0.5]	24.6 [1.6]	3.5 [0.0]	1,204.6 [181.7]	6.9 [0.5]	24.7 [1.6]	3.6 [0.1]
GL	H	683.0 [0.0]	6.6 [0.5]	39.2 [2.9]	5.9 [0.0]	683.0 [0.0]	6.2 [0.5]	39.6 [3.1]	6.4 [0.4]	1,397.9 [212.7]	6.6 [0.5]	39.2 [2.9]	5.9 [0.0]	1,487.2 [241.9]	6.2 [0.5]	39.6 [3.1]	6.4 [0.4]
	R	1,575.1 [0.0]	6.0 [0.4]	38.3 [2.6]	6.4 [0.0]	1,575.1 [0.0]	5.9 [0.4]	38.4 [2.7]	6.5 [0.3]	1,541.7 [239.4]	6.0 [0.4]	38.3 [2.6]	6.4 [0.0]	1,564.4 [266.3]	5.9 [0.4]	38.4 [2.7]	6.5 [0.3]
	L	1,575.1 [0.0]	7.0 [0.5]	38.0 [2.6]	5.4 [0.0]	1,575.1 [0.0]	6.8 [0.5]	38.2 [2.7]	5.6 [0.3]	1,315.8 [204.7]	7.0 [0.5]	38.0 [2.6]	5.4 [0.0]	1360.1 [233.7]	6.8 [0.5]	38.2 [2.7]	5.6 [0.3]
GM	H	1,558.0 [0.0]	6.2 [0.5]	40.2 [3.0]	6.5 [0.0]	1,558.0 [0.0]	5.9 [0.5]	40.5 [3.1]	6.9 [0.4]	2,558.9 [389.7]	6.2 [0.5]	40.2 [3.0]	6.5 [0.0]	2,710.8 [440.7]	5.9 [0.5]	40.5 [3.1]	6.9 [0.4]
	R	3,115.5 [0.0]	5.2 [0.4]	40.6 [2.7]	7.8 [0.0]	3,115.5 [0.0]	5.1 [0.4]	40.7 [2.8]	7.9 [0.4]	3,047.9 [474.5]	5.2 [0.4]	40.6 [2.7]	7.8 [0.0]	3,097.4 [533.9]	5.1 [0.4]	40.7 [2.8]	7.9 [0.4]
	L	3,115.5 [0.0]	6.0 [0.4]	39.4 [2.6]	6.6 [0.0]	3,115.5 [0.0]	5.8 [0.4]	39.6 [2.7]	6.8 [0.4]	2,635.5 [409.9]	6.0 [0.4]	39.4 [2.6]	6.6 [0.0]	2,731.9 [479.6]	5.8 [0.4]	39.6 [2.7]	6.8 [0.4]
SO	H	3,549.0 [0.0]	5.2 [0.4]	25.8 [1.9]	5.0 [0.0]	3,549.0 [0.0]	4.9 [0.5]	26.0 [2.0]	5.3 [0.5]	5,262.4 [802.3]	5.2 [0.4]	25.8 [1.9]	5.0 [0.0]	5,537.9 [875.6]	4.9 [0.5]	26.0 [2.0]	5.3 [0.5]
	R	6,194.8 [0.0]	4.5 [0.3]	28.3 [2.0]	6.3 [0.0]	6,194.8 [0.0]	4.4 [0.4]	28.4 [2.0]	6.5 [0.5]	6,032.5 [935.0]	4.5 [0.3]	28.3 [2.0]	6.3 [0.0]	6,172.5 [1,047.2]	4.4 [0.4]	28.4 [2.0]	6.5 [0.5]
	L	6,194.8 [0.0]	4.5 [0.3]	28.8 [2.0]	6.4 [0.0]	6,194.8 [0.0]	4.4 [0.4]	28.8 [2.0]	6.6 [0.6]	6,041.8 [938.1]	4.5 [0.3]	28.8 [2.0]	6.4 [0.0]	6,192.7 [1,050.8]	4.4 [0.4]	28.8 [2.0]	6.6 [0.6]

10.3389/fbioe.2022.1002731

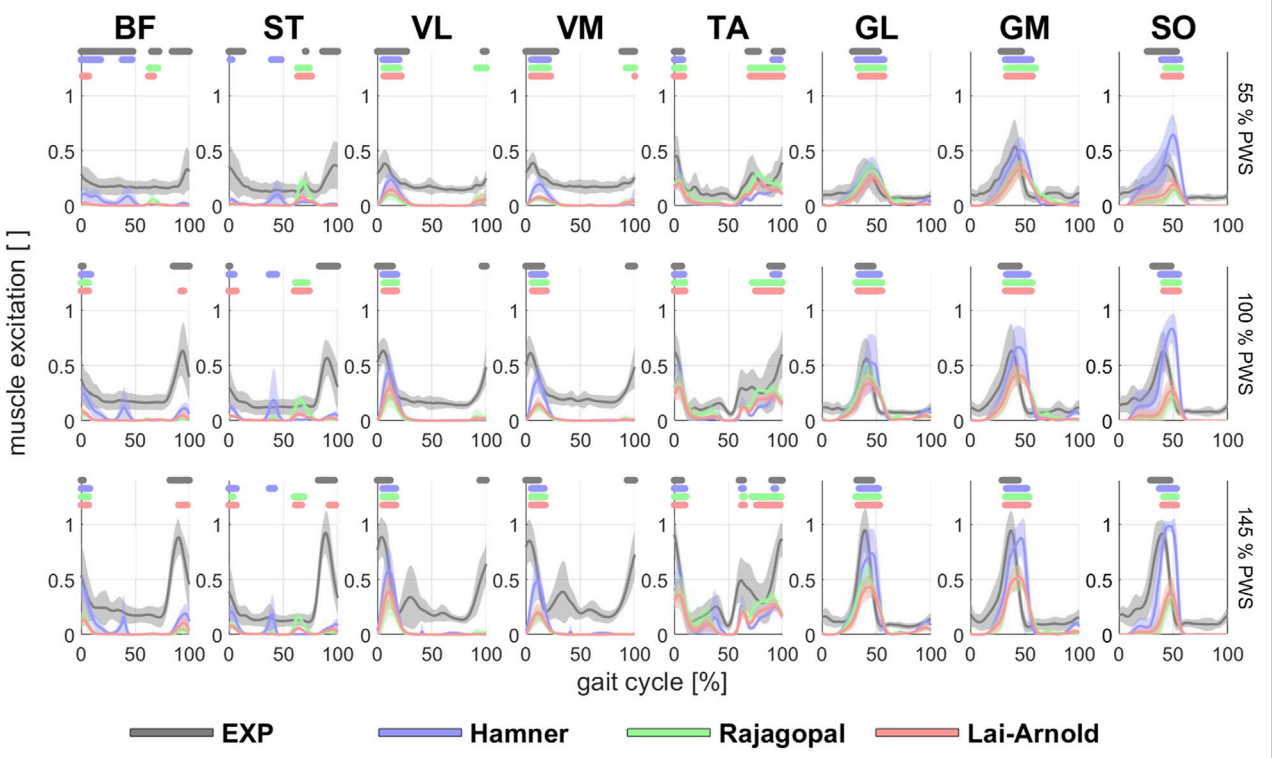

FIGURE 1
EMGs and estimated/modelled muscle excitations (average +/- 1 SD of all subjects) in 8 muscles with performance criterion J2 and scaling variant S1 at walking speeds of 55%, 100% and 145% PWS. EMGs were normalized to the maximum value at 145% PWS. Horizontal lines above each time series indicate on/off timing for EMG and each model, defined as >50% excitation.

length (L_M) relative to optimal fiber length (OFL): steep ascending limb (L_M/OFL< 0.75), shallow ascending limb (0.75 ≤L_M/OFL < 0.95), plateau (0.95 ≤L_M/OFL < 1.05), and descending limb (1.05< L_M/OFL) (Arnold and Delp, 2011).

Results

We found that muscle parameters estimated with scaled OFL and TSL were similar to those reported by Ward et al. (Ward et al., 2009) in most muscles and in all models. Scaling MIF had a larger effect on estimated muscle parameters in the Hamner model than in the other models (Table 1). Estimated OFLs with OFL and TSL linearly (S1) and non-linearly (S2) scaled in the Rajagopal model were within the expected values reported by Ward et al. (Ward et al., 2009), whereas VL, TA, and GM in the Hamner model, and GL in the Lai-Arnold model were not (Supplementary Table S1). OFL tended to be smaller with non-linearly scaled OFL and TSL in TA, GL, GM, and SO, but larger in BF and ST than linearly scaled OFL and TSL in all models. MTU compliance tended to be higher with non-linearly scaled in TA, GL, GM, and SO and lower in BF and ST than with linearly scaled OFL and TSL in all models. The Rajagopal and Lai-Arnold models estimated higher MIF than the Hamner model, with or without scaled MIF, for most muscles, except GL, VL, and VM.

As an indicator of simulation validity, the number of gait cycles that required excessive reserve actuators, defined as >2.5 N·m, were computed (Supplementary Table S2). This threshold represented approximately 5% of the average peak values of all the joint torques at the slowest walking speed. Acceptable reserve actuators were achieved in most muscles with most of the model combinations. The Hamner model required higher reserve actuators when MIF was not scaled (S1 and S2), compared to the Rajagopal and Lai-Arnold model using any scaling variant. Notably, higher reserve actuator magnitudes were found in the Hamner model at the ankle and hip joint in the sagittal plane, particularly at high walking speeds (not reported).

Estimated on/off timing in most muscles was similar for all model combinations. Estimated muscle excitations from all model combinations presented some similar discrepancies to EMGs, including lower co-activation and an excitation delay.

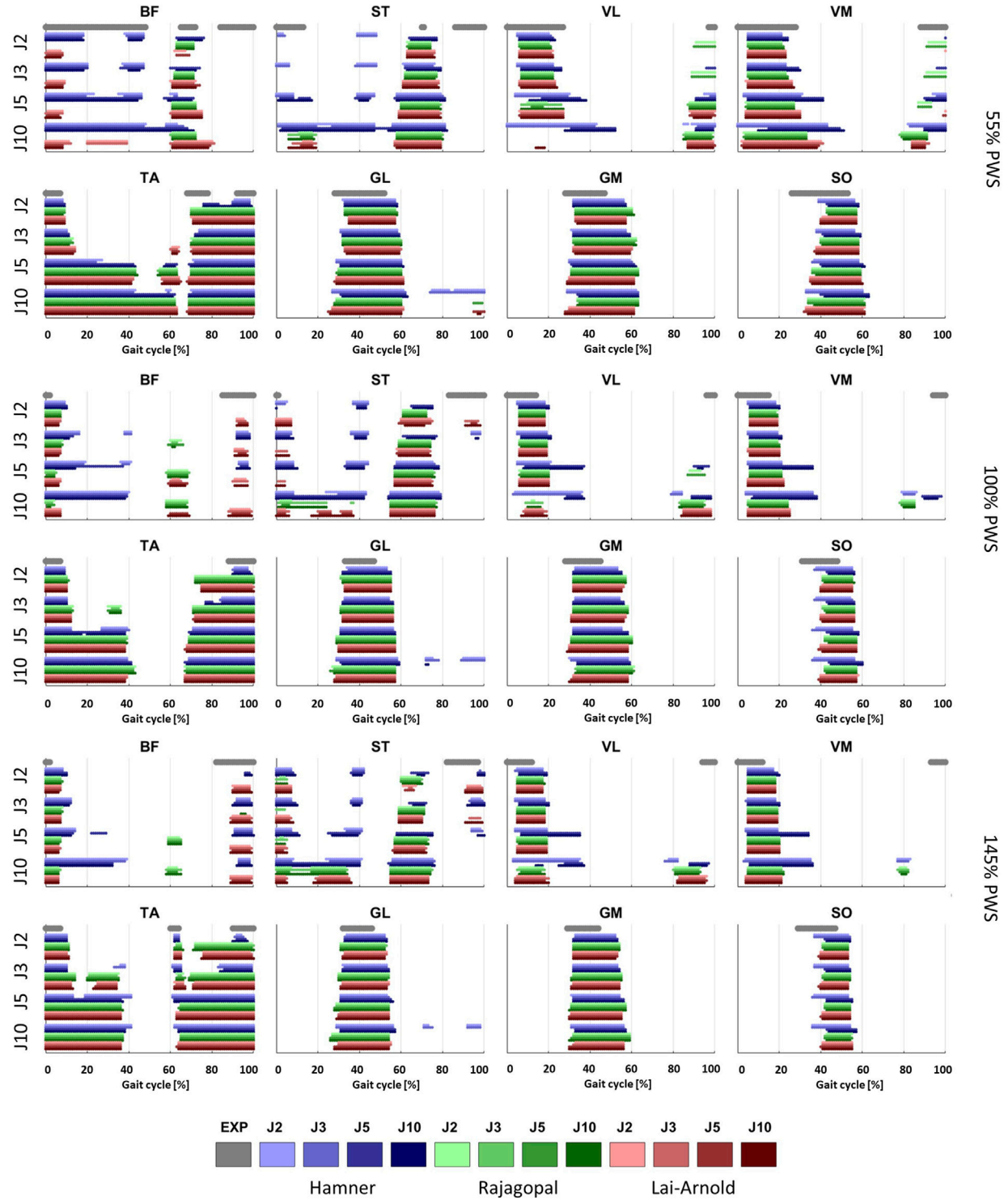

FIGURE 2
On/off timing of EMGs, averaged over all subjects, and estimated muscle excitations of 8 muscles at 3 walking speeds, with performance criteria based on minimization of muscle effort to the power of 2 (J2), 3 (J3), 5 (J5) and 10 (J10), and scaling variants with linear scaling of OFL and TSL and generic MIF (S1), non-linear scaling of OFL and TSL and generic MIF (S2), linear scaling of OFL and TSL and scaled MIF (S3), and non-linear scaling of OFL and TSL and scaled MIF (S4).

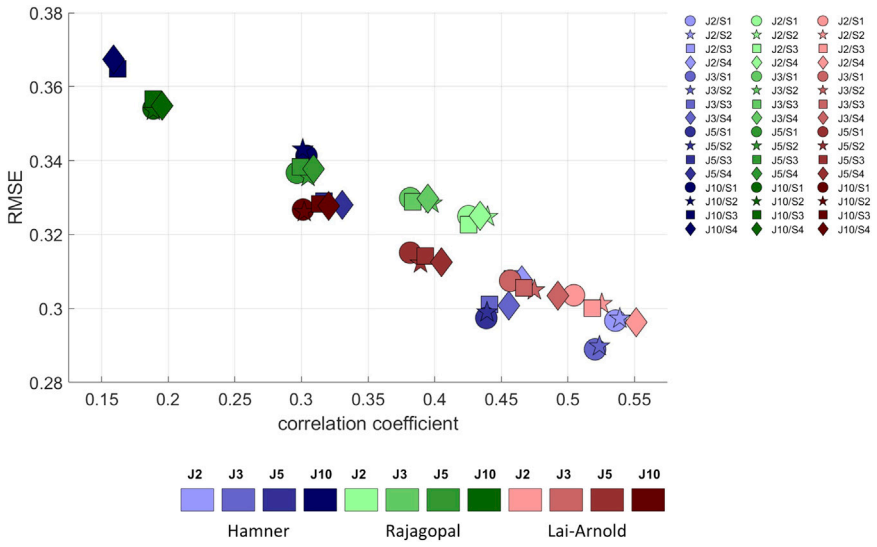

FIGURE 3
RMSE *versus* correlation coefficient (r) between normalized EMGs and estimated muscle excitations, averaged values among all subjects, speeds, and muscles, with performance criteria based on minimization of muscle effort to the power of 2 (J2), 3 (J3), 5 (J5), and 10 (J10), illustrated with darkening colors, and scaling variants of linear scaling of OFL and TSL and generic MIF (S1), non-linear scaling of OFL and TSL and generic MIF (S2), linear scaling of OFL and TSL and scaled MIF (S3), and non-linear scaling of OFL and TSL and scaled MIF (S4).

Estimated on/off timing agreed well with EMGs for most models and across walking speeds in ankle plantar- and dorsiflexors TA, GL, GM, and SO, and to a lesser degree, in knee extensors VL and VM, with performance criterion J2 and with any scaling variant (Figures 1, 2). Estimated on/off timing in GL, GM, and SO for all models agreed well with EMGs and did not substantially change among speeds, nor were they substantially influenced by performance criterion or scaling variant. Estimated on/off timing in VL, VM, and TA agreed least with EMGs with J10 compared to other performance criteria (Supplementary Figure S1), particularly in the Hamner model (Figure 2). All model combinations failed to capture VL and VM excitation in late swing at high speeds. Estimated ST excitation with all model combinations agreed poorly with EMGs across speeds, wherein on/off timing varied throughout the gait cycle among models, particularly in the Hamner model. Similar disagreements with EMGs can be observed for a few muscles in all models. For instance, all model combinations estimated very low or no excitation within certain periods of the gait cycle, whereas average EMG values never reached zero excitation. Thus, all model combinations estimated less co-activation than were observed in EMGs. In addition, for all model combinations, VL, VM, GL, GM, and SO estimates closely resembled EMG patterns, but with a delayed onset across all speeds.

For all models and scaling variants, excitation patterns estimated with performance criterion J2 agreed better with EMG, demonstrated by lower RMSE and higher correlation coefficients, than excitation patterns estimated by with performance criteria with higher powers (Figure 3). Muscle excitations estimated with Hamner, and Lai-Arnold models agreed better with EMG than those with the Rajagopal model when combined with performance criterion J2. Among the models, performance criterion had the largest influence on estimated muscle excitations with the Hamner model. Estimated muscle activation with the Lai-Arnold model agreed better with EMG than with Rajagopal model for all performance criteria.

The scaling variant had a smaller influence on agreement between estimated muscle excitations and EMG than the model or performance criterion. With Hamner model, regardless of performance criterion, the agreement between estimated muscle excitations and EMG was better when MIF was not scaled (Supplementary Figure S1). With the Lai-Arnold model, the agreement between estimated muscle excitations and EMG was best with non-linearly scaled OFL and TSL and scaled MIF (S4). With the Rajagopal model, the scaling variant had little influence on the agreement between estimated muscle excitations and EMG.

While muscle excitation time-series agreement with EMG was higher with Hamner and Lai-Arnold models than with the Rajagopal model, no single model estimated excitation time-series with highest agreement for all muscles (Figures 1, 4, Supplementary Tables S3, S4). The best time-series agreement of TA and SO are obtained with the Hamner

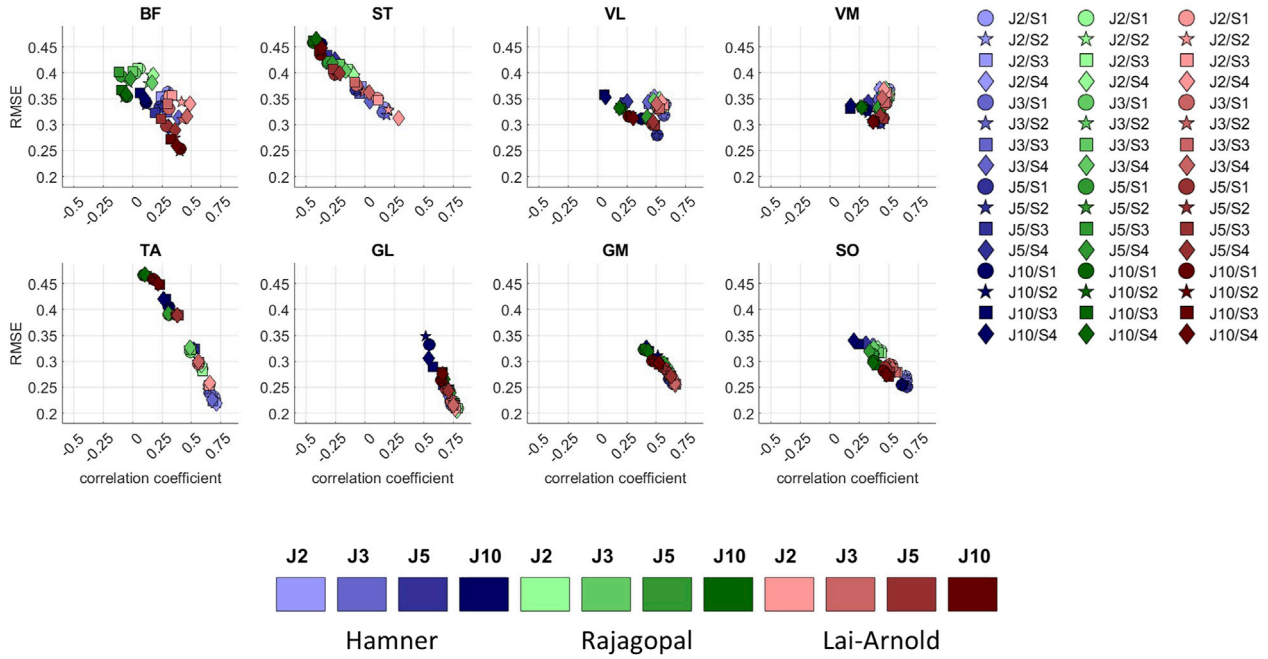

FIGURE 4
RMSE *versus* correlation coefficient (r) between normalized EMGs and estimated muscle excitations in 8 muscles, averaged values among all subjects and speeds, with performance criteria based on minimization of muscle effort to the power of 2 (J2), 3 (J3), 5 (J5), and 10 (J10), illustrated with darkening colors, and scaling variants of linear scaling of OFL and TSL and generic MIF (S1), non-linear scaling of OFL and TSL and generic MIF (S2), linear scaling of OFL and TSL and scaled MIF (S3), and non-linear scaling of OFL and TSL and scaled MIF (S4).

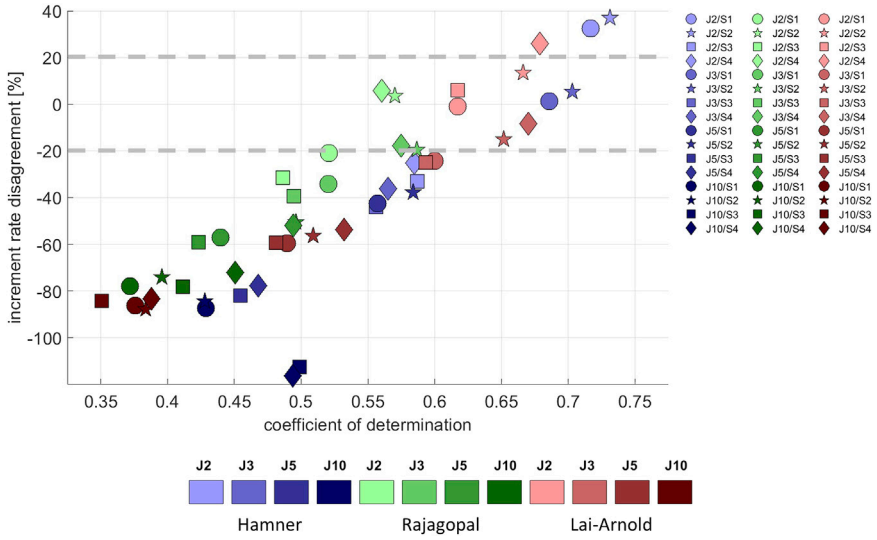

FIGURE 5
Increment rate disagreement between experimental and estimated excitations *versus* the coefficient of determination, averaged values among all subjects, speeds and muscles, with performance criteria based on minimization of muscle effort to the power of 2 (J2), 3 (J3), 5 (J5), and 10 (J10), and scaling variants with linear scaling of OFL and TSL and generic MIF (S1), non-linear scaling of OFL and TSL and generic MIF (S2), linear scaling of OFL and TSL and scaled MIF (S3), and non-linear scaling of OFL and TSL and scaled MIF (S4). The best estimates can be considered to lie approximately +/- 20%.

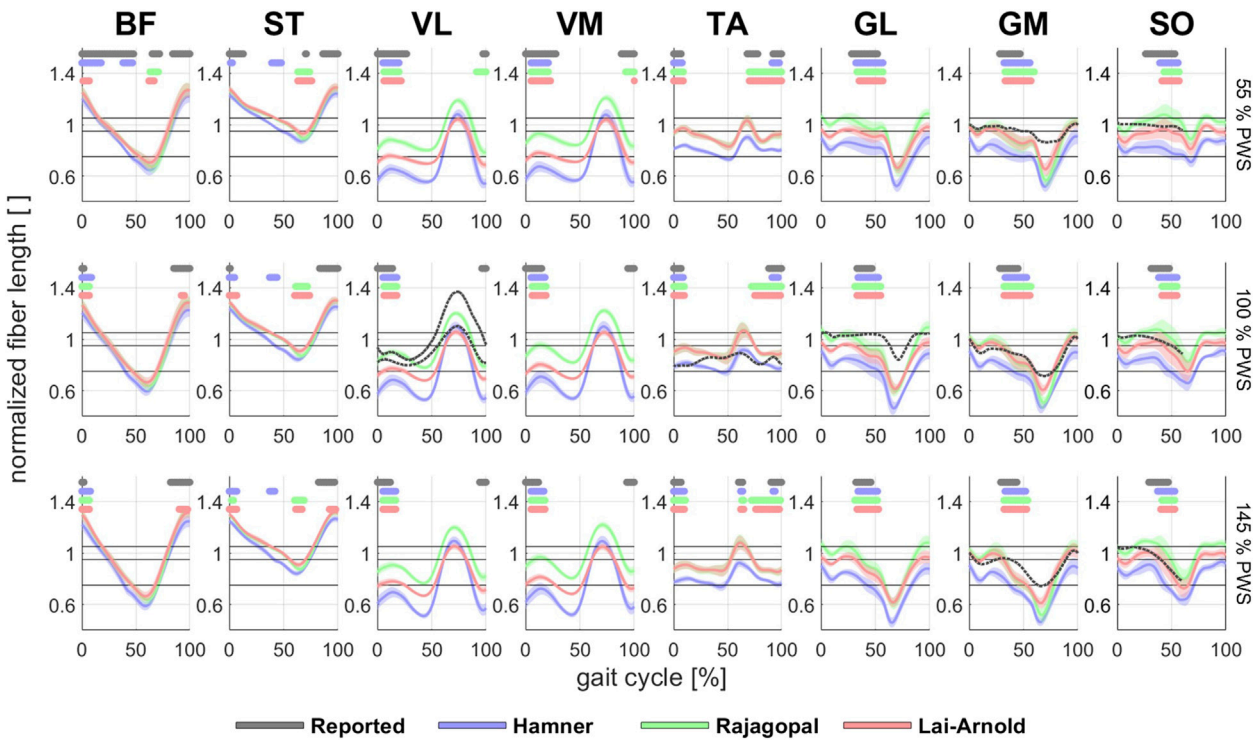

FIGURE 6
Estimated normalized fiber length (average +/- 1 SD of all subjects) in 8 muscles with performance criterion J2 and scaling variant S1 at walking speeds of 55%, 100% and 145% PWS. Reported experimental normalized fiber lengths of SO (Lai et al., 2015), GM (Farris and Sawicki, 2012), GL (Farris and Raiteri, 2017), and VL (Chleboun et al., 2007; Bohm et al., 2018) are shown. Experimental fiber lengths were normalized based on average values reported from a muscle architecture data set (Ward et al., 2009) if experimental studies did not provide normalized values. Horizontal lines above time series indicate on/off timing for EMG and each model. Dashed horizontal lines indicate operating ranges between steep and shallow ascending limb (lower), shallow ascending limb and plateau (middle), and plateau and descending limb (upper).

model and scaling variants without scaled MIF (S1 and S2) and the Lai-Arnold model with scaling method. Time-series agreement in GM and GL were similar in all models with any scaling variant. Time-series agreement in VL and VM were similar with Rajagopal and Lai-Arnold models and any scaling variant, and with the Hamner model and scaling variants without scaled MIF (S1 and S2). Time-series agreement in ST and BF was poor in all models (Figures 1, 4).

Average EMG increased approximately linearly with increasing walking speed (Supplementary Figure S2), as did estimated muscle excitation in all models, scaling variants and performance criteria (Supplementary Figure S3). The performance criterion had the largest influence on the agreement between the predicted and observed excitation/speed increments, with performance criteria J2 and J3 resulting in the best agreement (lowest increment rate disagreement and highest coefficient of determination with EMG increment rate) in all models (Figure 5). Increment rate agreement with the Hamner model was more influenced with MIF scaling (S3 and S4) than with OFL and TSL scaling (S1 and S2), but agreement was not notably better in any model with any specific scaling variant.

In estimated excitation/speed increments in individual muscles from all models, the lowest increment rate disagreement was observed with performance criterion J2, followed by J3. Increment rate agreement varied among model combinations and muscles; no single model combination best estimated increment rate for all muscles (Supplementary Table S5). The increment rates in SO were best estimated with the Rajagopal model, in GM and VM with the Lai-Arnold model, and in GL and TA with the Hamner model using scaling variants without scaled MIF (S1 and S2). The increment rate of VL was highly influenced by scaling variant. Increment rates in ST and BF were not estimated accurately with any model or scaling variant. The Hamner model with scaling variants without scaled MIF (S1 and S2) tended to overestimate increment rates in GM, VM, and VL and to underestimate them in SO. The Rajagopal model tended to underestimate increment rates in GM, GL, and TA and to overestimate them in VL. The Lai-Arnold model tended to underestimate increment rates in SO, GL, and TA.

Computed muscle fiber lengths varied among the different models and scaling variants. All models with linearly scaled OFL and TSL (S1) estimated different fiber lengths, largely visible as length offsets but similar length changes. Fiber lengths estimated by the Rajagopal model agreed best with reported experimental findings in VL, GL, GM, and SO (Figure 6). MTU actuators of VL and GM were active during shallow ascending limb region, and SO, during shallow ascending limb and plateau regions, which coincided with reported values in the literature. Fiber lengths of BF, ST and TA estimated by Rajagopal, and Lai-Arnold models operated at similar regions. The Hamner model estimated shorter muscle fibers than the other models in all muscles. The most notable fiber length differences between models were observed in the VL, VM, and SO, where the muscles contracted at distinct operating ranges within the gait cycle. All models overestimated the excursion of the fiber lengths in GL and GM (especially the Rajagopal model), none of them estimated an isometric contraction in the VL during stance (Chleboun et al., 2007; Bohm et al., 2018), and none of them estimated the TA fiber length nor length changes well. In addition, slight differences were observed when OFL and TSL were linearly (S1) and non-linearly (S2) scaled (Supplementary Figure S4). For example, larger GL an GM fiber excursion was estimated with non-linear vs. linear OFL and TSL scaling, associated with higher MTU compliance (Table 1).

Discussion

We have performed an extensive sensitivity analysis to investigate the influence of musculoskeletal models, scaling variants and optimization criteria for solving muscle redundancy, as well on the interactions between them, on estimation of muscle excitation as time series and over a range of walking speed, specifically how well they agree with experimentally observed EMG signals from a group of able-bodied adults. For each gait cycle, 48 different model combinations were computed and analyzed. We have illustrated which combination(s) of musculoskeletal model, MTU scaling variant, and performance criterion estimates 1) muscle excitations as time series and as excitation/speed increments that agree best with observed EMGs, and 2) muscle fiber lengths that best agree with reported experimentally-measured fiber lengths. We found that the best excitation on/off timing agreement was estimated with performance criterion J2 in all models The best time-series agreement was estimated using a performance criterion J2 with the Lai-Arnold model and any scaling variant, and with the Hamner model and scaling variant without scaled MIF (S1 and S2). The best excitation/speed increment rate agreement was estimated with performance criterion J2, followed by, J3 in all models. No single models best estimated muscle excitation time series or increment rates for all muscles; the agreement varied among model combinations. The Rajagopal model predicted fiber lengths and length change patterns that most closely resembled those reported in literature, though some discrepancies were observed in all models.

Among performance criteria, muscle excitations across walking speeds were estimated best when minimizing muscle effort to a power of 2 (J2) than to higher powers, which corroborates findings in a recent study evaluating the effect of performance criterion for walking at a self-selected speed (Zargham et al., 2019). Ackermann and van den Bogert proposed that neural commands were estimated better by minimizing muscle effort to the power of 10 (Ackermann and van den Bogert, 2010), which is practically equivalent to a min/max criterion (Rasmussen et al., 2001). The results in the present study contradict these findings to some degree; for instance, we observed that a higher exponent produced higher excitations during the swing phase, which did not correspond to observed EMGs time-series profiles (Supplementary Figure S1). This contradiction might be due in part to model sophistication; Ackermann and van den Bogert used a simplified 2D musculoskeletal model with eight muscles and estimated ground reaction force and kinematics, whereas we used 3D musculoskeletal models with a large number of muscles and prescribed inverse kinematics and inverse dynamics solutions, similar to Zargham et al. (Zargham et al., 2019). In addition, a simulation study from Arnold et al. (Arnold et al., 2013) reported good on/off timing estimations using computed muscle control (Thelen et al., 2003), with performance criterion of minimization of muscle effort to the power of 2. Our findings therefore support a recommendation to optimize for muscle redundancy base on a minimization of muscle effort to a power of 2 or perhaps 3 to estimate muscle excitations over walking speeds when kinematics and reaction forces are known.

Our findings do not clearly support any single MTUs scaling variant. It is unlikely that simple methods to scale MTUs accurately represent muscle architecture since muscle properties do not correlate well with anthropometric measurements, but scaling may improve muscle excitation estimation. Medical imaging studies using MRI have shown that muscle volume correlates reasonably well with height, and with body mass in young, healthy adults (Handsfield et al., 2014; Charles et al., 2019b). However, OFL did not correlate well with leg length (Ward et al., 2009; Charles et al., 2019b). It is hard to scale based on anthropometric measurements, and its accuracy will affect MIF estimation (Eq. 1). Specific tension at each muscle (Maganaris et al., 2001) is not well known. In this regard, we found that no single scaling method improved estimated muscle excitations, i.e., agreement with EMGs, for all muscles and all models, though some degree of personalization could result in better estimations of muscle excitation. Using non-linear scaling of OFL and TSL and scaled MIF (S4), the Lai-Arnold model had better time-series estimations

(Figure 3), and the Rajagopal model had better increment rate agreement (Figure 5), than without scaling. Despite this improvement, MIF scaling was based on estimating observations in young adults (Handsfield et al., 2014). Thus, these findings should not be extrapolated to other populations, such as children or persons with neuromuscular disorders.

Estimations of muscle excitations with the Hamner model were not improved with non-linear vs. linear OFL and TSL scaling and were even worse when MIF was scaled. Good estimations of on/off timing were achieved at different speeds in most muscles, but the magnitudes (Figure 1) were considerably higher than those estimated by other models, and normalized fiber lengths were shorter than those from reported experimental observations (Figure 6). Substantially high muscle excitations can be attributable to low MIF values and shorter normalized fiber lengths, which also disagreed with their corresponding values derived from experimental observations. The Hamner model adopted MIF values from the model developed by Delp et al. (Delp et al., 1990) with some modifications. MIF was computed based on physiological cross-sectional area from both cadavers (Delp et al., 1990) as in the Delp model and also healthy individuals (Carhart, 2000), and incorporated scaling factors that varied between muscles. These tuned values were substantially lower than MIF values derived from a single dataset based on muscle volume in healthy adults (Handsfield et al., 2014), which the Rajagopal and Lai-Arnold model incorporate. The scaled MIF values in the Hamner model were slightly smaller than those in the Rajagopal and Lai-Arnold models, except in VL and VM, where incidentally the lowest time-series and excitation/speed increment agreement were found. The scaled MIF in VL from the Hamner model was even higher than those reported from maximal isometric knee extension (Bohm et al., 2018). Also, normalized fiber lengths estimated from musculoskeletal modelling are typically lower than those measured experimentally with ultrasound (Figure 6). The combination of low MIF values and short normalized fiber lengths produced a low force-generation capacity, which, for instance, resulted in an estimation that the SO reaches full excitation at high walking speeds (Figure 1).

Some disagreements between estimated muscle excitations and EMGs were common across models, scaling methods, and performance criteria, which indicates that other modeling simplifications or experimental limitations might underlie these discrepancies. Estimated plantarflexor excitation was delayed with respect to EMG, which may be attributable to inaccuracies in representing MTU parameters and activation dynamics. Delabastita et al. demonstrated better temporal agreement with observed excitations when OFL, TSL, PA, and tendon stiffness parameters were personalized using ultrasound information and recorded EMGs (Delabastita et al., 2020). Also, activation dynamics, rate encoding, and motor unit recruitment were simplified into a first-order differential model with the same activation and deactivation time constants for all muscles and all subjects, whereas these parameters have been reported as functions of muscle fiber-type composition (Winters, 1995) and age (Thelen, 2003). The electromechanical delays, i.e. the duration between muscle twitch and force production, also depends on several factors such as muscle fiber-type composition, firing rate dynamics, and viscoelastic properties of the muscle and connective tissue (De Luca, 1997), none of which were modeled in the current study.

All simulations estimated lower co-activation compared to observed EMGs, which might be related to the optimization and performance criteria. MTU controls generally minimize overall muscle effort, whereas co-activation is a likely response to increase stability in dynamics tasks (Oomen et al., 2015). A high exponent in the performance criterion increased co-activation (Supplementary Figure S1) but resulted in excitation estimates that agreed poorly for all models and scaling variants (Figures 3, 5). Modeling approaches in which MTU controls are solved by minimizing muscle effort and including feedforward and feedback control to account for sensory and motor noise (Van Wouwe et al., 2022) or by regulating mechanical impedance at the joints (Shourijeh and Fregly, 2020), better represent intrinsic motor coordination characteristics; these approaches are more likely to better estimate co-activation than minimizing muscle effort with a high exponent.

Some disagreements between estimated fiber lengths and reported experimentally-measured fiber lengths in literature are also common across models, scaling variants, and performance criteria, and are related to the models' simplified muscle geometry. The Rajagopal model best estimated fiber lengths in VL, GL, GM, and SO, though the estimated fiber excursions were larger than those reported in the literature. A major reason for this is that modelling a muscle as unidimensional actuators does not provide a sufficient representation to capture muscle contraction throughout the volume; Aeles et al. report variations in fiber length and length changes in different fascicles of the same muscle (Aeles et al., 2022). Similarly, muscle attachments are modelled as points, whereas they in reality are surface areas. A study compared a three-dimensional fiber geometry and a lumped parameter model and showed that lumped parameter models overestimated fiber excursion (Blemker and Delp, 2006). Another factor involved in overestimating muscle excursion might be the tendon stiffness value. Modeling tendon as compliance seems a critical assumption as its influences fiber length excursion during walking (Lichtwark and Wilson, 2007; Lai et al., 2015). This study adopted the value of the Achilles tendon's stiffness from a previous study (Delabastita et al., 2020) which allowed us to estimate similar fiber length patterns in GL, GM, and SO similar to reported with experimental observations. Nonetheless, it was assumed that triceps surae muscles shared the same normalized stiffness (equal to 15), which affected each

model differently as its absolute (non-normalized) value depended upon MIF and TSL and, therefore, varied among muscles.

Also, other modeling simplifications have likely influenced fiber length estimations. For instance, patellar and quadriceps tendons were not modeled independently in any of the models, whereas they have been demonstrated to have different functions and mechanical properties (Sprague et al., 2019). In addition, measuring skeletal motion in the foot requires multi-segmental foot models, which in turn influence fiber lengths in triceps surae muscles (Zandbergen et al., 2020). By incorporating a more detailed description of patellar and quadriceps tendons, and bone foot geometry, it would be expected to capture muscle paths better and improve the representativeness of MTU mechanics in generic models.

Further limitations in studying the validity of musculoskeletal models should be noted. First, evaluation of estimated muscle excitations as time series largely consisted of comparing them to observed surface EMGs, but surface EMG signals in turn are sensitive to electrode placement, muscle fatigue, crosstalk from nearby muscles, and data post-processing methods. Furthermore, surface EMGs were measured with one bipolar sensor per muscle. It has been reported that EMG signals may vary among different regions of the same muscle (Vigotsky et al., 2018). In addition, modelled MTU time-dependent behavior will change if a different simulation approach is adopted, for instance, in dynamically consistent or in EMG-informed simulations. Thus, the results of these studies should be interpreted in the context of the modelling approach.

In terms of the generalizability of the results, the evaluation was performed using a direct collocation dynamic optimization which represents some advantages with respect to other algorithms used to solve muscle redundancies such as static optimization and computed muscle control (Thelen et al., 2003). For instance, the tendon deformation is neglected in static optimization, which might not be an appropriate assumption in large tendons such as the Achilles tendon (Lai et al., 2015) and patellar tendon (Bohm et al., 2018), and computed muscle control is sensitive to mass and inertia properties, as well as the initial time of the simulation (Wesseling et al., 2014). In contrast, the algorithm developed by DeGroote et al. incorporates tendon compliance and has a more robust formulation of the dynamic optimization than using direct shooting methods (De Groote et al., 2016). In addition, the software toolkit OpenSim Moco has been recently implemented in OpenSim, and uses direct collocation methods similar to the algorithm used in this study (Dembia et al., 2020). In this regard, our results should be compatible with the ones provided by OpenSim Moco when the inverse kinematic and inverse dynamic solutions are prescribed.

Future work to improve biofidelity of estimated muscle excitations from generic musculoskeletal models may include more detailed descriptions of muscle and bone geometry and paths and incorporate more experimental observations for their validation. We also conclude that evaluating biofidelity with on/off timing agreement and reliance on reserve actuators is insufficient to characterize MTU mechanics, as different musculoskeletal models, scaling methods, and optimization criteria estimate different fiber length patterns with good on/off timing agreement and no dependency in reserve actuators. As such, caution must be taken in interpreting estimations across different load conditions, for instance, the prediction of metabolic energetics within different walking speeds, as estimates might be misleading if MTU time-dependent behavior such as muscle excitations or fiber lengths are not adequately validated.

Finally, the Lai-Arnold model using non-linear scaling of OFL and TSL and scaled MIF with a performance criterion based on muscle effort squared better captured muscle excitations among all the variants evaluated in this study. Interestedly, the Rajagopal model, using either linear or non-linear scaling of OFL and TSL and scaled MIF with a performance criterion based on muscle effort squared, better captured fiber lengths compared to reported data in the literature. The Lai-Arnold model was derived from the Rajagopal model, and similarities were therefore expected. However, the modifications performed by Lai et al. (Lai et al., 2018) in the original formulation of the Rajagopal model improved muscle excitation estimations across walking speeds, particularly in the BF, and ST (Figures 1, 4), but yielded a higher disagreement of fiber lengths, especially in the VL. Thus, it is suggested that, among all the variants evaluated in this study, the Lai-Arnold model using non-linear scaling of OFL and TSL and scaled MIF with performance criterion based on muscle effort squared might be preferred if muscle excitation estimates are the outcomes of interest, but caution is advised in interpreting fiber length estimations. On the other hand, the Hamner model had the lowest biofidelity, which also led to the low force-generation capacity of the MTU actuators compared to other models. Therefore, the accuracy of the estimations of the muscle-tendon dynamics, particularly at high walking speeds, should be considered in the context of its application.

Conclusion

In this study, three generic musculoskeletal models, four scaling variants, and four performance criteria based on muscle effort minimization were performed to examine how they influence estimated muscle excitations as time series, based on experimental data at different walking speeds. Interactions between them were analyzed to determine which modelling combination estimated muscle excitations and fiber lengths that best agreed with observed EMGs at different walking speeds. We found best on/off timing and excitation/speed increment rates agreement

with the performance criterion of minimized muscle effort to the power of 2 in all models and scaling methods, compared to criteria with higher powers. Among models and scaling variants, we found best time-series agreements with the Hamner model without scaled MIF and with the Lai-Arnold model with non-linearly scaled OFL and TSL and scaled MIF. Overall, muscle excitations were best estimated with the Lai-Arnold model, but fiber lengths best agreed with previously reported experimentally-measured fiber lengths with the Rajagopal model. Despite moderately good estimated excitations in most muscles, the Hamner model required higher reserve actuators and estimated fiber lengths that agreed least with those reported in the literature. Common disagreements with EMG were observed in all model combinations, such as excitation delays and underestimated co-activation, which point to both model simplifications and to human motor behavior complexity.

Data availability statement

The raw data supporting the conclusion of this article will be made available by the authors, without undue reservation.

Ethics statement

The studies involving human participants were reviewed and approved by Swedish Ethical Review Authority. The patients/participants provided their written informed consent to participate in this study.

Author contributions

IL and EMG-F conceived the study concept and design. IL performed the data collection, processed the data, scaled the musculoskeletal models, and drafted the manuscript. IL and MA set up the simulation pipeline. EMG-F, MA, and FD analyzed and interpreted the results, and edited the manuscript. EMG-F obtained funding and supervised the study. All authors revised the final version of the manuscript.

Funding

This work was conducted with support from the Swedish Research Council (nr 2018-00750) and Promobilia Foundation (nr 18200).

Acknowledgments

The authors thank Lara Wehrmeyer, Antea Destro, and Davíð Ármann for their support in the data collection and processing.

Conflict of interest

The authors declare that the research was conducted in the absence of any commercial or financial relationships that could be construed as a potential conflict of interest.

Publisher's note

Supplementary material

The Supplementary Material for this article can be found online at: https://www.frontiersin.org/articles/10.3389/fbioe.2022.1002731/full#supplementary-material

References

Ackermann, M., and van den Bogert, A. J. (2010). Optimality principles for model-based prediction of human gait. *J. Biomech.* 43, 1055–1060. doi:10.1016/j.jbiomech.2009.12.012

Aeles, J., Bolsterlee, B., Kelp, N. Y., Dick, T. J. M., and Hug, F. (2022). Regional variation in lateral and medial gastrocnemius muscle fibre lengths obtained from diffusion tensor imaging. *J. Anat.* 240, 131–144. doi:10.1111/joa.13539

Arnold, A. S., Asakawa, D. J., and Delp, S. L. (2000). Do the hamstrings and adductors contribute to excessive internal rotation of the hip in persons with cerebral palsy? *Gait Posture* 11, 181–190. doi:10.1016/S0966-6362(00)00046-1

Arnold, E. M., and Delp, S. L. (2011). Fibre operating lengths of human lower limb muscles during walking. *Phil. Trans. R. Soc. B* 366, 1530–1539. doi:10.1098/rstb.2010.0345

Arnold, E. M., Hamner, S. R., Seth, A., Millard, M., and Delp, S. L. (2013). How muscle fiber lengths and velocities affect muscle force generation as humans walk and run at different speeds. *J. Exp. Biol.* 216, 2150–2160. doi:10.1242/jeb.075697

Arnold, E. M., Ward, S. R., Lieber, R. L., and Delp, S. L. (2010). A model of the lower limb for analysis of human movement. *Ann. Biomed. Eng.* 38, 269–279. doi:10.1007/s10439-009-9852-5

Blemker, S. S., and Delp, S. L. (2006). Rectus femoris and vastus intermedius fiber excursions predicted by three-dimensional muscle models. *J. Biomech.* 39, 1383–1391. doi:10.1016/j.jbiomech.2005.04.012

Bohannon, R. W. (1997). Comfortable and maximum walking speed of adults aged 20-79 years: Reference values and determinants. *Age Ageing* 26, 15–19. doi:10.1093/ageing/26.1.15

Bohm, S., Marzilger, R., Mersmann, F., Santuz, A., and Arampatzis, A. (2018). Operating length and velocity of human vastus lateralis muscle during walking and running. *Sci. Rep.* 8, 5066–5110. doi:10.1038/s41598-018-23376-5

Carhart, M. R. (2000). *Biomechanical analysis of compensatory stepping: Implications for paraplegics standing via FNS [dissertation/PhD's thesis*. Tempe, Arizona: Arizona State University.

Charles, J. P., Grant, B., D'Août, K., and Bates, K. T. (2020). Subject-specific muscle properties from diffusion tensor imaging significantly improve the accuracy of musculoskeletal models. *J. Anat.* 237, 941–959. doi:10.1111/joa.13261

Charles, J. P., Moon, C. H., and Anderst, W. J. (2019a). Determining subject-specific lower-limb muscle architecture data for musculoskeletal models using diffusion tensor imaging. *J. Biomech. Eng.* 141. doi:10.1115/1.4040946

Charles, J. P., Suntaxi, F., and Anderst, W. J. (2019b). *In vivo* human lower limb muscle architecture dataset obtained using diffusion tensor imaging. *PLoS One* 14, 02235311–e223618. doi:10.1371/journal.pone.0223531

Chleboun, G. S., Busic, A. B., Graham, K. K., and Stuckey, H. A. (2007). Fascicle length change of the human tibialis anterior and vastus lateralis during walking. *J. Orthop. Sports Phys. Ther.* 37, 372–379. doi:10.2519/jospt.2007.2440

De Groote, F., Kinney, A. L., Rao, A. V., and Fregly, B. J. (2016). Evaluation of direct collocation optimal control problem formulations for solving the muscle redundancy problem. *Ann. Biomed. Eng.* 44, 2922–2936. doi:10.1007/s10439-016-1591-9

De Luca, C. J. (1997). The use of surface electromyography in biomechanics. *J. Appl. Biomech.* 13, 135–163. doi:10.1123/jab.13.2.135

Delabastita, T., Afschrift, M., Vanwanseele, B., and De Groote, F. (2020). Ultrasound-based optimal parameter estimation improves assessment of calf muscle–tendon interaction during walking. *Ann. Biomed. Eng.* 48, 722–733. doi:10.1007/s10439-019-02395-x

Delp, S. L., Loan, J. P., Hoy, M. G., Zajac, F. E., Topp, E. L., and Rosen, J. M. (1990). An interactive graphics-based model of the lower extremity to study orthopaedic surgical procedures. *IEEE Trans. Biomed. Eng.* 37, 757–767. doi:10.1109/10.102791

Dembia, C. L., Bianco, N. A., Falisse, A., Hicks, J. L., and Delp, S. L. (2020). OpenSim Moco: Musculoskeletal optimal control. *PLoS Comput. Biol.* 16, 10084933–e1008521. doi:10.1371/journal.pcbi.1008493

Farris, D. J., and Raiteri, B. J. (2017). Elastic ankle muscle-tendon interactions are adjusted to produce acceleration during walking in humans. *J. Exp. Biol.* 220, 4252–4260. doi:10.1242/jeb.159749

Farris, D. J., and Sawicki, G. S. (2012). Human medial gastrocnemius force-velocity behavior shifts with locomotion speed and gait. *Proc. Natl. Acad. Sci. U. S. A.* 109, 977–982. doi:10.1073/pnas.1107972109

Hamner, S. R., Seth, A., and Delp, S. L. (2010). Muscle contributions to propulsion and support during running. *J. Biomech.* 43, 2709–2716. doi:10.1016/j.jbiomech.2010.06.025

Handsfield, G. G., Meyer, C. H., Hart, J. M., Abel, M. F., and Blemker, S. S. (2014). Relationships of 35 lower limb muscles to height and body mass quantified using MRI. *J. Biomech.* 47, 631–638. doi:10.1016/j.jbiomech.2013.12.002

Heintz, S., and Gutierrez-Farewik, E. M. (2007). Static optimization of muscle forces during gait in comparison to EMG-to-force processing approach. *Gait Posture* 26, 279–288. doi:10.1016/j.gaitpost.2006.09.074

Hermens, H. J., Freriks, B., Disselhorst-Klug, C., and Rau, G. (2000). Development of recommendations for SEMG sensors and sensor placement procedures. *J. Electromyogr. Kinesiol.* 10, 361–374. doi:10.1016/s1050-6411(00)00027-4

Hicks, J. L., Uchida, T. K., Seth, A., and Delp, S. L. (2015). Is my model good enough ? best practices for verification and validation of musculoskeletal models and simulations of movement. *J. Biomech. Eng.* 137. doi:10.1115/1.4029304

Krogt, M. M. Van Der, Bar-on, L., Kindt, T., Desloovere, K., and Harlaar, J. (2016). Neuro-musculoskeletal simulation of instrumented contracture and spasticity assessment in children with cerebral palsy. *J. Neuroeng. Rehabil.* 1, 64–11. doi:10.1186/s12984-016-0170-5

Lai, A. K. M., Arnold, A. S., Wakeling, J. M., Biology, E., and Station, C. F. (2018). Why are antagonist muscles co-activated in my simulation? A musculoskeletal model for analysing human locomotor tasks. *Ann. Biomed. Eng.* 45, 2762–2774. doi:10.1007/s10439-017-1920-7

Lai, A., Lichtwark, G. A., Schache, A. G., Lin, Y. C., Brown, N. A. T., and Pandy, M. G. (2015). *In vivo* behavior of the human soleus muscle with increasing walking and running speeds. *J. Appl. Physiol. (1985).* 118, 1266–1275. doi:10.1152/japplphysiol.00128.2015

Lichtwark, G. A., and Wilson, A. M. (2007). Is Achilles tendon compliance optimised for maximum muscle efficiency during locomotion? *J. Biomech.* 40, 1768–1775. doi:10.1016/j.jbiomech.2006.07.025

Lotti, N., Xiloyannis, M., Durandau, G., Galofaro, E., Sanguineti, V., Masia, L., et al. (2020). Adaptive model-based myoelectric control for a soft wearable arm exosuit: A new generation of wearable robot control. *IEEE Robot. Autom. Mag.* 27, 43–53. doi:10.1109/MRA.2019.2955669

Maganaris, C. N., Baltzopoulos, V., Ball, D., and Sargeant, A. J. (2001). *In vivo* specific tension of human skeletal muscle. *J. Appl. Physiol. (1985).* 90, 865–872. doi:10.1152/jappl.2001.90.3.865

Modenese, L., Ceseracciu, E., Reggiani, M., and Lloyd, D. G. (2016). Estimation of musculotendon parameters for scaled and subject specific musculoskeletal models using an optimization technique. *J. Biomech.* 49, 141–148. doi:10.1016/j.jbiomech.2015.11.006

Oomen, N. M. C. W., Reeves, N. P., Priess, M. C., and van Dieën, J. H. (2015). Trunk muscle coactivation is tuned to changes in task dynamics to improve responsiveness in a seated balance task. *J. Electromyogr. Kinesiol.* 25, 765–772. doi:10.1016/j.jelekin.2015.07.001

Rajagopal, A., Dembia, C. L., DeMers, M. S., Delp, D. D., Hicks, J. L., and Delp, S. L. (2016). Full-body musculoskeletal model for muscle-driven simulation of human gait. *IEEE Trans. Biomed. Eng.* 63, 2068–2079. doi:10.1109/TBME.2016.2586891

Rasmussen, J., Damsgaard, M., and Voigt, M. (2001). Muscle recruitment by the min/max criterion - a comparative numerical study. *J. Biomech.* 34, 409–415. doi:10.1016/S0021-9290(00)00191-3

Rubenson, J., Pires, N. J., Loi, H. O., Pinniger, G. J., and Shannon, D. G. (2012). On the ascent: The soleus operating length is conserved to the ascending limb of the force-length curve across gait mechanics in humans. *J. Exp. Biol.* 215, 3539–3551. doi:10.1242/jeb.070466

Shourijeh, M. S., and Fregly, B. J. (2020). Muscle synergies modify optimization estimates of joint stiffness during walking. *J. Biomech. Eng.* 142, 011011–011019. doi:10.1115/1.4044310

Son, J., Indresano, A., Sheppard, K., Ward, S. R., and Lieber, R. L. (2018). Intraoperative and biomechanical studies of human vastus lateralis and vastus medialis sarcomere length operating range. *J. Biomech.* 67, 91–97. doi:10.1016/j.jbiomech.2017.11.038

Sprague, A., Epsley, S., and Silbernagel, K. G. (2019). Distinguishing quadriceps and patellar tendinopathy : Semantics or significant? *J. Orthop. Sports Phys. Ther.* 49, 627–630. doi:10.2519/jospt.2019.0611

Swinnen, W., Hoogkamer, W., De Groote, F., and Vanwanseele, B. (2019). Habitual foot strike pattern does not affect simulated triceps surae muscle metabolic energy consumption during running. *J. Exp. Biol.* 22, jeb212449–19. doi:10.1242/jeb.212449

Thelen, D. G. (2003). Adjustment of muscle mechanics model parameters to simulate dynamic contractions in older adults. *J. Biomech. Eng.* 125, 70–77. doi:10.1115/1.1531112

Thelen, D. G., Anderson, F. C., and Delp, S. L. (2003). Generating dynamic simulations of movement using computed muscle control. *J. Biomech.* 36, 321–328. doi:10.1016/S0021-9290(02)00432-3

Van Wouwe, T., Ting, L. H., and De Groote, F. (2022). An approximate stochastic optimal control framework to simulate nonlinear neuromusculoskeletal models in the presence of noise. *PLoS Comput. Biol.* 18, 10093388–e1009430. doi:10.1371/journal.pcbi.1009338

Vigotsky, A. D., Halperin, I., Lehman, G. J., Trajano, G. S., and Vieira, T. M. (2018). Interpreting signal amplitudes in surface electromyography studies in sport and rehabilitation sciences. *Front. Physiol.* 8, 985–1015. doi:10.3389/fphys.2017.00985

Ward, S. R., Eng, C. M., Smallwood, L. H., and Lieber, R. L. (2009). Are current measurements of lower extremity muscle architecture accurate? *Clin. Orthop. Relat. Res.* 467, 1074–1082. doi:10.1007/s11999-008-0594-8

Wesseling, M., de Groote, F., and Jonkers, I. (2014). The effect of perturbing body segment parameters on calculated joint moments and muscle forces during gait. *J. Biomech.* 47, 596–601. doi:10.1016/j.jbiomech.2013.11.002

Winby, C. R., Lloyd, D. G., and Kirk, T. B. (2008). Evaluation of different analytical methods for subject-specific scaling of musculotendon parameters. *J. Biomech.* 41, 1682–1688. doi:10.1016/j.jbiomech.2008.03.008

Winters, J. M. (1995). An improved muscle-reflex actuator for use in large-scale neuromusculoskeletal models. *Ann. Biomed. Eng.* 23, 359–374. doi:10.1007/BF02584437

Zajac, F. E. (1989). Muscle and tendon: Properties, models, scaling, and application to biomechanics and motor control. *Crit. Rev. Biomed. Eng.* 17, 359–411.

Zandbergen, M. A., Schallig, W., Stebbins, J. A., Harlaar, J., and van der Krogt, M. M. (2020). The effect of mono- versus multi-segment musculoskeletal models of the foot on simulated triceps surae lengths in pathological and healthy gait. *Gait Posture* 77, 14–19. doi:10.1016/j.gaitpost.2020.01.010

Zargham, A., Afschrift, M., De Schutter, J., Jonkers, I., and De Groote, F. (2019). Inverse dynamic estimates of muscle recruitment and joint contact forces are more realistic when minimizing muscle activity rather than metabolic energy or contact forces. *Gait Posture* 74, 223–230. doi:10.1016/j.gaitpost.2019.08.019

frontiers | Frontiers in Bioengineering and Biotechnology

TYPE Original Research
PUBLISHED 02 December 2022
DOI 10.3389/fbioe.2022.1038116

OPEN ACCESS

EDITED BY
Navrag B. Singh,
ETH Zürich, Switzerland

REVIEWED BY
Gregorio Marchiori,
Rizzoli Orthopedic Institute (IRCCS), Italy
Tjarco ALTA,
Spaarne Gasthuis, Netherlands

*CORRESPONDENCE
Qing Han,
my.hanqing@163.com
Jincheng Wang,
jinchengwangjlu@163.com

†These authors have contributed equally to this work and share first authorship

SPECIALTY SECTION
This article was submitted to Biomechanics, a section of the journal Frontiers in Bioengineering and Biotechnology

RECEIVED 06 September 2022
ACCEPTED 22 November 2022
PUBLISHED 02 December 2022

CITATION
Wan Q, Zhang A, Bai H, Liu Y, Chen H, Zhao X, Wang X, Han Q and Wang J (2022), Cause analysis of the liner dissociation of a customized reverse shoulder prosthesis based on finite element analysis.
Front. Bioeng. Biotechnol. 10:1038116.
doi: 10.3389/fbioe.2022.1038116

Cause analysis of the liner dissociation of a customized reverse shoulder prosthesis based on finite element analysis

Qian Wan†, Aobo Zhang†, Haotian Bai, Yang Liu, Hao Chen, Xin Zhao, Xiaonan Wang, Qing Han* and Jincheng Wang*

Department of Orthopedics, The Second Hospital of Jilin University, Changchun, China

Background: Dissociation of the polyethylene liner after reverse shoulder arthroplasty could cause shoulder dislocation that could not achieve closed reduction. The cause of liner dissociation is currently unclear.

Method: Non-homogeneous model of the bone was constructed and dynamic finite element analysis was utilized to simulate the impingement of the polyethylene liner and scapula during humeral adduction. The stress distribution of the fixation claws, their degree of deformation (DOD), and the stress of the impingement sites in three initial humeral postures (neutral, 30° flexion, and 30° extension) were measured and analyzed. The influence of the liner material stiffness was also investigated.

Result: The impingement stress on the liner and scapula was 100–200 MPa, and different humeral postures caused different locations of impingement points. The fixation claws' maximum principal stress (MPS) results were below 5 MPa. In the connection area between some fixation claws and the liner, compressive stresses on the inside and tensile stresses on the outside were observed, which showed that the fixation claws were prone to deform toward the center direction. The maximum DOD results of three initial humeral postures (neutral, 30° flexion, and 30° extension) were 3.6%, 2.8%, and 3.5%, respectively. The maximum DOD results of neutral initial humeral posture were 0.51% and 11.4% when the elastic modulus of the liner was increased and decreased by a factor of 10, respectively.

Conclusion: The humeral adduction impingement could lead to the deformation of the claw-shaped liner fixation structure, which might be one of the reasons for the liner dissociation. The increased stiffness of the liner material helped to reduce the deformation of the fixation structure.

KEYWORDS

reverse total shoulder arthroplasty, finite element analysis, polyethylene liner dissociation, shoulder dislocation, fixation, impingement

1 Introduction

The reverse shoulder prosthesis was invented to compensate for the loss of rotator cuff function in the 1970s, which was the opposite design of the anatomic shoulder prosthesis (Hansen and Routman, 2019). The incidence of primary reverse total shoulder arthroplasty (RTSA) has increased substantially in recent years. It reached 19.3 cases per 100,000 in 2017 in the United States, which was 2.64 times the incidence in 2012 (Best et al., 2021). However, the design of reverse shoulder prosthesis frequently causes impingement between the scapular pillar and the polyethylene liner of the humeral component (Friedman et al., 2019). This impingement was considered related to scapular notching, polyethylene wear, and glenoid implant loosening (Mollon et al., 2017; Griffiths et al., 2020). Efforts were made to reduce impingement by altering the design or placement of the prosthesis. Inferior tilt of the glenosphere, lateral offset of the glenosphere, placing the glenosphere inferiorly, and decreasing the neck shaft angle of the humeral component are considered to decrease the tendency of the impingement. However, these parameters are not independent, they influence each other and affect the deltoid moment, the stress on the prosthesis, etc (Ackland et al., 2015). Therefore, the optimal prosthesis design and placement are not yet conclusive.

Dislocation of the shoulder joint is a common complication after RTSA, sometimes accompanied by the dissociation between the polyethylene liner and the metal tray in some cases, which prevents closed reduction and necessitates operative revision. This poses significant challenges for surgeons (Nizlan et al., 2009; Patel et al., 2017; Paynter et al., 2020). There have been some case reports of polyethylene liner dissociation (Nizlan et al., 2009; Patel et al., 2017; Paynter et al., 2020). However, the biomechanical mechanism of liner dissociation is still unclear. In a case series of four patients with liner dissociation reported by Patel et al, (2017), the fixation structure of the liner was severely deformed, resulting in fixation failure. Patel speculated that the cause of the liner dissociation might be the impingement between the liner and the scapula (Figure 1A). Nevertheless, further mechanism investigation was not conducted. The liner dissociation also happened to one of our patients. The used polyethylene liner of the prosthesis had a similar claw-shaped fixation structure to that used in Patel's case, which was found to be deformed (Figure 1B). There was a clinical study showed that 80% of late postoperative shoulder dislocations had evidence of adduction impingement and polyethylene liner failure (Kohan et al., 2017), so it is reasonable to suppose that the liner dissociation is related to the adduction impingement between the liner and the scapula.

To verify this hypothesis, observation of the liner fixation structure deformation during the adduction impingement is necessary. However, it is hard to capture the deformation *via* video radiography because of the precision limitation of the radiography system and the non-visualization of the polyethylene liner (Miranda et al., 2011; Patel et al., 2017). Computer simulation is a suitable method to investigate this question. Finite element analysis (FEA) has increasingly been used in the medical field, particularly in orthopedics where it can guide the design and optimization of prostheses (Liu et al., 2020;

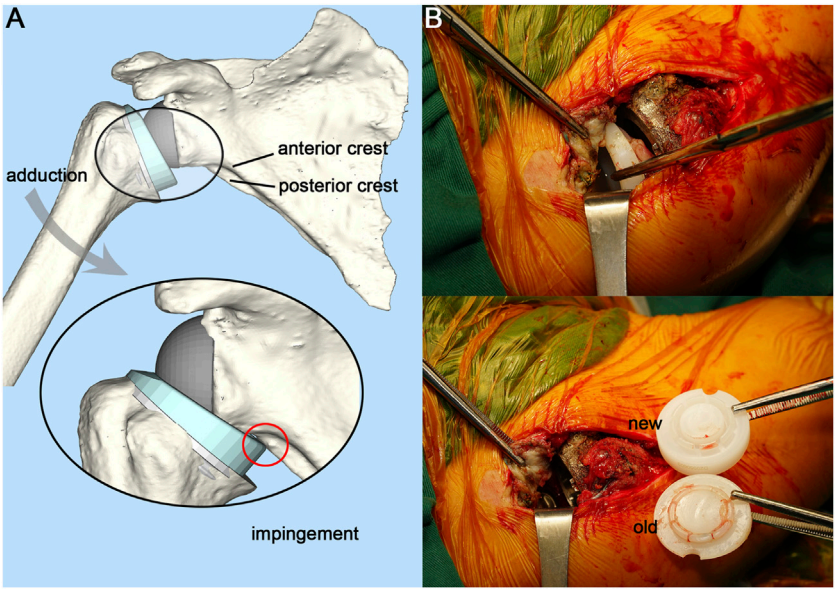

FIGURE 1
Illustration of adduction impingement and intraoperative photograph. **(A)**, Illustration of adduction impingement. **(B)**, Exposed joint cavity with visible polyethylene liner dissociation and intraoperative comparison of the new and the old liner.

Zhang et al., 2021). Using this technique, we could dynamically simulate the impingement between the liner and the scapula, and precisely observe the deformation and the stress state of the polyethylene liner.

In this study, based on a case of shoulder dislocation with liner dissociation after RSTA, the FEA was selected to investigate whether adduction impingement is a cause of the liner dissociation of the prosthesis with this kind of claw-shaped fixation structure. The impingement between the polyethylene liner and the scapula during humeral adduction was dynamically simulated. Meanwhile, solutions to decrease the incidence of liner dissociation were also proposed.

2 Materials and methods

2.1 Clinical data

The patient was a 52-year-old male with a complaint of right shoulder joint pain and limited movement for two months. The patient had undergone an anatomical shoulder arthroplasty 11 years ago. Due to prosthesis loosening and limited shoulder movement, the patient underwent a customized 3D printed reverse shoulder prosthesis (AK Medical, Beijing, China) revision surgery 7 years ago. The neck shaft angle of the prosthesis was 140°. The baseplate was positioned neutrally and centrally on the glenoid. Detailed treatment information was presented in a case report (Zou et al., 2018). The postoperative functional examination of the shoulder joint revealed that when the patient's arm was adducted close to the chest wall, the deltoid muscle was tense due to stretching. This is caused by the leverage generated by the contact between the liner and the scapula. At subsequent follow-up, the patient reported feeling friction within the joint during the walking arm swing. These demonstrated the presence of impingement and friction between the polyethylene liner and the scapula. The patient now has shoulder pain and limited movement. X-rays showed that the right shoulder was dislocated. After clinical evaluation, the surgeon decided to perform revision surgery.

2.2 Surgical procedure

The patient was placed in the left lateral position, and the right shoulder joint was routinely disinfected with iodophor. The right shoulder joint was incised from the rostral process, along the anterior border of the deltoid muscle, and ends at the humeral stop of the deltoid muscle, about 15 cm long. The patient had intact infraspinatus, teres minor, and teres major muscles. There was a moderate tear in the supraspinatus and subscapularis muscles. The deltoid muscle was separated under direct vision, and the anterior portion of the humeral shaft was incised at its stop to prevent damage to the axillary nerve branches. The short head of the biceps tendon was held medially, and the shoulder joint was flexed to reveal the joint cavity. The polyethylene liner was found to be completely detached and was removed. The fixation claws of the old liner had deformed and contracted towards the middle disc-shaped protrusion (Figure 1B), which caused the fixation claws to fail to snap into the metal tray. The scapular component of the prosthesis was properly polished and fitted with a suitable new liner. Accordingly, the humeral component was cleaned and trimmed to the proper size. The shoulder joint was reset and had good mobility and stability. The postoperative X-ray showed a satisfactory position of the shoulder joint. The patient had satisfactory shoulder function and was able to complete daily life activities at the 3-month follow-up.

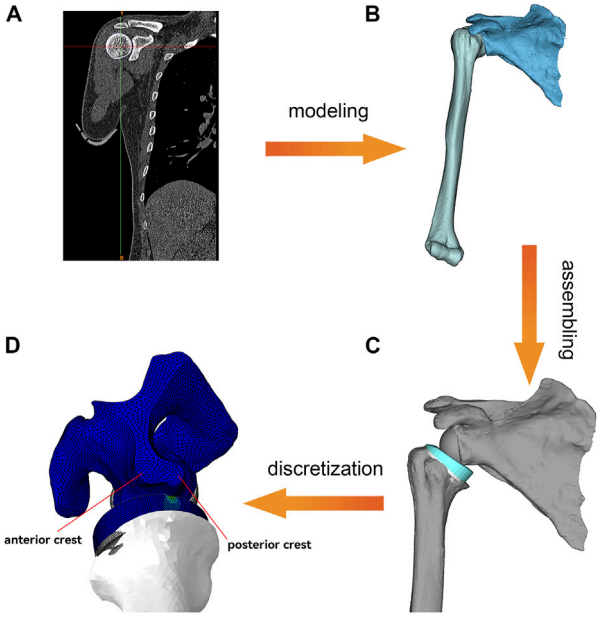

FIGURE 2
Overview of the FEA process. **(A)**, Shoulder CT data processing. **(B)**, Generation of scapula and humerus 3D models. **(C)**, Bone model and prosthesis model assembly and Meshing. **(D)**, Dynamic FEA. The lower border of the scapula is divided into a flat anterior crest and a narrow posterior crest.

2.3 Finite element analysis

A finite element (FE) model was developed to dynamically simulate the impingement between the polyethylene liner and the scapular pillar during humeral adduction. The entire experimental procedure is summarized in Figure 2. Supplementary Video S1 shows the impingement process and the Von Mises stress distribution.

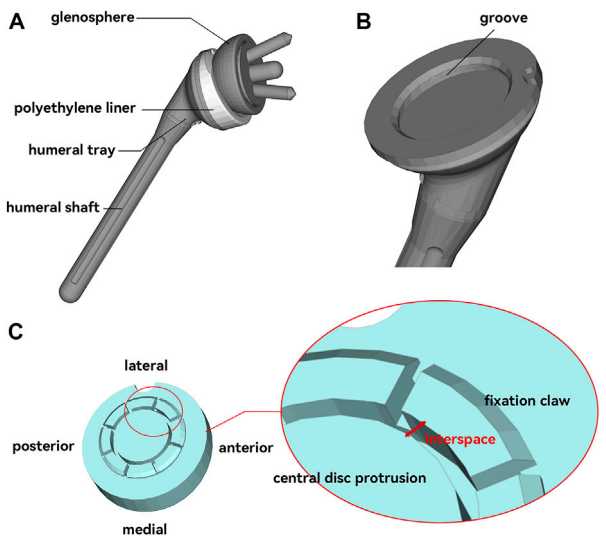

FIGURE 3
Reverse shoulder joint prosthesis model. **(A)**, Composition of the reverse shoulder joint prosthesis. **(B)**, Metal humeral tray with a groove that can catch the polyethylene liner. **(C)**, Polyethylene liner with eight symmetrical "claw" structures for fixation to the tray. The interspace between the claws and the intermediate disc-like protrusion was used as an indicator for this study.

2.3.1 Model building

This study was approved by the ethics committee of The Second Hospital of Jilin University approved. Informed consent was offered by the volunteer. The CT data of the volunteer's shoulder were collected through the Philips iCT 256 CT scanner at 156 mA and 120 kVp with a slice thickness of 0.602 mm and exported in DICOM format. MIMICS 21.0 (Materialise, Belgium) was used to reconstruct the shoulder joint. Then the shoulder joint model was exported in standardized trigonometric language (STL) format. The medial part of the scapula was truncated to improve the simulation efficiency. The type of prosthesis was customized to the shape of the patient's bone defect and 3D printed by the prosthesis manufacturer (AK Medical, Beijing, China). Its fixation structure was the claws on the underside of the liner (Figure 3C). The reverse shoulder prosthesis used in this study consisted of a scapular component and a humeral component. The scapular component included the glenoid base and glenosphere. The humeral component included the polyethylene liner, metal tray, and shaft (Figure 3). The assembly of the prosthesis and bone was performed under the supervision of an experienced surgeon. Both the humeral component and the glenosphere were placed in a neutral position without lateralization or tilt.

2.3.2 Meshing and boundary condition setting

For discretization, all components were imported into Hypermesh 2020 (Altair Engineering, Troy, MI, United States) software. The components were divided into tetrahedral meshes of different sizes. A convergence test was performed to ensure the precision of the analysis. Three mesh sizes (1.5 mm, 1.2 mm, and 1.0 mm) of the liner were tested. The stress results difference for 1.2 mm and 1.0 mm was 1.1%. Four mesh sizes (4 m, 3 mm, 2.5 mm, and 2.0 mm) of the scapula were tested. The stress results difference for 2.5 mm and 2.0 mm was 6.0%. The mesh size of 1.0 mm for the liner and 2.0 mm for the scapula could meet the accuracy requirements of the analysis. The mesh size of the scapular component, glenosphere, and humeral shaft was set to 2 mm. Due to the small features and the region of interest to observe the stress distribution, the mesh size of the polyethylene liner and the humeral tray was refined to 0.75 and 1 mm, respectively.

The model was then imported into Abaqus 2021 (Dassault Systèmes, France) for the boundary conditions setting. Contact between the glenosphere and the shoulder glenoid, as well as the contact between the humeral shaft and the metal tray, were set to tie constraint (no relative movement was allowed between the parts in contact). All other surface contacts were set to be friction contacts with a friction coefficient of 0.07 (Quental et al., 2015). Because of the large difference in the elastic modulus between the metallic components and the polyethylene, all metallic materials were set up as analytical rigid bodies to improve the simulation efficiency. The material property of polyethylene liner was defined as isotropic linear elastic. The Young's modulus was 850 MPa, the Poisson's ratio was 0.44, and the density was 0.94 g/cm^3. The Poisson's ratio value used for bone was 0.3. The density (ρ) and the elastic modulus (E) of the bone were calculated from the following formulas based on the grayscale values (HU) of the CT images (Mo et al., 2019):

$$\rho\left(\mathrm{g/m^3}\right) = -13.4 + 1017\,\mathrm{HU} \quad (1)$$

$$\mathrm{E(Pa)} = -388.8 + 5925\rho\left(\mathrm{g/m^3}\right) \quad (2)$$

The rotator cuff in the shoulder joint aids in internal rotation, external rotation, and abduction. It also squeezes the humeral head toward the scapular glenoid to stabilize the shoulder joint and prevent dislocation (Ackland et al., 2015). Since the active force processes of the muscles were not involved in this study, the rotator cuff was simplified to two nonlinear springs assemblies with anterior-posterior symmetry, which served to stabilize the shoulder joint and prevent dislocation (Hettrich et al., 2015) (Figure 4A). A 3.5 kg point mass was placed at the end of the humeral shaft (near the arm's center of gravity) to represent the arm's weight. The initial posture of the humeral component was set to 40° of abduction (Figure 4A). Except for the neutral initial posture, 40° abduction accompanied by 30° flexion or extension was also simulated (Figure 4B) to investigate the effect of different arm initial postures on the impingement. The medial plane of the scapula was set to be fully fixed, and then a gravitational acceleration of 9.8 m/s^2 was applied to the entire system. The entire simulation was performed as an explicit dynamic analysis with an analysis time of 0.4 s. The arm was

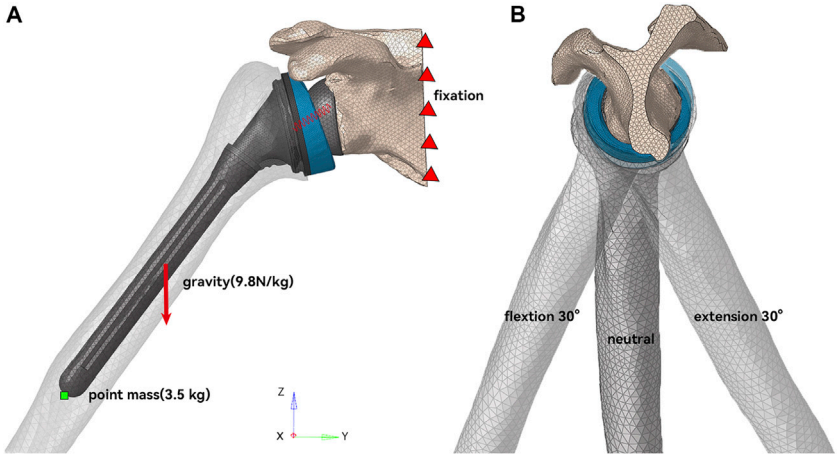

FIGURE 4
Schematic diagram of model working condition setting. **(A)** In the coronal plane, the humerus was initially abducted at 40°. **(B)** In the sagittal plane, the humerus had three initial postures of neutral, 30° flexion, and 30° extension.

simulated to adduct under gravity and impinge. In addition, the cases of 10* and 0.1* elastic modulus of the liner were simulated to study the effect of liner material stiffness.

2.3.3 Evaluation indicators

The Von Mises stress at the impingement location and the maximum principal stress (MPS) on the polyethylene liner were obtained. The Von Mises stress was used to assess the material failure of the polyethylene liner and the bone. The MPS was obtained to show the tendency of the fixation claw's deformation. The interspaces between the fixation claws and the central disc protrusion before and after impingement were also recorded and analyzed to quantify the degree of deformation (DOD) of the fixation claw (Figure 3C). It was measured at four randomly selected points on each claw. The DOD was defined as the percentage change in the interspace before and after the impingement, which could be expressed as the following formula:

$$\mathrm{DOD} = \mathrm{average}\left(\frac{intb - inta}{inta} * 100\%\right) \quad (3)$$

where *intb* was the interspace before impingement, *inta* was the interspace after impingement.

3 Result

3.1 Von Mises stress of the impingement point

The Von Mises stress at the impingement point in neutral, flexion, and extension humeral postures is shown in Figure 5. In the neutral posture, the liner impinged on both the anterior and posterior crest of the scapular pillar, with a maximum stress of 120 MPa on the scapula. There were two impingement points on the liner, located posteromedially, with a maximum stress of 145.7 MPa at the impingement point. In the 30° flexion posture, the impingement point for the scapular pillar and the liner was the anterior crest and posteromedial of the liner. The maximum stress on the scapula and the liner were 125.4 MPa and 152.9 MPa, respectively. In the 30° extension posture, the impingement point for the scapular pillar and the liner was the posterior crest and medial of the liner. The maximum stress on the scapular pillar and the liner were 160.7 MPa and 211.3 MPa, respectively.

3.2 Maximum principal stress distribution in fixation claws

Unlike the impingement point, the magnitude of the stress value on the fixation claws was much smaller, with the absolute value mostly less than 5 MPa (Figure 6). In the connection area between some fixation claws and the liner, compressive stress on the inside (Figure 6B) and tensile stress on the outside (Figure 6C) were observed. It represented a tendency for this part of the fixation claws to deform inward during liner impingement. Such regions were observed in the liner's anterior-medial, anterior, and lateral positions when the humerus was in neutral, flexion, and extension postures, respectively (Figure 6A).

3.3 Degree of deformation

The DOD results are shown in Table 1 and Figure 7, consistent with the fixation claws' MPS results. The DOD was

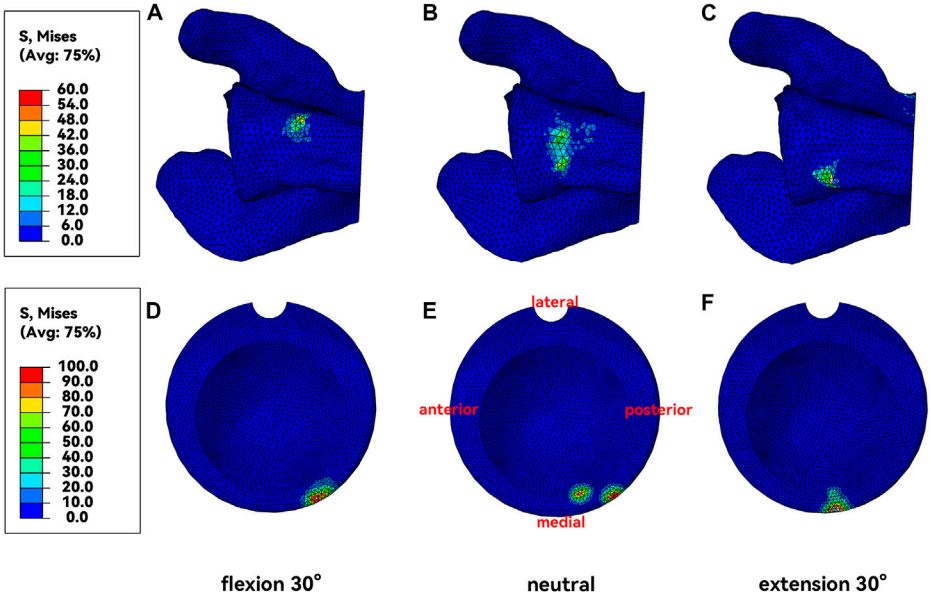

FIGURE 5
Von Mises Stress at the impingement point. **(A&D)**, Neural posture. **(B&E)**, Flexion posture. **(C&F)**, Extension posture.

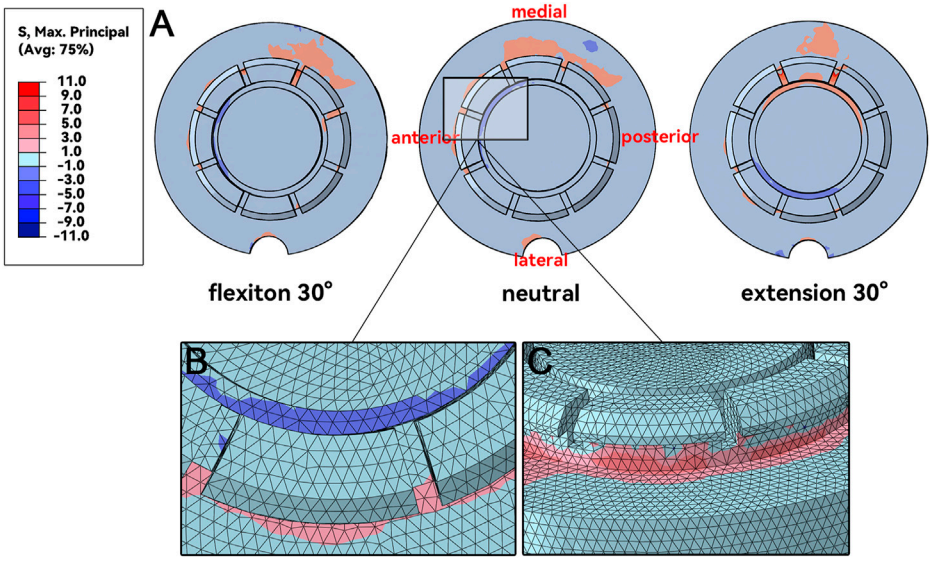

FIGURE 6
MPS at fixation claws. **(A)**, maximum principal stresses distribution. **(B&C)**, details of the inner side and outer side of the connection area.

relatively large in the area where high MPS occurred. In neutral, flexion, and extension postures, the maximum DOD were 3.6%, 2.8%, and 3.5%, respectively (Figure 7A). Changing the elastic modulus of the liner could affect the deformation of the fixation claws (Figure 7B). In the neutral initial posture, when the elastic modulus of the liner was multiplied by 10, the maximum DOD was only 0.51%. Furthermore, due to the significant elastic modulus difference between cortical bone and UHMWPE, the maximum Von Mises stress at the scapular impingement point was 155.8 MPa, similar to the results of normal liner stiffness.

TABLE 1 DOD*100% for different fixation claws.

	Neutral	Flexion	Extension	High elastic modulus	Low elastic modulus
Lateral	0.52	0.90	3.48	0.17	2.20
Lateral-anterior	1.28	2.10	2.99	0.26	7.25
Anterior	3.04	2.78	1.44	0.51	11.36
Anterior-medial	3.55	1.76	−0.47	0.42	9.63
Medial	2.59	1.02	0.24	0.19	6.62
Medial-posterior	1.76	0.71	−0.56	0.15	6.48
Posterior	0.99	0.11	−0.17	0.09	0.64
Posterior-lateral	0.58	0.17	1.97	0.04	−1.10

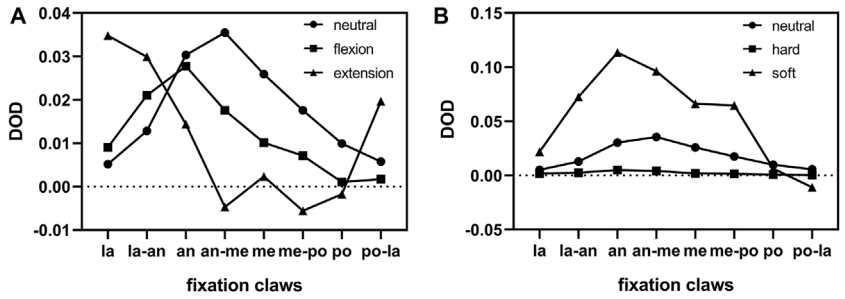

FIGURE 7
Distribution of DOD for different fixation claws. **(A)**, Comparison of different humeral postures. **(B)**, Comparison of different liner stiffnesses. la = lateral, an = anterior, me = medial, po = posterior.

When the elastic modulus was reduced by 10 times, DOD reached 11.4%. The maximum Von Mises stress at the scapular impingement point was 45.8 MPa.

4 Discussion

Polyethylene liner wear and deformation is one of the most common causes of late failure after reverse shoulder arthroplasty, which originates from the impingement of the scapula and the polyethylene liner (Friedman et al., 2019). Dislocation of the shoulder joint after RTSA causes great trouble when accompanied by the dissociation of the polyethylene liner (Garberina and Williams, 2008; Nizlan et al., 2009; Patel et al., 2017). In this study, FEA was used to investigate whether the liner dissociation of the prosthesis with this kind of claw-shaped fixation structure was related to adduction impingement.

Most FEA studies of reverse shoulder prosthesis used the static analysis method, so the role of inertia was not essential and could be ignored (Denard et al., 2017; Ingrassia et al., 2018; Zhang et al., 2020). However, the impingement is a high-speed and dynamic process, and a fully dynamic finite element model is necessary (Cooper et al., 2019). It is tough to apply muscle forces with constantly changing magnitude and direction during this fully dynamic process. Therefore, the process of arm adduction under gravity and without the active muscle forces was simulated in this study. Nevertheless, in real life, the adduction of the arm is often accompanied by muscle force control, making the impingement of the scapula with the liner less intense than under the action of gravity alone. Thus, the stress and deformation due to the impingement obtained were higher due to the neglect of muscle forces.

The acquired results indicated two impingement points on the liner when the humerus was in neutral posture during the adduction process (Figure 5B). This was due to an anatomical detail that was easily overlooked. The lower edge of the scapular pillar is divided into two crests: the anterior and posterior crest, where the anterior crest is flatter, and the posterior crest is narrower (Figures 1A, Figure 2D). When the humerus adducted from the neutral posture, the liner impinged with both crests. The impingement points were located on the posteromedial side (Figure 5A), which was consistent with

previous clinical studies (Lewicki et al., 2017). The impingement point of the liner was directly medial (Figure 5F) only when the humerus was in extension posture during adduction. At this time, the liner impinged with the narrower posterior crest, resulting in a stress of 160.7 MPa, higher than that of neutral posture and flexion posture. Nevertheless, humerus adduction from extension posture is less common in daily life than neutral and flexion posture.

Whether the impingement started from flexion, extension, or neutral posture inward, the stress generated on the liner exceeded 100 MPa, far beyond the yield stress of the UHMWPE (Pascual et al., 2012). There was no obvious difference in the magnitude of impingement stress generated by different impingement postures. Even though the real-life impingement with muscle control might not be that fierce, the liner was easily damaged. The maximum stress at the impingement point of the scapula reached 160 MPa in the extension posture and 120 MPa in both the flexion and neutral postures, which is less than the yield stress of the cortical bone (Heiner, 2008). According to these results, we might suspect that the scapular notch was not generated based on direct stress damage brought by adduction impingement, but based on the frictional wear. The particle debris produced by polyethylene wear was reported to contribute to the generation of the scapular notch (Levigne et al., 2008). The mechanism of the scapular notch generation needs further study.

The locations and the stress of the impingement points were discussed above. However, the direct reason for the liner dissociation was the failure of the fixation structure. In order to reflect the deformation direction of the fixation claws, the MPS was chosen to demonstrate the stress state of the liner fixation structure. When the stress on the structure was positive or negative, it meant that the structure was under tension or compression. The MPS distribution indicated that some fixation claws tended to deform inward. In the adjacent area between the fixation claws and the liner, the inner side was subjected to compressive stress while the outer side was subjected to tensile stress (Figures 6B,C). The fixation claws with high MPS varied when the impingement postures varied (Figure 6A). It is worth mentioning that the stress on the fixation claws did not reach the yield stress (Pascual et al., 2012), so the fixation claws did not enter the plastic deformation stage. The deformation might be the creep deformation caused by long-term stress (Glyn-Jones et al., 2008). A study of the creep behavior of polyethylene liner in hip prosthesis showed that creep deformation accounted for a large portion (up to 63%) of polyethylene liner deformation during gait simulation (Penmetsa et al., 2006). However, the creep behavior of polyethylene liner in reverse shoulder prosthesis has not been studied.

The MPS distribution was verified by the DOD results of the fixation claws. Figure 7 shows that most fixation claws deformed inward after the impingement. The areas with the greatest deformation were those with high MPS. The location where the maximum deformation occurred changed with the impingement posture, which explained the deformation of almost all fixation claws in our clinical case. Our arms are regularly in a neutral or flexion posture in daily life. Thus, when the impingement occurs in these postures, the fixation claws' anterolateral, anterior, and anterolateral regions are more prone to deform (Figure 6A). In a case reported by Patel et al., a portion of the fixation claws were deformed (Patel et al., 2017). However, it is unknown whether this was the anterior fixation claw from the pictures in the paper. Therefore, the results above need to be validated by more multicenter long-term follow-ups.

To find a solution to reduce the incidence of liner dissociation, whether changing the elastic modulus of the liner material contributes to reducing the deformation of the liner fixation structure was investigated. As we know, the higher the elastic modulus of a material, the smaller its deformation at the same state of stress. However, the results of our analysis showed that increasing the elastic modulus of the polyethylene liner also increased the stress on its fixation claws. So, the effect of the change in the elastic modulus on the deformation of the fixation structure is worth exploring. The elastic modulus of the liner was increased or decreased tenfold, respectively. The results showed that changing the elastic modulus of the liner material could affect the deformation of the liner (Figure 7A). After the elastic modulus of the liner was multiplied by 10, the average deformation of the fixation claws was reduced to only 12.9% of the original. At the same time, the maximum impingement stress on the scapula was 155.8 MPa, which increased by 29.8% compared to the original. Based on this result, ideas for liner improvement could be proposed: we could improve the elastic modulus of UHMWPE by modifying the manufacturing process to decrease the deformation of the fixation structure (Ansari et al., 2016). We could use ceramic material, which also significantly reduces the osteolysis from debris generation (Sonntag et al., 2012). Besides, the claw-shaped fixation structure may be one of the important reasons for deformation and causing dissociation of the liner, and further research on improved fixation structure is needed.

In addition to improving the material of the liner to reduce liner dissociation, changing the shape parameter and placement of the prosthesis to reduce the impingement is also a viable option and has been studied extensively (Friedman et al., 2019). Reducing the neck shaft angle of the humeral component, and inferior overhang/inferior tilt/lateral offset of the glenosphere could reduce the impingement and improve the adduction angle (Gutierrez et al., 2008; Roche et al., 2013; Langohr et al., 2016). There are also eccentric glenospheres designed to increase inferior overhang while keeping screw fixation in the glenoid (Poon et al., 2014). However, some alterations might have a negative impact at the same time. Inferior tilt of the glenosphere would cause uneven distribution of the joint reaction load compared to the neutral tilt (Gutierrez et al., 2011). An excessive inferior overhang of the glenosphere might cause hypertonicity of the deltoid muscle (Friedman et al., 2019). Reducing the neck shaft angle of the humeral component causes the glenosphere to contact at the edge of the polyethylene liner, increasing contact pressure and increasing the generation of wear particles (Langohr et al., 2016). Therefore, the surgeon has to choose

the appropriate prosthesis and its placement according to the anatomical characteristics of the patient's shoulder.

Some aspects of this study need to be improved in the future. Firstly, the UHMWPE was defined as a linear elastic material. Since the stress at the impingement point already exceeded the yield stress of UHMWPE, the linear elastic material did not fully reflect the properties of UHWPMPE. However, the stresses of the fixation claws, which were the focus of this study, did not exceed the yield stress. Liner elastic material definition was enough and would not affect the significance of the results. Secondly, this study was based on a clinical case, and the results acquired in this simulation study need to be validated by more multicenter long-term follow-ups.

5 Conclusion

In this paper, based on a case of dissociation of the polyethylene liner in a reverse shoulder prosthesis, the adduction impingement of the liner and the scapular pillar was analyzed using finite element analysis, and the results showed contraction and deformation of the fixation claws of the liner, consistent with the case observation. Thus adduction impingement may be one of the reasons for the dissociation of the liner with this claw-shaped fixation structure. Creep might be one of the mechanisms for the permanent deformation of fixed structures, however, further experimental verification is needed. The stiffness of the liner material could affect the degree of deformation of the fixation claws. In the future, we can prevent liner dissociation by reducing the occurrence of impingement (by modifying the prosthesis design) or by strengthening the liner material.

Data availability statement

The raw data supporting the conclusion of this article will be made available by the authors, without undue reservation.

Ethics statement

The studies involving human participants were reviewed and approved by the ethics committee of The Second Hospital of Jilin University approved. The patients/participants provided their written informed consent to participate in this study. Written informed consent was obtained from the individual(s) for the publication of any potentially identifiable images or data included in this article.

Author contributions

QW: Investigation, Methodology, Visualization, Writing–Original Draft, Writing–Review and Editing; AZ: Investigation, Methodology, Supervision, Validation, Visualization, Writing–Review and Editing; HB: Clinical Data Collection, Software; YL: Software, Validation, Writing–Review and Editing. HC: Software, Validation, Writing–Review and Editing. XZ: Clinical Data Collection, Project Administration. XW: Clinical Data Collection, Project Administration. QH: Conceptualization, Funding Acquisition, Project Administration, Resources, Supervision, Validation, Writing–Review and Editing. JW: Conceptualization, Funding Acquisition, Project Administration, Resources, Supervision, Validation.

Funding

1) National Natural Science Foundation of China (grant numbers 82072456&81802174); 2) National Key R&D Program of China (grant numbers 2018YFB1105100); 3) Department of Science and Technology of Jilin Province, P.R.C (grant numbers 20200404202YY &220200201453JC); 4) Department of finance in jilin province (grant number 2019SCZT046&2020SCZT037); 5) Undergraduate teaching reform research project of Jilin University (grant number 4Z2000610852); 6) Key training plan for outstanding young teachers of Jilin University (grant number 419080520253); 7) Bethune plan of Jilin University (grant number 470110000692); 8) Jilin Province Development and Reform Commission, P.R.C (grant numbers 2018C010).

Conflict of interest

The authors declare that the research was conducted in the absence of any commercial or financial relationships that could be construed as a potential conflict of interest.

Publisher's note

Supplementary material

The Supplementary Material for this article can be found online at: https://www.frontiersin.org/articles/10.3389/fbioe.2022.1038116/full#supplementary-material

References

Ackland, D. C., Patel, M., and Knox, D. (2015). Prosthesis design and placement in reverse total shoulder arthroplasty. *J. Orthop. Surg. Res.* 10, 101. doi:10.1186/s13018-015-0244-2

Ansari, F., Ries, M. D., and Pruitt, L. (2016). Effect of processing, sterilization and crosslinking on UHMWPE fatigue fracture and fatigue wear mechanisms in joint arthroplasty. *J. Mech. Behav. Biomed. Mat.* 53, 329–340. doi:10.1016/j.jmbbm.2015.08.026

Best, M. J., Aziz, K. T., Wilckens, J. H., McFarland, E. G., and Srikumaran, U. (2021). Increasing incidence of primary reverse and anatomic total shoulder arthroplasty in the United States. *J. Shoulder Elb. Surg.* 30 (5), 1159–1166. doi:10.1016/j.jse.2020.08.010

Cooper, R. J., Wilcox, R. K., and Jones, A. C. (2019). Finite element models of the tibiofemoral joint: A review of validation approaches and modelling challenges. *Med. Eng. Phys.* 74, 1–12. doi:10.1016/j.medengphy.2019.08.002

Denard, P. J., Lederman, E., Parsons, B. O., and Romeo, A. A. (2017). Finite element analysis of glenoid-sided lateralization in reverse shoulder arthroplasty. *J. Orthop. Res.* 35 (7), 1548–1555. doi:10.1002/jor.23394

Friedman, R. J., Barcel, D. A., and Eichinger, J. K. (2019). Scapular notching in reverse total shoulder arthroplasty. *J. Am. Acad. Orthop. Surg.* 27 (6), 200–209. doi:10.5435/JAAOS-D-17-00026

Garberina, M. J., and Williams, G. R., Jr. (2008). Polyethylene dissociation after reverse total shoulder arthroplasty: The use of diagnostic arthroscopy. *J. Shoulder Elb. Surg.* 17 (1), e16–e18. doi:10.1016/j.jse.2007.02.131

Glyn-Jones, S., McLardy-Smith, P., Gill, H. S., and Murray, D. W. (2008). The creep and wear of highly cross-linked polyethylene: A three-year randomised, controlled trial using radiostereometric analysis. *J. Bone Jt. Surg. Br. volume* 90 (5), 556–561. doi:10.1302/0301-620X.90B5.20545

Griffiths, M. W., Athwal, G. S., Medley, J. B., Johnson, J. A., and Langohr, G. D. G. (2020). Wear of humeral polyethylene cups in reverse total shoulder arthroplasty with simulated rim damage from scapular notching. *Biotribology* 22, 100123. doi:10.1016/j.biotri.2020.100123

Gutierrez, S., Levy, J. C., Frankle, M. A., Cuff, D., Keller, T. S., Pupello, D. R., et al. (2008). Evaluation of abduction range of motion and avoidance of inferior scapular impingement in a reverse shoulder model. *J. Shoulder Elb. Surg.* 17 (4), 608–615. doi:10.1016/j.jse.2007.11.010

Gutierrez, S., Walker, M., Willis, M., Pupello, D. R., and Frankle, M. A. (2011). Effects of tilt and glenosphere eccentricity on baseplate/bone interface forces in a computational model, validated by a mechanical model, of reverse shoulder arthroplasty. *J. Shoulder Elb. Surg.* 20 (5), 732–739. doi:10.1016/j.jse.2010.10.035

Hansen, M. L., and Routman, H. (2019). The biomechanics of current reverse shoulder replacement options. *Ann. Jt.* 4, 17. doi:10.21037/aoj.2019.01.06

Heiner, A. D. (2008). Structural properties of fourth-generation composite femurs and tibias. *J. Biomech.* 41 (15), 3282–3284. doi:10.1016/j.jbiomech.2008.08.013

Hettrich, C. M., Permeswaran, V. N., Goetz, J. E., and Anderson, D. D. (2015). Mechanical tradeoffs associated with glenosphere lateralization in reverse shoulder arthroplasty. *J. Shoulder Elb. Surg.* 24 (11), 1774–1781. doi:10.1016/j.jse.2015.06.011

Ingrassia, T., Nalbone, L., Nigrelli, V., Ricotta, V., and Pisciotta, D. (2018). Biomechanical analysis of the humeral tray positioning in reverse shoulder arthroplasty design. *Int. J. Interact. Des. Manuf.* 12 (2), 651–661. doi:10.1007/s12008-017-0418-8

Kohan, E. M., Chalmers, P. N., Salazar, D., Keener, J. D., Yamaguchi, K., and Chamberlain, A. M. (2017). Dislocation following reverse total shoulder arthroplasty. *J. Shoulder Elb. Surg.* 26 (7), 1238–1245. doi:10.1016/j.jse.2016.12.073

Langohr, G. D., Willing, R., Medley, J. B., Athwal, G. S., and Johnson, J. A. (2016). Contact mechanics of reverse total shoulder arthroplasty during abduction: The effect of neck-shaft angle, humeral cup depth, and glenosphere diameter. *J. Shoulder Elb. Surg.* 25 (4), 589–597. doi:10.1016/j.jse.2015.09.024

Levigne, C., Boileau, P., Favard, L., Garaud, P., Mole, D., Sirveaux, F., et al. (2008). Scapular notching in reverse shoulder arthroplasty. *J. Shoulder Elb. Surg.* 17 (6), 925–935. doi:10.1016/j.jse.2008.02.010

Lewicki, K. A., Bell, J. E., and Van Citters, D. W. (2017). Analysis of polyethylene wear of reverse shoulder components: A validated technique and initial clinical results. *J. Orthop. Res.* 35 (5), 980–987. doi:10.1002/jor.23353

Liu, Y., Zhang, A., Wang, C., Yin, W., Wu, N., Chen, H., et al. (2020). Biomechanical comparison between metal block and cement-screw techniques for the treatment of tibial bone defects in total knee arthroplasty based on finite element analysis. *Comput. Biol. Med.* 125, 104006. doi:10.1016/j.compbiomed.2020.104006

Miranda, D. L., Schwartz, J. B., Loomis, A. C., Brainerd, E. L., Fleming, B. C., and Crisco, J. J. (2011). Static and dynamic error of a biplanar videoradiography system using marker-based and markerless tracking techniques. *J. Biomech. Eng.* 133 (12), 121002. doi:10.1115/1.4005471

Mo, F., Zhang, H., Zhao, S., Xiao, Z., and Liu, T. (2019). Coupling musculoskeletal dynamics and subject-specific finite element analysis of femoral cortical bone failure after endoprosthetic knee replacement. *Appl. Bionics Biomech.* 2019, 1–8. doi:10.1155/2019/4650405

Mollon, B., Mahure, S. A., Roche, C. P., and Zuckerman, J. D. (2017). Impact of scapular notching on clinical outcomes after reverse total shoulder arthroplasty: An analysis of 476 shoulders. *J. Shoulder Elb. Surg.* 26 (7), 1253–1261. doi:10.1016/j.jse.2016.11.043

Nizlan, N. M., Campbell, P. T., and Skirving, A. P. (2009). Dissociated polyethylene liner after a reverse shoulder replacement: A case report. *J. Shoulder Elb. Surg.* 18 (5), e26–e28. doi:10.1016/j.jse.2009.01.016

Pascual, F. J., Przybilla, C., Gracia-Villa, L., Puertolas, J. A., and Fernandez-Canteli, A. (2012). Probabilistic assessment of fatigue initiation data on highly crosslinked ultrahigh molecular weight polyethylenes. *J. Mech. Behav. Biomed. Mat.* 15, 190–198. doi:10.1016/j.jmbbm.2012.06.004

Patel, K. A., Boyd, K. L., Renfree, K. J., and Hattrup, S. J. (2017). Polyethylene dissociation from humeral stem status after reverse total shoulder arthroplasty. *J. Shoulder Elb. Surg.* 26 (11), e346–e351. doi:10.1016/j.jse.2017.05.004

Paynter, J. W., Griswold, B. G., DeFoor, M. T., Crosby, L. A., and Parada, S. A. (2020). Polyethylene liner dissociation after reverse shoulder arthroplasty dislocation: A case series. *J. Radiol. Case Rep.* 14 (8), 14–23. doi:10.3941/jrcr.v14i8.3836

Penmetsa, J. R., Laz, P. J., Petrella, A. J., and Rullkoetter, P. J. (2006). Influence of polyethylene creep behavior on wear in total hip arthroplasty. *J. Orthop. Res.* 24 (3), 422–427. doi:10.1002/jor.20042

Poon, P. C., Chou, J., Young, S. W., and Astley, T. (2014). A comparison of concentric and eccentric glenospheres in reverse shoulder arthroplasty: A randomized controlled trial. *J. Bone Jt. Surg.* 96 (16), e138. doi:10.2106/JBJS.M.00941

Quental, C., Folgado, J., Fernandes, P. R., and Monteiro, J. (2015). Computational analysis of polyethylene wear in anatomical and reverse shoulder prostheses. *Med. Biol. Eng. Comput.* 53 (2), 111–122. doi:10.1007/s11517-014-1221-3

Roche, C. P., Stroud, N. J., Martin, B. L., Steiler, C. A., Flurin, P. H., Wright, T. W., et al. (2013). The impact of scapular notching on reverse shoulder glenoid fixation. *J. Shoulder Elb. Surg.* 22 (7), 963–970. doi:10.1016/j.jse.2012.10.035

Sonntag, R., Reinders, J., and Kretzer, J. P. (2012). What's next? Alternative materials for articulation in total joint replacement. *Acta Biomater.* 8 (7), 2434–2441. doi:10.1016/j.actbio.2012.03.029

Zhang, A. B., Chen, H., Liu, Y., Wu, N. C., Chen, B. P., Zhao, X., et al. (2021). Customized reconstructive prosthesis design based on topological optimization to treat severe proximal tibia defect. *Biodes. Manuf.* 4 (1), 87–99. doi:10.1007/s42242-020-00102-7

Zhang, M., Junaid, S., Gregory, T., Hansen, U., and Cheng, C.-K. (2020). Impact of scapular notching on glenoid fixation in reverse total shoulder arthroplasty: An *in vitro* and finite element study. *J. Shoulder Elb. Surg.* 29 (10), 1981–1991. doi:10.1016/j.jse.2020.01.087

Zou, Y., Yang, Y., Han, Q., Yang, K., Zhang, K., Wang, J., et al. (2018). Novel exploration of customized 3D printed shoulder prosthesis in revision of total shoulder arthroplasty A case report. *Medicine* 97 (47), e13282. doi:10.1097/md.0000000000013282

frontiers | Frontiers in Bioengineering and Biotechnology

TYPE Original Research
PUBLISHED 19 December 2022
DOI 10.3389/fbioe.2022.967411

OPEN ACCESS

EDITED BY
Yih-Kuen Jan,
University of Illinois at Urbana-Champaign, United States

REVIEWED BY
Ben-Yi Liau,
Hungkuang University, Taiwan
Andreas Martin Seitz,
Ulm University Medical Center, Germany

*CORRESPONDENCE
Cheng-Kung Cheng,
ckcheng2020@sjtu.edu.cn

†These authors have contributed equally to this work and share first authorship

SPECIALTY SECTION
This article was submitted to Biomechanics, a section of the journal Frontiers in Bioengineering and Biotechnology

RECEIVED 12 June 2022
ACCEPTED 06 December 2022
PUBLISHED 19 December 2022

CITATION
Wang H, Fang C, Tao M, Shi Q, He K and Cheng C-K (2022), Hourglass-shaped grafts are superior to conventional grafts for restoring knee stability and graft force at knee flexion angle of 30° following anterior cruciate ligament reconstruction: A finite element analysis.
Front. Bioeng. Biotechnol. 10:967411.
doi: 10.3389/fbioe.2022.967411

Hourglass-shaped grafts are superior to conventional grafts for restoring knee stability and graft force at knee flexion angle of 30° following anterior cruciate ligament reconstruction: A finite element analysis

Huizhi Wang[1†], Chaohua Fang[1,2†], Mingzhu Tao[1], Qinyi Shi[1], Kaixin He[1] and Cheng-Kung Cheng[1*]

[1]Engineering Research Center for Digital Medicine of the Ministry of Education, School of Biomedical Engineering, Shanghai Jiao Tong University, Shanghai, China., [2]Department of Joint Surgery, The 6th Hospital of Ningbo, Ningbo, Zhejiang, China

Background: Anterior cruciate ligament reconstruction (ACLR) using a generally columnar graft is considered the gold standard for treating anterior cruciate ligament ruptures, but such grafts cannot replicate the geometry and mechanical properties of the native anterior cruciate ligament.

Purpose: To evaluate the effectiveness of an innovative hourglass-shaped graft versus a traditional columnar graft for restoring joint stability and graft force, while avoiding notch impingement following anterior cruciate ligament reconstruction.

Methods: Finite element models of a human knee were developed to simulate ① An intact state, ② anterior cruciate ligament reconstruction using columnar grafts with different diameters (7.5–12 mm in 0.5 mm increments), ③ anterior cruciate ligament reconstruction using columnar grafts with different Young's moduli (129.4, 168.0 and 362.2 MPa) and ④ anterior cruciate ligament reconstruction using hourglass-shaped grafts with different Young's moduli. The knee model was flexed to 30° and loaded with an anterior tibial load of 103 N, internal tibial moment of 7.5 Nm, and valgus tibial moment of 6.9 Nm. The risk of notch impingement, knee stability and graft forces were compared among the different groups.

Results: This study found that columnar grafts could not simultaneously restore knee stability in different degree of freedoms (DOFs) and graft force to a level similar to that of the intact knee. The anterior tibial translation and graft force were restored to a near-normal condition when the internal tibial rotation was over-restrained and valgus tibial rotation was lax. A graft diameter of at least 10 mm was needed to restore knee stability and graft force to physiological levels, but such large grafts were found to be at high risk of notch impingement.

In contrast, the hourglass-shaped graft was able to simultaneously restore both knee stability and graft force at knee flexion of 30° while also having a much lower risk of impingement.

Conclusion: Under knee flexion angle of 30°, an hourglass-shaped graft was better able to restore joint stability and graft force to a near-physiological level than columnar grafts, while also reducing the risk of notch impingement.

KEYWORDS

ACL reconstruction, graft geometry, graft force, notch impingement, knee stability

1 Introduction

The anterior cruciate ligament (ACL) is important for normal functionality and movement of the knee joint. However, given the substantial multi-directional loads placed on the ACL, the ligament is prone to injury, particularly from non-contact athletic activities involving side-step cutting, heavy landing and rapid deceleration with the knee near full extension (Hashemi et al., 2007). In cases of ACL rupture when conservative non-invasive treatment is not viable, reconstruction surgery is considered the gold standard treatment. Replacing the ruptured ligament with a graft is expected to restore normal joint kinematics and function. Commonly used ACL grafts include autologous tendons such as the hamstring tendon and the patellar tendon, allogeneic tendons and artificial grafts (Wang et al., 2020a). Different positions, shapes and quantities of bone tunnels have also been used to achieve anatomic and non-anatomic reconstructions of the bone insertions (Yao et al., 2012; Wang et al., 2020b; Cheng et al., 2021; Cheng et al., 2022). Clinical outcomes have been reported to be good to excellent at 2 years post-surgery (Komzak et al., 2021). However, the long-term outcome of reconstruction is less encouraging, with a high incidence of secondary knee osteoarthritis (OA) at 14 years after surgery (Barenius et al., 2014). Other common complications following ACL reconstruction include impingement of the graft on the femoral intercondylar notch and graft rupture (Orsi et al., 2017; Schmucker et al., 2021).

The geometric features and material properties of common graft materials have been found to be significantly different to those of the native ACL. The graft size is often chosen regardless of the size of the native ACL, while the material properties are dependent on the source of the graft (Musahl et al., 2022). The ACL has an hourglass shape, with the areas of its bone insertion sites being over three times larger than the midsubstance (Wang et al., 2022). In contrast, tendon grafts typically have a relatively constant cross-sectional area (Han and Lee, 2019; Ayanoglu et al., 2022), termed a "columnar" shape in this study. Such differences may result in different mechanical behaviors. Similarly, studies have reported variations in the elasticity of commonly used ACL grafts (Wilson et al., 1999), which can have a direct effect on the resulting mechanical behavior (Han and Lee, 2019). Snaebjornsson et al. (2017) found that each incremental increase of 0.5 mm in graft diameter reduced the likelihood of needing revision surgery by 86%. Wang et al. (2020b) reported that larger graft diameters could better restore joint stability, allowing the graft to withstand greater forces while reducing stress concentrations on the articular cartilage. However, Orsi et al. (2017) found a potential for graft impingement on the femoral intercondylar notch if the mid-section of the graft was too large, with small differences in graft size leading to a considerable increase in impingement forces. Wang et al. (2020a) reported that more flexible grafts (low stiffness) may induce less bone tunnel enlargement and exhibit lower graft wear by reducing the stress concentrations at the contact area between the tunnel entrance and the graft. These studies indicate that a small diameter on a columnar graft may compromise joint stability and function, while an overly large diameter may lead to impingement. Also, the graft material is critical for proper functionality of the knee joint. Achieving a balance between these factors may be key to improving the longevity and performance of ACL reconstruction. However, it is unclear whether the size and properties of columnar grafts can be effectively tailored to replace the function of the hourglass-shaped native ACL.

As such, using finite element modeling, this study aims to assess 1) whether the diameter and elasticity of columnar grafts can be tailored to fully restore knee joint stability and graft force while avoiding graft impingement, and 2) whether an hourglass-shaped graft or columnar graft can better replicate the function of the native ACL. Finite element analysis (FEA) was used in this study because it allows the variate to be repeatedly changed without damaging the sample and the variate can be strictly controlled to one factor when the other factors are maintained constant. These advantages allow for different diameters, material properties and shapes of grafts used for ACLR to be assessed individually in this study. The outcomes of this study may provide a scientific basis for improving the design of ACL grafts and improving the clinical outcome of ACL reconstruction.

2 Materials and methods

2.1 Finite element model of the human knee joint

This study used a previously validated finite element (FE) model (Figures 1A, 3A) for all simulations (Wang et al., 2020c). The geometry of the femur, tibia, fibula, articular cartilage,

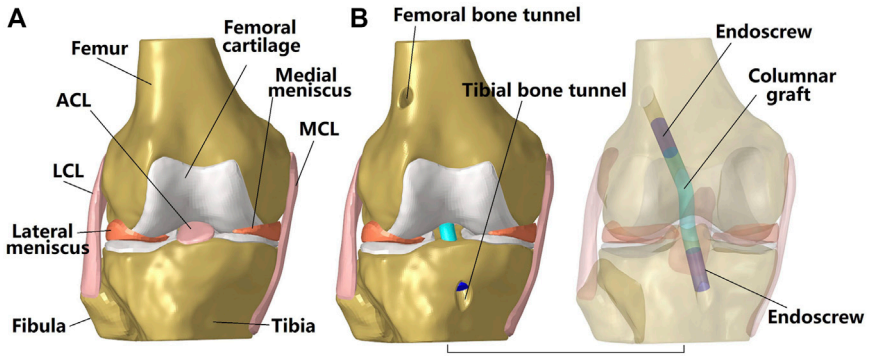

FIGURE 1
Three dimensional model of a cadaveric knee. **(A)** Intact knee; **(B)** Knee after ACL reconstruction using a columnar graft. The transparent model shows the fixation of the graft to the bone tunnel using an endoscrew. One end of the endoscrew was tied with the graft while the outside surface of the screw was tied with the inside wall of the bone tunnel. LCL, lateral collateral ligament; MCL, medial collateral ligament.

menisci, ACL, posterior cruciate ligament, medial collateral ligament and lateral collateral ligament were segmented from MRI images taken with a scan resolution of 0.2 mm × 0.2 mm and slice thickness of 0.2 mm. The model was meshed in HyperMesh 12.0 (Altair Engineering, Tokyo, Japan) using 4-node tetrahedron elements. A mesh convergence test was used to optimize the element size, whereby a 2.5-mm translational load was applied to the tibia while the femur was fixed at full extension of the knee joint to calculate the *in situ* force in the ACL. The element size was decreased until there was a negligible change in the *in situ* force in the ACL. The resulting element size was 1 mm. The model had a total of 659,251 elements. The material properties of the tissues were defined according to previous literature (Song et al., 2004; Wang et al., 2019). Bones (Young's modulus = 0.4 GPa, Poisson's ratio v = 0.33) and cartilage (Young's modulus = 5 MPa, Poisson's ratio v = 0.46) were assumed to be linear isotropic elastic tissues. Menisci were assumed to be orthotropic elastic tissues (E_θ = 125 MPa, E_R = E_Z =27.5 MPa, $G_{\theta R}$ = $G_{\theta Z}$ = 2 MPa, G_{RZ} = 10.34, $V_{\theta R}$ = $V_{\theta Z}$ = 0.1 and V_{RZ} = 0.33). Ligaments were defined as isotropic hyperelastic tissues using strain energy functions. The Veronda-Westmann function was used to define the properties of the ACL and PCL (α_{ACL} = 0.3 MPa, β_{ACL} = 12.20, α_{PCL} = 0.18 MPa and β_{PCL} = 17.35), while the Mooney-Rivlin material model was used to define the mechanical properties of the MCL and LCL. The coefficients of the LCL were assumed to be identical to those of the MCL (C1 = 30.1 MPa and C2 = −27.1 MPa). The model was validated using data from cadaveric experiments in terms of joint kinematics and ACL forces under an anterior tibial load, valgus tibial moment and internal tibial moment. The model had a calculation accuracy of 0.1 mm for anterior tibial translation, 1 ° for valgus tibial rotation and 1 N for ACL force.

2.2 Simulation groups, boundary and loading conditions, and evaluation indicators

The following simulation groups were included in this study: 1) Intact state (group I); 2) ACL reconstruction (ACLR) using a columnar graft with different graft diameters (group II); 3) ACLR using a columnar graft with different graft elasticities (group III); 4) ACLR using an hourglass-shaped graft resembling the dimensions of the native ACL in terms of the cross-sectional area (CSA) of its bone insertion sites and isthmus (group IV).

Using the software Abaqus/CAE 6.14–2 (Simulia, Inc., United States), all simulation groups were assigned the same boundary and loading conditions (Figure 2A). First, the tibial shaft was fixed in 6 degrees of freedom (DOFs) and the femur was flexed to 30°. Next, the femoral shaft was fixed in six DOFs while the tibial shaft was fixed only in flexion-extension. The bottom surface of the tibial shaft was then subjected to an anterior tibial load of 103 N, internal tibial moment of 7.5 Nm, and valgus tibial moment of 6.9 Nm. A flexion angle of 30° was used because a previous study has shown the peak ACL force during normal gait to occur at this joint position. Besides, the ACL was previously reported to be mainly functional for restraining anterior tibial loads and pivot shift loads (internal and valgus tibial moments) (Sakane et al., 1997; Kanamori et al., 2000), thus the combined loads used in this study represented the maximum values experienced during normal gait and were considered as a worst case for tensioning the ACL (Kutzner et al., 2010).

Joint stability under the above loading conditions were recorded to evaluate the stability and stiffness of the knee, including the anterior tibial translation (ATT), internal tibial rotation (ITR) and valgus tibial rotation (VTR). Greater knee displacement than the intact state indicates knee instability in the

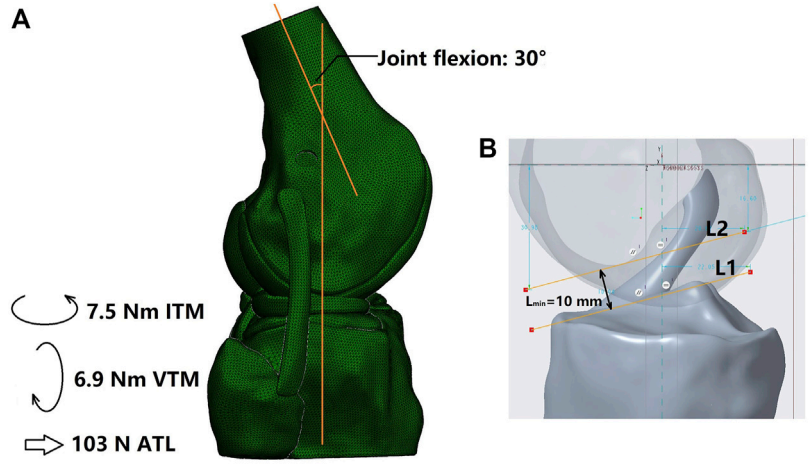

FIGURE 2
(A) Loading conditions and **(B)** Measurement of the minimum width of the space between the femoral notch and tibial plateau (L_{min}). L1 was plotted as a line tangent to the tibial plateau and parallel to L2 and L2 was tangent to the top contour of the femoral notch. ITM, internal tibial moment; VTM, valgus tibial moment; ATL, anterior tibial load.

corresponding DOFs, and less knee movement may indicate over-restraint of the joint. The *in situ* forces in the ACL and grafts were also obtained to evaluate the restoration of normal functionality. A lower force borne by the graft in comparison to the native ACL would indicate insufficient restoration, which may produce greater loading in other joint tissues and increase the risk of secondary damage.

The risk of graft impingement on the femoral notch was evaluated by comparing the effective diameter at the graft isthmus (D) against the minimum width of the space between the femoral notch and the tibial plateau (L_{min}) (Figure 2B). For the columnar graft, the diameter was constant along the whole graft, while the D value for the hourglass-shaped graft was calculated by Eq. 1. Then, Eq. 2 was used to calculate the risk for graft impingement on the femoral notch. Higher values for R_{ImP} indicate a greater risk of graft impingement, and a value greater than 1 indicates that the graft cannot be adequately accommodated within the femoral intercondylar notch at full knee extension.

$$D = 2 \times \sqrt{\frac{S_{isthmus}}{\pi}} \quad (1)$$

$$R_{ImP} = \frac{D}{L_{min}} \times 100\% \quad (2)$$

where D is the effective diameter at the graft isthmus, $S_{isthmus}$ is the cross-sectional area of the graft isthmus, and R_{ImP} is the risk of impingement.

The results from the ACLR groups (group II, III, IV) were compared with the intact group (group I) to evaluate the effectiveness of each technique at restoring graft and knee function.

2.3 ACL reconstruction using columnar grafts with different diameters

This study simulated anatomical single bundle ACL reconstruction (Figure 1B). The centers of the femoral and tibial bone insertion sites were set as the entrances for the femoral and tibial bone tunnels respectively. The angles between the femoral tunnel axis and the horizontal and sagittal planes were 45° and 25°, respectively, and the angles between the tibial tunnel axis and the horizontal and sagittal planes were 65° and 25°, respectively (Wan et al., 2012). The columnar grafts were modeled as cylindrical bodies using Creo Parametric 7.0 (Parametric Technology Corporation, United States) to simulate the geometry of an auto-hamstring tendon graft or an artificial graft. The Endoscrew was similarly modeled as a cylinder of length 10 mm and with the same diameter as the graft to fix the graft to the bone tunnel (Hung et al., 2014). One end of the endoscrew was tied with the end of the graft and its exterior wall was tied with the bone tunnel wall to simulate a secure fixation (no relative motion was allowed between the tied contact surfaces). The length of the graft inside the femoral tunnel was 20 mm and inside of the tibial tunnel was 10 mm due to a shorter tunnel. The length of the graft inside the femoral tunnel was decreased by 10 mm to explore the effect of fixation position on the main outcomes of this study. The endoscrew had a Young's modulus of 110 GPa and Poison's ratio of 0.35 to simulate a Titanium material.

For the simulation group II, different graft diameters were evaluated, but the material properties were constant across all models (Young's moduli = 129.4 MPa), thus to simulate different diameters of a certain type of graft tendon (e.g., hamstring

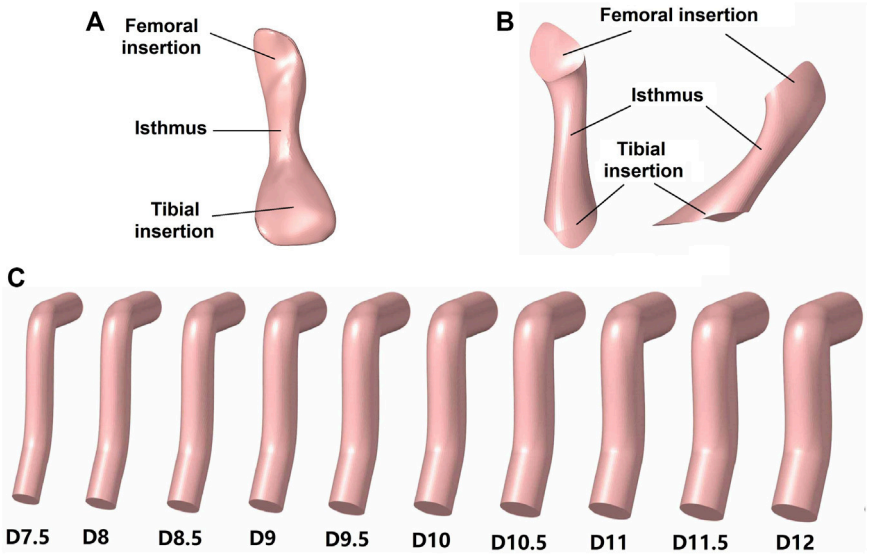

FIGURE 3
Models of the ACL and grafts. **(A)** Native ACL; **(B)** Hourglass-shaped ACL; **(C)** Columnar grafts with different diameters (D).

tendon with a diameter of 8 mm vs. 10 mm). Pujol et al. (2013) reported that the effective diameter of an auto-hamstring tendon graft is approximately 10% larger than the native ACL, and, accordingly, this study considered graft diameters ranging from 7.5 to 12 mm, increasing in increments of 0.5 mm (Figure 3C). The diameter of the bone tunnels was the same as the graft diameter used.

2.4 ACL reconstruction using columnar grafts with different material elasticity

Previous studies reported a wide variation in the elasticity of commonly used materials for ACL reconstruction (Butler et al., 1984; Wilson et al., 1999; Smeets et al., 2017; Chivot et al., 2020). For groups III and IV, the grafts were modeled with three different Young's moduli (129.4, 168.0, and 362.2 MPa) (Butler et al., 1984; Wilson et al., 1999) and a Poisson's ratio of 0.45 to assess whether the material properties of columnar grafts can be effectively tailored to replicate the functionality of the native ACL. All values for the Young's moduli were obtained from literature. The Young's modulus of 129.4 MPa was sourced from a previous experimental study on a subject of a similar age to the current study (Wilson et al., 1999), simulating an auto-graft source. And the moduli of 168.0 MPa (Wilson et al., 1999) and 362.2 MPa (Butler et al., 1984) were obtained from anatomical data from younger people, which may be considered as the properties of allografts obtained from younger tissue donors.

2.5 ACL reconstruction using hourglass-shaped grafts

Group IV used an hourglass-shaped graft to replace the native ACL in the knee joint (Figure 3B). The graft model was built in Creo Parametric 7.0 (Parametric Technology Corporation, United States) using mixed scanning whereby three sections of the graft (proximal, isthmus and distal sections) were defined and then connected by a smooth wrapped surface. The proximal and distal sections were centered on the bone insertion sites, and the isthmus was aligned with the native ACL. The cross-sectional area of the three sections replicated those of the native ACL (121.3, 35.3, and 185.6 mm^2, respectively). The normal lines of the proximal and distal sections were parallel to the tunnel axes in group II and the normal line of the isthmus section was parallel to the cross-sectional plane of the native ACL isthmus.

3 Results

3.1 Evaluation of risk of notch impingement

The minimum height between the femoral notch and tibial plateau was measured as 10 mm. The corresponding values of R_{ImP} for the columnar and hourglass-shaped grafts are shown in Figure 4. The red dotted line represents a value of 1 for R_{ImP}. Grafts with data points lying at and above the red dotted line

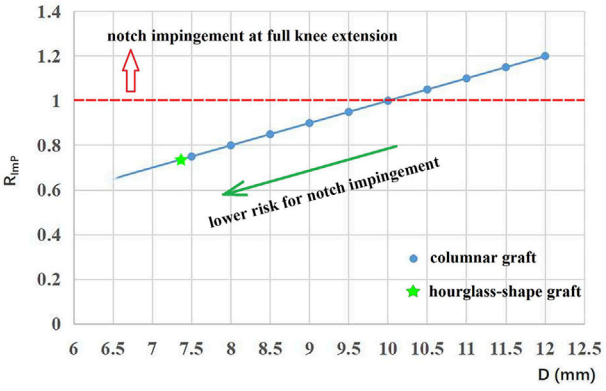

FIGURE 4
Plot of R_{imp} for columnar grafts with different diameters and the hourglass-shaped graft.

(columnar grafts with a diameter of 10–12 mm) could not be adequately accommodated within the femoral intercondylar notch at full knee extension, and thus were at higher risk of impingement (R_{imp} = 100%–120%). Grafts with data points below the red dotted line (columnar grafts with a diameter of 7.5–9.5 mm, and the hourglass-shaped graft) were at lower risk of notch impingement (R_{imp} = 75%–95%), and the risk decreased as the diameter was reduced. The hourglass-shaped graft had a lower risk of notch impingement than all of the columnar grafts (R_{imp} = 74%).

3.2 Evaluation of knee stability and graft force using columnar grafts with different diameters

Knee stability in different DOFs and ligament force for groups I and II are shown in Table 1. Compared with the intact knee (group I), ACLR using a columnar graft with a diameter of 7.5 mm resulted in increased anterior tibial translation (ATT) (4.2 mm vs. 4.7 mm) and valgus tibial rotation (VTR) (0.9° vs. 1.3°), but a reduced *in situ* force in the graft (128 N vs. 111 N). However, internal tibial rotation (ITR) was consistent with the intact knee (12.1°). Increasing the graft diameter resulted in a reduction in ATT, ITR and VTR, but lead to greater force on the graft. None of the columnar grafts simulated were capable of replicating both the stability and ligament force of the intact knee at the knee flexion angle of 30°. Although the results from the knee with a 11.5 mm graft could be considered most similar to the intact knee, the ITR was still over-restrained (12.1° vs. 11.0°) and the VTR was under-restrained (0.9° vs. 1.1°).

3.3 Evaluation of knee stability and graft force using columnar grafts with different elasticity

As shown in Table 2, increasing the Young's modulus of the graft resulted in a reduction in ATT, ITR and VTR and an increased force in the graft. The results also indicate that smaller diameter grafts are needed to maintain physiological knee stability and graft force when stiffer materials (high Young's modulus) are used for the graft. A graft with a Young's modulus of 168.0 MPa required a diameter of 9 mm to fully restore ATT in line with the intact knee at the knee flexion angle of 30°, which was 2.5 mm smaller than the graft diameter needed for a material of lower Young's modulus (129.4 MPa). With a larger Young's modulus of 362.2 MPa, the knee was over-restrained in ATT even with a relatively small graft diameter of 7.5 mm. The ITR for all ACLR knees was all over-restrained regardless of graft diameter or Young's modulus, except for when using the most flexible graft (129.4 MPa) with the smallest diameter (7.5 mm).

3.4 Evaluation of knee stability and graft force using hourglass-shaped grafts with different elasticity

As shown in Table 3, an hourglass-shaped graft resembling the dimensions of the native ACL with a Young's modulus of 129.4 MPa could restore joint stability and graft force in line with the intact knee at the knee flexion angle of 30°. Similar to the columnar grafts, increasing the Young's modulus of the hourglass graft lead to a reduction in ATT, ITR and VTR, but an increase in graft force. Using stiffer grafts with a higher Young's modulus (168.0 and 362.2 MPa) caused the knee to be over-constrained in all DOFs assessed, and also lead to a considerable increase in force on the graft in comparison to the intact knee.

3.5 Comparing the restoration of knee stability and graft force between the conventional columnar graft and hourglass-shaped graft with the same elasticity

Figure 5 shows that with grafts of the same elasticity (Young's modulus = 129.4 MPa), the hourglass-shaped graft was better able to simultaneously restore the knee stability and graft force to a level resembling the intact knee at the knee flexion angle of 30°. In contrast, the conventional columnar graft with varying diameters resulted in a lax ATT and VTR, but with the ITR over-constrained and a graft force lower than the intact ACL.

TABLE 1 ATT, Anterior tibial translation; IRT, internal tibial rotation; VTR, valgus tibial rotation and ACL/graft force in the intact knee and knee after ACLR using columnar grafts of different diameters.

		ATT (mm)	ITR (°)	VTR (°)	ACL/graft force (N)
Intact knee with the native ACL		4.2	12.1	0.9	128
Diameter of columnar graft in ACLR (mm) (Young's modulus of the graft = 129.4 MPa)	7.5	4.7	12.1	1.3	111
	8	4.5	11.9	1.3	113
	8.5	4.5	11.8	1.3	116
	9	4.5	11.7	1.2	117
	9.5	4.4	11.6	1.2	119
	10	4.4	11.5	1.2	119
	10.5	4.3	11.3	1.2	122
	11	4.3	11.2	1.2	124
	11.5	4.2	11.0	1.1	129
	12	4.0	10.8	1.0	133

3.6 Effect of the position for graft fixation inside the bone tunnel on the main outcomes

As shown in Figure 6, comparing with the simulation group using a graft length of 20 mm inside the bone tunnel, a shorter graft length (10 mm) inside the bone tunnel caused less ITR, when the ATT, VTR and graft force were not changed. Changing the length of the graft inside the bone tunnel did not change the outcome that comparing with the conventional ACLR group, the hourglass-shaped graft was better able to simultaneously restore the knee stability and graft force at the knee flexion angle of 30°.

4 Discussion

This study found that the diameter and elasticity of columnar grafts in ACLR could not be tailored to simultaneously replicate the knee stability and graft force of an intact knee at the knee flexion angle of 30°. Although increasing the diameter and/or Young's modulus of the graft could improve knee stability and graft force, it was not possible to restore both the joint stability and graft force at the same time. Larger diameter columnar grafts were also found to be at risk of impingement with the femoral notch. In contrast, an hourglass-shaped graft resembling the dimensions of the native ACL was better able to simultaneously restore knee stability and graft function at the knee flexion angle of 30°, while avoiding graft impingement, and thus may be at lower risk of rupture, instability and over-restraint of the knee.

In comparison to the intact knee, the results showed an increase in ATT and VTR after ACLR using a columnar graft of diameter 7.5 mm with a Young's modulus of 129.4 MPa. Notably, a graft diameter of 7.5 mm is commonly used in clinical practice when using an auto-hamstring tendon graft (Pujol et al., 2013). Higher values of ATT and VTR represented greater knee instability than the intact knee, which may cause an abnormal stress environment on the articular cartilage and, in the long term, may lead to knee OA. Meanwhile, the graft force was lower than the force in the native ACL, indicating the graft may not be capable of withstanding physiological joint forces at the knee flexion angle of 30°. This may impart larger forces on other tissues in the knee joint, such as the menisci or articular cartilage. Increasing the graft diameter improved knee stability and increased the force in the graft, indicating that choosing a suitable graft diameter is critical for restoring knee kinematics and forces in the tissues (Snaebjornsson et al., 2017; Wang et al., 2020b). However, this study found that columnar grafts could not replicate both the knee stability and ligament force of the intact joint at the same time. It was possible to restore one parameter to a physiological level, but at the expense of the other. For example, ATT was restored to the level of the intact joint only when ITR was over-restrained, indicating that the knee joint after conventional ACLR might be in the state of instability in one DOF while being over-restrained in another. When the knee moves in a different way to the intact knee, this may change the magnitude and distribution of articular stress (Wang et al., 2020b), which may cause degeneration of the cartilage in the long term (Arokoski et al., 2000). The results also showed that graft diameters larger than 10 mm are at high risk of impingement with the intercondylar femoral notch. This may be problematic when the data suggests that a graft diameter larger than 10 mm is needed to adequately restore knee functionality to a physiological level. Similarly, Howell et al. (1991) found that most columnar grafts suffer impingement on the femoral notch if

TABLE 2 ATT, Anterior tibial translation; IRT, internal tibial rotation; VTR, valgus tibial rotation and ACL/graft force in the intact knee and knee after ACLR using columnar grafts with different elasticity.

		ATT (mm)	ITR (°)	VTR(°)	ACL/graft force (N)
Intact knee with the native ACL		4.2	12.1	0.9	128
Diameter of columnar graft in ACLR (mm) (Young's modulus of the graft = 129.4 MPa)	7.5	4.7	12.1	1.3	111
	8	4.5	11.9	1.3	113
	8.5	4.5	11.8	1.3	116
	9	4.5	11.7	1.2	117
	9.5	4.4	11.6	1.2	119
	10	4.4	11.5	1.2	119
	10.5	4.3	11.3	1.2	122
	11	4.3	11.2	1.2	124
	11.5	4.2	11.0	1.1	129
	12	4.0	10.8	1.0	133
Diameter of columnar graft in ACL reconstruction (mm) (Young's modulus of the graft = 168.0 MPa)	7.5	4.4	11.8	1.3	115
	8	4.3	11.6	1.2	116
	8.5	4.3	11.5	1.2	120
	9	4.2	11.4	1.2	122
	9.5	4.2	11.3	1.2	124
	10	4.2	11.2	1.1	127
	10.5	4.1	11.0	1.1	129
	11	4.1	10.9	1.1	134
	11.5	4.0	10.7	1.0	139
	12	3.8	10.4	0.9	147
Diameter of columnar graft in ACL reconstruction (mm) (Young's modulus of the graft = 362.2 MPa)	7.5	3.8	11.2	1.1	127
	8	3.6	11.0	1.0	132
	8.5	3.6	10.8	1.0	139
	9	3.6	10.6	0.9	142
	9.5	3.6	10.5	0.9	147
	10	3.6	10.3	0.9	152
	10.5	3.6	10.0	0.8	157

TABLE 3 ATT, Anterior tibial translation; IRT, internal tibial rotation; VTR, valgus tibial rotation and ACL/graft force in the intact knee and knee after ACLR using an hourglass-shaped graft with different elasticity.

	ATT (mm)	ITR (°)	VTR(°)	ACL/graft force (N)
Intact knee with the native ACL	4.2	12.1	0.9	128
ACLR using an Hourglass-shaped graft with a Young's modulus of 129.4 MPa	4.2	11.7	0.9	129
ACLR using an Hourglass-shaped graft with a Young's modulus of 168.0 MPa	4.1	11.6	0.8	142
ACLR using an Hourglass-shaped graft with a Young's modulus of 362.2 MPa	4.1	11.3	0.5	169

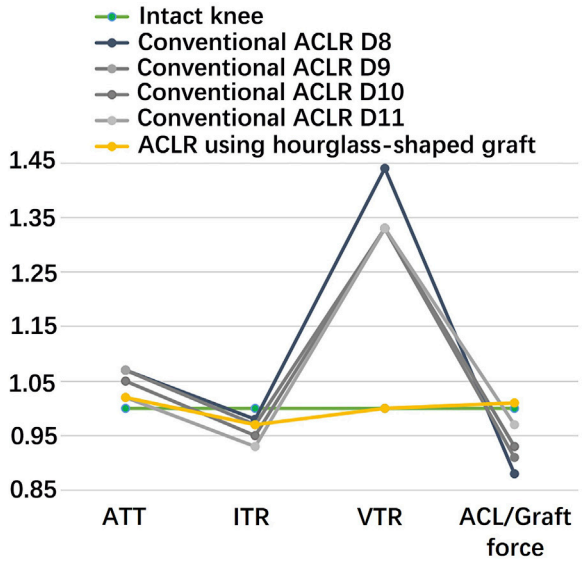

FIGURE 5
Comparison of a conventional columnar graft to an hourglass-shaped graft for restoring knee stability and ligament force. The values were standardized against an intact knee. D8 signifies a graft diameter of 8 mm. ATT, anterior tibial translation; ITR, internal tibial rotation; VTR, valgus tibial rotation.

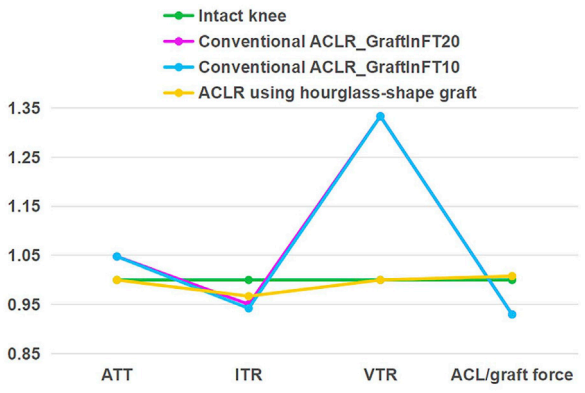

FIGURE 6
Comparison of a conventional columnar graft (diameter 10 mm, Young's moduli = 129.4 MPa) to an hourglass-shaped graft for restoring knee stability and ligament force, with varying position of graft fixation in the femoral tunnel (10 mm vs. 20 mm) for the conventional ACLR. GraftInFT20 means the graft length inside the femoral tunnel was 20 mm. The values were standardized against an intact knee. ATT, anterior tibial translation; ITR, internal tibial rotation; VTR, valgus tibial rotation.

the bone tunnels are placed at the centers of the bone insertion sites of the native ACL, and thus roofplasty or posterior placement of the tibial tunnel are often required to prevent such impingement. Unfortunately, from the author's point of view, placing the bone tunnels away from the native bone insertion sites may result in abnormal joint movement and damage to the knee. Notchplasty is also commonly performed by the surgeons to avoid the impingement. However, notchplasty disrupts the normal structure of the knee and may introduce other unforeseen complications. In this case, use of an hourglass-shaped graft may be helpful for avoiding these issues.

Increasing the Young's modulus of the graft was shown to restrict joint movement and increase the graft force, which could be expected to improve knee stability and reduce the risk of secondary damage to the other joint tissues. Beveridge et al. (2019) reported that 90% of the variability in gross cartilage changes (measured by macroscopic scoring) was associated with ACL stiffness (obtained by *ex vivo* tensile testing) at 6 months after ACL repair, with a higher ACL stiffness producing less cartilage damage (Beveridge et al., 2019). This finding is supported by the results of this current study, where an increase in graft elasticity was shown to improve knee stability and graft force, and thus may improve the articular stress and reduce damage to the cartilage. Also, increasing the Young's modulus allowed for a smaller graft diameter to be used while maintaining similar levels of knee stability and graft force, meaning less tissue needs to be harvested from the donor site. However, regardless of the Young's modulus or diameter, this study found that columnar grafts were not able to simultaneously restore both knee function and graft force to a near-physiological level at the knee flexion angle of 30°.

In contrast, using an hourglass-shaped graft resembling the dimensions of the native ACL may allow for the graft isthmus to be more easily accommodated by the femoral notch. This may reduce the risk of graft impingement after ACLR. The hourglass-shaped graft was also able to simultaneously restore both knee stability and graft force to levels resembling the intact knee at the knee flexion angle of 30°. The graft was developed by measuring the area of the native bone insertion sites and ACL isthmus and then blending these areas to create a smooth graft model. This development method is both accurate and easy to replicate, making it suitable for clinical applications in cases where the bone insertion sites and ACL isthmus can be measured *in vivo*. It should be noted that increasing the Young's modulus of the hourglass graft restricted knee movement and increased graft force, indicating that choosing suitable mechanical properties based on the required graft size is critical for the success of ACLR surgery. Also, given that an hourglass-shaped graft may be difficult to obtain directly from human tissue, allografts or artificial grafts may be a more suitable way for applying this method to clinical practice.

This study has some limitations. 1) The Young's moduli of the grafts were obtained from literature, but the reported properties of grafts in literature can vary considerably and so the moduli used in this study may be different from those

used in clinical practice. As shown by this study, larger graft elasticity resulted in lower knee laxity and greater graft force. This study suggests that the mechanical properties of ACL grafts should be carefully evaluated and selected for ACLR to adequately restore knee functionality. 2) All grafts were considered to have isotropic material properties. However, in clinical practice, the graft properties is anisotropic and can undergo minor changes during implantation due to its viscoelasticity. Nevertheless, the main function of the ACL is to bear tensile forces and the loading conditions used in this study primarily act to tension the ACL and grafts. Assigning isotropic properties to the ligaments should have little effect on the main findings of this study. The models in this study did not consider graft viscoelasticity, which may result in a stiffer joint than a physical knee. As such, future studies may further explore the effect of viscoelasticity on graft functionality after ACLR. 3) The internal tibial rotation (ITR) may be over-constrained in this FE model in comparison to the native ACL because the longitudinal fibers of the ligament were not considered, and thus the rotations of fibers could not be simulated. This may result in a lower simulated ITR of the knee. 4) Only a static loading condition was considered. Effectiveness of using the hourglass-shaped graft may vary in different knee flexions and different loadings such as dynamic loadings representing different daily activities. Future studies should further evaluate its effectiveness under more complex loading environments. 5) Different fixation techniques may lead to variation in the stiffness of the bone-graft-bone complex. In the current study, a good fixation between the graft and bone tunnel was assumed, which permits no relative motion between them. Such a completely rigid fixation neglected the graft sliding along the longitudinal axis of the bone tunnels and may result in a lower knee laxity after ACLR than the real situation.

In the current clinical practice, auto-grafts are often more convenient to use and can reduce the risk of immune reactions, but they can also compromise knee functionality, as shown in the current study. The currently used graft size is usually depending on the used tendon. We thus look forward to future developments of advanced biotechniques for better processing allografts and biomaterials to produce more effective artificial grafts for better restoring the joint functionality.

5 Conclusion

At the knee flexion angle of 30°, the hourglass-shaped graft was better able to restore joint stability and graft force after ACLR than columnar grafts. The hourglass graft might also be beneficial for reducing the risk of impingement on the femoral notch. The findings of this study provide information on designing and choosing suitable grafts depending on the conditions of the native knee, and thus may improve the clinical outcome of ACLR.

This study provides innovative concepts for designing and choosing suitable grafts for ACLR, especially when using allografts or artificial grafts, and thus may improve the clinical outcome of ACLR.

Data availability statement

The original contributions presented in the study are included in the article/Supplementary Material, further inquiries can be directed to the corresponding author.

Author contributions

HW, CF, and C-KC conceived and designed the study. HW, MT, QS, and KH collaborated in developing finite element models and conducting the simulations. MT and HW processed and analyzed the data. HW, CF, and C-KC interpreted the data. All authors participated in preparation, revision and approval of the version to be published.

Funding

This work was supported by the National Natural Science Foundation of China (grant number 32101050) and the China Postdoctoral Science Foundation (grant number 2021M702129).

Acknowledgments

We would like to thank Colin McClean for his assistance with editing this manuscript.

Conflict of interest

The authors declare that the research was conducted in the absence of any commercial or financial relationships that could be construed as a potential conflict of interest.

Publisher's note

References

Arokoski, J. P. A., Jurvelin, J. S., Vaatainen, U., and Helminen, H. J. (2000). Normal and pathological adaptations of articular cartilage to joint loading. *Scand. J. Med. Sci. Sports* 10 (4), 186–198. doi:10.1034/j.1600-0838.2000.010004186.x

Ayanoglu, T., Arikan, E., Yilmaz, O., Gokkus, H., Kaya, Y. E., and Ozturan, K. E. (2022). Investigating the magnetic resonance imaging cross-section area that best correlates with intraoperative hamstring autograft size. *Acta Orthop. Traumatol. Turc.* 56 (5), 311–315. doi:10.5152/j.aott.2022.21183

Barenius, B., Ponzer, S., Shalabi, A., Bujak, R., Norlen, L., and Eriksson, K. (2014). Increased risk of osteoarthritis after anterior cruciate ligament reconstruction A 14-year follow-up study of a randomized controlled trial. *Am. J. Sports Med.* 42 (5), 1049–1057. doi:10.1177/0363546514526139

Beveridge, J. E., Proffen, B. L., Karamchedu, N. P., Chin, K. E., Sieker, J. T., Badger, G. J., et al. (2019). Cartilage damage is related to ACL stiffness in a porcine model of ACL repair. *J. Orthop. Res.* 37 (10), 2249–2257. doi:10.1002/jor.24381

Butler, D. L., Grood, E. S., Noyes, F. R., Zernicke, R. F., and Brackett, K. (1984). Effects of structure and strain measurement technique on the material properties of young human tendons and fascia. *J. Biomech.* 17 (8), 579–596. doi:10.1016/0021-9290(84)90090-3

Cheng, R. S., Wang, H. Z., Dimitriou, D., Jiang, Z., Cheng, C. K., and Tsai, T. Y. (2022). Central femoral tunnel placement can reduce stress and strain around bone tunnels and graft more than anteromedial femoral tunnel in anterior cruciate ligament reconstruction. *Int. J. Numer. Method. Biomed. Eng.* 38 (5), e3590. doi:10.1002/cnm.3590

Cheng, R. S., Wang, H. Z., Jiang, Z., Dimitriou, D., Cheng, C. K., and Tsai, T. Y. (2021). The femoral tunnel drilling angle at 45° coronal and 45° sagittal provided the lowest peak stress and strain on the bone tunnels and anterior cruciate ligament graft. *Front. Bioeng. Biotechnol.* 9, 797389. doi:10.3389/fbioe.2021.797389

Chivot, M., Pioger, C., Cognault, J., Sharma, A., Pailhe, R., Cavaignac, E., et al. (2020). Every layer of quadriceps tendon's central and medial portion offers similar tensile properties than Hamstrings or Ilio-Tibial Band Grafts. *J. Exp. Orthop.* 7 (1), 50. doi:10.1186/s40634-020-00261-7

Han, H. S., and Lee, M. C. (2019). Anatomic anterior cruciate ligament reconstruction using the quadriceps tendon. *Ann. Jt.* 4 (1), 2. doi:10.21037/aoj.2018.12.10

Hashemi, J., Chandrashekar, N., Jang, T., Karpat, F., Oseto, M., and Ekwaro-Osire, S. (2007). An alternative mechanism of non-contact anterior cruciate ligament injury during jump-landing: *In-vitro* simulation. *Exp. Mech.* 47 (3), 347–354. doi:10.1007/s11340-007-9043-y

Howell, S. M., Usafr, M. M., Clark, J. A., and Farley, T. E. (1991). A rationale for predicting anterior cruciate graft impingement by the intercondylar roof - a magnetic-resonance-imaging study. *Am. J. Sports Med.* 19 (3), 276–282. doi:10.1177/036354659101900312

Hung, C-C., Chen, W-C., Yang, C-T., Cheng, C-K., Chen, C-H., and Lai, Y-S. (2014). Interference screw versus endoscrew fixation for anterior cruciate ligament reconstruction: A biomechanical comparative study in sawbones and porcine knees. *J. Orthop. Transl.* 2 (2), 82–90. doi:10.1016/j.jot.2014.02.001

Kanamori, A., Woo, S. L. Y., Ma, C. B., Zeminski, J., Rudy, T. W., Li, G. A., et al. (2000). The forces in the anterior cruciate ligament and knee kinematics during a simulated pivot shift test: A human cadaveric study using robotic technology. *Arthrosc. J. Arthrosc. Relat. Surg.* 16 (6), 633–639. doi:10.1053/jars.2000.7682

Komzak, M., Hart, R., Nahlik, D., and Vysoky, R. (2021). *In vivo* knee rotational stability 2 years after the ACL reconstruction using a quadriceps tendon graft with bone block and bone-patellar tendon-bone graft. *Arch. Orthop. Trauma Surg.* 142 (8), 1995–1999. doi:10.1007/s00402-021-04195-2

Kutzner, I., Heinlein, B., Graichen, F., Bender, A., Rohlmann, A., Halder, A., et al. (2010). Loading of the knee joint during activities of daily living measured *in vivo* in five subjects. *J. Biomech.* 43 (11), 2164–2173. doi:10.1016/j.jbiomech.2010.03.046

Musahl, V., Nazzal, E. M., Lucidi, G. A., Serrano, R., Hughes, J. D., Margheritini, F., et al. (2022). Current trends in the anterior cruciate ligament part 1: Biology and biomechanics. *Knee Surg. Sports Traumatol. Arthrosc.* 30 (1), 20–33. doi:10.1007/s00167-021-06826-y

Orsi, A. D., Canavan, P. K., Vaziri, A., Goebel, R., Kapasi, O. A., and Nayeb-Hashemi, H. (2017). The effects of graft size and insertion site location during anterior cruciate ligament reconstruction on intercondylar notch impingement. *Knee* 24 (3), 525–535. doi:10.1016/j.knee.2017.02.010

Pujol, N., Queinnec, S., Boisrenoult, P., Maqdes, A., and Beaufils, P. (2013). Anatomy of the anterior cruciate ligament related to hamstring tendon grafts. A cadaveric study. *Knee* 20 (6), 511–514. doi:10.1016/j.knee.2012.10.006

Sakane, M., Fox, R. J., Woo, S. L. Y., Livesay, G. A., Li, G., and Fu, F. H. (1997). *In situ* forces in the anterior cruciate ligament and its bundles in response to anterior tibial loads. *J. Orthop. Res.* 15 (2), 285–293. doi:10.1002/jor.1100150219

Schmucker, M., Haraszuk, J., Holmich, P., and Barfod, K. W. (2021). Graft failure, revision ACLR, and reoperation rates after ACLR with quadriceps tendon versus hamstring tendon autografts: A registry study with review of 475 patients. *Am. J. Sports Med.* 49 (8), 2136–2143. doi:10.1177/03635465211015172

Smeets, K., Bellemans, J., Scheys, L., Eijnde, B. O., Slane, J., and Claes, S. (2017). Mechanical Analysis of Extra-Articular Knee Ligaments. Part two: Tendon grafts used for knee ligament reconstruction. *Knee* 24 (5), 957–964. doi:10.1016/j.knee.2017.07.011

Snaebjornsson, T., Senorski, E. H., Ayeni, O. R., Alentorn-Geli, E., Krupic, F., Norberg, F., et al. (2017). Graft diameter as a predictor for revision anterior cruciate ligament reconstruction and KOOS and EQ-5D values A cohort study from the Swedish national knee ligament register based on 2240 patients. *Am. J. Sports Med.* 45 (9), 2092–2097. doi:10.1177/0363546517704177

Song, Y. H., Debski, R. E., Musahl, V., Thomas, M., and Woo, S. L. Y. (2004). A three-dimensional finite element model of the human anterior cruciate ligament: A computational analysis with experimental validation. *J. Biomech.* 37 (3), 383–390. doi:10.1016/s0021-9290(03)00261-6

Wan, C., Hao, Z., and Wen, S. (2012). Influence of various mechanical properties of anterior cruciate ligament on finite element simulation of knee joint. *J. Med. Biomechanics* 27 (4), 375–380.

Wang, H. Z., Kang, H. J., Yao, J., Cheng, C. K., and Woo, S. L. Y. (2019). Evaluation of a magnesium ring device for mechanical augmentation of a ruptured ACL: Finite element analysis. *Clin. Biomech. (Bristol, Avon.* 68, 122–127. doi:10.1016/j.clinbiomech.2019.06.002

Wang, H. Z., Zhang, B., and Cheng, C. K. (2020). Stiffness and shape of the ACL graft affects tunnel enlargement and graft wear. *Knee Surg. Sports Traumatol. Arthrosc.* 28 (7), 2184–2193. doi:10.1007/s00167-019-05772-0

Wang, H. Z., Zhang, M., and Cheng, C. K. (2020). A novel protection liner to improve graft-tunnel interaction following anterior cruciate ligament reconstruction: A finite element analysis. *J. Orthop. Surg. Res.* 15 (1), 232. doi:10.1186/s13018-020-01755-x

Wang, H. Z., Zhang, M., and Cheng, C. K. (2020). Changing the diameter of the bone tunnel is more effective than changing the tunnel shape for restoring joint functionality after ACL reconstruction. *Front. Bioeng. Biotechnol.* 8, 173. doi:10.3389/fbioe.2020.00173

Wang, H. Z., Zhang, Z. Y., Qu, Y., Shi, Q. Y., Ai, S. T., and Cheng, C. K. (2022). Correlation between ACL size and dimensions of bony structures in the knee joint. *Ann. Anat. - Anatomischer Anzeiger* 241, 151906. doi:10.1016/j.aanat.2022.151906

Wilson, T. W., Zafuta, M. P., and Zobitz, M. (1999). A biomechanical analysis of matched bone-patellar tendon-bone and double-looped semitendinosus and gracilis tendon grafts. *Am. J. Sports Med.* 27 (2), 202–207. doi:10.1177/03635465990270021501

Yao, J., Wen, C. Y., Cheung, J. T. M., Zhang, M., Hu, Y., Yan, C. H., et al. (2012). Deterioration of stress distribution due to tunnel creation in single-bundle and double-bundle anterior cruciate ligament reconstructions. *Ann. Biomed. Eng.* 40 (7), 1554–1567. doi:10.1007/s10439-012-0517-4

frontiers | Frontiers in Bioengineering and Biotechnology

TYPE Original Research
PUBLISHED 07 February 2023
DOI 10.3389/fbioe.2023.1033590

OPEN ACCESS

EDITED BY
Cheng-Feng Lin,
National Cheng Kung University, Taiwan

REVIEWED BY
Luiz H. Palucci Vieira,
São Paulo State University, Brazil
Bruno Luiz Souza Bedo,
University of São Paulo, Brazil

*CORRESPONDENCE
Siddhartha Bikram Panday,
siddartha@hanyang.ac.kr

SPECIALTY SECTION
This article was submitted to Biomechanics, a section of the journal Frontiers in Bioengineering and Biotechnology

RECEIVED 31 August 2022
ACCEPTED 23 January 2023
PUBLISHED 07 February 2023

CITATION
Moon J, Koo D, Kim S and Panday SB (2023), Effect of sprinting velocity on anterior cruciate ligament and knee load during sidestep cutting.
Front. Bioeng. Biotechnol. 11:1033590.
doi: 10.3389/fbioe.2023.1033590

Effect of sprinting velocity on anterior cruciate ligament and knee load during sidestep cutting

Jeheon Moon[1], Dohoon Koo[2], Sungmin Kim[3] and Siddhartha Bikram Panday[4,5]*

[1]Department of Physical Education, Korea National University of Education, Chungbuk, Republic of Korea, [2]Department of Exercise Prescription, Jeonju University, Chonbuk, Republic of Korea, [3]Institute of School Physical Education, Korea National University of Education, Chungbuk, Republic of Korea, [4]Department of Physical Education, Hanyang University, Seoul, Republic of Korea, [5]Department of Art and Sportainment, Hanyang University, Seoul, Republic of Korea

The purpose of the study was to investigate the effect of an increase in sprinting velocity on the anterior cruciate ligament (ACL) load, knee joint load, and activation of femoral muscles using the musculoskeletal modeling approach. Fourteen high school male athletes were recruited (age: 17.4 ± 0.7 years, height: 1.75 ± 0.04 m, weight: 73.3 ± 8.94 kg), with the right foot dominant and physical activity level of about 3–4 h per day. The kinematics, kinetics, and co-contraction index (CCI) of the extensors and flexors of the right leg's femoral muscles were calculated. The anterior cruciate ligament load was estimated using the musculoskeletal modeling method. In the results, it was observed that the anterior cruciate ligament load ($p < 0.017$) increased as sidestep cutting velocity increased, resulting in increased adduction ($p < 0.017$) and the internal rotation moment of the knee joint. This was significantly higher than when sprinting at a similar velocity. The co-contraction index result, which represents the balanced activation of the femoral extensor and flexor muscles, showed a tendency of decrement with increasing sprinting velocity during sidestep cutting ($p < 0.017$), whereas no significant differences were observed when running at different sprinting conditions. Therefore, we postulate that factors such as knee joint shear force, extended landing posture with increasing sprinting velocity, internal rotation moment, and femoral muscle activity imbalance influence the increase of anterior cruciate ligament load during a sidestep cutting maneuver.

KEYWORDS

musculoskeletal modeling, ACL injury, velocity, cutting, opensim

1 Introduction

Anterior Cruciate Ligament (ACL) injuries frequently occur when the knee joint is subjected to high loading during a sudden change in the whole body velocity (Pflum et al., 2004; Kernozek and Ragan 2008; O'Connor et al., 2009; Laughlin et al., 2011) such as a stop jump (Lin et al., 2009) or sidestep cutting (McLean et al., 2004; Pollard et al., 2005; McLean et al., 2008). Various biomechanical approaches have been employed to speculate on the mechanism of ACL injury by quantifying changes in kinematics, kinetics, and muscle activities (Weinhandl et al., 2010; Weinhandl et al., 2011). Studies report ACL injuries occur when landing with the knee elongated in the abduction position (Olsen et al., 2004; Krosshaug et al., 2005). Particularly, knee joint angles in the range of 9°~27° while impacting the ground after jumping and the height of the knee were reported to significantly increase the risk of an ACL injury (Olsen et al., 2005). Moreover, changes in shear force and internal rotation of the

knee joint have a greater effect on ACL load than the external rotation of the knee (Markolf et al., 1995).

The involvement of femoral muscle activation should be emphasized to better understand the ACL injury mechanism. When both agonistic and antagonistic muscles contract simultaneously, this is known as the "co-contraction of muscles" (Kellis et al., 2003). Hurd and Snyder-Mackler (2007) observed that high antagonistic muscle co-contraction can exhibit a knee stiffening strategy and improve the stability of the knee joint. The strong quadriceps femoris contraction increases ACL load and also correlates with ground reaction force (GRF). Further, when the knee is extended, the coupled moment acts on the posterior joint, increasing the risk of ACL injury (Fleming et al., 2001; DeMorat et al., 2004). Boden et al. (2000) reported that co-contraction of the quadriceps femoris and the biceps femoris (BF) decreases ACL strain. Khandha et al. (2019), on the contrary, argued that prolonged high muscle co-contraction may result in high joint loads, adversely affecting knee cartilage integrity. Additionally, several studies indicate that pre-activation of the quadriceps femoris before landing and co-contraction of the quadriceps femoris with the biceps femoris may aid in preventing the ACL load from increasing (Hewett et al., 2005; Kernozek and Ragan 2008; Hashemi et al., 2010).

Studies that investigated the factors contributing to ACL injuries caused during the sidestep cutting maneuver were conducted at a constant sprinting velocity (McLean et al., 2004; O'Connor et al., 2009; Weinhandl et al., 2013). ACL loading has been reported to occur as a result of a complex interaction between sagittal plane shear forces (i.e., quadriceps, hamstrings, and tibiofemoral) and frontal and transverse plane knee moments (Bedo et al., 2021; Weinhandl et al., 2013). Importantly, the findings of previous studies suggest that unanticipated movements such as sidestep cutting increase anterior cruciate ligament loading. Although the majority of non-contact ACL injuries in sporting scenarios are caused by excessive pressure or load on the knee joint during the weight-shifting process, little attention has been paid to the effect of running velocity and weight-shifting situations (i.e., sidestep cutting) on ACL injuries. According to Olsen et al. (2004), when running at a high velocity (5–8 m/s), increased ACL loading in the sagittal plane increases the vulnerability of injury. The increased ACL load was attributed to increased peak posterior GRF, knee extension moment, and stiffness, as well as decreased knee flexion range of motion (Yu and Garrett 2007; Lin et al., 2009; Taylor et al., 2011; Dai et al., 2012; Taylor et al., 2013).

Therefore, the purpose of the study was to investigate whether increasing sprinting velocity (3 m/s, 4 m/s, or 5 m/s) has an influence on ACL load, knee joint load, and femoral muscle co-activation using a musculoskeletal modeling technique. We hypothesize that 1) an increase in running velocity will increase the knee joint angle in all three directions, 2) an increase in running velocity will increase ACL load, and 3) an increase in velocity will decrease the co-contraction index.

2 Materials and methods

2.1 Participants

The study included fourteen high school male athletes (age: 17.4 ± 0.7 years, height: 1.75 ± 0.04 m, weight: 73.3 ± 8.94 kg). All of the individuals were right-foot dominant and engaged in varied sports activities for an average of 3–4 h per day. None of the subjects had a history of morbidity or musculoskeletal injury within the preceding 6 months. All individuals volunteered to participate in the experiment and gave their consent after reading the research instructions and signed the consent forms. The Institutional Review Board of Seoul National University (IRB Number: 1511/022-001) approved the research to ensure that it adhered to the Declaration of Helsinki's ethical principles (1975, revised 1983).

2.2 Apparatus

Nineteen infrared cameras (Oqus 7+, Gothenburg, Sweden) and a single force plate (Kistler Type 9287BA, Winterthur, Switzerland) were used to measure the motion data and the GRF. The muscle activities were measured using a wireless electromyography (EMG) system (Noraxon DTS, Scottsdale, AZ, United States). The three measurement systems were synchronized, and the set of synchronized data was sent to the main computer. The sampling rates were set at 200 Hz for the motion data, GRF at 2,000 Hz, and EMG at 1,500 Hz.

2.3 Experimental procedures

The participants were provided with a set of experimental attire and shoes prepared by the experimenter. Before the main experiment, the participants performed warm-up exercises for about 15 min. Thereafter, their skin was shaved with an alcohol pad to clean the skin and reduce the skin's impedance. Disposable dual-electrodes (Noraxon TM, Scottsdale, Arizona) were also attached to the belly of five muscle sites (Hermens et al., 1999) in the right lower extremities, including the rectus femoris, vastus medialis, and vastus lateralis, as well as flexors such as the biceps femoris and semitendinosus. The electrodes were further secured with adhesive cotton tape to minimize motion artifacts during the tasks. We then measured the manual isometric maximum voluntary contraction (MVC) test for extensors and flexors separately with the method described by Konrad (Konrad 2005). For the MVC test of the rectus femoris, vastus medialis, and vastus lateralis, participants were instructed to do a single-leg knee extension from a seated posture with the leg strapped to the chair and the knee flexed from 90° to 70°. For the MVC flexor test, participants lay in a prone position with their hips firmly fastened with a belt and conducted a unilateral knee flexion at 20–30°. In both tests, participants were asked to slowly increase the force until they reached their maximum after 3–5 s, hold for at least 5 s, and relax promptly. Throughout the MVC test, the experimenter verbally encouraged the participants to perform at their maximum. For each muscle group, the MVC test was repeated three times, and a 1-min rest was given after each repetition (Rutherford et al., 2011). The MVC values of each muscle site from three trials were averaged and later used for EMG normalization. After the MVC tests, participants were given 10–15 min for recovery. We then attached spherical passive reflective markers (12.7 mm in diameter) at the anatomically bony landmarks to define joints and segments (Cappozzo et al., 1997; Wu et al., 2002; Wu et al., 2005; Collins et al., 2009). A 13-segment kinematic model was employed, which consisted of the head, trunk, pelvis, and bilateral upper arms, lower arms, thighs, shanks, and feet.

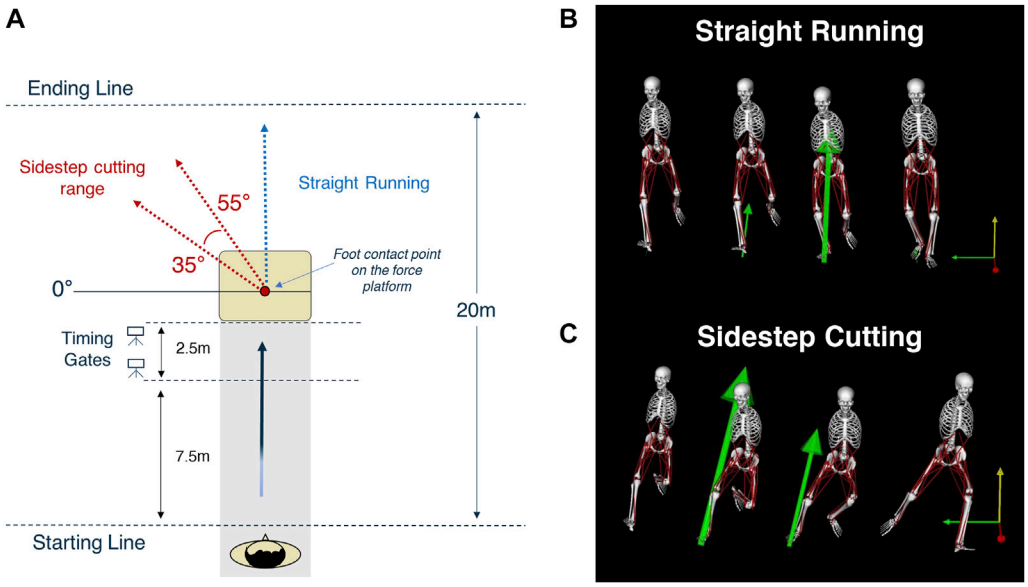

FIGURE 1
Experimental Procedure. **(A)** The sidestep cutting technique was carried out between 35° and 55° to the left of the path of travel. Sprinting velocity was controlled by monitoring the participant's velocity in the 2.5 m range prior to contact with the ground reaction force measurement apparatus. **(B,C)** The two running condition types performed in the study. The image were extracted at using open source model provided in OpenSim (Stanford University, Stanford, CA, United States).

The main experiment included two sprinting *TYPES*, i.e., sidestep cutting and straight running at three constrained sprinting velocities (3 m/s, 4 m/s, and 5 m/s) (McLean et al., 2004; Weinhandl et al., 2013; Xu et al., 2018). We monitored the participants' sprinting velocity using two timing gates (Witty Microgate, Bolzano, Italy), which measure the average passage time. The timing gates were installed at intervals of 2.5 m before the force plate (Figure 1). Considering the variability in performance, we collected data for only successful trials that came within ±5% for each velocity condition. Participants in both the sidestep cutting and straight running conditions ran a total of 10 m and were required to plant their right foot on the force plate. They were asked to maintain a constant velocity throughout the run and were given enough time for practice runs for each condition and type. Before the initiation of trials, the participants were notified of the types and velocities required for each trial. For the sidestep cutting condition, the participants were instructed to change their running direction to the left after planting on the force plate with the right leg. The range of sidestep cutting was set at 35°–55° to the left of the proceeding direction (Donnelly et al., 2012; McLean et al., 2004; McLean et al., 2008; Weinhandl et al., 2013). For the straight running condition, the participants were instructed to plant their right foot at the same location and run straight forward without any deceleration (Weinhandl et al., 2013). The order of conditions was randomized using MATLAB's random number generator function (version 2016b, MathWorks, Inc., United States). Each participant performed five trials for each condition, and a 3-min rest was given between each trial. Thus, a total of 30 trials were collected (5 trials × 3 velocities × 2 running types).

2.4 Data analysis

The measured data was labeled and extracted to a C3D file for further processing with Visual3D software. For kinematics data, spline interpolation up to 10 frames and a Butterworth 4th order low-pass filter at a cut-off frequency of 15 Hz was applied (Donnelly et al., 2012; Mudie et al., 2017). The kinetics data were filtered using a Butterworth 4th-order low-pass filter at a cut-off frequency of 20 Hz (Weinhandl et al., 2013). Similarly, raw EMG signals were filtered using a Butterworth 4th-order high-pass filter at a cut-off frequency of 20 Hz (De Luca et al., 2010). This was followed by full-wave rectification and re-filtering conducted with a Butterworth 4th-order low-pass filter at a cut-off frequency of 15 Hz (Laughlin et al., 2011).

2.4.1 Kinematic and kinetic data analysis

The femoral epicondyle markers (Fonseca et al., 2020) and the malleoli markers (Wu et al., 2002) were used to define the knee and ankle joint centers, respectively. The three-dimensional knee joint angle was calculated using an inverse kinematics algorithm. Negative values for flexion, abduction and external rotation were used to define the knee joint angles. The knee joint force and moment were calculated using an inverse dynamics algorithm. Positive values for extension, adduction and internal rotation were used to define the knee joint moments. The shear force that acts in the anterior-posterior and medial-lateral directions was referred to as the knee joint force. Peak values for different parameters were calculated at the instant of planting for each trial, which was identified by a force profile in the vertical direction (Fz). For interparticipant comparability, body mass was used to normalize the shear force and body mass and height to normalize the knee joint moment.

2.4.2 ACL modeling

The ACL force was calculated using the OpenSim musculoskeletal simulation software (version 3.3, Stanford University, Stanford, CA, United States). We employed the gait2354 model, which has twelve

segments with twenty-three degrees of freedom, including the lower leg and trunk (DOF). Fifty-four muscles were included, but only one DOF (flexion/extension) for the knee joint (Delp et al., 1990; Anderson and Pandy 1999). The ACL load was calculated using a model that took into account the knee joint's flexion/extension, adduction/abduction, internal/external rotation, and the maximum isometric force of the muscles acting around the knee joint. As a result, the improved model was a 3-DOF ball-and-socket joint with flexion/extension ranges of −120 to +10°, adduction/abduction ranges of +15 to −15°, and internal/external rotation ranges of +30 to −45° (Kar and Quesada 2012; Kar and Quesada 2013). Previous studies were used to obtain detailed ACL parameters such as location, length, cross-section, and strain (Cohen et al., 2009; Kar and Quesada 2012; Kar and Quesada 2013).

The inverse kinematics and dynamics calculations were performed after the participants' static standing information data was scaled on the modified ACL model. After reproducing the measured motion using the residual reduction algorithm, the computed muscle control (CMC) was used to construct a set of muscle excitations (Delp et al., 1990; Thelen et al., 2003; Thelen and Anderson 2006). Finally, the ACL force was computed using Hill's model, which may be found in the formula below (Hill 1938; Kar and Quesada 2012; Kar and Quesada 2013).

$$f^*_m = \left[a^*_m f_{lv}\left(l^*_m, i^*_m\right) + f_{psv}\left(l^*_m\right)\right] \cos\ \left(\alpha^*_m\right)$$

Here, a^*_m refers to muscle activity, f_{lv} refers to the active force exerted by the force-length-velocity curve based on Hill's model, l^*_m is the muscle's length, i^*_m refers to the velocity of the tendon acting in the muscle direction, f_{psv} is the passive force, a^*_m is the pennation angle of the muscle. The model was validated using a standard protocol, for which the residual force values of the RRA and CMC were considered. The outputs were compared to the threshold values presented in the OpenSim software used to evaluate simulations of walking and running (Lee et al., 2020).

2.4.3 Co-contraction index of electromyography

The co-contraction index (CCI) was calculated for the femoral extensors (rectus femoris, vastus medialis, vastus lateralis) and flexors (biceps femoris, semitendinosus) muscles following normalization with the MVC test. The analytical duration was set to 100 milliseconds before and following the GRF peak. All calculations were performed using Matlab (R2009b, MathWorks, Inc., Natick, MA, United States), and the following formula was used to perform the computations (Park et al., 2011).

$$\mathrm{CCI} = 1 - \frac{|M_{Extensor}| - |M_{Flexor}|}{|M_{Extensor}| + |F_{Flexor}|} = 2\frac{|M_{Flexor}|}{|M_{Extensor}| + |M_{Flexor}|}$$

2.5 Statistical analysis

Repeated-measured ANOVAs were used to explore the effect of the main outcome variables by the two factors, *VELOCITY* (3 levels: 3, 4, and 5 m/s) and *TYPE* (2 levels: straight-run and cutting-run). Mauchly's sphericity test was employed to confirm or reject the assumptions of sphericity. The Greenhouse-Geisser corrections were used when the sphericity assumption was rejected. The statistical power for all comparisons was computed, and for all planned comparisons, the power was over 0.7 from the pool of fourteen participants. For *post-hoc* comparison, paired *t*-tests were performed to explore further significant effects of three levels of velocity with Bonferroni *p*-value adjustments for multiple comparisons ($p < 0.0083$ instead of the nominal $p < 0.05$). For all statistical tests, the level of significance was set at p 0.05.

3 Results

3.1 Knee joint angle

In general, the knee flexion angles and knee abduction angles increased with running velocity, while there was no clear effect of the running velocity on the maximal internal rotation of the knee joint (Figure 2) (See Supplementary Files for details). For the knee flexion angle and knee abduction angle, the significant difference between the running types (e.g., straight and sidestep cutting runs) was only observed at the highest velocity (i.e., 5 m/s), which showed a larger knee flexion angle during straight running than during side step cutting. There was no significant difference in the knee internal rotation angle between the two running types. These findings were supported by a two-way repeated measure ANOVA separately on knee flexion angle, knee abduction angle, and knee internal rotation angle with factors *TYPE* (two levels: sidestep cutting and straight running) and *VELOCITY* (three levels: 3, 4, and 5 m/s). The main effects of *VELOCITY* ($F_{[2,\ 24]} = 31.46$, $p < 0.001$) and *TYPE* ($F_{[1,\ 12]} = 5.49$, $p < 0.05$) were significant on knee flexion angle only. The factor interaction *TYPE* × *VELOCITY* was significant on both the knee flexion angle and the knee abduction angle, which reflected the fact that a significant effect of *TYPE* on both the knee flexion angle and the knee abduction angle was observed only at the 5 m/s condition ($p < 0.001$ for flexion angle, $p < 0.01$ for abduction angle). A *post-hoc* comparison on knee flexion angle showed that knee flexion angle of 3 m/s < 5 m/s during the sidestep cutting condition ($p < 0.017$), and a knee flexion angle of 3 and 4 m/s < 5 m/s during the straight running condition ($p < 0.017$). Similarly, *post-hoc* comparison on knee abduction angle only showed a knee abduction angle of 3 m/s < 5 m/s during the sidestep cutting condition ($p < 0.017$), which confirmed a significant factor interaction on knee flexion angle and knee abduction angle.

3.2 ACL force and knee shear force

The ACL force normalized by the body mass ($\mathrm{ACLF_{NORM}}$) increased with running velocity in both sidestep cutting and straight running conditions, and $\mathrm{ACLF_{NORM}}$ in sidestep cutting and straight running conditions was similar in magnitude for 3 and 4 m/s velocity conditions (Figure 3) (See Supplementary Files for details). These findings were supported by the results of a two-way repeated measures ANOVA, which confirmed a significant main effect of *VELOCITY* on $\mathrm{ACLF_{NORM}}$ ($F_{[2,\ 24]} = 14.95$, $p < 0.001$) with a significant factor interaction ($F_{[2,\ 24]} = 9.95$, $p < 0.01$). Post-hoc comparisons showed $\mathrm{ACLF_{NORM}}$ at 3 m/s < 4 m/s < 5 m/s for the sidestep cutting condition ($p < 0.017$), and 3 m/s < 4 m/s and 5 m/s for the straight running condition ($p < 0.017$), which confirmed a significant factor interaction.

The knee shear force (KSF) normalized by the body mass of individual subjects ($\mathrm{KSF_{NORM}}$) increased with running velocity in both

10.3389/fbioe.2023.1033590

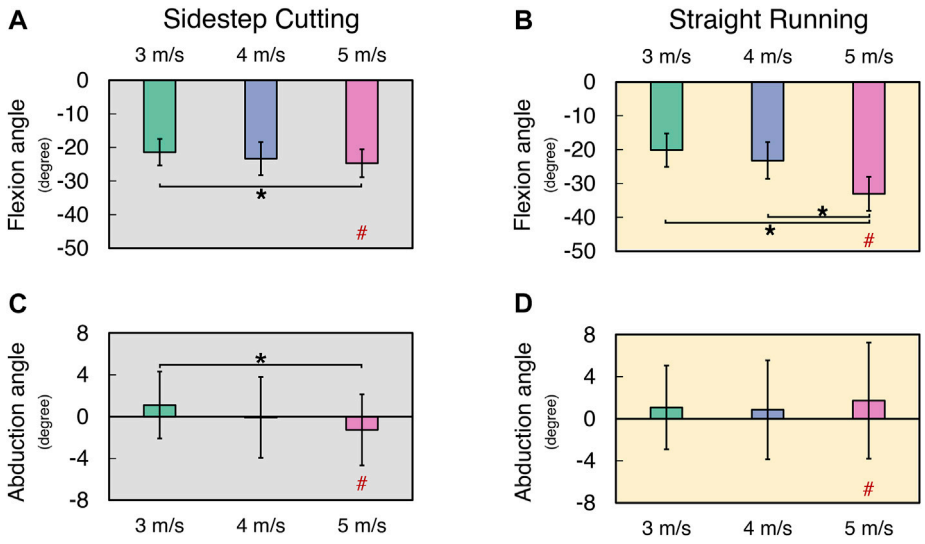

FIGURE 2
The mean and standard deviation of calculated variables during sidestep cutting (*Gray*) and straight running (*Yellow*). **(A,B)** Peak knee flexion angle, **(C,D)** Peak knee abduction angle. Note: Units expressed in degrees. Knee extension, adduction, and internal rotation are positive. Significant differences between *VELOCITY* denoted by asterisks (*) ($p < 0.05$). Significant differences between running *TYPES* for each condition denoted by hash (#) ($p < 0.05$).

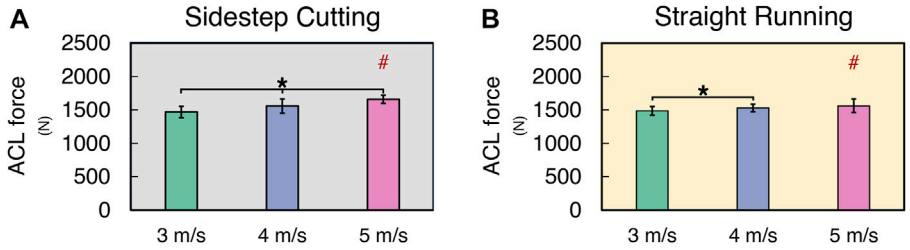

FIGURE 3
The mean and standard deviation of ACL force during **(A)** sidestep cutting (*Gray*) and **(B)** straight running (*Yellow*). Note: Units expressed in newton. Significant differences between *VELOCITIES* denoted by asterisks (*) ($p < 0.05$). Significant differences between running *TYPES* for each condition denoted by hash (#) ($p < 0.05$).

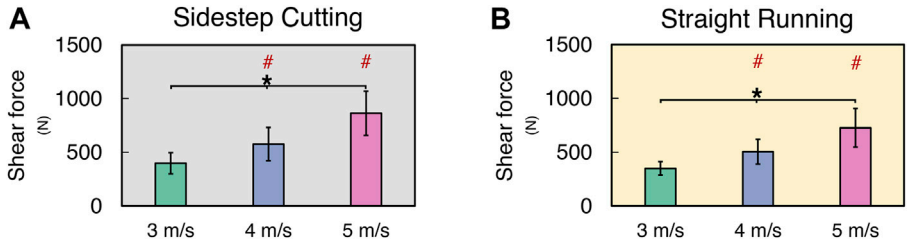

FIGURE 4
The mean and standard deviation of knee shear force during **(A)** sidestep cutting (*Gray*) and **(B)** straight running (*Yellow*). Note: Units expressed in newton. Significant differences between *VELOCITIES* denoted by asterisks (*) ($p < 0.05$). Significant differences between running *TYPES* for each condition denoted by hash (#) ($p < 0.05$).

sidestep cutting and straight running conditions (Figure 4) (See Supplementary Files for details). Also, KSF_{NORM} at 4 and 5 m/s velocities were larger in the sidestep cutting condition than in the straight running condition. A two-way repeated measures ANOVA with factor *TYPE* and *VELOCITY* confirmed the significant main effect of *VELOCITY* ($F_{[2, 24]} = 76.46, p < 0.001$) with a significant factor

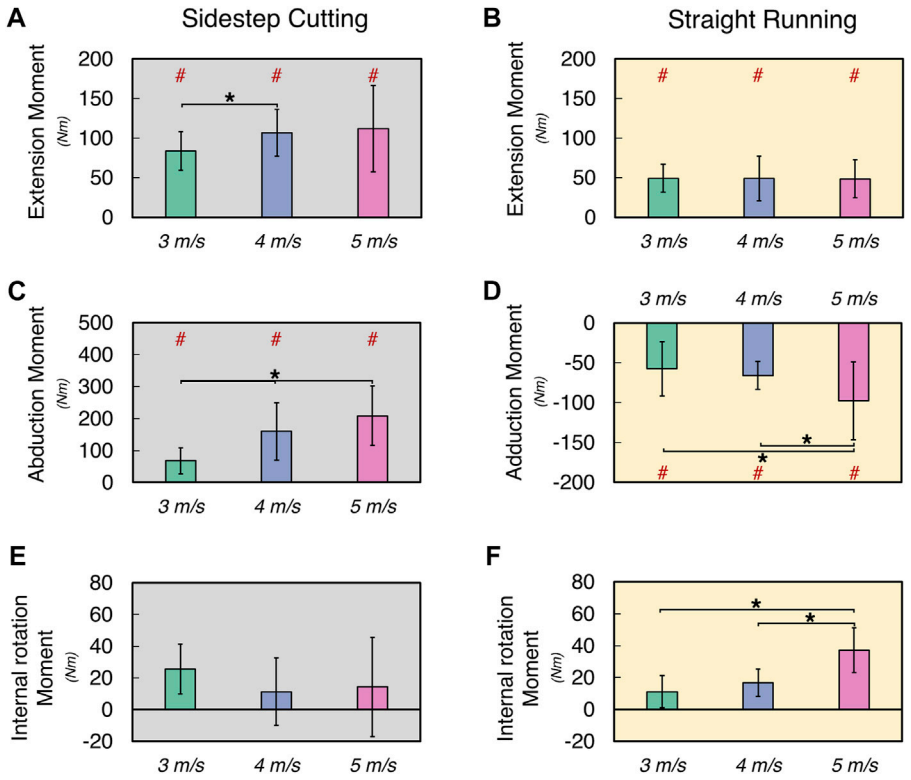

FIGURE 5
The mean and standard deviation of calculated variables during sidestep cutting (*Gray*) and straight running (*Yellow*). **(A,B)** Peak knee extension moment, **(C)** Peak knee abduction moment, **(D)** Peak knee adduction movement, **(E,F)** Internal rotation moment. Note: Units expressed in Newton-meters (Nm). Knee extension, adduction, and internal rotation are positive. Significant differences between *VELOCITY* denoted by asterisks (*) ($p < 0.05$). Significant differences between running *TYPES* for each condition denoted by hash (#) ($p < 0.05$).

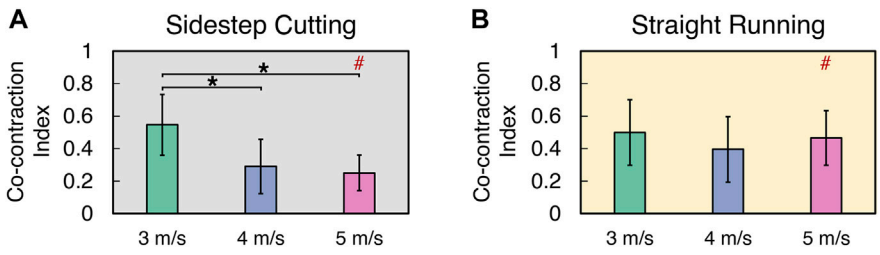

FIGURE 6
The mean and standard deviation of co-contraction index during **(A)** sidestep cutting (*Gray*) and **(B)** straight running (*Yellow*). Note: Significant differences between *VELOCITIES* denoted by asterisks (*) ($p < 0.05$). Significant differences between running *TYPES* for each condition denoted by hash (#) ($p < 0.05$).

interaction ($F_{[2,\ 24]} = 6.68$, $p < 0.01$). The *post-hoc* comparison showed KSF_{NORM} in sidestep cutting > straight running at 4 and 5 m/s conditions ($p < 0.017$), not at 3 m/s conditions.

3.3 Knee joint moment

The normalized knee extension moment (KEM_{NORM}) increased only at medium velocity (i.e., 4 m/s) in the sidestep cutting condition, while no differences were observed in the straight running condition (Figures 5A, B) (See Supplementary Files for details). A two-way repeated measure ANOVA with factor *TYPE* and *VELOCITY* confirmed the significant main effect of *TYPE* ($F_{[1,\ 12]} = 44.83$, $p < 0.001$). The *post-hoc* comparison showed KEM_{NORM} at 3 m/s < 4 m/s for the sidestep cutting condition ($p < 0.017$), and KEM_{NORM} in sidestep cutting > straight running at 3, 4, and 5 m/s conditions ($p < 0.017$).

The normalized knee adduction moment ($KADM_{NORM}$) increased with running velocity in the sidestep cutting condition, while the normalized knee abduction moment ($KABM_{NORM}$) increased only at the highest velocity (i.e., 5 m/s) in the straight running (Figures 5C, D) (See Supplementary Files for details). These findings were supported by the results of a two-way repeated measures ANOVA, which confirmed the significant main effects of *TYPE* on $KADM_{NORM}$ ($F_{[1,\ 12]} = 168.76$, $p < 0.001$) and *VELOCITY* on $KADM_{NORM}$ ($F_{[2,\ 24]} = 18.97$, $p < 0.001$) with a significant factor interaction ($F_{[2,\ 24]} = 38.89$, $p < 0.001$). The *post-hoc* comparison showed $KADM_{NORM}$ at 3 m/s < 4 m/s < 5 m/s for the sidestep cutting condition ($p < 0.017$), and $KABM_{NORM}$ at 3 and 4 m/s < 5 m/s for the straight running condition ($p < 0.017$), which confirmed a significant factor interaction.

In the straight running condition, the normalized internal rotation moment ($KIRM_{NORM}$) increased with running velocity, while no clear effect of running velocity was observed for $KIRM_{NORM}$ in the sidestep cutting condition (Figures 5E, F) (See Supplementary Files for details). The results of the two-way repeated measure ANOVA revealed that the main effects of *VELOCITY* and *TYPE* had no statistical significance, but the factor interaction was significant on $KIRM_{NORM}$ ($F_{[2,\ 24]} = 21.28$, $p < 0.001$). Post-hoc comparison only showed $KIRM_{NORM}$ at 3 and 4 m/s < 5 m/s for the straight running condition ($p < 0.017$).

3.4 Co-contraction index (CCI)

The CCI of the flexors and extensors of femoral muscles decreased with running velocity during the sidestep cutting, while no clear effect of running velocity was observed in the straight running (Figure 6) (See Supplementary Files for details). Also, CCI at 4 and 5 m/s velocity were larger in the sidestep cutting condition than in the straight running condition. A two-way repeated measures ANOVA with factor *TYPE* and *VELOCITY* confirmed the significant main effects of *TYPE* ($F_{[1,\ 12]} = 10.24$, $p < 0.01$) and *VELOCITY* ($F_{[2,\ 24]} = 14.85$, $p < 0.001$) with a significant factor interaction ($F_{[2,\ 24]} = 19.86$, $p < 0.001$). Post-hoc comparisons showed CCI at 3 m/s < 4 and 5 m/s in the sidestep cutting condition ($p < 0.017$), while CCI during sidestep cutting < straight running and statistical significance was observed only in the 5 m/s condition ($p < 0.017$), but not at 3 and 5 m/s.

4 Discussion

The purpose of the study was to investigate the effect of increasing sprinting velocity on ACL load, knee kinematics, and CCI, for which we employed a musculoskeletal modeling approach. Our findings indicated that an increase in running velocity during the sidestep cutting condition increased knee abduction angles, while the increase in velocity during straight running increased knee flexion angles. In line with our initial hypothesis, the $ACLF_{NORM}$, KSF_{NORM}, KEM_{NORM}, $KADM_{NORM}$, and CCI increased with running velocity, as predicted, and had higher values in the sidestep cutting condition than in the straight running condition. $KIRM_{NORM}$, on the other hand, showed no differences in running velocity or type.

4.1 Mechanism of changes in ACL loading with running velocities and types

The amplitude of ACL load is known to be influenced by knee flexion, with the maximum load found when the knee is flexed beyond 30° (DeMorat et al., 2004; Gabriel et al., 2004). The cadaveric investigation by Gabriel et al. (2004) confirmed this, revealing that the peak magnitude of ACL load was around 120 N at 15°–20° of knee flexion. The angle of knee flexion at the maximum magnitude of ACL load was also in the same range as the results of the current study. The angle of knee flexion increased with increasing running velocity, which coincided with an increase in ACL loading force during both the sidestep cutting and straight running. The highest ACL loading force was detected during the cutting run (5 m/s), although a considerably greater degree of knee flexion was observed during the straight running, which had a lower ACL loading force than the sidestep cutting. This indicates that knee flexion is not the only element to consider when estimating the risk of ACL injury (i.e., the ACL loading force). Running with cutting (rapid directional shift) at a faster velocity is likely to be more damaging to ACL damage, as shown by a greater loading force. The observed findings are consistent with the general assumption of ACL injury in terms of the level of ACL loading as a function of running velocity and type. Aside from knee flexion kinematics, the knee abduction/adduction kinematics differed across the two running types used in this study. The knee was adducted during straight running and abducted as the velocity increased. Even during the sidestep cutting, the knee was adducted at a slower pace.

In the study conducted by Markolf et al. (1995) applied a 100 N shear force to the tibia while varying the knee flexion (−)/extension (+) angles between −10° and 90°. The study found that knee abduction and internal rotation moments were the primary factors contributing to the increase in ACL load. While another female study found a knee abduction angle of 15°–20° during the sidestep cutting and landing (McLean et al., 2004; Olsen et al., 2004). When abrupt directional changes or deceleration were undertaken, analysis of real video from matches revealed external to internal tibial rotation (Boden et al., 2000). This type of situation can be referred to as movement behavior that frequently occurs with athletes during competitive matches. However, individuals in our study were able to predict the direction of the sidestep cutting in advance, which resulted in the direction switching being carried out in a state with the knee internal rotation angle.

4.2 Effect of running velocity and type on ACL load

Using our musculoskeletal model, we demonstrated the effect of running *VELOCITY* (i.e., the greater the running velocity, the greater the ACL loading force) and *TYPE* on the estimated maximal ACL load during the sidestep cutting. Previous studies have indicated a maximal ACL load of 681 N during sidestep cutting at a running velocity of 4.5–5.0 m/s, which is similar to our findings (Kernozek and Ragan 2008; Weinhandl et al., 2013). In comparison to our investigation, the result of the knee joint moment from Weinhandl et al., (2013) was significantly lower. Although the movement differed, when executing a double leg landing task at a height of 50 cm, the ACL loading was reported to be 1,150 N for the

right and 1,136 N for the left in a study by Kar and Quesada (2012), who used a similar biomechanical model as our work. Additionally, the ACL load estimated using this musculoskeletal model is more likely to be true, given that the ACL injury threshold is approximately 2,000 N (Stapleton et al., 1998).

Previously, research indicated that the ACL load was influenced by the knee shear force acting on the knee adduction and internal moments as well as the contraction of the quadriceps femoris (Markolfet al., 1995; Fukuda et al., 2003; DeMorat et al., 2004). However, there are conflicting perspectives regarding the effect of the external rotation moment on the rise in ACL load (Markolfet al., 1995; Fleming et al., 2001). Similarly, several investigations have indicated that when a force of 2,000 N or greater is applied, the shear force causes an ACL injury (Shin et al., 2007; McLean et al., 2008). The knee shear force at 5 m/s was the greatest in our study, at 864.2 ± 204.7 N (1.156 ± 0.241 N/BW) in the sidestep cutting condition, but it was much lower than the 2,000 N reported in other investigations. Furthermore, our findings are consistent with the findings of McLean et al., 2004, who concluded that the shear force acting on the knee joint cannot cause the injury on its own.

The adduction moment of the knee joint has been implicated in prior research as a factor impacting ACL loading (Markolfet al., 1995; Fukuda et al., 2003; McLean et al., 2004; McLean et al., 2008). Additionally, when executing a sidestep cutting, the adduction moment of the knee was greater than the abduction moment (Weinhandl et al., 2013). Furthermore, previous research has indicated that the internal rotation moment of the knee joint is a significant factor in increasing ACL load (Markolfet al., 1995; Shin et al., 2009). Markolfet al, (1995) used a shear force of 100 N and a moment of 10 Nm at a constant knee angle (flexion from 5° to 90°) to observe variations in ACL stress. As a result, the ACL load of shear force and internal rotation moment was around 180 N when the knee joint was flexed at 15°, which is nearly 2.6 times higher than a load of shear force and external rotation moment of 70 N. However, in this investigation, the internal rotation moment at the ACL maximum load was unaffected by increasing running velocity during sidestep cutting but was greatest at 5 m/s during straight running. These findings suggest that the task performed in this study can be predicted in advance, thereby shortening the time spent in the transverse plane (Weinhandl et al., 2013). Additionally, further research is required to determine the degree of injury threshold for internal rotation moments (McLean et al., 2004).

4.3 Effect of running velocity and type on the femoral muscle

Another factor that has been shown to affect ACL load around knee joints is quadriceps and biceps femoris muscle contractions. Previous research has found that excessive quadriceps femoris muscle contraction causes forward displacement of the tibia, which increases ACL load (Markolfet al., 1995; Fleming et al., 2001; DeMorat et al., 2004). Furthermore, it has been reported that if the femoral muscles are imbalanced, they become less mobilized or fatigued, causing a delay in muscle contraction time, which increases the ACL load (Boden et al., 2000; Hewett et al., 2005). However, Simonsen et al. (2000) hypothesized that the biceps femoris would have a negligible effect on ACL load reduction during the sidestep cutting since the biceps femoris has a low level of muscle activity (34%–39% of MVC). Additionally, the CCI of the extensor and flexor muscles during the sidestep cutting at 5 m/s was 0.244 ± 0.107%, which was found to be statistically less than the CCI in the 3 m/s condition. When the running velocity was increased, the ratio of muscular activity in the rectus femoris, vastus medialis, and vastus lateralis (extensor muscles) increased. While the flexor muscle's biceps femoris and semitendinosus muscular activation ratios were observed to be relatively lower and are considered to increase the risk of injury.

5 Conclusion

The goal of this study was to determine the effect of increasing sprinting velocity on ACL load, knee kinematics, and CCI, which was achieved using musculoskeletal modeling. As a result, the shear force, extended landing posture with increased running velocity, and femoral muscle imbalance activity all influenced the ACL load during a sidestep cutting. We suggest that to compensate for muscular imbalances in the lower limb and the increased load associated with increasing sidestep cutting velocity, it would be beneficial to strengthen the hamstring muscles and concentrate on knee flexion during landing.

Data availability statement

The raw data supporting the conclusion of this article will be made available by the authors, without undue reservation.

Ethics statement

The studies involving human participants were reviewed and approved by JM, Seoul National University. The patients/participants provided their written informed consent to participate in this study.

Author contributions

Conceptualization: JM and SP; Data curation: DK and SK; Formal analysis: JM and DK; Investigation: JM, DK, and SK; Methodology: JM, DK, and SP; Project administration: JM and SP; Resources: JM, SK, and SP; Software: JM and SK; Supervision: JM and SK; Validation: JM and DK; Visualization: JM and SP; Writing—original draft: JM and SP; Writing—review and editing: JM and SP.

Conflict of interest

The authors declare that the research was conducted in the absence of any commercial or financial relationships that could be construed as a potential conflict of interest.

Publisher's note

All claims expressed in this article are solely those of the authors and do not necessarily represent those of their affiliated

organizations, or those of the publisher, the editors and the reviewers. Any product that may be evaluated in this article, or claim that may be made by its manufacturer, is not guaranteed or endorsed by the publisher.

Supplementary material

The Supplementary Material for this article can be found online at: https://www.frontiersin.org/articles/10.3389/fbioe.2023.1033590/full#supplementary-material

References

Anderson, F. C., and Pandy, M. G. (1999). A dynamic optimization solution for vertical jumping in three dimensions. *Comput. methods biomechanics Biomed. Eng.* 2, 201–231. doi:10.1080/10255849908907988

Bedo, B. L. S., Cesar, G. M., Moraes, R., Mariano, F. P., Vieira, L. H. P., Andrade, V. L., et al. (2021). Influence of side uncertainty on knee kinematics of female handball athletes during sidestep cutting maneuvers. *J. Appl. Biomechanics* 37, 188–195. doi:10.1123/jab.2020-0141

Boden, B. P., Dean, G. S., Feagin, J. A., and Garrett, W. E. (2000). *Mechanisms of anterior cruciate ligament injury*. NJ: SLACK Incorporated Thorofare.

Cappozzo, A., Cappello, A., Croce, U. D., and Pensalfini, F. (1997). Surface-marker cluster design criteria for 3-D bone movement reconstruction. *IEEE Trans. Biomed. Eng.* 44, 1165–1174. doi:10.1109/10.649988

Cohen, S. B., VanBeek, C., Starman, J. S., Armfield, D., Irrgang, J. J., and Fu, F. H. (2009). MRI measurement of the 2 bundles of the normal anterior cruciate ligament. *Orthopedics* 32, 687. doi:10.3928/01477447-20090728-35

Collins, T. D., Ghoussayni, S. N., Ewins, D. J., and Kent, J. A. (2009). A six degrees-of-freedom marker set for gait analysis: Repeatability and comparison with a modified helen hayes set. *Gait posture* 30, 173–180. doi:10.1016/j.gaitpost.2009.04.004

Dai, B., Herman, D., Liu, H., Garrett, W. E., and Yu, B. (2012). Prevention of ACL injury, part I: Injury characteristics, risk factors, and loading mechanism. *Res. sports Med.* 20, 180–197. doi:10.1080/15438627.2012.680990

De Luca, C. J., Gilmore, L. D., Kuznetsov, M., and Roy, S. H. (2010). Filtering the surface EMG signal: Movement artifact and baseline noise contamination. *J. biomechanics* 43, 1573–1579. doi:10.1016/j.jbiomech.2010.01.027

Delp, S. L., Loan, J. P., Hoy, M. G., Zajac, F. E., Topp, E. L., and Rosen, J. M. (1990). An interactive graphics-based model of the lower extremity to study orthopaedic surgical procedures. *IEEE Trans. Biomed. Eng.* 37, 757–767. doi:10.1109/10.102791

DeMorat, G., Weinhold, P., Blackburn, T., Chudik, S., and Garrett, W. (2004). Aggressive quadriceps loading can induce noncontact anterior cruciate ligament injury. *Am. J. sports Med.* 32, 477–483. doi:10.1177/0363546503258928

Donnelly, C. J., Lloyd, D. G., Elliott, B. C., and Reinbolt, J. A. (2012). Optimizing whole-body kinematics to minimize valgus knee loading during sidestepping: Implications for ACL injury risk. *J. biomechanics* 45, 1491–1497. doi:10.1016/j.jbiomech.2012.02.010

Fleming, B. C., Renstrom, P. A., Beynnon, B. D., Engstrom, B., Peura, G. D., Badger, G. J., et al. (2001). The effect of weightbearing and external loading on anterior cruciate ligament strain. *J. biomechanics* 34, 163–170. doi:10.1016/s0021-9290(00)00154-8

Fonseca, M., Gasparutto, X., Leboeuf, F., Dumas, R., and Armand, S. (2020). Impact of knee marker misplacement on gait kinematics of children with cerebral palsy using the Conventional Gait Model-A sensitivity study. *PLoS One* 15 (4), e0232064. doi:10.1371/journal.pone.0232064

Fukuda, Y., Woo, S. L. Y., Loh, J. C., Tsuda, E., Tang, P., McMahon, P. J., et al. (2003). A quantitative analysis of valgus torque on the ACL: A human cadaveric study. *J. Orthop. Res.* 21, 1107–1112. doi:10.1016/s0736-0266(03)00084-6

Gabriel, M. T., Wong, E. K., Woo, S. L. Y., Yagi, M., and Debski, R. E. (2004). Distribution of *in situ* forces in the anterior cruciate ligament in response to rotatory loads. *J. Orthop. Res.* 22, 85–89. doi:10.1016/s0736-0266(03)00133-5

Hashemi, J., Breighner, R., Jang, T-H., Chandrashekar, N., Ekwaro-Osire, S., and Slauterbeck, J. R. (2010). Increasing pre-activation of the quadriceps muscle protects the anterior cruciate ligament during the landing phase of a jump: An *in vitro* simulation. *knee* 17, 235–241. doi:10.1016/j.knee.2009.09.010

Hermens, H. J., Freriks, B., Merletti, R., Stegeman, D., Blok, J., Rau, G., et al. (1999). European recommendations for surface electromyography. *Roessingh Res. Dev.* 8, 13–54.

Hewett, T. E., Myer, G. D., Ford, K. R., Heidt, R. S., Jr, Colosimo, A. J., McLean, S. G., et al. (2005). Biomechanical measures of neuromuscular control and valgus loading of the knee predict anterior cruciate ligament injury risk in female athletes: A prospective study. *Am. J. sports Med.* 33, 492–501. doi:10.1177/0363546504269591

Hill, A. V. (1938). The heat of shortening and the dynamic constants of muscle. *Proc. R. Soc. Lond. Ser. B-Biological Sci.* 126, 136–195. doi:10.1098/rspb.1938.0050

Hurd, W. J., and Snyder-Mackler, L. (2007). Knee instability after acute ACL rupture affects movement patterns during the mid-stance phase of gait. *J. Orthop. Res.* 25, 1369–1377. doi:10.1002/jor.20440

Kar, J., and Quesada, P. M. (2013). A musculoskeletal modeling approach for estimating anterior cruciate ligament strains and knee anterior–posterior shear forces in stop-jumps performed by young recreational female athletes. *Ann. Biomed. Eng.* 41, 338–348. doi:10.1007/s10439-012-0644-y

Kar, J., and Quesada, P. M. (2012). A numerical simulation approach to studying anterior cruciate ligament strains and internal forces among young recreational women performing valgus inducing stop-jump activities. *Ann. Biomed. Eng.* 40, 1679–1691. doi:10.1007/s10439-012-0572-x

Kellis, E., Arabatzi, F., and Papadopoulos, C. (2003). Muscle co-activation around the knee in drop jumping using the co-contraction index. *J. Electromyogr. Kines* 13, 229–238. doi:10.1016/s1050-6411(03)00020-8

Kernozek, T. W., and Ragan, R. J. (2008). Estimation of anterior cruciate ligament tension from inverse dynamics data and electromyography in females during drop landing. *Clin. Biomech.* 23, 1279–1286. doi:10.1016/j.clinbiomech.2008.08.001

Khandha, A., Manal, K., Capin, J., Wellsandt, E., Marmon, A., Snyder-Mackler, L., et al. (2019). High muscle co-contraction does not result in high joint forces during gait in anterior cruciate ligament deficient knees. *J. Orthop. Research®* 37, 104–112. doi:10.1002/jor.24141

Konrad, P. (2005). The abc of emg. *A Pract. Introd. Kinesiol. Electromyogr.* 1, 30–35.

Krosshaug, T., Andersen, T. E., Olsen, O. O., Myklebust, G., and Bahr, R. (2005). Research approaches to describe the mechanisms of injuries in sport: Limitations and possibilities. *Br. J. sports Med.* 39, 330–339. doi:10.1136/bjsm.2005.018358

Laughlin, W. A., Weinhandl, J. T., Kernozek, T. W., Cobb, S. C., Keenan, K. G., and O'Connor, K. M. (2011). The effects of single-leg landing technique on ACL loading. *J. biomechanics* 44, 1845–1851. doi:10.1016/j.jbiomech.2011.04.010

Lee, J., Pathak, P., Panday, S. B., and Moon, J. (2020). Effect of foot-planting strategy on anterior cruciate ligament loading in women during a direction diversion maneuver: A musculoskeletal modeling approach. *Orthop. J. Sports Med.* 8, 232596712096318. doi:10.1177/2325967120963180

Lin, C-F., Gross, M., Ji, C., Padua, D., Weinhold, P., Garrett, W. E., et al. (2009). A stochastic biomechanical model for risk and risk factors of non-contact anterior cruciate ligament injuries. *J. biomechanics* 42, 418–423. doi:10.1016/j.jbiomech.2008.12.005

Markolf, K. L., Burchfield, D. M., Shapiro, M. M., Shepard, M. F., Finerman, G. A., and Slauterbeck, J. L. (1995). Combined knee loading states that generate high anterior cruciate ligament forces. *J. Orthop. Res.* 13, 930–935. doi:10.1002/jor.1100130618

McLean, S. G., Huang, X., Su, A., and Van Den Bogert, A. J. (2004). Sagittal plane biomechanics cannot injure the ACL during sidestep cutting. *Clin. Biomech.* 19, 828–838. doi:10.1016/j.clinbiomech.2004.06.006

McLean, S. G., Huang, X., and van den Bogert, A. J. (2008). Investigating isolated neuromuscular control contributions to non-contact anterior cruciate ligament injury risk via computer simulation methods. *Clin. Biomech.* 23, 926–936. doi:10.1016/j.clinbiomech.2008.03.072

Mudie, K. L., Gupta, A., Green, S., Hobara, H., and Clothier, P. J. (2017). A comparison of vertical stiffness values calculated from different measures of center of mass displacement in single-leg hopping. *J. Appl. biomechanics* 33, 39–47. doi:10.1123/jab.2016-0037

O'Connor, K. M., Monteiro, S. K., and Hoelker, I. A. (2009). Comparison of selected lateral cutting activities used to assess ACL injury risk. *J. Appl. biomechanics* 25, 9–21. doi:10.1123/jab.25.1.9

Olsen, O-E., Myklebust, G., Engebretsen, L., and Bahr, R. (2004). Injury mechanisms for anterior cruciate ligament injuries in team handball: A systematic video analysis. *Am. J. sports Med.* 32, 1002–1012. doi:10.1177/0363546503261724

Olsen, O-E., Myklebust, G., Engebretsen, L., Holme, I., and Bahr, R. (2005). Exercises to prevent lower limb injuries in youth sports: Cluster randomised controlled trial. *Bmj* 330, 449. doi:10.1136/bmj.38330.632801.8f

Park, J., Sun, Y., Zatsiorsky, V. M., and Latash, M. L. (2011). Age-related changes in optimality and motor variability: An example of multifinger redundant tasks. *Exp. brain Res.* 212, 1–18. doi:10.1007/s00221-011-2692-1

Pflum, M. A., Shelburne, K. B., Torry, M. R., Decker, M. J., and Pandy, M. G. (2004). Model prediction of anterior cruciate ligament force during drop-landings. *Med. Sci. sports Exerc.* 36, 1949–1958. doi:10.1249/01.mss.0000145467.79916.46

Pollard, C. D., Heiderscheit, B. C., Van Emmerik, R. E., and Hamill, J. (2005). Gender differences in lower extremity coupling variability during an unanticipated cutting maneuver. *J. Appl. biomechanics* 21, 143–152. doi:10.1123/jab.21.2.143

Rutherford, D. J., Hubley-Kozey, C. L., and Stanish, W. D. (2011). Maximal voluntary isometric contraction exercises: A methodological investigation in

moderate knee osteoarthritis. *J. Electromyogr. Kinesiol.* 21, 154–160. doi:10.1016/j.jelekin.2010.09.004

Shin, C. S., Chaudhari, A. M., and Andriacchi, T. P. (2009). The effect of isolated valgus moments on ACL strain during single-leg landing: A simulation study. *J. biomechanics* 42, 280–285. doi:10.1016/j.jbiomech.2008.10.031

Shin, C. S., Chaudhari, A. M., and Andriacchi, T. P. (2007). The influence of deceleration forces on ACL strain during single-leg landing: A simulation study. *J. biomechanics* 40, 1145–1152. doi:10.1016/j.jbiomech.2006.05.004

Simonsen, E., Magnusson, S., Bencke, J., Naesborg, H., Havkrog, M., Ebstrup, J., et al. (2000). Can the hamstring muscles protect the anterior cruciate ligament during a side-cutting maneuver? *Scand. J. Med. Sci. sports* 10, 78–84. doi:10.1034/j.1600-0838.2000.010002078.x

Stapleton, T. R., Waldrop, J. I., Ruder, C. R., Parrish, T. A., and Kuivila, T. E. (1998). Graft fixation strength with arthroscopic anterior cruciate ligament reconstruction. *Am. J. sports Med.* 26, 442–445. doi:10.1177/03635465980260031801

Taylor, K., Cutcliffe, H., Queen, R., Utturkar, G., Spritzer, C., Garrett, W., et al. (2013). *In vivo* measurement of ACL length and relative strain during walking. *J. biomechanics* 46, 478–483. doi:10.1016/j.jbiomech.2012.10.031

Taylor, K., Terry, M., Utturkar, G., Spritzer, C., Queen, R., Irribarra, L., et al. (2011). Measurement of *in vivo* anterior cruciate ligament strain during dynamic jump landing. *J. biomechanics* 44, 365–371. doi:10.1016/j.jbiomech.2010.10.028

Thelen, D. G., Anderson, F. C., and Delp, S. L. (2003). Generating dynamic simulations of movement using computed muscle control. *J. biomechanics* 36, 321–328. doi:10.1016/s0021-9290(02)00432-3

Thelen, D. G., and Anderson, F. C. (2006). Using computed muscle control to generate forward dynamic simulations of human walking from experimental data. *J. biomechanics* 39, 1107–1115. doi:10.1016/j.jbiomech.2005.02.010

Weinhandl, J. T., Earl-Boehm, J. E., Ebersole, K. T., Huddleston, W. E., Armstrong, B. S., and O'Connor, K. M. (2013). Anticipatory effects on anterior cruciate ligament loading during sidestep cutting. *Clin. Biomech.* 28, 655–663. doi:10.1016/j.clinbiomech.2013.06.001

Weinhandl, J. T., Joshi, M., and O'Connor, K. M. (2010). Gender comparisons between unilateral and bilateral landings. *J. Appl. biomechanics* 26, 444–453. doi:10.1123/jab.26.4.444

Weinhandl, J. T., Smith, J. D., and Dugan, E. L. (2011). The effects of repetitive drop jumps on impact phase joint kinematics and kinetics. *J. Appl. Biomechanics* 27, 108–115. doi:10.1123/jab.27.2.108

Wu, G., Siegler, S., Allard, P., Kirtley, C., Leardini, A., Rosenbaum, D., et al. (2002). ISB recommendation on definitions of joint coordinate system of various joints for the reporting of human joint motion—part I: Ankle, hip, and spine. *J. biomechanics* 35, 543–548. doi:10.1016/s0021-9290(01)00222-6

Wu, G., Van der Helm, F. C., Veeger, H. D., Makhsous, M., Van Roy, P., Anglin, C., et al. (2005). ISB recommendation on definitions of joint coordinate systems of various joints for the reporting of human joint motion—Part II: Shoulder, elbow, wrist and hand. *J. biomechanics* 38, 981–992. doi:10.1016/j.jbiomech.2004.05.042

Xu, S. D., Liang, Z. Q., Liu, Y. W., and Fekete, G. (2018). Biomechanical performance of habitually barefoot and shod runners during barefoot jogging and running. *Proc. J. Biomimetics, Biomaterials Biomed. Eng.* 38, 1–10. doi:10.4028/www.scientific.net/JBBBE.38.1

Yu, B., and Garrett, W. E. (2007). Mechanisms of non-contact ACL injuries. *Br. J. sports Med.* 41, i47–i51. doi:10.1136/bjsm.2007.037192

frontiers | Frontiers in Bioengineering and Biotechnology

TYPE Original Research
PUBLISHED 15 February 2023
DOI 10.3389/fbioe.2023.1110099

OPEN ACCESS

EDITED BY
Cheng-Feng Lin,
National Cheng Kung University, Taiwan

REVIEWED BY
Filippo Bertozzi,
Politecnico di Milano, Italy
Tao Liu,
Zhejiang University, China

*CORRESPONDENCE
Bergita Ganse,
✉ Bergita.ganse@uks.eu

SPECIALTY SECTION
This article was submitted to Biomechanics, a section of the journal Frontiers in Bioengineering and Biotechnology

RECEIVED 28 November 2022
ACCEPTED 03 February 2023
PUBLISHED 15 February 2023

CITATION
Wolff C, Steinheimer P, Warmerdam E, Dahmen T, Slusallek P, Schlinkmann C, Chen F, Orth M, Pohlemann T and Ganse B (2023), Effects of age, body height, body weight, body mass index and handgrip strength on the trajectory of the plantar pressure stance-phase curve of the gait cycle.
Front. Bioeng. Biotechnol. 11:1110099.
doi: 10.3389/fbioe.2023.1110099

Effects of age, body height, body weight, body mass index and handgrip strength on the trajectory of the plantar pressure stance-phase curve of the gait cycle

Christian Wolff[1], Patrick Steinheimer[2], Elke Warmerdam[3], Tim Dahmen[1], Philipp Slusallek[1], Christian Schlinkmann[1], Fei Chen[1], Marcel Orth[2], Tim Pohlemann[2] and Bergita Ganse[2,3]*

[1]German Research Center for Artificial Intelligence (DFKI), Saarbrücken, Germany, [2]Department of Trauma, Hand and Reconstructive Surgery, Saarland University, Homburg, Germany, [3]Werner Siemens-Endowed Chair for Innovative Implant Development (Fracture Healing), Saarland University, Homburg, Germany

The analysis of gait patterns and plantar pressure distributions *via* insoles is increasingly used to monitor patients and treatment progress, such as recovery after surgeries. Despite the popularity of pedography, also known as baropodography, characteristic effects of anthropometric and other individual parameters on the trajectory of the stance phase curve of the gait cycle have not been previously reported. We hypothesized characteristic changes of age, body height, body weight, body mass index and handgrip strength on the plantar pressure curve trajectory during gait in healthy participants. Thirty-seven healthy women and men with an average age of 43.65 ± 17.59 years were fitted with Moticon OpenGO insoles equipped with 16 pressure sensors each. Data were recorded at a frequency of 100 Hz during walking at 4 km/h on a level treadmill for 1 minute. Data were processed *via* a custom-made step detection algorithm. The loading and unloading slopes as well as force extrema-based parameters were computed and characteristic correlations with the targeted parameters were identified *via* multiple linear regression analysis. Age showed a negative correlation with the mean loading slope. Body height correlated with $Fmean_{load}$ and the loading slope. Body weight and the body mass index correlated with all analyzed parameters, except the loading slope. In addition, handgrip strength correlated with changes in the second half of the stance phase and did not affect the first half, which is likely due to stronger kick-off. However, only up to 46% of the variability can be explained by age, body weight, height, body mass index and hand grip strength. Thus, further factors must affect the trajectory of the gait cycle curve that were not considered in the present analysis. In conclusion, all analyzed measures affect the trajectory of the stance phase curve. When analyzing insole data, it might be useful to correct for the factors that were identified by using the regression coefficients presented in this paper.

KEYWORDS

gait, motion analysis, ground reaction (forces), ageing, obesity, insoles, handgrip strengh, smart healthcare

1 Introduction

The analysis of gait patterns and pressure distributions under the feet *via* insoles is increasingly used to study specific questions in the everyday lives of people, i.e., to analyze recovery after surgeries (Braun et al., 2017) and to monitor training or health (Subramaniam et al., 2022). Instrumented insoles have become more usable in recent years, as several technical issues could be resolved. These include durability, usability, calibration, hysteresis and drift, limited battery life and data storage capacity, and related to that, the restriction to low sample frequencies that are associated with higher error rates (North et al., 2012; Elstub et al., 2022; Subramaniam et al., 2022). Currently, the usability is still limited by the complexities of data analysis and the need for advanced algorithms and tools to be able to draw meaningful conclusions from these data (Anderson et al., 2022; Chatzaki et al., 2022). For machine-learning-based analyses, it is important to find parameters that are known to have an effect on the stance phase curve and could serve as input variables. This is why the authors conducted the present study in the first place. In addition, one could correct for such confounders when analyzing insole data. Characteristic effects of anthropometric and other individual parameters on the trajectory of the stance phase curve measured by insoles have not been previously reported.

Known gait alterations typical for higher age include a more cautious gait, reductions of the preferred walking speed, cadence, step and stride length plus width, as well as increases in speed-normalized cadence and gait speed variability (Herssens et al., 2018; Niederer et al., 2021). The underlying causes include physical performance declines in advancing age that are associated with progressive losses of muscle mass, decreased joint flexibility, declines in force- and power-generating capacity, as well as age-related changes of the cardiovascular system (Ganse and Degens, 2021). In obesity, the spatiotemporal gait parameters, parameters of pedography and joint kinematics differed compared with normal-weight matched control groups (Choi et al., 2021; Pau et al., 2021). In detail, during walking significantly greater peak pressure values were reported for the front and rear of the foot in normal compared to obese people (Choi et al., 2021). In addition, obese people had a lower gait speed and stride length, shorter stance and swing phases, as well as longer double support phases (Pau et al., 2021). The ankle, knee and hip ranges of motion were smaller in the obese compared to the non-obese (Pau et al., 2021). Compared to obese people, people who are both, obese and old walked with higher center of pressure (CoP) velocity, shorter stride, and spent more time in the support phase (Maktouf et al., 2020). Known gait changes associated with body height include negative correlations of height with cadence (every 10 cm increase in height decreased cadence by 5.6 steps/min), ankle velocity, stride time and stride length (every 10 cm increase in height extended the stride length by 5 cm) (Mikos et al., 2018). In a study with 120 healthy subjects by Senden et al. (2012), together, height, age and gender explained 51% of the variability in step length, 41% of the variability in cadence, and 34% of the variability in age. In addition, age and gender accounted for 34% of the variability in walking speed.

Muscle power is likely to influence the stance phase curve, i.e., *via* more forceful movements and a stronger or weaker push-off (Kim et al., 2022). Maximal voluntary contraction measurements of the legs due to risks of re-injury and worsening are problematic in patients with injuries or degenerative conditions of the lower extremities. In clinical settings, handgrip strength measurements are already widely established, also since they are much easier to perform, and far less time-consuming than leg force measurements. Handgrip strength varies substantially with sex, age and body height, and it correlates with the remaining years of life (Scherbov et al., 2022). Low handgrip strength and gait speed are associated with cardiovascular mortality and markers of neurodegeneration (Chainani et al., 2016; Jacob et al., 2022). It is known that stride length at preferred walking speed correlates positively with muscle mass, and the variance in the double support phase correlates with muscle strength (Kim et al., 2022).

Apart from these known characteristic gait changes, it is currently unknown how these factors affect the trajectory of the stance-phase curve derived from plantar-pressure data. The M-shaped curve of ground reaction forces during the stance phase is defined by two maxima, one minimum, the loading and unloading slope, as well as the force during defined periods (Larsen et al., 2008). We hypothesized characteristic changes of age, body height, body weight, body mass index (BMI) and handgrip strength on the plantar pressure stance-phase curve trajectory in healthy participants. In detail, we hypothesized higher forces and steeper loading and unloading slopes in younger, stronger and taller people, and in those with a higher body mass and body mass index.

2 Materials and methods

Ethical approval was obtained from the IRB of Saarland Medical Board (Ärztekammer des Saarlandes, Germany, application number 30/21). The study is part of the project Smart Implants 2.0 – Weight-bearing and Gait Observation for Early Monitoring of Fracture Healing and Individualized Therapy after Trauma, funded by the Werner Siemens Foundation. It is registered in the German Clinical Trials Register (DRKS-ID: DRKS00025108).

2.1 Measurement protocol

Data were collected from healthy volunteers. The inclusion criteria were the ability to walk on a treadmill, and age 18 years and older. Exclusion criteria were immobility, previous injury of the lower legs or pelvis, use of walking aids, inability to give consent, pregnancy, and age under 18 years.

The healthy participants of both sexes (none of them identified as diverse) were fitted with OpenGO insoles (Moticon GmbH, Munich, Germany) matching their shoe size that were individually calibrated.

Forces were recorded from both feet with one insole each. Measurements were conducted in the record mode of the device with a recording frequency of 100 Hz. Each insole is fitted with 16 pressure sensors. Raw data were exported for further analyses. The participants walked on a level treadmill at 4 km/h (Mercury, HP Cosmos, Nussdorf-Traunstein, Germany) for 1 minute, while insole data were collected. The participants were asked to walk for 1 minute straight, and recording was only commenced when the walking was already in progress to avoid bias by including altered steps upon gait initiation. Age was calculated from the date of birth. Body weight was measured with a Beurer MS 50 scale. Body height was measured with a Seca 206 roll-up measuring tape with wall attachment (Seca, Hamburg, Germany). Handgrip strength was measured with a hand dynamometer (Kern MAP 130K1, Kern, Balingen, Germany) by asking the participant while standing to hold the device in the dominant hand with the elbow extended and the arm hanging down (Ireland et al., 2014; Xu et al., 2021; Chen et al., 2022). Participants were asked to perform three maximal contractions with breaks, and the highest of the three values was chosen for statistical analysis. Handgrip strength is reported in kg. Of note, handgrip strength measured while standing with the elbow fully extended is greater than that measured while sitting (Xu et al., 2021).

2.2 Data management

The data obtained by the 16 force sensors in the insole devices were aggregated by the inbuilt data processing units and exported as described previously (Braun et al., 2015; Stöggl and Martiner, 2017). In detail, the pressure readings of the individual force sensors present in the insole device yield a weighted sum as the total vertical ground reaction force reading. Every summand is weighted by its sensor area (to compute the force) and a respective scaling factor accounting for the sensor's surrounding area, as well as gaps between sensors, which also depend on the insole size. This process is conducted by the Moticon software as an automated processing step before the file export takes place. The raw data acquired by the devices were transferred to desktop computers and converted into csv-formatted ASCII-files. The resulting files were then loaded into a custom-developed data platform for further processing and parameter calculation.

2.3 Data processing

As a first processing step, stance phases of the gait cycles were identified and extracted from the time-series data (step detection). For this, any activity with consecutive force readings above 30N was considered. We applied a tolerance of up to three missing values due to possible recording device faults and discarded any activity with a duration of less than 300 ms or more than 2000 ms. To allow for inter-subject comparability of the derived gait parameters, normalization is required. Since the parameters presented in this publication are based on total force (force extrema and averages), as well as force over time (slope -based parameters), this applies to both the force and time axes. Force readings were transformed from Newton to proportion of body weight of the respective subject. It should be noted that since ground reaction force was measured instead of weight, due to acceleration, this value regularly exceeds the body weight for peak load bearing instances. Normalizing the time axis requires a more complex approach, as lack of a fixed cadence results in varying step activity lengths and thus amounts of true measurements for each step. Hence, a natural cubic spline interpolation was conducted on the original raw data. Based on the resulting curve for each stance phase, 100 equidistant samples were taken, yielding one (interpolated) force measurement point for every 1% of overall stance phase length.

When compared with other conventional gait measuring tools, such as sensor-equipped treadmills or ground-mounted force plates, insole sensors feature a lower recording frequency and higher sensor noise. Similar to the different gait phases, further parameters are usually based on or derived from the characteristic local extrema (first and second force peak, local minimum in between force peaks, which are also considered parameters themselves); sensor jitter can cause the issue of having multiple ambiguous candidates for those extrema. To remedy this problem, a Gaussian filter was applied to the original raw data while repeating the normalization process. This filtering strategy with the corresponding parameters (Sigma = 3, kernel size 7) prioritized the elimination of extrema ambiguity at the expense of signal precision, which can result in overcorrection in areas where a higher signal volatility is to be naturally expected (e.g., at the start and end of the stance phase). Therefore, in order to avoid losing high-frequency detail, the filtered and normalized curve was only used to determine unambiguous time-axis positions (indices) for the extremum candidates; those indices were then re-applied to the non-filtered, normalized data to yield the corresponding ground reaction force measurement closer to the original raw data. For cases in which using the filtered data still yielded inconclusive extremum candidates, additional detection strategies were applied in the following order: (a) Time plausibility: Extremum candidates occurring within the first or last 10 indices (first/last 10% of overall time span) are eliminated. (b) Max/Min-pool filtering: Should multiple extremum candidates occur within a pool size of five indices (equals to 5% of overall time span), choose candidate with highest/lowest force value. (c) Monotony-check: In case of multiple extremum candidates remaining, eliminate those candidates from which the curve does not display a strict monotonous decrease/increase in both directions within five indices each. (d) Monotony grace: In case monotony-check has eliminated too many candidates (less than two maximum candidates or less than one minimum candidate remaining), reinstate eliminated candidates in descending order of their highest achieved monotony distance until the target number of candidates is reached.

Every stance activity with an irregular amount of unambiguous extremum candidates remaining after the application of those strategies in the context of step detection was considered a non-step event, and thus removed from the dataset. In total, an average of 96.51 stance phase curves were extracted per participant, out of which an average of 7.35 had the additional extremum elimination strategies applied, as outlined above. An average of 14.86 events per participant had to be excluded over the entire experiment.

2.4 Parameters of the stance phase curve

Figure 1 shows the analyzed parameters of the stance phase curve, which we computed for each step after applying the pre-processing procedure as described (Larsen et al., 2008; Stöggl and

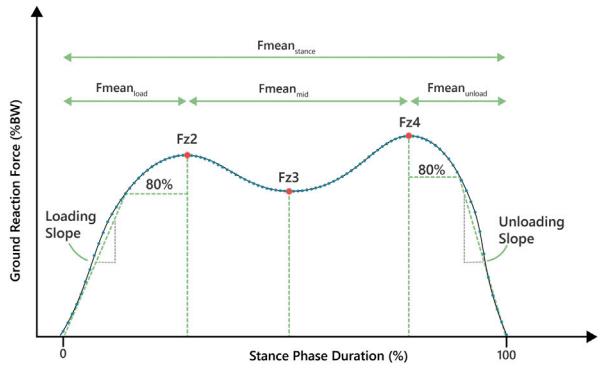

FIGURE 1
The plantar pressure gait curve with the determined parameters.

Martiner, 2017). In detail, the underlying curves for parameter extraction were not filtered, but are instead a product of the normalization process described in 2.3. Since the time-normalization in most cases produces more interpolated data points than the raw data provides, this can cause a smoothing effect similar to filtering. All curves were time-normalized to yield 100 force data points. The average was calculated by the mean of every data point at the same time index, respectively (0–99), which again produces a curve with 100 averaged force data points. All stance phase curves were extracted for each participant across the minute of walking. Mean forces were acquired using the arithmetic mean of all force values in a defined section given as proportions of body weight. Descriptions of all parameters are shown in Table 1.

2.5 Statistical analyses

All statistical tests were executed with IBM SPSS Statistics version 29 (IBM SPSS Statistics, Armonk, NY, United States). Normal distribution of data was tested by the Kolmogorov-Smirnov and Shapiro-Wilk tests. Significance was defined as $p < 0.05$. Multiple linear regression analyses were conducted with forced entry for each of the nine parameters of the stance phase trajectory separate (Figure 1; Table 1) as the dependent variable. Forced entry was chosen, as the number of independent variables is low and all variables have an explainable influence (Kucuk et al., 2016). The relationships of each of these parameters with age, weight, BMI, body height and handgrip strength as independent variables were explored. As body height, body weight and BMI intercorrelate, they could not be entered in the same model. Instead, two separate models were run, the main one including body weight and height, and a second one with BMI instead of body weight and height, but otherwise identical. Data visualization was conducted using the Matplotlib in Python. Due to lack of comparable data in the literature, the authors could not run an *a priori* sample size calculation. The sample size of 37 was an estimate based on what is common in the field, and taking into account the aim to measure a very diverse group of volunteers.

3 Results

A total of 37 participants (18 women and 19 men) with an average age of 43.65 ± 17.59 years were included in the study (for participant characteristics see Table 2). All models were significant, which means all models could be used. Table 3 shows the adjusted R^2 values and non-standardized and standardized (Beta) regression coefficients for all parameters. Figure 2 serves to illustrate differences in the trajectory of the insole-derived stance phase curve for younger and older, taller and shorter, heavier and lighter people, as well as those with a lower and higher handgrip strength.

3.1 Age

The only parameter of the stance phase curve that showed a significant negative correlation with age was the mean loading slope ($p = 0.014$). Younger participants had higher loading slope values, indicating a steeper increase. All other analyzed parameters were independent of age.

TABLE 1 Parameter definitions and units.

Parameter name	Definition	Unit
$Fmean_{stance}$	Mean force over the entire stance phase	% body weight
$Fmean_{load}$	Mean force between start of loading-phase and Fz2	% body weight
$Fmean_{mid}$	Mean force between Fz2 and Fz4	% body weight
$Fmean_{unload}$	Mean force between Fz4 and the end of the unloading-phase	% body weight
Fz2	First force maximum marking the end of the loading-phase	% body weight
Fz3	Force minimum during the mid-phase between Fz2 and Fz4	% body weight
Fz4	Second force maximum marking the end of mid-phase and beginning of unloading-phase	% body weight
Loading slope	Slope of the line between the start of the loading-phase and the first force reading equal or higher than 80% of Fz2	% body weight/% stance phase duration
Unloading slope	Slope of the line between the first force reading in the unloading-phase below 80% of Fz4 and the end of the stance phase event	% body weight/% stance phase duration

TABLE 2 Participant characteristics.

	Total	Women	Men
N	37	18	19
Mean age [years] ± SD (range)	43.65 ± 17.59 (18–87)	38.35 ± 15.28 (23–65)	48.57 ± 18.49 (18–87)
Mean height [cm] ± SD (range)	173.70 ± 11.22 (157–203)	165.47 ± 6.03 (157–174)	181.23 ± 8.83 (163–103)
Mean weight [kg] ± SD (range)	79.81 ± 27.85 (43.9–170.8)	63.01 ± 13.42 (43.9–78.9)	96.67 ± 32.71 (63.4–170.8)
Mean BMI [kg/m^2] ± SD (range)	22.78 ± 7.04 (13.81–45.63)	19.03 ± 3.98 (13.81–27.66)	26.56 ± 8.49 (18.11–45.63)
Mean handgrip force [kg] ± SD (range)	35.41 ± 12.46 (19.6–68.7)	26.14 ± 4.60 (19.6–38.0)	43.30 ± 11.59 (21.0–68.7)

TABLE 3 Adjusted R^2 values of the main model that includes body weight and height, and of the model that includes BMI instead. In addition, non-standardized and standardized (Beta) coefficients of the computed parameters are shown, if significant, separated by a comma. The values shown for BMI are derived from the BMI model, the others from the main model. Units are either kg, cm, or years per percent body weight, or in case of slope kg, cm or years per percent body weight per percent stance phase duration. The non-standardized coefficients can be used to correct for age, height, weight, BMI and handgrip strength when analysing such data.

	Adjusted R^2 (main model)	Adjusted R^2 (BMI model)	Age [years]	Body height [cm]	Body weight [kg]	BMI [kg/m^2]	Handgrip strength [kg]
$Fmean_{stance}$ [% body weight]	0.400	0.365			−0.007, −0.882	−0.022, −0.761	0.120, 0.696
$Fmean_{load}$ [% body weight]	0.460	0.391		−0.008, −0.413	−0.005, −0.715	−0.018, −0.595	
$Fmean_{mid}$ [% body weight]	0.285	0.267			−0.007, −0.818	−0.026, −0.716	0.130, 0.652
$Fmean_{unload}$ [% body weight]	0.335	0.338			−0.006, −0.946	−0.019, −0.831	0.010, 0.764
Fz2 [% body weight]	0.376	0.350			−0.008, −0.748	−0.028, −0.646	
Fz3 [% body weight]	0.199	0.182			−0.006, −0.734	−0.020, −0.646	0.012, 0.672
Fz4 [% body weight]	0.282	0.278			−0.010, −0.899	−0.035, −0.790	0.019, 0.763
Loading slope [% body weight/% stance phase duration]	0.292	0.177	−0.067, −0.394	−0.145, −0.543			
Unloading slope [% body weight/% stance phase duration]	0.264	0.255			0.083, 0.835	0.283, 0.723	−0.150, −0.677

3.2 Body height

The body height correlated negatively with $Fmean_{load}$ (p = 0.046) and the loading slope (p = 0.023). All other analyzed parameters were independent of body height.

3.3 Body weight and BMI

The body weight correlated with all the analyzed parameters of the stance phase, except the loading slope ($Fmean_{stance}$: $p < 0.001$, $Fmean_{load}$: $p = 0.002$, $Fmean_{mid}$: $p = 0.002$, $Fmean_{unload}$: $p < 0.001$, Fz2: $p = 0.002$, Fz3: $p = 0.007$, Fz4: $p < 0.001$, unloading slope: $p = 0.002$). Identical to the body weight, the BMI (separate model) also correlated with all parameters, except the loading slope ($Fmean_{stance}$: $p < 0.001$, $Fmean_{load}$: $p = 0.005$, $Fmean_{mid}$: $p = 0.002$, $Fmean_{unload}$: $p = 0.002$, Fz2: $p = 0.003$, Fz3: $p = 0.008$, Fz4: $p < 0.001$, unloading slope: $p = 0.002$).

3.4 Handgrip strength

The handgrip strength correlated positively with the parameters of the mid and unloading phase, $Fmean_{stance}$ (p = 0.015), $Fmean_{mid}$ (p = 0.036), $Fmean_{unload}$ (p = 0.012), Fz3 (p = 0.041), Fz4 (p = 0.015) and the unloading slope (p = 0.032). There was no correlation with $Fmean_{load}$, Fz2 and the loading slope, which are the parameters of the early stance phase.

3.5 Variability

The adjusted R^2 values shown in Table 3 indicate that only up to 46% of the variability in the analyzed parameters can be explained by age, body weight, height, BMI and hand grip strength. Thus, further factors must affect the trajectory of the gait cycle curve, that have not been considered in the present analysis.

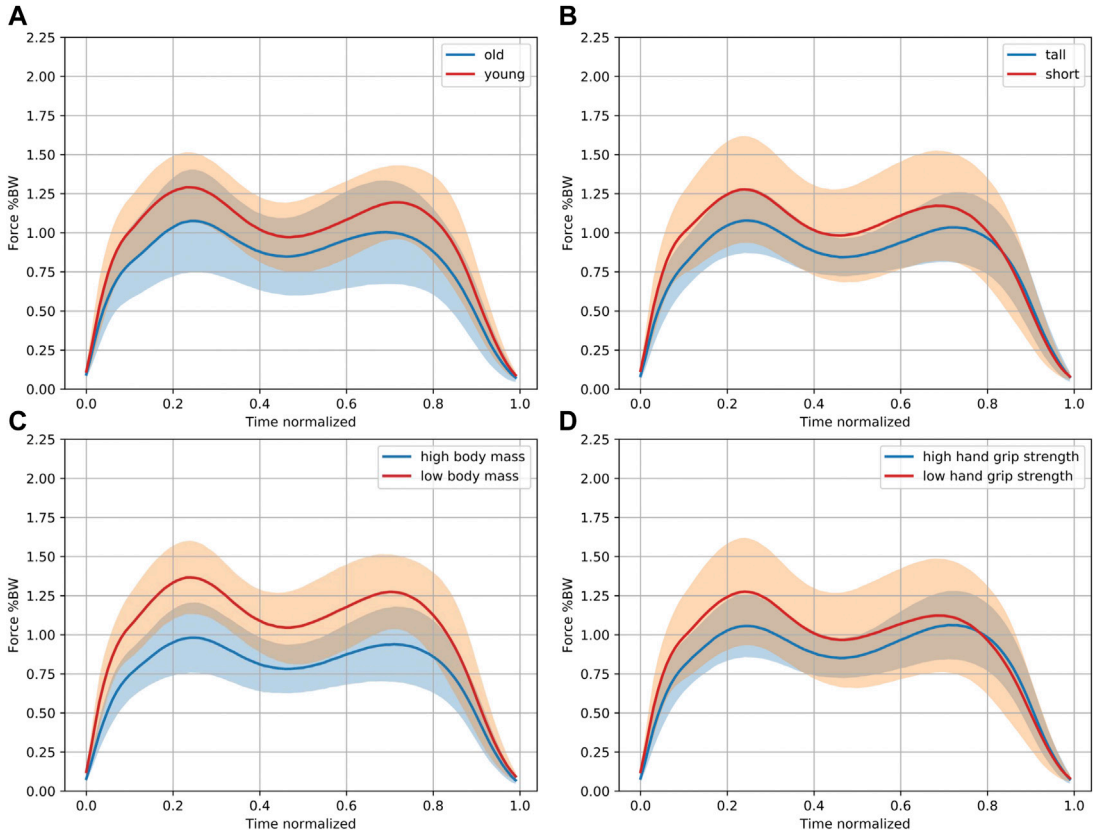

FIGURE 2
Characteristic differences in the stance phase curve. This figure is independent of the multiple regression analysis purely for illustration purposes. Pooled data of 18 out of 37 participants in each group are shown comparing the 18 **(A)** oldest and youngest participants, **(B)** tallest and smallest participants, **(C)** with the highest and lowest body mass, and **(D)** those with the highest and lowest handgrip strength. The solid lines indicate the mean. The 95% confidence intervals are shown in orange and blue, while the overlap shows up in brown. Higher normalized force values (in % body weight) can be observed in the younger and shorter participants with a lower body mass and handgrip strength.

4 Discussion

In summary, the present study demonstrated influences of age, body height, body weight, body mass index and handgrip force with parameters derived from the trajectory of the stance phase curve in healthy participants. However, only up to 46% of the variability in the analyzed parameters can be explained by age, body weight, height, BMI and hand grip strength. Thus, further factors affect the trajectory of the gait cycle curve, that have not been considered in the present analysis. When analyzing insole data, it might be useful to use the identified factors as input for machine-learning algorithms, or to correct for them by using the regression coefficients presented in this paper.

Pressure insoles are increasingly used to study gait in patients, as well as for lifestyle and health monitoring (Braun et al., 2017; Subramaniam et al., 2022). In addition to continuous measurements with insoles in patients with injuries, insoles are used in neurological patients for home-based treatment monitoring and as a rehabilitation tool for neuro-impaired gait, such as in Parkinson's disease (Sica et al., 2021; Das et al., 2022). Such long-term monitoring, especially if combined with further sensors, may produce large amounts of data that require automated analyses. Among the possibilities is the use of machine-learning algorithms trained with annotated data for pattern recognition of which activities a person is performing or has been able to perform (Harris et al., 2022). Such algorithms could be trained to recognize not only level walking and running, but also activities such as climbing stairs, cycling, driving a car, riding a train or bus, indicate falls and events with excessive loads, and quantify the overall time a person has been active. In addition, prediction algorithms could be implemented for falls and diseases. Machine-learning algorithms are already in use for many applications in gait analyses, including spatiotemporal human gait recognition (Harris et al., 2022; Konz et al., 2022). Such analyses in real time open up the possibility to deliver patient feedback, including warning of excessive forces and movements, as well as to remind patients that it is time to get up and exercise (Zheng and Chen, 2017). The inherent limitations in computing power of small wearable devices are increasingly targeted by both algorithmic optimization techniques in machine-learning like reservoir computing, network pruning, dimensionality reduction and so on, as well as hardware innovations. Together, these advances will ultimately allow real-time feedback based on data from various sources combined in the near future (Chiasson-Poirier et al., 2022; Zhang et al., 2022). Alternatively, extracting decision making systems (symbolic artificial intelligence), such as threshold-based methods, might offer an immediate route to real-time feedback.

As shown in the present study, individual characteristics of gait should be taken into account when analyzing continuous gait data in the field and daily life, and especially when deriving advice and warnings or alarms from these data. The present study revealed that the loading slope decreased with increasing age. This finding is novel, but in line with previous studies that showed a more cautious gait (more focus on gait combined with a slower walking speed) as well as age-related reductions of the preferred walking speed, and cadence (Herssens et al., 2018; Niederer et al., 2021). The more cautious gait in the present study is reflected in the slower loading of the foot, while the force maxima did not change with age. Larsen et al. (2008) showed that elderly compared to young participants had elevated muscular coactivation along with greater electromyographic activation when walking stairs, which illustrated the more cautious gait. Interestingly, in a different study, in participants 70 years and older, the center of mass push-off power was shown to be significantly decreased (Sloot et al., 2021). This effect did not show up in the present study, likely as the average participant age was relatively low. The finding, however, matches the increasing decline in performance with age that accelerates from the age of around 70 years onward (Ganse et al., 2020; Ganse et al., 2021). It should thus be assumed that the force maxima of the plantar pressure stance phase curve might decrease in the oldest-old, and particularly the second maximum that reflects the push-off force.

The body height affected $Fmean_{load}$ and the loading slope, and thereby delivered a characteristic change in the curve trajectory. This finding is not surprising, as devices are usually calibrated to body weight, but not to body height. Known changes in gait characteristics in taller participants include lower cadence due to longer steps, lower ankle velocity due to fewer steps, and increased stride time and stride length (Mikos et al., 2018). Taller people with longer legs often prefer higher walking speeds than smaller people. Walking speed has been shown to impact spatio-temporal gait parameters, and the perception of what the most comfortable walking speed is certainly varies among individuals (Andriacchi et al., 1977; Kirtley et al., 1985). The walking speed of 4 km/h, however, that was used in the present study, is usually in the range of what healthy participants consider comfortable. In patients with walking impairments, however, 4 km/h might be too fast, and slower speeds should be selected when studying gait (Linder et al., 2022; Zhu et al., 2022).

The body weight and BMI both had an influence on all the analyzed parameters of the stance phase curve, except the loading slope. The latter is an interesting detail, since age only affected the loading slope, which allows to determine the influence of weight/BMI independent from the effect of age.

The handgrip strength affected the mean force values of the later stance phase curve, the minimum and the push-off force (second maximum), as well as the unloading slope. There was, however, no effect on the average force of the initial phase, the first maximum and the loading slope. This very clear picture shows that the handgrip strength correlates only with the second half of the stance phase curve, while it leaves the first half unaffected. The underlying cause is likely the muscle force available for push-off, that is usually stronger in individuals who also have more handgrip strength. The hip abductors and adductors contribute the most muscle power in adult normal walking and are thus the muscles that would need to be studied more closely in future studies that deal with correlations of muscle strength and gait (Bogey and Barnes, 2017).

In future studies, also further parameters should be assessed that may affect the stance phase curve to enable for advanced analyses in the daily life. These may include the shoe and surface type, as well as a variety of characteristic activities. In addition, children and people aged 70 years and older should be studied. It is currently unknown how different injury types and degenerative musculoskeletal conditions affect the gait cycle curve, such as bone fractures, ligament injuries or arthritis of the legs. In case characteristic differences can be found among injury types, analyses of the stance phase curve may even have diagnostic and potentially even predictive value.

The main limitation of the study is that the effect of walking speed was not considered, as only one pre-defined walking speed was used for the measurements. Another limitation is that the data were recorded on a treadmill that is known to differ from walking on a ramp or on normal ground (Strutzenberger et al., 2022). The setup and walking speed were chosen to get the best standardization possible. In addition, differences in the pressure distribution under the feed *via* the 16 sensors were not analyzed per sensor in the present study and could be assessed in the future. Of note, the parameters analyzed in the present study can only be used when a regular gait curve is present. If this is not the case, other methods need to be applied, i.e., machine-learning or the analysis of other parameters, including possibly slopes and averages.

5 Conclusion

Age, body height, body weight, body mass index and handgrip force affect the trajectory of the stance phase curve in characteristic ways, but only explain up to 46% of the variability. When analyzing insole and ground-reaction-force data, it might be useful to correct for such factors, especially in automated data analyses *via* wearables, when the data are analyzed to give warnings and deliver live feedback. Smart healthcare applications that use insole data could help to improve patient health and facilitate treatment after injuries.

Data availability statement

The original contributions presented in the study are included in the article/Supplementary Material, further inquiries can be directed to the corresponding author.

Ethics statement

The studies involving human participants were reviewed and approved by IRB of Saarland Medical Board (Ärztekammer des Saarlandes, Germany), application number 30/21. The patients/participants provided their written informed consent to participate in this study.

Author contributions

CW contributed the data processing platform, data analysis, methods and Figure 2. PS conducted the measurements. BG contributed the idea, ran the statistical analyses, interpreted the data,

made the tables, drafted and submitted the manuscript. TD, CS, and FC took part in the data platform implementation. EW, TD, PS, CS, FC, MO, and TP helped with data interpretation. All authors have contributed to manuscript drafting and revision, read, and approved the submitted version of the manuscript.

Funding

The Werner Siemens Foundation (project Smart Implants 2.0) funded this work.

Acknowledgments

The authors would like to acknowledge the help of the study nurses Aynur Gökten and Jacqueline Orth during the measurements and of Lisa-Marie Jost for her support with graphics design and Figure 1.

Conflict of interest

TP is president elect and board member of the AO Foundation, Switzerland, and extended board member of the German Society of Orthopedic Trauma Surgery (DGU), the German Society of Orthopedic Surgery and Traumatology (DGOU), and the German Society of Surgery (DGCH). TP is also the speaker of the medical advisory board of the German Ministry of Defense.

The remaining authors declare that the research was conducted in the absence of any commercial or financial relationships that could be construed as a potential conflict of interest.

Publisher's note

Supplementary material

The Supplementary Material for this article can be found online at: https://www.frontiersin.org/articles/10.3389/fbioe.2023.1110099/full#supplementary-material

References

Anderson, W., Choffin, Z., Jeong, N., Callihan, M., Jeong, S., and Sazonov, E. (2022). Empirical study on human movement classification using insole footwear sensor system and machine learning. *Sensors (Basel).* 22 (7), 2743. doi:10.3390/s22072743

Andriacchi, T., Ogle, J., and Galante, J. (1977). Walking speed as a basis for normal and abnormal gait measurements. *J. Biomechanics* 10 (4), 261–268. doi:10.1016/0021-9290(77)90049-5

Bogey, R. A., and Barnes, L. A. (2017). Estimates of individual muscle power production in normal adult walking. *J. Neuroeng Rehabil.* 14 (1), 92. doi:10.1186/s12984-017-0306-2

Braun, B. J., Veith, N. T., Hell, R., Döbele, S., Roland, M., Rollmann, M., et al. (2015). Validation and reliability testing of a new, fully integrated gait analysis insole. *J. Foot Ankle Res.* 8, 54. doi:10.1186/s13047-015-0111-8

Braun, B. J., Veith, N. T., Rollmann, M., Orth, M., Fritz, T., Herath, S. C., et al. (2017). Weight-bearing recommendations after operative fracture treatment-fact or fiction? Gait results with and feasibility of a dynamic, continuous pedobarography insole. *Int. Orthop.* 41 (8), 1507–1512. doi:10.1007/s00264-017-3481-7

Chainani, V., Shaharyar, S., Dave, K., Choksi, V., Ravindranathan, S., Hanno, R., et al. (2016). Objective measures of the frailty syndrome (hand grip strength and gait speed) and cardiovascular mortality: A systematic review. *Int. J. Cardiol.* 215, 487–493. doi:10.1016/j.ijcard.2016.04.068

Chatzaki, C., Skaramagkas, V., Kefalopoulou, Z., Tachos, N., Kostikis, N., Kanellos, F., et al. (2022). Can gait features help in differentiating Parkinson's disease medication states and severity levels? A machine learning approach. *Sensors (Basel)* 22 (24), 9937. doi:10.3390/s22249937

Chen, X., Liu, G., Li, S., Lin, X., Han, Z., Hu, X., et al. (2022). Handgrip measurement method affects asymmetry but not weakness identification in community-dwelling older adults. *J. Am. Med. Dir. Assoc.* 8610 (22), 00795–802. doi:10.1016/j.jamda.2022.10.013

Chiasson-Poirier, L., Younesian, H., Turcot, K., and Sylvestre, J. (2022). Detecting gait events from accelerations using reservoir computing. *Sensors (Basel).* 22 (19), 7180. doi:10.3390/s22197180

Choi, H., Lim, J., and Lee, S. (2021). Body fat-related differences in gait parameters and physical fitness level in weight-matched male adults. *Clin. Biomech. (Bristol, Avon)* 81, 105243. doi:10.1016/j.clinbiomech.2020.105243

Das, R., Paul, S., Mourya, G. K., Kumar, N., and Hussain, M. (2022). Recent trends and practices toward assessment and rehabilitation of neurodegenerative disorders: Insights from human gait. *Front. Neurosci.* 16, 859298. doi:10.3389/fnins.2022.859298

Elstub, L. J., Grohowski, L. M., Wolf, D. N., Owen, M. K., Noehren, B., and Zelik, K. E. (2022). Effect of pressure insole sampling frequency on insole-measured peak force accuracy during running. *J. Biomech.* 145, 111387. doi:10.1016/j.jbiomech.2022.111387

Ganse, B., and Degens, H. (2021). Current insights in the age-related decline in sports performance of the older athlete. *Int. J. Sports Med.* 42 (10), 879–888. doi:10.1055/a-1480-7730

Ganse, B., Drey, M., Hildebrand, F., Knobe, M., and Degens, H. (2021). Performance declines are accelerated in the oldest-old track and field athletes 80 to 94 Years of age. *Rejuvenation Res.* 24 (1), 20–27. doi:10.1089/rej.2020.2337

Ganse, B., Kleerekoper, A., Knobe, M., Hildebrand, F., and Degens, H. (2020). Longitudinal trends in master track and field performance throughout the aging process: 83,209 results from Sweden in 16 athletics disciplines. *Geroscience* 42 (6), 1609–1620. doi:10.1007/s11357-020-00275-0

Harris, E. J., Khoo, I. H., and Demircan, E. (2022). A survey of human gait-based artificial intelligence applications. *Front. Robot. AI* 8, 749274. doi:10.3389/frobt.2021.749274

Herssens, N., Verbecque, E., Hallemans, A., Vereeck, L., Van Rompaey, V., and Saeys, W. (2018). Do spatiotemporal parameters and gait variability differ across the lifespan of healthy adults? A systematic review. *Gait Posture* 64, 181–190. doi:10.1016/j.gaitpost.2018.06.012

Ireland, A., Maden-Wilkinson, T., Ganse, B., Degens, H., and Rittweger, J. (2014). Effects of age and starting age upon side asymmetry in the arms of veteran tennis players: A cross-sectional study. *Osteoporos. Int.* 25 (4), 1389–1400. doi:10.1007/s00198-014-2617-5

Jacob, M. E., O'Donnell, A., Samra, J., Gonzales, M. M., Satizabal, C., Pase, M. P., et al. (2022). Grip strength, gait speed and plasma markers of neurodegeneration in asymptomatic middle-aged and older adults. *J. Frailty Aging* 11 (3), 291–298. doi:10.14283/jfa.2022.17

Kim, B., Youm, C., Park, H., Lee, M., and Choi, H. (2022). Association of muscle mass, muscle strength, and muscle function with gait ability assessed using inertial measurement unit sensors in older women. *Int. J. Environ. Res. Public Health* 19 (16), 9901. doi:10.3390/ijerph19169901

Kirtley, C., Whittle, M. W., and Jefferson, R. (1985). Influence of walking speed on gait parameters. *J. Biomed. Eng.* 7 (4), 282–288. doi:10.1016/0141-5425(85)90055-X

Konz, L., Hill, A., and Banaei-Kashani, F. (2022). ST-DeepGait: A spatiotemporal deep learning model for human gait recognition. *Sensors (Basel).* 22 (20), 8075. doi:10.3390/s22208075

Kucuk, U., Kucuk, H. O., Eyuboglu, M., and Dogan, M. (2016). eComment. The importance of choosing a proper predictor variable selection method in logistic

regression analyses. *Interact. Cardiovasc Thorac. Surg.* 22 (3), 258. doi:10.1093/icvts/ivv403

Larsen, A. H., Puggaard, L., Hämäläinen, U., and Aagaard, P. (2008). Comparison of ground reaction forces and antagonist muscle coactivation during stair walking with ageing. *J. Electromyogr. Kinesiol* 18 (4), 568–580. doi:10.1016/j.jelekin.2006.12.008

Linder, S. M., Baron, E., Learman, K., Koop, M. M., Penko, A., Espy, D., et al. (2022). An 8-week aerobic cycling intervention elicits improved gait velocity and biomechanics in persons with Parkinson's disease. *Gait Posture* 98, 313–315. doi:10.1016/j.gaitpost.2022.10.007

Maktouf, W., Durand, S., Boyas, S., Pouliquen, C., and Beaune, B. (2020). Interactions among obesity and age-related effects on the gait pattern and muscle activity across the ankle joint. *Exp. Gerontol.* 140, 111054. doi:10.1016/j.exger.2020.111054

Mikos, V., Yen, S. C., Tay, A., Heng, C. H., Chung, C. L. H., Liew, S. H. X., et al. (2018). Regression analysis of gait parameters and mobility measures in a healthy cohort for subject-specific normative values. *PLoS One* 13 (6), e0199215. doi:10.1371/journal.pone.0199215

Niederer, D., Engeroff, T., Fleckenstein, J., Vogel, O., and Vogt, L. (2021). The age-related decline in spatiotemporal gait characteristics is moderated by concerns of falling, history of falls & diseases, and sociodemographic-anthropometric characteristics in 60-94 years old adults. *Eur. Rev. Aging Phys. Act.* 18 (1), 19. doi:10.1186/s11556-021-00275-9

North, K., Kubiak, E. N., and Hitchcock, R. W. (2012). Sensor packaging design for continuous underfoot load monitoring. *Biomed. Microdevices* 14 (1), 217–224. doi:10.1007/s10544-011-9599-2

Pau, M., Capodaglio, P., Leban, B., Porta, M., Galli, M., and Cimolin, V. (2021). Kinematics adaptation and inter-limb symmetry during gait in obese adults. *Sensors (Basel)* 21 (17), 5980. doi:10.3390/s21175980

Scherbov, S., Spitzer, S., and Steiber, N. (2022). Thresholds for clinical practice that directly link handgrip strength to remaining years of life: Estimates based on longitudinal observational data. *BMJ Open* 12 (7), e058489. doi:10.1136/bmjopen-2021-058489

Senden, R., Meijer, K., Heyligers, I. C., Savelberg, H. H., and Grimm, B. (2012). Importance of correcting for individual differences in the clinical diagnosis of gait disorders. *Physiotherapy* 98 (4), 320–324. doi:10.1016/j.physio.2011.06.002

Sica, M., Tedesco, S., Crowe, C., Kenny, L., Moore, K., Timmons, S., et al. (2021). Continuous home monitoring of Parkinson's disease using inertial sensors: A systematic review. *PLoS One* 16 (2), e0246528. doi:10.1371/journal.pone.0246528

Sloot, L. H., Malheiros, S., Truijen, S., Saeys, W., Mombaur, K., Hallemans, A., et al. (2021). Decline in gait propulsion in older adults over age decades. *Gait Posture* 90, 475–482. doi:10.1016/j.gaitpost.2021.09.166

Stöggl, T., and Martiner, A. (2017). Validation of Moticon's OpenGo sensor insoles during gait, jumps, balance and cross-country skiing specific imitation movements. *J. Sports Sci.* 35 (2), 196–206. doi:10.1080/02640414.2016.1161205

Strutzenberger, G., Leutgeb, L., Claußen, L., and Schwameder, H. (2022). Gait on slopes: Differences in temporo-spatial, kinematic and kinetic gait parameters between walking on a ramp and on a treadmill. *Gait Posture* 91, 73–78. doi:10.1016/j.gaitpost.2021.09.196

Subramaniam, S., Majumder, S., Faisal, A. I., and Deen, M. J. (2022). Insole-based systems for health monitoring: Current solutions and research challenges. *Sensors (Basel)* 22 (2), 438. doi:10.3390/s22020438

Xu, Z. Y., Gao, D. F., Xu, K., Zhou, Z. Q., and Guo, Y. K. (2021). The effect of posture on maximum grip strength measurements. *J. Clin. Densitom.* 24 (4), 638–644. doi:10.1016/j.jocd.2021.01.005

Zhang, Q., Jin, T., Cai, J., Xu, L., He, T., Wang, T., et al. (2022). Wearable triboelectric sensors enabled gait analysis and waist motion capture for IoT-based smart healthcare applications. *Adv. Sci. (Weinh).* 9 (4), e2103694. doi:10.1002/advs.202103694

Zheng, Q., and Chen, H. (2017). A monitoring system for walking rehabilitation after THR or TKR surgeries. *Annu. Int. Conf. IEEE Eng. Med. Biol. Soc.* 2017, 2373–2376. doi:10.1109/EMBC.2017.8037333

Zhu, T., Wang, Y., Tian, F., Wang, W., Zhong, R., Zhai, H., et al. (2022). Clinical assessments and gait analysis for patients with Trimalleolar fractures in the early postoperative period. *BMC Musculoskelet. Disord.* 23 (1), 663. doi:10.1186/s12891-022-05615-z

frontiers | Frontiers in Bioengineering and Biotechnology

TYPE Original Research
PUBLISHED 25 April 2023
DOI 10.3389/fbioe.2023.1176054

OPEN ACCESS

EDITED BY
Fuyuan Liao,
Xi'an Technological University, China

REVIEWED BY
Yifang Fan,
Fujian Normal University, China
Peng Chen,
Southwest Jiaotong University, China

*CORRESPONDENCE
Huijing Hu,
huhuijing@nwpu.edu.cn
Le Li,
lile5@nwpu.edu.cn

†These authors have contributed equally to this work

RECEIVED 28 February 2023
ACCEPTED 14 April 2023
PUBLISHED 25 April 2023

CITATION
Wang X, Luo Z, Zhang M, Zhao W, Xie S, Wong SF, Hu H and Li L (2023), The interaction between changes of muscle activation and cortical network dynamics during isometric elbow contraction: a sEMG and fNIRS study.
Front. Bioeng. Biotechnol. 11:1176054.
doi: 10.3389/fbioe.2023.1176054

The interaction between changes of muscle activation and cortical network dynamics during isometric elbow contraction: a sEMG and fNIRS study

Xiaohan Wang[1†], Zichong Luo[2†], Mingxia Zhang[1], Weihua Zhao[3], Songyun Xie[4], Seng Fat Wong[2], Huijing Hu[1*] and Le Li[1*]

[1]Institute of Medical Research, Northwestern Polytechnical University, Xi'an, China, [2]Faculty of Science and Technology, University of Macau, Taipa, China, [3]Hospital of Northwestern Polytechnical University, Xi'an, China , [4]School of Electronics and Information, Northwestern Polytechnical University, Xi'an, China

Objective: The relationship between muscle activation during motor tasks and cerebral cortical activity remains poorly understood. The aim of this study was to investigate the correlation between brain network connectivity and the non-linear characteristics of muscle activation changes during different levels of isometric contractions.

Methods: Twenty-one healthy subjects were recruited and were asked to perform isometric elbow contractions in both dominant and non-dominant sides. Blood oxygen concentrations in brain from functional Near-infrared Spectroscopy (fNIRS) and surface electromyography (sEMG) signals in the biceps brachii (BIC) and triceps brachii (TRI) muscles were recorded simultaneously and compared during 80% and 20% of maximum voluntary contraction (MVC). Functional connectivity, effective connectivity, and graph theory indicators were used to measure information interaction in brain activity during motor tasks. The non-linear characteristics of sEMG signals, fuzzy approximate entropy (fApEn), were used to evaluate the signal complexity changes in motor tasks. Pearson correlation analysis was used to examine the correlation between brain network characteristic values and sEMG parameters under different task conditions.

Results: The effective connectivity between brain regions in motor tasks in dominant side was significantly higher than that in non-dominant side under different contractions ($p < 0.05$). The results of graph theory analysis showed that the clustering coefficient and node-local efficiency of the contralateral motor cortex were significantly varied under different contractions ($p < 0.01$). fApEn and co-contraction index (CCI) of sEMG under 80% MVC condition were significantly higher than that under 20% MVC condition ($p < 0.05$). There was a significant positive correlation between the fApEn and the blood oxygen value in the contralateral brain regions in both dominant or non-dominant sides ($p < 0.001$). The node-local efficiency of the contralateral motor cortex in the dominant side was positively correlated with the fApEn of the EMG signals ($p < 0.05$).

Conclusion: In this study, the mapping relationship between brain network related indicators and non-linear characteristic of sEMG in different motor tasks was verified. These findings provide evidence for further exploration of the interaction

between the brain activity and the execution of motor tasks, and the parameters might be useful in evaluation of rehabilitation intervention.

KEYWORDS

fNIRS, electromyography, brain network, fuzzy approximate entropy, muscle isometric contraction

1 Introduction

Human execute motor tasks and promote individuals to complete activities of daily life and social interaction (Shumway-Cook and Woollacott, 2014). The completion of motor tasks consists of corresponding muscle contractions and stretches, so it is important to generate accurate motor control, which is considered to be the fundamental factor of movement (Yokoyama et al., 2019). Previous studies, such as electroencephalography (EEG) and functional magnetic resonance imaging (fMRI), have found that upper limb movement is regulated by corresponding regions of the cerebral cortex (Long et al., 2016; Lin et al., 2017). It is believed that the relationship between the muscle contractions and correlated cerebral hemodynamic is essential to the understanding of motor control such as the planning and execution of motor tasks (Winter 2009; Zhou et al., 2022). However, the low spatial resolution of EEG and the high costs of fMRI limit the development of relevant motor studies and it is also very challenging to combine the fMRI with human daily activity due to the strict requirement of subject's stabilization during the scan.

Functional Near-infrared Spectroscopy (fNIRS) is a non-invasive brain functional imaging technology based on optical principles (Ferrari and Quaresima, 2012) and it has the advantages of being safe and non-invasive, easy to move, anti-motion and electromagnetic interference, high spatial resolution, and allowing long-term monitoring (Herold et al., 2018). Neuroscience research has highlighted the importance of brain networks between different brain regions in motor tasks (Felleman and Van Essen, 1991). fNIRS technique facilitated the investigation of elucidating cerebral hemodynamic changes during muscle contraction motor tasks (Zimmermann et al., 2013). Functional connectivity, effective connectivity and graph theory analysis between different brain regions have been applied to the study of neural function and motor function. Xu et al. found that brain network indicators, including clustering coefficient and global efficiency, could be used to evaluate the rehabilitation effects of post-stroke exercise training (Xu et al., 2022). However, it remains unclear whether the connections between the cerebral cortex are related to motor performance during execution of motor tasks, so the relationship between muscle excitability and brain network changes warrants further investigation.

Recording of muscle activity by electromyography (EMG) from skin surface, so called sEMG, has proved to be useful for evaluating central and peripheral determinants of motor function (Donaldson et al., 2003). The analysis of sEMG signals can explore the activity state of muscle tissue and the control mechanism of the nerve center under different task states, which is of great significance for the training and evaluation of rehabilitation intervention (Vigotsky et al., 2017). sEMG is characterized by high complexity and chaos (Hong-Chun et al., 2005), so it is imperative to use non-linear characteristic analysis methods to analyze sEMG signals (Sun et al., 2014). Entropy indicates the complicated properties of the researched signal with a simple yet effective approach and high consistency in order to analyze biological signals such as sEMG. Chen et al. proposed fuzzy approximate entropy (fApEn) based on the entropy theory by introducing the idea of a fuzzy set (Chen et al., 2007). Previous studies have shown that fApEn can be used as an indicator of changes in the complexity of sEMG signals to determine the alterations in motor control during task execution (Ao et al., 2015; Deng et al., 2021). However, the relationship between changes in muscle complexity and brain network during task execution remains unclear. Understanding the coupling mechanism between the cerebral cortex and muscle is essential in the study of human motor control (Bao et al., 2021; Colamarino et al., 2021).

Therefore, in current study, fNIRS and sEMG were used to investigate the interaction between brain region activation and peripheral muscle contraction in different motor control tasks. The connectivity parameters between brain regions in motor tasks (functional connectivity, effective connectivity and graph theory indicators) and the non-linear analysis of muscle activation from fApEn were conducted. We hypothesize that the brain network connectivity is correlated to the efficiency of peripheral motor control, and the findings of current study may help to understand the underlying mechanism of corticomuscular coupling.

2 Methods

2.1 Participants

Twenty-one healthy subjects (mean age: 23.86 ± 1.35, 12 males and 9 females) were recruited from Northwestern Polytechnical University for this study. All of the subjects were right-hand dominant with normal vision and did not have any history of epilepsy or other psychiatric disorders according to the Edinburgh Handedness Inventory. This study was approved by the local institutional ethics committee and was registered in the Chinese Clinical Trial Registry (ChiCTR2200057839). All participants understood the content of the experiment and signed the informed consent before participating in the study. In addition, subjects were allowed enough time to rest to ensure their attention during the experiment.

2.2 Experimental procedures

Before the data collection, the operator explained the entire procedure to each participant until they fully understood. Figure 1A

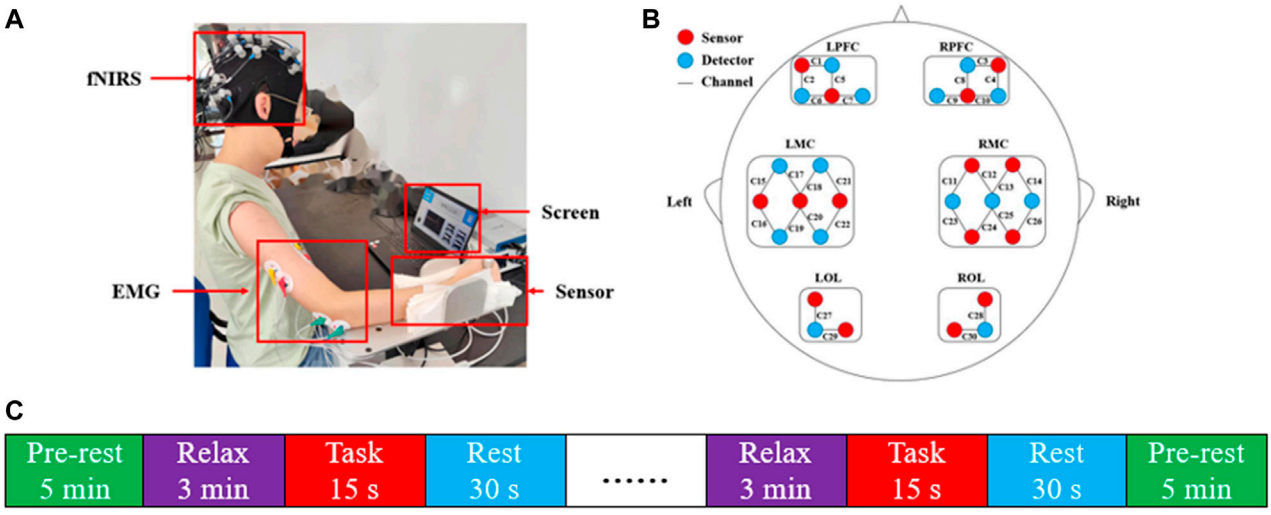

FIGURE 1
The experimental design of the evaluation test. **(A)** Experimental set-up. **(B)** The layout of fNIRS channels. The red dots represented sources, and the blue dots represented detectors. The 15 sources and 15 detectors constitute 30 channels, overlaying six brain regions: LPFC, RPFC, LMC, RMC, LOL, and ROL. **(C)** Experiment procedure. Each trial consisted of a combination of a 15 s task and a 30 s rest and was repeated five times in each condition.

shows the experimental setup in this study. In the process of experiment, participants were asked to sit on a chair, facing the computer screen. The subject's forearm was fixed to the slot of the homemade handrail. Their elbows were flexed at 90°, and their shoulders were turned at 90° of abduction. All participants practiced muscle contraction to achieve the target values in response to visual feedback. The visualization experiment program was provided by a custom LabVIEW (LabVIEW 2012; National Instruments, Austin, TX, United States) program. First, the subjects were asked to produce consecutive maximum voluntary contractions (MVC) lasting 5 s each, repeating three times with a 2-min rest interval to avoid muscle fatigue. Secondly, subjects completed isometric elbow contraction under visual feedback regulation. Each trial included two conditions, 20% MVC and 80% MVC, repeated five times each. Subjects were required to complete 20 trials in both the dominant and non-dominant sides. Each trial consisted of a 3-min relaxation phase, a 15-s task phase, and a 30-s rest phase. The experimental procedure is shown in Figure 1C.

2.3 Data acquisition

fNIRS signals with NIR wavelengths of 730 and 850 nm were collected using a multichannel fNIRS system (NirSmart, Danyang Huichuang Medical Equipment Co. Ltd., China) at a sampling rate of 11 Hz. Figure 1B demonstrates the usage of a standard cap with an international 10–20 system to reference the NIR probe layout. The distance between the source and the detector was 30 mm to ensure that the signal was detected from the brain's gray matter. A total of 30 channels were used to cover the left and right prefrontal cortex (LPFC, RPFC), left and right motor cortex (LMC, RMC), and left and right occipital lobe (LOL, ROL). To collect the sEMG signals, the skin above the subjects' muscle was scraped and cleaned with alcohol. Ag-AgCl bipolar electrodes were placed on the belly of muscle with a constant distance of 20 mm between electrodes. sEMG signals were recorded by a custom sEMG amplifier and sampled by a data converter at 1,000 Hz. fNIRS and sEMG were synchronized through the LabVIEW program. A two-channel sEMG amplifier with a gain of 5,000 was applied to record the sEMG signals. The acquisition rate of the sEMG signals was at 1,000 Hz, sampled by a 16-bit data converter (DAQ-6341, National Instruments, Austin, TX, United States). A LabVIEW program was used to monitor and save the raw sEMG signals. To synchronize the EMG and fNIRS devices, timestamp signals were sent simultaneously to two devices at the beginning and end of each task recording using the same computer that presented the task and visual feedback, and each "go" cue was stored by each device as its time reference (Ortega et al., 2020; Wang et al., 2020). In addition, EMG and FNIRS signals were aligned using the synchronization program developed in LabView (Jian et al., 2021).

2.4 Data analysis

2.4.1 Data preprocess

In this experiment, raw sEMG signals of BIC and TRI were first filtered with a fourth-order bandpass Butterworth filter (20–450 Hz) and then filtered with a notch filter (50 Hz). For the preprocessing of fNIRS signal, the original fNIRS signal was first converted into the hemodynamic signal by the modified bill-lambert law. Each fNIRS channel could obtain an oxygenated hemoglobin (HbO_2) concentration signal and a deoxyhemoglobin (HbR) concentration signal. Since the HbO_2 signal showed a better signal noise ratio than the HbR signal, the HbO_2 signal was chosen as a marker of cortical activation, and the task-related HbO_2 concentration was calculated (Ye et al., 2009). After

removing invalid channels and motion artifacts, the HbO_2 signal was bandpass Butterworth filtered (0.01–0.2 Hz) to remove physiological signal interference, including interference caused by heartbeat and respiratory activity.

2.4.2 EMG data analysis

Off-line EMG signals were digitally filtered by a zero-phase-shift fourth-order Butterworth bandpass filter with 10–490 Hz and a notch filter with a notch point at 50 Hz to cancel noise and power-line interference. Manual visual inspection was performed on each trial to determine segments of the 5-s EMG signal, with a consistent, steady flat response after RMS-smoothing.

2.4.2.1 fApEn of EMG

Entropy is an effective non-linear method to represent physiological signals (Ao et al., 2015). The increase of entropy indicates the increase of complexity and the decrease of regularity of motor tasks. fApEn analysis was performed to calculate the complexity of EMG signal for each chopped segment. The theory of fApEn has been developed in previous studies so that a brief of the algorithm is described here (Xie et al., 2010; Sun et al., 2014):

For the time series T containing N EMG signal data point {e(i): $1 \le i \le N$}, the following vector sequence can be formed as:

$$S_i^m = e(i), e(i+1), \cdots e(i+m-1) - e0(i) \tag{1}$$

where S_i^m represents m consecutive e values, commencing with the ith point. $e0(i)$ is the baseline of the vector to be removed:

$$e0(i) = \frac{1}{m}\sum_{j=0}^{m-1} e(i+j) \tag{2}$$

Then, the distance d_{ij}^m between two vectors S_i^m and S_j^m is defined as:

$$\begin{aligned} d_{ij}^m &= d\left[S_i^m, S_j^m\right] \\ &= \max_{k \in (0, m-1)} \left|\left(e(i+k) - e0(i) - \left(e(j+k) - e0(j)\right)\right|\right. \end{aligned} \tag{3}$$

The similarity degree of d_{ij}^m between S_i^m and S_j^m can be determined by an ambiguity function $\mu(d_{ij}^m, n, r)$, where n and r represent the width and gradient parameters of the boundary of the exp function respectively.

$$D_{ij}^m(n,r) = \mu\left(d_{ij}^m, n, r\right) = exp\left(-\left(d_{ij}^m\right)^n / r\right) \tag{4}$$

The function ϕ^m is defined as:

$$\phi^m(n) = \frac{1}{N-m+1}\sum_{i=1}^{N-m+1} \ln\left(\frac{1}{N-m-1}\sum_{j=1, j\neq i}^{N-m+1} D_{ij}^m\right) \tag{5}$$

Repeatedly, the function ϕ^{m+1} can be defined as:

$$\phi^{m+1}(n) = \frac{1}{N-m+1}\sum_{i=1}^{N-m+1} \ln\left(\frac{1}{N-m-1}\sum_{j=1, j\neq i}^{N-m+1} D_{ij}^{m+1}\right) \tag{6}$$

Finally, the function of fApEn of the EMG signal can be expressed as:

$$fApEn(m, r, n, N) = \phi^m(r) - \phi^{m+1}(r) \tag{7}$$

2.4.2.2 Co-contraction index estimation

Co-contraction Index (CCI) is the EMG-based model to estimate the simultaneous contraction of antagonists and agonists during dynamic movement base. Several CCI calculation methods have been discussed in a previous study (Souissi et al., 2017). The method proposed by winter was applied in this study (Winter, 2009).

$$\%CCI = \frac{2 \times common\ Area}{Area\ A + Area\ B} \times 100 \tag{8}$$

Area A and Area B represent the area under the enveloped EMG antagonists and agonists curve, and the common area is the overlap area between Area A and Area B. Trapezoidal method is suggested for the integral calculation to estimate the areas. The CCI should vary from 0 to 100, where 0 indicates no overlap of the two EMG envelopes and 100 indicates that both muscles were fully activated to 100% MVC during the trial.

2.4.3 fNIRS data analysis

The general linear model is a standard linear estimation method commonly used to extract hemodynamic responses from fNIRS data to examine brain-activated regions (Zhou et al., 2022). NirSpark software was used to process the original data to obtain the data on brain activation and functional connectivity strength under different task conditions (https://openfnirs.org/). After brain activation analysis, brain network analysis was performed to explore connectivity between brain regions further (Friston et al., 2013). Thus, there are dynamic interactions between each functional brain region to coordinate and respond to specific environmental and task demands.

Finally, common brain network indicators, including node-local efficiency and clustering coefficient, were calculated to characterize the functional connectivity of brain regions (http://www.brain-connectivity-toolbox.net) (Bullmore and Sporns, 2009; Rubinov and Sporns, 2010). The clustering coefficient measures network isolation and global efficiency index network integration (Wang et al., 2019). In contrast, node-local efficiency represents the ability to integrate neighboring nodes of a given node corresponding to brain regions (Yuan et al., 2022).

2.4.4 Statistical analysis

All experimental data were statistically analyzed using IBM SPSS Statistics 26 (IBM Inc., WA, United States) and MATLAB R2021a (The MathWorks, United States) software. Data of functional connectivity were analyzed by independent sample t-test. The functional connectivity and effective connectivity of brain regions between different groups were analyzed by one-way ANOVA. Paired sample t-test was performed on the indexes such as clustering coefficient and node-local efficiency calculated in graph theory analysis as well as the EMG correlation characteristic values. Finally, Pearson correlation analysis was used to test the correlation between the activation intensity of each brain region and the fApEn of the EMG signal under different task conditions. $p < 0.05$ was considered statistically significant for all the statistical analyses and false discovery rate (FDR) correction was performed.

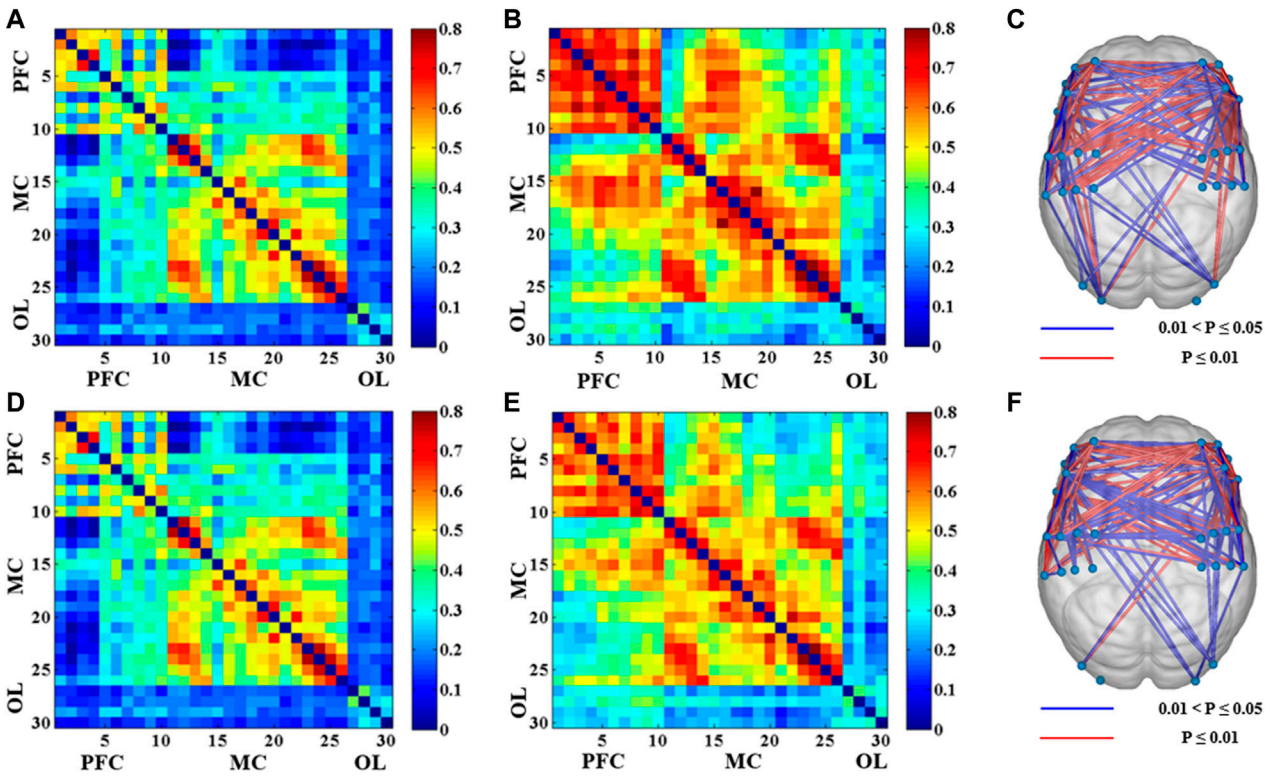

FIGURE 2
The results of the functional connectivity between 30 channels in different conditions ($p < 0.05$). **(A)** Correlation matrix between 30 channels under 20% MVC of the dominant side. **(B)** Correlation matrix between 30 channels under 80% MVC of the dominant side. **(C)** The significant difference of functional connectivity of the 80% MVC relative to the 20% MVC between 30 channels under the dominant side. **(D)** Correlation matrix between 30 channels under 20% MVC of the non-dominant side. **(E)** Correlation matrix between 30 channels under 80% MVC of the non-dominant side. **(F)** The significant difference of functional connectivity of the 80% MVC relative to the 20% MVC between 30 channels under the non-dominant side.

3 Results

3.1 Functional connectivity

Figure 2 showed the functional connectivity matrix of brain channels of the dominant and non-dominant side during different levels of muscle contraction. Compared with the resting state, the functional connectivity between the corresponding channels in the contralateral and ipsilateral motor cortex was more robust under the 20% MVC condition of the dominant side (LMC-RMC: 0.44 ± 0.17). In contrast, the functional connectivity between other brain regions was weaker. Similarly, functional connectivity was stronger between the contralateral and ipsilateral motor cortex and between the contralateral and ipsilateral prefrontal cortex in the dominant side, with 80% MVC condition compared to the resting state (LPFC-RPFC: 0.63 ± 0.16; LMC-RMC: 0.52 ± 0.23) (Figures 2A–C). Under the 20% MVC condition of the non-dominant side, the functional connectivity between the corresponding channels of the contralateral motor cortex and the ipsilateral motor cortex was also stronger compared with the resting state (LMC-RMC: 0.44 ± 0.19). In comparison, the functional connectivity between other brain regions was weaker. Similarly, functional connectivity between the contralateral motor cortex and ipsilateral prefrontal cortex was also more significant in the 80% MVC of the non-dominant side compared to the resting state, as was functional connectivity between the contralateral prefrontal cortex and ipsilateral prefrontal cortex (LPFC-RPFC: 0.59 ± 0.17; LMC-RMC: 0.51 ± 0.20) (Figures 2D–F).

The comparison results of functional connectivity of brain regions under different muscle contraction levels showed that the functional connectivity between the motor cortex and prefrontal cortex (LPFC-RMC: $p = 0.017$; RPFC-ROL: $p = 0.020$; LMC-LOL: $p = 0.025$; LMC-ROL: $p = 0.049$) was significantly enhanced under 80% MVC condition compared with 20% MVC condition of the dominant side, especially the functional connectivity between the contralateral motor cortex, contralateral prefrontal cortex and ipsilateral prefrontal cortex (LPFC-RPFC: $p = 0.000$; LPFC-LMC: $p = 0.000$; LPFC-LOL: $p = 0.001$; LPFC-ROL: $p = 0.005$; RPFC-LMC: $p = 0.000$; RPFC-RMC: $p = 0.003$; RPFC-LOL: $p = 0.005$) was significantly enhanced (Figures 3A, B). Similarly, functional connectivity between the motor cortex and prefrontal cortex (LPFC-LMC: $p = 0.012$; LPFC-RMC: $p = 0.014$; LPFC-ROL: $p = 0.019$; RPFC-ROL: $p = 0.013$) was significantly enhanced in the non-dominant side 80% MVC condition compared to 20% MVC, especially between contralateral motor cortex, contralateral prefrontal cortex, and ipsilateral prefrontal cortex (LPFC-RPFC: $p = 0.000$; RPFC-LMC: $p = 0.009$; RPFC-RMC: $p = 0.006$) (Figures 3C, D).

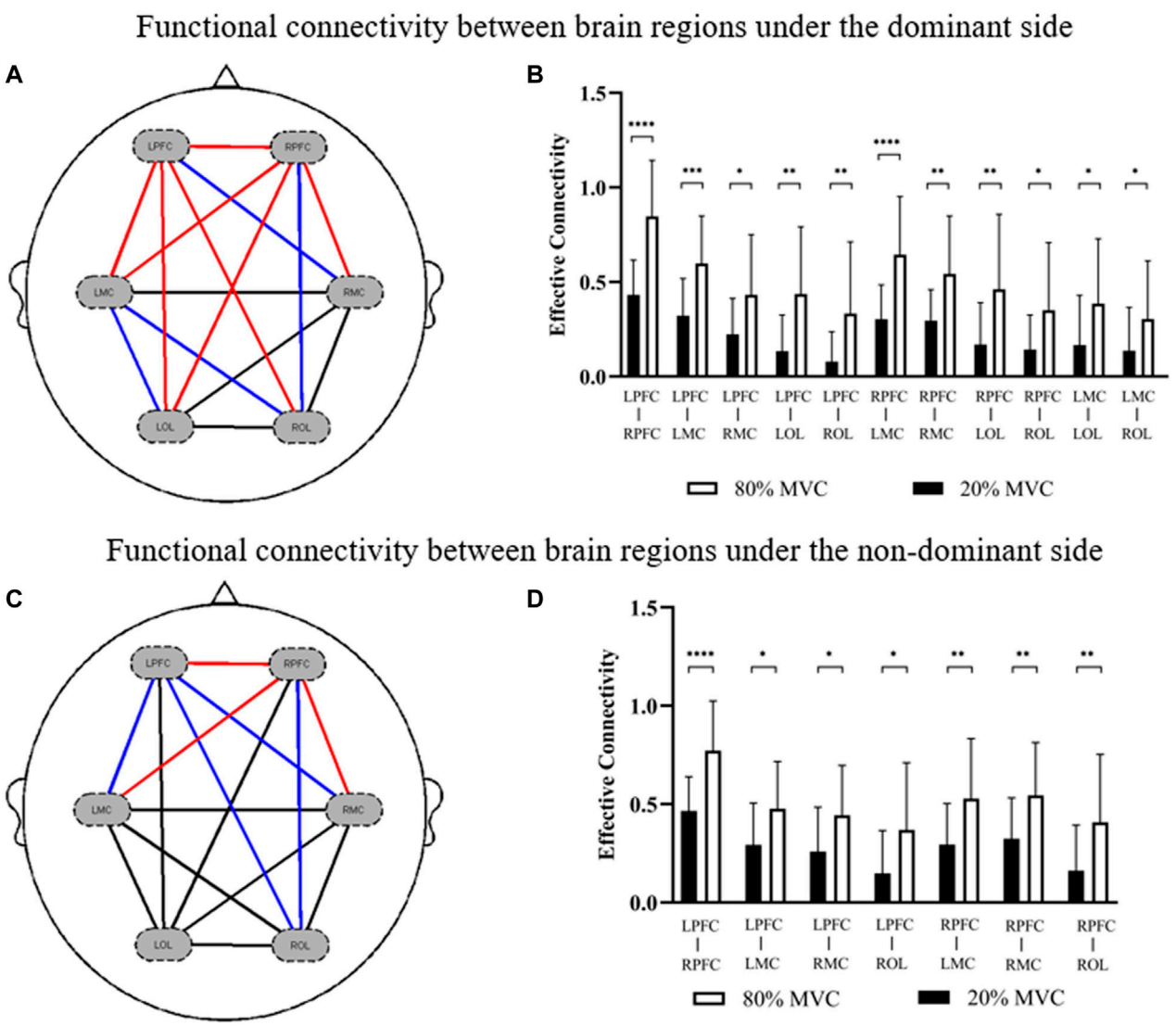

FIGURE 3
The results of significant differences in functional connections between brain regions in different conditions. **(A,B)** The change is represented by the functional connectivity of the 80% MVC relative to the 20% MVC under the dominant side. **(C,D)** The change is represented by the functional connectivity of the 80% MVC relative to the 20% MVC under the non-dominant side. The red line ($p < 0.01$) and blue line ($0.01 < p < 0.05$) indicate significant increase statistically.

3.2 Effective connectivity

Figure 4 showed the effective connectivity between the different brain regions of the dominant and non-dominant sides under the same force conditions. Under the 80% MVC condition, the effective connectivity between other brain regions of the dominant and non-dominant sides showed that the effective connectivity was significantly enhanced under the dominant side condition from RMC to LMC ($p = 0.046$), from LMC to the RMC ($p = 0.049$), and from LMC to LOL ($p = 0.032$) (Figures 4A, B). Under the 20% MVC condition, the effective connectivity between different brain regions of the dominant and non-dominant sides showed that the effective connectivity from RPFC to LRPC ($p = 0.039$), from RPFC to LMC ($p = 0.033$), from RPFC to RMC ($p = 0.047$), from RMC to LPFC ($p = 0.016$), from RMC to LOL ($p = 0.022$), from RMC to LOL ($p = 0.035$) and from LMC to LOL ($p = 0.028$) was significantly enhanced under the dominant side condition (Figures 4C, D).

3.3 Brain network analysis

As shown in Figure 5, only significant differences were observed in the clustering coefficient ($p = 0.008$) and node-local efficiency ($p = 0.006$) of the contralateral motor cortex under different force conditions of the dominant side. However, no significant difference was observed in the contralateral motor cortex under other force conditions of the non-dominant side. But the clustering coefficient of the dominant side under the same

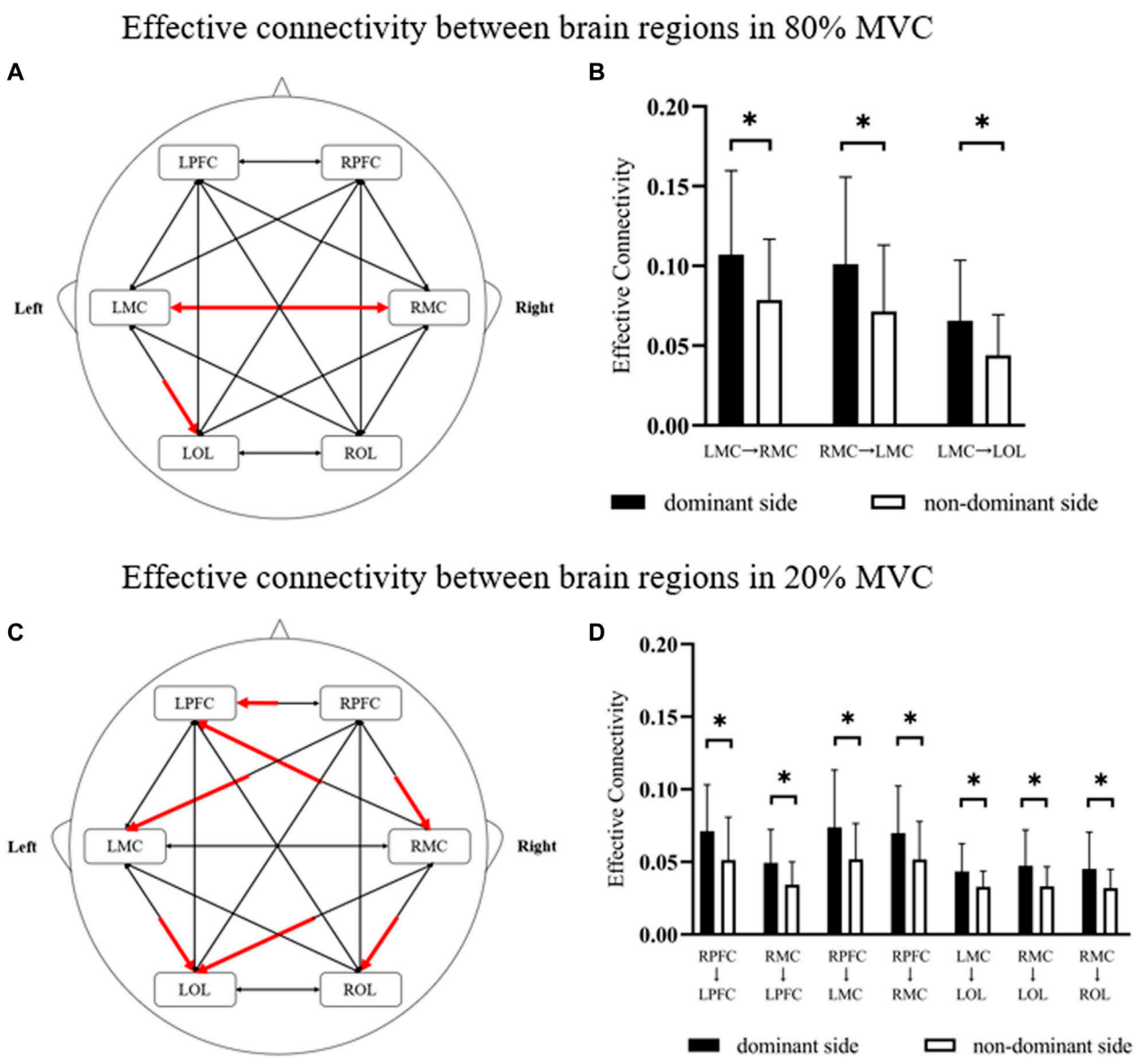

FIGURE 4
The results of significant differences in effective connectivity between brain regions in different conditions. **(A,B)** The change is represented by the effective connectivity of the dominant side relative to the non-dominant side under 80% MVC. **(C,D)** The change is represented by the effective connectivity of the dominant side relative to the non-dominant side under 20% MVC. The red line indicates a significant increase statistically ($p < 0.05$), where * indicates $p < 0.05$.

conditions was higher than those of the non-dominant side ($C_{\text{dominant side\_80\%}} = 0.21$; $C_{\text{non-dominant side\_80\%}} = 0.18$; $C_{\text{dominant side\_20\%}} = 0.18$; $C_{\text{non-dominant side\_20\%}} = 0.17$). Similarly, the node-local efficiency of the dominant side under the same conditions was higher than that of the non-dominant side ($E_{\text{dominant side\_80\%}} = 0.25$; $E_{\text{non-dominant side\_80\%}} = 0.20$; $E_{\text{dominant side\_20\%}} = 0.22$; $E_{\text{non-dominant side\_20\%}} = 0.19$). The results showed that the information connection efficiency was higher in the brain network of the contralateral motor cortex under 80% MVC condition of the dominant side. The information connection efficiency was lower in the brain network of the contralateral motor cortex with the non-dominant side.

3.4 EMG analysis

Figures 6A, B depicted the fApEn of the EMG signal extracted from the BIC and TRI under different conditions as the window N increases from 100 points to 5,000 points in the step of 100 points size. Figures 6C, D respectively depicted the fApEn of the EMG signal when the admissible window r is increased from 0.02 to 1 at a step r of 0.02 for the picked EMG signal of BIC and TRI under four different conditions, respectively. Combined with the results reported in previous studies and the test results in this study, N was set as 5,000, r was fixed as 0.15, and the five repeated tests were averaged. Comparing the fApEn of EMG

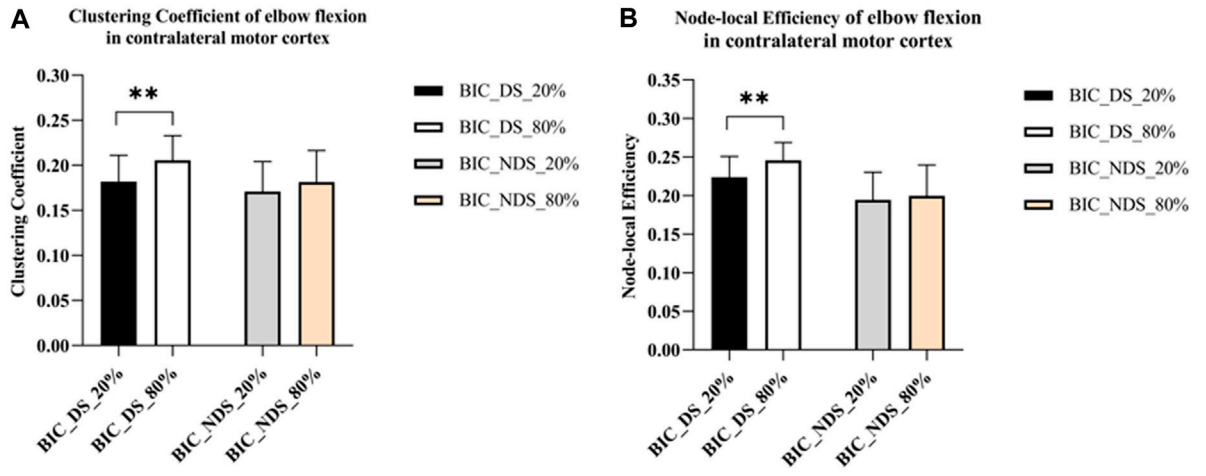

FIGURE 5
Significant global and local metric changes of elbow flexion in the contralateral motor cortex. **(A)** Global metrics results of the clustering coefficient (ΔHbO_2). **(B)** Local metrics results of the node-local efficiency (ΔHbO_2), where ** indicates $p < 0.01$. Abbreviation: DS, dominant side; NDS, non-dominant side.

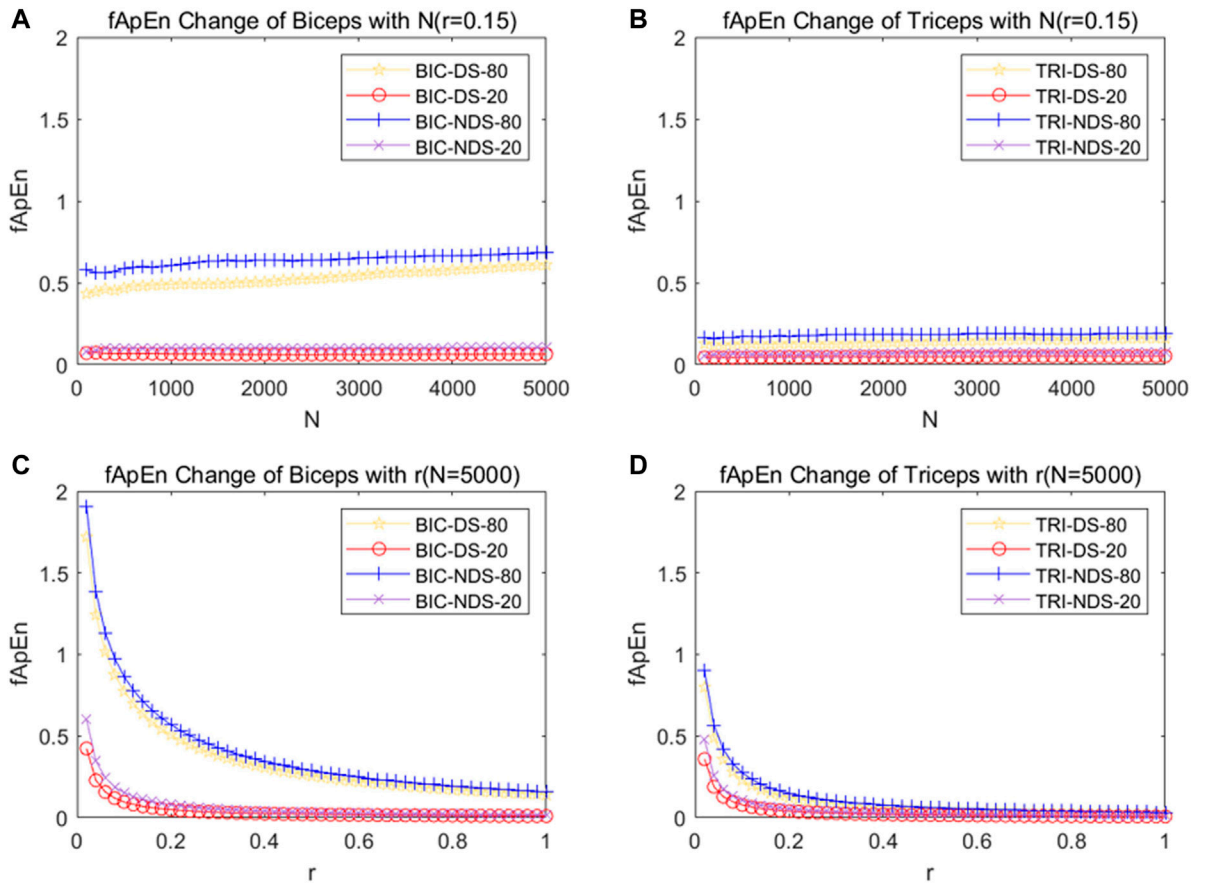

FIGURE 6
(A) Change of fApEn of BIC with the change of window N. **(B)** Change of fApEn of TRI with the change of window N. **(C)** Change of fApEn of BIC with the change of tolerance r. **(D)** Change of fApEn of TRI with the change of tolerance r. EMG signals were picked out from four different conditions from a subject. Abbreviation: DS, dominant side; NDS, non-dominant side.

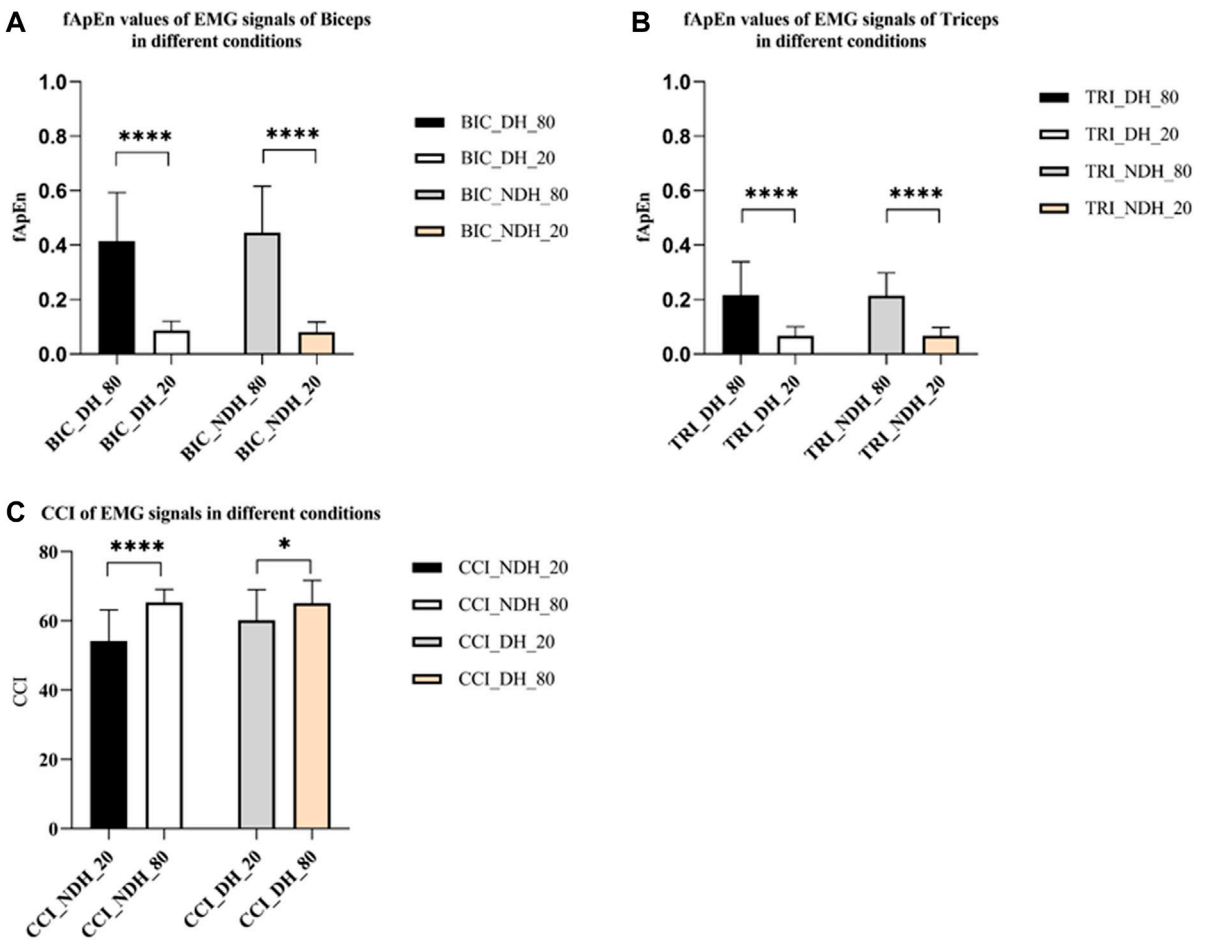

FIGURE 7
(A) fApEn values of EMG signals of BIC. **(B)** fApEn values of EMG signals of TRI. **(C)** The CCI of EMG signals in different conditions. The significant difference between different conditions was represented by *$p < 0.05$ and ****$p < 0.0001$. Abbreviation: DS, dominant side; NDS, non-dominant side.

signals of the BIC, the results showed that fApEn under the condition of 80% MVC was significantly higher than that under the condition of 20% MVC, no matter it was dominant or non-dominant sides ($p < 0.0001$) (Figure 7A). Comparing the fApEn of EMG signals of the TRI, the results showed that the value under the 80% MVC condition was significantly higher than that under the 20% MVC condition, whether it was the dominant or non-dominant sides ($p < 0.0001$) (Figure 7B). The results showed that in the non-dominant side condition, the CCI of 80% MVC was significantly higher than that of 20% MVC ($p = 0.000$) (Figure 7C). Similarly, in the dominant side condition, the CCI of 80% MVC was significantly higher than that of 20% MVC ($p = 0.048$) (Figure 7C).

3.5 Correlation analysis

As shown in Figure 8, fApEn of EMG signals in both dominant and non-dominant conditions was significantly correlated with activation in the contralateral prefrontal cortex, contralateral motor cortex, and contralateral occipital lobe regions. The results showed that there was a significant positive correlation between the fApEn of EMG signal of the BIC and the HbO_2 integral value of the contralateral motor cortex under the dominant side condition ($r = 0.6268$, $p < 0.0001$) (Figure 8B). In addition, the results showed that fApEn of EMG signal of the BIC was significantly positively correlated with HbO_2 integral value in both contralateral prefrontal cortex ($r = 0.6995$, $p < 0.0001$) and contralateral occipital lobe ($r = 0.4815$, $p = 0.0012$) under the dominant side condition (Figures 8A, C). The same trend was observed during elbow isometric contractions of the non-dominant side. The results showed that the fApEn of EMG signal of BIC was also significantly positively correlated with the HbO_2 integral value of the contralateral prefrontal cortex ($r = 0.5949$, $p < 0.0001$), contralateral motor cortex ($r = 0.5091$, $p = 0.0006$) and contralateral occipital lobe ($r = 0.5749$, $p < 0.0001$) under the non-dominant side condition (Figures 8D–F).

fApEn of EMG signals and brain network related indicators, mainly including node-local efficiency and clustering coefficient were further analyzed. The results showed that fApEn of EMG signal of BIC was significantly positively correlated with node-local

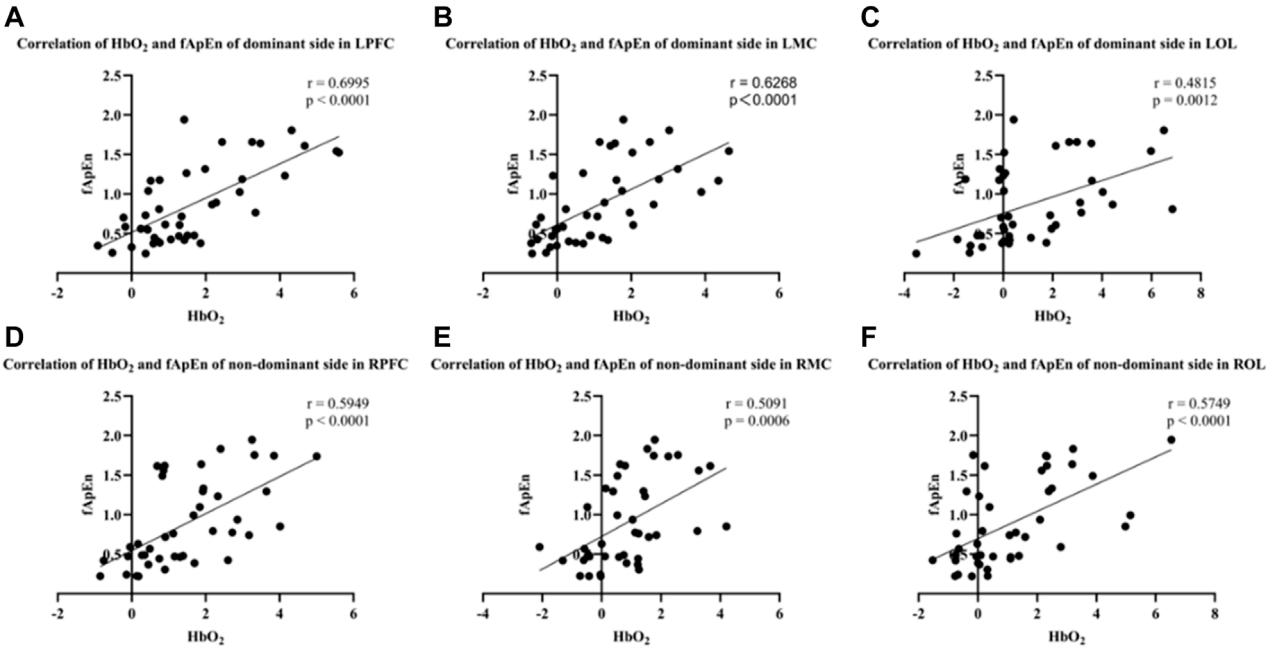

FIGURE 8
(A–C) Correlation of HbO_2 and fApEn of the dominant side in LPFC (r = 0.6995, $p < 0.0001$), LMC (r = 0.6268, $p < 0.0001$) and LOL (r = 0.4815, $p = 0.0012$). **(D–F)** Correlation of HbO_2 and fApEn of the non-dominant side in RPFC (r = 0.5945, $p < 0.0001$), RMC (r = 0.5091, $p = 0.0006$) and ROL (r = 0.5749, $p < 0.0001$).

efficiency of contralateral motor cortex under the dominant side condition (r = 0.3789, $p = 0.0133$) (Figure 9A). However, no significant correlation was found between the fApEn of EMG signal of BIC and clustering coefficient of contralateral motor cortex under the dominant side condition (r = 0.2797, $p = 0.0728$) (Figure 9C). Similarly, no significant correlation was found between the fApEn of EMG signal of BIC and node-local efficiency (r = 0.0371, $p = 0.8157$) and clustering coefficient (r = 0.2045, $p = 0.1939$) of contralateral motor cortex under the non-dominant side condition (Figures 9B, D).

4 Discussion

In this study, the correlation between muscle coordination, cerebral cortex activation, and brain networks during isometric elbow contraction were investigated by simultaneously collecting and analyzing EMG and fNIRS signals. The results showed fApEn of EMG signals was significantly positively correlated with changes in HbO_2 integral value in the contralateral brain region of the dominant and non-dominant sides. In addition, fApEn of EMG signals was significantly positively correlated with the changes in node-local efficiency of the contralateral motor cortex under the dominant side. The results also revealed that the effective connectivity between brain networks was significantly enhanced when the dominant side exerted muscle contraction, compared with that of the non-dominant side. This implies that there might be a mapping correlation between the central nervous system of the brain and peripheral muscle contractions during motor tasks.

4.1 The change in brain networks during motor tasks

Previous studies using fNIRS on relevant mechanisms of action in motor tasks have focused on brain region activation analysis (Lee et al., 2019; Shamsi and Najafizadeh, 2019; Shamsi and Najafizadeh, 2021; Kim et al., 2022). Based on the activation analysis of brain regions, the changes related to the brain network during exercise tasks and compared functional connectivity, effective connectivity, and graph theory analysis of the brain network under different motor tasks were investigated in current study. As shown in figure 2 and figure 3, it was found that functional connections between the prefrontal cortex, motor cortex, and occipital cortex were significantly enhanced in both dominant and non-dominant sides with greater contraction level, especially between the contralateral prefrontal cortex, ipsilateral prefrontal cortex, and contralateral motor cortex. Previous studies have shown the correlation between the complexity of neural activity in the brain and the complexity of the task caused by the level of force applied (Spraker et al., 2012; Alahmadi et al., 2015). The results of our study are consistent with those of previous studies.

Although many neuroimaging studies have analyzed handedness, the mechanism of the relationship between handedness and brain networks in motor tasks still needs to be fully understood (Klöppel et al., 2007; Lin et al., 2017). Many studies have shown that dominant hands perform better than non-dominant hands in motor tasks (Pool et al., 2014; Xiao et al., 2019). As shown in Figure 5, the results revealed that the contralateral motor cortex's clustering coefficient and node-local efficiency increased significantly when the dominant side exerted

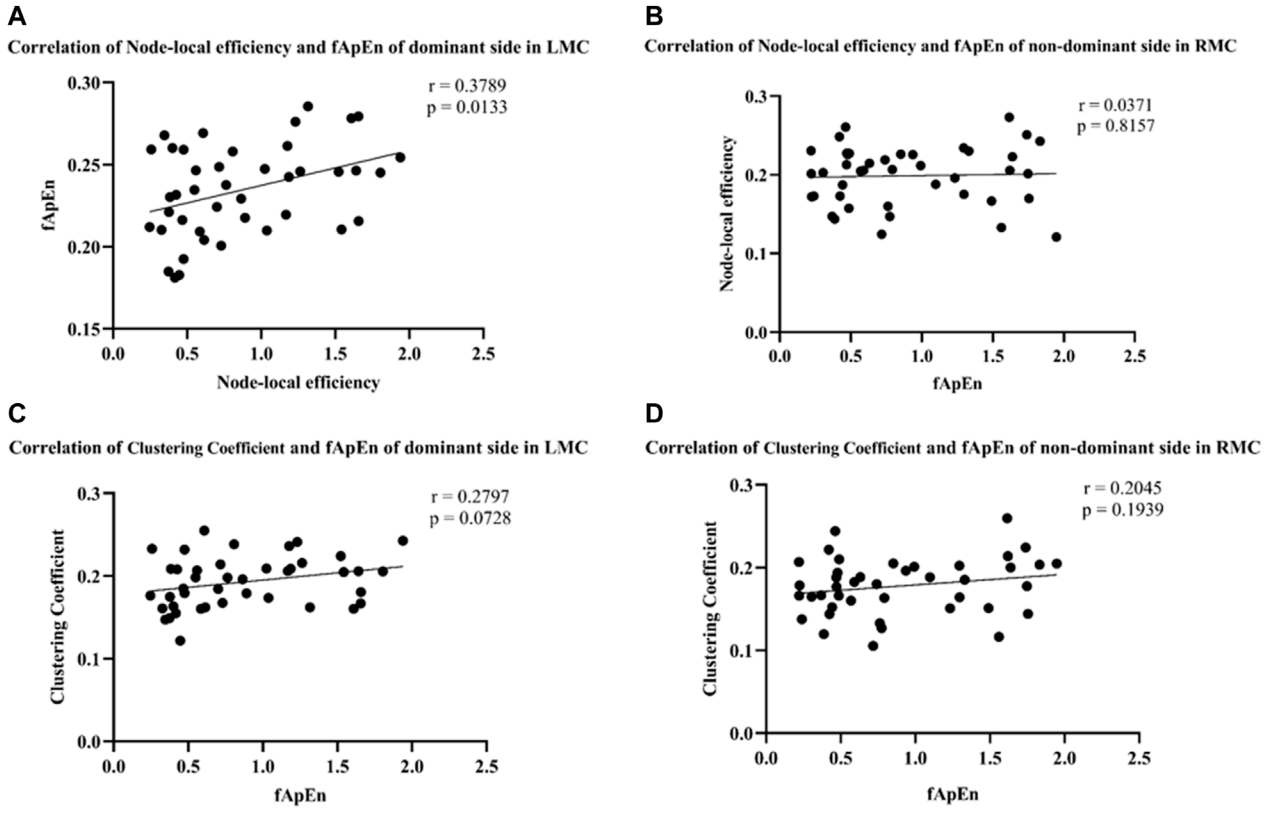

FIGURE 9
(A,B) Correlation of node-local efficiency and fApEn of the dominant side in LMC (r = 0.3789, p = 0.0133) and the non-dominant side in RMC (r = 0.0371, p = 0.8157). **(C,D)** Correlation of clustering coefficient and fApEn of the dominant side in LMC (r = 0.2797, p = 0.0728) and the non-dominant side in RMC (r = 0.2045, p = 0.1939).

force in a larger MVC. Meanwhile, under the same force conditions in this study, the effective connectivity of the brain network in the dominant side was significantly higher than that in the non-dominant side (Figure 4). In a review article from Hammond, the author also concluded the similar findings of the correlates of the handedness in primary motor cortex (Hammond, 2002). In addition, a fNIRS study from Yokoyama et al. showed that non-dominant side had greater variability in adjustment time than the dominant side under the same muscle relaxation and contraction conditions (Yokoyama et al., 2019). These findings suggest that there are significant differences in motor control between the dominant and non-dominant sides of healthy adults, and motor control might be more difficult on the non-dominant side.

4.2 The change in muscle control during motor tasks

Some of previous studies on approximate entropy or sample Entropy recommended using the standard deviation of segmented data for the determination of the r value (Zhou et al., 2011; Zhang and Zhou, 2012). But Sun and others asserted that the r value should be upheld as a universal constant for fuzzy approximate entropy analysis, with the aim of mitigating the impact of noise on the complexity of EMG signals (Sun et al., 2014). Figures 6C, D illustrate the response of tolerance r and fApEn and our results were similar with Sun's finding and the N was set at 5,000 and r was fixed at 0.15. As shown in Figure 7, the study revealed that the fApEn of the EMG signals were significantly higher under the larger MVC force than under the smaller MVC force in both dominant and non-dominant sides, indicating more MUs were involved and more complicated motor firing pattern were triggered in the larger contraction force. Previous studies revealed the composition of EMG signals were the summation of a temporal superposition of the motor unit action potentials (MUAPs) sequence produced by the various motor units of the contracted muscles (De Luca, 1984; Gazzoni et al., 2004; Chen and Zhou, 2016). As the task intensity increased, the neuromuscular control strategy adjusted and structure in motor execution increased, leading to more complicated muscle firing patterns (Enders et al., 2015; Ma et al., 2017; Deng et al., 2021). As muscle power increases, more motor units are recruited, increasing the fApEn of the EMG signals (Kamavuako et al., 2012; Chen et al., 2018). Our results confirm that the complexity of BIC activation increases considerably with increasing strength levels, suggesting the motor control strategy may be adjusted accordingly.

The CCI can evaluate the degree of upper limb muscle activation and muscle coordination (Sheng et al., 2022). As shown in Figure 7, the results revealed that the CCI of EMG signals increased significantly in both dominant and non-dominant sides with

higher MVC force. This may be because increased strength levels require more muscles to maintain strength output, leading to a significant increase in muscle co-contraction. A previous study reported that expert drummers reduced co-contraction in wrist flexor and extensor muscles (Beveridge et al., 2021). The lower CCI value hypothesized the for more exercised side qualified more precise and more efficient movement control.

4.3 The effects of corticomuscular interaction during motor tasks

As shown in Figure 8, we found that the fApEn of EMG signals was positively correlated with the changes in blood oxygen in contralateral motor cortex under both dominant and non-dominant sides (Figures 8B, E). Kumai et al. also found a significant correlation between brain activation and lower limb muscle activity during postural control tasks (Kumai et al., 2022). In addition, Liu et al. showed a substantial correlation between EEG and EMG and coherence in the beta band during both arm flexion and extension tasks (Liu et al., 2021). At high strength levels, muscles produce stronger contractions and activate more motor neurons (Xi et al., 2021). Therefore, the above findings might provide evidence that the higher the force intensity, the more numbers of motor units are involved in the motor task and correlated with the higher activation of corresponding brain regions. As the increase in the number of motor units leads to the increase in the density of the EMG signal, the non-linear characteristic (fApEn) of the EMG signal also increases. However, the number of motor units may not be the only factor for the variation of the non-linear characteristics of the EMG signal. The coherence of motor units and the firing rate may also change the variation of the EMG signal (Cashaback et al., 2013). McManus et al. showed a significant correlation between sEMG-based non-linear features and the underlying motor unit coherence. The results of our study are consistent with those previous studies (McManus et al., 2019). In addition, the motor control of the corresponding brain regions is strengthened, resulting in the increase of oxygen metabolism rate in local brain regions, thus enhancing the activation of the cerebral cortex (Leff et al., 2011). Takahashi et al. used a combination of EMG and fNIRS to study changes during muscle fatigue in healthy adults (Takahashi et al., 2021). The results showed that there was a correlation between peripheral muscles and cerebral blood oxygen during muscle fatigue, and the premotor cortex was specifically activated. The results of our study showed a consistent trend with this study (Takahashi et al., 2021). Another interesting finding from current study is that the fApEn of EMG was positively correlated with the changes of blood oxygen in the prefrontal and occipital cortex on both dominant and non-dominant sides (Figures 8A, C, D, F). Although many previous studies have suggested that motor tasks are primarily controlled by the motor cortex, the prefrontal cortex which is related to cognitive function may also be highly involved (Dayan and Cohen, 2011; Rizzolatti et al., 2014). Zou and coworkers' finding also revealed that cognitive control plays an important role in complex motor tasks in a subject group of stroke patients (Zou et al., 2018). Since the task of 80% MVC is more challenging and the subject kept increasing their attention on screen to continuously follow the target line, it may cause the significant correlations between occipital cortex hemodynamics and complexity of muscle contraction. Therefore, all these findings provide evidence of a mapping relationship between the brain activity and the execution of motor tasks. The results also imply that exploring the coupling mechanism between the cerebral cortex and muscle contraction might provide a new evaluation method for rehabilitation intervention for motor function.

Previous studies have shown dynamic changes in corticomuscular coupling and brain network during muscle contraction (Siemionow et al., 2010; Xi et al., 2021). Similarly, we found that the fApEn of EMG signals was significantly positively correlated with changes in the node-local efficiency of the contralateral motor cortex (LMC) on the dominant side (Figure 9A). However, we did not find the significant relationship on the non-dominant side (Figure 9B). Furthermore, no significant correlation was found between the fApEn of EMG signals and clustering coefficient of the contralateral motor cortex on both dominant and non-dominant sides (Figures 9C, D). In previous studies of brain network, node-local efficiency reflects the integration ability and fault-tolerant ability of neighboring nodes (Li et al., 2013). This might mean that the brain network efficiency of contralateral motor cortex is still vital in the performance of motor tasks (Zimmermann et al., 2013). Clustering coefficient can be used to characterize the efficiency and ability of local information transmission in the network (Watts and Strogatz, 1998). However, due to the limited number of nodes in the brain network in this study, this might cause the non-significant correlation between node efficiency and muscle contraction tasks. By comparing Figures 8, 9, it indicated that the activations of local brain regions are different with the brain network node connections during elbow contractions. It means the connectivity between different brain regions might play a more important role to coordinate the completion of motor tasks than the local hemodynamic changes, but further evidence is needed (Thiebaut de Schotten and Forkel, 2022). Previous studies have also shown better recovery of local brain networks in stroke patients after completion of motor task training (Rehme and Grefkes, 2013; Xu et al., 2022). In general, our correlation results of brain network indicators demonstrated that the complexity of muscle contraction is significant related to the node-local efficiency of the contralateral motor cortex when performing isometric elbow contraction. This might provide a useful method for future clinical research to evaluate the rehabilitation of motor function and help us understand the mechanism behind these interventions.

4.4 Limitations

There were several limitations in the study. First, the experiment only recruited young, healthy people, and the interpretation may not be directly applied in older people and those with neurological conditions such as stroke. Second, the task of elbow isometric stretching was not set in the study, so the results did not address the task of the TRI as an active muscle to detect the co-contraction changes during elbow extension. In future studies, the relevant aspects of the elbow isometric stretch task will be further

explored. Finally, only the cerebral hemodynamics in the time domain were analyzed, but not in the frequency domain. The physiological significance of cerebral hemodynamics in different frequency domains remains to be further studied.

5 Conclusion

In summary, this study demonstrated the changes of brain network related indexes and the non-linear characteristics of EMG signals under different motor task conditions, and explored the differences between dominant and non-dominant sides in motor tasks. The results found that effective connectivity between brain networks was significantly enhanced when the dominant side performed muscle contractions compared to the non-dominant side, which may imply that brain network analysis is a potential way to explore brain function during motor tasks. At the same time, fApEn of EMG signals increased significantly under greater MVC force, which was related to the increasing complexity of motor tasks. Finally, this study demonstrated a significant positive correlation between cerebral oxygen changes and EMG signals during motor tasks. This finding provides evidence for further exploration of the mapping relationship between the brain activity and the execution of motor tasks and can guide the movement function damage in patients with clinical rehabilitation.

Data availability statement

The datasets analyzed during the current study are available from the corresponding authors upon reasonable request.

Ethics statement

The studies involving human participants were reviewed and approved by the ethics committee of Northwestern Polytechnical University and was registered in the Chinese Clinical Trial Registry (ChiCTR2200057839). The patients/participants provided their written informed consent to participate in this study.

Author contributions

HH, WZ, SX, SF, and LL conceived and designed the study, made contributions to experiments, and reviewed and edited the manuscript, XW, ZL, and MZ performed the experiments and collected data, XW, ZL, MZ and SX analyzed the data, XW, ZL, and LL wrote the manuscript. All authors read and approved the final manuscript.

Funding

This work was supported by the National Natural Science Foundation of China (Nos 32071316, 32211530049), the Key Research and Development Project of Shaanxi province (2022SF-117), the Natural Science Foundation of Shaanxi province (2022-JM482), and the Education and Teaching Reform Funds for the Central Universities (No. 22GZ230101).

Acknowledgments

We acknowledge the help of Mr. Yuzhao Chen during the performance of this study and Ambrose WL Lo for the language improvement of the manuscript.

Conflict of interest

The authors declare that the research was conducted in the absence of any commercial or financial relationships that could be construed as a potential conflict of interest.

Publisher's note

References

Alahmadi, A. A., Pardini, M., Samson, R. S., D'Angelo, E., Friston, K. J., Toosy, A. T., et al. (2015). Differential involvement of cortical and cerebellar areas using dominant and nondominant hands: An FMRI study. *Hum. Brain Mapp.* 36 (12), 5079–5100. doi:10.1002/hbm.22997

Ao, D., Sun, R., Tong, K. Y., and Song, R. (2015). Characterization of stroke- and aging-related changes in the complexity of EMG signals during tracking tasks. *Ann. Biomed. Eng.* 43 (4), 990–1002. doi:10.1007/s10439-014-1150-1

Bao, S. C., Chen, C., Yuan, K., Yang, Y., and Tong, R. K. (2021). Disrupted cortico-peripheral interactions in motor disorders. *Clin. Neurophysiol.* 132 (12), 3136–3151. doi:10.1016/j.clinph.2021.09.015

Beveridge, S., Herff, S. A., Buck, B., Madden, G. B., and Jabusch, H. C. (2021). Corrigendum: Expertise-related differences in wrist muscle co-contraction in drummers. *Front. Psychol.* 12, 706228. doi:10.3389/fpsyg.2021.706228

Bullmore, E., and Sporns, O. (2009). Complex brain networks: Graph theoretical analysis of structural and functional systems. *Nat. Rev. Neurosci.* 10 (3), 186–198. doi:10.1038/nrn2575

Cashaback, J. G., Cluff, T., and Potvin, J. R. (2013). Muscle fatigue and contraction intensity modulates the complexity of surface electromyography. *J. Electromyogr. Kinesiol* 23 (1), 78–83. doi:10.1016/j.jelekin.2012.08.004

Chen, M., and Zhou, P. (2016). A novel framework based on fastICA for high density surface EMG decomposition. *IEEE Trans. Neural Syst. Rehabil. Eng.* 24 (1), 117–127. doi:10.1109/tnsre.2015.2412038

Chen, W., Wang, Z., Xie, H., and Yu, W. (2007). Characterization of surface EMG signal based on fuzzy entropy. *IEEE Trans. Neural Syst. Rehabil. Eng.* 15 (2), 266–272. doi:10.1109/tnsre.2007.897025

Chen, Y., Hu, H., Ma, C., Zhan, Y., Chen, N., Li, L., et al. (2018). Stroke-related changes in the complexity of muscle activation during obstacle crossing using fuzzy approximate entropy analysis. *Front. Neurol.* 9, 131. doi:10.3389/fneur.2018.00131

Colamarino, E., de Seta, V., Masciullo, M., Cincotti, F., Mattia, D., Pichiorri, F., et al. (2021). Corticomuscular and intermuscular coupling in simple hand movements to enable a hybrid brain-computer interface. *Int. J. Neural Syst.* 31 (11), 2150052. doi:10.1142/s0129065721500520

Dayan, E., and Cohen, L. G. (2011). Neuroplasticity subserving motor skill learning. *Neuron* 72 (3), 443–454. doi:10.1016/j.neuron.2011.10.008

De Luca, C. J. (1984). Myoelectrical manifestations of localized muscular fatigue in humans. *Crit. Rev. Biomed. Eng.* 11 (4), 251–279.

Deng, L., Luo, J., Lyu, Y., and Song, R. (2021). Effects of future information and trajectory complexity on kinematic signal and muscle activation during visual-motor tracking. *Entropy (Basel)* 23 (1), 111. doi:10.3390/e23010111

Donaldson, S., Donaldson, M., and Snelling, L. (2003). SEMG evaluations: An overview. *Appl. Psychophysiol. Biofeedback* 28 (2), 121–127. doi:10.1023/a:1023858524879

Enders, H., Tscharner, V., and Nigg, B. M. (2015). Neuromuscular strategies during cycling at different muscular demands. *Med. Sci. Sports Exerc* 47 (7), 1450–1459. doi:10.1249/mss.0000000000000564

Felleman, D. J., and Van Essen, D. C. (1991). Distributed hierarchical processing in the primate cerebral cortex. *Cereb. Cortex* 1 (1), 1–47. doi:10.1093/cercor/1.1.1

Ferrari, M., and Quaresima, V. (2012). A brief review on the history of human functional near-infrared spectroscopy (fNIRS) development and fields of application. *Neuroimage* 63 (2), 921–935. doi:10.1016/j.neuroimage.2012.03.049

Friston, K., Moran, R., and Seth, A. K. (2013). Analysing connectivity with Granger causality and dynamic causal modelling. *Curr. Opin. Neurobiol.* 23 (2), 172–178. doi:10.1016/j.conb.2012.11.010

Gazzoni, M., Farina, D., and Merletti, R. (2004). A new method for the extraction and classification of single motor unit action potentials from surface EMG signals. *J. Neurosci. Methods* 136 (2), 165–177. doi:10.1016/j.jneumeth.2004.01.002

Hammond, G. (2002). Correlates of human handedness in primary motor cortex: A review and hypothesis. *Neurosci. Biobehav Rev.* 26 (3), 285–292. doi:10.1016/s0149-7634(02)00003-9

Herold, F., Wiegel, P., Scholkmann, F., and Müller, N. G. (2018). Applications of functional near-infrared spectroscopy (fNIRS) neuroimaging in exercise¯cognition science: A systematic, methodology-focused review. *J. Clin. Med.* 7 (12), 466. doi:10.3390/jcm7120466

Hong-Chun, Y., Du-Ming, W., and Jian, W. (2005). Linear and non-linear features of surface EMG during fatigue and recovery period. *Conf. Proc. IEEE Eng. Med. Biol. Soc.* 2005, 5804–5807. doi:10.1109/iembs.2005.1615808

Jian, C., Liu, H., Deng, L., Wang, X., Yan, T., and Song, R. (2021). Stroke-induced alteration in multi-layer information transmission of cortico-motor system during elbow isometric contraction modulated by myoelectric-controlled interfaces. *J. Neural Eng.* 18 (4), 0460e1. doi:10.1088/1741-2552/ac18ae

Kamavuako, E. N., Farina, D., Yoshida, K., and Jensen, W. (2012). Estimation of grasping force from features of intramuscular EMG signals with mirrored bilateral training. *Ann. Biomed. Eng.* 40 (3), 648–656. doi:10.1007/s10439-011-0438-7

Kim, D. H., Lee, K. D., Bulea, T. C., and Park, H. S. (2022). Increasing motor cortex activation during grasping via novel robotic mirror hand therapy: A pilot fNIRS study. *J. Neuroeng Rehabil.* 19 (1), 8. doi:10.1186/s12984-022-00988-7

Klöppel, S., van Eimeren, T., Glauche, V., Vongerichten, A., Münchau, A., Frackowiak, R. S., et al. (2007). The effect of handedness on cortical motor activation during simple bilateral movements. *Neuroimage* 34 (1), 274–280. doi:10.1016/j.neuroimage.2006.08.038

Kumai, K., Ikeda, Y., Sakai, K., Goto, K., Morikawa, K., and Shibata, K. (2022). Brain and muscle activation patterns during postural control affect static postural control. *Gait Posture* 96, 102–108. doi:10.1016/j.gaitpost.2022.05.017

Lee, S. H., Jin, S. H., and An, J. (2019). The difference in cortical activation pattern for complex motor skills: A functional near-infrared spectroscopy study. *Sci. Rep.* 9 (1), 14066. doi:10.1038/s41598-019-50644-9

Leff, D. R., Orihuela-Espina, F., Elwell, C. E., Athanasiou, T., Delpy, D. T., Darzi, A. W., et al. (2011). Assessment of the cerebral cortex during motor task behaviours in adults: A systematic review of functional near infrared spectroscopy (fNIRS) studies. *Neuroimage* 54 (4), 2922–2936. doi:10.1016/j.neuroimage.2010.10.058

Li, W., Huang, Y., Li, Y., and Chen, X. (2013). Brain network evolution after stroke based on computational experiments. *PLoS One* 8 (12), e82845. doi:10.1371/journal.pone.0082845

Lin, Q., Li, H., Mao, Y. R., Lo, W. L., Zhao, J. L., Chen, L., et al. (2017). The difference of neural networks between bimanual antiphase and in-phase upper limb movements: A preliminary functional magnetic resonance imaging study. *Behav. Neurol.* 2017, 1–9. doi:10.1155/2017/8041962

Liu, J., Wang, J., Tan, G., Sheng, Y., Chang, H., Xie, Q., et al. (2021). Correlation evaluation of functional corticomuscular coupling with abnormal muscle synergy after stroke. *IEEE Trans. Biomed. Eng.* 68 (11), 3261–3272. doi:10.1109/tbme.2021.3068997

Long, J., Tazoe, T., Soteropoulos, D. S., and Perez, M. A. (2016). Interhemispheric connectivity during bimanual isometric force generation. *J. Neurophysiol.* 115 (3), 1196–1207. doi:10.1152/jn.00876.2015

Ma, C., Chen, N., Mao, Y., Huang, D., Song, R., and Li, L. (2017). Alterations of muscle activation pattern in stroke survivors during obstacle crossing. *Front. Neurol.* 8, 70. doi:10.3389/fneur.2017.00070

McManus, L., Flood, M. W., and Lowery, M. M. (2019). Beta-band motor unit coherence and nonlinear surface EMG features of the first dorsal interosseous muscle vary with force. *J. Neurophysiol.* 122 (3), 1147–1162. doi:10.1152/jn.00228.2019

Ortega, P., Zhao, T., and Faisal, A. A. (2020). Hygrip: Full-Stack characterization of neurobehavioral signals (fNIRS, EEG, EMG, Force, and Breathing) during a bimanual grip force control task. *Front. Neurosci.* 14, 919. doi:10.3389/fnins.2020.00919

Pool, E. M., Rehme, A. K., Fink, G. R., Eickhoff, S. B., and Grefkes, C. (2014). Handedness and effective connectivity of the motor system. *Neuroimage* 99, 451–460. doi:10.1016/j.neuroimage.2014.05.048

Rehme, A. K., and Grefkes, C. (2013). Cerebral network disorders after stroke: Evidence from imaging-based connectivity analyses of active and resting brain states in humans. *J. Physiol.* 591 (1), 17–31. doi:10.1113/jphysiol.2012.243469

Rizzolatti, G., Cattaneo, L., Fabbri-Destro, M., and Rozzi, S. (2014). Cortical mechanisms underlying the organization of goal-directed actions and mirror neuron-based action understanding. *Physiol. Rev.* 94 (2), 655–706. doi:10.1152/physrev.00009.2013

Rubinov, M., and Sporns, O. (2010). Complex network measures of brain connectivity: Uses and interpretations. *Neuroimage* 52 (3), 1059–1069. doi:10.1016/j.neuroimage.2009.10.003

Shamsi, F., and Najafizadeh, L. (2019). "Multi-class classification of motor execution tasks using fNIRS," in Proceeding of the 2019 IEEE Signal Processing in Medicine and Biology Symposium (SPMB), Philadelphia, PA, USA, December 2019 (IEEE), 1–5.

Shamsi, F., and Najafizadeh, L. (2021). "Multi-class fNIRS classification of motor execution tasks with application to brain-computer interfaces," in *Biomedical signal processing: Innovation and applications*. Editors I. Obeid, I. Selesnick, and J. Picone (Cham: Springer International Publishing), 1–32.

Sheng, W., Li, S., Zhao, J., Wang, Y., Luo, Z., Lo, W. L. A., et al. (2022). Upper limbs muscle co-contraction changes correlated with the impairment of the corticospinal tract in stroke survivors: Preliminary evidence from electromyography and motor-evoked potential. *Front. Neurosci.* 16, 886909. doi:10.3389/fnins.2022.886909

Shumway-Cook, A., and Woollacott, M. (2014). *Motor control: Translating research into clinical practice*. Fourth edition.

Siemionow, V., Sahgal, V., Yue, G. H., and Yue, G. H. (2010). Single-Trial EEG-EMG coherence analysis reveals muscle fatigue-related progressive alterations in corticomuscular coupling. *IEEE Trans. Neural Syst. Rehabil. Eng.* 18 (2), 97–106. doi:10.1109/tnsre.2010.2047173

Souissi, H., Zory, R., Bredin, J., and Gerus, P. (2017). Comparison of methodologies to assess muscle co-contraction during gait. *J. Biomech.* 57, 141–145. doi:10.1016/j.jbiomech.2017.03.029

Spraker, M. B., Corcos, D. M., Kurani, A. S., Prodoehl, J., Swinnen, S. P., and Vaillancourt, D. E. (2012). Specific cerebellar regions are related to force amplitude and rate of force development. *Neuroimage* 59 (2), 1647–1656. doi:10.1016/j.neuroimage.2011.09.019

Sun, R., Song, R., and Tong, K. Y. (2014). Complexity analysis of EMG signals for patients after stroke during robot-aided rehabilitation training using fuzzy approximate entropy. *IEEE Trans. Neural Syst. Rehabil. Eng.* 22 (5), 1013–1019. doi:10.1109/tnsre.2013.2290017

Takahashi, R., Fujita, K., Kobayashi, Y., Ogawa, T., Teranishi, M., and Kawamura, M. (2021). Effect of muscle fatigue on brain activity in healthy individuals. *Brain Res.* 1764, 147469. doi:10.1016/j.brainres.2021.147469

Thiebaut de Schotten, M., and Forkel, S. J. (2022). The emergent properties of the connected brain. *Science* 378 (6619), 505–510. doi:10.1126/science.abq2591

Vigotsky, A. D., Halperin, I., Lehman, G. J., Trajano, G. S., and Vieira, T. M. (2017). Interpreting signal amplitudes in surface electromyography studies in sport and rehabilitation sciences. *Front. Physiol.* 8, 985. doi:10.3389/fphys.2017.00985

Wang, M., Yuan, Z., and Niu, H. (2019). Reliability evaluation on weighted graph metrics of fNIRS brain networks. *Quant. Imaging Med. Surg.* 9 (5), 832–841. doi:10.21037/qims.2019.05.08

Wang, Y., Lü, J., Rong, J., Song, L., Wang, W., Jiang, Y., et al. (2020). Acute effects of two types of dumbbell exercise on oxygenated hemodynamic concentration of cerebral activation in healthy young male adults: A functional near-infrared spectroscopy study. *Front. Hum. Neurosci.* 14, 519171. doi:10.3389/fnhum.2020.519171

Watts, D. J., and Strogatz, S. H. (1998). Collective dynamics of 'small-world' networks. *Nature* 393 (6684), 440–442. doi:10.1038/30918

Winter, D. A. (2009). *Biomechanics and motor control of human movement*. Wiley.

Xi, X., Pi, S., Zhao, Y. B., Wang, H., and Luo, Z. (2021). Effect of muscle fatigue on the cortical-muscle network: A combined electroencephalogram and electromyogram study. *Brain Res.* 1752, 147221. doi:10.1016/j.brainres.2020.147221

Xiao, X., Hu, H. J., Li, L. F., and Li, L. (2019). Comparison of dominant hand to non-dominant hand in conduction of reaching task from 3D kinematic data: Trade-off between successful rate and movement efficiency. *Math. Biosci. Eng.* 16 (3), 1611–1624. doi:10.3934/mbe.2019077

Xie, H. B., Guo, J. Y., and Zheng, Y. P. (2010). Fuzzy approximate entropy analysis of chaotic and natural complex systems: Detecting muscle fatigue using electromyography signals. *Ann. Biomed. Eng.* 38 (4), 1483–1496. doi:10.1007/s10439-010-9933-5

Xu, G., Huo, C., Yin, J., Li, W., Xie, H., Li, X., et al. (2022). Effective brain network analysis in unilateral and bilateral upper limb exercise training in subjects with stroke. *Med. Phys.* 49 (5), 3333–3346. doi:10.1002/mp.15570

Ye, J. C., Tak, S., Jang, K. E., Jung, J., and Jang, J. (2009). NIRS-SPM: Statistical parametric mapping for near-infrared spectroscopy. *Neuroimage* 44 (2), 428–447. doi:10.1016/j.neuroimage.2008.08.036

Yokoyama, N., Ohtaka, C., Kato, K., Kubo, H., and Nakata, H. (2019). The difference in hemodynamic responses between dominant and non-dominant hands during muscle contraction and relaxation: An fNIRS study. *PLoS One* 14 (7), e0220100. doi:10.1371/journal.pone.0220100

Yuan, Z., Xu, W., Bao, J., Gao, H., Li, W., Peng, Y., et al. (2022). Task-state cortical motor network characteristics by functional near-infrared spectroscopy in subacute stroke show hemispheric dominance. *Front. Aging Neurosci.* 14, 932318. doi:10.3389/fnagi.2022.932318

Zhang, X., and Zhou, P. (2012). Sample entropy analysis of surface EMG for improved muscle activity onset detection against spurious background spikes. *J. Electromyogr. Kinesiol* 22 (6), 901–907. doi:10.1016/j.jelekin.2012.06.005

Zhou, P., Barkhaus, P. E., Zhang, X., and Rymer, W. Z. (2011). Characterizing the complexity of spontaneous motor unit patterns of amyotrophic lateral sclerosis using approximate entropy. *J. Neural Eng.* 8 (6), 066010. doi:10.1088/1741-2560/8/6/066010

Zhou, G., Chen, Y., Wang, X., Wei, H., Huang, Q., and Li, L. (2022). The correlations between kinematic profiles and cerebral hemodynamics suggest changes of motor coordination in single and bilateral finger movement. *Front. Hum. Neurosci.* 16, 957364. doi:10.3389/fnhum.2022.957364

Zimmermann, R., Marchal-Crespo, L., Edelmann, J., Lambercy, O., Fluet, M. C., Riener, R., et al. (2013). Detection of motor execution using a hybrid fNIRS-biosignal BCI: A feasibility study. *J. Neuroeng Rehabil.* 10, 4. doi:10.1186/1743-0003-10-4

Zou, Y., Zhao, Z., Yin, D., Fan, M., Small, M., Liu, Z., et al. (2018). Brain anomaly networks uncover heterogeneous functional reorganization patterns after stroke. *Neuroimage Clin.* 20, 523–530. doi:10.1016/j.nicl.2018.08.008

frontiers | Frontiers in Bioengineering and Biotechnology

TYPE Original Research
PUBLISHED 05 May 2023
DOI 10.3389/fbioe.2023.1140262

OPEN ACCESS

EDITED BY
Navrag B. Singh,
ETH Zürich, Switzerland

REVIEWED BY
Yaodong Gu,
Ningbo University, China
Wenxin Niu,
Tongji University, China

*CORRESPONDENCE
Cai-Hua Xiong,
chxiong@hust.edu.cn
Wen-Bin Chen,
wbchen@hust.edu.cn

RECEIVED 08 January 2023
ACCEPTED 03 April 2023
PUBLISHED 05 May 2023

CITATION
Xv X-W, Chen W-B, Xiong C-H, Huang B, Cheng L-F and Sun B-Y (2023), Exploring the effects of skeletal architecture and muscle properties on bipedal standing in the common chimpanzee (*Pan troglodytes*) from the perspective of biomechanics.
Front. Bioeng. Biotechnol. 11:1140262.
doi: 10.3389/fbioe.2023.1140262

Exploring the effects of skeletal architecture and muscle properties on bipedal standing in the common chimpanzee (*Pan troglodytes*) from the perspective of biomechanics

Xiao-Wei Xv, Wen-Bin Chen*, Cai-Hua Xiong*, Bo Huang, Long-Fei Cheng and Bai-Yang Sun

State Key Lab of Digital Manufacturing Equipment and Technology, School of Mechanical Science and Engineering, Institute of Medical Equipment Science and Engineering, Huazhong University of Science and Technology, Wuhan, Hubei, China

Introduction: It is well known that the common chimpanzee, as both the closest living relative to humans and a facultative bipedal, has the capability of bipedal standing but cannot do so fully upright. Accordingly, they have been of exceeding significance in elucidating the evolution of human bipedalism. There are many reasons why the common chimpanzee can only stand with its hips–knees bent, such as the distally oriented long ischial tubercle and the almost absent lumbar lordosis. However, it is unknown how the relative positions of their shoulder–hip–knee–ankle joints are coordinated. Similarly, the distribution of the biomechanical characteristics of the lower-limb muscles and the factors that affect the erectness of standing as well as the muscle fatigue of the lower limbs remain a mystery. The answers are bound to light up the evolutional mechanism of hominin bipedality, but these conundrums have not been shed much light upon, because few studies have comprehensively explored the effects of skeletal architecture and muscle properties on bipedal standing in common chimpanzees.

Methods: Thus, we first built a musculoskeletal model comprising the head-arms-trunk (HAT), thighs, shanks, and feet segments of the common chimpanzee, and then, the mechanical relationships of the Hill-type muscle-tendon units (MTUs) in bipedal standing were deduced. Thereafter, the equilibrium constraints were established, and a constrained optimization problem was formulated where the optimization objective was defined. Finally, thousands of simulations of bipedal standing experiments were performed to determine the optimal posture and its corresponding MTU parameters including muscle lengths, muscle activation, and muscle forces. Moreover, to quantify the relationship between each pair of the parameters from all the experimental simulation outcomes, the Pearson correlation analysis was employed.

Results: Our results demonstrate that in the pursuit of the optimal bipedal standing posture, the common chimpanzee cannot simultaneously achieve maximum erectness and minimum muscle fatigue of the lower limbs. For uni-articular MTUs, the relationship between muscle activation, relative muscle lengths, together with relative muscle forces, and the corresponding joint angle is generally negatively correlated for extensors and positively correlated

for flexors. For bi-articular MTUs, the relationship between muscle activation, coupled with relative muscle forces, and the corresponding joint angles does not show the same pattern as in the uni-articular MTUs.

Discussion: The results of this study bridge the gap between skeletal architecture, along with muscle properties, and biomechanical performance of the common chimpanzee during bipedal standing, which enhances existing biomechanical theories and advances the comprehension of bipedal evolution in humans.

KEYWORDS

common chimpanzee, bipedal standing, musculoskeletal model, Hill-type MTU, constrained optimization, simulation experiments

1 Introduction

Apart from modern humans (*Homo sapiens*), there are various other species of primates, such as the common chimpanzee (*Pan troglodytes*), that have acquired the ability of bipedal standing; however, they cannot stand fully upright (Jenkins, 1972). As our closest living relative (Goodman, 1999; Waterson et al., 2005), common chimpanzees (chimps) share with us the post-cranial features related to orthograde modes of locomotion (Hunt, 1991) while lacking the human-like skeletal architecture that aligns the shoulder, hip, knee, and ankle joints in the sagittal plane (Thorpe et al., 1999; Payne et al., 2006b; Pontzer, 2018). Circumscribed to the distally oriented long ischial tubercle and the almost absent lumbar lordosis (Robinson, 1972; McHenry, 1975), chimps are unable to extend their hip joint so that they stand bipedally in a bent-hip, bent-knee manner, a position in which the center of mass (CoM) is located anterior to the hip (Sockol et al., 2007). When a human stands upright, the CoM, hip, knee, and ankle joints approximately line up (Neumann, 2013), diminishing the necessity for the lower-limb muscles to be activated (Pontzer et al., 2009). In the case of a chimp, muscle activation of the hind limbs is required to generate muscle forces and joint moments on account of balance when it comes to standing on two feet. However, how do chimps coordinate the relative positions of their shoulder, hip, knee, and ankle joints? How is the muscle activation of the hind limbs assigned in pursuit after maintaining balance? How do biomechanical factors such as skeletal architecture and muscle properties affect the erectness of standing? Although the bipedal locomotion pattern of chimps has been studied since 1944 (Elftman, 1944), few studies have explored this topic in depth.

The road to uncovering the aforementioned questions is paved with challenging puzzles. Although laboratory-based experiments have been widely conducted in the bipedal walking or running of chimps (Demes et al., 2015; Thompson et al., 2015; Kozma et al., 2018), their application remains unfeasible in bipedal standing since it is barely possible to keep untrained chimps standing bipedally for a sufficient amount of time (Doran, 1992a; Doran, 1992b; Hunt, 1992; Hunt, 1994). Training may not be a feasible alternative either because trained primates have been proven to develop changes in the musculoskeletal structure (Nakatsukasa, 2004). Modeling and simulation can not only overcome these problems but can also provide internal parameters that are difficult to measure. However, existing musculoskeletal models (Yamazaki, 1985; O'Neill et al., 2013; O'Neill et al., 2015; O'Neill et al., 2018; O'Neill et al., 2022; Sellers et al., 2013) are still far from effective for investigating the biomechanical performance of chimps during bipedal standing. Yamazaki (1985) measured the net joint moments of chimps during bipedal locomotion under controlled conditions and derived the corresponding muscle forces using computer simulations. However, Yamazaki assumed constant values of the muscle moment arms that apparently vary with joint angles and did not specify whether anatomical or physiological cross-sectional areas were used to estimate muscle forces from stresses. O'Neill et al. (2013, 2015, 2018, 2022) quantified the variation in moment arms and muscle forces of hind limb muscles with joint angles during bipedal locomotion in chimps through modeling and simulations on the OpenSim platform, combined with detailed muscle–tendon parameters. However, their model merely contained the pelvis and hind limbs and could not predict the maximum erectness that chimps can achieve during bipedal standing and the corresponding posture. Sellers et al. (2013) established a whole-body model of the common chimpanzee on the GaitSym platform to explore changes in performance, such as footfall sequences, locomotion velocity, and energy expenditure during quadrupedal locomotion within the domain. However, their model simplified the pattern of muscle activation according to the motor function, which is solely applicable to rhythmic movements.

Numerical optimization is recognized as a viable technique for predicting animal behavior (Pandy, 2001), where it is crucial to translate appropriate biomechanical metrics into optimization objectives (Lee and Umberger, 2016). Experimental studies have indicated that the larger the hip and knee joint angles, that is, the greater the erectness, the smaller the activation volume of the hind limb muscles during bipedal walking in chimps (Pontzer et al., 2014). This implies that erectness and muscle activation can be considered as the objective function for optimization. Furthermore, muscle fatigue, as a pivotal biomechanical indicator, can be regarded as an objective function that characterizes muscle activation (Crowninshield and Brand, 1981). The constrained optimization is thus applicable for exploring the bipedal standing postures (BSPs) of chimps and corresponding biomechanical factors. This methodology thoroughly assesses multiple biomechanical factors of the skeletal muscles, such as the isometric force, deformation, and muscle fatigue. To the best of our knowledge, this approach is the first-ever attempt to predict the optimal bipedal standing posture of chimps and is a valuable complement to existing biomechanical theories.

This study aimed to investigate the biomechanical effects of skeletal architecture and muscle properties on bipedal standing in chimps. First, a musculoskeletal model based on anatomical data

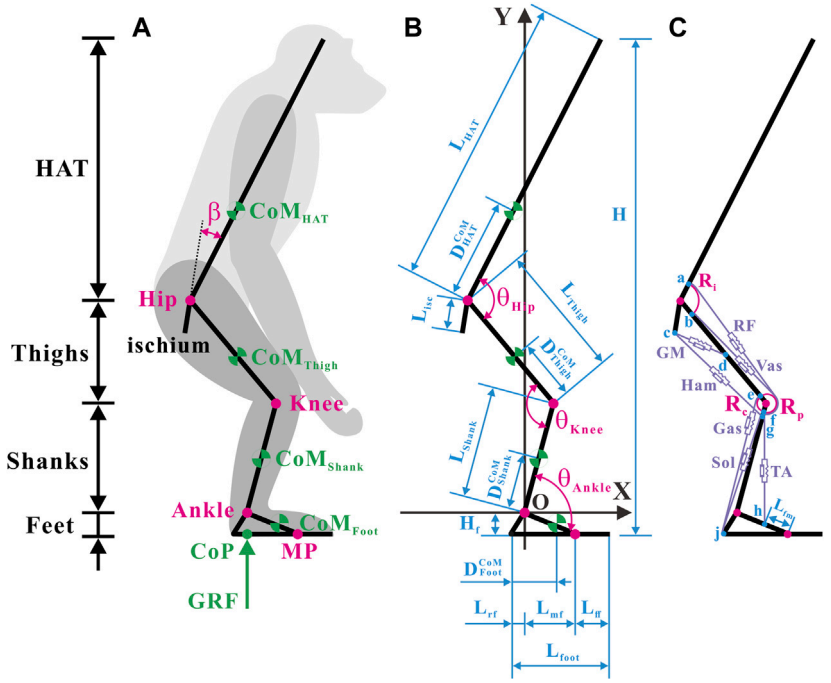

FIGURE 1
Musculoskeletal model of a bipedally standing common chimpanzee in the sagittal plane. **(A)** The skeletal elements include seven segments (HAT, bilateral thighs, bilateral shanks, and bilateral feet) and the ischium, with mobile articulations at the hip, knee, ankle, and metatarsal-phalangeal joints. **(B)** Annotations of segmental parameters (length of each segment and sub-segment, and position of CoM in each segment) and joint angles. **(C)** The muscular elements include the primary extensors and flexors of each lower limb [gluteus maximus (GM), hamstrings (Ham) (biceps femoris long head, semimembranosus, and semitendinosus), vastus (Vas), rectus femoris (RF), gastrocnemius (Gas) (gastrocnemius lateralis and gastrocnemius medialis), soleus (Sol), and tibialis anterior (TA)]. Blue dots: a) anterior-inferior iliac spine; b) the combined origin point of the vastus intermedius, vastus lateralis, and vastus medialis; c) midpoint of the most superior and to the most inferior points of the ischial tuberosity face; d) midpoint of the posterior femur shaft; e) medial and lateral femoral condyles and knee capsule; f) patella; g) fibular head; h) proximal end of the metatarsal I; j) distal end of the rear foot. Adapted from Diogo et al. (2013), Thorpe et al. (1999), Payne et al. (2006b), Myatt et al. (2011).

comprising the head–arms–trunk (HAT), thighs, shanks, and feet segments of the common chimpanzee was developed. Second, the static relationships among the Hill-type muscle–tendon units (MTUs) in bipedal standing were deduced. Next, the equilibrium constraints and the optimization objective were set up, which transformed the investigation into a constrained optimization problem. Subsequently, thousands of simulations of bipedal standing experiments in chimps were conducted. Finally, the optimal posture that simultaneously maximizes erectness and minimizes muscle fatigue of the hind limbs was determined *via* numerical searching within the domain, and MTU parameters including muscle activation, muscle length, and muscle force were drawn. In addition, the biomechanical effects under investigation were stipulated by the Pearson correlation analysis of the outcomes from simulating experiments.

2 Materials and methods

2.1 Musculoskeletal modeling

In the strictest sense, the analysis of bipedal standing in chimps should be conducted in three dimensions. However, reckoning with the reality that the mechanical behaviors of bipedal standing in chimps mainly occur in the sagittal plane, we subsequently generated the musculoskeletal model in the sagittal plane.

2.1.1 Segmental and skeletal properties

The body of the common chimpanzee can be represented as seven segments: the HAT (including the pelvis), bilateral thighs (including femurs), bilateral shanks (including tibias and fibulas), and bilateral feet.

Without loss of generality and to ensure computational efficiency, the following hypotheses were presented: 1) the thigh length and femur length were the same; 2) the shank length was the same as the tibia length; 3) the foot was subdivided into the forefoot, midfoot, and rearfoot, and the midfoot and rearfoot were integrated as one rigid piece; 4) the hip joint connecting the HAT and the thigh, the knee joint connecting the thigh and the shank, the ankle joint connecting the shank and the foot, and the metatarsophalangeal (MP) joint connecting the forefoot and midfoot were all simplified as smooth hinges; 5) the ground reaction force was evaluated as a resultant force and its acting point at the foot was the center of pressure (CoP); and 6) the external force only involved the gravitational force and the support force from the ground, and friction was neglected.

The segments, CoMs, joints, segmental angles, and ground reaction force (GRF) are shown in Figure 1A. Annotations of the segmental

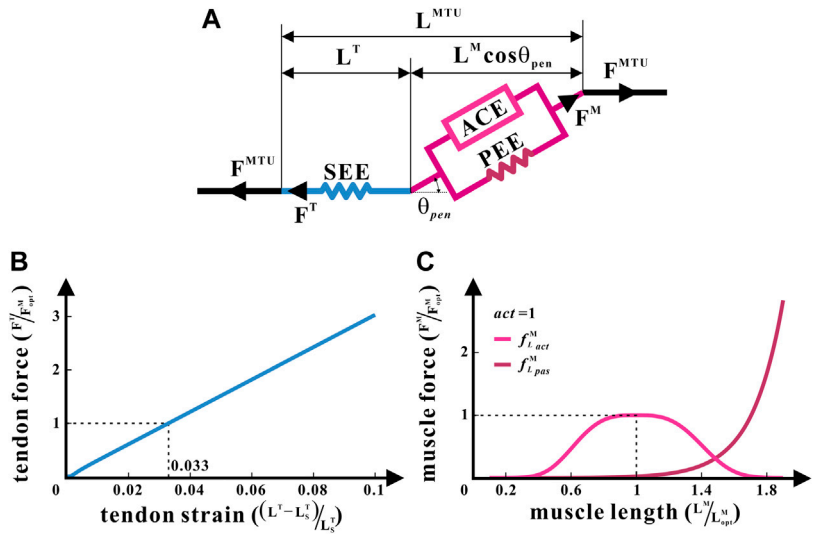

FIGURE 2
Hill-type MTU of the common chimpanzee. **(A)** Structure of the Hill-type MTU. **(B)** Non-linear relationship between the tendon force and tendon strain for SEE. **(C)** Non-linear relationships between the relative muscle force and relative muscle length, respectively, for ACE and PEE.

parameters and joint angles are shown in Figure 1B. The precise values of the segmental parameters are listed in Supplementary Table S1, and their sources are disclosed in Section 2.1.3. The positive direction of the joint angles was defined as the hip joint extension, knee joint extension, and ankle joint extension. Given that the hip joint of chimps cannot be entirely extended owing to the orientation and length of the ischium (Kozma et al., 2018), the acute angle between the ischium and HAT was fixed as a constant β.

Considering computational efficiency, a global Cartesian coordinate system with the rotation center of the ankle joint as the origin was created.

2.1.2 Muscle geometry and Hill-type MTU

Conscientious observations of the anatomy of chimps (Thorpe et al., 1999; Payne et al., 2006b; Myatt et al., 2011; Diogo et al., 2013) have revealed that the extensor and flexor muscles, which primarily produce forces and joint moments in the sagittal plane in each hind limb, incorporate a total of 10 muscles in seven muscle groups, as shown in Figure 1C. It should be noted that the gluteus maximus (GM) only comprises the gluteus maximus ischiofemoralis according to Stern (1972), Tuttle et al. (1978), and Lieberman et al. (2006).

After careful estimation of bone landmarks and muscle maps of chimps (Thorpe et al., 1999; Payne et al., 2006b; Myatt et al., 2011; Diogo et al., 2013), the points of origin and insertion for each muscle were designated, located as close to the center of the attachment area as possible, as shown in Figure 1C. In accordance with the attachment points and wrapping paths of muscles, the functional relationship between the lengths and moment arms of muscles with respect to joint angles can be verified. In particular, because the femoral condyle contour in chimps is significantly more circular than that in humans (Heiple and Lovejoy, 1971), the femoral condyle was approximated as a circular arc in the sagittal plane. The tibia was presumed to move wholly along the femoral condyle contour, and the patella was presumed to move completely along the femoral–tibial condyle contour (O'Neill et al., 2013). Consequently, the moment arms of the rectus femoris (RF) and vastus (Vas) around the knee joint were constant (R_p), and the moment arm of gastrocnemius lateralis and gastrocnemius medialis (Gas) around the knee joint was constant (R_e) when tangential to the femoral condyle. With reference to the measurements (Thorpe et al., 1999; Payne et al., 2006a), the moment arm of RF about the hip joint was assumed constant (R_i).

A generic Hill-type model (Zajac, 1989) was applied to enumerate metrics such as the lengths and forces of muscles and tendons in each hind limb under isometric contraction as the joint angle changed (Sawicki and Khan, 2015), as illustrated in Figure 2. It was the posture of bipedal standing that this study intended to analyze. Therefore, the muscle contraction velocity v^M was approximated to zero, and the bipedal standing of the common chimpanzee was statically analyzed.

The Hill-type model treats each muscle as an MTU. Every MTU consists of two portions: a part associated with the traits of the muscle fibers and another part equated to the tendon. They are in series with each other, between which is the pennation angle θ_{pen}. The muscle part is composed of an active contractile element (ACE) arranged in parallel with a passive non-linear elastic element (PEE), while the tendon part consists of a series elastic unit (SEE). Because no θ_{pen} of any MTU in chimps is greater than 30°, which means $\cos\theta_{pen} \approx 1$ (Thorpe et al., 1999), all θ_{pen} were approximated to zero (Payne et al., 2006). Furthermore, the muscle and tendon in MTUs were confined to the following force and length relationships:

$$F^{MTU} = F^M = F^T, \quad (1)$$

$$L^{MTU} = L^M + L^T, \quad (2)$$

where F^{MTU} denotes the force of MTU, F^M denotes the muscle force, F^T denotes the tendon force, L^{MTU} denotes the length of MTU, L^M denotes the muscle length, and L^T denotes the tendon length.

10.3389/fbioe.2023.1140262

TABLE 1 Hill-type MTU parameters.

	m^{MTU} (g)	$PCSA$ (cm²)	L^M_{opt} (mm)	F^M_{opt} (N)	L^T_S (mm)
Gluteus maximus	300	27.9	101	837	35.4
Biceps femoris (long head)	85	5.1	157	153	123.6
Semimembranosus	67	4.0	158	120	122.4
Semitendinosus	100	3.6	260	108	74.9
Rectus femoris	93	11.3	78	339	260.4
Vastus	455	44.7	95.3	1,341	196.6
Gastrocnemius lateralis	67	7.9	80	237	206.6
Gastrocnemius medialis	90	10.6	80	318	207.2
Soleus	128	22	55	660	212.1
Tibialis anterior	50	5.3	88	159	137.9

The biomechanical characteristics of each MTU were confirmed by five internal parameters: the mass of MTU (m^{MTU}), optimal fiber length (L^M_{opt}), physiological cross-sectional area ($PCSA$), optimal isometric muscle force (F^M_{opt}), and tendon slack length (L^T_S), the values of which are shown in Table 1 and explained in Section 2.1.3.

With the aforementioned parameters, F^M and F^T can be addressed by the following formula:

$$F^M = F^M_{opt} \cdot \left(act \cdot f^M_{L\ act} + f^M_{L\ pas} \right), \tag{3}$$

$$F^T = K^T \cdot \left(L^T - L^T_S \right), \tag{4}$$

where act is the muscle activation between $[0, 1]$, $f^M_{L\ act}$ is the active coefficient of the muscle force–length relationship, $f^M_{L\ pas}$ is the passive coefficient of the muscle force–length relationship, and K^T is the coefficient of the tendon stiffness. In addition, $f^M_{L\ act}$ and $f^M_{L\ pas}$ are both functions of L^M. K^T is a function of F^T, and $F^T = F^M_{opt}$ when $(L^T - L^T_S)/L^T_S = 0.033$ (Zajac, 1989). Subsequently, under circumstances wherein every L^{MTU} has been counted from θ_{Hip}, θ_{Knee}, and θ_{Ankle}, together with the knowledge of L^M_{opt}, F^M_{opt}, and L^T_S, all the unknown variables in MTUs can be articulated as functions of L^M.

2.1.3 Musculoskeletal dataset

Full sets of anatomical data of the common chimpanzee are limited (Zihlman and Cramer, 1978; Thorpe et al., 1999; Wang and Crompton, 2004; Isler et al., 2006; Kozma et al., 2018), among which source sample Chimp 95 (Thorpe et al., 1999) stands out for integrity. To construct the complete dataset of the skeletal and muscular parameters in need, the anatomical data from other sources were scaled to match that of sample Chimp 95 (Thorpe et al., 1999), depending on the geometric similarity between different individuals of the same species.

The segmental masses of sample Pa1 in Table 3 from Isler et al. (2006) were scaled according to the ratio of the mass of Chimp 95 $m_{Chimp95}$ to that of Pa1 m_{Pa1} for obtaining the corresponding head mass m_{Head}, trunk mass m_{Trunk}, upper arm mass m_{Uarm}, forearm mass m_{Farm}, hand mass m_{Hand}, thigh mass m_{Thigh}, shank mass m_{Shank}, and foot mass m_{Foot} of Chimp 95. The HAT mass m_{HAT} of Chimp 95 was calculated as follows:

$$m_{HAT} = m_{Head} + m_{Trunk} + 2 \times (m_{Uarm} + m_{Farm} + m_{Hand}). \tag{5}$$

The segmental lengths of sample Pa1 in Table 3 from Isler et al. (2006) were scaled according to the ratio of masses as $(\frac{m_{Chimp95}}{m_{Pa1}})^{\frac{1}{3}}$ for attaining the corresponding head length l_{Head}, trunk length l_{Trunk}, and foot length l_{Foot} of Chimp 95. The HAT length L_{HAT} of Chimp 95 was calculated as follows:

$$L_{HAT} = l_{Head} + l_{Trunk}. \tag{6}$$

The relative position of each segmental CoM of sample Pa1 in Table 3 from Isler et al. (2006) was, respectively, multiplied by the segmental lengths of Chimp 95 worked out previously to attain the corresponding segmental CoM positions of Chimp 95, that is, the distance from the HAT CoM to the hip joint D^{CoM}_{HAT}, the distance from the thigh CoM to the knee joint D^{CoM}_{Thigh}, the distance from the shank CoM to the ankle joint D^{CoM}_{Shank}, and the distance from the foot CoM to the heel D^{CoM}_{Foot}.

The average fibular length $\bar{X}_{fibula}$ of samples *Pan troglodytes* in Table 1 from Zihlman and Cramer (1978) was scaled according to the ratio of the tibial length of Chimp 95 L_{tibia} to the average tibial length of *Pan troglodytes* $\bar{X}_{tibia}$ for obtaining the corresponding fibula length L_{fibula} of Chimp 95.

The foot length parameters of the chimpanzee species in Table 1 in the paper by Wang and Crompton (2004) were scaled by the ratio of the foot length of Chimp 95 L_{Foot} to that of the species chimpanzee FL for attaining the corresponding foot height H_f, rearfoot length L_{rf}, midfoot length L_{mf}, forefoot length L_{ff}, and third metatarsal length L_{fm} of Chimp 95.

To obtain the corresponding ischial length L_{isc} of Chimp 95, the ischial lengths of the 20 samples of *Pan troglodytes* in Supplementary Table S1 from the study by Kozma et al. (2018) were averaged.

The value of β was elicited from the maximum hip angle (162°) in the presence of the dimensionless mechanical advantage of samples of *Pan troglodytes* in Table S1 from Kozma et al. (2018):

$$\beta = 180° - 162° = 18°. \tag{7}$$

The values of m^{MTU}, L^M_{opt}, and $PCSA$ were obtained from sample Chimp 95 by Thorpe et al. (1999). The value of F^M_{opt}, which

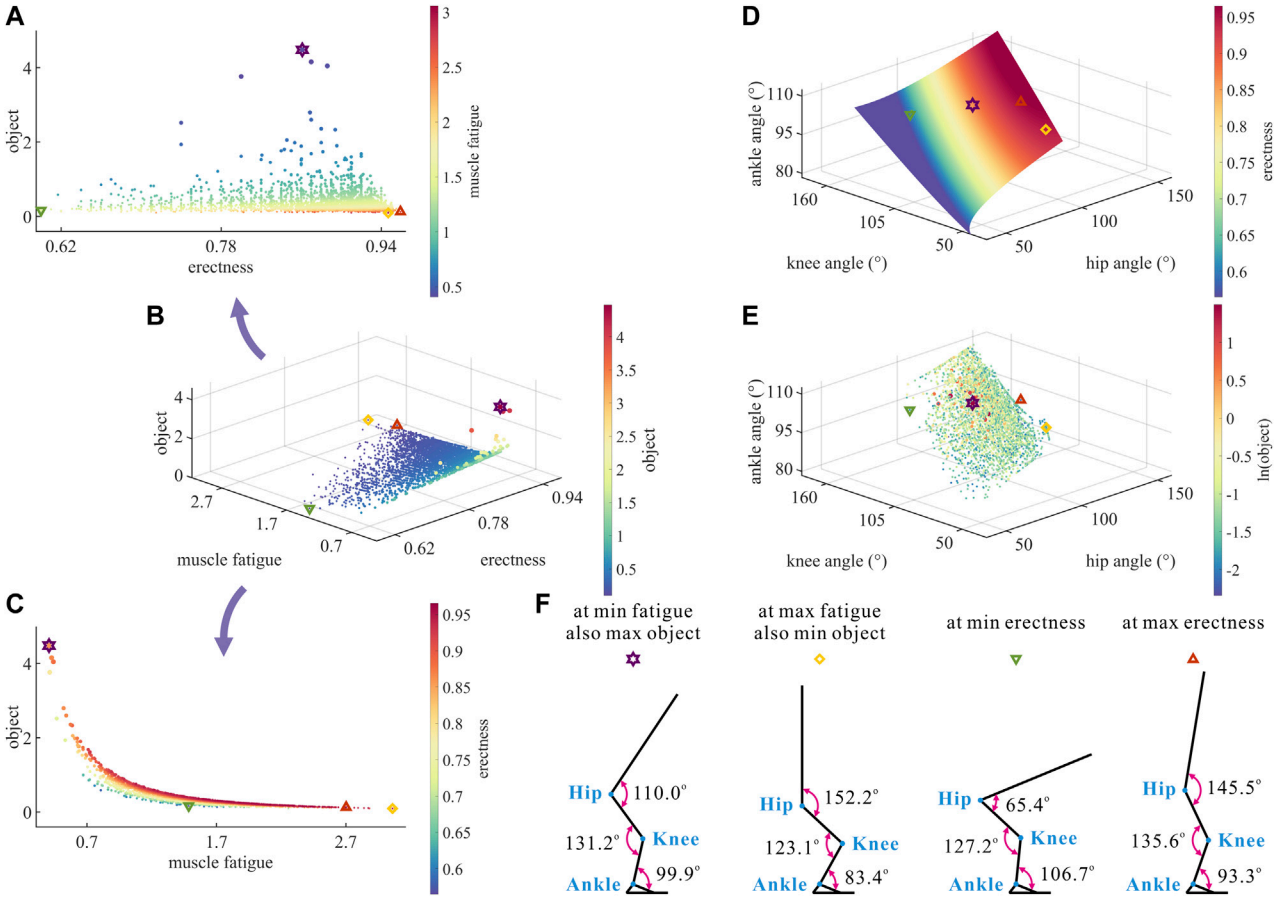

FIGURE 3
(A–C) Results of optimization objective, standing erectness, and muscle fatigue of the lower limb in the 3,536 simulation experiments of bipedal standing. Marked points: purple hexagram: both the optimal and easiest BSP; yellow diamond: both the worst and hardest BSP; green downward-pointing triangle: lowest BSP; red upward-pointing triangle: highest BSP. **(D)** Domain of the hip, knee, and ankle joint angles. **(E)** Results of the hip, knee, and ankle joint angles in the 3,536 simulation experiments of bipedal standing. **(F)** Joint angles, respectively, at (purple hexagram) both the optimal and easiest BSP, (yellow diamond) both the worst and hardest BSP, (green downward-pointing triangle) lowest BSP, and (red upward-pointing triangle) highest BSP.

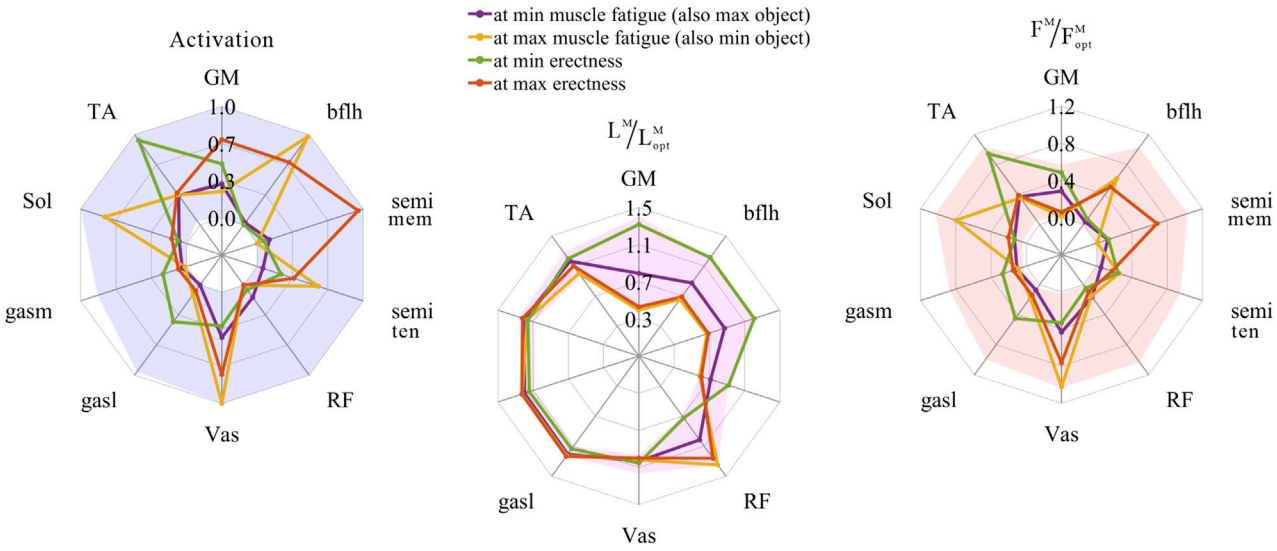

FIGURE 4
Distribution and value ranges of activation, relative muscle lengths, and relative muscle forces of the lower-limb MTUs. Marked lines: purple: both the optimal and easiest BSP; yellow: both the worst and hardest BSP; green: lowest BSP; red: highest BSP.

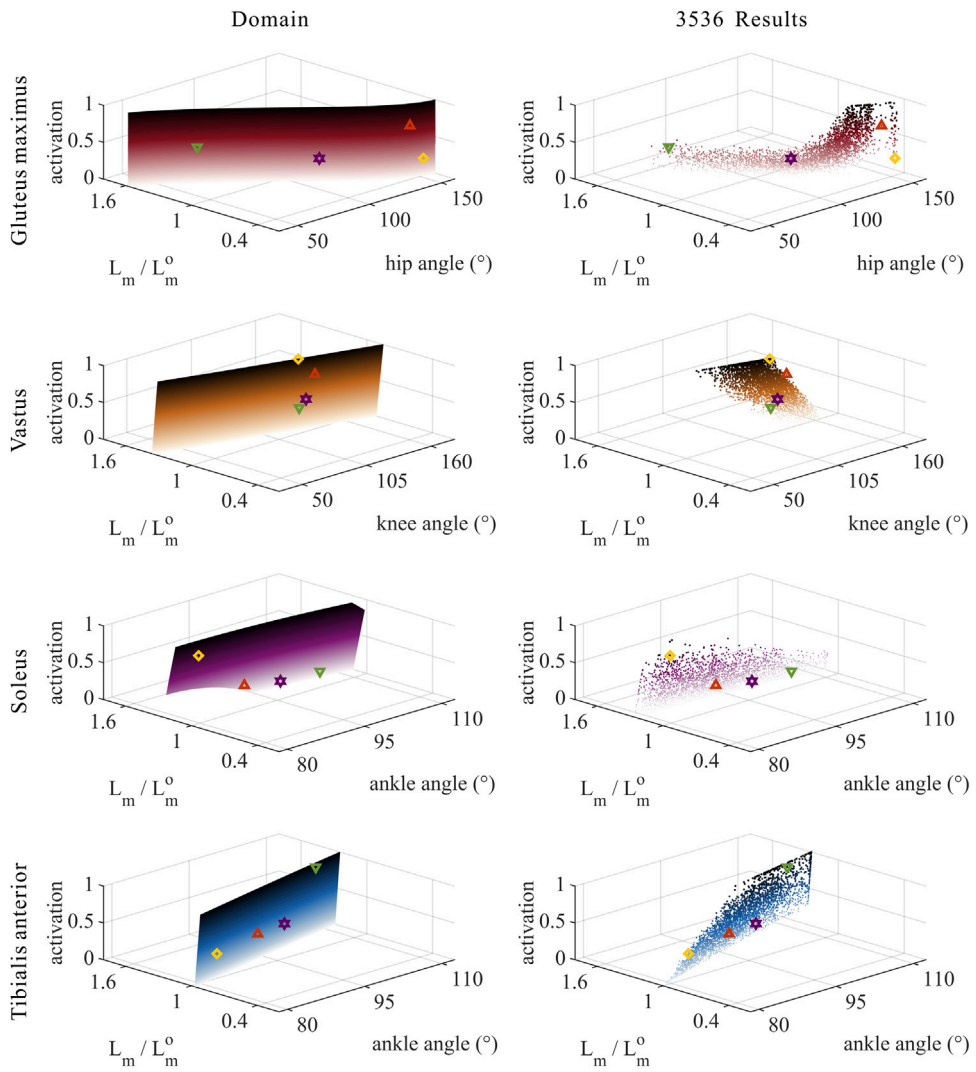

FIGURE 5
Domains (surfaces) and results in the 3,536 simulation experiments (scatters) of activation, relative muscle lengths, and joint angles for the uni-articular MTUs (gluteus maximus, vastus, soleus, and tibialis anterior). Marked points: purple hexagram: both the optimal and easiest BSP; yellow diamond: both the worst and hardest BSP; green downward-pointing triangle: lowest BSP; red upward-pointing triangle: highest BSP.

characterizes the capacity of muscle force production, can be acquired by multiplying the *PCSA* with the maximum isometric muscle stress, which was set to 0.3 MPa according to previous studies (Wells, 1965; Thorpe et al., 1999). The value of L_S^T was obtained using the constrained non-linear optimization function (fmincon) in the MATLAB optimization toolbox (MathWorks, Natick, MA, United States) (O'Neill et al., 2013), following the force and length relationships between muscles and tendons in MTUs (Zajac, 1989; Manal and Buchanan, 2004; Sawicki and Khan, 2015).

2.2 Search of solutions

It is well-known that chimps, like any primate, are constrained in their erectness when standing bipedally by their skeletal architecture and muscle properties; for example, they must maintain balance and stability, and their muscles and tendons should not exceed the force ranges (O'Neill et al., 2013). These constraints were translated into numerical boundaries merged with the geometric and mechanical relationships of the musculoskeletal system, as described in Section 2.1. Subsequently, the objective function was interpreted in accordance with the principle of simultaneously maximizing erectness and minimizing the muscle fatigue of the hind limbs. Finally, the constrained optimization was carried out through random initial values and random directions within the domain, and this process was repeated to globally search for the bipedal standing postures (BSPs) of chimps. During the procedure, every set of optimization results was equivalent to one simulation experiment of bipedal standing in chimps.

10.3389/fbioe.2023.1140262

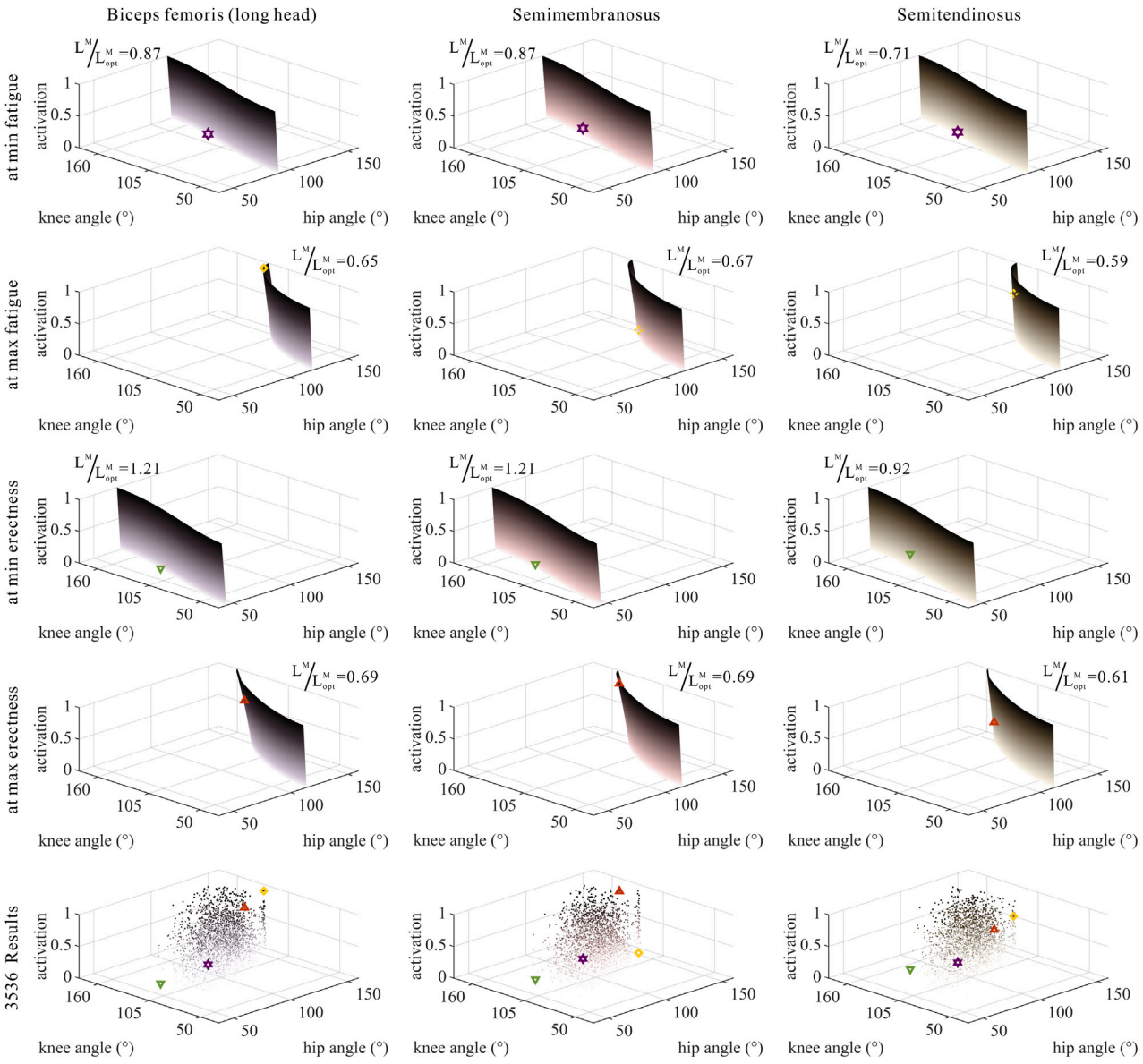

FIGURE 6
Domains (surfaces) and results in the 3,536 simulation experiments (scatters) of activation, relative muscle lengths, and joint angles for bi-articular MTUs [biceps femoris (long head), semimembranosus, and semitendinosus]. Marked points: purple hexagram: both the optimal and easiest BSP; yellow diamond: both the worst and hardest BSP; green downward-pointing triangle: lowest BSP; red upward-pointing triangle: highest BSP.

2.2.1 Biomechanical constraints

To guarantee the stability of bipedal standing, the overall CoM of the common chimpanzee was assumed to be maintained directly above the ankle joint:

$$X^{CoM} = 0, \tag{8}$$

where X^{CoM} is the horizontal coordinate of the CoM about the origin, which is a function of θ_{Hip}, θ_{Knee}, and θ_{Ankle}.

To ensure the balance of bipedal standing in chimps, the MTU of the hind limbs must be able to produce the torque desired by the hip, knee, and ankle joints:

$$M_i^{need} = M_i^{prod} \quad (i = Hip, Knee, Ankle), \tag{9}$$

where M_i^{need} is the required moment of the hip, knee, and ankle joints, and M_i^{prod} is the moment produced by the hip, knee, and ankle joints. Referring to Figure 1A, M_i^{need} can be expressed as a function of θ_{Hip}, θ_{Knee}, and θ_{Ankle}. Referring to Figure 1C, combined with Section 2.1, M_i^{prod} can be, respectively, expressed as functions of θ_{Hip}, θ_{Knee}, θ_{Ankle}, and L^M.

2.2.2 Constrained optimization

Considering that chimps seek the maximum erectness and minimum muscle fatigue of hind limbs during bipedal standing, the optimization objective was defined as the square of the ratio of erectness to the muscle fatigue of hind limbs:

$$Object = Erectness^2 / Fatigue^2, \tag{10}$$

10.3389/fbioe.2023.1140262

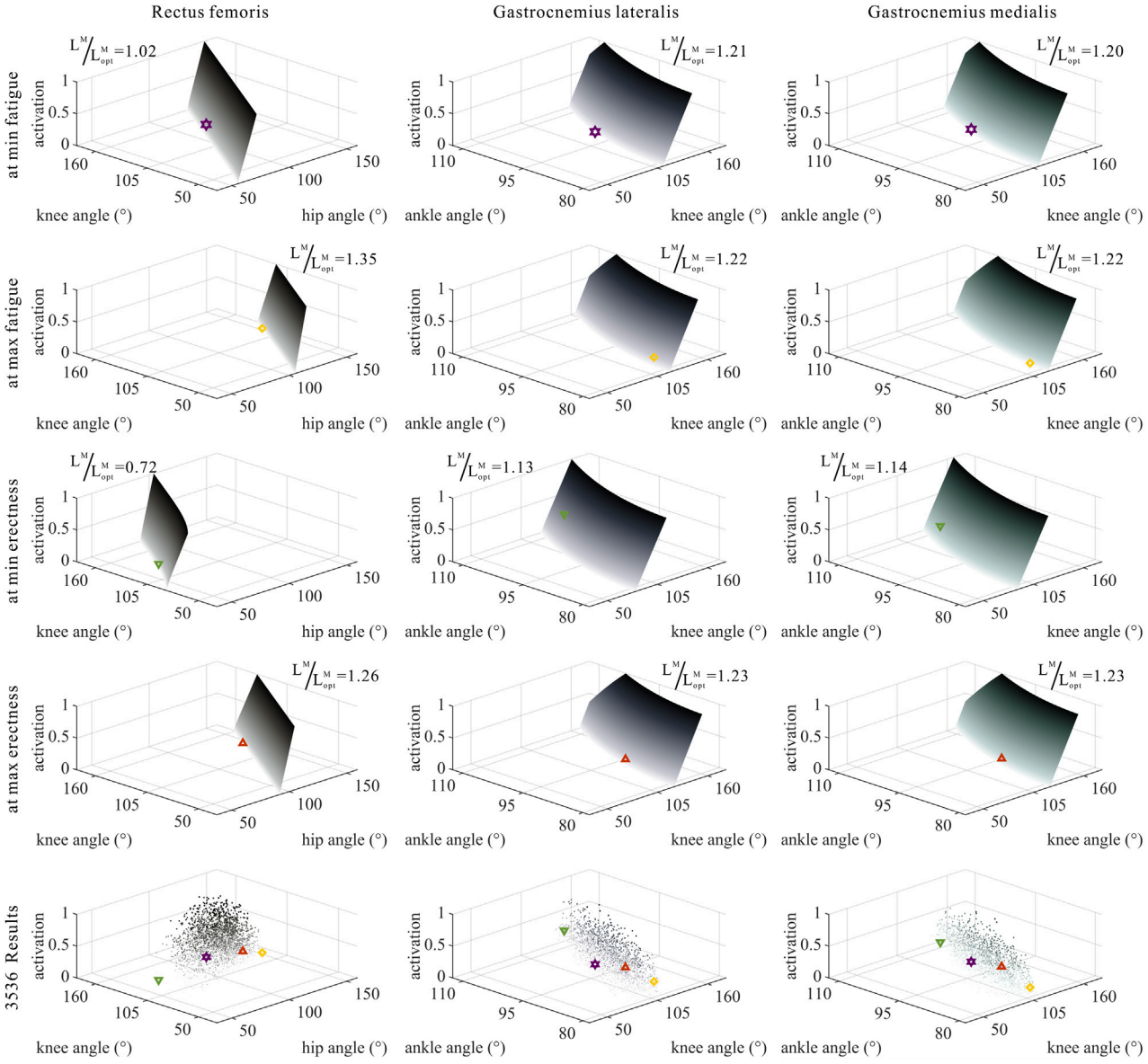

FIGURE 7
Domains (surfaces) and results in the 3,536 simulation experiments (scatters) of activation, relative muscle lengths, and joint angles for bi-articular MTUs (rectus femoris, gastrocnemius lateralis, and gastrocnemius medialis). Marked points: purple hexagram: both the optimal and easiest BSP; yellow diamond: both the worst and hardest BSP; green downward-pointing triangle: lowest BSP; red upward-pointing triangle: highest BSP.

where *Erectness* is the ratio of height to the full length of the body during bipedal standing:

$$Erectness = \frac{H}{H_f + L_{Shank} + L_{Thigh} + L_{HAT}}, \tag{11}$$

where H is the height during bipedal standing. Thus, *Erectness* is a function of θ_{Hip}, θ_{Knee}, and θ_{Ankle}.

The muscle fatigue of hind limbs was manifested as follows (Anderson and Pandy, 2001):

$$Fatigue = \sum_i (act_i)^2$$
$$(i = GM, bflh, semimem, semiten, Vas, RF, Gasl, Gasm, Sol, TA). \tag{12}$$

Consequently, *Fatigue* is a function of L^M.

To sum up, *Object* is a function of θ_{Hip}, θ_{Knee}, θ_{Ankle}, and L^M.

2.2.3 Data analysis

To obtain the numerical solution of *Object* that is as close to the global optimal solution as possible, the values of θ_{Hip}, θ_{Knee}, θ_{Ankle}, and L^M were randomly initiated within the range of $0.60 \leq Erectness \leq 1$ and every variable threshold. In addition, the search direction was randomly selected on the foundation of the gradient descent method; this process was repeated 3,536 times. The largest *Object* among these 3,536 sets of numerical results was approximated as the global optimal solution. During the course, other sets of optimization results were also weighted as simulation experiments of bipedal standing in chimps.

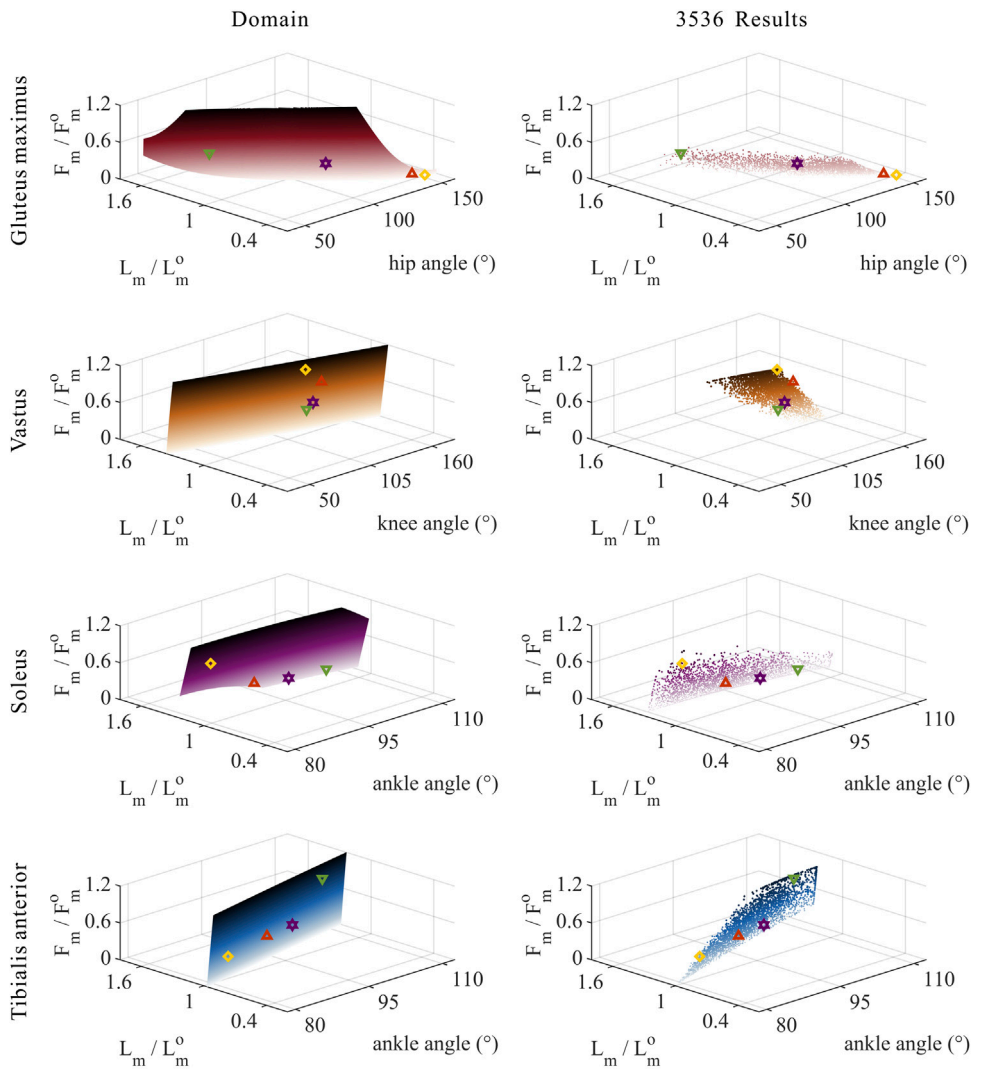

FIGURE 8
Domains (surfaces) and results in the 3,536 simulation experiments (scatters) of relative muscle forces, relative muscle lengths, and joint angles for uni-articular MTUs (gluteus maximus, vastus, soleus, and tibialis anterior). Marked points: purple hexagram: both the optimal and easiest BSP; yellow diamond: both the worst and hardest BSP; green downward-pointing triangle: lowest BSP; red upward-pointing triangle: highest BSP.

Probing deeper into the relationship between each pair of the biomechanical parameters, the Pearson correlation analysis of the outcomes from simulating experiments was accomplished.

3 Results

In this study, the effects of skeletal architecture and muscle properties on bipedal standing in chimps were investigated using modeling and simulation. The global optimal solution of *Object* was achieved from 3,536 sets of optimization results to ascertain the optimal posture for bipedal standing in chimps. It is worth noting that these 3,536 sets of numerical results can also be considered as 3,536 simulations of bipedal standing experiments. Based on these simulations, the numerical relationships among *Object*, *Erectness*, and *Fatigue* can be analyzed, and the biomechanical relationships among the hip, knee, and ankle joint angles; muscle activation; muscle lengths; and muscle forces of the hind limbs can be further analyzed.

3.1 Numerical trade-offs between erectness and fatigue

Taking *Object* as the objective function, simultaneously maximizing *Erectness* and minimizing *Fatigue*, numerical optimization was conducted 3,536 times, and 3,536 randomized simulations of bipedal standing experiments in chimps were performed.

As shown in Figures 3A–C, the same degree of *Erectness* may correspond to different degrees of *Fatigue*, and in turn, the same degree of *Fatigue* may correspond to different degrees of

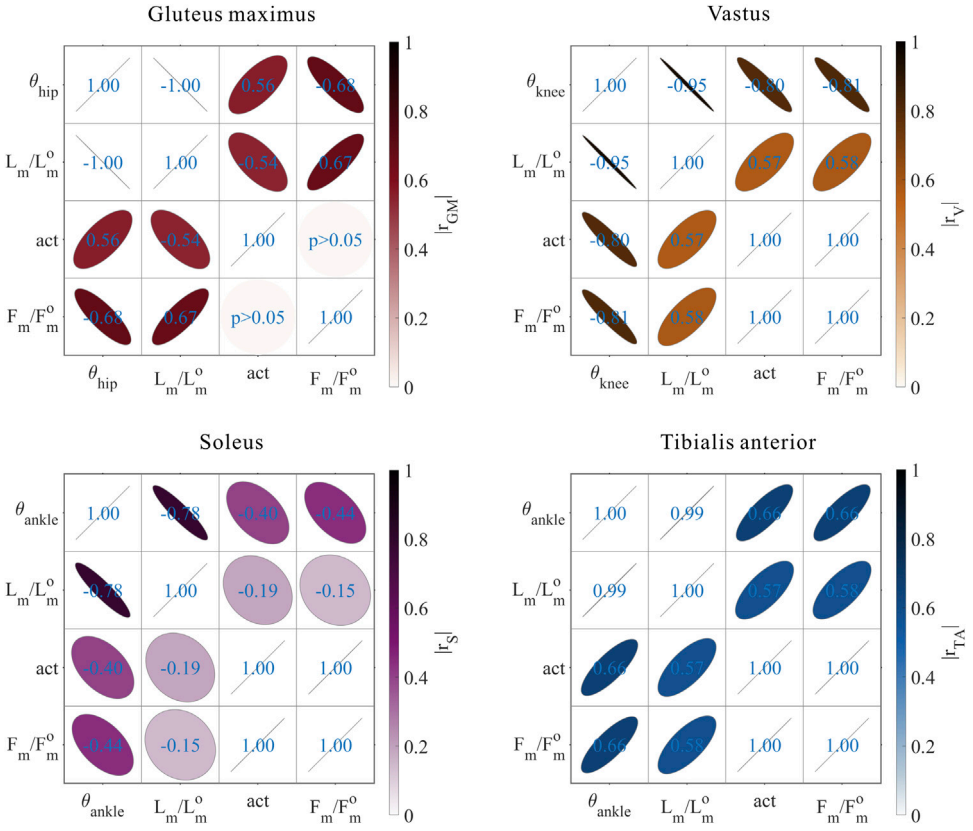

FIGURE 9
Results of the correlation analysis of joint angles, relative muscle lengths, activation, and relative muscle forces among the 3,536 simulation experiments for the uni-articular MTUs (gluteus maximus, vastus, soleus, and tibialis anterior).

Erectness. As the value of *Object* gradually increased from a minimum of 0.096 to a maximum of 4.480, the degree of *Fatigue* generally decreased from a maximum of 3.060 to a minimum of 0.407, whereas the degree of *Erectness* did not show a clear pattern of change. When *Object* reached a maximum of 4.480, which is the optimal BSP, although *Fatigue* also reached a minimum of 0.407 (the easiest BSP), *Erectness* reached neither the minimum of 0.600 nor the maximum of 0.959, but 0.861. This indicated that *Fatigue* is higher than 0.407 when *Erectness* is either less than or more than 0.861, so that *Object* is reduced. Moreover, when *Fatigue* reached a maximum of 3.060 (the hardest BSP), *Erectness* was 0.947, which is not significantly different from its maximum of 0.959. Additionally, the degree of *Fatigue* was higher at the maximum value of *Erectness* (the highest BSP) than at the minimum value of *Erectness* (the lowest BSP), which were 2.702 and 1.486, respectively. This result is rather counterintuitive, indicating that too high a degree of *Erectness* would not lead to a decrease in *Fatigue*. These results contrast with those for humans, where the optimal BSP corresponds to both the highest *Erectness* and the lowest *Fatigue* (Pontzer et al., 2009), with *Erectness* and *Fatigue* being almost negatively correlated (Neumann, 2013).

As a result, there is a numerical trade-off between the degree of *Erectness* and the degree of *Fatigue* in the quest of the optimal BSP for chimps.

Although *Object* is the ratio of *Erectness* to *Fatigue*, the latter two are not completely independent variables. The degree of *Erectness* is directly dependent on θ_{Hip}, θ_{Knee}, and θ_{Ankle}. The degree of *Fatigue* is directly dependent on the muscle activation of hind limb MTUs act_i ($i = GM, bflh, semimem, semiten, Vas, RF, Gasl, Gasm, Sol, TA$), which indirectly depends on L^{MTU} and L^{M} (see Section 2.1.2 for details). Because L^{MTU} depends directly on θ_{Hip}, θ_{Knee}, and θ_{Ankle}, *Fatigue* is indirectly affected by θ_{Hip}, θ_{Knee}, θ_{Ankle}, and L_i^M ($i = GM, bflh, semimem, semiten, Vas, RF, Gasl, Gasm, Sol, TA$).

In summary, the numerical trade-off between the degree of *Erectness* and the degree of *Fatigue* requires a comprehensive consideration of θ_{Hip}, θ_{Knee}, θ_{Ankle}, *act*, and L^M.

3.2 Numerical trade-offs among hip–knee–ankle angles by skeletal architecture

As shown in Figure 3D, the degree of *Erectness* increased with θ_{Hip}, θ_{Knee}, and θ_{Ankle}, wherein the change caused by θ_{Hip} was the most evident. This is attributable to the fact that the hip, knee, and ankle joints, respectively, drive the HAT, thigh, and shank segments, among which the HAT segment is the longest.

As shown in Figure 3E, the motion range of θ_{Hip} was 105.59 ± 48.49°, the motion range of θ_{Knee} was 118.07 ± 43.83°,

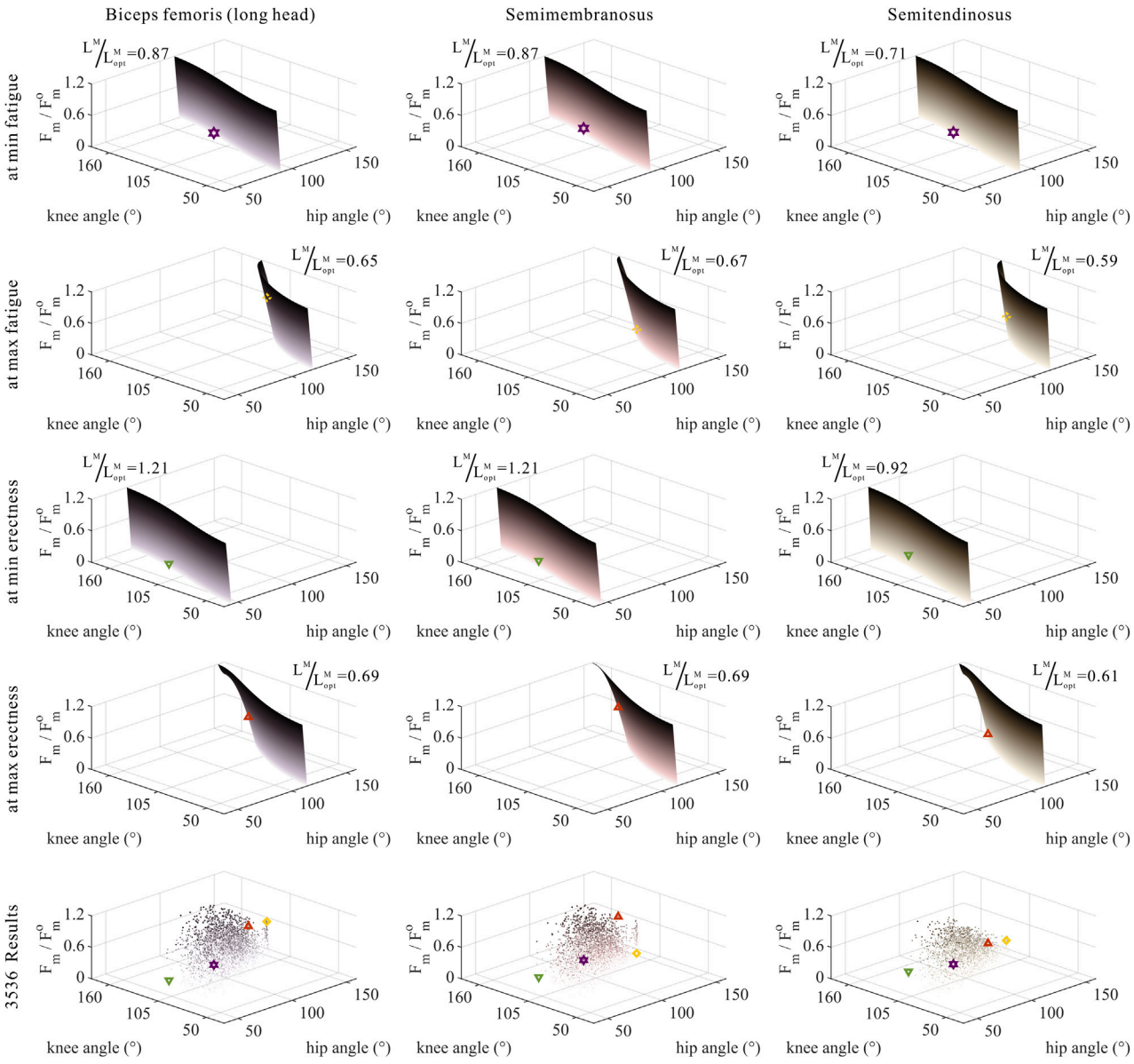

FIGURE 10
Domains (surfaces) and results in the 3,536 simulation experiments (scatters) of relative muscle forces, relative muscle lengths, and joint angles for bi-articular MTUs [biceps femoris (long head), semimembranosus, and semitendinosus]. Marked points: purple hexagram: both the optimal and easiest BSP; yellow diamond: both the worst and hardest BSP; green downward-pointing triangle: lowest BSP; red upward-pointing triangle: highest BSP.

and the motion range of θ_{Ankle} was 95.42 ± 17.05° in 3,536 simulation experiments of bipedal standing in chimps.

As shown in Figure 3F, the corresponding θ_{Hip}, θ_{Knee}, and θ_{Ankle} of the optimal BSP and easiest BSP were, respectively, 110.02°, 131.19°, and 99.92°, which is consistent with the existing measurement data of the middle stance during bipedal walking in chimps (Jenkins, 1972; O'Neill et al., 2015).

Taking the optimal BSP as the benchmark, the lowest BSP showed a significant decrease in θ_{Hip} (−40.60%) and insignificant changes in θ_{Knee} (−3.07%) and θ_{Ankle} (+6.80%), while the highest BSP showed a significant increase in θ_{Hip} (+32.24%) and insignificant changes in θ_{Knee} (+3.36%) and θ_{Ankle} (−6.59%). This is not only consistent with the pattern shown in Figure 3D, but also suggests that θ_{Hip}, θ_{Knee}, and θ_{Ankle} cannot be increased or decreased at the same time compared to the optimal BSP in the effort to maintain balance in chimps.

It is noteworthy that the maximum degree of *Fatigue* (the hardest BSP) did not correspond to the highest or lowest BSP, whereas θ_{Hip} increased significantly (+38.32%), θ_{Knee} decreased slightly (−6.18%), and θ_{Ankle} decreased significantly (−16.55%) compared to the optimal BSP. This signifies that simultaneous changes in θ_{Hip} and θ_{Ankle} cause a greater degree of *Fatigue* than simultaneous changes in θ_{Hip} and θ_{Knee}.

10.3389/fbioe.2023.1140262

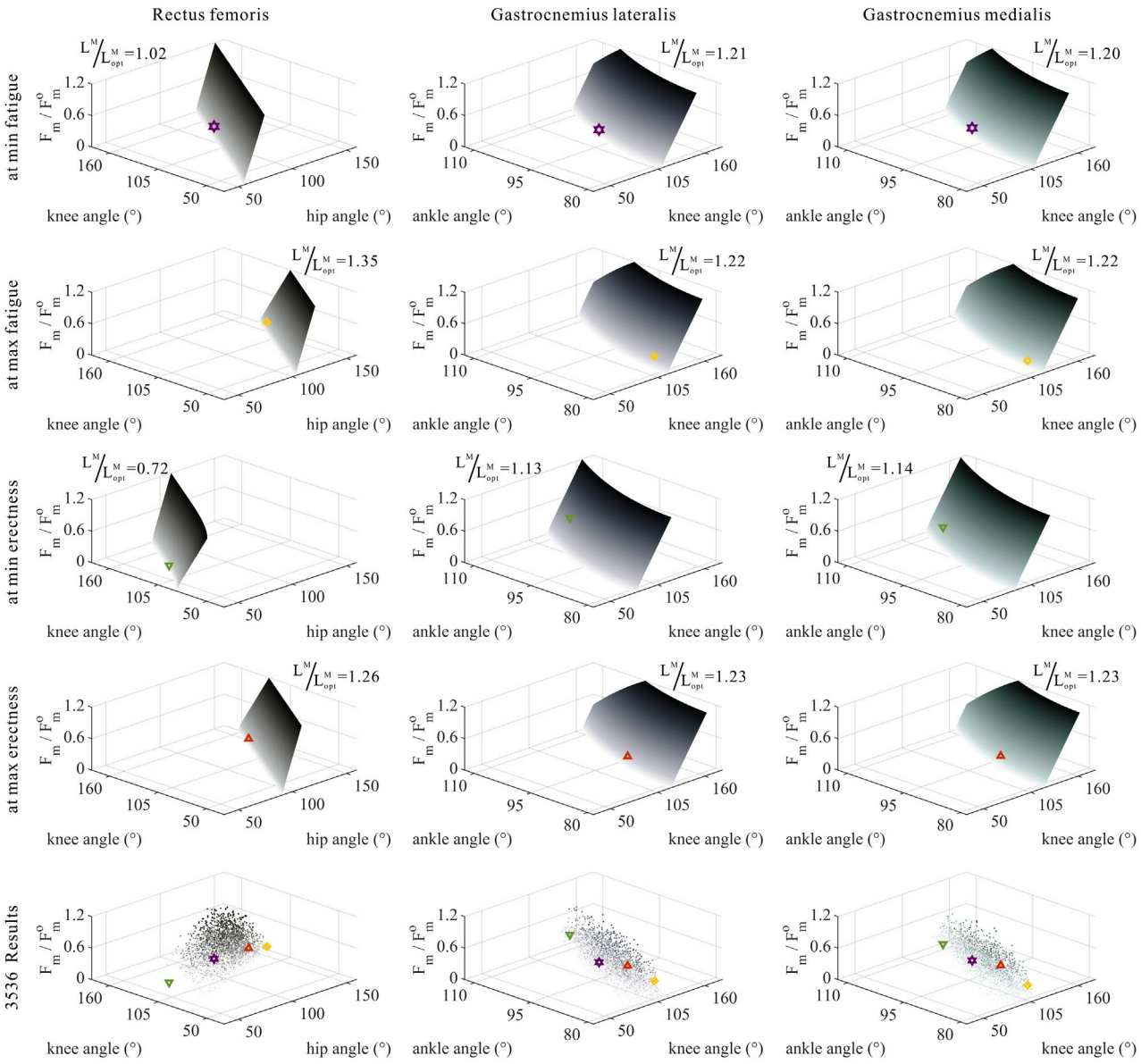

FIGURE 11
Domains (surfaces) and results in the 3,536 simulation experiments (scatters) of relative muscle forces, relative muscle lengths, and joint angles for bi-articular MTUs (rectus femoris, gastrocnemius lateralis, and gastrocnemius medialis). Marked points: purple hexagram: both the optimal and easiest BSP; yellow diamond: both the worst and hardest BSP; green downward-pointing triangle: lowest BSP; red upward-pointing triangle: highest BSP.

Therefore, there is a numerical trade-off between the hip–knee–ankle joint angles in the quest of the optimal BSP for chimps.

The hip–knee–ankle joint angles directly decided L^{MTU} of the hind limbs, thereby influencing the range of values for L^M, which, in turn, indirectly influenced the value of the degree of *Fatigue*.

For uni-articular MTUs, the larger the θ_{Hip} was, the smaller the L^{MTU} of the extensor GM; the larger the θ_{Knee} was , the smaller the L^{MTU} of the extensor Vas; the larger the θ_{Ankle} was, the smaller the L^{MTU} of the extensor Sol and the larger the L^{MTU} of the flexor TA.

For bi-articular MTUs, bflh, semimem, and semiten were both hip extensors and knee flexors, RF was both the hip flexor and knee extensor, and gasl and gasm were both knee flexors and ankle extensors. The variation in the L^{MTU} in bi-articular MTUs depended on the specific magnitude of the angular variations.

As shown in Figures 5–7, as long as θ_{Hip}, θ_{Knee}, θ_{Ankle}, and L_i^M $(i = GM, bflh, semimem, semiten, Vas, RF, Gasl, Gasm, Sol, TA)$ were settled, act_i $(i = GM, bflh, semimem, semiten, Vas, RF, Gasl, Gasm, Sol, TA)$ could be uniquely certified. Ergo, *Fatigue* can be derived.

To summarize, the numerical trade-offs between θ_{Hip}, θ_{Knee}, and θ_{Ankle} also demand the contemplation of muscle activation of lower-limb MTUs.

10.3389/fbioe.2023.1140262

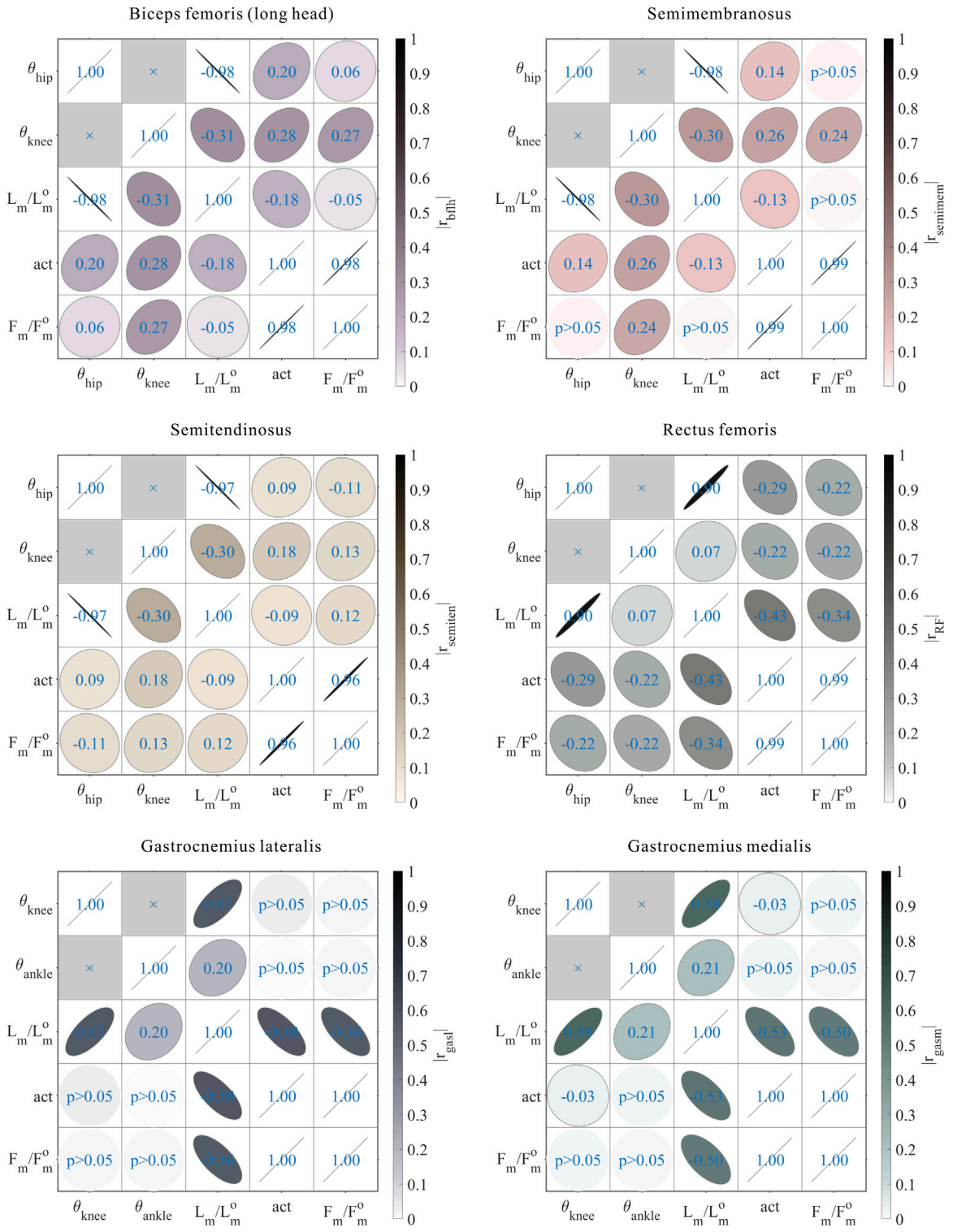

FIGURE 12
Results of the correlation analysis of joint angles, relative muscle lengths, activation, and relative muscle forces among the 3,536 simulation experiments for the bi-articular MTUs [biceps femoris (long head), semimembranosus, semitendinosus, rectus femoris, gastrocnemius lateralis, and gastrocnemius medialis].

10.3389/fbioe.2023.1140262

3.3 Numerical trade-offs among muscle parameters of MTUs by muscle properties

The distribution and value ranges of the activation, relative muscle lengths, and relative muscle forces of the lower-limb MTUs in the 3,536 experimental simulations are shown in Figure 4.

3.3.1 Relative muscle lengths

According to Section 2.1.2, the degree of muscle activation in the lower-limb MTUs directly depends on the relative muscle lengths.

As shown in Figures 5, 8, 9, for uni-articular MTUs, there was a correspondence between the relative muscle lengths and joint angles. For the hip extensor GM, $\frac{l_m^{GM}}{l_{opt}^{GM}}$ was negatively correlated with θ_{Hip} ($r = -1.00$, $p < 0.05$). For the knee extensor Vas, $\frac{l_m^{Vas}}{l_{opt}^{Vas}}$ was negatively correlated with θ_{Knee} ($r = -0.95$, $p < 0.05$). For the ankle extensor Sol, $\frac{l_m^{Sol}}{l_{opt}^{Sol}}$ was negatively correlated with θ_{Ankle} ($r = -0.78$, $p < 0.05$). For the ankle flexor TA, $\frac{l_m^{TA}}{l_{opt}^{TA}}$ was positively correlated with θ_{Ankle} ($r = 0.99$, $p < 0.05$).

As shown in Figures 6, 7, 10, 11, and 12, for bi-articular MTUs, the correspondence between the relative muscle lengths and joint angles still existed but the degree varied among joints. For bflh, semimem, and semiten, which are both hip extensors and knee flexors, the relative muscle lengths were negatively correlated with θ_{Hip} ($\frac{l_m^{bflh}}{l_{opt}^{bflh}}$: $r = -0.98$, $p < 0.05$; $\frac{l_m^{semimem}}{l_{opt}^{semimem}}$: $r = -0.98$, $p < 0.05$; $\frac{l_m^{semiten}}{l_{opt}^{semiten}}$: $r = -0.97$, $p < 0.05$) and less correlated with θ_{Knee} ($\frac{l_m^{bflh}}{l_{opt}^{bflh}}$: $r = -0.31$, $p < 0.05$; $\frac{l_m^{semimem}}{l_{opt}^{semimem}}$: $r = -0.30$, $p < 0.05$; $\frac{l_m^{semiten}}{l_{opt}^{semiten}}$: $r = -0.30$, $p < 0.05$). For RF, both the hip flexor and knee extensor, the relative muscle length was positively correlated with θ_{Hip} ($\frac{l_m^{RF}}{l_{opt}^{RF}}$: $r = 0.90$, $p < 0.05$) and less correlated with θ_{Knee} ($\frac{l_m^{RF}}{l_{opt}^{RF}}$: $r = 0.07$, $p < 0.05$). For gasl and gasm, which are both knee flexors and ankle extensors, the relative muscle lengths were positively correlated with θ_{Knee} ($\frac{l_m^{Gasl}}{l_{opt}^{Gasl}}$: $r = 0.57$, $p < 0.05$; $\frac{l_m^{Gasm}}{l_{opt}^{Gasm}}$: $r = 0.59$, $p < 0.05$) and less correlated with θ_{Ankle} ($\frac{l_m^{Gasl}}{l_{opt}^{Gasl}}$: $r = 0.20$, $p < 0.05$; $\frac{l_m^{Gasm}}{l_{opt}^{Gasm}}$: $r = 0.21$, $p < 0.05$).

3.3.2 Muscle activation

As shown in Figures 5, 9, for uni-articular MTUs, there was a correspondence between the muscle activation and joint angles. For the hip extensor GM, act^{GM} was positively correlated with θ_{Hip} ($r = 0.56$, $p < 0.05$). For the knee extensor Vas, act^{Vas} was negatively correlated with θ_{Knee} ($r = -0.80$, $p < 0.05$). For the ankle extensor Sol, act^{Sol} was negatively correlated with θ_{Ankle} ($r = -0.40$, $p < 0.05$). For the ankle flexor TA, act^{TA} was positively correlated with θ_{Ankle} ($r = 0.66$, $p < 0.05$). Among them, GM did not satisfy the rule that muscle activation is negatively correlated with joint angles for extensors and positively correlated with joint angles for flexors, which will be discussed in detail in Section 4.

As shown in Figures 6, 7, 12, for bi-articular MTUs, the correspondence between the muscle activation and joint angles still existed in some but the degree was much lower. For bflh, semimem, and semiten, which are both hip extensors and knee flexors, the muscle activation was positively correlated with θ_{Hip} (act^{bflh}: $r = 0.20$, $p < 0.05$; $act^{semimem}$: $r = 0.14$, $p < 0.05$; $act^{semiten}$: $r = 0.09$, $p < 0.05$) and also positively correlated with θ_{Knee} (act^{bflh}: $r = 0.28$, $p < 0.05$; $act^{semimem}$: $r = 0.26$, $p < 0.05$; $act^{semiten}$: $r = 0.18$, $p < 0.05$). For RF, both the hip flexor and knee extensor, the muscle activation was negatively correlated with θ_{Hip} (act^{RF}: $r = -0.29$, $p < 0.05$) and also negatively correlated with θ_{Knee} (act^{RF}: $r = -0.22$, $p < 0.05$). For gasl and gasm, which are both knee flexors and ankle extensors, the correlation was neglectable.

These results suggest that the corresponding relationship between muscle activation and joint angles in bi-articular MTUs does not match that in uni-articular MTUs. It was speculated that bi-articular MTUs play a paramount role in regulating balance during bipedal standing in chimps.

3.3.3 Relative muscle forces

As shown in Figures 8, 9, for uni-articular MTUs, there was a correspondence between the relative muscle forces and joint angles. For the hip extensor GM, $\frac{F_m^{GM}}{F_{opt}^{GM}}$ was negatively correlated with θ_{Hip} ($r = -0.68$, $p < 0.05$). For the knee extensor Vas, $\frac{F_m^{Vas}}{F_{opt}^{Vas}}$ was negatively correlated with θ_{Knee} ($r = -0.81$, $p < 0.05$). For the ankle extensor Sol, $\frac{F_m^{Sol}}{F_{opt}^{Sol}}$ was negatively correlated with θ_{Ankle} ($r = -0.44$, $p < 0.05$). For the ankle flexor TA, $\frac{F_m^{TA}}{F_{opt}^{TA}}$ was positively correlated with θ_{Ankle} ($r = 0.66$, $p < 0.05$).

These results satisfied the rule that relative muscle forces are negatively correlated with joint angles for extensors and positively correlated with those for flexors.

As shown in Figures 10, 11, 12, for bi-articular MTUs, the correspondence between the relative muscle forces and joint angles was too weak to form a pattern. These results indicate that the relative muscle forces of bi-articular MTUs cannot be conjectured directly from θ_{Hip}, θ_{Knee}, and θ_{Ankle}, which likewise took the next step in validating that bi-articular MTUs play a fundamental role in regulating balance during bipedal standing in chimps.

4 Discussion

Our study substantiated the premise that when the common chimpanzee is bipedal standing, 1) it cannot simultaneously achieve the maximum *Erectness* and the minimum *Fatigue*, and excessive *Erectness* would not lead to the reduction of *Fatigue*; 2) the hip–knee–ankle joint angles corresponding to the optimal BSP are consistent with the measurement data (Jenkins, 1972; O'Neill et al., 2015) of the middle stance during bipedal walking of chimps; 3) for uni-articular MTUs, the relationship between the muscle activation and the corresponding joint angle, that between the relative muscle lengths and the corresponding joint angle, together with that between the relative muscle forces and the corresponding joint angle is, generally negatively correlated for extensors and positively correlated for flexors; and 4) for bi-articular MTUs, the relationship between the relative muscle lengths and the corresponding joint angles is still negatively correlated for extensors and positively correlated for flexors, but that between the muscle activation and the corresponding joint angles, coupled with the relationship between the relative muscle forces and the corresponding joint angles, is hardly correlated.

4.1 Biomechanical effects of skeletal architecture on the bipedal standing posture of chimps

The lumbar lordosis is absent in chimps; their almost-rigid lumbar spine restrains further extension of the HAT, which compels the lower-limb MTUs to bear greater lumbar-bending stresses during bipedal standing (Lovejoy et al., 2009). In this study, the pelvis was included in the HAT segment, and not as a separate segment, when we established the musculoskeletal model, ignoring the degree of freedom between the lumbar spine and pelvis.

The lower limbs of chimps are evidently shorter than the slender legs of humans (Schultz, 1937; Young et al., 2010); evidently, their HAT segment is longer than the thigh and shank segments. The results presented in Section 3.1 unmasked that this very skeletal architecture leads to the variation in the degree of *Erectness*, which was induced mainly by the hip joint angle.

The elongated and laterally oriented ischia of chimps limit the range of motion of the hip joint. When the hip joint is extended, the moment arms of the GM and hamstrings (bflh, semimem, and semiten), together with the length of the GM, rapidly decrease (Robinson, 1972; McHenry, 1975; Kozma et al., 2018). The results obtained in Section 3.3.1 suggest that this very skeletal architecture leads to the relative muscle lengths of bi-articular MTUs that span the hip and knee joints, namely, the bflh, semimem, semiten, and RF, to be more susceptible to the hip joint angle.

The elongated and dorsally oriented ilia of chimps entail that only the movement of the gluteus maximus ischiofemoralis is regulated in the sagittal plane, whereas the movement of the gluteus maximus poprius is mainly curbed in the coronal plane (Stern, 1972; Tuttle et al., 1979; Lieberman et al., 2006). The results obtained in Section 3.3.2 indicate that this skeletal architecture leads to a positive correlation between the muscle activation of GM, uni-articular extensor, and hip joint angle, in contrast to the pattern satisfied by other uni-articular MTUs, where muscle activation was negatively correlated with joint angles for extensors and positively correlated with joint angles for flexors.

4.2 Biomechanical effects of muscle properties on the bipedal standing posture of chimps

The structure of the MTU governs its muscle–tendon length distribution and its ability to produce force (Biewener and Roberts, 2000; Charles et al., 2022). For instance, the MTU with a shorter muscle and longer tendon is designed to generate more economic force, and that with a longer muscle and shorter tendon is suitable for maintaining the stability of joints. The skeletal muscles of chimps have, on average, longer muscle fibers (Isler, 2005); thus, the maximum dynamic force output in muscles of the same size is 1.35 times greater than that of humans (O'Neill et al., 2017). The results presented in Section 3.3.2 and Section 3.3.3 suggest that this muscle property leads the muscle activation and relative muscle forces of bi-articular MTUs to the violation of the pattern conformed by uni-articular MTUs, where these parameters were negatively correlated with joint angles for extensors and positively correlated with joint angles for flexors. It was meditated that during the bipedal standing of chimps, bi-articular MTUs mainly played a role in harmonizing balance, owing to the longer muscle fibers than those of uni-articular MTUs.

The gluteus maximus of chimps originates from the sacro-iliac region, coccyx, sacrotuberous ligament, and ischial tuberosity, while it inserts in the vastus lateralis aponeurosis (a part of the iliotibial tract) and along the lateral side of the femoral diaphysis (Stern, 1972). Therefore, compared with humans, the gluteus maximus of chimps faces more laterally and then acts more in the coronal plane than that in the sagittal plane (Lovejoy et al., 2002). The results of Section 3.3.2 indicated that this muscle property leads to a positive correlation between the muscle activation and the hip joint angle for the uni-articular extensor GM, in contrast to the pattern met by other uni-articular MTUs where muscle activation was negatively correlated with joint angles for extensors and positively correlated with joint angles for flexors.

The gluteus maximus of chimps is considerably smaller than that of humans, deteriorating the complementary function of the hamstrings in extending the hip joint (Stern and Susman, 1981; Lieberman et al., 2006). The results presented in Section 3.3.2 and Section 3.3.3 indicate that this muscle property leads to a further increase in both the muscle activation and muscle forces of the hamstrings when the hip joint is extended.

Unlike humans, chimps lack the external Achilles tendon in the triceps surae (gasl, gasm, and Sol), the PCSAs of which are relatively small. Therefore, the force production of all these MTUs is small within the motion range of the ankle joint (Thorpe et al., 1999; Payne et al., 2006b).

4.3 Limitations and practical implications

Due to the incompleteness of anatomical information from a single specimen of the common chimpanzee, multiple different specimens were used to build the musculoskeletal model. Therefore, parameters of the skeletal architecture and muscle properties were scaled based on the principle of geometric similarity, which might not be an appropriate assumption. Muscle force-generating capacities of mammals in general were found to be proportional to the body mass raised to the power of 0.8 (Alexander et al., 1981) and to differ in divergent muscles. However, research studies also suggested that while peak isometric muscle forces calculated by the scaling method significantly differed from those measured, the gleaned muscle-force functions were quite similar (Scovil et al., 2006; Redl et al., 2007; Correa & Pandy, 2011). This indication supports the application of mass–length scaling in the musculoskeletal model development.

Though mainly lower-limb MTUs were considered in the musculoskeletal model, core muscles, such as multifidus, also play a critical role in the bipedalism (Wang et al., 2023). Research studies implied that multifidus controls trunk movement primarily in the sagittal plane during the bipedal and quadrupedal movements in chimps (Shapiro & Jungers, 1988; Shapiro & Jungers, 1994). Consequently, multifidus is

worth being used in the model, only if the anatomical data are available.

The musculoskeletal model proposed in this paper is able to predict how changes in the skeletal architecture and muscle properties could alter the force-generating capacity of MTUs. This will enhance the understanding of causal relationships between the musculoskeletal system and locomotor characteristics in primates and advance the comprehension of bipedal evolution in humans.

The biomechanical limitations of the common chimpanzee were elucidated in this paper, which inspire the design of prosthetic devices and assistive technologies for people with impaired mobility, and of robotic systems that better mimic the movements of humans.

5 Conclusion

In this study, to explore the effects of skeletal architecture and muscle properties on bipedal standing in chimps from the perspective of biomechanics, we established a whole-body musculoskeletal model of the common chimpanzee and developed experimental simulations of bipedal standing. Chimps bipedally stand in a "bent-hip, bent-knee" posture due to their skeletal architecture, such as the almost rigid lumbar spine, relatively long HAT segment, elongated and laterally oriented ischia, and elongated and dorsally oriented ilia. The relationship between muscle activation, relative muscle lengths, together with relative muscle forces, and the corresponding joint angle varies between uni-articular and bi-articular MTUs because of muscle properties, such as the muscle–tendon length distribution, insertion, and shape. It would appear that bi-articular MTUs chiefly contribute to balance. Future research could continue to complete the anatomical dataset of chimps, refine the relationships between the musculoskeletal system and locomotor characteristics in primates, and even design wearable equipment or bipedal robotics based on the drawn mechanism.

Data availability statement

The original contributions presented in the study are included in the article/Supplementary Material; further inquiries can be directed to the corresponding author.

Author contributions

CHX conceived and directed the study. XWX, WBC, CHX, BH, and LFC constructed the model. XWX collected the data, wrote the codes, conducted the simulation, and performed the statistical analysis. XWX, WBC and CHX interpreted the results. XWX, WBC, CHX, BH, LFC, and BYS wrote the manuscript. All authors approved the submitted version.

Funding

This work was partially supported by the National Natural Science Foundation of China (grant no. 52027806, U1913601).

Acknowledgments

The authors would like to thank Dr. Di Hu, Dr. Chang He, Dr. Lei He, Dr. Jun Fan, Quan-Lin Li, Jin-Hao Yang, and Han-Wen Zhang for their academic advice and technical assistance during the study.

Conflict of interest

The authors declare that the research was conducted in the absence of any commercial or financial relationships that could be construed as a potential conflict of interest.

Publisher's note

Supplementary material

The Supplementary Material for this article can be found online at: https://www.frontiersin.org/articles/10.3389/fbioe.2023.1140262/full#supplementary-material

References

Alexander, R. M., Jayes, A., Maloiy, G., and Wathuta, E. (1981). Allometry of the leg muscles of mammals. *J. Zool* 194, 539–552. doi:10.1111/j.1469-7998.1981.tb04600.x

Anderson, F. C., and Pandy, M. G. (2001). Static and dynamic optimization solutions for gait are practically equivalent. *J. Biomech* 34, 153–161. doi:10.1016/s0021-9290(00)00155-x

Biewener, A. A., and Roberts, T. J. (2000). Muscle and tendon contributions to force, work, and elastic energy savings: A comparative perspective. *Exerc. Sport Sci. Rev* 28, 99–107.

Charles, J., Kissane, R., Hoehfurtner, T., and Bates, K. T. (2022). From fibre to function: Are we accurately representing muscle architecture and performance? *Biol. Rev* 97, 1640–1676. doi:10.1111/brv.12856

Correa, T. A., and Pandy, M. G. (2011). A mass–length scaling law for modeling muscle strength in the lower limb. *J. Biomech.* 44, 2782–2789. doi:10.1016/j.jbiomech.2011.08.024

Crowninshield, R. D., and Brand, R. A. (1981). A physiologically based criterion of muscle force prediction in locomotion. *J. Biomech* 14, 793–801. doi:10.1016/0021-9290(81)90035-x

Demes, B., Thompson, N. E., O'Neill, M. C., and Umberger, B. R. (2015). Center of mass mechanics of chimpanzee bipedal walking. *Am. J. Phys. Anthropol* 156, 422–433. doi:10.1002/ajpa.22667

Diogo, R., Potau, J. M., and Pastor, J. F. (2013). *Photographic and descriptive musculoskeletal atlas of chimpanzees: With notes on the attachments, variations, innervation, function and synonymy and weight of the muscles*. Boca Raton, FL, USA: CRC Press.

Doran, D. M. (1992a). Comparison of instantaneous and locomotor bout sampling methods: A case study of adult male chimpanzee locomotor behavior and substrate use. *Am. J. Phys. Anthropol* 89, 85–99. doi:10.1002/ajpa.1330890108

Doran, D. M. (1992b). The ontogeny of chimpanzee and pygmy chimpanzee locomotor behavior: A case study of paedomorphism and its behavioral correlates. *J. Hum. Evol* 23, 139–157. doi:10.1016/0047-2484(92)90104-H

Elftman, H. (1944). The bipedal walking of the chimpanzee. *J. Mammal* 25, 67–71. doi:10.2307/1374722

Goodman, M. (1999). The genomic record of Humankind's evolutionary roots. *Am. J. Hum. Genet* 64, 31–39. doi:10.1086/302218

Heiple, K. G., and Lovejoy, C. O. (1971). The distal femoral anatomy of Australopithecus. *Am. J. Phys. Anthropol* 35, 75–84. doi:10.1002/ajpa.1330350109

Hunt, K. D. (1991). Positional behavior in the hominoidea. *Int. J. Primatol* 12, 95–118. doi:10.1007/BF02547576

Hunt, K. D. (1992). Positional behavior of *Pan troglodytes* in the Mahale Mountains and Gombe stream national parks, Tanzania. *Am. J. Phys. Anthropol* 87, 83–105. doi:10.1002/ajpa.1330870108

Hunt, K. D. (1994). The evolution of human bipedality: Ecology and functional morphology. *J. Hum. Evol* 26, 183–202. doi:10.1006/jhev.1994.1011

Isler, K. (2005). 3D-kinematics of vertical climbing in hominoids. *Am. J. Phys. Anthropol* 126, 66–81. doi:10.1002/ajpa.10419

Isler, K., Payne, R. C., Günther, M. M., Thorpe, S. K., Li, Y., Savage, R., et al. (2006). Inertial properties of hominoid limb segments. *J. Anat* 209, 201–218. doi:10.1111/j.1469-7580.2006.00588.x

Jenkins, F. A. (1972). Chimpanzee bipedalism: Cineradiographic analysis and implications for the evolution of gait. *Science* 178, 877–879. doi:10.1126/science.178.4063.877

Kozma, E. E., Webb, N. M., Harcourt-Smith, W. E. H., Raichlen, D. A., D'Août, K., Brown, M. H., et al. (2018). Hip extensor mechanics and the evolution of walking and climbing capabilities in humans, apes, and fossil hominins. *Proc. Natl. Acad. Sci. U. S. A* 115, 4134–4139. doi:10.1073/pnas.1715120115

Lee, L. F., and Umberger, B. R. (2016). Generating optimal control simulations of musculoskeletal movement using OpenSim and MATLAB. *PeerJ* 4, e1638. doi:10.7717/peerj.1638

Lieberman, D. E., Raichlen, D. A., Pontzer, H., Bramble, D. M., and Cutright-Smith, E. (2006). The human gluteus maximus and its role in running. *J. Exp. Biol* 209, 2143–2155. doi:10.1242/jeb.02255

Lovejoy, C. O., Meindl, R. S., Ohman, J. C., Heiple, K. G., and White, T. D. (2002). The maka femur and its bearing on the antiquity of human walking: Applying contemporary concepts of morphogenesis to the human fossil record. *Am. J. Phys. Anthropol* 119, 97–133. doi:10.1002/ajpa.10111

Lovejoy, C. O., Suwa, G., Simpson, S. W., Matternes, J. H., and White, T. D. (2009). The great divides: Ardipithecus ramidus reveals the postcrania of our last common ancestors with African apes. *Science* 326, 73–106. doi:10.1126/science.1175833

Manal, K., and Buchanan, T. S. (2004). Subject-specific estimates of tendon slack length: A numerical method. *J. Appl. Biomech* 20, 195–203. doi:10.1123/jab.20.2.195

McHenry, H. M. (1975). The ischium and hip extensor mechanism in human evolution. *Am. J. Phys. Anthropol* 43, 39–46. doi:10.1002/ajpa.1330430107

Myatt, J. P., Crompton, R. H., and Thorpe, S. K. (2011). Hindlimb muscle architecture in non-human great apes and a comparison of methods for analysing inter-species variation. *J. Anat* 219, 150–166. doi:10.1111/j.1469-7580.2011.01383.x

Nakatsukasa, M. (2004). Acquisition of bipedalism: The miocene hominoid record and modern analogues for bipedal protohominids. *J. Anat* 204, 385–402. doi:10.1111/j.0021-8782.2004.00290.x

Neumann, D. A. (2013). *Kinesiology of the musculoskeletal system: Foundations for rehabilitation*. St. Louis, MO, USA: Elsevier Inc.

O'Neill, M. C., Demes, B., Thompson, N. E., Larson, S. G., Stern, J. T., and Umberger, B. R. (2022). Adaptations for bipedal walking: Musculoskeletal structure and three-dimensional joint mechanics of humans and bipedal chimpanzees (*Pan troglodytes*). *J. Hum. Evol* 168, 103195. doi:10.1016/j.jhevol.2022.103195

O'Neill, M. C., Demes, B., Thompson, N. E., and Umberger, B. R. (2018). Three-dimensional kinematics and the origin of the hominin walking stride. *J. R. Soc. Interface* 15, 20180205. doi:10.1098/rsif.2018.0205

O'Neill, M. C., Lee, L. F., Demes, B., Thompson, N. E., Larson, S. G., Stern, J. T., et al. (2015). Three-dimensional kinematics of the pelvis and hind limbs in chimpanzee (*Pan troglodytes*) and human bipedal walking. *J. Hum. Evol* 86, 32–42. doi:10.1016/j.jhevol.2015.05.012

O'Neill, M. C., Lee, L. F., Larson, S. G., Demes, B., Stern, J. T., Jr, and Umberger, B. R. (2013). A three-dimensional musculoskeletal model of the chimpanzee (*Pan troglodytes*) pelvis and hind limb. *J. Exp. Biol* 216, 3709–3723. doi:10.1242/jeb.079665

O'Neill, M. C., Umberger, B. R., Holowka, N. B., Larson, S. G., and Reiser, P. J. (2017). Chimpanzee super strength and human skeletal muscle evolution. *Proc. Natl. Acad. Sci. U. S. A* 114, 7343–7348. doi:10.1073/pnas.1619071114

Pandy, M. G. (2001). Computer modeling and simulation of human movement. *Annu. Rev. Biomed. Eng* 3, 245–273. doi:10.1146/annurev.bioeng.3.1.245

Payne, R. C., Crompton, R. H., Isler, K., Savage, R., Vereecke, E. E., Günther, M. M., et al. (2006a). Morphological analysis of the hindlimb in apes and humans. II. Moment arms. *J. Anat* 208, 725–742. doi:10.1111/j.1469-7580.2006.00564.x

Payne, R. C., Crompton, R. H., Isler, K., Savage, R., Vereecke, E. E., Günther, M. M., et al. (2006b). Morphological analysis of the hindlimb in apes and humans. I. Muscle architecture. *J. Anat* 208, 709–724. doi:10.1111/j.1469-7580.2006.00563.x

Pontzer, H. (2018). "Locomotor ecology and evolution in chimpanzees and humans," in *Chimpanzees and human evolution*. Editors M. Muller, R. Wrangham, and D. Pilbeam (Cambridge, MA, USA: Harvard University Press).

Pontzer, H., Raichlen, D. A., and Rodman, P. S. (2014). Bipedal and quadrupedal locomotion in chimpanzees. *J. Hum. Evol* 66, 64–82. doi:10.1016/j.jhevol.2013.10.002

Pontzer, H., Raichlen, D. A., and Sockol, M. D. (2009). The metabolic cost of walking in humans, chimpanzees, and early hominins. *J. Hum. Evol* 56, 43–54. doi:10.1016/j.jhevol.2008.09.001

Redl, C., Gfoehler, M., and Pandy, M. G. (2007). Sensitivity of muscle force estimates to variations in muscle-tendon properties. *HumanMovementScience* 26, 306–319. doi:10.1016/j.humov.2007.01.008

Robinson, J. T. (1972). *Australopithecine anatomy: Early hominid posture and locomotion*. Chicago, IL, USA: University of Chicago Press.

Sawicki, G. S., and Khan, N. S. (2016). A simple model to estimate plantarflexor muscle–tendon mechanics and energetics during walking with elastic ankle exoskeletons. *IEEE Trans. Bio Med. Eng* 63, 914–923. doi:10.1109/TBME.2015.2491224

Schultz, A. H. (1937). Proportions, variability and asymmetries of the long bones of the limbs and the clavicles in man and apes. *Hum. Biol* 9, 281–328.

Scovil, C. Y., and Ronsky, J. L. (2006). Sensitivity of a Hill-based muscle model to perturbations in model parameters. *J. Biomech* 39, 2055–2063. doi:10.1016/j.jbiomech.2005.06.005

Sellers, W. I., Margetts, L., Bates, K. T., and Chamberlain, A. T. (2013). Exploring diagonal gait using a forward dynamic three-dimensional chimpanzee simulation. *Folia Primatol. (Basel)* 84, 180–200. doi:10.1159/000351562

Shapiro, L. J., and Jungers, W. L. (1988). Back muscle function during bipedal walking in chimpanzee and gibbon: Implications for the evolution of human locomotion. *Am. J. Phys. Anthropol* 77, 201–212. doi:10.1002/ajpa.1330770208

Shapiro, L. J., and Jungers, W. L. (1994). Electromyography of back muscles during quadrupedal and bipedal walking in primates. *Am. J. Phys. Anthropol* 93, 491–504. doi:10.1002/ajpa.1330930408

Sockol, M. D., Raichlen, D. A., and Pontzer, H. (2007). Chimpanzee locomotor energetics and the origin of human bipedalism. *Proc. Natl. Acad. Sci. U. S. A* 104, 12265–12269. doi:10.1073/pnas.0703267104

Stern, J. T. (1972). Anatomical and functional specializations of the human gluteus maximus. *Am. J. Phys. Anthropol* 36, 315–339. doi:10.1002/ajpa.1330360303

Stern, J. T., and Susman, R. L. (1981). Electromyography of the gluteal muscles in Hylobates, Pongo, and Pan: Implications for the evolution of hominid bipedality. *Am. J. Phys. Anthropol* 55, 153–166. doi:10.1002/ajpa.1330550203

Thompson, N. E., Demes, B., O'Neill, M. C., Holowka, N. B., and Larson, S. G. (2015). Surprising trunk rotational capabilities in chimpanzees and implications for bipedal walking proficiency in early hominins. *Nat. Commun.* 6, 8416. doi:10.1038/ncomms9416

Thorpe, S. K., Crompton, R. H., Günther, M. M., Ker, R. F., and McNeill Alexander, R. (1999). Dimensions and moment arms of the hind-and forelimb muscles of common chimpanzees (*Pan troglodytes*). *Am. J. Phys. Anthropol* 110, 179–199. doi:10.1002/(SICI)1096-8644(199910)110:2<179:AID-AJPA5>3.0.CO;2-Z

Tuttle, R. H., Basmajian, J. V., and Ishida, H. (1978). Activities of pongid thigh muscles during bipedal behavior. *Am. J. Phys. Anthropol* 50, 123–135. doi:10.1002/ajpa.1330500113

Wang, K., Deng, Z., Chen, X., Shao, J., Qiu, L., Jiang, C., et al. (2023). The role of multifidus in the biomechanics of lumbar spine: A musculoskeletal modeling study. *Bioengineering* 10, 67. doi:10.3390/bioengineering10010067

Wang, W. J., and Crompton, R. H. (2004). Analysis of the human and ape foot during bipedal standing with implications for the evolution of the foot. *J. Biomech* 37, 1831–1836. doi:10.1016/j.jbiomech.2004.02.036

Waterson, R. H., Lander, E. S., and Wilson, R. K. (2005). Initial sequence of the chimpanzee genome and comparison with the human genome. *Nature* 437, 69–87. doi:10.1038/nature04072

Wells, J. B. (1965). Comparison of mechanical properties between slow and fast mammalian muscles. *J. Physiol* 178, 252–269. doi:10.1113/jphysiol.1965.sp007626

Yamazaki, N. (1985). "Primate bipedal walking: Computer simulation," in *Primate morphophysiol. Locomot. Anal. Human biped* (Tokyo: University of Tokyo Press).

Young, N. M., Wagner, G. P., and Hallgrímsson, B. (2010). Development and the evolvability of human limbs. *Proc. Natl. Acad. Sci. U. S. A* 107, 3400–3405. doi:10.1073/pnas.0911856107

Zajac, F. E. (1989). Muscle and tendon: Properties, models, scaling, and application to biomechanics and motor control. *Crit. Rev. Biomed. Eng* 17, 359–411.

Zihlman, A. L., and Cramer, D. L. (1978). Skeletal differences between pygmy (*Pan paniscus*) and common chimpanzees (*Pan troglodytes*). *Folia Primatol. (Basel)* 29, 86–94. doi:10.1159/000155830

frontiers | Frontiers in Bioengineering and Biotechnology

TYPE Original Research
PUBLISHED 01 June 2023
DOI 10.3389/fbioe.2023.1182265

OPEN ACCESS

EDITED BY
Yih-Kuen Jan,
University of Illinois at Urbana-Champaign, United States

REVIEWED BY
Zhan Liu,
Sichuan University, China
Tung-Wu Lu,
National Taiwan University, Taiwan

*CORRESPONDENCE
Weng-Pin Chen,
wpchen@mail.ntut.edu.tw

RECEIVED 08 March 2023
ACCEPTED 22 May 2023
PUBLISHED 01 June 2023

CITATION
Hsieh M-K, Tai C-L, Li Y-D, Lee D-M, Lin C-Y, Tsai T-T, Lai P-L and Chen W-P (2023), Finite element analysis of optimized novel additively manufactured non-articulating prostheses for cervical total disc replacement.
Front. Bioeng. Biotechnol. 11:1182265.
doi: 10.3389/fbioe.2023.1182265

Finite element analysis of optimized novel additively manufactured non-articulating prostheses for cervical total disc replacement

Ming-Kai Hsieh[1], Ching-Lung Tai[1,2], Yun-Da Li[1,2], De-Mei Lee[3], Cheng-Yi Lin[4], Tsung-Ting Tsai[1], Po-Liang Lai[1] and Weng-Pin Chen[4]*

[1]Department of Orthopaedic Surgery, Spine Section, Bone and Joint Research Center, Chang Gung Memorial Hospital and Chang Gung University College of Medicine, Taoyuan, Taiwan, [2]Department of Biomedical Engineering, Chang Gung University, Taoyuan, Taiwan, [3]Department of Mechanical Engineering, Chang Gung University, Taoyuan, Taiwan, [4]Department of Mechanical Engineering, National Taipei University of Technology, Taipei, Taiwan

Ball-and-socket designs of cervical total disc replacement (TDR) have been popular in recent years despite the disadvantages of polyethylene wear, heterotrophic ossification, increased facet contact force, and implant subsidence. In this study, a non-articulating, additively manufactured hybrid TDR with an ultra-high molecular weight polyethylene core and polycarbonate urethane (PCU) fiber jacket, was designed to mimic the motion of normal discs. A finite element (FE) study was conducted to optimize the lattice structure and assess the biomechanical performance of this new generation TDR with an intact disc and a commercial ball-and-socket Baguera®C TDR (Spineart SA, Geneva, Switzerland) on an intact C5-6 cervical spinal model. The lattice structure of the PCU fiber was constructed using the Tesseract or the Cross structures from the IntraLattice model in the Rhino software (McNeel North America, Seattle, WA) to create the hybrid I and hybrid II groups, respectively. The circumferential area of the PCU fiber was divided into three regions (anterior, lateral and posterior), and the cellular structures were adjusted. Optimal cellular distributions and structures were A2L5P2 in the hybrid I and A2L7P3 in the hybrid II groups. All but one of the maximum von Mises stresses were within the yield strength of the PCU material. The range of motions, facet joint stress, C6 vertebral superior endplate stress and path of instantaneous center of rotation of the hybrid I and II groups were closer to those of the intact group than those of the Baguera®C group under 100 N follower load and pure moment of 1.5 Nm in four different planar motions. Restoration of normal cervical spinal kinematics and prevention of implant subsidence could be observed from the FE analysis results. Superior stress distribution in the PCU fiber and core in the hybrid II group revealed that the Cross lattice structure of a PCU fiber jacket could be a choice for a next-generation TDR. This promising outcome suggests the feasibility of implanting an additively manufactured multi-material artificial disc that allows for better physiological motion than the current ball-and-socket design.

KEYWORDS

biomechanics, hybrid artificial cervical disc, additive manufacture technology, polycarbonate urethane, finite element analysis, lattice structure

Introduction

Total disc replacement (TDR) has been proven to preserve level motion at the treated level and reduce adjacent segment degeneration, which are advantages over anterior cervical discectomy and fusion (ACDF) (Findlay et al., 2018). Between 2006 and 2013, a total of 1,059,403 ACDF and 13,099 TDR surgeries were performed in the United States. During this same time period, the annual number of ACDF and TDR increased non-linearly by 5.7% and 190% (Saifi et al., 2018). The preservation of physiologic motion at the treated level leads to longevity of the facet joints and decreases the adjacent segment degeneration rate, which would otherwise lead to additional revision surgery (Bhattacharya et al., 2019; Rajakumar et al., 2017; Yang et al., 2017). Ball-and-socket TDR have been more popular than other designs in recent years, but their potential disadvantages include polyethylene (PE) wear, heterotrophic ossification, increased contact forces, and disc subsidence and migration (Virk et al., 2021; Shen et al., 2021; Shen et al., 2022; Cao et al., 1976; Parish et al., 2020). A new-generation prosthesis with a compressible central core allows for six kinematic degrees of freedom and mimics normal biomechanics has been developed and used (Patwardhan et al., 2012; Phillips et al., 2021; Oltulu et al., 2019). The non-articulating TDR was designed to model normal discs by using PE fiber as the annulus, polycarbonate urethane (PCU) core as the nucleus pulposus, and covered polymer to catch soft tissue growth and debris. However, the overall biomechanical performance of the fiber network of the TDR was determined not only by the geometric properties of the layered material but also by the physical similarity, complexity, lattice geometry, and distributions of the materials, which should be taken into consideration (Mahbod and Asgari, 2019; Maconachie et al., 2019). The open porous cellular architecture of the lattice plays an important role in energy absorption and stress distribution (Mahbod and Asgari, 2019; Maconachie et al., 2019; Gutiérrez, 2020).

The applications of additive manufacturing (AM) technologies, also known as rapid prototyping or three-dimensional (3-D) printing, in the biomedical field have increased substantially in recent years (Puppi and Chiellini, 2020; Kumar et al., 2021). Five key benefits that AM has over traditional manufacturing include cost, speed, quality, innovation/transformation, and impact. Small volume, on-demand and component manufacturing enables quality improvement and time and cost savings (Attaran, 2017). AM 3D printing has been used in several biomedical applications, including anatomical models, customized implants, and tissue and organ fabrication (Attaran, 2017; Mobbs et al., 2017). Preoperative planning in the reconstruction of C1-2 chordoma, sacral osteosarcoma, and vertebral fracture was also successfully applied (Siu et al., 2018; Kim et al., 2017; Phan et al., 2016).

With recent progress in micro-fabrication technology by AM, lattice structures can now be made with diameters ranging from millimeter to submicron levels (Tancogne-Dejean et al., 2016). The mechanical and biological performance of implants can be greatly affected by internal architecture, and implant design can be tailored by using AM techniques.

Our study utilized additive manufacturing to create a TDR with a multi-material elastomeric design consisting of a PE core and a PCU fiber jacket. This design was chosen to replicate the anisotropic mechanical properties of natural discs at the frequently degenerated C5-6 cervical level (Teraguchi et al., 2014). The purpose of our finite element (FE) study was to optimize the cellular structure, density and distribution of the PCU fibers in the TDR produced by AM. The core stress, C6 superior endplate stress, facet joint force, and range of motion at the treated level of the cervical spine were compared between the two optimized AM TDR and a commercial product (Baguera®C, Spineart SA, Geneva, Switzerland). Biomechanical comparison and finite element analysis of various commercially available cervical artificial discs have been conducted in recent years (Kowalczyk et al., 2011; Lin et al., 1976; Chen et al., 2018; Choi et al., 2020). To the best of the author's knowledge, this is the first finite element study optimizing an additively manufactured hybrid TDR and comparing them with a commercially available TDR with ball-and-socket designs.

Materials and methods

Development of an FE C5-6 intact cervical spine model

An FE model of a C5-C6 spine segment was developed from computed tomography (CT) images of the cervical spine of a 55 years/o male subject (The Visible Human Project, National Library of Medicine, Bethesda, MD, United States) at 1-mm intervals with an original disc height of 5.5 mm as the baseline model (Kamal and Rouhi, 2016a). The development process included the following steps: (1) The 3-D reconstruction of the solid volume based on the CT images was set up by using commercial segmentation and visualization software (Amira 4.1, TGS, San Diego, CA). (2) The solid model was then exported into a readable input file for the SolidWorks 2014 CAD software (Solidworks Corp., Boston, MA, United States), where the intervertebral disc was created. (3) The bony components and intervertebral disc were meshed using linear tetrahedral elements by FE pre-processing software (HyperMesh 2017, Altair Engineering, Inc., Troy, MI, United States). The thickness of the cortex and endplate were set as 0.5 mm (Kamal and Rouhi, 2016a; Kwon et al., 2020; Liu et al., 2020). (4) The material properties and loading/boundary conditions of the FE analysis were set up, and nonlinear, quasi-static analysis was performed using Abaqus 2018/CAE software (Simulia Corp., Prvidence, RI, United States).

The detailed material parameters used for the parts of the C5-C6 spine model, including cortical bone, cancellous bone, posterior bony elements, endplates, nucleus pulposus, annulus fibrosus, and annulus ground substance, are shown in Table 1. All materials were assumed to be linear elastic, homogeneous and

TABLE 1 Material parameters used for the C5-C6 spine model.

	Young's modulus (MPa)	Poisson's ratio (v)	Element type	References
Cortical Bone	10,000	0.3	C3D4	Mackiewicz et al. (2016)
Cancellous Bone	E_{xx} = 100	v_{xy} = 0.3 v_{xz} = 0.1	C3D4	Mackiewicz et al., 2016, Whyne et al., 2001
	E_{yy} = 100			
	E_{zz} = 300			
	G_{xy} = 38			
	G_{yz} = 77			
	G_{zx} = 77			
Posterior Bone	3,500	0.3	C3D4	Toosizadeh and Haghpanahi (2011)
Endplate	500	0.4	C3D4	Zhang et al. (2006)
Annulus Ground Substance (Mooney–Rivlin)	C_{10} = 0.56	0.45	C3D4	Toosizadeh and Haghpanahi, (2011), SchmidtHeuer et al., 2006
	C_{01} = 0.14			
Annulus	175	0.3	SFM3D4	
Fibrosus				
Nucleus	C_{10} = 0.12	0.4999	C3D4	Mackiewicz et al. (2016)
Pulposus (Mooney–Rivlin)	C_{01} = 0.09			
Rigid Body	10^{12}	0.3	C3D4	Toosizadeh and Haghpanahi, (2011), SchmidtHeuer et al., 2006

TABLE 2 Force-displacement data used for the ligaments in the spine model (Wheeldon et al., 2008).

All		PLL		ISL, SSL		LF		FCL	
Displacement (mm)	Force (N)	Displacement (mm)	Force (N)	Displacement (mm)	Force (N)	Displacement (mm)	Force (N)	Displacement (mm)	Force (N)
0	0	0	0	0	0	0	0	0	0
1	35.5	0.9	1.33	1.2	0.75	1.7	2.2	1.7	2.452
2	64.9	2	29.0	2.7	16.9	3.74	45.9	3.9	53.6
4	89.7	3	51.4	4.0	24.4	5.6	82.9	5.8	87.9
5	108.6	4	71.38	5.4	29.5	7.48	119.6	7.7	109.4
6	119.6	5	85.8	6.7	32.9	9.35	133.7	9.7	125.8
-	-	6	94.7	8.1	34.9	11.3	147.2	11.5	134.8

isotropic, except orthotropic in cancellous bone and hyperelastic in nucleus pulposus and annulus ground substance (Kowalczyk et al., 2011; Lin et al., 1976; Chen et al., 2018; Choi et al., 2020).

Six major groups of ligaments of the C5-C6 spine model, including anterior longitudinal (ALL), posterior longitudinal (PLL), ligament flavum (LF), facet capsular (FCL), interspinous (ISL), and supraspinous (SSL), were created. The points of attachment of the ALL and PLL were along the anterior and posterior surfaces of the vertebral bodies. The FCL was attached between the articular processes, the LF between the lower margin of the C5 laminae to the upper-third of the C6 laminae, and the ISL between the two spinous processes. The ligaments were modeled using two-node wire nonlinear link elements that permitted only nonlinear tensile force transmission and are listed in Table 2 (Wheeldon et al., 2008).

Development and optimization of the AM hybrid TDRs

The overall design process of the additive manufacturing of hybrid TDRs consisted of four steps.

A

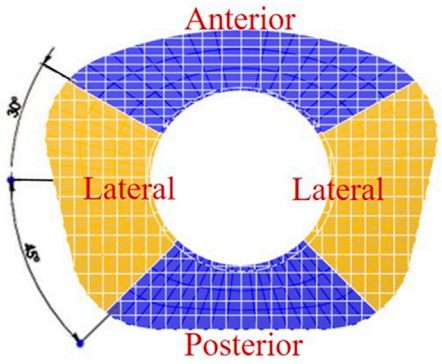

B

Definition of different Tesseract structure models for hybrid I group

Anterior region	Lateral region	Posterior region	Group name
Number of structure	Number of structure	Number of structure	
3	5	2	A3L5P2
2	5	2	A2L5P2
1	5	2	A1L5P2
1	5	3	A1L5P3

C

Definition of different Cross structure models for hybrid II group

Anterior region	Lateral region	Posterior region	Group name
Number of structure	Number of structure	Number of structure	
2	6	3	A3L5P2
2	7	3	A2L5P2
2	7	4	A1L5P2
1	7	4	A1L5P3

FIGURE 1
Division of circumferential regions of the artificial fiber jacket structure **(A)**. Definition of different Tesseract structure models for the hybrid I group **(B)** and Cross structure models for the hybrid II group **(C)**.

First, the referenced geometric parameters were input. The additively manufactured TDR, a multi-material elastomeric design with ultra-high molecular weight PE (UHMWPE) core and PCU fiber jacket, was designed. The superior and inferior plates of the AM TDR were constructed with stainless steel (316L). The geometric data of the UHMWPE core were 5.8 mm in height, 14.0 mm in anterior-posterior length, and 17.9 mm in width, and the distance between the core and the superior plate was 0.08 mm (Moroney et al., 1988). The lattice structure of the PCU fiber jacket was constructed using the Tesseract or the Cross structures from the IntraLattice model in the Rhinoceros 6 software (Rhino, McNeel North America, Seattle, WA) to create the Hybrid I and Hybrid II groups, respectively (Figure 1). The circumferential area of the PCU fiber jacket was divided into three different regions (Figure 1A), and the lattice structures were adjusted into different models: A3L5P2, A2L5P2, A1L5P2 and A1L5P3 in the Hybrid I group (Figure 1B) and A2L6P3, A2L7P3, A2L7P4 and A1L7P4 in the Hybrid II group (Figure 1C). According to the biomechanical performance in the range of motion (ROM) under various loadings compared to the intact model, the optimal lattice structures from the Hybrid I and Hybrid II groups were chosen, and their biomechanical performances were then compared with a commercially available Baguera®C cervical joint prosthesis (Spineart SA, Geneva, Switzerland).

Development of the FE model of the Baguera®C TDR

The 3D computer-aided design (CAD) model of the Baguera®C TDR was reconstructed through an ATOS scanning system (GOM mbH, Braunschweig, Germany) with dimensions of 13, 16, and 7 mm in length, width and height, respectively (Figure 2). The internal nucleus of the Baguera group is able to translate ±0.3 mm, anterior-posteriorly and laterally. Two degrees of axial rotation of the nucleus and 8 degrees of sagittal and coronal rotation of the entire implant were set before the analysis. The CAD model was exported into a readable input file for Solidworks 2014 software (Solidworks Corp., Boston, MA, United States), and then a finite element model was created with tetrahedral elements in Hypermesh 2017 FE pre-processing software (HyperMesh, Altair Engineering, Inc., Troy, MI). The material properties and loading/boundary conditions were set up, and FE analysis was performed with Abaqus 2018/CAE software (Simulia Corp., Prvidence, RI, United States).

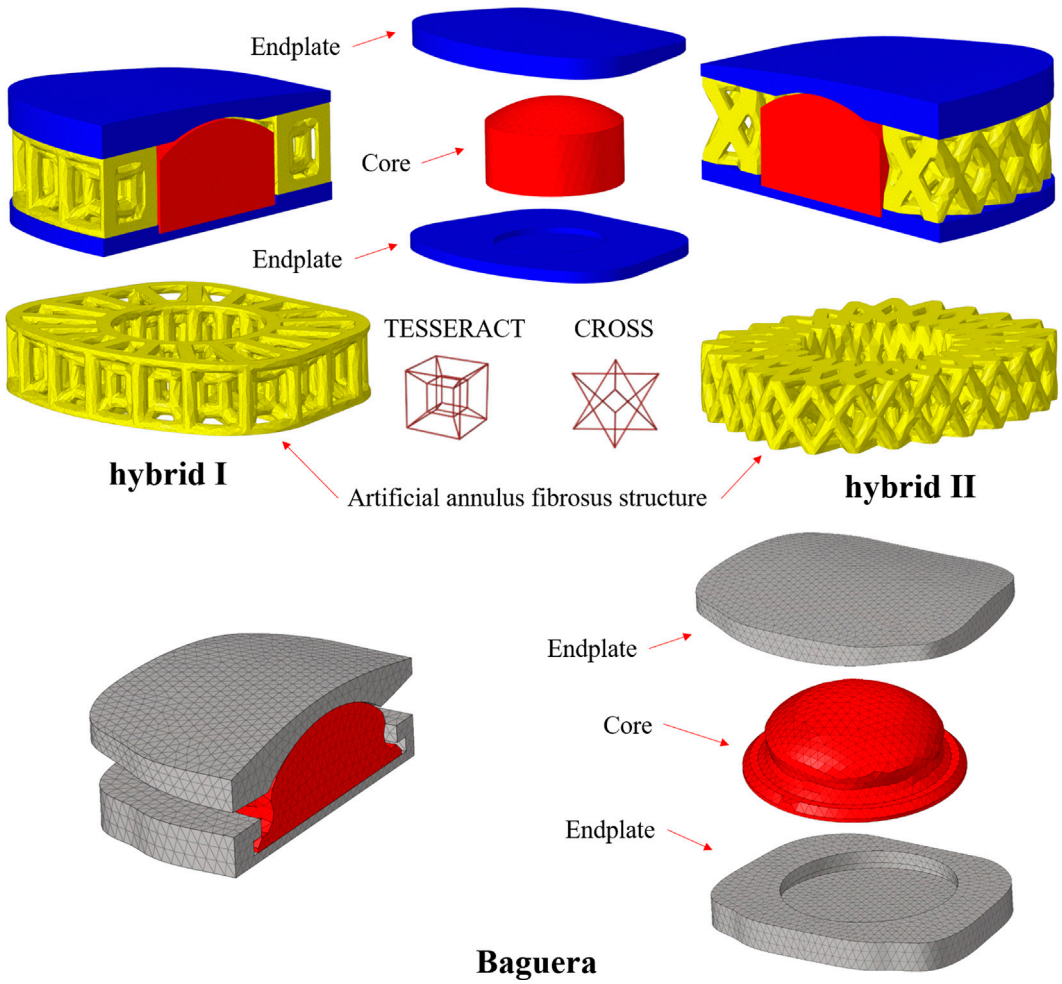

FIGURE 2
Detailed parts of the hybrid I, hybrid II and Baguera®C TDR models.

TABLE 3 Material parameters used for the artificial disc materials (Kamal and Rouhi, 2016b), (Jacobs et al., 2017).

	Young's modulus (MPa)	Poisson's ratio (ν)	Element type	References
Ti-6-Al-4-V	110,000	0.3	C3D4	Kamal and Rouhi (2016b)
316 L	52,000	0.3	C3D4	
Stainless Steel				
PCU 75D	188	0.3	C3D4	Jacobs et al. (2017)
UHMWPE	800	0.3	C3D4	Kamal and Rouhi (2016b)

Material parameters setup for TDR finite element models

The detailed parts of the Hybrid I and Hybrid II models included endplates, a fiber jacket, and a core and the Baguera®C model included an endplate and a core. The material parameters were set up and are listed in Table 3. All materials were assumed to be linear elastic and homogeneous. The schematic diagrams for the three TDR implantation models are shown in Figure 3.

Loading and boundary conditions

The inferior surface of the C6 vertebra was fixed in all degrees of freedom, while a follower load of 100 N that simulating the head weight and local muscle motion during daily activity was applied on the superior surface of the C5 vertebra (Bell et al., 2018; Finn et al., 2009). In loading control, pure moments of 1.5 Nm were generated by a force couple during flexion, extension, lateral bending, and axial rotation of the cervical spine respectively (Figure 4) (Bell et al., 2018;

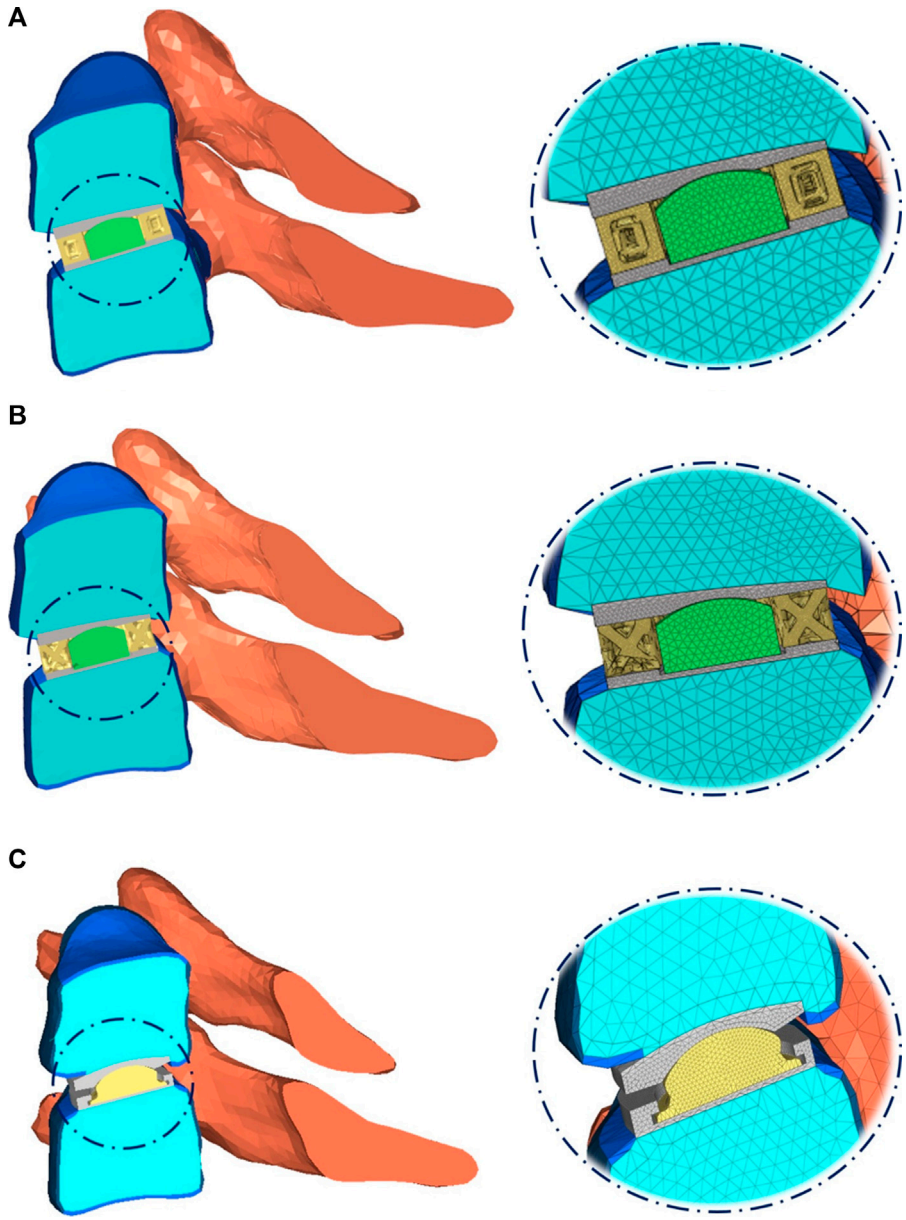

FIGURE 3
Schematic diagram of three TDR implantation models: **(A)** hybrid I group, **(B)** hybrid II group, **(C)** Baguera®C group.

Finn et al., 2009). A friction coefficient of 0.1 was established for the ball and socket joints of the implants (Galbusera et al., 2008). The boundary condition between the implant endplates and vertebral bodies was set to merge to achieve fully restrained components. To prevent any relative sliding, a Tie contact was implemented between the artificial annulus fibrosus and implant endplates.

Finite element model convergence test

The convergence criteria for the FE models were selected as the total strain energy (ALLSE in Abaqus 2018/CAE software) between different mesh refinements to be less than 5%. The final analysis mesh sizes were chosen to be 1.3 mm for the intact group, 0.2 mm for the Hybrid I group, 0.15 mm for the Hybrid II group and 0.2 mm for the Baguera group after the mesh convergence tests (Supplementary Table S1).

Biomechanical evaluation

To compare the primary stabilizing properties of the three TDR groups, the ROMs of the operated C5-C6 motion segment with the Hybrid I, Hybrid II, and Baguera groups were compared to those of the Intact group under loadings of 100 N follower load and pure moment of 1.5 Nm in four different motions (flexion, extension,

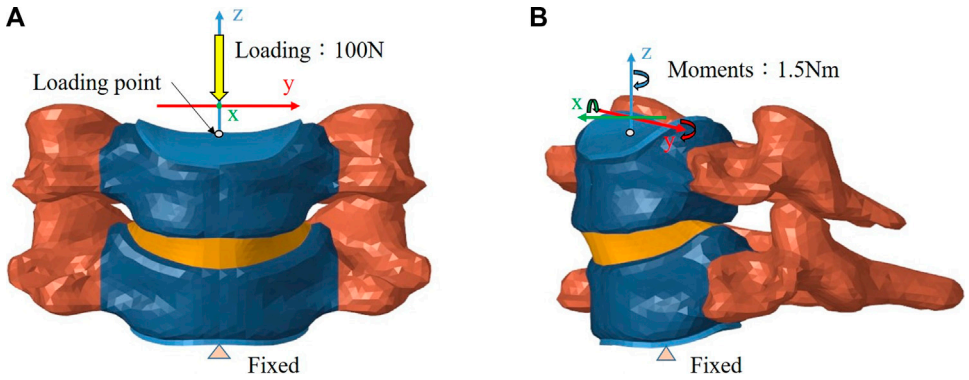

FIGURE 4
Finite element model of the intact C5–C6 motion segment with loading/boundary conditions: **(A)** coronal view, **(B)** sagittal view.

lateral bending, and axial rotation). To evaluate the strength of the TDRs and the tendency of prosthesis subsidence, the stress distributions of the core, facet joint and C6 vertebral superior endplate were analyzed for different motions. The quality of the spine movement was evaluated by the instantaneous center of rotation (ICR). The detailed ICR paths were calculated from the relative positions of the vertebrae during motion as described in the literature (Muhlbauer et al., 2020).

Results

Model validation

Figure 5 shows the comparison of ROMs for the intact C5-C6 model and those obtained in previous biomechanical studies for moments of 1.5 Nm (Finn et al., 2009; Purushothaman et al., 2020). The ROMs of the intact C5-C6 FE model were 7.25, 3.7 and 2.31° during flexion/extension, lateral bending and axial rotation, respectively. All ROMs of the intact model were comparable with previously obtained experimental data, and the comparison successfully verified the intact model used in the current study for further biomechanical analysis of implantation groups.

Optimization of two AM TDR groups

According to the comparison of the biomechanical performance of the intact model for the range of motion under various loadings, the optimal lattice structure distributions from the Hybrid I and Hybrid II groups were A2L5P2 in the Hybrid I groups and A2L7P3 in the Hybrid II group, and they were selected to be compared with the Baguera®C group (Figure 6). All the maximum von Mises stresses of the PCU fiber jacket were within the yield strength of the PCU material (less than 41.1 MPa) (Inyang and Vaughan, 2020; Ford et al., 2018) except for one value of 41.28 MPa in the Hybrid I group under axial rotation (Figure 7).

Range of motion results for the two optimized hybrid groups, Baguera®C group and intact group

To compare the primary stabilizing properties of the three TDR groups, the ROMs of the operated C5-C6 motion segments were compared. The ROMs of the C5-C6 models of the Hybrid I, Hybrid II, and Baguera groups were compared with those of the intact group under the follower load of 100 N and pure moment of 1.5 Nm, and the ROMs 33% less, 23% less, and 150.2% more in flexion; unchanged (0%), 20.5% more, and 28.7% more in extension; 7.0% more, 11.1% more, and 279.5% more in lateral bending; and 179.7% more, 165.4% more, and 638.1% more in axial rotation, respectively (Figure 8).

Stress analysis among the two optimized hybrid groups, Baguera®C group, and intact group

Core stress

To evaluate the durability of the prostheses, the von Mises stress distributions of the cores during four different motions were analyzed (Figure 9). In flexion, the stress distribution in the Hybrid I group was the lowest (0.28 MPa in the Hybrid I group, 10.77 MPa in the Hybrid II group and 34.47 MPa in the Baguera®C group). In extension, lateral bending and axial rotation, both the Hybrid I and Hybrid II groups showed considerably lower stress values (0.01 MPa, 0.01 MPa and 0.02 MPa in the Hybrid I group; 0.03 MPa, 0.03 MPa and 0.02 MPa in the Hybrid II group) than the Baguera group (25.88 MPa, 41.23 MPa, and 27.86 MPa, respectively).

C6 vertebral superior endplate stress

To predict the tendency of prosthesis subsidence, the von Mises stress distribution on the interface between the prosthesis and C6 vertebral superior end plate was evaluated (Figure 10). In flexion, the stress values were 52.56 MPa in the Hybrid I group, 64.01 MPa in the Hybrid II group and 129.6 MPa in the Baguera group. In extension,

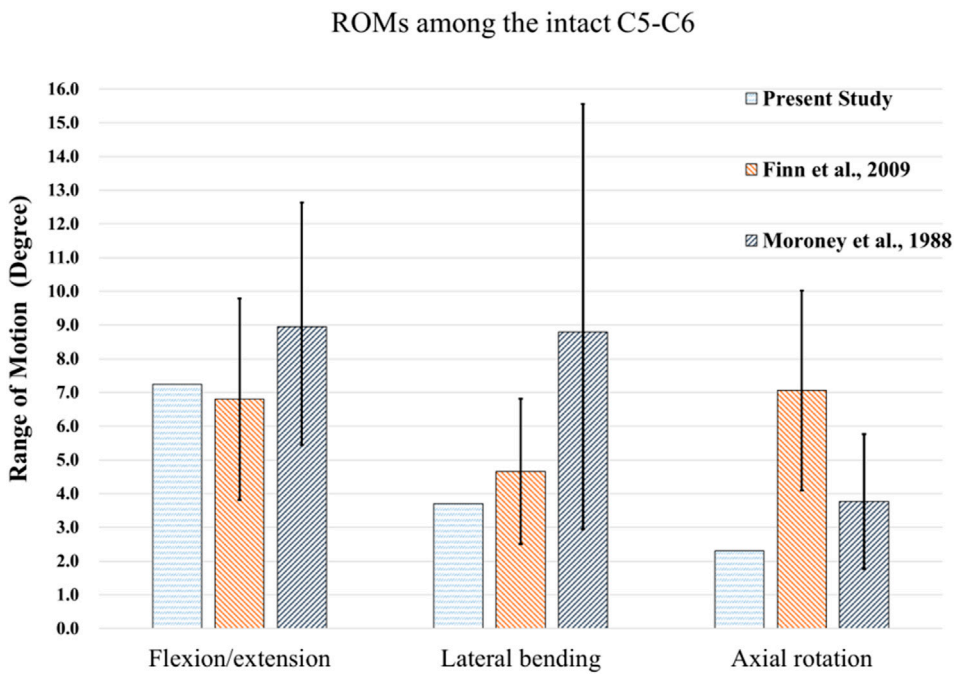

FIGURE 5
Comparisons of ROMs for the intact C5-C6 model and those obtained from previous biomechanical studies (Moroney et al., 1988), (Finn et al., 2009).

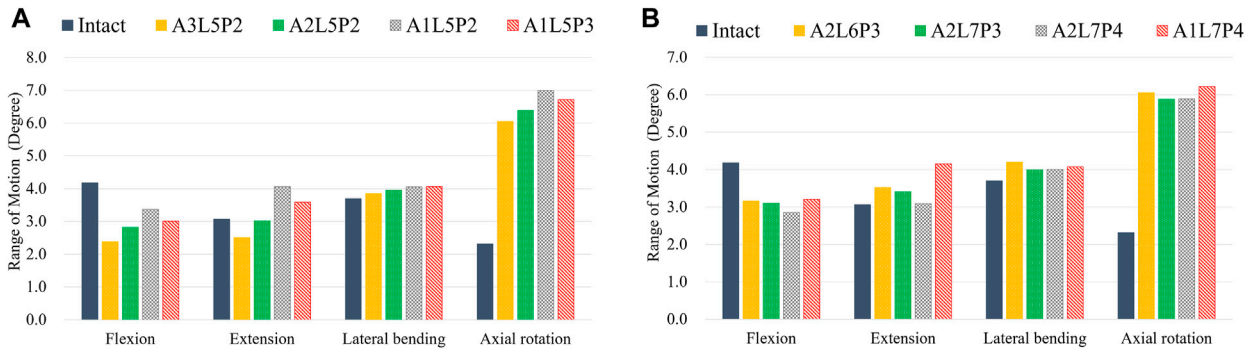

FIGURE 6
ROMs for different lattice structure models for the hybrid I and hybrid II groups for different motions (FL: flexion, EX: extension, LB: lateral bending, and AR: axial rotation) compared to those of the intact group: **(A)** hybrid I group, **(B)** hybrid II group.

the results were 61.08 MPa in the Hybrid I group, 56.27 MPa in the Hybrid II group and 35.02 MPa in the Baguera®C group. In lateral bending, the results were 44.80 MPa in the Hybrid I group, 41.52 MPa in the Hybrid II group and 65.28 MPa for the Baguera group. In axial rotation, the results were 36.89 MPa for the Hybrid I group, 34.73 MPa for the Hybrid II group and 61.03 MPa for the Baguera®C group. Overall, the von Mises stress level on the C6 superior endplate was much greater in the Baguera group than in the Hybrid I and Hybrid II groups, as shown in Figure 10. In flexion, extension and axial rotation, a larger stress concentration on the margin of the Baguera group was observed, which indicated a greater risk of subsidence.

Facet stress

The facet stress distributions of the four groups during three different motions (extension, lateral bending and axial rotation) are shown in Figure 11. In extension, the stress values were 1.53 MPa in the intact group, 0.0 MPa in the Hybrid I group, 0.0 MPa in the Hybrid II group and 4.03 MPa in the Baguera group. In lateral bending, 0.16 MPa in the intact group, 1.29 MPa in the Hybrid I group, 0.92 MPa in the Hybrid II group and 17.70 MPa in the Baguera group. In axial rotation, 0.10 MPa in the intact group, 3.01 MPa in the Hybrid I group, 1.60 MPa in the Hybrid II group and 6.19 MPa in the Baguera group. Both the Hybrid I and Hybrid II

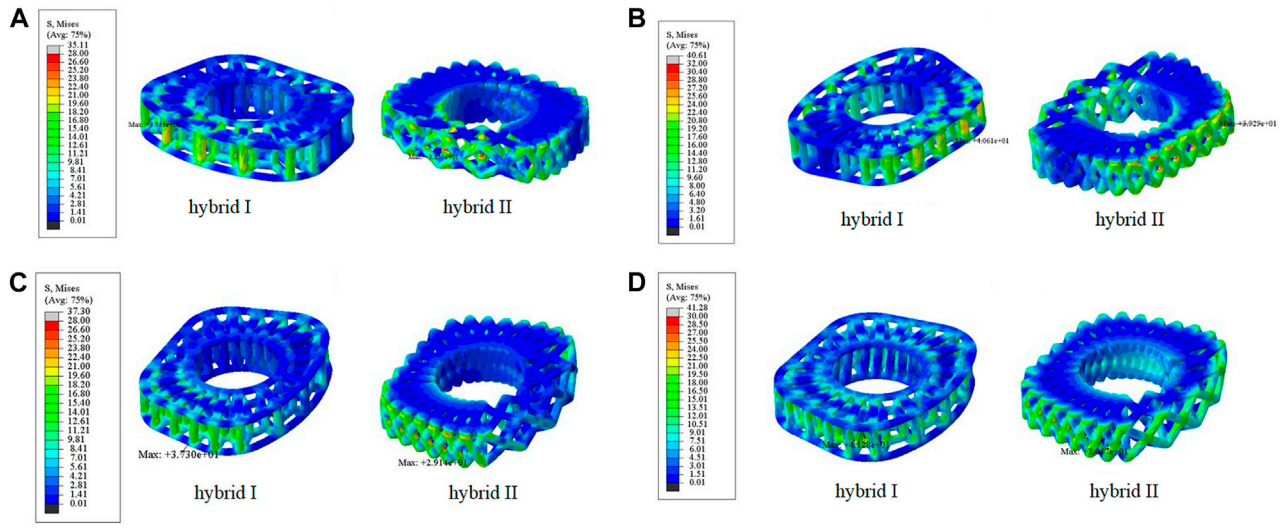

FIGURE 7
Von Mises stress distributions on the lattice fiber jacket for the hybrid I and hybrid II groups for different motions: **(A)** flexion, **(B)** extension, **(C)** lateral bending, and **(D)** axial rotation. (unit: MPa).

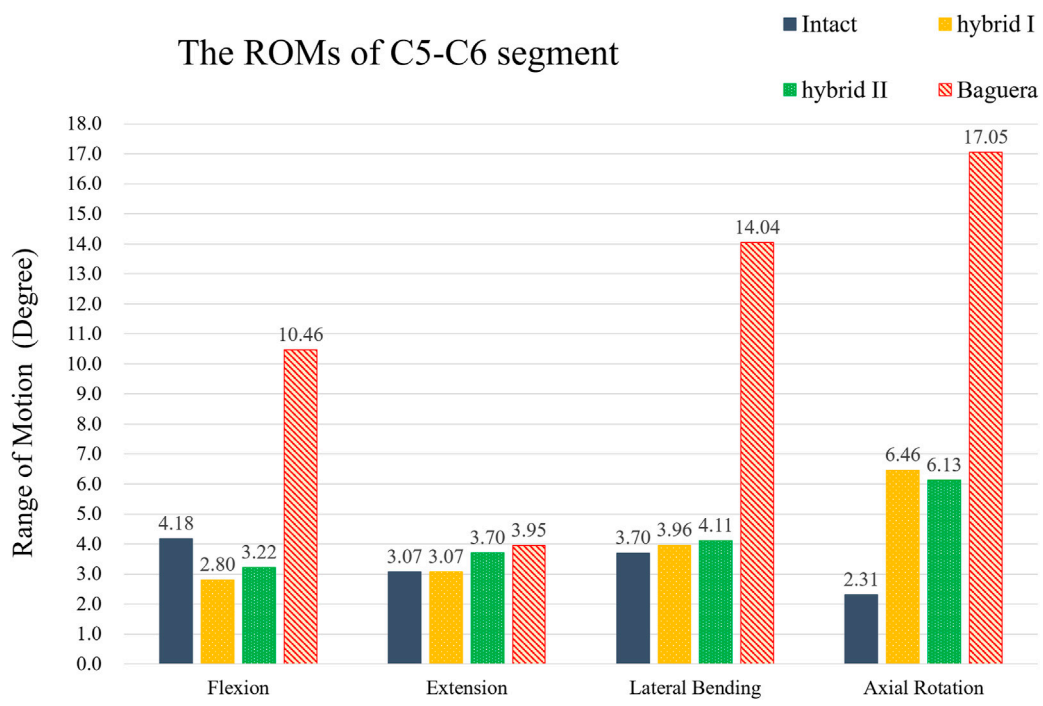

FIGURE 8
ROMs of the C5-C6 segment of hybrid I, hybrid II and Baguera®C groups compared to those of the intact group.

groups showed relatively lower facet stress than the Baguera group; furthermore, facet stress values of the Hybrid II group showed a similar tendency to the intact group than the Hybrid I group. Among the three different motions in the Baguera group, significantly increased facet stress was observed in lateral bending, which indicated that lateral constraint of the prosthesis was lacking.

Paths of ICRs among the two optimized hybrid groups, Baguera®C group, and intact group

The path of the ICR, an alternative of ROM, has been proposed to evaluate the quality of spine movement and to identify abnormal

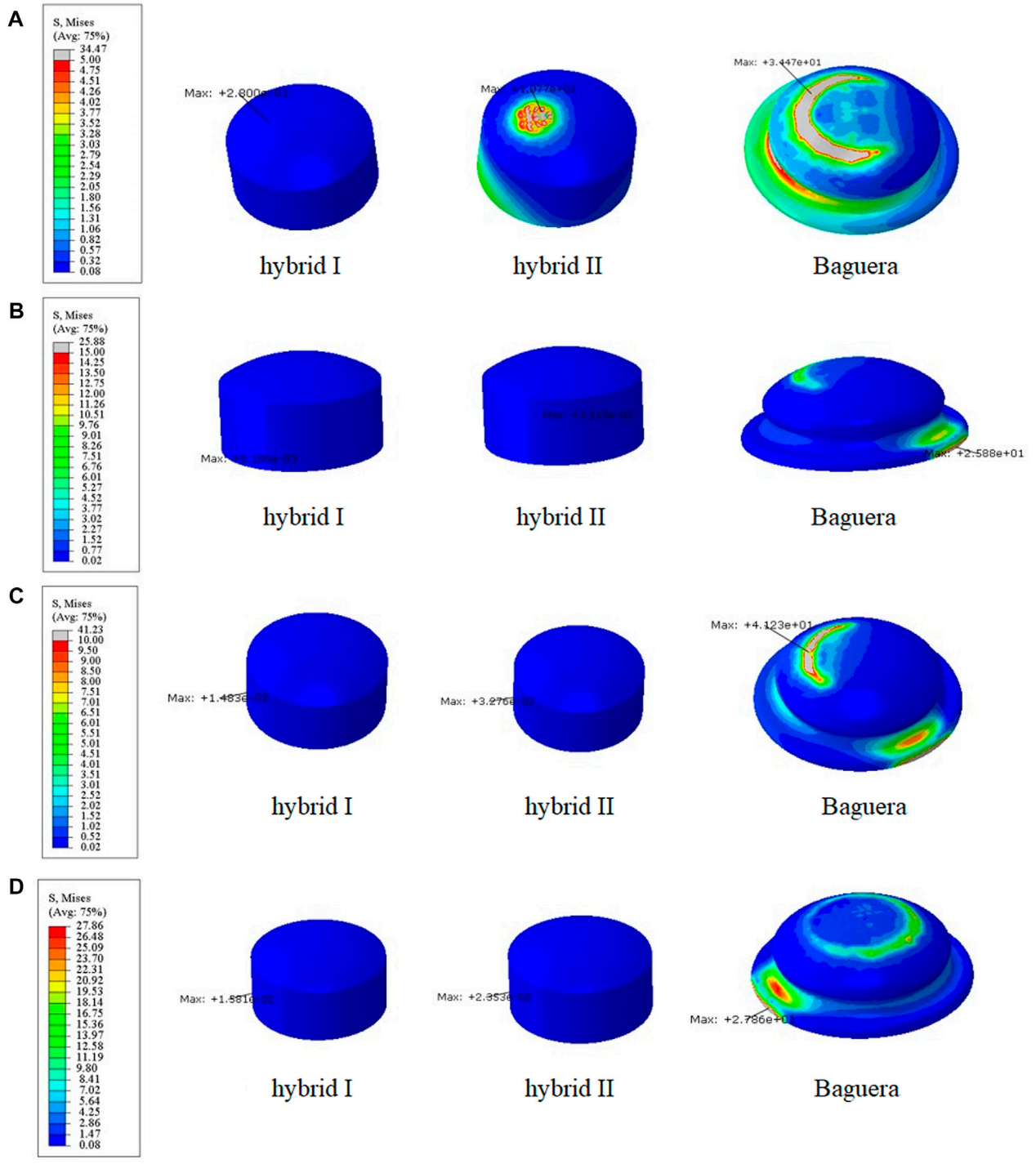

FIGURE 9
Core stress distribution patterns for the Hybrid I, Hybrid II, and Baguera groups for different motions: **(A)** flexion, **(B)** extension, **(C)** lateral bending, and **(D)** axial rotation. (unit: MPa).

cervical spine kinematics (Kamal and Rouhi, 2016b; Kim et al., 2019). The detailed ICR paths were calculated through the relative positions of the vertebrae during motion as described in the literature. During C5-C6 treated level movement, a total of 20 ICRs from each individual segment were calculated to form the path of ICRs. In flexion, extension and lateral bending, the ICR paths of the Hybrid I and Hybrid II groups did not change much, whereas the ICR path of the intact group shifted sagittally in flexion/extension and shifted coronally in lateral bending (Figure 12). In axial rotation, the ICR paths of the intact and hybrid groups shifted posteriorly, which was in agreement with other studies (Muhlbauer et al., 2022; Venegas et al., 2020; Claessens, 2017). In the Baguera® C

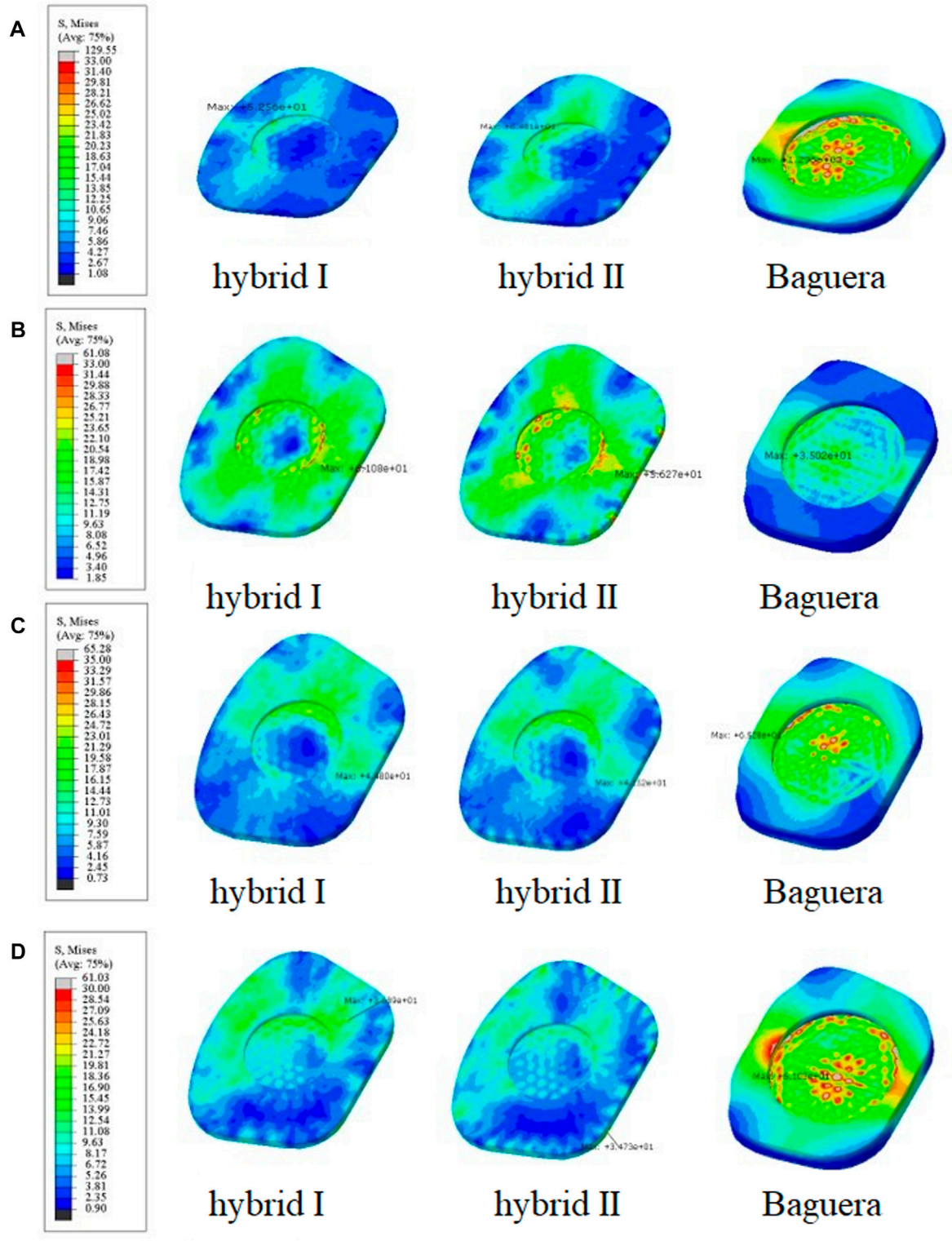

FIGURE 10
Von Mises stress distributions on the C6 superior endplate for the hybrid I, hybrid II and Baguera®C groups for different motions: **(A)** flexion, **(B)** extension, **(C)** lateral bending, and **(D)** axial rotation. (unit: MPa).

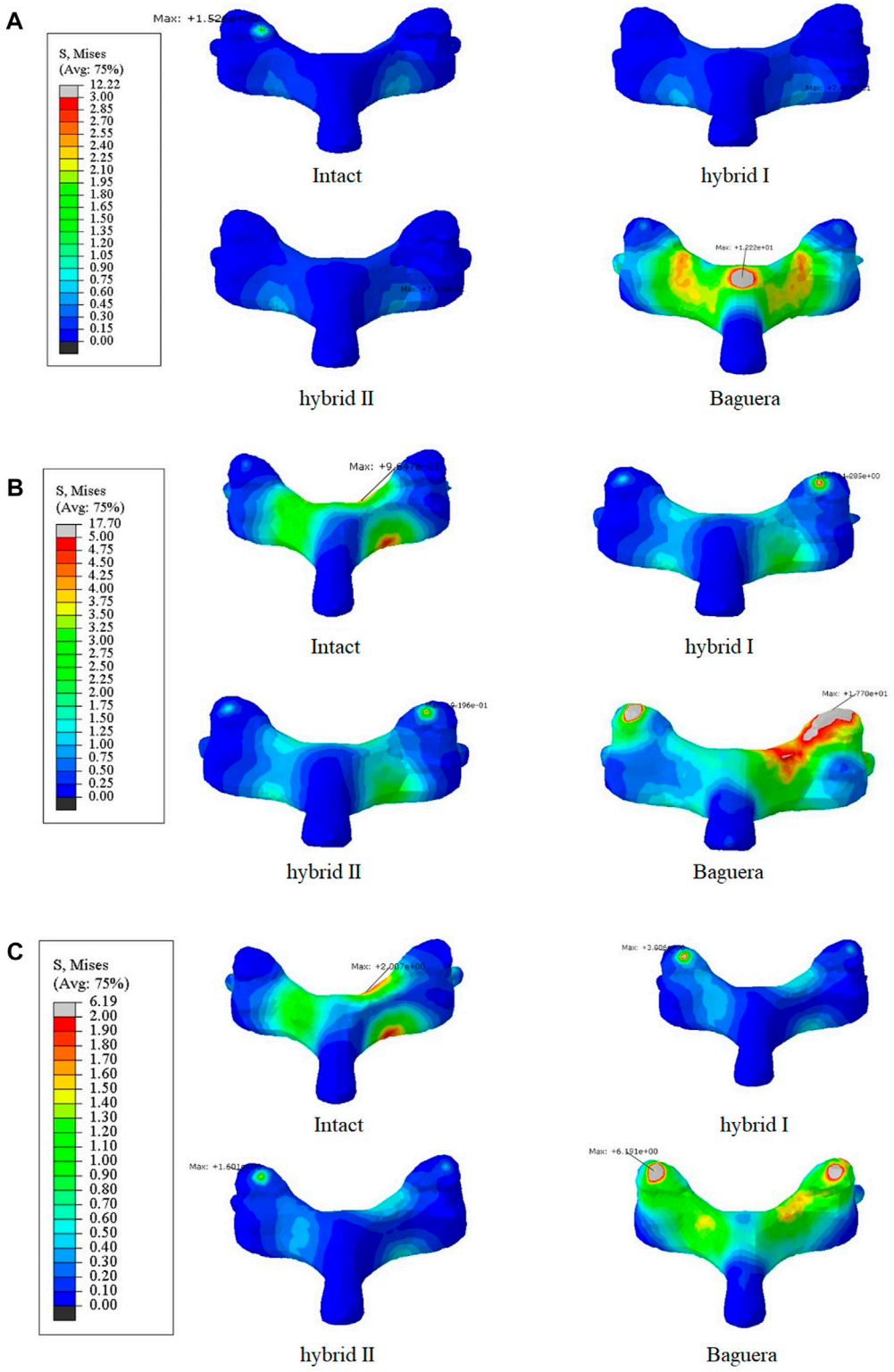

FIGURE 11
Von Mises stress distributions on the facet joints for the intact, hybrid I, hybrid II and Baguera® C groups for three different motions: **(A)** extension, **(B)** lateral bending, and **(C)** axial rotation. (unit: MPa).

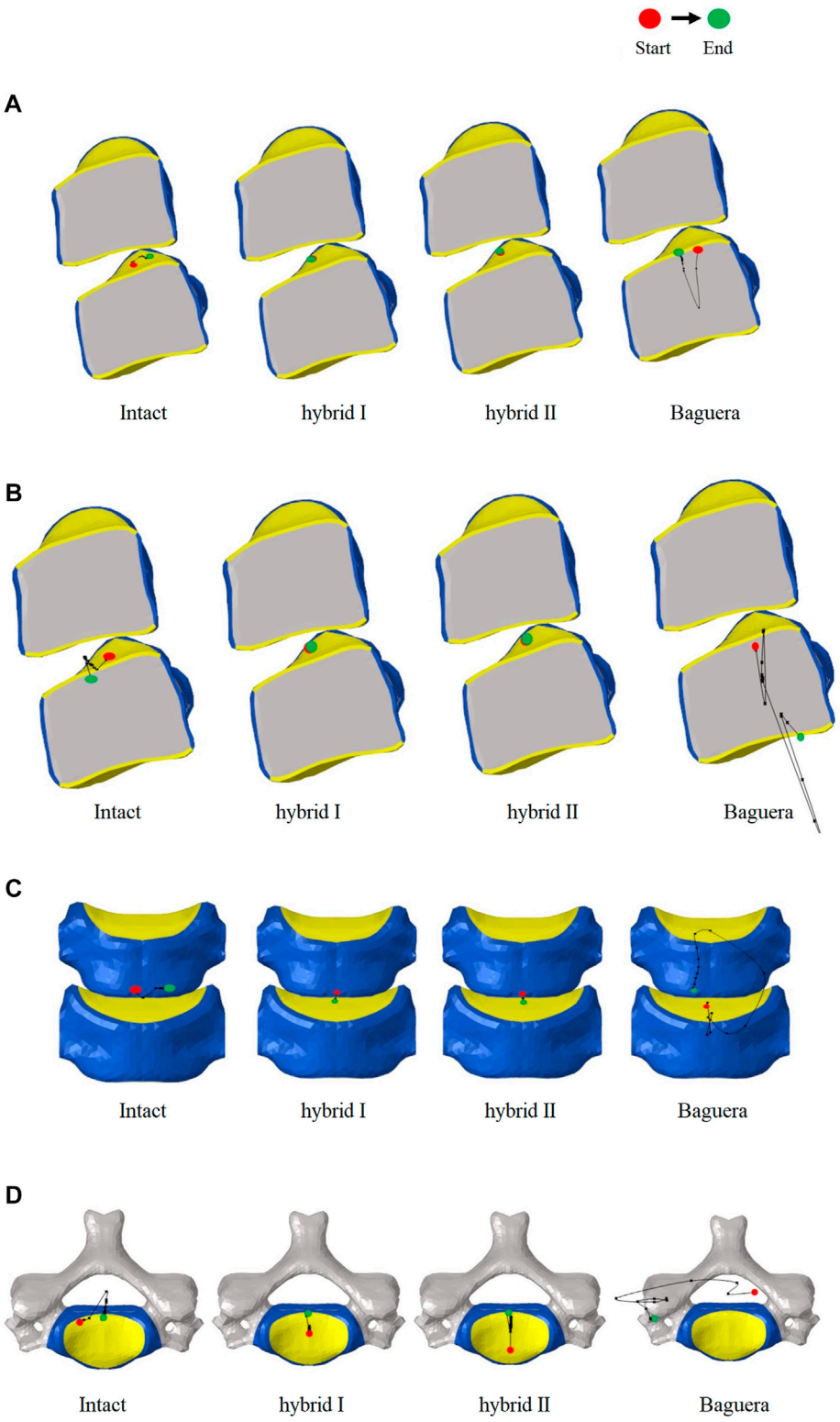

FIGURE 12
Paths of ICR for the intact, hybrid I, hybrid II and Baguera® C groups for different motions: **(A)** flexion, **(B)** extension, **(C)** lateral bending, and **(D)** axial rotation.

group, obvious anterior shift of the ICR in flexion, posterior-inferior shift in extension, and deviated and irregular movements in lateral bending and axial rotation were recorded.

Discussion

As observed in the literature, total disc replacement at the C5–C6 segment with a non-articulating prosthesis, such as the M6 cervical disk prosthesis (Spinal Kinetics, Sunnyvale, CA, United States) with PCU core and PE fiber to mimic normal disc anatomy, has been proven clinically to be a superior alternative because of the benefits of maintaining ROM and smaller heterotopic ossification rate (Patwardhan et al., 2012; Phillips et al., 2021; Oltulu et al., 2019). The kinematic response and postoperative flexion/extension stiffness were proven to be biomechanically compatible with the intact motion segment. However, significantly greater stiffnesses in lateral bending and axial rotation were still obstacles (Patwardhan et al., 2012). Due to the load-bearing capabilities and complexity of motion exposure to daily activities, the importance of evaluating the material characteristics of the prosthesis intended to replace the disc cannot be underestimated. Furthermore, current failures associated with existing implants, such as heterotopic ossification, insufficient stiffness, dislocation, wear and improper ICR further buttress the need for assessing the mechanical behavior of a material proposed to replace the disc (Virk et al., 2021; Shen et al., 2021; Shen et al., 2022; Cao et al., 1976; Parish et al., 2020). Thus, an appropriate material attribute design using a PE core and PCU fiber jacket with adequate native geometry could represent a suitable candidate for replacing the disc. polycarbonate urethane (PCU) could be customized and adapted based on a suitable choice of reinforcement fiber, and the property of fiber-reinforced composite enabled the load-bearing nucleus from dislocation and have been applied in joint replacement (Inyang and Vaughan, 2020; Ford et al., 2018). Biomechanical properties such as modulus of elasticity compatible to the annulus fibrosus make PCU a more suitable surrounding fiber candidate than PE.

Lattice structures have become a key factor for AM prostheses since AM processes enable the fabrication of cellular materials with complex microstructures and mimic disc spatial biomechanical behavior (dellaRipa et al., 2021; Pan et al., 2020; Chen et al., 2017). Several lattice cell structures could be used in this study, including X, Star, Tesseract, Vintiles, Cross, and Octet. However, due to the potential for implant instability, lattice structures that exhibited stress over-concentration at the implant endplate in X and Vintiles, as well as a micro-buckling effect under compressive loads in Octet, were excluded. Ultimately, the Tesseract (Hybrid I group) and Cross (Hybrid II group) structures were selected for analysis due to their stable and nonlinear mechanical properties, as well as their ability to mimic the biomechanical behavior of natural discs (Weeger et al., 2019). Because the material properties of the annulus fibrosus were varied linearly in the circumferential and radial directions histologically (Zhu et al., 2008), the circumferential area of the PCU fiber jacket was divided into three different regions, and the cellular density was adjusted. According to the biomechanical performance in the range of motion under various loadings compared to the intact disc, the optimal cellular densities were A2L5P2 from the Hybrid I group and A2L7P3 from the Hybrid II group. From the values and distributions of von Mises stress of both chosen Hybrid groups, the Hybrid II group showed more symmetric and lower stress than the Hybrid I group. The Tesseract structure in the Hybrid I group was the four-dimensional analog of a cube and lacked the ability to resist torsion due to vertical alignment, whereas the Cross structure in the Hybrid II group absorbed direct force and efficiently buffered the impact. In Figure 6, a Cross structure with smaller size than the Tesseract structure was made by the innate programed lattice structure, which induced greater cellular density in the Hybrid II group than the Hybrid I group and thus, more even stress distribution was found in the Hybrid II group.

The main purpose of this finite element study was to investigate the biomechanical performance of the newly designed additively manufactured hybrid TDR and compare it to the performance of the Baguera®C prosthesis with downward mobile core under loadings that simulated the daily activities of patients by imposing a pure moment of 1.5 Nm combined with a follower load of 100 N. Our data showed a difference in the lateral bending and axial rotation at C5/C6 compared to a previous *in vivo* study using ten young asymptomatic adults, which reported values of 6.11 and 3.01°, respectively (Lin et al., 2014). It should be noted that the *in vivo* study measured dynamic cervical intervertebral ROMs during active motion in the sitting position, while our study imposed a pure moment and a follower load passively. However, the ROMs of our intact C5-C6 FE model were comparable to previously obtained experimental data using the same moment and follower load (Finn et al., 2009; Purushothaman et al., 2020).

From the results for each implant group, both hybrid groups underwent similar ROMs and had core stress distributions similar to that of the intact group in contrast to the Baguera®C group (Figures 8, 9). The deformation property of the intervertebral disc allowed flexibility under smaller loadings and restricted excessive motion under larger loadings. TDRs with ball-and-socket designs can theoretically provide benefits as movable articulating prostheses, but facts have shown that moments cannot be constrained in flexion, lateral bending or axial rotation. The Baguera®C disc prosthesis had been proven to have stiffness similar to that of the intact disc and mobile core design in contrast to prostheses with other ball-and-socket designs (Kamal and Rouhi, 2016a), but they still showed obviously higher ROM values than our two hybrid groups.

One of the major complications of current commercial TDR designs is subsidence resulting from interfacial stress concentration on the bony endplate. Anchorage of ball-and-socket TDR using central fins or teeth might cause higher stress concentrations, thus initiating stress shielding and bone resorption (Lin et al., 1976). Another reason for subsidence is hypermobility, which causes excessive strain over the facet joint and surrounding capsular ligaments and indirectly increases stress over the anchorage area between the prosthesis and bone (Kerferd et al., 2017; Matgé et al., 2015). The C6 vertebral superior endplate stress was focused unevenly and mostly on the central regions in the Baguera group but was evenly distributed in the peripheral region of both hybrid groups in all ROMs (Figure 10). The top and bottom boundaries of both hybrid groups were chosen to conform evenly to the vertebral endplates with stainless steel. The nonlinear behavior of the lattice structure arrangement in the PCU fiber jacket can resist compression, constrain expansion and dissipate the concentrated load.

In extension, lateral bending and axial rotation, both the hybrid I and hybrid II groups showed facet stress distributions similar to that of the intact group (Figure 11). In the Baguera®C group, stress focused on the lamina in extension, unilateral facet in lateral bending and both facets in axial rotation due to the lack of a constraint of the artificial annulus fibrosus, which was compatible with other finite element studies (Rong et al., 1976). Increased facet joint stress after ball-and-socket TDR has been discussed as a reason for degenerative changes at the surgical level and leads to poor clinical results (Rong et al., 1976; Rousseau et al., 1976; Wang et al., 2021). Rousseau et al. showed an increase in facet stress from 18% to 86% with increasing load from 0.8 to 1.6 Nm in a FE model and recommended posterior implantation of a larger radius prosthesis to diminish the elevated stress (Rousseau et al., 1976). Gandhi et al. compared two TDRs (Bryan and Prestige LP) in the C2-T1 reconstructed finite element model and found that the facet contact force increased by 50%–100% compared with the intact disc in the C5-6 operated level (Rong et al., 1976). Wang et al. measured the facet pressure in six C5-C6 cadaveric spines implanted with different sizes of ball-and- socket TDRs and found significantly elevated facet joint pressures from 25.2 to 44.6 psi in flexion and from 58.9 to 90.3 psi with a 2 mm increment in prosthesis height (Wang et al., 2021). Improper positioning or size of the device and intrinsic design defects might have been the reasons for elevated stress. Elastomers including a polymer fiber jacket resulted in nonlinear behavior similar to that of an intact disc (van denBroek et al., 2012). This nonlinearity provides a neutral zone to protect surrounding tissues from high loading.

The ICR path has been proposed as an alternative to the ROM for evaluating the quality of spine movement and for identifying abnormal cervical spine kinematics. In normal discs, the average location of the ICR path was observed to be posterior to the geometric center of the inferior vertebral body and move anterior-posteriorly during flexion/extension (Anderst et al., 1976). The ICR location was not significantly affected superior-inferiorly during motion. In our study, the ICR paths of the Hybrid I and Hybrid II groups were similar to that of the intact group in all ROMs; however, in the Baguera group, an obvious anterior shift of the ICR in flexion, posterior-inferior shift in extension, and deviated and irregular movement of lateral bending and axial rotation were also observed. A systematic review showed that the ICR of ball-and-socket TDR tended to shift anteriorly or superiorly in finite element studies or *in vitro* biomechanical studies and may have been easily affected by the prosthesis implantation position (Patwardhan et al., 2012; Sang et al., 2020). The Baguera®C group, with a two-piece articulation design, constrained the ICR to the center of the radius of curvature of the prosthesis, and a downward center of rotation of Baguera®C caused ROMs to be more similar to the intact model than other implant design (Kowalczyk et al., 2011; Kamal and Rouhi, 2016a). In studies using ProDisc-C® (Synthes, West Chester, PA, United States), the ball on the lower endplate (possessing the same radius of curvature as the socket on the upper plate) provided an ICR at a more inferior location at the ROM. Studies comparing the sagittal kinematics of postoperative ICRs above the midline of the disc space with an upper-located ball design, Prestige LP®, and a lower-located design, ProDisc-C®, suggested that the location of postoperative ICR was strongly correlated with the artificial disc design, and neither design could not fully replicate the physiological ICR path (Rong et al., 1976).

In this study, we aimed to determine which additively manufactured hybrid group was a cervical joint prostheses that mimicked an intact disc and compared it to a commercial product for further clinical recommendation. There were some limitations in our study. First, certain assumptions were made in this parametrized finite element model, and an *in vivo* animal study should be performed for validation in the future. Second, more commercially available cervical joint prostheses, including one with a lower ball or a six-degree prosthesis with a PCU core and PE fiber design, are still needed to make a comprehensive comparison. Third, partial ALL or PLL should be removed to reveal the clinical operative segment. Finally, a longer cervical segment could be created for further evaluation of adjacent segment stress and degeneration.

Conclusion

Ranges of motion and core stresses similar to those of the intact group indicate the possible longevity of the proposed additively manufactured hybrid TDR. Lower endplate stress and facet force compared to those of the Baguera®C group offer a solution for preventing implant subsidence. The ICR path of the additively manufactured hybrid groups in all ROMs were similar to those of the intact disc and can restore normal cervical spine kinematics. Superior stress distribution of the PCU fiber jacket and core in the additively manufactured hybrid II group compared to the Hybrid I group revealed that the Cross lattice structure of the PCU fiber jacket could be a choice for a next-generation TDR. In summary, this promising outcome suggests the feasibility of implanting an additively manufactured multi-material artificial disc that allows for better physiological motion than the current ball-and-socket design.

Data availability statement

The original contributions presented in the study are included in the article/Supplementary Material, further inquiries can be directed to the corresponding author.

Author contributions

All authors listed have made a substantial, direct, and intellectual contribution to the work and approved it for publication.

Acknowledgments

The authors would like to acknowledge and thank the financial grant (109-2221-E-027-021-MY3) from National Science and Technology Council, Taiwan.

Conflict of interest

The authors declare that the research was conducted in the absence of any commercial or financial relationships that could be construed as a potential conflict of interest.

Publisher's note

All claims expressed in this article are solely those of the authors and do not necessarily represent those of their affiliated organizations, or those of the publisher, the editors and the reviewers. Any product that may be evaluated in this article, or claim that may be made by its manufacturer, is not guaranteed or endorsed by the publisher.

Supplementary material

The Supplementary Material for this article can be found online at: https://www.frontiersin.org/articles/10.3389/fbioe.2023.1182265/full#supplementary-material

References

Anderst, W., Baillargeon, E., Donaldson, W., Lee, J., and Kang, andJ. (1976). Motion path of the instant center of rotation in the cervical spine during *in vivo* dynamic flexion-extension: Implications for artificial disc design and evaluation of motion quality after arthrodesis. *Spine (Phila. pa.* 38 (10), E594–E601. doi:10.1097/BRS.0B013E31828CA5C7

Attaran, M. (2017). The rise of 3-D printing: The advantages of additive manufacturing over traditional manufacturing. *Bus. Horiz.* 60 (5), 677–688. doi:10.1016/j.bushor.2017.05.011

Bell, K. M., Yan, Y., Hartman, R. A., and Lee, J. Y. (2018). Influence of follower load application on moment-rotation parameters and intradiscal pressure in the cervical spine. *J. Biomech.* 76, 167–172. doi:10.1016/j.jbiomech.2018.05.031

Chen, T., Mueller, J., and Shea, K. (2017). Integrated design and simulation of tunable, multi-state structures fabricated monolithically with multi-material 3D printing. *Sci. Rep.* 7 (1), 45671–45678. doi:10.1038/srep45671

Chen, W. M., Jin, J., Park, T., Ryu, K. S., and Lee, S. J. (2018). Strain behavior of malaligned cervical spine implanted with metal-on-polyethylene, metal-on-metal, and elastomeric artificial disc prostheses – a finite element analysis. *Clin. Biomech.* 59, 19–26. doi:10.1016/J.CLINBIOMECH.2018.08.005

Choi, H., Purushothaman, Y., Baisden, J., and Yoganandan, N. (2020). Unique biomechanical signatures of bryan, prodisc C, and Prestige LP cervical disc replacements: A finite element modelling study. *Eur. Spine J.* 29 (11), 2631–2639, Nov. doi:10.1007/S00586-019-06113-Y

Claessens, T. (2017). Finding the location of the instantaneous center of rotation using a particle image velocimetry algorithm. *Am. J. Phys.* 85 (3), 185–192. doi:10.1119/1.4973427

Lin, C. Y., Kang, H., Rouleau, J. P., Hollister, S. J., and LaMarca, F., "Stress analysis of the interface between cervical vertebrae end plates and the Bryan, Prestige LP, and ProDisc-C cervical disc prostheses: An *in vivo* image-based finite element study," *Spine (Phila. pa.* 1976)., vol. 34, no. 15, pp. 1554–1560, Jul. doi:10.1097/BRS.0b013e3181aa643b

della Ripa, M., Paolino, D. S., Amorese, A., and Tridello, A., "Numerical modelling of the mechanical response of lattice structures produced through AM," *Procedia Struct. Integr.*, vol. 33, no., pp. 714–723. 2021. doi:10.1016/j.prostr.2021.10.079

Findlay, C., Ayis, S., and Demetriades, A. K. (2018). Total disc replacement versus anterior cervical discectomy and fusion. *Bone Jt. J.* 100B (8), 991–1001. doi:10.1302/0301-620X.100B8.BJJ-2018-0120.R1

Finn, M. A., Brodke, D. S., Daubs, M., Patel, A., and Bachus, K. N. (2009). Local and global subaxial cervical spine biomechanics after single-level fusion or cervical arthroplasty. *Eur. Spine J.* 18 (10), 1520–1527. doi:10.1007/S00586-009-1085-7

Ford, A. C., Gramling, H., Li, S. C., Sov, J. V., Srinivasan, A., and Pruitt, L. A. (2018). Micromechanisms of fatigue crack growth in polycarbonate polyurethane: Time dependent and hydration effects. *J. Mech. Behav. Biomed. Mat.* 79, 324–331. doi:10.1016/J.JMBBM.2018.01.008

Galbusera, F., Bellini, C. M., Raimondi, M. T., Fornari, M., and Assietti, R. (2008). Cervical spine biomechanics following implantation of a disc prosthesis. *Med. Eng. Phys.* 30 (9), 1127–1133, Nov. doi:10.1016/J.MEDENGPHY.2008.02.002

Gutiérrez, H. R. (2020). Two-dimensional layered materials offering expanded applications in flatland. *ACS Appl. Nano Mat.* 3 (7), 6134–6139, Jul. doi:10.1021/ACSANM.0C01763

Schmidt, H., Heuer, F., Simon, U., Kettler, A., Rohlmann, A., Claes, L., et al. 2006 Application of a new calibration method for a three-dimensional finite element model of a human lumbar annulus fibrosus," *Clin. Biomech. (Bristol, Avon)*, vol. 21, no. 4, pp. 337–344. doi:10.1016/J.CLINBIOMECH.2005.12.001

Inyang, A. O., and Vaughan, C. L., "Functional characteristics and mechanical performance of PCU composites for knee meniscus replacement," *Mat. (Basel, Switz.*, vol. 13, no. 1886, 2020. doi:10.3390/MA13081886

Jacobs, E., Roth, A. K., Arts, J. J., vanRhijn, L. W., and Willems, P. C., "Reduction of intradiscal pressure by the use of polycarbonate-urethane rods as compared to titanium rods in posterior thoracolumbar spinal fixation," *J. Mat. Sci. Mat. Med.*, vol. 28, no. 148, 2017. doi:10.1007/S10856-017-5953-0

Kamal, Z., and Rouhi, G. (2016). A parametric investigation of the effects of cervical disc prostheses with upward and downward nuclei on spine biomechanics. *J. Mech. Med. Biol.* 16, 1650092. doi:10.1142/S0219519416500925

Kerferd, J. W., Abi-Hanna, D., Phan, K., Rao, P., and Mobbs, R. J. (2017). Focal hypermobility observed in cervical arthroplasty with Mobi-C. *J. Spine Surg.* 3 (4), 693–696. doi:10.21037/JSS.2017.08.19

Kim, D., Lim, J. Y., Shim, K. W., Han, J. W., Yi, S., Yoon, D. H., et al. (2017). Sacral reconstruction with a 3D-printed implant after hemisacrectomy in a patient with sacral osteosarcoma: 1-Year follow-up result. *Yonsei Med. J.* 58 (2), 453–457. doi:10.3349/YMJ.2017.58.2.453

Kim, S. H., Ham, D. W., Lee, J. I., Park, S. W., Ko, M. J., Koo, S. B., et al. (2019). Locating the instant center of rotation in the subaxial cervical spine with biplanar fluoroscopy during *in vivo* dynamic flexion-extension. *CiOS Clin. Orthop. Surg.* 11 (4), 482–489. doi:10.4055/CIOS.2019.11.4.482

Kowalczyk, I., Lazaro, B. C. R., Fink, M., Rabin, D., and Duggal, andN. (2011). Analysis of *in vivo* kinematics of 3 different cervical devices: Bryan disc, ProDisc-C, and Prestige LP disc. Clinical article. *J. Neurosurg. Spine* 15 (6), 630–635. doi:10.3171/2011.8.SPINE11273

Kumar, R., Kumar, M., and Chohan, J. S. (2021). The role of additive manufacturing for biomedical applications: A critical review. *J. Manuf. Process.* 64, 828–850. doi:10.1016/j.jmapro.2021.02.022

Lin, C. C., Lu, T. W., Wang, T. M., Hsu, C. Y., Hsu, S. J., and Shih, T. F. (2014). *In vivo* three-dimensional intervertebral kinematics of the subaxial cervical spine during seated axial rotation and lateral bending via a fluoroscopy-to-CT registration approach. *J. Biomech.* 47 (13), 3310–3317, Oct. doi:10.1016/J.JBIOMECH.2014.08.014

Liu, J., Wang, R., Wang, H., Wang, Y., Lv, D., Diao, P., et al. (2020). Biomechanical comparison of a new memory compression alloy plate versus traditional titanium plate for anterior cervical discectomy and fusion: A finite element analysis. *Biomed. Res. Int.* 2020, 1–10. doi:10.1155/2020/5769293

Mackiewicz, A., Banach, M., Denisiewicz, A., and Bedzinski, R. (2016). Comparative studies of cervical spine anterior stabilization systems - finite element analysis. *Clin. Biomech.* 32, 72–79. doi:10.1016/j.clinbiomech.2015.11.016

Maconachie, T., Leary, M., Lozanovski, B., Zhang, X., Qian, M., Faruque, O., et al. (2019). SLM lattice structures: Properties, performance, applications and challenges. *Mat. Des.* 183 (Dec), 108137. doi:10.1016/j.matdes.2019.108137

Mahbod, M., and Asgari, M. (2019). Elastic and plastic characterization of a new developed additively manufactured functionally graded porous lattice structure: Analytical and numerical models. *Int. J. Mech. Sci.* 155, 248–266. doi:10.1016/j.ijmecsci.2019.02.041

Matgé, G., Berthold, C., Gunness, V. R. N., Hana, A., and Hertel, F. (2015). Stabilization with the dynamic cervical implant: A novel treatment approach following cervical discectomy and decompression. *J. Neurosurg. Spine* 22 (3), 237–245. doi:10.3171/2014.10.SPINE131089

Moroney, S. P., Schultz, A. B., Miller, J. A. A., and Andersson, G. B. J. (1988). Load-displacement properties of lower cervical spine motion segments. *J. Biomech.* 21 (9), 769–779. doi:10.1016/0021-9290(88)90285-0

Muhlbauer, M. K., Tomasch, E., Sinz, W., Trattnig, S., and Steffan, H., "Cervical disc prostheses need a variable center of rotation for flexion/extension below disc level, plus a separate COR for lateral bending above disc level to more closely replicate *in-vivo* motion: MRI-based biomechanical *in-vivo* study," *BMC Musculoskelet. Disord.*, vol. 23, no. 227, 2022. doi:10.1186/S12891-022-05121-2

Muhlbauer, M., Thomasch, E., Sinz, W., Trattnig, S., and Steffan, H. (2020). In cervical arthroplasty, only prosthesis with flexible biomechanical properties should be used for achieving a near-physiological motion pattern. *J. Orthop. Surg. Res.* 15 (1), 391. doi:10.1186/S13018-020-01908-Y

Oltulu, I., Korkmaz, Ö., Sarioğlu, E., and Aydoğan, M. (2019). A retrospective review of radiographic and clinical findings from the M6 cervical prosthesis. *Asian Spine J.* 13 (6), 913–919. doi:10.31616/ASJ.2018.0346

Pan, C., Han, Y., and Lu, J., "Design and optimization of lattice structures: A review," *Appl. Sci.* 2020, vol. 10, no. 18, p. 6374. doi:10.3390/APP10186374

Parish, J. M., Asher, A. M., and Coric, D. (2020). Complications and complication avoidance with cervical total disc replacement. *Int. J. Spine Surg.* 14, S50–S56. doi:10.14444/7091

Patwardhan, A. G., Tzermiadianos, M. N., Tsitsopoulos, P. P., Voronov, L. I., Renner, S. M., Reo, M. L., et al. (2012). Primary and coupled motions after cervical total disc replacement using a compressible six-degree-of-freedom prosthesis. *Eur. Spine J.* 21, 618–629. doi:10.1007/S00586-010-1575-7

Phan, K., Sgro, A., Maharaj, M. M., D'Urso, P., and Mobbs, R. J. (2016). Application of a 3D custom printed patient specific spinal implant for C1/2 arthrodesis. *J. spine Surg. Hong. Kong)* 2 (4), 314–318. doi:10.21037/JSS.2016.12.06

Phillips, F. M., Coric, D., Sasso, R., Lanman, T., Lavelle, W., Blumenthal, S., et al. (2021). Prospective, multicenter clinical trial comparing M6-C compressible six degrees of freedom cervical disc with anterior cervical discectomy and fusion for the treatment of single-level degenerative cervical radiculopathy: 2-year results of an FDA investigational device exemption study. *Spine J.* 21 (2), 239–252. doi:10.1016/J.SPINEE.2020.10.014

Puppi, D., and Chiellini, F., "Biodegradable polymers for biomedical additive manufacturing," *Appl. Mat. Today*, vol. 20, 100700, 2020. doi:10.1016/j.apmt.2020.100700

Purushothaman, Y., Yoganandan, N., Jebaseelan, D., Choi, H., and Baisden, J. (2020). External and internal responses of cervical disc arthroplasty and anterior cervical discectomy and fusion: A finite element modeling study. *J. Mech. Behav. Biomed. Mat.* 106, 103735. doi:10.1016/j.jmbbm.2020.103735

Rajakumar, D. V., Hari, A., Krishna, M., Konar, S., and Sharma, A. (2017). Adjacent-level arthroplasty following cervical fusion. *Neurosurg. Focus* 42 (2), E5. doi:10.3171/2016.11.FOCUS16412

Mobbs, R. J., Coughlan, M., Thompson, R., Sutterlin, C. E., and Phan, K., "The utility of 3D printing for surgical planning and patient-specific implant design for complex spinal pathologies: Case report," *J. Neurosurg. Spine*, vol. 26, no. 4, pp. 513–518.2017. doi:10.3171/2016.9.SPINE16371

Rousseau, M. A., Bonnet, X., and Skalli, W., "Influence of the geometry of a ball-and-socket intervertebral prosthesis at the cervical spine: A finite element study.," *Spine (Phila. pa.* 1976)., vol. 33, no. 1, pp. E10–E14. doi:10.1097/BRS.0B013E31815E62EA

Saifi, C., Fein, A. W., Cazzulino, A., Lehman, R. A., Phillips, F. M., An, H. S., et al. (2018). Trends in resource utilization and rate of cervical disc arthroplasty and anterior cervical discectomy and fusion throughout the United States from 2006 to 2013. *Spine J.* 18 (6), 1022–1029, Jun. doi:10.1016/j.spinee.2017.10.072

Sang, H., Cui, W., Sang, D., Guo, Z., and Liu, B. (2020). How center of rotation changes and what affects these after cervical arthroplasty: A systematic review and meta-analysis. *World Neurosurg.* 135, e702–e709. –e709. doi:10.1016/j.wneu.2019.12.111

Bhattacharya, S., Roy, S., Rana, M., Banerjee, S., Karmakar, S. K., and Biswas, K., "Biomechanical performance of A modified design of dynamic cervical implant compared to conventional ball and socket design of an artificial intervertebral disc implant: A finite element study," *J. Mech. Med. Biol.*, vol. 19, no. 1950017.2019. doi:10.1142/S0219519419500179

Cao, S., Zhao, Y., Sun, Y., Li, W., Zhou, F., Zhang, F., et al. Single-level cervical arthroplasty with prodisc-C vivo artificial disc: Five-year follow-up results from one center," *Spine (Phila. pa.* 1976)., vol. 47, no. 2, pp. 122–127. doi:10.1097/BRS.0000000000004119

Yang, S. D., Zhu, Y. B., Yan, S. Z., Di, J., Yang, D. L., and Ding, W. Y., "Anterior cervical discectomy and fusion surgery versus total disc replacement: A comparative study with minimum of 10-year follow-up," *Sci. Rep.*, vol. 7, no. 164432017. doi:10.1038/S41598-017-16670-1

Shen, Y.-W., Yang, Y., Liu, H., Wang, B. Y., Ding, C., Meng, Y., et al. (2022). The effect of preoperative cervical spondylosis on heterotopic ossification after cervical disc replacement. *Glob. spine J.* 2022, 219256822210942. doi:10.1177/21925682221094265

Siu, T. L., Rogers, J. M., Lin, K., Thompson, R., and Owbridge, M. (2018). Custom-made titanium 3-dimensional printed interbody cages for treatment of osteoporotic fracture-related spinal deformity. *World Neurosurg.* 111, 1–5. doi:10.1016/J.WNEU.2017.11.160

Tancogne-Dejean, T., Spierings, A. B., and Mohr, D. (2016). Additively-manufactured metallic micro-lattice materials for high specific energy absorption under static and dynamic loading. *Acta Mater* 116, 14–28. doi:10.1016/j.actamat.2016.05.054

Teraguchi, M., Yoshimura, N., Hashizume, H., Muraki, S., Yamada, H., Minamide, A., et al. (2014). Prevalence and distribution of intervertebral disc degeneration over the entire spine in a population-based cohort: The wakayama spine study. *Osteoarthr. Cartil.* 22 (1), 104–110. doi:10.1016/J.JOCA.2013.10.019

Toosizadeh, N., and Haghpanahi, M. (2011). Generating a finite element model of the cervical spine: Estimating muscle forces and internal loads. *Sci. Iran.* 18 (6), 1237–1245. doi:10.1016/J.SCIENT.2011.10.002

van denBroek, P. R., Huyghe, J. M., Wilson, W., and Ito, K. (2012). Design of next generation total disk replacements. *J. Biomech.* 45 (1), 134–140. doi:10.1016/J.JBIOMECH.2011.09.017

Venegas, W., Inglés, M., Page, Á., and Serra-Añó, P. (2020). Paths of the cervical instantaneous axis of rotation during active movements—Patterns and reliability. *Med. Biol. Eng. Comput.* 58 (5), 1147–1157. doi:10.1007/S11517-020-02153-5

Virk, S., Phillips, F., Khan, S., and Qureshi, S. (2021). A cross-sectional analysis of 1347 complications for cervical disc replacements from medical device reports maintained by the United States Food and Drug Administration. *Spine J.* 21 (2), 265–272. doi:10.1016/j.spinee.2020.09.005

Weeger, O., Boddeti, N., Yeung, S. K., Kaijima, S., and Dunn, M. L. (2019). Digital design and nonlinear simulation for additive manufacturing of soft lattice structures. *Addit. Manuf.* 25, 39–49. doi:10.1016/J.ADDMA.2018.11.003

Wheeldon, J. A., Stemper, B. D., Yoganandan, N., and Pintar, F. A. (2008). Validation of a finite element model of the young normal lower cervical spine. *Ann. Biomed. Eng.* 36 (9), 1458–1469, Sep. doi:10.1007/S10439-008-9534-8

Whyne, C. M., Hu, S. S., and Lotz, J. C. (2001). Parametric finite element analysis of verterbral bodies affected by tumors. *J. Biomech.* 34 (10), 1317–1324, Oct. doi:10.1016/S0021-9290(01)00086-0

wonKwon, J., Bang, S. H., Park, T. H., Lee, S. J., Lee, H. M., Lee, S. B., et al. (2020). Biomechanical comparison of cervical discectomy/fusion model using allograft spacers between anterior and posterior fixation methods (lateral mass and pedicle screw). *Clin. Biomech.* 73, 226–233. doi:10.1016/j.clinbiomech.2020.01.018

Wang, X. F., Meng, Y., Liu, H., Wang, B. Y., and Hong, Y., "The impact of different artificial disc heights during total cervical disc replacement: An *in vitro* biomechanical study," *J. Orthop. Surg. Res.*, vol. 16, no. 12, 2021. doi:10.1186/S13018-020-02157-9

Rong, X., Gong, Q., Liu, H., Hong, Y., Lou, J., Wu, W., et al. The effect of deviated center of rotation on flexion-extension range of motion after single-level cervical arthroplasty," *Spine (Phila. pa.* 1976)., vol. 39, pp. B12–B18. doi:10.1097/BRS.0000000000000634

Shen, Y. W., Yang, Y., Liu, H., Rong, X., Ding, C., Meng, Y., et al. Effects of endplate coverage and intervertebral height change on heterotopic ossification following cervical disc replacement," *J. Orthop. Surg. Res.*, vol. 16, no. 693, 2021. doi:10.1186/s13018-021-02840-5

Zhang, Q. H., Teo, E. C., Ng, H. W., and Lee, V. S. (2006). Finite element analysis of moment-rotation relationships for human cervical spine. *J. Biomech.* 39 (1), 189–193. doi:10.1016/j.jbiomech.2004.10.029

Zhu, D., Gu, G., Wu, W., Gong, H., Zhu, W., Jiang, T., et al. (2008). Micro-structure and mechanical properties of annulus fibrous of the L4-5 and L5-S1 intervertebral discs. *Clin. Biomech.* 23, S74–S82. SUPLL.1. doi:10.1016/J.CLINBIOMECH.2008.04.007

Kamal, Z., and Rouhi, G., "A parametric investigation of the effects of cervical disc prostheses with upward and downward nuclei on spine biomechanics," *J. Mech. Med. Biol.*, vol. 16, no. 1650092, 2016. doi:10.1142/S0219519416500925

frontiers | Frontiers in Bioengineering and Biotechnology

TYPE Original Research
PUBLISHED 14 June 2023
DOI 10.3389/fbioe.2023.1199944

OPEN ACCESS

EDITED BY
Cheng-Feng Lin,
National Cheng Kung University, Taiwan

REVIEWED BY
Yuqi He,
University of Pannonia, Hungary
William Dias Belangero,
State University of Campinas, Brazil

*CORRESPONDENCE
Yangyang Xu,
youngerxv@buaa.edu.cn
Ruijiang Wang,
15635580115@163.com
Fei Tian,
999tianfei99@sina.com

†These authors share first authorship

RECEIVED 04 April 2023
ACCEPTED 06 June 2023
PUBLISHED 14 June 2023

CITATION
Wei G, Niu X, Li Y, Chang T, Zhang J, Wang H, Li X, He Y, Wang R, Tian F and Xu Y (2023), Biomechanical analysis of internal fixation system stability for tibial plateau fractures.
Front. Bioeng. Biotechnol. 11:1199944.
doi: 10.3389/fbioe.2023.1199944

Biomechanical analysis of internal fixation system stability for tibial plateau fractures

Guoqiang Wei[1†], Xiaofen Niu[1†], Yuan Li[2], Tingjie Chang[2], Jianfang Zhang[1], Haiyan Wang[3], Xiaohe Li[3], Yujie He[3], Ruijiang Wang[4*], Fei Tian[5,6*] and Yangyang Xu[7*]

[1]Department of Rehabilitation Medicine, Changzhi Medical College Affiliated Changzhi People's Hospital, Changzhi, China, [2]Department of Orthopedics, Changzhi Medical College Affiliated Peace Hospital, Changzhi, China, [3]Department of Anatomy, School of Basic Medical Sciences, Inner Mongolia Medical University, Hohhot, China, [4]Department of Orthopedics, Changzhi Second People's Hospital, Changzhi, China, [5]Department of Health Management, Changzhi Medical College, Changzhi, China, [6]Department of Rehabilitation Medicine, Changzhi Medical College Affiliated Peace Hospital, Changzhi, China, [7]Beijing Key Laboratory for Design and Evaluation Technology of Advanced Implantable and Interventional Medical Devices, Beijing Advanced Innovation Center for Biomedical Engineering, School of Biological Science and Medical Engineering, Beihang University, Beijing, China

Background: Complex bone plateau fractures have been treated with bilateral plate fixation, but previous research has overemphasized evaluating the effects of internal fixation design, plate position, and screw orientation on fracture fixation stability, neglecting the internal fixation system's biomechanical properties in postoperative rehabilitation exercises. This study aimed to investigate the mechanical properties of tibial plateau fractures after internal fixation, explore the biomechanical mechanism of the interaction between internal fixation and bone, and make suggestions for early postoperative rehabilitation and postoperative weight-bearing rehabilitation.

Methods: By establishing the postoperative tibia model, the standing, walking and running conditions were simulated under three axial loads of 500 N, 1000 N, and 1500 N. Accordingly, finite element analysis (FEA) was performed to analyze the model stiffness, displacement of fractured bone fragments, titanium alloy plate, screw stress distribution, and fatigue properties of the tibia and the internal fixation system under various conditions.

Results: The stiffness of the model increased significantly after internal fixation. The anteromedial plate was the most stressed, followed by the posteromedial plate. The screws at the distal end of the lateral plate, the screws at the anteromedial plate platform and the screws at the distal end of the posteromedial plate are under greater stress, but at a safe stress level. The relative displacement of the two medial condylar fracture fragments varied from 0.002–0.072 mm. Fatigue damage does not occur in the internal fixation system. Fatigue injuries develop in the tibia when subjected to cyclic loading, especially when running.

Conclusion: The results of this study indicate that the internal fixation system tolerates some of the body's typical actions and may sustain all or part of the weight early in the postoperative period. In other words, early rehabilitative exercise is recommended, but avoid strenuous exercise such as running.

KEYWORDS

biomechanical study, finite element analysis, internal fixation, tibial plateau fracture, weight bearing, interfragmentary motion

1 Introduction

The optimal treatment of complicated bicondylar tibial plateau fractures has been a source of contention for decades (McNamara et al., 2015), and bicondylar tibial plateau fractures provide several challenges to surgical treatment techniques. To achieve appropriate bone consolidation, surgical implants must offer mechanical stability at the fracture location. As a result, during the healing process, the internal fixation operation should give the best possible placement and fixation of the bone fragment (Bucholz et al., 2010). Bilateral plate fixation is a well-known therapeutic technique with strong biomechanical stability (Lee et al., 2013; Lee et al., 2018). An analysis of complicated Schatzker V/VI fractures revealed that coronal posteromedial split fragments occurred in 28%–74% of cases (Barei et al., 2008; McGonagle et al., 2019), requiring separate posterior fixing (Samsami et al., 2020). In complicated tibial plateau fractures, the incidence and consequent displacement of posteromedial split pieces are commonly underestimated (Hua et al., 2019). The fracture pattern of complicated bicondylar tibial fractures is characterized by a combination of medial coronal and lateral multifragment depression fractures (Eggli et al., 2008). The treatment of tibial plateau fractures needs to be carried out with stable fixation to allow early mobility. The mechanical environment is an essential factor in fracture healing. Surgeons often prescribe a 6- to 8- week non-weight-bearing period following surgery (Burdin, 2013). This time of non-weight-bearing significantly hinders the patient's function, potentially delaying the outcome and increasing healthcare expenditures. Finally, a lack of mechanical stress in the knee joint may have an impact on the articular cartilage. During short-term reduced loading conditions there was a significant degree of cartilage thinning; in other words, the cartilage underwent some process of atrophy without mechanical stimulation (Eckstein et al., 2006). Previous research has overemphasized the effects of internal fixation design, plate position, and screw orientation on fracture fixation stability (Chen et al., 2017; Djuricic et al., 2022; Ren et al., 2022). However, the biomechanical environment and intensity of postoperative weight-bearing exercise training in complex tibial plateau fractures remain unknown, and more attention should be paid to the biomechanical characteristics of complex tibial plateau fractures postoperatively.

The AO/OTA classification and the Schatzker classification are the most commonly used fracture classifications. Maurice Muller, one of the founders of the Swiss AO/ASIF (Association for the Study of Internal Fixation), established the Comprehensive Classification of Fractures of the Long Bones, which describes the site, morphology, and severity of long bone fractures through a combination of letters and numbers. The American OTA (the Orthopaedic Trauma Association) adopted Professor Muller's classification system for long bone fractures and applied its classification method and principles to other bones throughout the body to form the AO/OTA fracture classification system. The principles of AO/OTA fracture classification, in general, follow Muller's principles of long bone fracture classification. By typing, grouping and subgrouping, fractures of one site or segment can have 27 subgroups. Schatzker typing is a proposed six-class classification based on the radiographic plain view of tibial plateau fractures. The strategies for reconstruction of the tibial plateau depend on the fracture lines identified in the preoperative CT scan. The established fracture classifications cannot be used for the definition of operative treatment algorithms for contemporary fracture management. In contrast, these classifications do not consider the 3D manifestation of the fracture offered by CT imaging. Its insufficiency has led to criticism of the idea of treating bicondylar tibial plateau fractures in the context of posteromedial coronal fractures (Pätzold et al., 2017). According to Samsami et al. (2020), the posteromedial split fragment has a significant biomechanical role in the structural rigidity of bicondylar tibial plateau fractures. Therefore, to conceptually comprehend the biomechanical principles of anteromedial fracture block and posteromedial fractured bone fragment fixation, a fracture model is required. Titanium alloy plates and screws serving as the primary biomechanical load-bearing mechanisms are used in the model, which is based on a genuine case with a typical fracture.

This study analyzed the biomechanical characteristics of a bilateral plate fixation method used to treat bicondylar tibial plateau fractures using FEA. The stability of the internal fixation system, the risk of implant failure, and the risk of fracture instability were evaluated under different motion conditions based on the interaction with the mechanical environment. The mechanical behavior of the fractured tibial plateau stability was determined in this way. The model stiffness, implant stress distribution, fracture block stress distribution, displacement distribution, and tibial and screw plate fatigue life were analyzed to assist surgeons and rehabilitation physicians in their evaluation. It is clinically relevant to explore the biomechanical environment features of internal fixation under three conditions common in standing, walking, and running using FEA. Exploring the biomechanical mechanism of the interaction between internal fixation and bone guides the timing of early postoperative rehabilitation. It provides a clinical reference for the stability of the internal fixation system and the safety of rehabilitation sports training after complex bicondylar tibial plateau fractures in the clinic. The use of digital medicine for fracture surgery and rehabilitation training guidance has been well integrated and tried, which is a worthy approach to promote.

2 Materials and methods

The research was approved by the Science and Ethics Committee of the School of Biological Science and Medical Engineering at Beihang University (protocol code: BM20220087).

2.1 Subject

A Schatzker type V fracture of the tibial plateau was reproduced using computer-aided-design (CAD) based on Computed

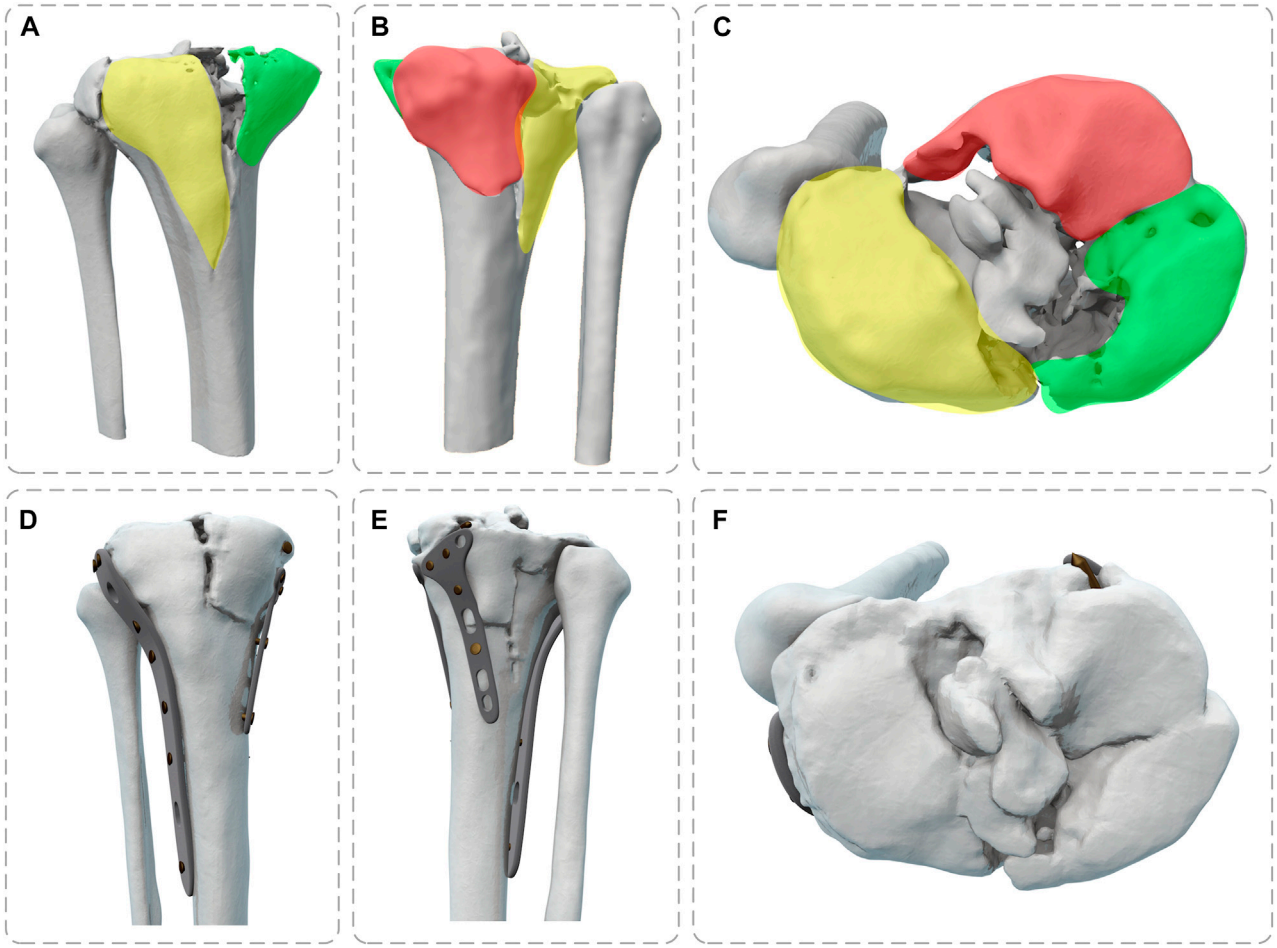

FIGURE 1
Full view of tibial plateau fracture before and after surgery (Yellow: lateral fracture block, Green: posteromedial fracture block, Red: posteromedial fracture block) **(A,D)** Front View; **(B,E)** Back View; **(C,F)** Top View.

Tomography (CT) images (female, 28 years old, height 164 cm, body weight 60 kg); the patient has signed an informed consent. This case is a typical fracture presentation and fits well with the research requirements. The surgeon removed the internal fixation from the patient 1.5 years after the surgery.

2.2 Surgical technique

The posteromedial incision of the right tibia revealed the fracture end. After the posterior bone block reduction, the Kirschner needle was temporarily fixed, the T-type plate was placed, and four-length screws were drilled in turn. The fractured end is reduced anteriorly at the medial plateau, and a moderate-length tension screw is placed anteriorly to posteriorly. The medial front fracture line is long, the 5-well bone plate is placed, and 4-length screws are drilled in turn. A curved incision was made through the middle and upper lateral segments (see the longitudinal fracture line of the right lateral tibial plateau), and plate was placed and drilled into the length screw fixation.

2.3 Creating the base model

Pre- and post-operative high-resolution CT scans of patients to obtain DICOM data (raw HD images from CT scanners) were imported into Mimics 21.0 (Materialise, Leuven, Belgium) to obtain the knee joint structure by threshold segmentation. The Schatzker type V fracture consists of a bicondylar fracture, and the tibial was divided into three fragments (Figure 1). The drawing of screws and plates was done in 3-Matic (Materialise, Leuven, Belgium). To obtain a high-quality tibia-fibula model, the model was processed in Geomagic Studio 2013 (Raindrop Geomagic Inc., Morrisville, NC, United States) for denoising, smoothing, and fitting the surface. The entire model meshed was created in Hypermesh (Altair Engineering Inc., Troy, MI, United States). Define material properties, set boundaries, loading conditions, and computational conditions, and complete the FEA in Abaqus (Simulia, Providence, Rhode Island, United States). Import the calculation file. odb into Fe-safe (Simulia, Providence, Rhode Island, United States) for fatigue life calculation (Figure 2).

To make the computation more precise, the threaded screws were simplified to smooth screws in this study, the screw holes of the

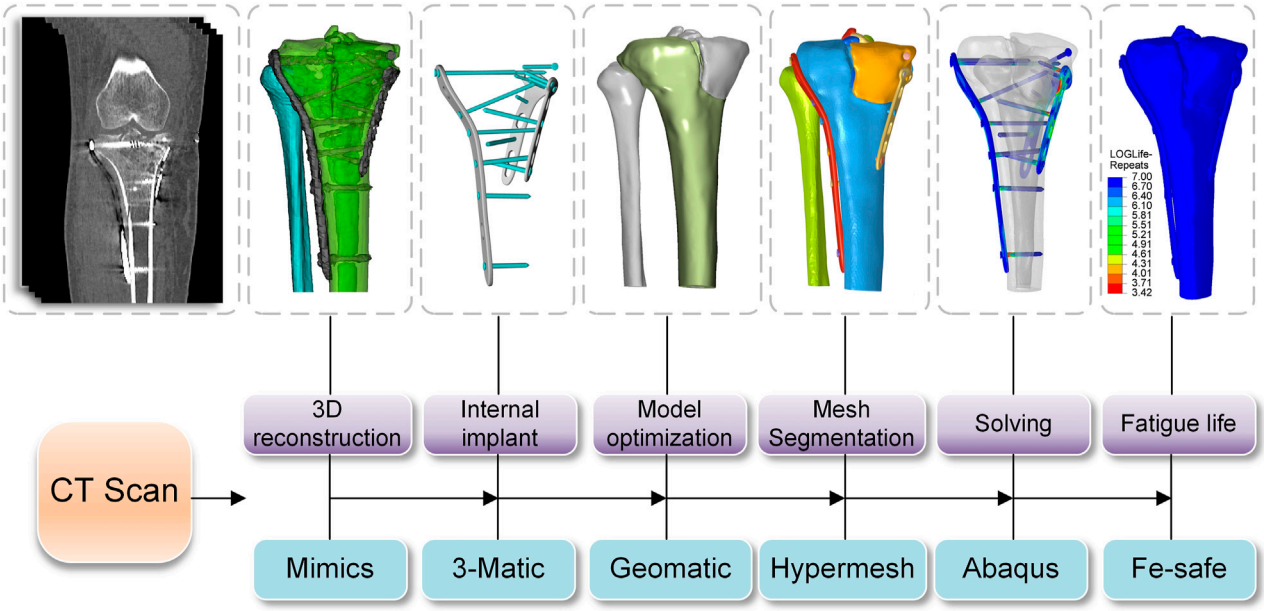

FIGURE 2
Flow chart of FEA experiments.

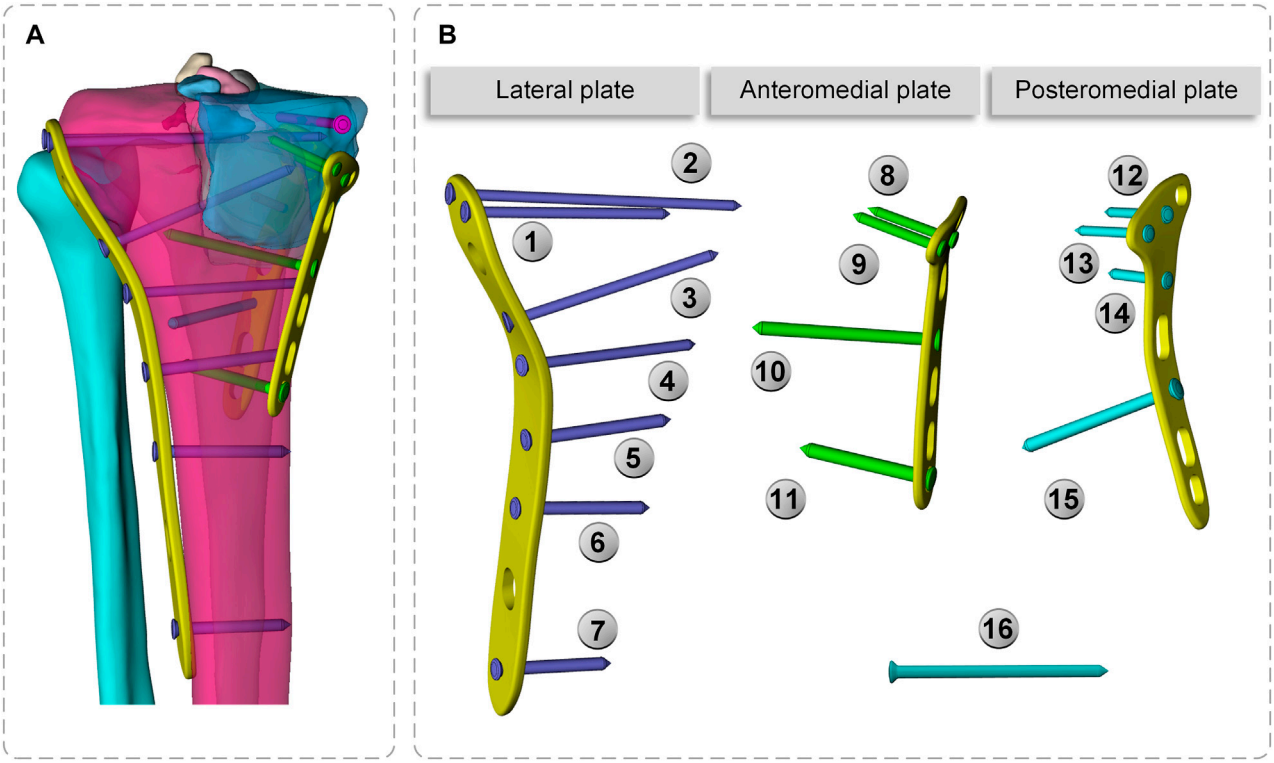

FIGURE 3
Final CAD models of the bone-implant sets. **(A)** 3D model **(B)** Plates and screws number.

steel plate were obtained using Boolean operations, and contact relations can be easily added (Ren et al., 2022; Zeng et al., 2022). The screws were numbered screws 1–16 (S1–S16), to assist in further analysis (Figure 3). Titanium alloy plate placement: along the longitudinal fracture line of the lateral tibial plateau, an osteotomy plate (lateral plate) was placed along the axial

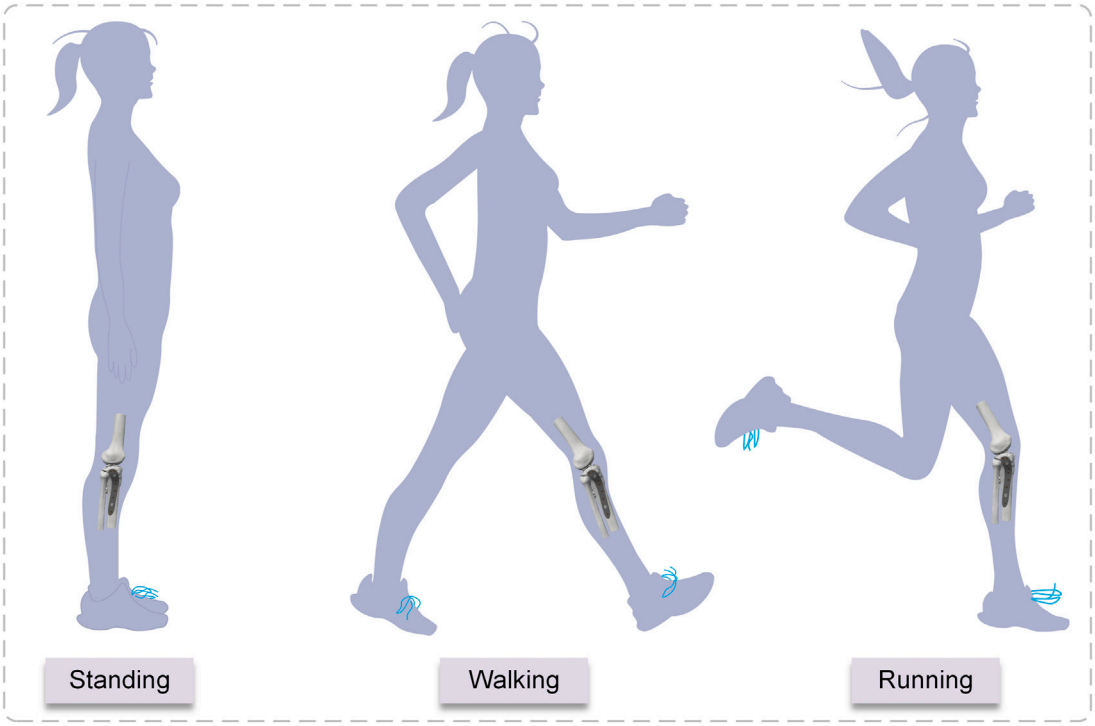

FIGURE 4
The three conditions of standing, walking, and running.

direction of the tibia. Along the anteromedial fracture line, a 5-hole osteotomy plate (posteromedial plate) was placed along the medial tibial condyle obliquely toward the anatomical axis of the tibia, and along the posteromedial fracture line, a T-shaped osteotomy plate (posteromedial plate) was placed along the medial tibial condyle obliquely toward the anatomical axis of the tibia. Screw S16 was a lag screw that was not attached to the plates. In this experiment, we ignored the components that influence knee joint stress, such as ligaments, muscles, and other soft tissues. The stiffness, stress, and displacement distributions of the fractured bone fragments and internal fixation system were determined for various motion states, and a comprehensive report was produced. Select the node with the largest tibial displacement value and plot the force-displacement curve to calculate the model stiffness value (Figure 5A). To achieve the main objective, the final relative displacement was evaluated in eight measurement points located at the fracture edge (Figure 8A). The magnitude of the relative displacement between the two relative nodes of the bone backbone and the fracture fragment was assessed at each site.

2.4 Loading conditions and boundary

The biomechanical load on the knee joint during normal gait is approximately two to three times the body weight (Taylor et al., 2004), and the percentage of load on the medial and lateral plateaus is approximately 55% and 45%, respectively (Zhao et al., 2007). When a healthy adult weighing 60 kg is standing, the pressure on the tibial plateau is 60 kg × 9.8 N/kg × 85.6% = 503.33 N (Gao et al., 2022). Walking and running generate two to three times the stress on the tibial plateau than standing (Tai et al., 2009). The majority of individuals spend their days standing, walking, and running. To simulate the stress condition of the tibial plateaus during standing, walking, and running in adults, three axial loads of 500, 1000, and 1500 N were chosen (Figure 4). Due to the incremental nature of the nonlinear analysis, the prescribed loads were applied to the structure in discrete increments. In this experiment, distributed coupling constraints were used to apply loads. Reference points were established medially and laterally on the tibial plateau, and then the reference point was coupled to the reference surface. An axial load was applied at the reference point. The fibula was bonded within the area of the proximal tibial of non-fractured bone by multi-point constraints (Wang et al., 2021). Fixed constraints of the distal tibia and distal fibula. The fractured bone fragments were designed to be frictionless, with a coefficient of friction of 0.3 between the implant and bone and the plate and screws (Koh et al., 2019; Dehoust et al., 2020). When the displacement under load is less than 2 mm, the bone is usually considered undamaged (Haller et al., 2015), and considering the brittle qualities of the material, cortical bone was defined as failing at pressures up to 115 Mpa (Consortium, 2014), and the screws and plates were of titanium alloy with a yield stress of 795 Mpa (Tian et al., 2018; Boluda-Mengod et al., 2021).

2.5 Adopted mesh and material properties

The mesh was tetrahedral; the mesh sensitivity analysis was performed under an axial load of 500 N and boundary conditions

TABLE 1 Material properties.

	Young modulus (MPa)	Poisson's ration
Cortical bone	E3 = 12,847	υ12 = 0.381
	E2 = 7,098	υ13 = 0.172
	E1 = 6,498	υ23 = 0.160
	G12 = 2,290	υ2 1 = 0.396
	G13 = 2,826	υ31 = 0.376
	G23 = 3,176	υ32 = 3.346
Cancellous bone	E3 = 370.6	υ12 = 0.381
	E2 = 123.4	υ13 = 0.104
	E1 = 123.4	υ23 = 0.104
	G12 = 44.84	υ21 = 0.381
	G13 = 58.18	υ31 = 0.312
	G23 = 58.18	υ32 = 0.312
Titanium alloy plate and screw	E = 110,000	υ = 0.3

(see Section 2.4). The final mesh size was obtained by adjusting the mesh size until the displacement value did not fluctuate by more than 1% (Belaid et al., 2018). The resulting mesh is a tetrahedral cell with an average size of 1.5–2 mm, which was consistent with previous research (Dehoust et al., 2020). The node and element numbers were 106,496 and 507,044, respectively. We assigned cortical and cancellous bone separately to the corresponding elastic, homogeneous, and orthotropic properties (Amini et al., 2015). The material properties of the other structures were assumed to have isotropic linear elasticity. Table 1 shows the material properties of all constructs and relevant literature sources.

2.6 Fatigue properties

The fatigue life analysis is based on static analysis, and the results of the static analysis are imported into Fe-safe software. The program defines fatigue damage as several cycles more than 10 to the power of 7 based on the stress amplitude and the estimated number of cycles that fatigue damage may occur. The stress field and strain field are calculated by Abaqus. The axial cyclic loads are set to 500, 1000, and 1500 N, the load amplitudes are set to 0 to +1, the material parameters are set to "E-N Curve," and the algorithm is selected as the maximum principal stress algorithm.

2.7 Validation of the model

The stiffness and Von Mises stress of the model were compared with the experimental data reported in previous studies to validate the plausibility of the model. Gao et al. (2022) showed that the max von Mises stress of the internal fixation system was 69.54, 112.10, and 155.71 MPa for the three conditions of 500, 1000, and 1500 N, respectively. Huang et al. (2015) showed that the maximal stress value in the plate-screw system was 256.20 MPa, while that of the screw was 225.12 MPa. In this study, the max von Mises stress of the plate was 201.52 MPa and the max von Mises stress of the screw was 197.73 MPa. Karunakar et al. (2002) measured stiffness of 2026–2666 N/mm by loading the knee joint after internal fixation. This study produced stiffness values of 2041–2129 N/mm for the model without internal fixation and 2,781–2,868/mm for the model with internal fixation. There were no significant differences in the data, proving that the model was reasonable.

3 Results

3.1 Stiffness

The stiffness of the tibia increased significantly after internal fixation by 738.57, 729.96, and 740.67 N/mm in the standing, walking, and running states, respectively. The stiffness values of the tibia did not vary significantly throughout sports (Figure 5B).

3.2 Von Mises stress distribution

3.2.1 Von Mises stress of plates

Under axial loads ranging from 500 to 1500 N, the stresses shared by the plates gradually increase. The anteromedial plate was most stressed, followed by the posteromedial plate, and the lateral plate primarily serves as a support (Figure 6B). The shape of the lateral plate is curved, and the stress cloud diagram shows that the stress of the lateral plate was mostly in the region of the concave edge, with a larger stress at the screw hole at the distal end. The forms of the anteromedial plate and posteromedial plate are T-shaped, and the stress was mostly in the corner of the near end of the plate, PII as a whole exhibits relatively high-stress conditions, but they do not reach the yield stress of titanium alloy and are in the safe stress range (Figure 7).

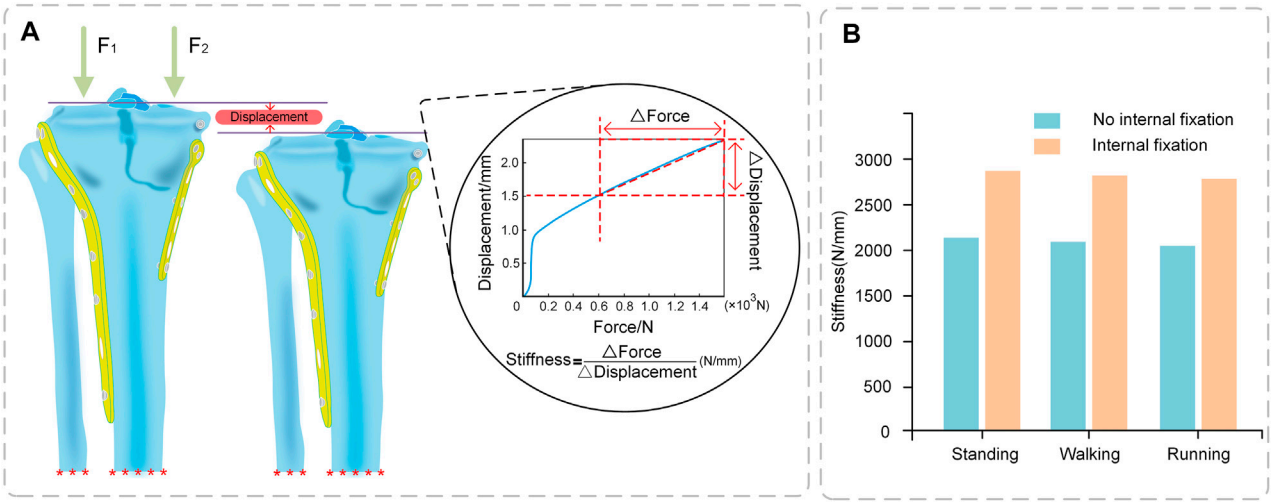

FIGURE 5
Stiffness of Tibia **(A)** Stiffness calculation (Force-displacement curve); **(B)** Comparison of stiffness between No internal fixation and internal fixation models under different conditions.

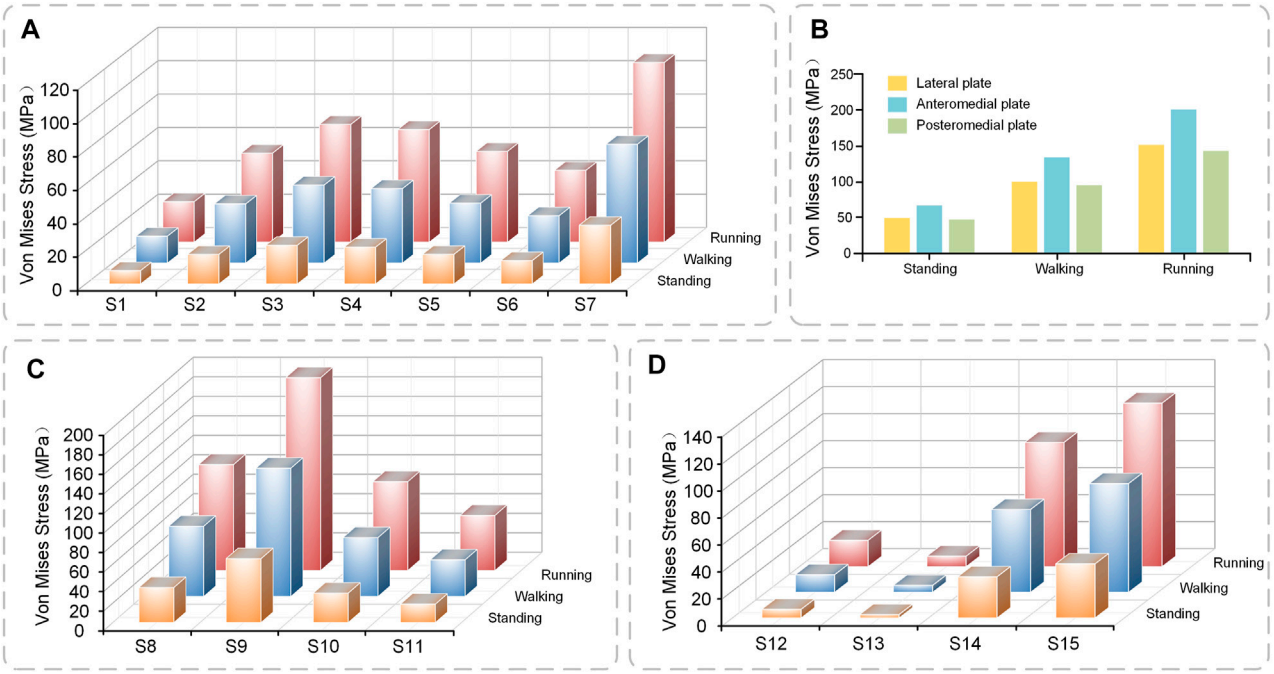

FIGURE 6
The stress value of plates and screws in postoperative FEMs under different conditions **(A)** Stress value of S1–7 **(B)** Stress value of plates **(C)** Stress value of S8–11 **(D)** Stress value of S12–15.

3.2.2 Von Mises stress of screws

The general trend of each set of screws was comparable in the three conditions of standing, walking, and running, and the screws at the same location rose with the increase in motion intensity. Screw S7 at the most distal end of the lateral plate, has the highest stress, whereas screws S1–S6 exhibit a rising and then declining pattern (Figure 6A). Screws S8 and S9 at the proximal end of the anteromedial plate have the largest stress, whereas the screw at the distal end of the anteromedial plate gradually diminishes (Figure 6C). The stresses in screws S12 and S13 near the proximal end of the posteromedial plate are low, whereas those in screw S14 were rather high (Figure 6D). S16 was not attached to

FIGURE 7
Plates and screws **(A)** Lateral plate and screw 1–7; screw 16 **(B)** Anteromedial plate and screw 8–11 **(C)** Posteromedial plate and screw 12–15.

the plates and did not appear in the bar graph. S16 did not experience substantial axial stress, with stress values of 3.08, 6.16, and 9.21 MPa for the three conditions of standing, walking, and running.

Through the stress cloud, similar stress distribution features can be seen, with large stress concentrations near the screw head. For screw S2, stress concentrations were also detected close to the screw tip due to the screw straddling the medial and lateral tibial plateaus (Figure 7).

3.3 Displacement distribution

The anteromedial bone fragment experienced a large relative displacement of 0.072 mm at the fracture line at the edge of the tibial plateau, extending medially and decreasing in displacement. The posteromedial bone fragment experienced a small relative displacement value and a relatively large displacement value of 0.042 mm at the axial split (Figure 8B).

The total displacement (the maximum value of the cloud map) variation in the anteromedial portion of the fractured bone fragments and the posteromedial portion of the fracture block differs for the two critical fractured bone fragments. The displacement values were somewhat bigger in the anteromedial portion than in the posteromedial portion under different conditions, and the displacement values increased with increasing motion intensity. The largest displacement occurred during running, 0.54 mm for the anteromedial portion and 0.51 mm for the posteromedial portion, neither of which exceeded 2 mm, indicating that the fractured bone fragments were in a stable state (Figure 8C).

3.4 Fatigue properties

The fatigue life of the internal fixation system under the action of the cyclic load was more than 10 to the power of 7 times in the three conditions of standing, walking, and running, which may be characterized as no damage. The screw path of S8 was damaged in the walking state, and the minimum LOGlife-Repeats was 4.28, so the fatigue life of this area was 10 to the power of 4.28 = 18973.164 times. In the running state, the screw path of S8 was damaged again, and the minimum LOGlife-Repeats was 3.42, so the fatigue life of this area was 10 to the power of 3.42 = 2605.264 times. The location where fatigue occurs is the location of bone-screw contact (Figure 9).

4 Discussion

The surgical treatment of comminuted tibial plateau fractures is challenging. The main purpose of surgery is to provide anatomic

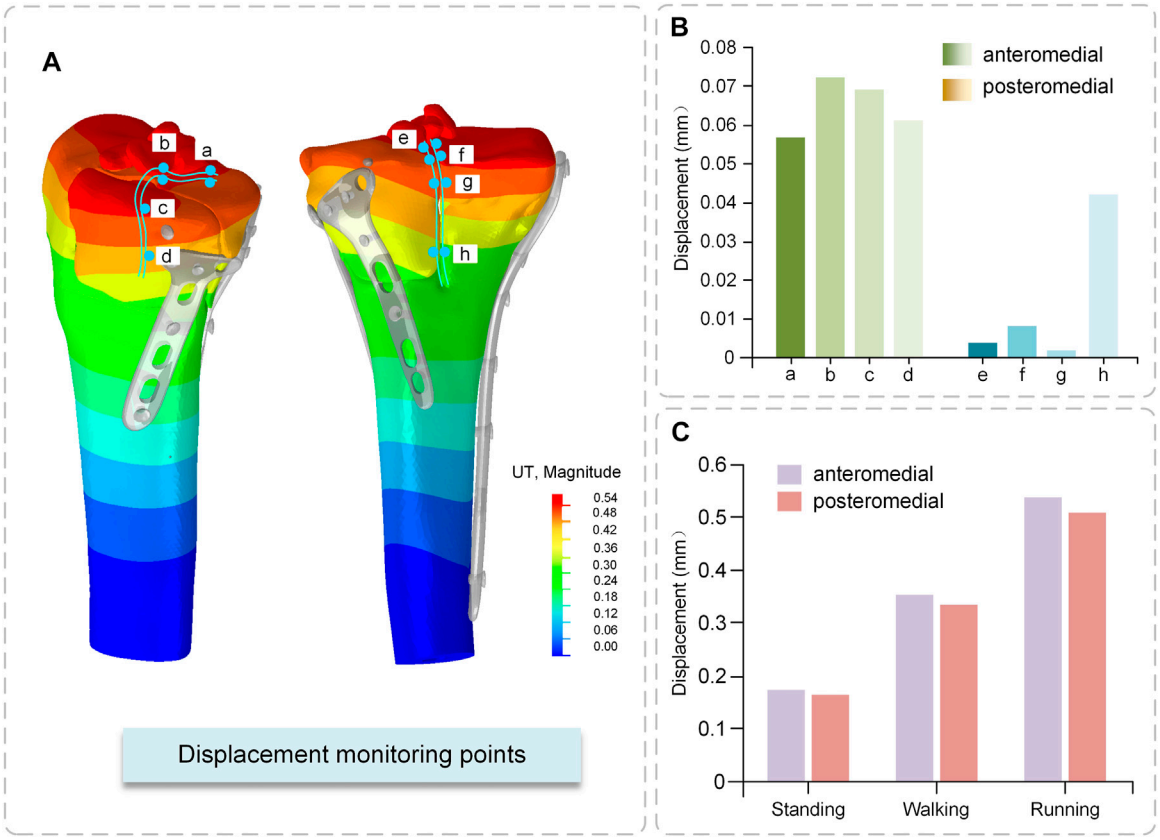

FIGURE 8
Displacement of fractured bone fragments **(A)** Displacement Cloud Map **(B)** Relative displacement of fractured fragments **(C)** Total displacement of fractured fragments.

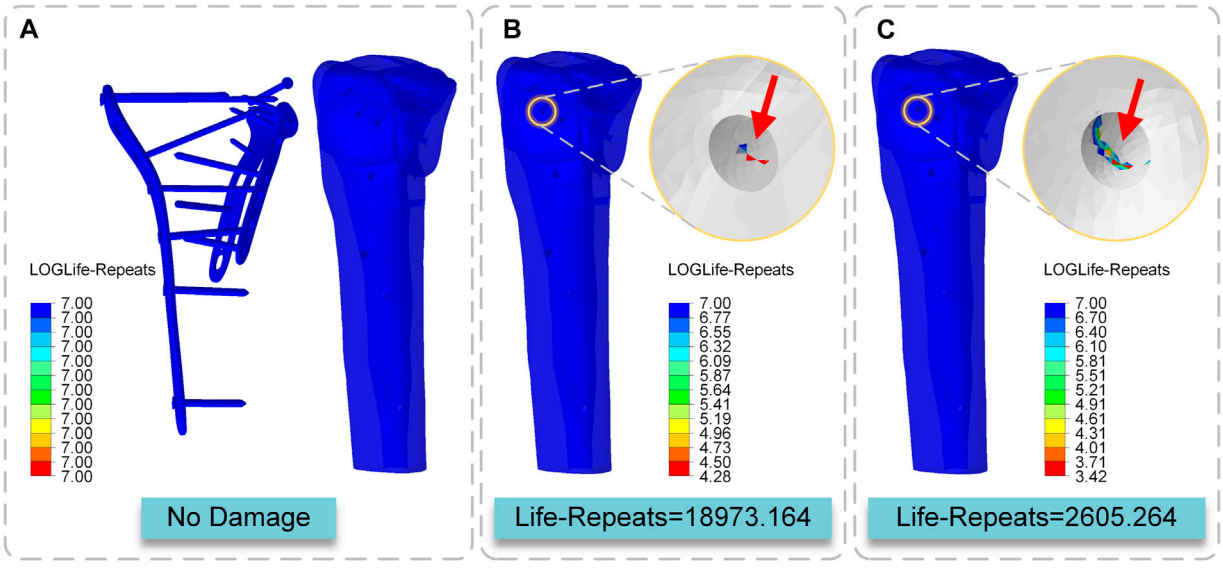

FIGURE 9
Cloud map of LOGLife-Repeats **(A)** Internal fixation system in three states and the tibia in the standing state **(B)** The tibia in the walking state **(C)** The tibia in the running state.

restoration of the articular surface and rigid fixation to allow early mobilization (Mueller et al., 2003). The displaced condyle must be reduced for a good clinical outcome, the depressed plateau must be elevated and adequately supported, and early rehabilitation must be encouraged. In clinical practice, surgeons provide conservative recommendations to ensure the solidity of internal fixation by instructing patients to rest in bed. Still, breaking the joint can bring about a loss of joint mobility. This study uses the finite element approach to examine three conditions typical of standing, walking, and running to understand the peculiarities of the internal fixation system's biomechanical environment. The study provides a theoretical foundation for the viability of early postoperative rehabilitation by examining the biomechanical mechanism of the interaction between internal fixation and bone. This study makes recommendations for rehabilitation, emphasizing that appropriate rehabilitation training is safe and helpful for postoperative rehabilitation whereas intense activity is harmful in the initial postoperative phase. A good combination and attempt of fracture surgery and rehabilitation guidance using a digital medicine approach is a worthy method to be promoted.

In one trial, 32 patients with tibial plateau fractures were treated with internal fixation with plates and either immediate postoperative weight-bearing (n = 12) or delayed weight-bearing (n = 20), with no fracture displacement in either group and comparable complication rates (Haak et al., 2012). In a large study of 51 patients with comminuted plateau fractures, nearly half were given internal fixation and early partial weight-bearing, with no differences in reoperation rates, post-traumatic osteoarthritis, or pain when compared to those given other external fixation braces and limited weight-bearing. Patients who had early weight-bearing treatment returned to work more frequently than those who had limited weight-bearing (Blauth et al., 2001). Kazemi and Archdeacon (2012), Thewlis et al. (2017) have demonstrated that weight bearing did not have a deleterious impact on the outcome of tibial plateau fractures and may thus be safe for postoperative care. Our study provides a detailed analysis of the internal fixation system's stability and fatigue characteristics during postoperative rehabilitation exercises, evaluates the mechanical characteristics of tibial plateau fractures after internal fixation, and makes recommendations for postoperative weight-bearing rehabilitation.

This study produced stiffness values of 2041–2129 N/mm for the model without internal fixation and 2,781–2,868 N/mm for the model with internal fixation. Karunakar et al. (2002) reported that the internal fixation model was 2,026–2,666 N/mm, which was similar to the present study. Ion Carrera et al. (2016) reported an internal fixation model of approximately 2,800–3,300 N/mm, which was greater than the present experimental results. Although, the values reported by Ion Carrera et al. (2016) are greater than the results of the present study, the results have the same order of magnitude. One reason may be that the experimental research focused on this comparison is limited. Another reason is that the types of fixation explored in their experiments differed from those used in the current study. It can be seen that the stiffness value significantly increases after implantation of the internal fixation system. Internal fixation implantation greatly improves the stability of the knee joint, which is the basis for the safety of rehabilitative exercise training.

Gao et al. (2022) used three axial loads of 500, 1000, and 1500 N to evaluate the stress of the internal attachment fixation system, and the stress value ranged from 48.92 to 155.71 MPa, similar to the results of this study. Many academics have studied the stability of the internal fixation system, but none have examined the sites of the stress distribution between the plate and the screw. The stress distribution features of the specific steel plate and screw are highlighted in detail in this experiment, and it is noted that the front section of the medial condyle has the greatest stress distribution. The tail of the screw attached to the steel plate has the highest stress, which is consistent with the findings of other investigations (Samsami et al., 2020). On the other hand, the maximum stress of the plate and screw is substantially lower than the maximum yield strength of titanium alloy. This indicates that the strength of the internal fixation system meets the normal activities of the body to some extent.

Displacement monitoring sites A, B, E, and F, which are situated on the top surface of the tibial plateau, are crucial for determining the relative displacement of the fractured bone fragments. This region is related to the distal femoral epiphysis and is covered in ligaments and articular cartilage. As a result, it is critical that this surface recovers optimally to restore joint stability. Independent movement of bone fragments is highly detrimental to fracture fixation. This scenario means that following compressive pressure, each bone fragment travels independently of the others. The posteromedial fractured bone fragments demonstrated a smooth transition of displacement on the fracture boundary, implying increased mechanical stability. Ferre et al. (2022) measured the relative displacement of the distal medial tibial condyle between 0.02 and 0.03 mm. They proposed that locking compression plate fixation of the medial tibial condyle reduced the independent movement of the fracture. In our study, the medial condyle was divided into anterior and posterior parts. The relative motion was 0.002–0.072 mm, which is extremely small and indicates the presence of micromovements between the fracture blocks, but does not affect the weight-bearing function of the bone and is within the safe range.

The implants should be developed to sustain the stress of the broken bone and achieve the needed durability, in addition to mechanical stability and biocompatibility. These implants are subjected to repeated fluctuating loads during regular activities, which can lead to implant fatigue failure. Several studies have looked at implant fatigue failure (Kanchanomai et al., 2008; Schüller et al., 2009; Gervais et al., 2016). These studies suggest that unexpected implant fatigue failure may occur. As a result, while proposing these implants for use in bone-damaged patients, extra consideration should be given to their fatigue characteristics. This study showed no fatigue damage to the implant when standing, walking, or running and that the implant's strength was enough for regular living activities. Under cyclic stress, however, fatigue damage was found in the tibia. In the standing condition, the bone was entirely safe under the strain. Fatigue damage to the bone occurred after 18973.164 cycles of loading in the walking mode. After 2605.564 cycles of loading in the running state, fatigue damage to the bone was seen. The location where fatigue occurs is the location of bone-screw contact. This

experiment did not consider the bone repair factor, which means that in the true case, bone fatigue should appear later than in the experiment, but to some extent, it means that when the stress on the tibia exceeds its body weight numerous times, the likelihood of bone disintegration increases significantly. The choice of rehabilitation training intensity affects bone repair, and the results of this study suggest that excessive loading can cause bone destruction, suggesting that the rehabilitator should choose an appropriate training level. As a result, regular standing weight-bearing and a modest amount of walking weight-bearing are allowed throughout the postoperative rehabilitation period, although the intense activity is discouraged.

Limitations of this study: firstly, bone heterogeneity and biological activity were not considered in the local calculation of bone stresses because bone tissue has a high capacity for repair and adaptation, which may be critical and needs to be investigated. Second, only the effect of axial loading was considered in this study, and shear forces from torsion and bending moment were not considered. Third, the model was simplified by ignoring the effects of the meniscus, cartilage, muscles, and ligaments, as well as by simplifying the threads. All these factors can nonetheless constitute a significant contribution to influencing the biomechanical model, and their contribution has to be studied. This study, combined with the calculation of patient-specific model geometry should be part of the future assessment of immediate bearing capacity after fracture reduction. For this purpose, population-based customization of FEM is both feasible and promising.

5 Conclusion

The method of creating a 3D internal fixation system from CT images, the segmentation of the bone model, and the modeling process described in this study demonstrate the high accuracy and usability of 3D virtual objects with mechanical properties. In the case of complicated tibial plateau fractures, the postoperative internal fixation system satisfies some of the body's normal activities. It can sustain all or part of the weight in a static condition at an early stage. When the load on the tibia exceeds the weight of the body multiple times, the risk of bone deterioration increases significantly. As a result, regular standing weight-bearing and limited amounts of walking weight-bearing are permitted throughout the postoperative rehabilitation phase, but vigorous movements such as running and leaping are discouraged. This study may not be enough to issue complete recommendations for the postoperative period, but it may be a good start to provide some ideas for that process. In the future, we will need more clinical cases to validate this process.

Data availability statement

The original contributions presented in the study are included in the article/supplementary material, further inquiries can be directed to the corresponding authors.

Ethics statement

The studies involving human participants were reviewed and approved by the Science and Ethics Committee of the School of Biological Science and Medical Engineering at Beihang University (protocol code: BM20220087). The patients/participants provided their written informed consent to participate in this study.

Author contributions

Conceptualization, GW and YX; methodology, YX; software, YX and YL; validation, TC and YL; investigation, FT; resources, YX and YH; data curation, GW and RW; writing—original draft preparation, GW; writing-review and editing, TC, HW, and XN; visualization, XN; supervision, JZ and XL; project administration, FT and HW; funding acquisition, GW and FT. All authors contributed to the article and approved the submitted version.

Funding

This research was funded by the National Natural Science Foundation of China (No. 11972065), Teaching Reform Innovation Project of Higher Education Institutions in Shanxi Province (No. J20220847).

Conflict of interest

The authors declare that the research was conducted in the absence of any commercial or financial relationships that could be construed as a potential conflict of interest.

Publisher's note

All claims expressed in this article are solely those of the authors and do not necessarily represent those of their affiliated organizations, or those of the publisher, the editors and the reviewers. Any product that may be evaluated in this article, or claim that may be made by its manufacturer, is not guaranteed or endorsed by the publisher.

References

Amini, M., Nazemi, S. M., Lanovaz, J. L., Kontulainen, S., Masri, B. A., Wilson, D. R., et al. (2015). Individual and combined effects of OA-related subchondral bone alterations on proximal tibial surface stiffness: A parametric finite element modeling study. *Med. Eng. Phys.* 37 (8), 783–791. doi:10.1016/j.medengphy.2015.05.011

Barei, D. P., O'Mara, T. J., Taitsman, L. A., Dunbar, R. P., and Nork, S. E. (2008). Frequency and fracture morphology of the posteromedial fragment in bicondylar tibial plateau fracture patterns. *J. Orthop. trauma* 22 (3), 176–182. doi:10.1097/BOT.0b013e318169ef08

Belaid, D., Vendeuvre, T., Bouchoucha, A., Brémand, F., Brèque, C., Rigoard, P., et al. (2018). Utility of cement injection to stabilize split-depression tibial plateau fracture by minimally invasive methods: A finite element analysis. *Clin. Biomech.* 56 (1), 27–35. doi:10.1016/j.clinbiomech.2018.05.002

Blauth, M., Bastian, L., Krettek, C., Knop, C., and Evans, S. (2001). Surgical options for the treatment of severe tibial pilon fractures: A study of three techniques. *J. Orthop. trauma* 15 (3), 153–160. doi:10.1097/00005131-200103000-00002

Boluda-Mengod, J., Guimerà-García, V., Olías-López, B., Renovell-Ferrer, P., Carrera, I., Herrera-Pérez, M., et al. (2021). A proposal of a new algorithm for decision-making approaches in open reduction and internal fixation of complex tibial plateau fractures-SOTA algorithm (Spanish Orthopaedic Trauma Association). *Injury* 52 (4), S87–S98. doi:10.1016/j.injury.2021.03.064

Bucholz, R. W., Heckman, J. D., Tornetta, P., McQueen, M. M., and Ricci, W. M. (2010). *Rockwood and Green's fractures in adults*. Berlin, Germany: Springer, 195–226.

Burdin, G. (2013). Arthroscopic management of tibial plateau fractures: Surgical technique. *Orthop. Traumatology Surg. Res.* 99 (1), S208–S218. doi:10.1016/j.otsr.2012.11.011

Carrera, I., Gelber, P. E., Chary, G., González-Ballester, M. A., Monllau, J. C., and Noailly, J. (2016). Fixation of a split fracture of the lateral tibial plateau with a locking screw plate instead of cannulated screws would allow early weight bearing: A computational exploration. *Int. Orthop.* 40 (10), 2163–2169. doi:10.1007/s00264-015-3106-y

Chen, P., Lu, H., Shen, H., Wang, W., Ni, B., and Chen, J. (2017). Newly designed anterolateral and posterolateral locking anatomic plates for lateral tibial plateau fractures: A finite element study. *J. Orthop. Surg. Res.* 12 (1), 35–39. doi:10.1186/s13018-017-0531-1

Consortium, G. H. B. M. (2014). *User manual: M50 occupant, version 4.3 for LS-dyna*. Clemmons, NC: Elemance LLC.

Dehoust, J., Münch, M., Seide, K., Barth, T., and Frosch, K.-H. (2020). Biomechanical aspects of the posteromedial split in bicondylar tibial plateau fractures—A finite-element investigation. *Eur. J. Trauma Emerg. Surg.* 46 (6), 1257–1266. doi:10.1007/s00068-020-01538-3

Djuricic, A., Gee, A., Schemitsch, E. H., Quenneville, C. E., and Zdero, R. (2022). Biomechanical design of a new percutaneous locked plate for comminuted proximal tibia fractures. *Med. Eng. Phys.* 104, 103801. doi:10.1016/j.medengphy.2022.103801

Eckstein, F., Hudelmaier, M., and Putz, R. (2006). The effects of exercise on human articular cartilage. *J. Anat.* 208 (4), 491–512. doi:10.1111/j.1469-7580.2006.00546.x

Eggli, S., Hartel, M. J., Kohl, S., Haupt, U., Exadaktylos, A. K., and Röder, C. (2008). Unstable bicondylar tibial plateau fractures: A clinical investigation. *J. Orthop. trauma* 22 (10), 673–679. doi:10.1097/bot.0b013e31818b1452

Ferre, L. S., Di Nisio, F. G., Mendonça, C. J. A., and Belo, I. M. (2022). Comparative analysis of tibial plateau fracture osteosynthesis: A finite element study. *J. Mech. Behav. Biomed. Mater.* 134, 105392. doi:10.1016/j.jmbbm.2022.105392

Gao, S., Yao, Q., Geng, L., Lu, J., Li, M., An, K., et al. (2022). A finite element analysis of the supportive effect of a new type of rotary support plate on lateral tibial plateau fractures. *Ann. Transl. Med.* 10 (18), 1020–1110. doi:10.21037/atm-22-4529

Gervais, B., Vadean, A., Raison, M., and Brochu, M. (2016). Failure analysis of a 316L stainless steel femoral orthopedic implant. *Case Stud. Eng. Fail. Analysis* 5, 30–38. doi:10.1016/j.csefa.2015.12.001

Haak, K. T., Palm, H., Holck, K., Krasheninnikoff, M., Gebuhr, P., and Troelsen, A. (2012). Immediate weight-bearing after osteosynthesis of proximal tibial fractures may be allowed. *Dan. Med. J.* 59 (10), A4515.

Haller, J. M., O'Toole, R., Graves, M., Barei, D., Gardner, M., Kubiak, E., et al. (2015). How much articular displacement can be detected using fluoroscopy for tibial plateau fractures? *Injury* 46 (11), 2243–2247. doi:10.1016/j.injury.2015.06.043

Hua, K., Jiang, X., Zha, Y., Chen, C., Zhang, B., and Mao, Y. (2019). Retrospective analysis of 514 cases of tibial plateau fractures based on morphology and injury mechanism. *J. Orthop. Surg. Res.* 14 (1), 267–310. doi:10.1186/s13018-019-1321-8

Huang, X., Zhi, Z., Yu, B., and Chen, F. (2015). Stress and stability of plate-screw fixation and screw fixation in the treatment of schatzker type IV medial tibial plateau fracture: A comparative finite element study. *J. Orthop. Surg. Res.* 10 (1), 182–189. doi:10.1186/s13018-015-0325-2

Kanchanomai, C., Phiphobmongkol, V., and Muanjan, P. (2008). Fatigue failure of an orthopedic implant–A locking compression plate. *Eng. Fail. Anal.* 15 (5), 521–530. doi:10.1016/j.engfailanal.2007.04.001

Karunakar, M. A., Egol, K. A., Peindl, R., Harrow, M. E., Bosse, M. J., and Kellam, J. F. (2002). Split depression tibial plateau fractures: A biomechanical study. *J. Orthop. Trauma* 16 (3), 172–177. doi:10.1097/00005131-200203000-00006

Kazemi, N., and Archdeacon, M. T. (2012). Immediate full weight bearing after percutaneous fixation of anterior column acetabulum fractures. *J. Orthop. Trauma* 26 (2), 73–79. doi:10.1097/BOT.0b013e318216b3e3

Koh, Y.-G., Lee, J.-A., Lee, H.-Y., Chun, H.-J., Kim, H.-J., and Kang, K.-T. (2019). Design optimization of high tibial osteotomy plates using finite element analysis for improved biomechanical effect. *J. Orthop. Surg. Res.* 14 (1), 219–310. doi:10.1186/s13018-019-1269-8

Lee, A. K., Cooper, S. A., and Collinge, C. (2018). Bicondylar tibial plateau fractures: A critical analysis review. *JBJS Rev.* 6 (2), e4. doi:10.2106/JBJS.RVW.17.00050

Lee, T.-C., Huang, H.-T., Lin, Y.-C., Chen, C.-H., Cheng, Y.-M., and Chen, J.-C. (2013). Bicondylar tibial plateau fracture treated by open reduction and fixation with unilateral locked plating. *Kaohsiung J. Med. Sci.* 29 (10), 568–577. doi:10.1016/j.kjms.2013.01.006

McGonagle, L., Cordier, T., Link, B. C., Rickman, M. S., and Solomon, L. B. (2019). Tibia plateau fracture mapping and its influence on fracture fixation. *J. Orthop. Traumatology* 20, 12–16. doi:10.1186/s10195-019-0519-1

McNamara, I. R., Smith, T. O., Shepherd, K. L., Clark, A. B., Nielsen, D. M., Donell, S., et al. (2015). Surgical fixation methods for tibial plateau fractures. *Cochrane Database Syst. Rev.* 4 (9), CD009679. doi:10.1002/14651858.CD009679.pub2

Mueller, K. L., Karunakar, M. A., Frankenburg, E. P., and Scott, D. S. (2003). Bicondylar tibial plateau fractures: A biomechanical study. *Clin. Orthop. Relat. Research®* 412, 189–195. doi:10.1097/01.blo.0000071754.41516.e9

Pätzold, R., Friederichs, J., von Rüden, C., Panzer, S., Bühren, V., and Augat, P. (2017). The pivotal role of the coronal fracture line for a new three-dimensional CT-based fracture classification of bicondylar proximal tibial fractures. *Injury* 48 (10), 2214–2220. doi:10.1016/j.injury.2017.06.019

Ren, W., Zhang, W., Jiang, S., Peng, J., She, C., Li, L., et al. (2022). The study of biomechanics and clinical anatomy on a novel plate designed for posterolateral tibial plateau fractures via anterolateral approach. *Front. Bioeng. Biotechnol.* 10, 818610. doi:10.3389/fbioe.2022.818610

Samsami, S., Herrmann, S., Pätzold, R., Winkler, M., and Augat, P. (2020). Finite element analysis of Bi-condylar Tibial Plateau fractures to assess the effect of coronal splits. *Med. Eng. Phys.* 84, 84–95. doi:10.1016/j.medengphy.2020.07.026

Schüller, M., Drobetz, H., Redl, H., and Tschegg, E. (2009). Analysis of the fatigue behaviour characterized by stiffness and permanent deformation for different distal volar radius compression plates. *Mater. Sci. Eng. C* 29 (8), 2471–2477. doi:10.1016/j.msec.2009.07.013

Tai, C.-L., Chen, W.-P., Chen, H.-H., Lin, C.-Y., and Lee, M. S. (2009). Biomechanical optimization of different fixation modes for a proximal femoral L-osteotomy. *BMC Musculoskelet. Disord.* 10 (1), 112–210. doi:10.1186/1471-2474-10-112

Taylor, W. R., Heller, M. O., Bergmann, G., and Duda, G. N. (2004). Tibio-femoral loading during human gait and stair climbing. *J. Orthop. Res.* 22 (3), 625–632. doi:10.1016/j.orthres.2003.09.003

Thewlis, D., Fraysse, F., Calgary, S. A., Verghese, V. D., Jones, C. F., Findlay, D. M., et al. (2017). Postoperative weight bearing and patient-reported outcomes at one year following tibial plateau fractures. *Injury* 48 (7), 1650–1656. doi:10.1016/j.injury.2017.05.024

Tian, L., Sheng, Y., Huang, L., Chow, D. H.-K., Chau, W. H., Tang, N., et al. (2018). An innovative Mg/Ti hybrid fixation system developed for fracture fixation and healing enhancement at load-bearing skeletal site. *Biomaterials* 180, 173–183. doi:10.1016/j.biomaterials.2018.07.018

Wang, Y., Qi, E., Zhang, X., Xue, L., Wang, L., and Tian, J. (2021). A finite element analysis of relationship between fracture, implant and tibial tunnel. *Sci. Rep.* 11 (1), 1781. doi:10.1038/s41598-021-81401-6

Zeng, C., Ren, X., Xu, C., Hu, M., Li, J., and Zhang, W. (2022). Stability of internal fixation systems based on different subtypes of schatzker II fracture of the tibial plateau: A finite element analysis. *Front. Bioeng. Biotechnol.* 1637, 973389. doi:10.3389/fbioe.2022.973389

Zhao, D., Banks, S. A., Mitchell, K. H., D'Lima, D. D., Colwell, C. W., and Fregly, B. J. (2007). Correlation between the knee adduction torque and medial contact force for a variety of gait patterns. *J. Orthop. Res.* 25 (6), 789–797. doi:10.1002/jor.20379

frontiers | Frontiers in Bioengineering and Biotechnology

TYPE Original Research
PUBLISHED 19 June 2023
DOI 10.3389/fbioe.2023.1185177

OPEN ACCESS

EDITED BY
Yih-Kuen Jan,
University of Illinois at Urbana-Champaign, United States

REVIEWED BY
Qiang Chen,
Southeast University, China
Vijay Kumar Meena,
Central Scientific Instruments Organization (CSIR), India

*CORRESPONDENCE
Minjun Liang,
liangminjun@nbu.edu.cn
Yufei Fang,
fyf369@126.com

RECEIVED 13 March 2023
ACCEPTED 09 June 2023
PUBLISHED 19 June 2023

CITATION
He Y, Liang M, Fang Y, Fekete G, Baker JS and Gu Y (2023), Lumbar and pelvis movement comparison between cross-court and long-line topspin forehand in table tennis: based on musculoskeletal model.
Front. Bioeng. Biotechnol. 11:1185177.
doi: 10.3389/fbioe.2023.1185177

Lumbar and pelvis movement comparison between cross-court and long-line topspin forehand in table tennis: based on musculoskeletal model

Yuqi He[1,2,3], Minjun Liang[1,4]*, Yufei Fang[1]*, Gusztáv Fekete[3], Julien S. Baker[5] and Yaodong Gu[1,4]

[1]Research Academy of Medicine Combining Sports, Ningbo No.2 Hospital, Ningbo, China, [2]Faculty of Engineering, University of Pannonia, Veszprém, Hungary, [3]Savaria Institute of Technology, Eötvös Loránd University, Szombathely, Hungary, [4]Faculty of Sports Science, Ningbo University, Ningbo, China, [5]Department of Sport, Physical Education and Health, Hong Kong Baptist University, Hong Kong, China

Introduction: Cross-court and the long-line topspin forehand is the common and basic stroke skill in table tennis. The purpose of this study was to investigate the differences in lumbar and pelvis movements between cross-court and long-line topspin forehand strokes in table tennis based on musculoskeletal demands using OpenSim.

Materials and Methods: The eight-camera Vicon system and Kistler force platform were used to measure kinematics and kinetics in the lumbar and pelvis movement of sixteen participants (Weight: 69.89 ± 1.58 kg; Height: 1.73 ± 0.03 m; Age: 22.89 ± 2.03 years; BMI: 23.45 ± 0.69 kg/m^2; Experience: 8.33 ± 0.71 years) during cross-court and long-line topspin forehand play. The data was imputed into OpenSim providing the establishment of the Giat2392 musculoskeletal model for simulation. One-dimensional statistical parametric mapping and independent samples t-test was performed in MATLAB and SPSS to analyze the kinematics and kinetics.

Results: The results show that the range of motion, peak moment, and maximum angle of the lumbar and pelvis movement in cross-court play were significantly higher than in the long-line stroke play. The moment of long-line in the sagittal and frontal plane was significantly higher than cross-court play in the early stroke phase.

Conclusion: The lumbar and pelvis embody greater weight transfer and greater energy production mechanisms when players performed cross-court compared to long-line topspin forehand. Beginners could enhance their motor control strategies in forehand topspin skills and master this skill more easily based on the results of this study.

KEYWORDS

pelvis rotation, lumbar movement, opensim, musculoskeletal model, trunk rotation, topspin forehand, table tennis

Introduction

Topspin forehand is regarded as one of the most attacking strokes in table tennis based on the high speed and fast rotation (Poizat et al., 2004; Qian et al., 2016; He et al., 2020; He et al., 2022a). The mastery of the topspin forehand is also considered an important factor in differentiating elite athletes (Iino and Kojima, 2011; He et al., 2020). The biomechanical mechanisms inherent in topspin forehand have been extensively reported in previous studies, such as the joint kinematics (Iino and Kojima, 2009; He et al., 2020; He et al., 2021a) and kinetics (Iino and Kojima, 2011), ground reaction force (GRF) (Zhou et al., 2021a), plantar pressure (Fu et al., 2016; Lam et al., 2019; He et al., 2021b), and electromyography (EMG) and information regarding muscle contraction dynamics (Le Mansec et al., 2018; Chen et al., 2022). These studies amply illustrate the value and significance of investigating the biomechanical intrinsic mechanisms of the topspin forehand.

The speed and accuracy of the ball, as well as the success rate, are the key determinants of the quality of strokes (Landlinger et al., 2012; Kolman et al., 2019). The key role of ball speed in table tennis supports the optimization of stroke skills and distinguishes the performance level of players. Trunk rotation was strongly correlated with the velocity of the racket (Akutagawa and Kojima, 2005). Due to the critical role of pelvic movement on the axial rotation of the trunk rotation and hitting speed, pelvic movement plays a crucial role in powerful hitting sports, such as table tennis, tennis, and baseball (Elliott and Zatsiorsky, 2000; Akutagawa and Kojima, 2005). In table tennis, the horizontal velocity of the racket during the topspin forehand stroke was benefited by the peak angular velocity of pelvic axial rotation and the pelvic axial rotation torque on the playing hand side (Iino, 2018; He et al., 2022a). In order to remain powerful and competitive, players need to increase the acceleration of their playing hand by optimizing their stroke skill and the efficiency of the power chain transmission, which brings gains to the spin effect and flight speed of the ball during the topspin forehand (Qian et al., 2016; Lam et al., 2019; He et al., 2020; Chen et al., 2022). In tennis, the rotational movement of the lower trunk in the horizontal plane was very frequent (Muyor et al., 2013). In baseball, the rotation of the trunk and leg has been reported as the important power source in ground strokes (Elliott and Zatsiorsky, 2000; Akutagawa and Kojima, 2005). Even though a great deal of previous research and evidence has strongly supported that the development of the optimal trunk rotation was one of the most important factors to master the topspin strokes (Akutagawa and Kojima, 2005), however, the movement characteristics of the human pelvis have hardly been specifically studied and reported in table tennis topspin forehand stroke.

The development of musculoskeletal models to investigate the mechanical performance of human structures during movement is an important and commonly used tool in the field of biomechanics research. Motion reconstruction based on captured data allows access to additional variables of interest to explain some phenomena and intrinsic patterns. Examples include the reconstruction of musculoskeletal models in OpenSim and Visual3D to calculate joint kinematics, kinetics, and muscle forces during movement (Seth et al., 2018; Dorschky et al., 2019; Nitschke et al., 2020). Iino (2018) created a musculoskeletal model in OpenSim and investigated the muscular effort of lower limb muscles during the topspin forehand stroke (Iino et al., 2018). Yang et al. (2022) calculated the angles and moments of lower limb joints of 36 elite table tennis players during chasse-step footwork by OpenSim to investigate the gender difference (Yang et al., 2022). He et al. (2022a) investigated lower limbs muscle force, joint kinematics, and joint kinetics in footwork during the topspin forehand using OpenSim (He et al., 2022b). That evidence suggests simulation using a musculoskeletal model to obtain key information is viable and recognized for explaining the mechanisms underlying table tennis topspin forehand stroke movements.

As a typical one-handed racket sport, table tennis has been proven to have a bad effect on the symmetry of the trunk, and the imbalance of symmetry is one of the key factors leading to sports injuries (Bańkosz and Barczyk-Pawelec, 2020). The revealing of the inner mechanism of the lumbar and pelvis movement during stroke play in table tennis can provide reference information for exploring sports injuries caused by symmetry imbalance. The constant interplay of technical and tactical skills is crucial to winning each point in a competition game (Kolman et al., 2019). To achieve tactical goals, athletes need to perform specific skills (Kolman et al., 2019). The importance of the cross-court (CC) topspin forehand is reflected in the fact that the CC has always been the object or vehicle of study in previous studies on the biomechanics of table tennis (Iino and Kojima, 2011; Malagoli Lanzoni et al., 2018; He et al., 2020; He et al., 2021a; Xing et al., 2022). Besides, the long-line (LL) topspin forehand, as one of the basic strokes in racket sports, has been widely studied not only in table tennis but also in tennis (Landlinger et al., 2010; Pedro et al., 2022). The functional role of the topspin forehand stroke skills in influencing tactics results in players being able to optimize their skills to enhance the success of their tactics and further ensure an advantageous position in the match. Although previous studies have investigated the kinematics difference between CC and LL (Malagoli Lanzoni et al., 2018; He et al., 2020), the lumbar and pelvis movement and the kinetic information have not been measured and analyzed. To summarize, this study aimed to simulate a musculoskeletal model using OpenSim software to investigate the difference in lumbar and pelvis movements between CC and LL topspin forehand strokes in table tennis. Firstly, this study can be applied to guide the coaching and training of table tennis players, especially for beginner players to recognize the role of lumbar and pelvis movement in optimizing topspin forehand stroke skills for application in the game. Secondly, the movement information could be provided to explore the injury risk in table tennis or other racket sports. The hypothesis of this study was that CC and LL topspin forehand show significantly different kinematics and kinetics, and the difference would be evident in the transverse plane.

Methods

Participants

Sixteen male table tennis players from the Ningbo University table tennis team volunteered to participate in this study and provided written informed consent after the purpose and process of this study were explained. All the participants were at the national-one performance level and right-handed, as well as free from any neuromuscular injury in the past 6 months. The demographic information of participants is shown in Table 1. The Ethics Committee of Ningbo University approved this study.

TABLE 1 Demographic information.

Weight (Kg)	Height (M)	Age (Y)	BMI (Kg/m^2)	Experience (Y)
69.89 ± 1.58	1.73 ± 0.03	22.89 ± 2.03	23.45 ± 0.69	8.33 ± 0.71

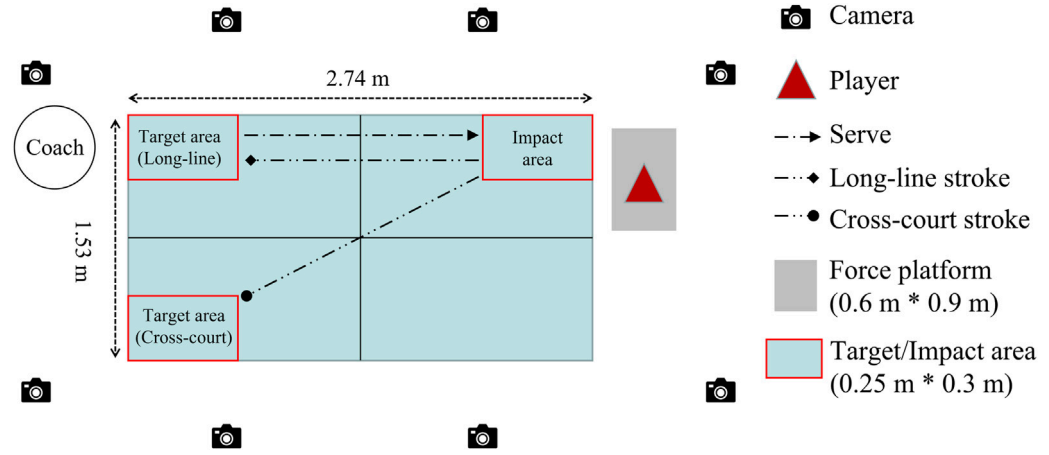

FIGURE 1
Experimental environment and set-up.

Experimental protocol and equipment

The experiment was performed in the biomechanics laboratory of the Ningbo University Research Academy of Grand Health. As shown in Figure 1, the kinematics of participants were captured by an eight-camera Vicon motion capture system (Oxford Metrics, Ltd., Oxford, United Kingdom) which was set at the sampling frequency of 200 Hz. The kinetics of participants was recorded by a force platform (Kistler, Switzerland) using a sampling frequency of 1,000 Hz. All devices used for data acquisition were electronically connected to achieve the multi-parameter synchronous acquisition of the test data. The Gait2392 model was selected to simulate the movement of the participant in the OpenSim (Stanford University, Stanford, CA, United States), and the thirty-nine reflective markers (12.5 mm in diameter) placement was replicated according to the previous studies (Delp et al., 2007).

Participants used uniform rackets (Butterfly Tenergy 05 Max and DHC Hurricane 3 rubber sheets), balls (D40+, Double Happiness Sports Company, Shanghai, China), and playing table (Rainbow, Double Happiness Sports Company, Shanghai, China), as well as match table tennis shoes and tights during the experiment.

Procedure

Prior to the commencement of the formal test, participants were allowed to complete 5 min of static stretching and 10 min of running in a spacious area to warm up. Subjects were required to stand on the force platform to complete the static coordinates collection process after putting the reflective markers on the subjects' bodies. To check the operation of all the equipment and help the subjects quickly familiarize themselves with the laboratory environment, subjects were asked to perform five topspin forehand stroke tasks before the formal data collection session.

As shown in Figure 1, in the formal test, the coach was shooting the ball with normal service to the impact area (0.25 m * 0.3 m). The subject stands on the right side of the playing table and was required to perform the topspin forehand stroke to return the ball to the long-line target area (0.25 m * 0.3 m) and cross-court target area (0.25 m * 0.3 m), respectively. The CC topspin forehand started first, then perform the LL topspin forehand. There is no rest time during the formal test until the successfully recorded 5 trials data of the CC and the LL topspin forehand for each participant, respectively. The subject and a qualified coach judged the quality of motion during the test. The test data were excluded if the drop point of the ball was out of the target area and the motion quality was questioned. Meanwhile, the data performance was also used to evaluate the validity of data collection. The size set of the impact and target area was as same as in previous studies (Zhou et al., 2021a; He et al., 2022b).

Definition

In this study, only the data in the forward swing phase during the stroke were collected and analyzed. The pelvis movement in the transverse plane was defined as pelvis axial rotation (PAR), as well as

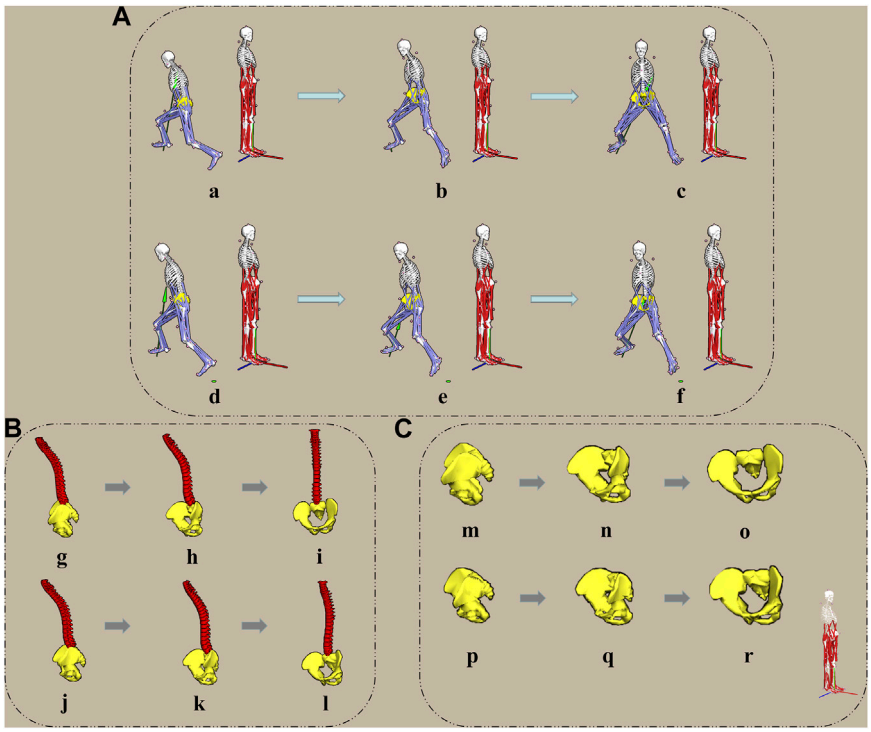

FIGURE 2
Diagram of the human musculoskeletal model of the CC and LL topspin forehand stroke. **(A)** indicate the topspin forehand stroke process. (a–c) and (d–f) indicate the CC and LL, respectively. **(B)** shows the lumbar and pelvis movement during the topspin forehand stroke. (g–i) and (j–l) indicate the CC and LL, respectively. **(C)** shows the pelvis movement during the topspin forehand stroke. (m–o) and (p–r) indicate the CC and LL, respectively.

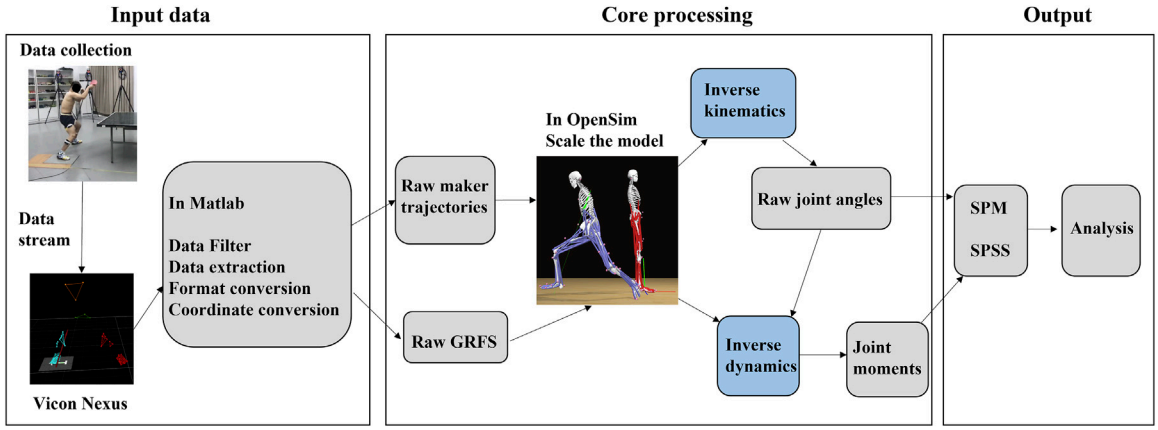

FIGURE 3
Flow chart and data processing.

the lumbar movement in the sagittal, frontal, and transverse plane, was defined as lumber flexion (LF), lumbar left lateral bending (LLB), and lumbar axial rotation (LAR) in this study.

As shown in Figure 2, "A", "B", and "C" are the CC and LL topspin forehand stroke process in the full body, lumbar, and pelvis view, respectively. Besides, the "a-c", "g-I", and "m-o" in CC and "d-f", "j-l", and "p-r" in LL indicate the "end of the backward swing (EB)", "medium forward swing (MF)", and "end of the forward swing (EF)", respectively. The definition of EB, MF, and EF was completed in the Vicon Nexus 1.8.6 software (Oxford Metrics, Ltd., Oxford, United Kingdom). When the GRF wave reached the first

TABLE 2 The moment and angle results of the SPM analysis. (Unit: %).

Variables	Percentage (*p*)
LAR Moment	0–1.75 (0.045), 3.80–28.14 (<0.001), 34.51–57.98 (<0.001)
LLB Moment	1.30–19.81 (<0.001), 27.93–49.48 (<0.001), 55.56–72.87 (<0.001), 97.38–100 (0.043)
LF Moment	0–2.52 (0.04), 6.38–29.08 (<0.001), 37.81–58.06 (<0.001), 63.86–76.6 (<0.001), 90.29–99.25 (0.003)
PAR Moment	4.15–30.01 (<0.001), 45.01–80.63 (<0.001),
LAR Angle	3.30–22.79 (<0.001), 30.29–60.43 (<0.001)
LLB Angle	12.29–75.30 (<0.001), 85.68–100 (0.004),
LF Angle	5.26–10.63 (0.038), 18.40–39.10 (0.001), 55.13–100 (<0.001)
PAR Angle	0–1.69 (0.049), 10.29–78.31 (<0.001), 88.90–100 (0.027)

Note: the percentage indicates the process of the stroke play phase.

peak value was defined as EB. After the first peak in the GRF wave, the medium value was defined as MF. And the second peak value in the GRF wave was defined as EF.

Data processing

As shown in Figure 3, GRF and kinematic data during CC and LL topspin forehand were identified and acquired using Vicon Nexus 1.8.6 software. The data was exported from the Vicon Nexus with a c3d. format file, and use MATLAB R2019a (The MathWorks, Natick, MA, United States) to perform coordinate system conversion, lower pass filtering, data extraction, and format conversation for all data. The detailed process in MATLAB R2019 has been outlined in previous studies (Zhou et al., 2021b; He et al., 2022b) that as follows: convert the coordinate to the subsequent simulation coordinate system, filter the marker trajectory and the GRF, and convert the formats of data to the trc. and mot. formats that are required by OpenSim. The statics model of the subjects was imported into OpenSim and the anthropometric model was obtained. Then we identified the muscle's starting and ending points and ensured the moment arms were consistent with the length of the subject's limb (Delp et al., 2007; He et al., 2022b). We used the inverse kinematic tool (IK) to calculate the kinematics data of the subject during CC and LL topspin forehand and created a motion file using mot format. We then imported the GRF and markers files using the inverse dynamics tool (ID) and calculated the joint moment. In OpenSim, the weighted least square problem was solved by the IK function to minimize the distance of markers' placements between the experimental and virtual; the generalized positions, velocities, and accelerations defined the motion of the model, which resulted in the unknown generalized forces were calculated by those known motion variables.

Statistical analysis

Kinematics and the moment of the pelvis and lumbar were analyzed by one-dimensional statistical parametric mapping (SPM1d) analysis in MATLAB R2019a. The Rom and peak moment of the pelvis and lumbar were analyzed by independent samples t-test in SPSS 24.0 (SPSSs Inc., Chicago, IL, United States). In the SPM analysis, we performed the custom script in MATLAB to expend all data into a time series curve of 101 data points. The significance level in this study was set as $p < 0.05$.

Result

Lumbar movement

Table 2; Figure 4 show the SPM1d analysis result of the angle and moment in the LAR, LLB, and LF between the CC and LL topspin forehand. In the LAR, the LL showed a significantly higher moment than CC in the 0%–1.75% ($p = 0.045$, $t = 3.331$) and 3.80%–28.14% ($p < 0.001$, $t = 3.331$) phase, and a significantly higher angle in 3.30%–22.79% ($p < 0.001$, $t = 3.129$) phase. However, the LL showed a significantly lower moment and angle in the 34.51%–57.98% ($p < 0.001$, $t = 3.331$) and 30.29%–60.43% ($p < 0.001$, $t = 3.129$) phase than CC, respectively. In the LLB, CC showed a significantly higher moment than LL in the 27.93%–49.48% ($p < 0.001$, $t = 3.258$), 55.56%–72.87% ($p < 0.001$, $t = 3.258$), 97.38%–100% ($p = 0.043$, $t = 3.258$) phase, and a significantly higher angle in the 12.29%–75.30% ($p < 0.001$, $t = 3.125$) and 85.68%–100% ($p = 0.004$, $t = 3.125$) phase. The LL showed a significantly higher moment in the 1.30%–19.81% ($p < 0.001$, $t = 3.258$) phase than CC. In the LF, the moment of LL was significantly higher than CC in the 6.38%–29.08% ($p < 0.001$, $t = 3.344$) and 90.29%–99.25% ($p = 0.003$, $t = 3.344$) phase, and the angle were higher than CC in the 55.13%–100% ($p < 0.001$, $t = 3.08$) phase. The CC showed a significantly higher moment in the 0%–2.52% ($p = 0.04$, $t = 3.344$), 37.81%–58.06% ($p < 0.001$, $t = 3.344$), and 63.86%–76.60% ($p < 0.001$, $t = 3.344$) phase, and a significantly higher angle in the 5.26%–10.63% ($p = 0.038$, $t = 3.080$) and 18.40%–39.10% ($p = 0.001$, $t = 3.080$) phase than LL.

As shown in Table 3; Figure 5, the Rom and peak moment of LLB and LF in CC were significantly higher than LL (Rom: $t = 16.55$, $p = 0$; $t = 12.139$, $p = 0$. Peak moment: $t = -3.396$, $p = 0.002$; $t = 3.412$, $p = 0.003$). The maximum LAR, LLB, and LF in the CC were significantly higher than LL ($t = -2.84$, $p = 0.008$; $t = 13.206$, $p = 0$; $t = -3.307$, $p = 0.003$).

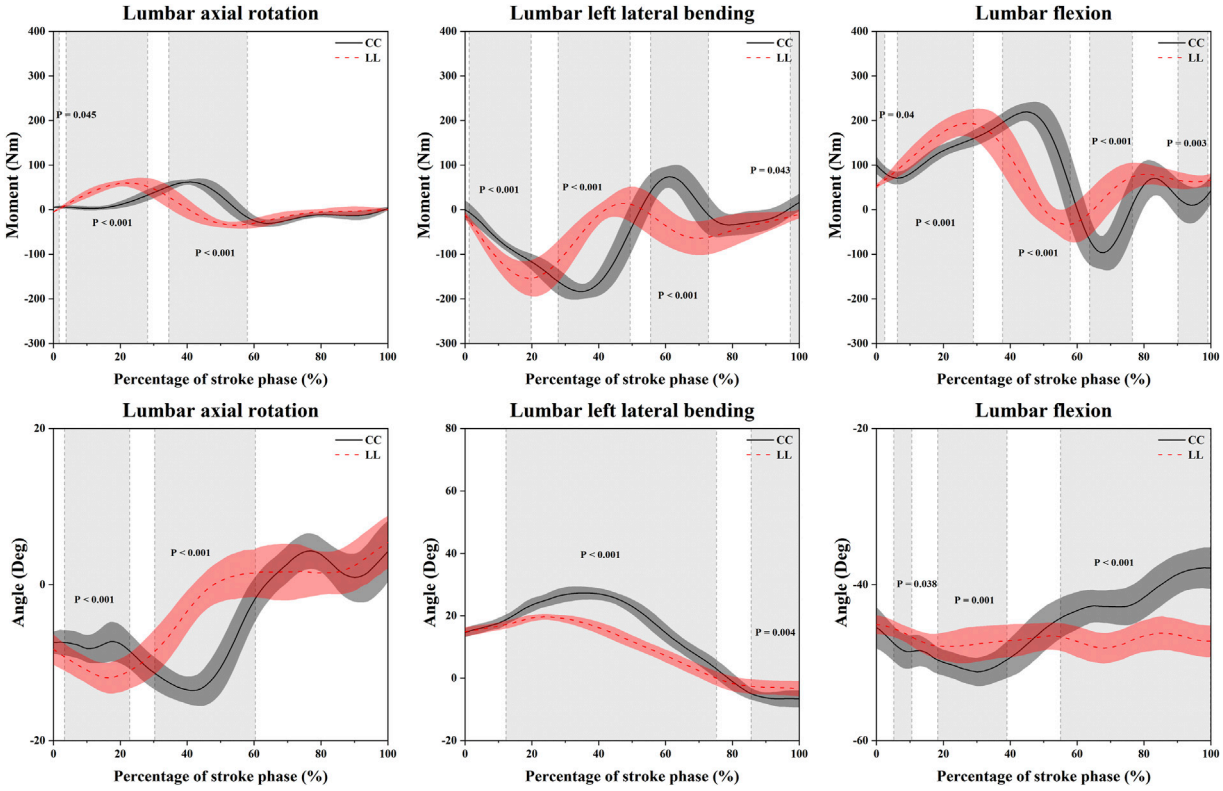

FIGURE 4
Illustration of the result of the angle and moment in the LAR, LLB, and LF between the CC and LL topspin forehand showing the SPM1d outputs. Grey-shaded areas indicate that there are significant differences ($p < 0.05$) between the CC and LL. LL indicates long-line topspin forehand, CC indicates cross-court topspin forehand.

TABLE 3 Comparison of Rom, Peak moment, and Maximum angle of lumbar and pelvis movement between CC and LL topspin forehand.

		Rom (Deg)				Peak moment (Nm)				Maximum angle (Deg)			
		Mean ± SD	*t*	*p*	*95%CI*	Mean ± SD	*t*	*p*	*95%CI*	Mean ± SD	*t*	*p*	*95%CI*
LAR	CC	20.10 ± 2.91	1.853	0.073	−1.90, 4.00	66.69 ± 3.97	1.06	0.30	−2.26, 7.13	−14.13 ± 1.80	−2.84	0.008*	−2.83, −0.47
	LL	18.19 ± 3.07				64.25 ± 8.29				−12.48 ± 1.57			
LLB	CC	35.39 ± 1.85	16.55	0*	10.16, 13.02	−194.0 ± 14.11	−3.396	0.002*	−54.72, 13.62	27.78 ± 2.19	13.206	0*	6.55, 8.94
	LL	23.80 ± 2.22				−159.82 ± 37.70				20.04 ± 1.03			
LF	CC	14.20 ± 2.44	12.139	0*	7.16, 10.06	231.10 ± 13.87	3.412	0.003*	11.43, 47.19	−51.46 ± 1.77	−3.307	0.003*	−2.84, −0.67
	LL	5.59 ± 1.61				201.79 ± 31.44				−49.71 ± 1.28			
PAR	CC	75.96 ± 5.64	12.798	0*	19.08, 26.31	597.68 ± 115.84	2.245	0.034*	6.01, 143.78	−52.02 ± 3.31	−9.627	0*	−15.08, −9.81
	LL	53.26 ± 4.65				522.78 ± 66.27				−39.57 ± 4.17			

Note: "*" indicate a significant difference between LL and CC. LL indicates long-line topspin forehand, CC indicates cross-court topspin forehand. LAR indicates lumbar axial rotation, LLB indicates lumbar left lateral bending, LF indicates lumbar flexion, and PAR indicates pelvis axial rotation.

Pelvis axial rotation

Table 2; Figure 6 show the SPM1d analysis result of the angle and moment of PAR between the CC and LL topspin forehand. The PAR angle of CC was significantly higher than LL in the 10.29%–78.31% ($p < 0.001$, $t = 2.86$) and 88.90%–100% ($p = 0.027$, $t = 2.86$) phase, but significantly lower than LL in 0%–1.69% ($p = 0.049$, $t = 2.86$) phase. The PAR moment of CC was significantly higher than LL in the 4.15%–30.01% ($p < 0.001$, $t = 3.288$) phase and significantly lower than LL in the 45.01%–80.63% ($p < 0.001$, $t = 3.288$) phase.

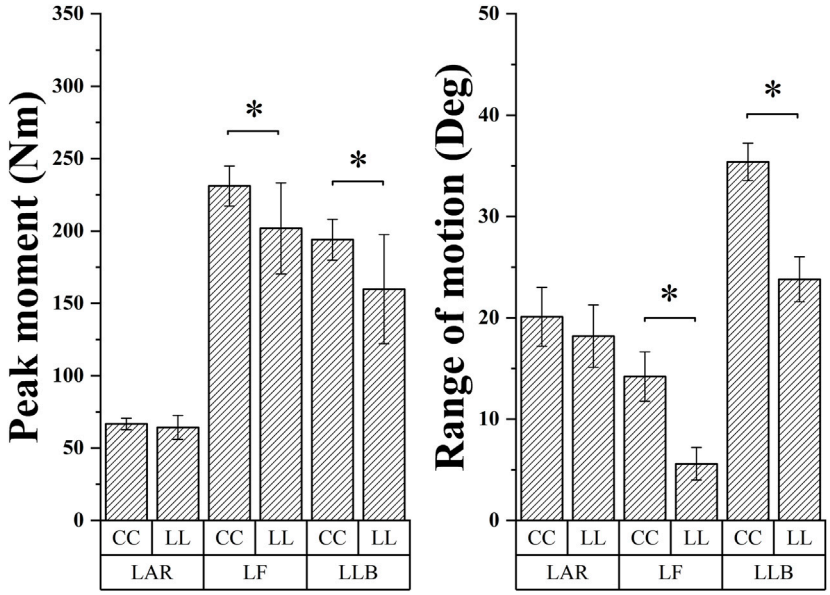

FIGURE 5
The Rom and peak moment comparison of lumbar movement between the CC and LL topspin forehand. "*" indicate a significant difference between LL and CC. LL indicates long-line topspin forehand, CC indicates cross-court topspin forehand. LAR indicates lumbar axial rotation, LLB indicates lumbar left lateral bending, and LF indicates lumbar flexion.

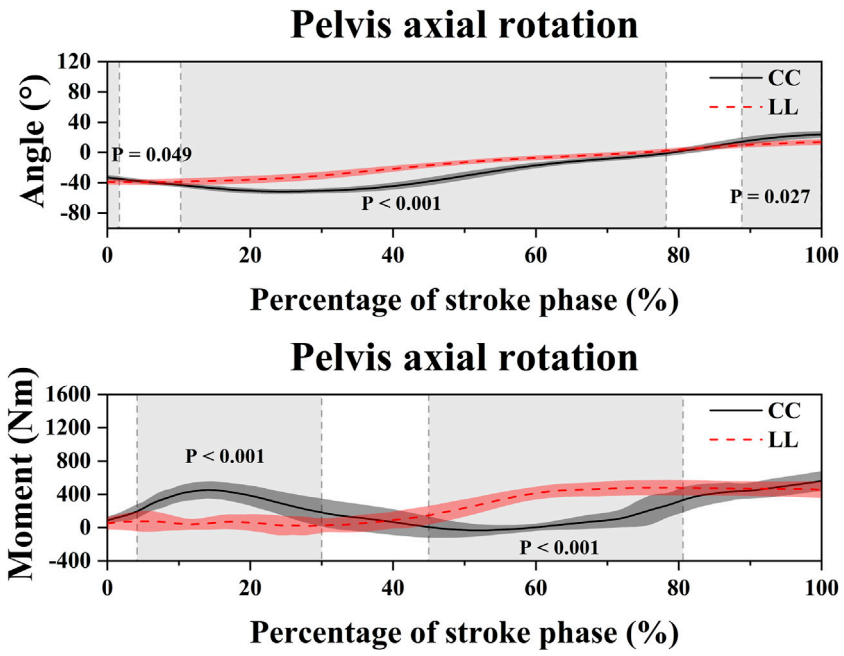

FIGURE 6
Illustration of the result of angle and moment of the PAR between the CC and LL topspin forehand showing the SPM1d outputs. Grey-shaded areas indicate that there are significant differences ($p < 0.05$) between the CC and LL. LL indicates long-line topspin forehand, CC indicates cross-court topspin forehand.

As shown in Table 3; Figure 7, The maximum PAR in the CC was significantly higher than LL ($t = -9.627$, $p = 0$), and Rom and peak moment of PAR in the CC was significantly higher than LL ($p = 0$, $t = 12.798$; $p = 0.034$, $t = 2.245$).

Discussion

This study simulated the musculoskeletal model in OpenSim to investigate the lumbar and pelvis movement difference

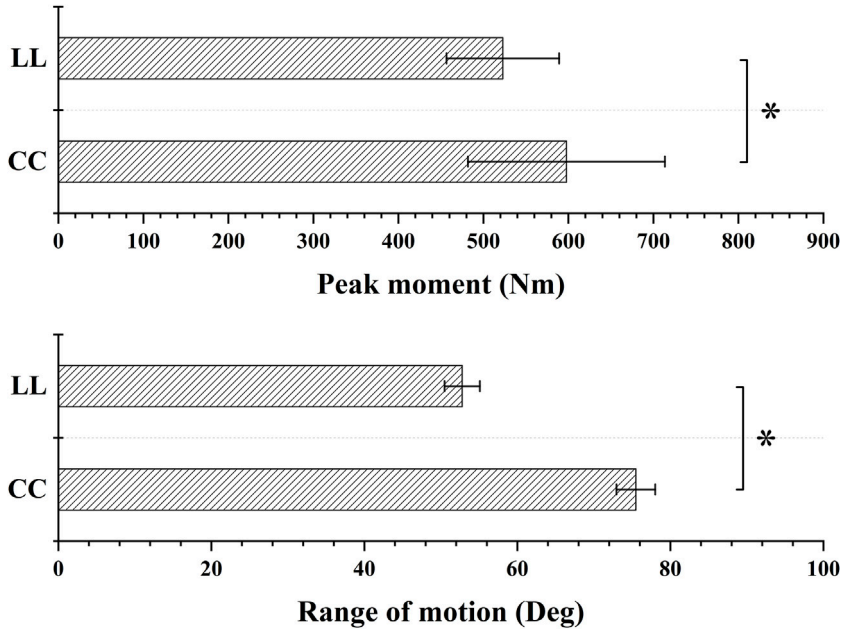

FIGURE 7
The Rom and peak moment comparison of PAR between CC and LL topspin forehand. "*" indicate a significant difference between LL and CC. LL indicates long-line topspin forehand, CC indicates cross-court topspin forehand.

between the CC and LL topspin forehand in table tennis. The key finding of this study was (Qian et al., 2016) the main difference between CC and LL topspin forehand in the lumbar movement was found in the LLB and LF, the Rom, peak moment, and maximum angle of the LLB and LF in CC were significantly higher than LL (He et al., 2022a); the Rom, peak moment and maximum angle of PAR in CC were significantly higher than LL (Poizat et al., 2004); the moment of LL in the LF and LLB was significantly higher than CC in the early stroke phase. The results of the current study were consistent with our hypothesis, the CC and LL showed a significant difference in lumbar and pelvis movement in the transverse plane. Investigating the difference in lumbar and pelvis movement between the CC and LL topspin forehand could provide guidelines for coaches and players to understand the mechanisms inherent from a biomechanical perspective, especially the information could help beginners to build awareness of CC and LL topspin forehand skills more easily for enhance their stroke skill and motor control.

The lumbar movement is widely focused, especially in racket sports. The Rom and maximum angle of the LLB and LF in CC were significantly higher than LL in this study. This could be explained by the fact that the target area in CC is the left side of the playing body, and the players need to adjust their bodies to hit the ball correctly. A higher LLB Rom and maximum angle could bring a completed body weight transfer which could benefit the energy transfer from the trunk to the upper limb following the proximal-to-distal segmental sequences in the kinetic chain (Fu et al., 2016; Bańkosz and Winiarski, 2018; Lam et al., 2019; He et al., 2022b). A higher LF in CC probably means a more forward shift of the center of gravity in the sagittal plane, furthermore, the shift in the center of gravity will result in greater energy transfer, which may mean greater racket acceleration during the forward swing phase. In previous studies, lower back pain (LBP) in athletes of racket sports has been thought to be closely associated with lumbar movement (Kawasaki et al., 2005; Campbell et al., 2013; Campbell et al., 2014; Connolly et al., 2020; Connolly et al., 2021). The lumbar section as the main core region of the body plays a coordinating role in the compound movement of the upper and lower extremities, however, this is also a major cause of LBP, because in the topspin forehand motor, the LLB, LAR, and LF have occurred simultaneously, the 'coupled movements' could bring more pressure and load to vertebral structures than the single plane movement (Gunzburg et al., 1992; Haberl et al., 2004). Previous studies have shown that 32% of athletes experience pain in the lumbar and spinal column during competition or immediately after training, and 36% of athletes even quit training due to pain (He et al., 2022a). In the topspin forehand, the athlete's unilateral upper extremity needs to hit the ball with maximum force, and this often leads to full body involvement, increasing the impact of the stroke through a large transfer of full body weight. However, the foot on the non-playing side needs to be locked on the ground to maintain dynamic body balance. Extensive repetition of this compensatory movement leads to severe overload of the posterior side of the disc and causes injury. Further, the significantly greater maximum angle and peak moment of LF and LLB exhibited in CC relative to LL may imply a greater risk of injury.

Extensive research on topspin forehand already exists, but few studies have reported detailed information on pelvis movement during topspin forehand stroke. The result shows that the Rom, peak moment and maximum angle of PAR in CC

were significantly higher than in LL. The ROM value of PAR in this study was basically consistent with the study of Bańkosz and Winiarski (2018) and Malagoli Lanzoni et al. (2018) respectively, this indicates that during the topspin forehand, the players follow a steady motor program and execute it repeatedly, which may be gradually fixed and standardized in daily training and practice. Players will make small adjustments to their own movement patterns according to the changes in the situation during the match, and finally complete the stroke task. Previous studies have reported the important role of pelvic axial rotation on racket acceleration (Iino, 2018; Xia et al., 2020), even trunk rotation is probably the most critical factor in the development of racket speed (Landlinger et al., 2010), a higher velocity was observed in CC as compared with LL in tennis (Landlinger et al., 2010). The CC has a longer trajectory than the LL (Malagoli Lanzoni et al., 2018), and the target area was on the left side of the playing body, these were the results obtained in players trying to get a racket acceleration during the forward swing phase through full muscle elongation and a greater axial rotation of the lower trunk in CC. The ROM and peak moment of PAR in CC was significantly higher than in LL in the current study, this also could be linked to a more weight transfer that could bring more energy transfer to further enhance the racket acceleration (He et al., 2022b), because the playing arm was the endpoint of the body during stroke motor program which follows the proximal-to-distal segmental sequences in the kinetic chain (Fu et al., 2016; Bańkosz and Winiarski, 2018; Lam et al., 2019; He et al., 2022b). However, the result of the pelvis movement between CC and LL was different from the study of Malagoli Lanzoni et al. (2018). This is due to the different calculations, in their study the angle of axial pelvic movement was calculated relative to the table and not based on the player's own body, and the position of the player's feet when hitting the ball was not taken into account, the player's position was different in CC and LL, so the movement information of the pelvis is not comprehensive enough if only the playing table was used as a reference in evaluation. The moment of LL in the LF and LLB was significantly higher than CC in the early stroke phase. This result could support the hypothesis of Xing et al. (2022) in the discussion section. Furthermore, this could probably be explained that LL has a shorter trajectory (Malagoli Lanzoni et al., 2018) and less forward swing time compared with CC (Xing et al., 2022), which results in the players having to pull their muscles as soon as possible in a limited time to gain more elastic energy to complete an attractive stroke. On the other hand, a shorter running trajectory of the ball in LL means a shorter reaction time for the player, which further requires the player to return to the ready position for the next stroke. This could explain the ROM and maximum angle of LF and LLB in the LL were significantly less than in the CC.

After understanding the differences between the lumbar and pelvis movements of CC and LL topspin forehand, players could enhance the motor control of lumbar and pelvis movements according to the movement characteristics, either by enhancing core strength to improve the explosive power of lumbar and pelvis movements or by flexibility training to enhance lumbar and pelvis synergy, as these modalities are able to enhance the level of energy transfer in the power chain and improve performance. Beginners could quickly understand the role and contribution of the lumbar and pelvis in topspin forehand skills based on the results of this study, thus making it easier to master CC and LL topspin forehand skills.

There are several limitations of this study that have to be mentioned (Qian et al., 2016): the result of this study was limited to male table tennis players; therefore, the result may not be generalizable to female players (He et al., 2022a); the results of this study were generated in a laboratory environment and the results may be inaccurate in relation to a real game environment, for example, where the player needs to judge the rotation and direction of the next ball, which may result in the player having to adjust their body to ensure they can move to the correct position at all time (Poizat et al., 2004); the motion time of stroke in each phase and racket velocity should be measured in further studies.

Conclusion

This study analyzed and compared the movement of the lumbar and pelvis during the CC and LL topspin forehand. The results showed that the lumbar and pelvis embody greater weight transfer and greater energy production mechanisms when players performed CC compared to LL, while it is important to note that players are also at greater risk of lumbar injury in CC. Beginners could enhance their motor control strategies in forehand topspin skills and master this skill more easily based on the findings of this study.

Data availability statement

The raw data supporting the conclusion of this article will be made available by the authors, without undue reservation.

Ethics statement

The studies involving human participants were reviewed and approved by ningbo university. The patients/participants provided their written informed consent to participate in this study.

Author contributions

YH, GF, and YF worked on the conception and experiment design. YH, ML, and GF were involved in the data processing and manuscript writing. JB and YF helped in manuscript revision and final approval of the manuscript. All authors contributed to the article and approved the submitted version.

Funding

This study was sponsored by the Zhejiang Provincial Natural Science Foundation of China for Distinguished Young Scholars (LR22A020002), Zhejiang Provincial Key Research and

Development Program of China (2021C03130), Zhejiang Provincial Natural Science Foundation (LTGY23H040003), János Bolyai Research Scholarship of the Hungarian Academy of Sciences (BO/00047/21/6), Research Academy of Medicine Combining Sports, Ningbo (No. 2023001), the Project of NINGBO Leading Medical and Health Discipline (No. 2022-F15 and No. 2022-F22), Ningbo Natural Science Foundation (20221JCGY010532 and 20221JCGY010607), Public Welfare Science and Technology Project of Ningbo, China (2021S134), and K. C. Wong Magna Fund in Ningbo University.

Acknowledgments

We would appreciate the participation of each participant.

Conflict of interest

The authors declare that the research was conducted in the absence of any commercial or financial relationships that could be construed as a potential conflict of interest.

Publisher's note

References

Akutagawa, S., and Kojima, T. (2005). Trunk rotation torques through the hip joints during the one-and two-handed backhand tennis strokes. *J. Sport Sci.* 23, 781–793. doi:10.1080/02640410400021609

Bańkosz, Z., and Barczyk-Pawelec, K. (2020). Habitual and ready positions in female table tennis players and their relation to the prevalence of back pain. *PeerJ* 8, e9170. doi:10.7717/peerj.9170

Bańkosz, Z., and Winiarski, S. (2018). The evaluation of changes of angles in selected joints during topspin forehand in table tennis. *Mot. Control* 22, 314–337. doi:10.1123/mc.2017-0057

Campbell, A., O'Sullivan, P., Straker, L., Elliott, B., and Reid, M. (2014). Back pain in tennis players: A link with lumbar serve kinematics and range of motion. *Med. Sci. Sport Exer* 46, 351–357. doi:10.1249/mss.0b013e3182a45cca

Campbell, A., Straker, L., O'Sullivan, P., Elliott, B., and Reid, M. (2013). Lumbar loading in the elite adolescent tennis serve: Link to low back pain. *Med. Sci. Sport Exer* 45, 1562–1568. doi:10.1249/mss.0b013e31828bea5e

Chen, M. Z., Wang, X., Chen, Q., Ma, Y., Malagoli Lanzoni, I., and Lam, W. K. (2022). An analysis of whole-body kinematics, muscle strength and activity during cross-step topspin among table tennis players. *Int. J. Perf. Anal. Spor* 22, 16–28. doi:10.1080/24748668.2022.2025712

Connolly, M., Middleton, K., Spence, G., Cant, O., and Reid, M. (2021). Effects of lumbar spine abnormality and serve types on lumbar kinematics in elite adolescent tennis players. *Sports Med-Open* 7, 7–10. doi:10.1186/s40798-020-00295-2

Connolly, M., Rotstein, A. H., Roebert, J., Grabinski, R., Malara, F., O'Shea, T., et al. (2020). Lumbar spine abnormalities and facet joint angles in asymptomatic elite junior tennis players. *Sports Med-Open* 6, 57–10. doi:10.1186/s40798-020-00285-4

Delp, S. L., Anderson, F. C., Arnold, A. S., Loan, P., Habib, A., John, C. T., et al. (2007). OpenSim: Open-source software to create and analyze dynamic simulations of movement. *IEEE T Bio-Med Eng.* 54, 1940–1950. doi:10.1109/TBME.2007.901024

Dorschky, E., Nitschke, M., Seifer, A. K., Van den Bogert, A. J., and Eskofier, B. M. (2019). Estimation of gait kinematics and kinetics from inertial sensor data using optimal control of musculoskeletal models. *J. Biomech.* 95, 109278. doi:10.1016/j.jbiomech.2019.07.022

Elliott, B. (2000). "Hitting and kicking," in *Biomechanics in sport*. Editor V. M. Zatsiorsky (Oxford: Blackwell Science), 487–504.

Fu, F., Zhang, Y., Shao, S., Ren, J., Lake, M., and Gu, Y. (2016). Comparison of center of pressure trajectory characteristics in table tennis during topspin forehand loop between superior and intermediate players. *Int. J. Sports Sci. Coa* 11, 559–565. doi:10.1177/1747954116654778

Gunzburg, R., Hutton, W. C., Crane, G., and Fraser, R. D. (1992). Role of the capsulo-ligamentous structures in rotation and combined flexion-rotation of the lumbar spine. *Clin. Spine Surg.* 5, 1–7. doi:10.1097/00002517-199203000-00001

Haberl, H., Cripton, P. A., Orr, T. E., Beutler, T., Frei, H., Lanksch, W. R., et al. (2004). Kinematic response of lumbar functional spinal units to axial torsion with and without superimposed compression and flexion/extension. *Eur. Spine J.* 13, 560–566. doi:10.1007/s00586-004-0720-6

He, Y., Fekete, G., Sun, D., Baker, J. S., Shao, S., and Gu, Y. (2022a). Lower limb biomechanics during the topspin forehand in table tennis: A systemic review. *Bioengineering* 9, 336. doi:10.3390/bioengineering9080336

He, Y., Lv, X., Zhou, Z., Sun, D., Baker, J. S., and Gu, Y. (2020). Comparing the kinematic characteristics of the lower limbs in table tennis: Differences between diagonal and straight shots using the forehand loop. *J. Sport Sci. Med.* 19, 522–528.

He, Y., Lyu, X., Sun, D., Baker, J. S., and Gu, Y. (2021a). The kinematic analysis of the lower limb during topspin forehand loop between different level table tennis athletes. *PeerJ* 9, e10841. doi:10.7717/peerj.10841

He, Y., Shao, S., Fekete, G., Yang, X., Cen, X., Song, Y., et al. (2022b). Lower limb muscle forces in table tennis footwork during topspin forehand stroke based on the OpenSim musculoskeletal model: A pilot study. *Mol. Cell. Biomech.* 19, 221–235. doi:10.32604/mcb.2022.027285

He, Y., Sun, D., Yang, X., Fekete, G., Baker, J. S., and Gu, Y. (2021b). Lower limb kinetic comparisons between the chasse step and one step footwork during stroke play in table tennis. *PeerJ* 9, e12481. doi:10.7717/peerj.12481

Iino, Y. (2018). Hip joint kinetics in the table tennis topspin forehand: Relationship to racket velocity. *J. Sport Sci.* 36, 834–842. doi:10.1080/02640414.2017.1344777

Iino, Y., and Kojima, T. (2009). Kinematics of table tennis topspin forehands: Effects of performance level and ball spin. *J. Sport Sci.* 27, 1311–1321. doi:10.1080/02640410903264458

Iino, Y., and Kojima, T. (2011). Kinetics of the upper limb during table tennis topspin forehands in advanced and intermediate players. *Sport Biomech.* 10, 361–377. doi:10.1080/14763141.2011.629304

Iino, Y., Yoshioka, S., and Fukashiro, S. (2018). Effect of mechanical properties of the lower limb muscles on muscular effort during table tennis forehand. *ISBS Proc. Arch.* 36, 770.

Kawasaki, S., Imai, S., Inaoka, H., Masuda, T., Ishida, A., Okawa, A., et al. (2005). The lower lumbar spine moment and the axial rotational motion of a body during one-handed and double-handed backhand stroke in tennis. *Int. J. Sports Med.* 26, 617–621. doi:10.1055/s-2004-830338

Kolman, N. S., Kramer, T., Elferink-Gemser, M. T., Huijgen, B. C., and Visscher, C. (2019). Technical and tactical skills related to performance levels in tennis: A systematic review. *J. Sport Sci.* 37, 108–121. doi:10.1080/02640414.2018.1483699

Lam, W. K., Fan, J. X., Zheng, Y., and Lee, W. C. C. (2019). Joint and plantar loading in table tennis topspin forehand with different footwork. *Eur. J. Sport Sci.* 19, 471–479. doi:10.1080/17461391.2018.1534993

Landlinger, J., Lindinger, S. J., Stöggl, T., Wagner, H., and Müller, E. (2010). Kinematic differences of elite and high-performance tennis players in the cross court and down the line forehand. *Sport Biomech.* 9, 280–295. doi:10.1080/14763141.2010.535841

Landlinger, J., Stöggl, T., Lindinger, S., Wagner, H., and Müller, E. (2012). Differences in ball speed and accuracy of tennis groundstrokes between elite and high-performance players. *Eur. J. Sport Sci.* 12, 301–308. doi:10.1080/17461391.2011.566363

Le Mansec, Y., Dorel, S., Hug, F., and Jubeau, M. (2018). Lower limb muscle activity during table tennis strokes. *Sport Biomech.* 17, 442–452. doi:10.1080/14763141.2017.1354064

Malagoli Lanzoni, I., Bartolomei, S., Di Michele, R., and Fantozzi, S. (2018). A kinematic comparison between long-line and cross-court top spin forehand in competitive table tennis players. *J. Sport Sci.* 36, 2637–2643. doi:10.1080/02640414.2018.1456394

Muyor, J. M., Sánchez-Sánchez, E., Sanz-Rivas, D., and López-Miñarro, P. A. (2013). Sagittal spinal morphology in highly trained adolescent tennis players. *J. Sport Sci. Med.* 12, 588–593.

Nitschke, M., Dorschky, E., Heinrich, D., Schlarb, H., Eskofier, B. M., Koelewijn, A. D., et al. (2020). Efficient trajectory optimization for curved running using a 3D musculoskeletal model with implicit dynamics. *Sci. Rep.* 10, 17655–17712. doi:10.1038/s41598-020-73856-w

Pedro, B., João, F., Lara, J. P., Cabral, S., Carvalho, J., and Veloso, A. P. (2022). Evaluation of upper limb joint contribution to racket head speed in elite tennis players using IMU sensors: Comparison between the cross-court and inside-out attacking forehand drive. *Sensors* 22, 1283. doi:10.3390/s22031283

Poizat, G., Thouvarecq, R., and Séve, C. (2004). *A descriptive study of the rotative topspin and of the striking topspin of expert table tennis players. A. lees, JF Kahn and IW Maynard, Science and racket sports III*. London and New York: Routledge.

Qian, J., Zhang, Y., Baker, J. S., and Gu, Y. (2016). Effects of performance level on lower limb kinematics during table tennis forehand loop. *Acta Bioeng. Biomech.* 18 (3), 149–155. doi:10.5277/ABB-00492-2015-03

Seth, A., Hicks, J. L., Uchida, T. K., Habib, A., Dembia, C. L., Dunne, J. J., et al. (2018). OpenSim: Simulating musculoskeletal dynamics and neuromuscular control to study human and animal movement. *PLoS Comput. Biol.* 14, e1006223. doi:10.1371/journal.pcbi.1006223

Xia, R., Dai, B., Fu, W., Gu, N., and Wu, Y. (2020). Kinematic comparisons of the shakehand and penhold grips in table tennis forehand and backhand strokes when returning topspin and backspin balls. *J. Sport Sci. Med.* 19, 637–644.

Xing, K., Hang, L., Lu, Z., Mao, C., Kang, D., Yang, C., et al. (2022). Biomechanical comparison between down-the-line and cross-court topspin backhand in competitive table tennis. *Int. J. Env. Res. Pub He* 19, 5146. doi:10.3390/ijerph19095146

Yang, X., Mei, Q., Shao, S., Gu, W., He, Y., Zhu, R., et al. (2022). Understanding sex-based kinematic and kinetic differences of chasse-step in elite table tennis athletes. *Bioengineering* 9, 246. doi:10.3390/bioengineering9060246

Zhou, H., He, Y., Yang, X., Ren, F., Ugbolue, U. C., and Gu, Y. (2021a). Comparison of kinetic characteristics of footwork during stroke in table tennis: Cross-step and chasse step. *J. Vis. Exp.* 172, e62571. doi:10.3791/62571

Zhou, H., Quan, W., Liang, M., Ugbolue, U. C., and Baker, J. S. (2021b). A pilot study of muscle force between normal shoes and bionic shoes during men walking and running stance phase using opensim. *Actuators* 10, 274. doi:10.3390/act10100274

frontiers | Frontiers in Bioengineering and Biotechnology

TYPE Original Research
PUBLISHED 21 July 2023
DOI 10.3389/fbioe.2023.1201421

OPEN ACCESS

EDITED BY
Yih-Kuen Jan,
University of Illinois at Urbana-Champaign, United States

REVIEWED BY
Marco Ghislieri,
Polytechnic University of Turin, Italy
Kimitaka Hase,
Kansai Medical University, Japan

*CORRESPONDENCE
Jingmin Liu,
ljm_th@mail.tsinghua.edu.cn

RECEIVED 06 April 2023
ACCEPTED 13 July 2023
PUBLISHED 21 July 2023

CITATION
Bai X, Huo H and Liu J (2023), Analysis of mechanical characteristics of walking and running foot functional units based on non-negative matrix factorization. *Front. Bioeng. Biotechnol.* 11:1201421. doi: 10.3389/fbioe.2023.1201421

Analysis of mechanical characteristics of walking and running foot functional units based on non-negative matrix factorization

Xiaotian Bai[1,2,3], Hongfeng Huo[2,3] and Jingmin Liu[1]*

[1]Department of Physical Education, Tsinghua University, Beijing, China, [2]College of Physical Education, Hebei Normal University, Shijiazhuang, China, [3]Key Laboratory of Bioinformatics Evaluation of Human Movement, Hebei Normal University, Shijiazhuang, China

Objective: To explore the characteristics of Non-Negative Matrix Factorization (NNMF) in analyzing the mechanical characteristics of foot functional units during walking and running.

Methods: Eighteen subjects (9 males and 9 females) were recruited, and the ground reaction force curves of each foot region during walking and running were collected using a plantar pressure measurement system. NNMF was used to extract the mechanical features of different foot regions and to determine the number of foot functional units. The differences between the base matrices of walking and running were compared by traditional t-tests, and the differences in coefficient matrices were compared by one-dimensional statistical parameter mapping.

Results: 1) When the number of foot functional units for walking and running were both 2, the Variability Accounted For (VAF) by the matrix exceeded 0.90 (VAF_{walk} = 0.96 ± 0.02, VAF_{run} = 0.95 ± 0.04); 2) In foot functional unit 1, both walking and running exhibited buffering function, with the heel region being the main force-bearing area and the forefoot also participating in partial buffering; 3) In foot functional unit 2, both walking and running exhibited push-off function, with the middle part of the forefoot having a higher contribution weight; 4) In foot functional unit 1, compared to walking, the overall force characteristics of the running foot were greater during the support phase of the 0%–20% stage, with the third and fourth metatarsal areas having higher contribution weights and the lateral heel area having lower weights; 5) In foot functional unit 2, compared to walking, the overall force was higher during the beginning and 11%–69% stages of running, and lower during the 4%–5% and 73%–92% stages. During running, the thumb area, the first metatarsal area and the midfoot area had higher contribution weights than during walking; in the third and fourth metatarsal areas, the contribution weights were lower during running than during walking.

Conclusion: Based on the mechanical characteristics of the foot, walking and running can both be decomposed into two foot functional units: buffering and push-off. The forefoot occupies a certain weight in both buffering and push-off functions, indicating that there may be a complex foot function transformation mechanism in the transverse arch of foot. Compared to walking, running completes push-off earlier, and the force region is more inclined towards the

inner side of the foot, with the hallux area having a greater weight during push-off. This study suggests that NNMF is feasible for analyzing foot mechanical characteristics.

KEYWORDS

non-negative matrix factorization, one-dimensional statistical parameter mapping, foot pressure, walking, running

1 Introduction

Walking and running are the most basic forms of human movement. The low cost and convenience make brisk walking and slow running a popular way of exercising (Wolf and Wohlfart, 2014). In the process of walking and running, the foot as the supporting part of the human body not only bears the weight of the body but also absorbs and releases energy, cushions ground impact, and completes extension (Natali et al., 2010; Hageman et al., 2011; Kelly et al., 2014). Therefore, functional analysis of the foot during walking and running has important value. Foot pressure is the most commonly used analysis index to reflect foot function. Measuring foot pressure can help understand the support method and pressure distribution of the foot., evaluate the balance, stability and motion control ability of the foot (Hu et al., 2023; Jia et al., 2023). At present, foot pressure testing and analysis have been applied to rehabilitation programs and sports training program development (Wikstrom and McKeon, 2014; Jiang et al., 2021; Conner et al., 2022), foot function evaluation (Hillstrom et al., 2013; Montagnani et al., 2021; Shen et al., 2021), and sports shoe research and development (Chen et al., 1994; Zhao and Li, 2019).

Currently, assessment of plantar pressure usually divides the foot into four major zones: toe zone, metatarsal zone, midfoot zone, and heel zone, and each zone can be further divided into different subzones based on anatomical features. Functional analysis of the foot is performed using metrics such as impulse, maximum pressure, maximum pressure intensity and force loading rate in different regions of the foot (Aminian et al., 2013; Hillstrom et al., 2013). However, the structure and function of the foot are often closely related, and it is insufficient to divide the plantar area based solely on anatomical features, which may overlook the same mechanical properties of different regions of the foot, resulting in redundant regional divisions. At the same time, traditional plantar pressure indicators cannot simultaneously consider the spatiotemporal characteristics of foot mechanics. Therefore, from the perspective of functional analysis of foot movement, the shortcomings of traditional plantar pressure analysis methods can lead to information loss in the data analysis process, making it difficult to explore the dynamic mechanical characteristics of the foot.

Non-Negative Matrix Factorization (NNMF) is a data analysis method used to process complex non-negative data. It completes dimensionality reduction by decomposing the original matrix into a base matrix that reflects the weight of each element and a coefficient matrix that reflects the overall characteristics of each element. This makes the extracted data have clustering and temporal characteristics (Lee and Seung, 1999). Existing research in sports science mostly applies NNMF to analyze Surface Electromyographic Signals (sEMG) to explore muscle coordination characteristics of complex human action control mechanisms and action learning rules (Hagio et al., 2015; Hajiloo et al., 2020; Bach et al., 2021). In the medical field, NNMF can be used to predict the potential relationship between drugs and diseases, or detect the distribution of tumors based on magnetic resonance imaging (Laudadioa et al., 2016; Wang et al., 2022). In addition, NNMF can also be used for signal processing applications such as audio separation and feature extraction (O'Grady and Pearlmutter, 2008; Li et al., 2017). As plantar pressure has non-negative characteristics, some researchers have applied this method to functional partitioning of the foot and it has been proven to be feasible (Van Hese et al., 2021). Although NNMF can be combined with motion forms to divide foot functional areas, traditional statistical methods still cannot meet the requirements of curve analysis because the coefficient matrix of NNMF is a continuous data model. One-Dimensional Statistical Parameter Mapping (SPM1D) based on random field theory can be used for topological analysis of continuous data models, which has been applied in one-dimensional biomechanical data such as torque and angle (Pataky, 2012; Pataky et al., 2013; Pataky et al., 2015). Based on the research of Van Hese et al. (Van Hese et al., 2021), this paper incorporates SPM1D to the traditional statistical method to achieve quantitative analysis of the decomposed matrix by NNMF.

Combining the above content, this study collected plantar pressure data during walking and running and applied NNMF and SPM1D methods to divide the foot according to the mechanical characteristics of walking and running, extract foot functional units, and compare the dynamic foot mechanical characteristics of walking and running. This provides methodological support and theoretical support for the simplified processing of complex foot mechanical data and dynamic mechanical feature comparison of the foot.

2 Materials and methods

2.1 Participants

According to the sample size estimation using PASS software (Version15, NCSS, United States) for paired sample experimental design, when the significance level is 0.05, statistical power is 0.80, and effect size is 0.80, the minimum required sample size is 15. Based on the sample size estimation results, our study recruited 18 young participants for walking and running plantar pressure tests, including 9 male participants (age 25.2 ± 3.2 years, height 176.2 ± 4.3 cm, weight 68.3 ± 5.7 kg) and 9 female participants (age 24.3 ± 4.1 years, height 161.3 ± 3.7 cm, weight 51.9 ± 7.2 kg).

The participants involved in this experiment were normal foot types [with a foot arch index between 0.21–0.26 (Cavanagh and Rodgers, 1987)], All participants were healthy and had no history of

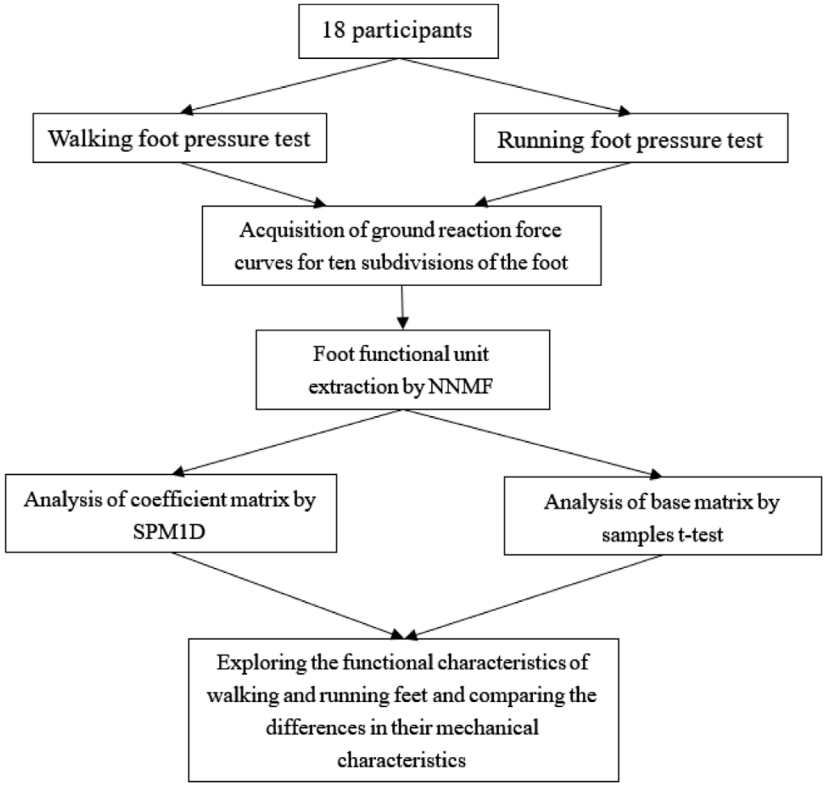

FIGURE 1
Technology roadmap.

lower limb surgery or lower limb injury within the past 3 months. They did not engage in strenuous exercise 48 h before the test. The dominant foot of the subjects was the right foot, and they ran with a rearfoot strike pattern. All subjects voluntarily participated in this experiment and signed an informed consent form. This experiment was approved by the Ethics Committee of Hebei Normal University (No. 2022LLSC026).

2.2 Experimental procedure and data acquisitions

Before the test began, the subjects were first familiarized with the experimental procedure under the explanation of the experimenter and completed warm-up under the guidance of the experimenter. After collecting basic information such as height, age, and weight, the subjects completed three barefoot walking and running tests in random order by drawing lots in a foot pressure test system with a length of 2 m and an extension runway of 1.5 m at both the starting point and the end point. According to previous research on the most suitable walking speed for young people (Lian et al., 2012; Baroudi et al., 2022), a speed closest to 1.50 m/s was recorded for the walking test, and the final walking speed range was 1.49 ± 0.09 m/s; in the running test, participants were selected to run at a speed close to twice walking speed (3.00 m/s) for recording purposes (Aghabayk et al., 2021), and the final running speed range was 3.08 ± 0.29 m/s. The Footscan high-frequency foot pressure test board produced by RSscan International Company was used in the test. The sampling frequency of the instrument was 126 Hz, the sensor density was 4 per square centimeter, the effective pressure measurement range was [1,60] N per square centimeter, and the minimum resolution was 0.25N. The technology roadmap of this study was shown in Figure 1.

2.3 Data processing

2.3.1 Foot pressure data preprocessing

Plantar pressure were divided into ten regions according to Footscan software (as shown in Figure 2), and the vertical ground reaction force changes of each region during walking and running support phases were collected. The collected foot pressure raw data of the ten regions were normalized according to the subject's weight, where the acceleration due to gravity was taken as 9.8 m/s. The weight-normalized foot pressure data were filtered in Origin2018 using a fourth-order Butterworth low-pass filter with the cutoff frequency set to 20 Hz (Limroongreungrat and Boonkerd, 2019), and the curve was interpolated using cubic B-Spline (Warmenhoven et al., 2018). The number of points after interpolation was set to 101, which normalizes the support phase to an interval of 0%–100% (Warmenhoven et al., 2018).

(Note: Where T1 represents the thumb area, T2-5 represents the second to fifth toe area, M1 represents the first metatarsal area, M2 represents the second metatarsal area, M3 represents the third

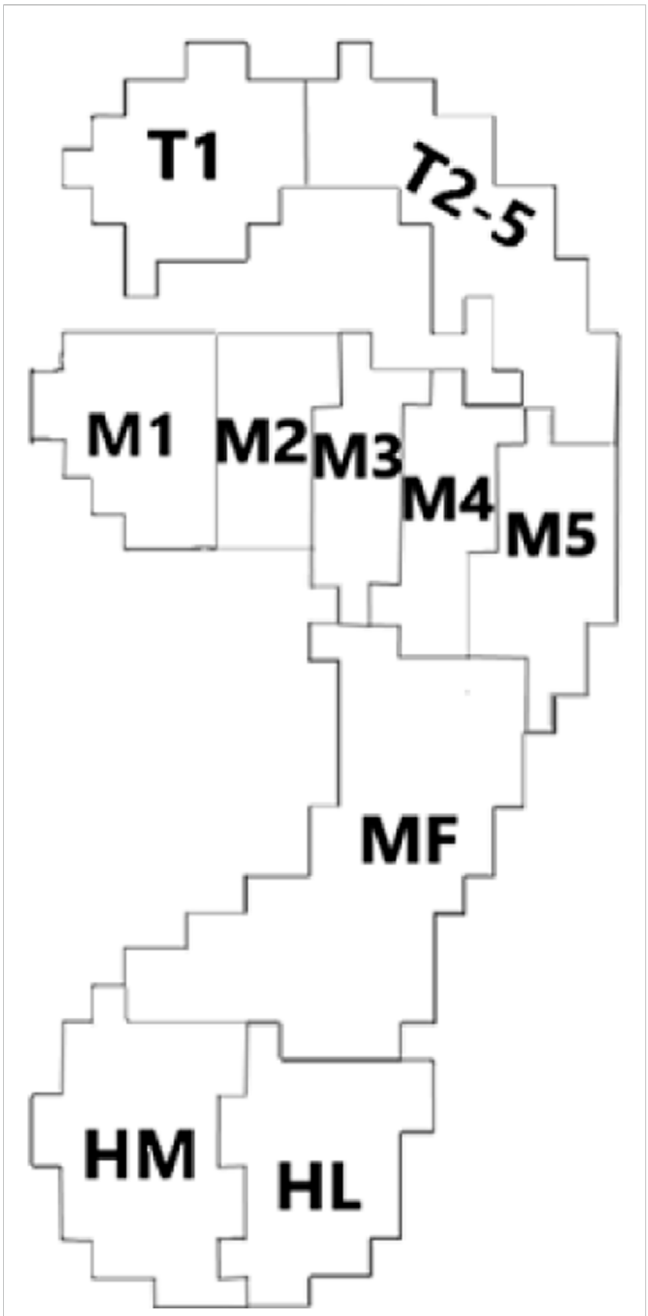

FIGURE 2
Foot partition schematic diagram.

metatarsal area, M4 represents the fourth metatarsal area, M5 represents the fifth metatarsal area, MF represents the midfoot area, HM represents the medial heel area, and HL represents the lateral heel area.).

2.3.2 Foot function unit extraction

The preprocessed plantar pressure data was arranged into a 10 row and 101 column matrix V based on 10 foot regions and 101 sampling points. NNMF was used to decompose matrix V into a 10-row k-column basis matrix W and a k-row 101-column coefficient matrix H, where k is the number of factors used in matrix decomposition (Lee and Seung, 1999) and represents the number of foot function units extracted (see Eq. 1). In order to eliminate the influence of random initialization matrix on the accuracy of results, NNMF was performed 10 times for each data, and the maximum VAF was extracted (Nishida et al., 2017). The matrix calculation was performed using the NNMF function combined with a loop statement in MATLAB 2022b. (Mathworks, USA), and the number of iterations was set to 5000 (Nishida et al., 2017; Sun, 2019).

$$\begin{bmatrix} V_{11} & V_{12} \dots V_{1101} \\ V_{21} & V_{22} \dots V_{2101} \\ \vdots & \vdots \quad \dots \quad \vdots \\ V_{101} & V_{102} \dots V_{10101} \end{bmatrix} \approx \begin{bmatrix} W_{11} \dots W_{1k} \\ W_{21} \dots W_{2k} \\ \vdots \quad \dots \quad \vdots \\ W_{101} \dots W_{10k} \end{bmatrix} \times \begin{bmatrix} H_{11} H_{12} \dots H_{1101} \\ \vdots \quad \vdots \quad \dots \quad \vdots \\ H_{k1} H_{k2} \dots W_{k101} \end{bmatrix} \tag{1}$$

The Variability Accounted For (VAF) was used to evaluate the quality of the reconstructed matrix after decomposition. The VAF value ranges from 0 to 1, and the larger value of VAF indicates the higher quality of matrix reconstruction (Lee and Seung, 1999; Hug et al., 2010). In this study, the final number of foot functional units was determined when the VAF was greater than 0.85 and the change in VAF did not exceed 0.05 as the number of factors k increased, the convergence tolerance (TolFun) was set to 10^{-6} (Rabbi et al., 2020; Van Hese et al., 2021). The VAF calculation method is shown in (2):

$$VAF = 1 - \frac{RSS}{TSS} = 1 - \frac{\sum \left(V_{mn} - V'_{mn}\right)^2}{\sum {V_{mn}}^2} \tag{2}$$

Where *RSS* is the residual sum of squares between the original matrix and the reconstructed matrix, *TSS* is the total sum of squares of the original matrix, V_{mn} is the original matrix, and $V'_{mn}$is the reconstructed matrix.

As the matrices extracted from the same sport appear in a random order, it is necessary to classify the foot functional units. In this study, the cosine similarity was used to classify the units based on the curve characteristics of the coefficient matrix, the coefficient matrix in the extracted foot functional units from different subjects was compared with the initial coefficient matrix to rank the cosine similarity and thus classify the extracted foot functional units (Sy et al., 2016; Ghislieri et al., 2020; Van Hese et al., 2021). The cosine similarity is calculated as follows (3):

$$\cos \theta_{i,k,n} = \frac{H_{i,k} \cdot H_{1,1}}{\|H_{i,k}\| \cdot \|H_{1,1}\|} \tag{3}$$

Where $H_{i,k}$ represents the k-th foot functional unit extracted from the i-th participant, and $H_{1,1}$ represents the initial coefficient matrix, and $\cos \theta_{i,k,n}$ represents the cosine similarity between $H_{i,k}$ and $H_{1,1}$.

In the two decomposed matrices, the coefficient matrix H was used to evaluate the overall force characteristics of the foot during the support phase, and the basis matrix W was used to reflect the contribution of each foot region to the overall force characteristics of each foot functional unit. To unify the quantification standard, the weight of each foot region in each foot functional unit in the basis matrix W was normalized (Cappellini et al., 2006; Nishida et al., 2017), as shown in Eq. 4:

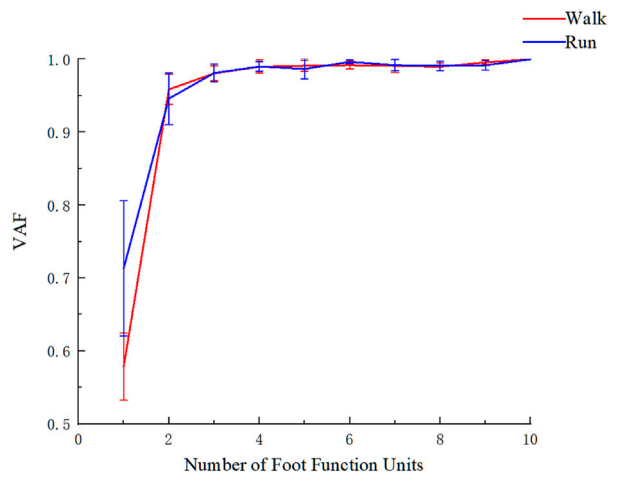

FIGURE 3
VAF vs. number of foot functional unit curve during walking and running.

$$C_{wi} = \frac{1}{10}\sum_{n=1}^{10} C_{in} \tag{4}$$

Where i represents different foot functional units, n represents various foot regions, and C_{wi} is the normalized weight of each foot region in each foot functional unit.

2.4 Data statistics

2.4.1 Statistical test of coefficient matrix

For the coefficient matrix obtained by NNMF, SPM1D of paired experimental design was used to compare the force characteristics of walking and running foot functional units. When the curve residual value conforms to a normal distribution, the SPM1D model was used for testing. Otherwise, the SnPM1D was used for non-parametric model testing. The significance level α was set to 0.05, and the t-value calculation method of SPM/SnPM is as follows (Pataky et al., 2015):

$$SPM/SnPM_{\{t\}} = \frac{\mu_d}{s_d/\sqrt{n}} \tag{5}$$

Where μ_d is the mean difference of the paired sample, s_d is the standard deviation of the mean difference of the paired sample, and n is the number of paired samples.

According to the α value set in this study, the threshold $t_{critical}$ is calculated through random field theory. When $SPM/SnPM_{\{t\}}$ exceeds the threshold $t_{critical}$, it is judged that there is statistical significance between the samples (Pataky et al., 2013; Pataky et al., 2015). The Eq. 5.

$$P\left(SPM/SnPM_{\{t\}} > t_{critical}\right) = 1 - exp\left(-\int_{t_{critical}}^{\infty} f_{0D}(x)dx - ED\right) = \alpha \tag{6}$$

Where $f_{0D}(x)$ is the probability density function of the t-test; ED is the Euler density function related to smoothing.

2.4.2 Statistical test of basic matrix

For the basic matrix obtained by NNMF, the weights of each plantar region were normalized and perform a normality test at first. If the data conforms to normal distribution, paired sample t-test was used for comparing the difference between walking and running basic matrices; if the data does not conform to normal distribution, Wilcoxon signed-rank test was used for statistics. When $p < 0.05$, indicating that the difference is significant.

3 Results

3.1 Number of foot functional units determined

3.1.1 Determination of foot functional units for walking and running

Based on Figure 3, it can be observed that when the number of foot functional units is 2, the VAF of the reconstruction matrix is around 0.90 in both walking and running (with the VAF of 0.96 ± 0.02 for walking and 0.95 ± 0.04 for running), and the VAF does not significantly change when the number of foot functional units is greater than 2. Therefore, 2 foot functional units were selected for analysis during both walking and running.

3.2 Characteristics of foot functional units during walking and running

3.2.1 Characteristics of foot functional units during walking

Based on the foot force characteristics during walking, the two foot functional units obtained through NNMF are shown in Figure 4, which respectively reflect the overall force characteristics (coefficient matrix) and the weight distribution across different foot regions (base matrix) of the two functional units. It can be observed from Figure 4 that during walking, the two foot functional units are dominated by the heel region and the mid-forefoot region consisting of the second, third, and fourth metatarsal bones, respectively. The overall force characteristics are concentrated around 20% and 80% of the stance phase.

(The gray lines show the foot force characteristics of each participant during walking, and the black line represents the average of the walking foot force characteristics of the 18 participants).

3.2.2 Characteristics of foot functional units during running

NNMF was performed on the foot force characteristics during running, as shown in Figure 5. Similar to walking, the foot force characteristics during running were dominated by the heel and the second and third metatarsal bones. The overall force characteristics of the two foot functional units were concentrated respectively prior to 40% and between 40% and 60% of the stance phase during running.

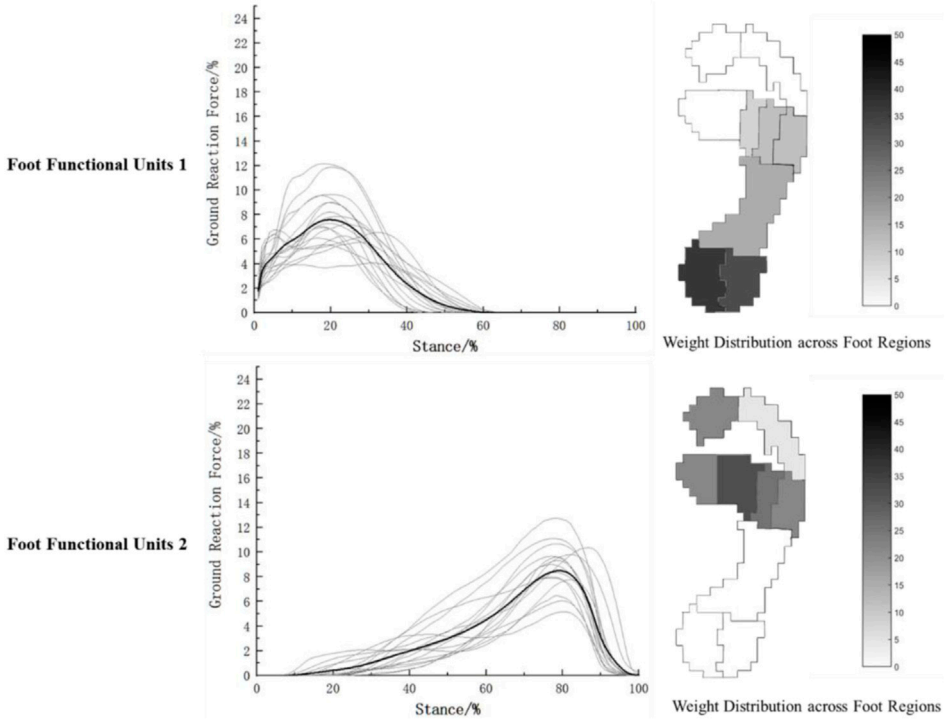

FIGURE 4
Characteristics of foot functional units during walking.

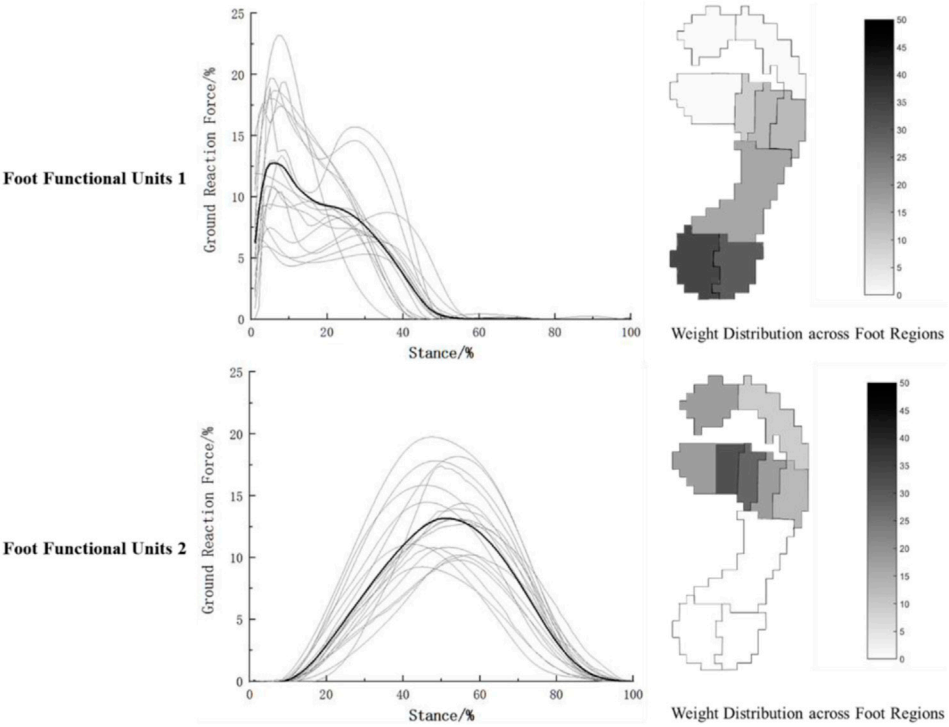

FIGURE 5
Characteristics of foot functional units during running.

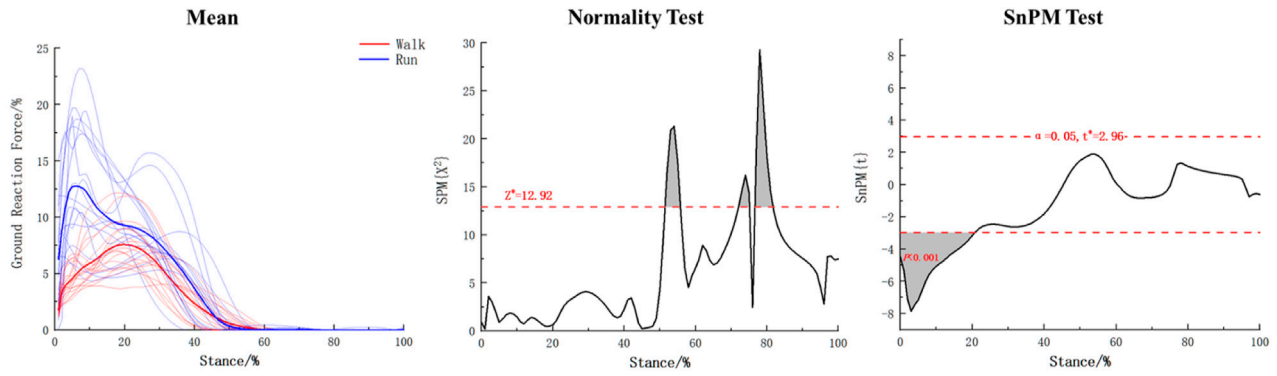

FIGURE 6
The coefficient matrix statistical results for walking and running in foot functional unit 1.

(The gray lines show the foot force characteristics of each participant during running, and the black line represents the average of the running foot force characteristics of the 18 participants).

3.3 Comparison of foot functional units between walking and running

3.3.1 Comparison of coefficient matrices between walking and running foot functional units

According to Figure 6, the coefficient matrix of walking and running in foot functional unit 1 does not follow a normal distribution. Therefore, a one-dimensional data test was performed using SnPM. The results showed that there was a significant difference ($p < 0.001$) in the coefficient matrix between walking and running during the 0%–20% stance phase in foot functional unit 1, with the overall force feature being higher during running than during walking in this phase.

Based on Figure 7, it is evident that the overall force characteristics of walking and running in foot function unit 2 do not follow a normal distribution. Therefore, a one-dimensional data test using SnPM was conducted. It was found that the thresholds were exceeded at the beginning of the stance phase, 4%–5%, 11%–69%, and 73%–92% stages during walking and running. Specifically, the overall force during walking was lower than that during running at the beginning ($p = 0.014$) and 11%–69% stages ($p < 0.001$), while the overall force during walking was higher than that during running at the 4%–5% ($p = 0.001$) and 73%–92% stages ($p < 0.001$).

3.3.2 Comparison of basic matrices between walking and running foot functional units

Table 1 presents the comparison results of the base matrices between walking and running in foot functional unit 1. It can be observed that the weights of M3, M4, and HL regions follow a normal distribution, and paired sample t-tests were performed, while the weights of other foot regions were examined using non-parametric tests. The results indicated that in foot functional unit 1, compared to walking, running had higher weight contributions to the total force from M3($p = 0.025$) and M4 regions ($p = 0.004$), while lower weight contribution from HL region ($p = 0.005$).

According to Table 2, in foot functional unit 2, the weights of M2, M3, and M4 areas conform to normal distribution, and paired sample t-tests were used for analysis, while Wilcoxon signed-rank test was used for the other foot regions. The results show that in the T1($p = 0.020$), M1($p = 0.006$), and MF($p = 0.017$) regions, the contribution of total force during running was higher than walking, while in M3($p < 0.001$) and M4($p = 0.004$) regions, the weights of both areas for total force during running were lower than walking.

4 Discussion

4.1 Feasibility analysis of non-negative matrix factorization in foot mechanics applications

Walking and rearfoot striking running, as basic movement patterns, exhibit different plantar foot mechanics during different phases of the support period. In traditional biomechanical analyses of human movement, peak forces, impulses, and loading rates are typically used to analyze foot-ground interactions. This method can provide detailed explanations of the mechanical changes in different regions, However, it cannot take into account the spatiotemporal characteristics and is unable to simplify the plantar area division from a functional perspective based on mechanical features. NNMF as an important feature extraction method can not only extract features from multidimensional data but also preserve the temporal and spatial variations in the data (Lee and Seung, 1999; Pataky et al., 2013; Nishida et al., 2017). Due to the non-negative characteristics of plantar pressure, NNMF can be used for simplified analysis of multiple regions of the foot. Van et al. used NNMF to perform functional segmentation of the foot based on plantar pressure characteristics, and found that this method had good discrimination for different types of running foot strikes (Van Hese et al., 2021). However, their study did not provide a specific quantitative analysis of the decomposed matrices. After applying NNMF to one-dimensional biomechanical data, a coefficient matrix and corresponding basis matrix are obtained. The coefficient matrix reflects the overall spatiotemporal features of the data in the form of

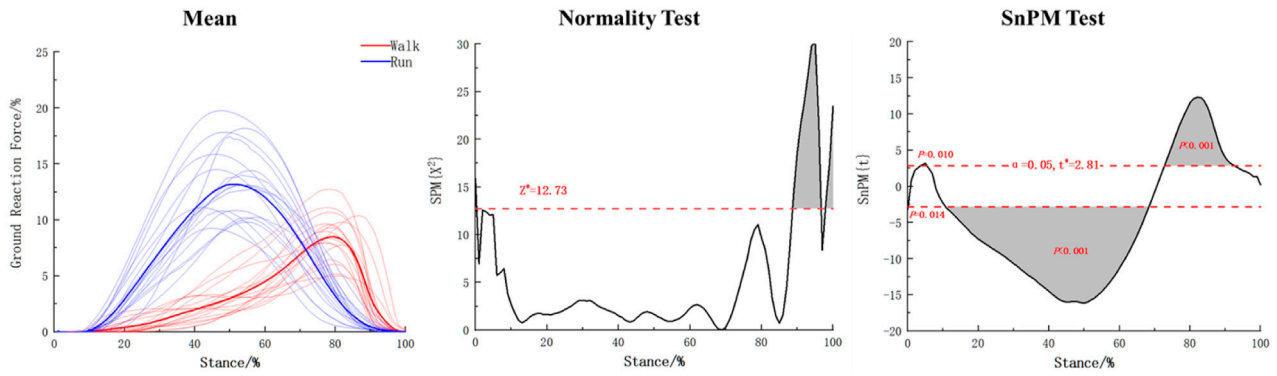

FIGURE 7
The coefficient matrix statistical results for walking and running in foot functional unit 2.

TABLE 1 Comparison of basic matrices for walking and running in foot function unit 1 (n = 18%).

Foot regions	Walk		Run		*p-value*
	Mean/ Median	Standard deviation/Interquartile range	Mean/ Median	Standard deviation/Interquartile range	
T1	0.00	(0.00.0.00)	0.00	(0.00.0.00)	1.000
T2-5	0.00	(0.00.0.00)	0.00	(0.00.0.00)	0.317
M1	0.00	(0.00.0.00)	0.00	(0.00.0.00)	0.593
M2	0.00	(0.00.0.376)	0.00	(0.00.0.715)	0.424
M3	**1.21**	(**0.00**,**2.24**)	**1.47**	(**0.00**,**3.60**)	**0.025**
M4	**2.87**	**1.84**	**4.56**	**2.71**	**0.004**
M5	3.00	(1.66.4.84)	4.02	(2.13.7.05)	0.170
MF	12.00	(7.20.18.70)	11.88	(8.56.20.95)	0.215
HM	41.01	7.68	40.57	10.22	0.829
HL	**37.08**	**1.75**	**30.21**	**8.31**	**0.005**

Bold values indicate $p < 0.05$.

TABLE 2 Comparison of basic matrices for walking and running in foot function unit 2 (n = 18,%).

Foot regions	Walk		Run		*p-value*
	Mean/ Median	Standard deviation/Interquartile range	Mean/ Median	Standard deviation/Interquartile range	
T1	**7.78**	(**5.16**,**11.96**)	**15.06**	(**6.94**,**16.78**)	**0.020**
T2-5	2.05	(1.06.4.03)	3.94	(1.41.5.10)	0.215
M1	**9.82**	(**4.31**,**20.77**)	**15.45**	(**10.43**,**25.33**)	**0.006**
M2	26.78	9.35	27.07	7.08	0.842
M3	**27.12**	**8.05**	**21.34**	**6.53**	**<0.001**
M4	**14.37**	**8.08**	**9.97**	**3.67**	**0.004**
M5	4.23	(1.59.9.39)	4.27	(1.60.7.17)	0.744
MF	**0.00**	(**0.00**,**0.23**)	**0.60**	(**0.03**,**1.60**)	**0.017**
HM	0.00	(0.00.0.00)	0.00	(0.00.0.00)	1.000
HL	0.00	(0.00.0.00)	0.00	(0.00.0.00)	1.000

Bold values indicate $p < 0.05$.

a curve, while the basis matrix shows the weight values of each element in the matrix (Lee and Seung, 1999). In the analysis of walking and running plantar pressure, traditional t-tests can be used to compare the statistical differences in the contribution of each foot region based on the basis matrix. However, traditional hypothesis testing methods cannot reflect the continuous change characteristics of the overall force curve for the coefficient matrix. The statistical parameter mapping based on the theory of random fields has been used for the analysis of continuous data, including kinematic and kinetic data (Pataky, 2012; Pataky et al., 2015). In this study, we applied this method to compare the coefficient matrices obtained from NNMF of walking and running data, in order to achieve quantitative analysis of the decomposed matrices. Our results showed that under both walking and rearfoot striking running, when the number of matrix factorization was set to 2, the fitting degree of the reconstructed matrices exceeded the VAF value of 0.85 set in this study. This indicates that the dimensionality reduction analysis of rearfoot striking running and walking can be simplified into two dynamic foot functional units.

4.2 Analysis of foot functional unit features during walking and running

Our study used NNMF to divide the two foot functional units based on the main force application time of the overall foot mechanics during walking and running. During walking, the first foot functional unit mainly exhibited mechanical characteristics in the support phase around 15%–35%, at this point, dorsiflexion of the foot and flexion of the knee joint are used to complete the deceleration of the body, which is the weight-bearing buffering stage of walking (Earls, 2018; Perry and Burnfield, 2018). According to Figure 4 and Table 1, the HM and HL regions occupied 78.09% of the weight of all foot regions, indicating that the heel region played a major role in buffering during weight-bearing, while the midfoot (12%) and M3-M5 regions (7.08%) also participated in buffering. This suggests that the heel receives the highest impact during weight-bearing buffering, and the arch and outer edge of the forefoot assist in completing the buffering. In the second foot functional unit during walking, as shown in Figure 4 and Table 2, the main force is concentrated around the support phase of 60%–80%, during this phase, the posterior muscles of the lower leg and the muscles of the foot plantar flex to perform push-off, while the muscles of the thigh and buttocks begin to exert force, extending the knee joint and propelling the body forward (Earls, 2018; Perry and Burnfield, 2018). The basic matrix shows that the M2-M4 region occupies 68.27% of the weight, indicating that the middle part of the forefoot is the main force application area during push-off. Early studies on foot mechanics during walking typically considered the foot to be supported by three points: the heel, lateral forefoot, and medial forefoot (Zheng, 2002). With advances in foot pressure testing methods, researchers found that the results of actual walking tests contradicted the three-point support theory. This may be due to traditional understanding not taking into account the mechanical characteristics of the metatarsal bone section (Zheng, 2002). Kanatli's research discovered that in a healthy population, the middle area of the forefoot bears the highest pressure during walking (Kanatli et al., 2008). This finding aligns with the our results, which show that the primary force regions during the support phase of walking are the heel and middle forefoot. In contrast to previous studies, our study provides a more detailed functional division based on foot mechanics, namely, that the heel is the main force area during the buffering phase of walking and the middle forefoot is the main force area during the push-off phase.

During running, the plantar mechanical characteristics are similar to walking. In the first functional unit, the main force is concentrated around 10%–30%, with the heel being the main force area (70.78%), and the midfoot (11.88%) and the medial-lateral forefoot (10.05%) assisting in cushioning, meanwhile, the hip joint, knee joint, and ankle joint sequentially flex to store kinetic and gravitational potential energy as elastic potential energy (Mcmahon and Cheng, 1990). In the second functional unit, as shown in Figure 5 and Table 2, the main force characteristics are concentrated around 40%–60% of the running support phase, with the M1, M2, and M3 regions accounting for 63.86% of the weight and the T1 region accounting for 15.06% of the weight. It can be seen that during the push-off phase of running, the main force areas are the medial and central parts of the forefoot and the toes, and the foot exhibits an outward and rotational posture during force exertion, gradually shifting the force from the lateral to the medial side of the foot. Venkadesan's team found that the transverse arch of foot provides over 40% of the foot's stiffness through variations in the arrangement of the metatarsal bones (Venkadesan et al., 2020). During the push-off phase of running, the metatarsophalangeal joint undergoes flexion to increase the tension of the plantar fascia, enhancing foot stiffness through the "windlass effect". Subsequently, the metatarsophalangeal joint extends, releasing stored elastic potential energy to improve the efficiency of push-off (Donatelli, 1987; Kelly et al., 2015). The significant role of the metatarsophalangeal joint in this process may be the reason for the prominent mechanical characteristics in the forefoot region observed in this study. At the same time, the results of this study show that, similar to walking, the forefoot area still plays a role in the buffering functional unit during rearfoot strike running. During the buffering phase of walking or rearfoot strike running, the foot plantarflexes around the heel axis and the forefoot assists in weight-bearing (Perry and Burnfield, 2018); after the heel lifts off, the foot rolls around the toe axis, and at this point, the forefoot completes the push-off phase (Perry and Burnfield, 2018). In these two processes, the transverse arch of the forefoot participates in both buffering and push-off, indicating its important role in the transition from elastic buffering to rigid lever function. However, since this study only investigated the foot's mechanical characteristics, further research on the arch should incorporate morphological changes in the foot during the support phase for deeper insights.

4.3 Comparison analysis of foot function units between walking and running

Quantitative analysis of the basic matrix and coefficient matrix within the two functional units of walking and running was conducted in this study. Results showed that in the first functional unit, as shown in Figure 6 and Table 1, during the first 20% of the support period, the overall force characteristics

of the foot were higher in running than in walking ($p < 0.001$). This study also found that in this functional unit, the contribution weights of the M3 ($p = 0.025$) and M4 ($p = 0.004$) regions were higher in running than in walking, while the weight of the HL region was lower in running than in walking ($p = 0.005$), indicating that the foot experiences greater impact during running in the first 20% of the support period, and that compared to walking, the weight of the lateral part of the heel is smaller during the buffering phase of rearfoot landing when running, with the weight-bearing area more biased towards the forefoot, suggesting that the forefoot may be more involved in buffering under high loads. In the second functional unit, as shown in Figure 7 and Table 2, it was found that at the beginning of the support period, the overall force characteristics of walking were lower than those of rearfoot running ($p = 0.014$). During the 4%–5% support phase, walking was higher than rearfoot landing when running ($p = 0.010$), due to these two phases are short in duration, they cannot reflect curve characteristics and are not further analyzed. During the support phase from 11% to 69%, the overall force characteristics of walking were lower than running ($p < 0.001$), while during the support phase from 73% to 92%, the overall force of walking was higher than that of running ($p < 0.001$). Combined with Figure 7, it can be seen that in the push-off unit, running completed the main force production process earlier than walking. For the basic matrix, the results of this study found that in the T1 ($p = 0.020$), M1 ($p = 0.006$), and MF ($p = 0.017$) areas, the weight of the heel strike during running was higher than that during walking, while in the M3 ($p < 0.001$) and M4 ($p = 0.004$) areas, the weight of running was lower than that of walking. This indicates that running places greater stress on the arch area of the foot during the heel strike phase compared to walking. Moreover, in the forefoot area, the force production area during running shifts from the lateral to the medial side compared to walking, which allows for more complete toe-off extension. Wang and Raychoudhury found that during running, the functional axis of the metatarsophalangeal joint moved forward by about 3% compared to walking (Raychoudhury et al., 2014; Wang et al., 2021), which may have contributed to the greater contribution of the toe region during running in this study.

There are also some limitations in this study. Although the quality of NNMF for both walking and running in this study reached 0.95, there still exists some error between the factorization and the real data. Future research could increase the number of matrix factorizations according to different needs to improve the quality of the reconstructed matrix. In addition, our study used NNMF to divide the plantar into ten regions and analyzed the differences in plantar mechanical characteristics between healthy individuals during walking and running. However, some studies have shown that individuals with symptoms, such as stroke, pes cavus, and flatfoot, exhibit differences in plantar mechanics compared to healthy individuals during walking (Hillstrom et al., 2013; Wang et al., 2019; Bai et al., 2022). Therefore, it is recommended to redefine the plantar regions and combine lower limb biomechanical features for functional classification when applying NNMF to symptomatic populations based on their movement patterns. Additionally, NNMF can be used to further analyze foot function from a mechanical perspective for different types of movements, such as cutting and sudden stops, in healthy individuals. Future research should increase sample sizes and apply NNMF to functional analysis in different populations and complex movements from a mechanical perspective.

5 Conclusion

In this study, NNMF was used to decompose walking and running into two foot functional units based on mechanical characteristics. According to the matrix structure of each unit, the two foot functional units corresponded to cushioning and push-off, respectively. The forefoot accounted for a certain weight in both cushioning and push-off functions, indicating the existence of complex foot functional transformation mechanisms in the transverse arch of foot. Compared with walking, running completed push-off earlier, with a force application area that was more inwardly biased towards the foot and with the big toe accounting for a larger weight during push-off. The use of NNMF to extract and quantify foot mechanics has certain application value.

Data availability statement

The original contributions presented in the study are included in the article/Supplementary material, further inquiries can be directed to the corresponding author.

Ethics statement

The studies involving human participants were reviewed and approved by the University Ethics Committee of Hebei Normal University (No. 2022LLSC026). The patients/participants provided their written informed consent to participate in this study.

Author contributions

XB and HH were in charge of designing the experiment. XB wrote the manuscript. HH and JL revised the manuscript. All authors contributed to the article and approved the submitted version.

Funding

This research was supported by Tsinghua University Initiative Scientific Research Program (2021THZWJC15), Hebei Science and Technology Plan Project (16275709).

Conflict of interest

The authors declare that the research was conducted in the absence of any commercial or financial relationships that could be construed as a potential conflict of interest.

Publisher's note

References

Aghabayk, K., Parishad, N., and Shiwakoti, N. (2021). Investigation on the impact of walk ways slope and pedestrians physical characteristics on pedestrians normal walking and jogging speeds. *Saf. Sci.* 133, 105012. doi:10.1016/j.ssci.2020.105012

Aminian, G., Safaeepour, Z., Farhoodi, M., Pezeshk, A. F., Saeedi, H., and Majddoleslam, B. (2013). The effect of prefabricated and proprioceptive foot orthoses on plantar pressure distribution in patients with flexible flatfoot during walking. *Prosthet. Orthot. Int.* 37 (3), 227–232. doi:10.1177/0309364612461167

Bach, M. M., Daffertshofer, A., and Dominici, N. (2021). Muscle synergies in children walking and running on a treadmill. *Front. Hum. Neurosci.* 15, 637157. doi:10.3389/fnhum.2021.637157

Bai, X. T., Huo, H. F., Lu, P., Luan, Y. S., Koga, A., and Liu, J. (2022). Analysis of plantar impact characteristics of walking in patients with flatfoot according to basic mechanical features and continuous wavelet transform. *Front. Phys-Lausanne* 10, 1058615. doi:10.3389/fphy.2022.1058615

Baroudi, L., Yan, X., Newman, M. W., Barton, K., Cain, S. M., and Shorter, K. A. (2022). Investigating walking speed variability of young adults in the real world. *Gait Posture* 98, 69–77. doi:10.1016/j.gaitpost.2022.08.012

Cappellini, G., Ivanenko, Y. P., Poppele, R. E., and Lacquaniti, F. (2006). Motor patterns in human walking and running. *J. Neurophysiol.* 95 (6), 3426–3437. doi:10.1152/jn.00081.2006

Cavanagh, P. R., and Rodgers, M. M. (1987). The arch index - a useful measure from footprints. *J. Biomech.* 20 (5), 547–551. doi:10.1016/0021-9290(87)90255-7

Chen, H., Nigg, B. M., and Dekoning, J. (1994). Relationship between plantar pressure distribution under the foot and insole comfort. *Clin. Biomech.* 9 (6), 335–341. doi:10.1016/0268-0033(94)90062-0

Conner, B. C., Fang, Y., and Lerner, Z. F. (2022). Under pressure: Design and validation of a pressure-sensitive insole for ankle plantar flexion biofeedback during neuromuscular gait training. *J. Neuroeng Rehabil.* 19 (1), 135. doi:10.1186/s12984-022-01119-y

Donatelli, R. A. (1987). Abnormal biomechanics of the foot and ankle. *J. Orthop. Sport Phys.* 9 (1), 11–16. doi:10.2519/jospt.1987.9.1.11

Earls, J. (2018). *Born to walk*. Beijing: Beijing Science and Technology Press.

Ghislieri, M., Agostini, V., and Knaflitz, M. (2020). Muscle synergies extracted using principal activations: Improvement of robustness and interpretability. *Ieee T Neur Sys Reh* 28 (2), 453–460. doi:10.1109/TNSRE.2020.2965179

Hageman, E. R., Hall, M., Sterner, E. G., and Mirka, G. A. (2011). Medial longitudinal arch deformation during walking and stair navigation while carrying loads. *Foot Ankle Int.* 32 (6), 623–629. doi:10.3113/FAI.2011.0623

Hagio, S., Fukuda, M., and Kouzaki, M. (2015). Identification of muscle synergies associated with gait transition in humans. *Front. Hum. Neurosci.* 948, 48. doi:10.3389/fnhum.2015.00048

Hajiloo, B., Anbarian, M., Esmaeili, H., and Mirzapour, M. (2020). The effects of fatigue on synergy of selected lower limb muscles during running. *J. Biomech.* 103, 103109692. doi:10.1016/j.jbiomech.2020.109692

Hillstrom, H. J., Song, J. S., Kraszewski, A. P., Hafer, J. F., Mootanah, R., Dufour, A. B., et al. (2013). Foot type biomechanics part 1: Structure and function of the asymptomatic foot. *Gait Posture* 37 (3), 445–451. doi:10.1016/j.gaitpost.2012.09.007

Hsi, W. L., Kang, J. H., and Lai, J. S. (2004). Distribution of plantar pressure on the second metatarsal head during walking. *J. Formos. Med. Assoc.* 103 (7), 540–545.

Hu, S. S., Ma, X. L., Ma, X. Y., Sun, W., Zhou, Z. P., Chen, Y., et al. (2023). Relationship of strength, joint kinesthesia, and plantar tactile sensation to dynamic and static postural stability among patients with anterior cruciate ligament reconstruction. *Front. Physiol.* 14, 141112708. doi:10.3389/fphys.2023.1112708

Hug, F., Turpin, N. A., Guevel, A., and Dorel, S. (2010). Is interindividual variability of emg patterns in trained cyclists related to different muscle synergies? *J. Appl. Physiol.* 108 (6), 1727–1736. doi:10.1152/japplphysiol.01305.2009

Jia, X. H., Li, J. R., Liu, J. Y., Li, T. J., and Yang, H. (2023). Study on abnormal gait and fall warning method using wearable sensors and a human musculoskeletal model. *Meas. Sci. Technol.* 34 (6), 065104. doi:10.1088/1361-6501/acbdb7

Jiang, X. Y., Li, S. D., Teo, E. C., and Zhou, Z. X. (2021). The effect of high-intensity intermittent training on the acute gait plantar pressure in healthy young adults. *J. Biomim. Biomater. Bi* 49, 4921–4932. doi:10.4028/www.scientific.net/JBBBE.49.21

Kanatli, U., Yetkin, H., Simsek, A., Ozturk, A. M., Esen, E., and Beşli, K. (2008). Pressure distribution patterns under the metatarsal heads in healthy individuals. *Acta Orthop. Traumato* 42 (1), 26–30. doi:10.3944/aott.2008.026

Kelly, L. A., Cresswell, A. G., Racinais, S., Whiteley, R., and Lichtwark, G. (2014). Intrinsic foot muscles have the capacity to control deformation of the longitudinal arch. *J. R. Soc. Interface* 11 (93), 20131188. doi:10.1098/rsif.2013.1188

Kelly, L. A., Lichtwark, G., and Cresswell, A. G. (2015). Active regulation of longitudinal arch compression and recoil during walking and running. *J. R. Soc. Interface* 12 (102), 20141076. doi:10.1098/rsif.2014.1076

Laudadioa, T., Anca, R. C. S. C., Wrightd, A. J., Arend, H., Nicola, M. A., Mastronardi, N., et al. (2016). Hierarchical non-negative matrix factorization applied to three-dimensional 3t mrsi data for automatic tissue characterization of the prostate. *Nmr Biomed.* 29 (6), 751–758. doi:10.1002/nbm.3527

Lee, D. D., and Seung, H. S. (1999). Learning the parts of objects by non-negative matrix factorization. *Nature* 401 (6755), 788–791. doi:10.1038/44565

Li, Y., Zhang, X., and Sun, M. (2017). Robust non-negative matrix factorization with beta-divergence for speech separation. *Etri J.* 39 (1), 21–29. doi:10.4218/etrij.17.0115.0122

Lian, Y., Wang, Z., Li, X., Wang, J., Mi, H., Li, M., et al. (2012). Research on the recommended brisk walking speed and stride frequency of ordinary adults aged from 20 to 59. *J. Beijing Sport Univ.* 35 (7), 49–51. doi:10.19582/j.cnki.11-3785/g8.2012.07.010

Limroongreungrat, W., and Boonkerd, C. (2019). Immediate effect of acl kinesio taping technique on knee joint biomechanics during a drop vertical jump: A randomized crossover controlled trial. *Bmc Sports Sci. Med. R.* 11 (1), 32–37. doi:10.1186/s13102-019-0144-6

Mcmahon, T. A., and Cheng, G. C. (1990). The mechanics of running: How does stiffness couple with speed? *J. Biomech.* 23, 65–78. doi:10.1016/0021-9290(90)90042-2

Montagnani, E., Price, C., Nester, C., and Morrison, S. C. (2021). Dynamic characteristics of foot development: A narrative synthesis of plantar pressure data during infancy and childhood. *Pediatr. Phys. Ther.* 33 (4), 275–282. doi:10.1097/PEP.0000000000000819

Natali, A. N., Pavan, P. G., and Stecco, C. (2010). A constitutive model for the mechanical characterization of the plantar fascia. *Connect. Tissue Res.* 51 (5), 337–346. doi:10.3109/03008200903389127

Nishida, K., Hagio, S., Kibushi, B., Moritani, T., and Kouzaki, M. (2017). Comparison of muscle synergies for running between different foot strike patterns. *Plos One* 12 (2), e0171535. doi:10.1371/journal.pone.0171535

O'Grady, P. D., and Pearlmutter, B. A. (2008). Discovering speech phones using convolutive non-negative matrix factorisation with a sparseness constraint. *Neurocomputing* 72 (1-3), 88–101. doi:10.1016/j.neucom.2008.01.033

Pataky, T. C. (2012). One-dimensional statistical parametric mapping in python. *Comput. Method Biomec* 15 (3), 295–301. doi:10.1080/10255842.2010.527837

Pataky, T. C., Robinson, M. A., and Vanrenterghem, J. (2013). Vector field statistical analysis of kinematic and force trajectories. *J. Biomech.* 46 (14), 2394–2401. doi:10.1016/j.jbiomech.2013.07.031

Pataky, T. C., Vanrenterghem, J., and Robinson, M. A. (2015). Zero-vs. One-dimensional, parametric vs. Non-parametric, and confidence interval vs. Hypothesis testing procedures in one-dimensional biomechanical trajectory analysis. *J. Biomech.* 48 (7), 1277–1285. doi:10.1016/j.jbiomech.2015.02.051

Perry, J., and Burnfield, J. M. (2018). *Gait analysis: Normal and pothological function*. Shanghai: Shanghai Science and Technology Press.

Rabbi, M. F., Pizzolato, C., Lloyd, D. G., Carty, C. P., Devaprakash, D., and Diamond, L. E. (2020). Non-negativematrixfactorisationisthemostappropriatemethodforextraction ofmusclesynergiesinwalking and running. *Sci. Rep-Uk* 10 (1), 8266. doi:10.1038/s41598-020-65257-w

Raychoudhury, S., Hu, D., and Ren, L. (2014). Three-dimensional kinematics of the human metatarsophalangeal joint during level walking. *Front. Bioeng. Biotech.* 273, 73. doi:10.3389/fbioe.2014.00073

Shen, L. B., Ouyang, H., Huang, Y. X., Pan, R., Lu, J. L., Xie, Z. W., et al. (2021). Establishing the normal gait of Chinese youth based on the plantar pressure test: An experimental study. *J. Mech. Med. Biol.* 21 (06), 2150038. doi:10.1142/S021951942150038X

Sun, W. (2019). *Simulation and experimental study of muscle synergy for human lower extremity*. Zhejiang University. Doctoral dissertation.

Sy, H. V. N., Nambu, I., and Wada, Y. (2016). "The adjustment of musclesynergy recruitment bycontrolling muscle contraction during the reaching movement," in 2016 IEEE International Conference on Systems, Man, and Cybernetics (SMC), Budapest, Hungary, 09-12 October 2016. 345 E 47TH ST, NEW YORK, NY 10017 USA.

Van Hese, P., Cabral, H., Aerts, W., and Tsiporkova, E. (2021). "Functional foot segmentation based on plantar pressure measurements for profiling subjects performing a running exercise," in 2021 International Conference on Data Mining Workshops (ICDMW), Auckland, New Zealand, 07-10 December 2021.

Venkadesan, M., Yawar, A., Eng, C. M., Dias, M. A., Singh, D. K., Tommasini, S. M., et al. (2020). Stiffness of the human foot and evolution of the transverse arch. *Nature* 579 (7797), 97–100. doi:10.1038/s41586-020-2053-y

Wang, K. Y., Raychoudhury, S., Hu, D., Ren, L., Liu, J., Xiu, H., et al. (2021). The impact of locomotor speed on the human metatarsophalangeal joint kinematics. *Front. Bioeng. Biotech.* 9644582, 644582. doi:10.3389/fbioe.2021.644582

Wang, M., Wang, X., Fan, Z., Chen, F., Zhang, S., and Peng, C. (2019). Research on feature extraction algorithm for plantar pressure image and gait analysis in stroke patients. *J. Vis. Commun. Image R.* 58, 525–531. doi:10.1016/j.jvcir.2018.12.017

Wang, M., Xie, X., You, Z., Ding, D., and Wong, L. (2022). A weighted non-negative matrix factorization approach to predict potential associations between drug and disease. *J. Transl. Med.* 20 (1), 552. doi:10.1186/s12967-022-03757-1

Warmenhoven, J., Harrison, A., Robinson, M. A., Vanrenterghem, J., Bargary, N., Smith, R., et al. (2018). A force profile analysis comparison between functional data analysis, statistical parametric mapping and statistical non-parametric mapping in on-water single sculling. *J. Sci. Med. Sport* 21 (10), 1100–1105. doi:10.1016/j.jsams.2018.03.009

Wikstrom, E. A., and McKeon, P. O. (2014). The effects of 2-weeks of sensory-targeted ankle rehabilitation strategies on single limb center of pressure velocity in those with chronic ankle instability. *Med. Sci. Sport Exer* 46 (5), 202. doi:10.1249/01.mss.0000493786.64766.67

Wolf, I. D., and Wohlfart, T. (2014). Walking, hiking and running in parks: A multidisciplinary assessment of health and well-being benefits. *Landsc. Urban Plan.* 130, 13089–13103. doi:10.1016/j.landurbplan.2014.06.006

Zhao, X. X., and Li, S. D. (2019). A biomechanical analysis of lower limb movement on the backcourt forehand clear stroke among badminton players of different levels. *Appl. Bionics Biomech.* 2019, 1–8. doi:10.1155/2019/7048345

Zheng, X. (2002). *Modern sports biomechanics*. Beijing: National Defense Industry Press.

frontiers | Frontiers in Bioengineering and Biotechnology

TYPE Original Research
PUBLISHED 04 August 2023
DOI 10.3389/fbioe.2023.1204115

OPEN ACCESS

EDITED BY
Navrag B. Singh,
ETH Zürich, Switzerland

REVIEWED BY
Simone Tassani,
Pompeu Fabra University, Spain
Nicola Francesco Lopomo,
University of Brescia, Italy

*CORRESPONDENCE
Johannes Burdack,
burdack@uni-mainz.de

RECEIVED 11 April 2023
ACCEPTED 25 July 2023
PUBLISHED 04 August 2023

CITATION
Burdack J, Giesselbach S, Simak ML, Ndiaye ML, Marquardt C and Schöllhorn WI (2023), Identifying underlying individuality across running, walking, and handwriting patterns with conditional cycle–consistent generative adversarial networks.
Front. Bioeng. Biotechnol. 11:1204115.
doi: 10.3389/fbioe.2023.1204115

Identifying underlying individuality across running, walking, and handwriting patterns with conditional cycle–consistent generative adversarial networks

Johannes Burdack[1]*, Sven Giesselbach[2,3], Marvin L. Simak[1], Mamadou L. Ndiaye[1], Christian Marquardt[4] and Wolfgang I. Schöllhorn[1]

[1]Department of Training and Movement Science, Institute of Sport Science, Johannes Gutenberg-University, Mainz, Germany, [2]Knowledge Discovery, Fraunhofer-Institute for Intelligent Analysis and Information Systems, Sankt Augustin, Germany, [3]Lamarr Institute for Machine Learning and Artificial Intelligence, Sankt Augustin, Germany, [4]Science&Motion GmbH, Munich, Germany

In recent years, the analysis of movement patterns has increasingly focused on the individuality of movements. After long speculations about weak individuality, strong individuality is now accepted, and the first situation–dependent fine structures within it are already identified. Methodologically, however, only signals of the same movements have been compared so far. The goal of this work is to detect cross-movement commonalities of individual walking, running, and handwriting patterns using data augmentation. A total of 17 healthy adults (35.8 ± 11.1 years, eight women and nine men) each performed 627.9 ± 129.0 walking strides, 962.9 ± 182.0 running strides, and 59.25 ± 1.8 handwritings. Using the conditional cycle-consistent generative adversarial network (CycleGAN), conditioned on the participant's class, a pairwise transformation between the vertical ground reaction force during walking and running and the vertical pen pressure during handwriting was learned in the first step. In the second step, the original data of the respective movements were used to artificially generate the other movement data. In the third step, whether the artificially generated data could be correctly assigned to a person via classification using a support vector machine trained with original data of the movement was tested. The classification F1–score ranged from 46.8% for handwriting data generated from walking data to 98.9% for walking data generated from running data. Thus, cross–movement individual patterns could be identified. Therefore, the methodology presented in this study may help to enable cross–movement analysis and the artificial generation of larger amounts of data.

KEYWORDS

cross-movement individuality, cross-signal individuality, CycleGAN, data augmentation, deep learning, generative adversarial network, movement pattern recognition, support vector machine

1 Introduction

After weak individuality had been used only sporadically for quite some time and, meanwhile, acquired the status of a buzzword, especially in connection with learning, training, and therapy, the investigation of strong individuality had increasingly been asked for (Schöllhorn, 1993; Bates, 1996). Often, a mixture of colloquial (weak) and science–oriented (strong) understanding can be observed, which is even more confusingly equated with "personalized" (Ginsburg and Willard, 2009; Ng et al., 2009; Chan and Ginsburg, 2011; Buford et al., 2013). Colloquially, weak individuality often serves as an excuse for a lack of statistically significant group differences (Davids et al., 1999; Button et al., 2000; Nuzzo, 2014) or for not finding commonalities across individuals (Schöner et al., 1992; Button et al., 2000; Hecksteden et al., 2015; Barth et al., 2019). In contrast, science on individuality is guided by the much stronger criteria of forensics, which must withstand legal proof for sentencing purposes. The two essential criteria are uniqueness and persistence (Jain et al., 2006; Kaye, 2010), for the proof of which, first, a larger amount of data is necessary, and, second, a different statistical method than the average oriented in social sciences is required. Both conditions explain why it is only with the more recent development of appropriate methods and techniques that the study of the strong individuality of selected forms of movement has increased almost inflationary. Originating from the visual perception of walking individuals (Johansson, 1973; Cutting and Kozlowski, 1977; Troje, 2002), followed by biomechanical analyses of gait movements (Schöllhorn et al., 1999; Windle et al., 1999; Schöllhorn et al., 2002) and sporadically single sports movements (Bauer and Schöllhorn, 1997; Schöllhorn and Bauer, 1998b), analyses of a wide variety of movements have become increasingly popular. Besides walking (Schöllhorn et al., 2002a; Begg et al., 2005; Begg and Kamruzzaman, 2005), the individuality of movements has also been shown in the field of sports in sprinting (Schöllhorn et al., 2001), running (Schöllhorn and Bauer, 1998a; Maurer et al., 2012; Hoerzer et al., 2015; Hoitz et al., 2021), javelin (Schöllhorn and Bauer, 1998b) and discus throwing (Bauer and Schöllhorn, 1997), and horseback riding (Schöllhorn et al., 2006), as well as in the field of music when playing the flute (Albrecht et al., 2014). Similar features could be shown for team behavior in volleyball (Westphal and Schöllhorn, 2001; Jäger and Schöllhorn, 2007), soccer (Grunz et al., 2012; Rein and Memmert, 2016), or basketball (Schmidt, 2012; Kempe et al., 2014). Typical parameters investigated are biomechanical data from video recordings (Kaur et al., 2023), force plates (Horst et al., 2016; Horst et al., 2017a; Horst et al., 2017b), pressure insoles (Schöllhorn et al., 2002b; Jacques et al., 2022), EMG (Jaitner et al., 2001; Aeles et al., 2021), and brain signals (Liao et al., 2014; Lee et al., 2022). Besides these, wearable sensors are becoming increasingly popular (Hammad and El-Sankary, 2020). Situated "perturbations" such as emotions (Janssen et al., 2008), fatigue (Burdack et al., 2020a), or time alone (Schöllhorn and Bauer, 1998b; Horst et al., 2016; Horst et al., 2017a; Horst et al., 2017b) were not able to move the patterns out of the strong individual space. Consequently, robust evidence for an important role of individuality is provided in short–term adaptive behavior. What all studies listed so far have in common is that they answer questions that could be carried out based on the comparison of a single movement technique. From this, the problem of individuality in longer–term learning, like in training or therapy, must be distinguished, especially with respect to the criterion of permanence. Repeating or learning the same movement by the same person never encounters comparable conditions again due to cognitive and body memory (Horst et al., 2020). To solve this problem, finding commonalities in learning different movements seems an appropriate approach but requires the identification of movement-independent individuality. In a first proposal, evidence for individual characteristics across three throwing techniques of the decathlon (final throwing phase of shot put, discus, and javelin) with similar kinematic structure was provided (Horst et al., 2020). The aim of this study is to identify individual commonalities of movement forms with different kinematic structures.

The problem with this is that the classification models cannot transfer among domains and thus only work on data from one domain. Consequently, it is not straightforward to train a classification model with walking data and test it on running data to identify any common underlying structures. However, new methods from the field of deep learning provide the potential to address this problem. Approaches from image generation offer solutions for analog problems. In image–to–image translation or style transfer, it is possible to learn a relationship between images from two domains, domain A (e.g., horses) and domain B (e.g., zebras), so that realistic images of domain B can then be generated from images of domain A. This has been done without losing the image content. Images of horses can become pictures of zebras, or images of a landscape can become pictures of the same landscape as it might look in summer or in winter.

In the area of data generation, Generative Adversarial Networks (GANs) (Goodfellow et al., 2014; Goodfellow et al., 2020) have proven to be extremely successful in generating new, previously unseen data that is somewhat similar to a given training data set. In order to solve "generative modeling" problems, the goal of a GAN is to learn the probability distribution of the data to be generated. Based on this probability distribution, the GAN then generates new data from this probability distribution. However, a major challenge with GANs is that they require a very large database of paired data to solve image-to-image translation (Zhu et al., 2017). This makes the GANs difficult to apply in the context of cross–movement studies for many problems. First, it is often not possible to generate the necessary large data sets, and second, due to the continuous change of movement patterns (Horst et al., 2019), finding matching pairs of movements between two movements can be problematic.

A further development of the GAN that circumvents the pairwise data problem that respectively offers a possible solution and can be successfully applied on relatively small data sets is the cycle–consistent GAN (CycleGAN) (Zhu et al., 2017). Here, images from domain A can be translated into domain B, but the basic content from domain A is preserved. A well–known example that makes use of this method is FaceApp (FaceApp Technology Limited, Cyprus). Given images of faces, the app allows for a transformation that makes someone's face laugh, look older, look younger, or appear in the style of the opposite sex.

While the CycleGANs work quite well on images, it has not been applied to movement measurements. Therefore, in this work, we will

TABLE 1 Participant characteristics.

	M	SD
Age (years)	35.8	11.1
Height (cm)	172.1	6.2
Body mass (kg)	68.0	9.3
Preferred walking speed (km/h)	4.2	0.5
Preferred running speed (km/h)	8.4	1.4

Data are presented as mean (M) and standard deviation (SD); preferred walking and running speed was determined while walking/running on the treadmill.

use CycleGAN to identify common individual patterns across different movements. Specifically, we aim to find individual commonalities underlying the walking, running, and handwriting patterns of the same person.

With the CycleGAN, we generate artificial movement data of movement B from the original data of movement A. Specifically, we generate the other two movements from the walking, running, and handwriting movements (i.e., walking to running, walking to handwriting, running to walking, running to handwriting, handwriting to walking, and handwriting to running). The movements were chosen from the point of view that with walking and running, we have two related movements, and with handwriting, one very different from them. Based on former studies on individuality (Bauer and Schöllhorn, 1997; Schöllhorn et al., 2002a; Schöllhorn et al., 2002b; Schöllhorn et al., 2006; Janssen et al., 2008; Janssen et al., 2011; Schmidt, 2012; Albrecht et al., 2014; Horst et al., 2016; Horst et al., 2017a; Horst et al., 2017b; Horst et al., 2019; Burdack et al., 2020a), we assume that individuals can be distinguished by their walking, running, and handwriting patterns. From this, we derive the following research questions: Can CycleGANs artificially generate pairwise data between walking, running, and handwriting movements, and can this artificial data be assigned to the correct individuals?

2 Materials and methods

2.1 Participants and ethics statement

The study participants were 17 athletically active, healthy adults (eight women and nine men; 1 left–handed and 16 right–handed) who regularly handwrote and ran for health reasons (the group characteristics are shown in Table 1). Before participating in the study, the participants signed informed consent forms. The study was conducted according to the guidelines of the Declaration of Helsinki and approved by the Ethics Committee of the Johannes Gutenberg–University Mainz (2022/05; 5/23/2022). Each participant visited the biomechanics laboratory once, where all measurements took place.

2.2 Experimental protocol

At the beginning of the study, the preferred walking speed (PWS) and preferred running speed (PRS) on the treadmill were determined for each participant (Dal et al., 2010). The PWS is a speed that the participants prefer in their leisure time, for example, when going for a walk, and the PRS is a speed at which they "feel comfortable" and "can keep going for a very long time". At the same time, the determination of PWS and PRS also served as a habituation to the treadmill. This was followed by familiarization with writing on the digitizing tablet with a pressure–sensitive pen, with everyone writing the sentence that was also written in the data collection (see below) five times.

As presented in Figure 1, the participants performed six sets of 4 min of running or walking. Each was followed by a 4–minute break during which they performed 10 handwriting trials. To achieve greater variation within participants (for more robust training of the Deep Learning models, we increased the variance), we varied the speed in each of the three walks and runs slightly from slow: 85% PWS/PRS, to normal: 100% PWS/PRS, and fast: 115% PWS/PRS. To avoid sequence effects, we randomly shuffled the order of the walking and running conditions across all participants, with the only restriction being that walking and running must always alternate due to load control. Between each walk and run, the phrase "Wellen folgen den Bewegungen" [English: "waves follow the movements"] was handwritten 10 times. The sentence was chosen because it was as neutral and as contentless as possible in terms of meaning. Again, to provoke greater variation in the data, a new instruction was given for each handwriting set, which was implemented at the discretion of the participants. The instructions included writing "normal" or "bigger", "smaller", "faster", "slower", and "more beautiful" as usual. Again, we randomized the order of each instruction.

2.3 Data acquisition

The movements investigated in this study are walking, running, and handwriting. Walking and running were performed on a treadmill (cos12148, h/p/cosmos, Leipzig, Germany) and recorded with pressure soles (pedar, novel, Munich, Germany) at a frequency of 100 Hz. The handwriting was performed using a pressure-sensitive pen (Wacom Pro Pen 3D, Wacom, Düsseldorf, Germany) with 4096 pressure levels on a digitizing tablet on which a paper was adjusted (Wacom Intuos Pro Paper Edition L, Wacom, Düsseldorf, Germany) with a recording frequency of 200 Hz and recorded with the software CSWin (CSWin 2016; MedCom Verlag, Munich, Germany).

FIGURE 1
Experimental sequence with the chronological sequence of the three walking, three running, and six handwriting conditions. The walking and running conditions were always alternated with handwriting. In addition, walking and running were always alternated for stress control reasons. The starting condition (walking or running) was randomized between participants.

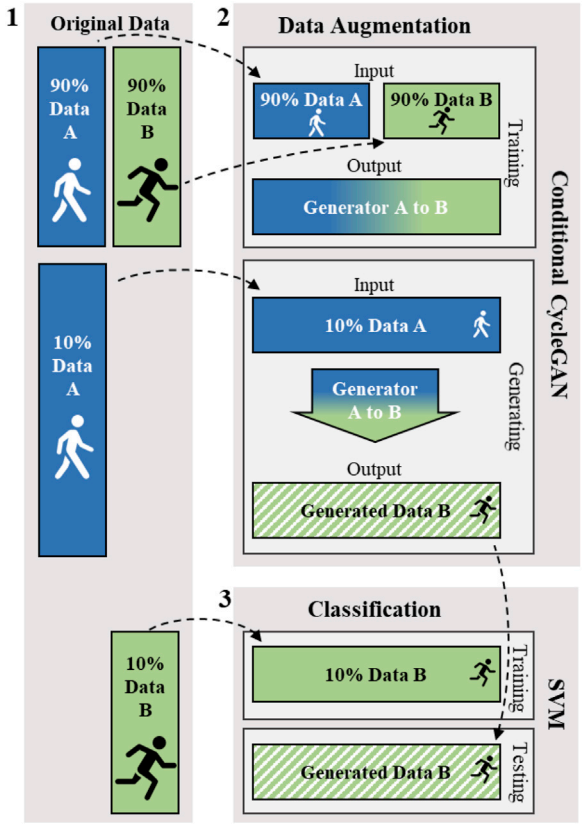

FIGURE 2
Description of the procedure from data generation to classification. For the sake of clarity, only the way of generating new data from data A is described in the figure. However, the way of generation from data B is analogous. For illustration purposes, data A corresponds to walking and data B to running. (1) Original Data: In each case, the original data was split 90:10. (2) The outlined process of the conditional CycleGAN: 90% of the data of A and B were used for training the conditional CycleGAN. The trained generators were then used to generate new data B from the remaining 10% of data A accordingly. (3) The outlined procedure of classification using a Support Vector Machine (SVM): the SVM was trained with the 10% of data B that was not used for training the conditional CycleGAN. In each case, the SVM was tested with the newly generated data B.

2.4 Data processing

For the locomotion tasks, the vertical ground reaction force (GRF) was calculated from the pressure data using Pedar Mobile Expert software (version 8.2). The stance phase from heel strike to toe–off of the left and right foot was determined using a vertical GRF threshold of 50N. Each ground contact with one foot was time-normalized to 128 values. Burdack et al. (2020b) showed that the exact vector length plays a minor role as long as the curve shape is preserved. In addition, the data were normalized by body weight and scaled to the range [0, 1] (Chau, 2001a; Chau, 2001b; Hsu et al., 2003). After scaling, the step pairs from the left and right ground contact were combined into one vector of 256 values (128 data points left foot + 128 data points right foot). Each vector begins with a left-ground contact and ends with the corresponding right one. If the data of ground contact was incorrect during recording, this and the corresponding ground contact of the other foot were deleted from the recording.

For handwriting, only the vertical pen pressure data where the pressure on the pen was greater than zero was considered. Furthermore, we considered only the first letter W for the handwriting analysis. If the W was not written in one piece, the test was discarded. In the case that the 'e' was written from the W without settling, the point with the least pressure between the W and the 'e' determined the end of the W. In addition, the handwriting data were filtered with a 1st–order Savitzky–Golay filter with a window size of 13 (Savitzky and Golay, 1964), which smoothens on the least squares method while maintaining the shape and height of the waveform peaks (Schafer, 2011). Data were also time–normalized to 256 data points to have the same length as the GRF data, z–standardized, and scaled to the range [0, 1]. The reduction of the entire sentence to the letter W had several reasons. First, preliminary measurements showed that compressing the signal of the entire sentence to 256 data points meant that the handwriting could no longer be generated sufficiently well. Derived from this, we wanted to obtain a signal that was similarly complicated and on a similar time scale in execution as that of the locomotion movements.

2.5 Data analysis

2.5.1 Data analysis procedure

Figure 2 shows a schematic example of the data analysis flow for a portion of the data (Data A). It is important to emphasize that the conditional CycleGAN training data is separate from the generation data and from the SVM training data. While the conditional CycleGAN training for data A and B occurs simultaneously, the paths of data A and B are strictly separated from the time of data

generation. The details of data generation and classification are described below.

2.5.2 Data generating–conditional CycleGAN

With the CycleGAN (Zhu et al., 2017), we want to translate the movements of walking, running, and handwriting, keeping individual features in each case. Again, an unpaired approach is particularly appropriate because we want to translate data from one movement domain (e.g., walking) into data from another movement domain (e.g., running) without knowing a possible mapping of the different movements of each domain to each other.

In doing so, our approach deviates somewhat from the original CycleGAN formulation. Since we want to preserve the individual component via the movement data transfer as well, we have added a class condition to the conventional CycleGAN in the following.

2.5.2.1 Formulation of the conditional CycleGAN

The goal of the conditional CycleGAN, conditioned on the participant's class label, is to learn mapping functions between two domains X and Y under the condition of the classes Z given the training samples $\{x_i\}_{i=1}^{N}$ where $x_i \in X$ and $\{y_j\}_{j=1}^{M}$ where $y_j \in Y$, and the class embedding $\{z_k\}_{k=1}^{P}$ where $z_k \in Z$. For simplicity, the indices i, j, and k are omitted in the following. The data distribution is denoted as $x \sim p_{data}(x)$ and $y \sim p_{data}(y)$, for the input of the original data, $z \sim p_{class}(z)$ for the class embedding, and $x, z \sim p_{data}(x, z)$ and $y, z \sim p_{data}(y, z)$ for the data under the class condition. The conditional CycleGAN includes two mappings G: $(X, Z) \rightarrow Y$ and F: $(Y, Z) \rightarrow X$. Furthermore, there are two adversarial discriminators D_X and D_Y, where the aim of D_X is to distinguish between data $\{x\}$ and translated data $\{F(y, z)\}$ and correspondingly for D_Y to distinguish between $\{y\}$ and $\{G(x, z)\}$. In the following, the terms adversarial loss (Goodfellow et al., 2014; Goodfellow et al., 2020), cycle–consistency loss (Zhu et al., 2017), and identity–mapping loss (Taigman et al., 2017), which are elementary for the conditional CycleGAN, are described and finally summarized in the objective function.

Adversarial Loss (Goodfellow et al., 2014; Goodfellow et al., 2020): To both functions, adversarial losses are applied. For the mapping function G: $(X, Z) \rightarrow Y$ and its discriminator D_Y, the adversarial loss is:

$$\mathcal{L}_{\mathrm{GAN}}(\mathbf{G}, \mathbf{D_Y}, \mathbf{X}, \mathbf{Y}, \mathbf{Z}) = \mathbb{E}_{\mathbf{y,z}\sim \mathbf{p_{data}}(\mathbf{y,z})}\left[\mathbf{log D_Y}(\mathbf{y}, \mathbf{z})\right] + \mathbb{E}_{\mathbf{x,z}\sim \mathbf{p_{data}}(\mathbf{x,z}), \mathbf{z}\sim \mathbf{p_{class}}(\mathbf{z})}\left[\mathbf{log}\left(\mathbf{1} - \mathbf{D_Y}(\mathbf{G}(\mathbf{x}, \mathbf{z}), \mathbf{z})\right)\right]$$

where G aims to generate data $G(x, z)$ that look similar to data from domain Y, while D_Y tries to distinguish them from the real samples y. G tries to minimize this goal against an adversary D, which in turn tries to maximize it: $min_G max_{D_Y} \mathcal{L}_{GAN}(G, D_Y, X, Y, Z)$. The adversarial loss for the mapping function F: $(Y, Z) \rightarrow X$ and its discriminator D_X is formulated accordingly.

Cycle–Consistency Loss (Zhu et al., 2017): In addition, to reduce the space of possible mapping functions G and F, the mapping functions should be cycle–consistent. For each data x from domain X, the data translation cycle should be able to return x to the original data: $x \rightarrow G(x, z) \rightarrow F(G(x, z), z) \approx x$, which is called *forward cycle consistency*. The *backwards cycle consistency* applies accordingly to y from domain Y. To achieve cycle consistency, the following cycle–consistency loss is expressed:

$$\mathcal{L}_{\mathrm{CYC}}(\mathbf{G}, \mathbf{F}) = \mathbb{E}_{\mathbf{x,z}\sim \mathbf{p_{data}}(\mathbf{x,z}), \mathbf{z}\sim \mathbf{p_{data}}(\mathbf{z}), \mathbf{x}\sim \mathbf{p_{data}}(\mathbf{x})}\left[\| \mathbf{F}(\mathbf{G}(\mathbf{x}, \mathbf{z}), \mathbf{z}) - \mathbf{x}\|_1\right] + \mathbb{E}_{\mathbf{y,z}\sim \mathbf{p_{data}}(\mathbf{y,z}), \mathbf{z}\sim \mathbf{p_{data}}(\mathbf{z}), \mathbf{y}\sim \mathbf{p_{data}}(\mathbf{y})}\left[\| \mathbf{G}(\mathbf{F}(\mathbf{y}, \mathbf{z}), \mathbf{z}) - \mathbf{y}\|_1\right]$$

Identity–mapping Loss (Taigman et al., 2017): To promote the successful reproduction of the input, an identity-mapping loss is formulated:

$$\mathcal{L}_{ID}(G, F) = \mathbb{E}_{y,z\sim p_{data}(y,z), y\sim p_{data}(y)}\left[\| G(y, z) - y\|_1\right] + \mathbb{E}_{x,z\sim p_{data}(x,z), x\sim p_{data}(x)}\left[\| F(x, z) - x\|_1\right]$$

Full Objective: To summarize, the complete objective is:

$$\mathcal{L}_{CYC}(G, F, D_X, D_Y) = \mathcal{L}_{GAN}(G, D_Y, X, Y) + \mathcal{L}_{GAN}(F, D_X, Y, X) + \lambda_{CYC}\mathcal{L}_{CYC}(G, F) + \lambda_{ID}\mathcal{L}_{ID}(G, F)$$

where λ_{CYC} and λ_{ID} control the relative importance of the two objectives, respectively.

The goal is to solve the following equation:

$$\mathbf{G}^{*}, \mathbf{F}^{*} = \mathbf{arg}\ \mathbf{min}_{\mathbf{G,F}}\ \mathbf{max}_{\mathbf{D_X, D_Y}}\ \mathcal{L}(\mathbf{G}, \mathbf{F}, \mathbf{D_X}, \mathbf{D_Y})$$

2.5.2.2 Architecture and training details

The basic architecture and training details are based on the CycleGAN architecture of Zhu et al. (Zhu et al., 2017) and its implementation on GitHub (https://github.com/junyanz/CycleGAN). Thereby, the generator architecture is in turn based on the GAN architecture of Johnson et al. (Johnson et al., 2016), and the discriminator architecture is based on PatchGANs (Li and Wand, 2016; Isola et al., 2017; Ledig et al., 2017). We implemented the class conditioning according to the conditional GAN model of Isola and colleagues (Isola et al., 2017). To implement the code, we used Tensorflow 2.9.2 (Abadi et al., 2015). In the following, we point out all differences in specifications from the originally proposed constructs and training parameters.

The specific layers used for the generator and discriminator models, including their filter and kernel sizes, are shown in Figure 3. We fitted all layers to a one–dimensional input. Moreover, for the convolutional layers shown, we initialized the model weights with a random Gaussian with a mean of 0.00 and a standard deviation of 0.02. In addition, we used the same padding.

Other specific settings not shown in Figure 3 for the discriminator and generator are noted below. For the discriminator, we used 70 × 1 PatchGANs according to Isola et al. (2017). The convolutional layers had a stride of two for all layers except the output layer, where the stride is one. In addition, the slope of the leaky ReLU layers was set to $\alpha = 0.2$. The generator model according to Johnson et al. (2016) consists of an encoder, nine consecutive residual networks (ResNet) for transformation, and a decoder. The stride of the first and last convolutional layers and ResNet convolutions is one, while it is two in every other convolutional layer. For all parameters of the discriminator and generator not mentioned, we used the default values of Tensorflow (version 2.9.2).

Furthermore, 200 epochs were trained with a batch size of 64. The discriminator used the Adam solver with a constant learning rate of 0.0002. While for the generator, we adjusted the learning rates

10.3389/fbioe.2023.1204115

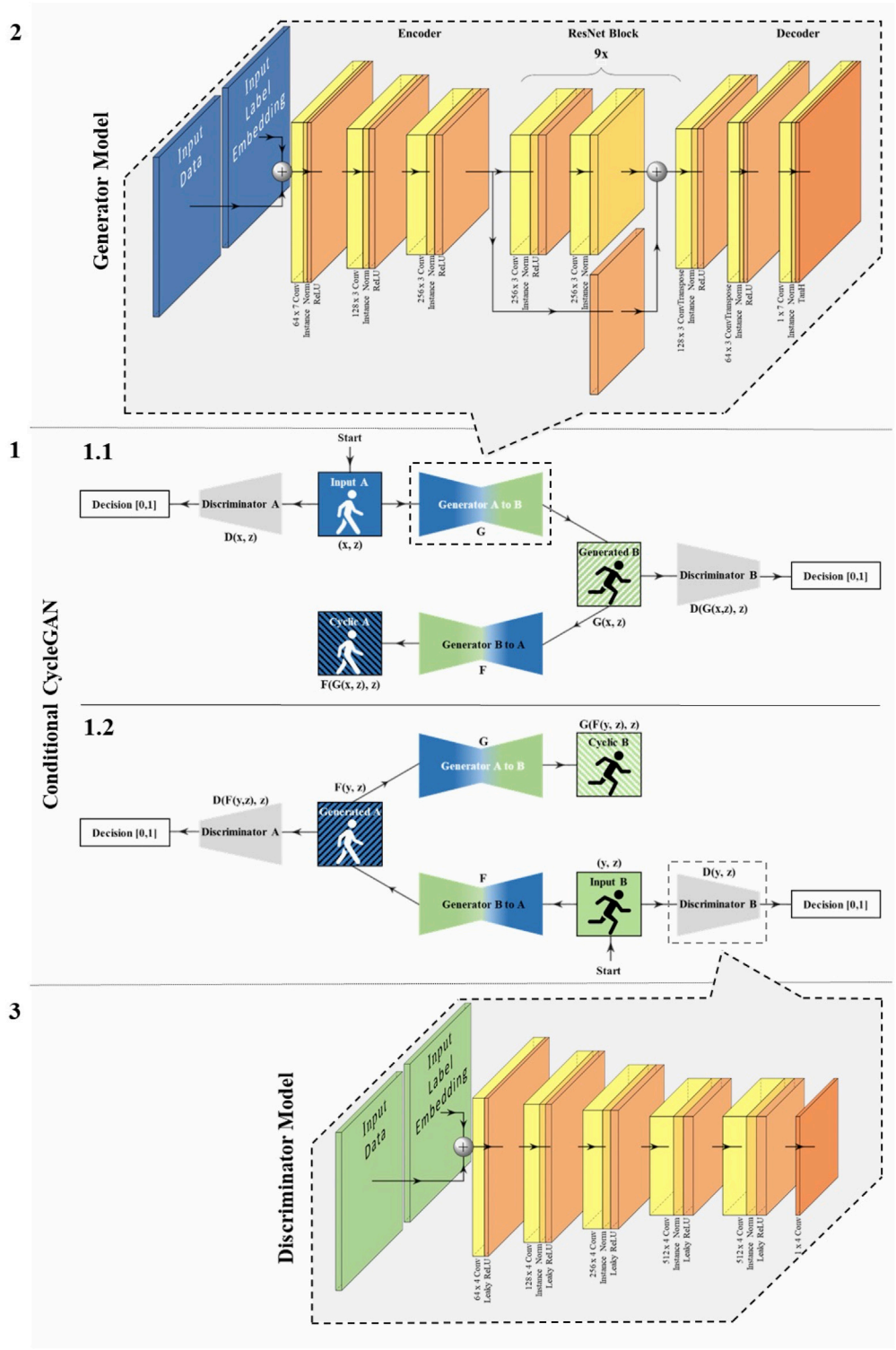

FIGURE 3
Schematic structure of the conditional CycleGAN, the generator, and the discriminator model. (1) The conditional CycleGAN with walking exemplary for Data A and running for Data B: In 1.1, the path is shown starting from Data A, and in 1.2 starting from Data B. It is important to emphasize that the identically named generators and discriminators are the same in each case and are trained from both directions. Furthermore, the basic generator and discriminator models are the same. (2) Generator model: presented are the layers including filter and kernel size (e.g., 64 × 7 Conv = convolutional Layer with 64 filters and a kernel size of seven). (3) PatchGAN discriminator model: presented are the layers including filter and kernel size.

TABLE 2 Description of the data of the baseline participant classification by means of SVM based on the original walking, running, and handwriting data.

Original data	SVM	
	Number of training data	Number of test data
Walking	9,594 (565.1 ± 110.7) [905 (53.3 ± 1.5)]	1,067 (62.9 ± 12.3) [101 (5.9 ± 0.3)]
Running	14,722 (866.6 ± 163.9) [905 (53.3 ± 1.5)]	1,636 (96.3 ± 18.1) [101 (5.9 ± 0.3)]
Writing	905 (53.3 ± 1.5)	101 (5.9 ± 0.3)

An SVM with five–fold cross–validation was applied. The table shows the total number of trials for the training and test data from all 17 participants. The mean amount and standard deviations of the trials of each participant are shown in round brackets. In square brackets, the number of trials of the walking and running data adjusted for the number of trials of the writing data is also shown.

according to the pair of data. For the conditional CycleGAN between walking and running data, as suggested in the study by Zhu et al. (2017), the learning rate was set to 0.0002 for the first 100 epochs and then linearly decreased to 0 for the next 100 epochs. For the conditional CycleGAN between walking and handwriting data or running and handwriting data, in the first 50 epochs, the learning rate was 0.0128 (= 0.0002 * 64 (batch size)); in the next 50 epochs, it was 0.0016 (0.0002 * 8 (square root of the batch size)); and in the last 100 epochs, it was linearly decreasing to 0. In addition, λ_{CYC} was set to 10 and λ_{ID} to 5 in Equation 4. The trained generator with the lowest loss value over each of the 200 epochs was selected for data generation.

2.5.2.3 Data classification

Since there are no theoretical or practical empirical values for the time series-based method used in this study in terms of the minimum amount of data, we roughly followed the sizes of the image datasets used in the CycleGAN article (Zhu et al., 2017). We collected 10,661 walking strides (627.9 ± 129.0 per person), 16,358 running strides (962.9 ± 182.0 per person), and 1,067 handwritings (59.25 ± 1.8 per person). Each vector of walking or running stride and handwriting included 256 data points (walking/running: 256 data points = 128 data points of left food contact + 128 data points of the right food contact).

Participant classifications were based on support vector machine (SVM) (Cortes and Vapnik, 1995; Boser et al., 1996; Müller et al., 2001; Scholkopf and Smola, 2002) with an extensive hyperparameter search in terms of kernel (linear, radial basis function, sigmoid, and polynomial) and cost parameter ($C = 2^{-5}, 2^{-4.75}, \ldots, 2^{15}$).

We examined the performance to discriminate walking, running, and handwriting patterns between participants using a multi-class classification with 17 classes, where each participant represented one class. As shown in Table 2 for the original data (and in more detail for the generated data in the Supplementary Table S1), the amount of training and testing data used for the classifications varied in size due to the different data sets. In addition, to relate the results of the participant classification based on the original data, we exactly matched the training and test splits of the walking and running classification to those of the writing classification.

To evaluate the results of the multi-class classifications, the performance indicators accuracy, F_1-score, precision, and recall were calculated after five-fold cross-validation. The number of true positives (TP), true negatives (TN), false positives (FP), and false negatives (FN) define these metrics:

$$Accuracy = \frac{TP + TN}{TP + TN + FP + FN}$$

$$Precision = \frac{TP}{TP + FP}$$

$$Recall = \frac{TP}{TP + FN}$$

$$F_1 - score = 2 * \frac{Precision * Recall}{Precision + Recall}$$

The baseline reference is the zero-rule baseline (ZRB), which results from the theoretical accuracy when the classifier always predicts the most frequented class of the training set. Since our dataset is unbalanced, the ZRB is calculated by dividing the number of training trials of the most frequent class by the number of all training trials in the corresponding classification task:

$$ZRB = \frac{Training\ Trials\ Most\ Frequent\ Class}{All\ Training\ Trials}$$

For a detailed overview of the calculated ZRB for each classification task, see Supplementary Table S2.

The classification was performed within Python version 3.9.12 (Python Software Foundation, Wilmington, DE, United States) using the scikit–learn toolbox version 1.1.3 (Pedregosa et al., 2011).

3 Results

3.1 Participant classification on original data

The basic assumption of this study is the existence of the distinguishability of the individual movement patterns between the persons. To test this assumption, an SVM was used to classify individuals based on walking, running, or handwriting data. As presented in Table 3, it is possible to distinguish the participants from each other in both the walking and running data, and the handwriting data with more than 98.0% classification F_1–score each.

3.2 Qualitative analysis of generated data

Figure 4 shows an example of the data of the participants p3 (Figure 4.1) and p5 (Figure 4.2). Looking at the shape of the curves, it is noticeable that the generated running (genRunning), generated

TABLE 3 Classification scores of person recognition using SVM based on original data.

Classification problem	Classification score [%]					Number of trials	
	Acc	F_1	Prec	Rec	ZRB	Train	Test
Walking	99.7 [98.0]	99.7 [98.0]	99.7 [98.4]	99.7 [98.0]	7.5 [6.0]	9,594 [905]	1,067 [101]
Running	99.6 [99.0]	99.6 [99.0]	99.6 [99.1]	99.6 [99.0]	6.7 [6.0]	14,722 [905]	1,636 [101]
Writing	99.0	99.0	99.2	99.0	6.0	905	101

In squared parentheses are the results of the original walking and running classification, where the number of trials was exactly matched to that of the writing classification. ZRB, Zero–Rule Baseline; Acc, Accuracy; F_1, F_1–Score; Prec, Precision; and Rec, Recall.

walking (genWalking), and generated handwriting (genWriting) data correspond to the curve of the respective original data. However, based on the examples, it is noticeable that genWalking and genRunning data generated from walking or running data show a distribution with lower variance. In addition, the examples of genRunning data from walking data show a small wave at the end of the left and right ground contact, which does not occur in the original running data. In the genWalking and genRunning data, which are based on the handwritten data, it can also be seen that there are sections within the curves that vary noticeably in variance (e.g., Figure 4.1.3: the right ground contact in each case for genWalking and genRunning). A more detailed look at the genWriting data shows that they deviate somewhat more from the original data than genRunning data and genWalking data. In addition, for example, there are also fewer smooth curve components (Figure 4.1.2). Furthermore, it is noticeable that the first value of the generated data tends to be too small (i.e., by 0.0) and does not match the original data (i.e., by 0.2).

Looking at the data at the individual participant level, we see that individual characteristics of the original walking, running, and handwriting data were carried over into the genWalking, genRunning, and genWriting data, respectively. For example, in both p3 and p5, the somewhat stronger impact peak of the right ground contact during running is also transferred accordingly in the respective genRunning data. In addition, in the genWalking data at p3 (Figure 4.1.2), the left ground contact shows a higher loading peak than the terminal stance peak, which is exactly the opposite in the right ground contact but corresponds to the original data in both cases. Also, in handwriting, for example, it can be seen that the pattern of p5 (Figure 4.2.3) is somewhat wavier than that of p3 (Figure 4.1.3), which is also reflected in the corresponding genWriting data.

3.3 Classification with generated test data

Table 4 presents the results of the person classifications with generated test data. The classification F_1–score of the genRunnings generated from walking data and the genWalkings from running data was 92.5% and 98.9%, respectively. The classification F_1–score of the genRunnings and genWalkings from handwriting data was 78.7% and 78.4%, respectively. For the genWriting data generated from the walking and running data, the F_1–score was 46.8% and 50.0%, respectively. Thus, the results are 7.7–14.0 times better than the ZRB guess probability.

4 Discussion

4.1 Person classification based on original data

To test the underlying assumption of the individuality of the collected walking, running, and handwriting patterns in the present study, person classifications were performed. The results of the person classifications based on the original data confirm our assumption that both vertical GRF in walking or running and vertical pen pressure in handwriting clearly differ between participants in each case (F_1–score: running: 99.6%, walking: 99.7%, and writing: 99.0%). These results are therefore within the range of previous studies on the individuality of movement patterns (Bauer and Schöllhorn, 1997; Schöllhorn et al., 2002a; Schöllhorn et al., 2002b; Schöllhorn et al., 2006; Janssen et al., 2008; 2011; Schmidt, 2012; Albrecht et al., 2014; Horst et al., 2016; Horst et al., 2017a; Horst et al., 2017b; Horst et al., 2019; Burdack et al., 2020a).

In order to be able to relate the results of the person classifications between the movements based on the original data, the data sets of the walking and running data were adjusted to the size of the data set of the writing data. Due to the reduction of the data set, the classification results of the original walking (99.7%–98.0% F_1–score) and running (99.6%–99.0% F_1–score) data slightly decreased. When comparing the classification results between the vertical GRF of walking and running and the vertical pen pressure patterns in handwriting, no differences were shown between the signals of running and those of writing. However, there is a difference, albeit very slight, between the results based on the signals of walking and those of walking or writing. A possible explanation for the somewhat more individual patterns in running compared to walking could be due to, for example, a different frequency spectrum or higher applied forces (Burdack et al., 2020a). Similar to the study by Schöllhorn et al. (2002a), where the most extreme heel heights of shoes resulted in the highest recognition rate, running can be seen as a more extreme movement that forces the participants to show their individuality. Whereas in walking speed there are many more possibilities for compensation. However, for larger data sets, the above points seem to play a minor role in influencing person classification. One approach to explaining the slightly better handwriting results compared to those of walking could be the different localization of the movement control in the central nervous system. The time normalization and accompanying possible interpolation of the vectors should have only a subordinate influence on the results of the classification (Burdack et al., 2020b).

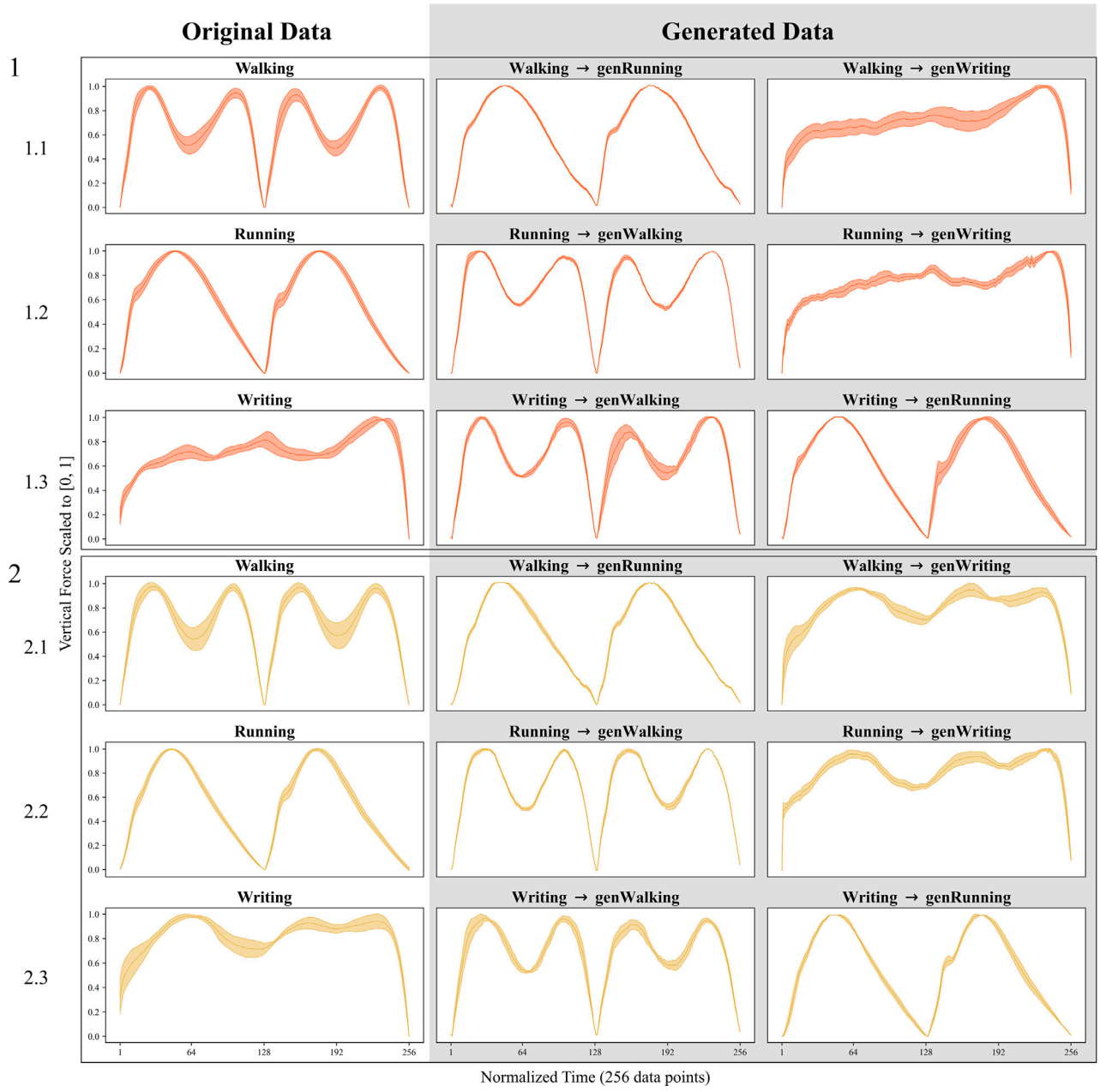

FIGURE 4
Original and CycleGAN-generated Data. Shown is the test set data of Participant 3 (1) and Participant 5 (2). Panels 1.1 and 2.1 show the original walking data and the genRunning and genHandwriting data generated from them. Accordingly, panels 1.2 and 2.2 refer to the original running data, and panels 1.3 and 2.3 to the original handwriting data each with the data generated from them. The mean values and standard deviation over the respective curves are shown in each case. On the *x*–axis, the respective courses over the 256 time points are shown. The *y*–axis shows the vertical force scaled to the interval [0, 1]. For the walking and running data, the values 1 to 128 represent the ground contact of the left foot and the values 129 to 256 of the right foot. genRunning, generated running data; genWalking, generated walking data; and genWriting, generated handwriting data.

4.2 Data generation and person classification based on generated data

In the first step of data analysis, transformations between the vertical GRF data of walking and running movements and the vertical pen pressure of handwriting were learned using the deep learning method CycleGAN (Zhu et al., 2017) with a participant's class conditioning. Then, based on the learned transformations, the data of each of the other two movements was artificially generated from the third movement. This generated data was then tested in a person classification trained with the original data.

The results ranged from 46.8% to 98.9% F1–score, corresponding to almost 8 times and up to 14 times the guess probability, respectively. Consequently, this provided the first

TABLE 4 Classification results of person recognition using SVM with generated test data.

Classification problem		Classification score [%]					Number of trials	
Test Data	Generated from	Acc	F1	Prec	Rec	ZRB	Train	Test
genRunning	←Walking	93.6	92.5	95.9	93.6	6.7	1,636	1,067
genWriting	←Walking	52.2	46.8	49.7	52.2	6.0	101	1,067
genWalking	←Running	98.9	98.9	98.9	98.9	7.5	1,067	1,636
genWriting	←Running	53.9	50.0	50.1	53.9	6.0	101	1,636
genRunning	←Writing	71.3	78.7	75.5	86.7	6.7	1,636	101
genWalking	←Writing	73.3	78.4	73.4	88.1	7.5	1,067	101

ZRB, Zero–Rule Baseline; Acc, Accuracy; F_1, F_1–score; Prec, Precision; Rec, Recall; genWalking, Generated walking data; genRunning, Generated running data; and genWriting, Generated handwriting data.

evidence that it is possible to learn pairwise transformations between the respective movement data on the one hand, and preservation of individual structures on the other hand.

The generation of the genRunning (92.5% F_1–score) and genWalking (98.9% F_1–score) data from the original walking and running data worked particularly well. This impression can be confirmed by looking at the figures (Figure 4) of the generated data. The generated genWalking and genRunning data from the original walking and running data are not only very similar in their general shape to the original data but also reflect the respective individual characteristics such as impact peak or time course features in their curves. However, the figures (Figure 4) also show differences between generated and original data. For example, the variance of the generated data was shown to be significantly lower than that of the original data. This observation could be attributed to the fact that GANs aim to learn probability distributions that accurately represent the underlying data generation process (Goodfellow et al., 2014; Goodfellow et al., 2020). Thus, the generator might have tried to stay as close as possible to the learned probability distribution. In addition, curve features were also uncovered that did not appear to have a substantial effect on classification but did not match the original data. On the one hand, this provides a reason for caution for the use of the generated data, and on the other hand, it reveals optimization potential that should be addressed in future research.

To be able to explain the approximated 6% difference in the classification results of the genRunning and genWalking data, several explanatory approaches come into question. One possible approach could be due to the highly non–convex optimization process of the conditional CycleGAN so that the generator was stuck in a local minimum, for example, or the initially learned weights negatively influenced the learning process of the genRunnings. Alternatively, it could be that the running data contains more or different information than the walking data, and it is therefore easier for the conditional CycleGAN to generate genWalking data from the running data than genRunning data from the walking data. However, if we put the classifications in relation to the guessing probability, we notice that the results with 13.2 and 13.8 times the ZRB roughly correspond.

The results of the genRunning and genWalking data from handwriting data are 78.7% and 78.4% F_1–score and the genWriting data from running (50.0% F_1–score) and walking (46.1% F_1–score) data are at least 7.7 times better than the ZRB. Thus, the results are worse than those of the genRunning and genWriting data generated from the walking and running data. The figures (Figure 4) provide a first explanation in this respect. At first glance, the genRunning and genWalking data from the handwriting data and the genWriting data from the running and walking data correspond quite closely to the original data, including the adoption of the curve–specific individual characteristics. The genRunning and genWalking data from the handwriting data, for example, show a relatively strong unequal distribution of the variance in certain curve segments, which does not occur in the original data. However, this could also be due to the relatively small amount of handwriting data generated so that individual trials with a greater deviation from the mean are more significant and are shown relatively overrepresented. The genWriting data also shows a lower variance than the original handwriting data and represents the original curve in part only in a rough form. A further potential explanation for the lower classification results compared to the data generated between walking and running, as well as the discrepancy between the genRunning and genWalking data and the genWriting data derived from walking and running data, could be attributed to the quantity of handwriting data. The limited training data available for the conditional CycleGAN could result in the generator learning a probability distribution that does not accurately represent the original data. One more possible explanation is that generating handwriting is inherently more challenging than generating walking or running. Additionally, the bipedal nature of walking and running may provide additional information about the relationship between the left and right steps, which could facilitate the generation, but this is not present in the case of handwriting. To what extent the different central nerves control locomotion movements such as walking or running and arm or wrist movements such as writing influences the identification of individual patterns remain a subject of future research. The extent to which analyzing the first letter of the sentence while handwriting, and a possible altered variation in movement associated with this, may also have influenced the results remains a subject for future investigation. A further possible explanation could lie in the architecture and training parameters of the conditional CycleGAN so that parameter tuning or optimization of the architecture of the generator or

discriminator (details in chapter IV.D) can achieve domain–specific improvements.

4.3 Identification of underlying individuality across movements

The results provide further evidence for the possibility of automatic recognition of movement patterns across movements. So far, this could only be done for very similar movements using the joint angle curves in shot put, discus, and javelin throwing, taking into account all kinematic variables except that of the throwing arm (Horst et al., 2020). With the proposed method, we can extend this approach considerably. As shown in this work, transferable individual movement features can also be found in movement data that differ significantly in their time course and originate from very different movements.

Other previous studies on the automatic identification of individual movement patterns investigated these in each case only based on single movement signals (Bauer and Schöllhorn, 1997; Schöllhorn et al., 2002a; Schöllhorn et al., 2002b; Schöllhorn et al., 2006; Janssen et al., 2008; Janssen et al., 2011; Schmidt, 2012; Albrecht et al., 2014; Horst et al., 2016; Horst et al., 2017a; Horst et al., 2017b; Horst et al., 2019; Burdack et al., 2020a).

Even though we can provide the first cross–movement approaches in this work, we are only at the beginning of cross–movement research. We were able to provide the first evidence in this study, using vertical forces and pressure data respectively, that it is possible to learn transformations between these data to generate artificial data that still preserve latent patterns of the original data. Thus, we provide a "proof of concept" of the presented method, which has the potential to represent a starting point for further research in this context.

In this respect, an extension of the study to other data signals as well as other biological data would be useful. It would be of interest to see how additional movement components such as three-dimensional GRF, which has been shown to be better than vertical GRF in classifying individuals (Horst et al., 2023), could convey additional information about the individual. While a transfer from kinematic data to GRF data during walking could be shown using GANs (Bicer et al., 2022), there is still great potential to be exploited cross–movement wise. For example, it is important to find out the extent to which the large thematic overlap of locomotion movements might affect inherent biases related to movement character or motor and neurological control compared to handwriting. It is therefore even more encouraging that more different movement signals, such as that of handwriting, could be adequately generated. This gives room for an experimental extension to other signals as well as to linkages with other signals such as audio (e.g., voice), ECG, or EEG (John et al., 2022), which, however, remain the subject of future research.

Furthermore, while we have found individual cross–movement commonalities, what these explicitly look like and what characteristics they exhibit should be addressed in future research. In addition to the individual movement component, it might also be possible to find further latent patterns or subcomponents across movements. Other movement components could be the movement technique or situational adaptations to fatigue, emotions, environment, etc.

The individual patterns across movements also suggest that there might be characteristic features of a person that are at least reflected in several movements. Whether a link can be established between movement and the psychological characteristics of a person could also be the subject of future work. In addition, it remains to be investigated whether individual movement patterns behave similarly and are consistent with patterns found in behavioral research (Buss and Plomin, 1975; Funder and Colvin, 1991; Sherman et al., 2010; Marcus and Roy, 2017). This could be of specific interest for economizing training or therapy. Whether changing the gait by training or therapy, which is sometimes observed after psychotherapy, and whether this has an effect on the handwriting or *vice versa* could be one area of a more holistic approach to future practical applications.

4.4 Data generation and cross–movement analysis by conditional CycleGANs

The methodology presented in this paper has overcome the problem of mapping two biomechanical time series signals to each other while transferring the individual component. It was thus possible to learn the transfer of movement A to movement B while obtaining latent patterns of movement A. This could provide fundamental new opportunities in future experiments where one is looking for latent structures between movements or movement–signals. In the following, we discuss optimization potentials and application possibilities of conditional CycleGANs.

First, it must be emphasized restrictively that in the context of this study, the person condition of the CycleGAN was necessary to learn the transformation including the preservation of the individual component from movement A to movement B. Specifically, this means that it was not possible, for example, to generate a person's individual handwriting data from the walking data without prior knowledge of that person's handwriting.

For the conditional CycleGANs, the amount of walking (approximately 10,000 steps), running (approximately 14,000 steps), and handwriting data (approximately 900 trials) appears to be sufficient to learn transformations between movements based on vertical ground reaction forces or vertical pen pressure. However, the results suggest that the quality of the learned transformation depends largely on the amount of data such that possibly the 900 handwritten trials were too few to produce deceptively real trials, while the amount of walking and running data provided a good basis to perform person classification with very high recognition rates; the generated curves also showed "errors". In order to use data for generation, domain–specific optimizations would need to be made (Saxena and Cao, 2022) so that the generated data are not only indistinguishable using a classifier but make biological sense and are indistinguishable from original data by experts. Apart from a larger data set, we see the greatest optimization potential in adjusting the learning rate of the generator's optimizer (especially in relation to the learning rate of the discriminator). In addition, the number of epochs, or the selected batch size also seems to provide the potential for domain–specific optimization.

The particular potential of the conditional CycleGAN lies in the possibility of cross–movement analysis due to the learnability of transformations from one movement signal to another movement signal. In addition, as in the setting of the present work, the conditional CycleGAN could be used to identify further latent patterns across movements. In doing so, it would also be possible to search for cross–person abstract patterns of, for example, fatigue, emotion, or illness. Another potential of the conditional CycleGAN could be especially in an area where it is difficult to collect large amounts of data. There, artificial augmentation of small data sets could open up the possibility of using data–intensive methods (e.g., deep learning approaches and machine–learning classification). The advantage of the conditional CycleGAN in this context is that this algorithm requires relatively little data and that the training data need not be paired, or the construction of artificial pairs is obsolete.

5 Conclusion

In recent years, the analysis of movement patterns has increasingly focused on the individuality of movements, revealing individual patterns with situation–dependent fine structures. However, previous research methods only allowed the comparison of very similar movement signals. In this study, we were able to identify similarities between individual walking, running, and handwriting patterns across different movements through data augmentation, revealing individual patterns across movements. This further extends the understanding of strong individuality.

Based on the results of movement science studies that use machine learning methods to investigate the uniqueness of individual movement patterns, and the findings presented in this study, it can be inferred that our understanding of the individuality of human movement and the influence of individuality on targeted development, improvement, or recovery is still in its beginning stages. Understanding individual cross–movement commonalities in movement may offer insights into the underlying more general individuality of the central nervous system physiology and structure. Future applications of this approach have the potential to investigate the extent to which the central nervous system or muscle physiology can be altered beyond the individual domain.

In addition, this study provides proof of concept that it is possible to use the conditional CycleGAN to artificially generate cross–movement data with latent movement characteristics of the original movement without relying on paired data. In summary, the methodology presented in this study helps to enable cross–movement analysis and artificially generate larger data sets.

Data availability statement

The raw data supporting the conclusion of this article will be made available by the authors, without undue reservation.

Ethics statement

The studies involving human participants were reviewed and approved by Ethics Committee of the Johannes Gutenberg–University Mainz. The patients/participants provided their written informed consent to participate in this study.

Author contributions

JB and MN recorded the data. JB, SG, and WS conceived the presented idea. JB, SG, and MS performed the data analysis and designed the figures. JB and WS wrote the manuscript. JB, SG, MS, MN, CM, and WS reviewed and approved the final manuscript. All authors contributed to the article and approved the submitted version.

Conflict of interest

CM was employed by the Company Science&Motion GmbH.

The remaining authors declare that the research was conducted in the absence of any commercial or financial relationships that could be construed as a potential conflict of interest.

Publisher's note

All claims expressed in this article are solely those of the authors and do not necessarily represent those of their affiliated organizations, or those of the publisher, the editors and the reviewers. Any product that may be evaluated in this article, or claim that may be made by its manufacturer, is not guaranteed or endorsed by the publisher.

Supplementary material

The Supplementary Material for this article can be found online at: https://www.frontiersin.org/articles/10.3389/fbioe.2023.1204115/full#supplementary-material

References

Abadi, M., Agarwal, A., Barham, P., Brevdo, E., Chen, Z., Citro, C., et al. (2015). *TensorFlow: Large-scale machine learning on heterogeneous systems*. arXiv. doi:10.5281/zenodo.5043456

Aeles, J., Horst, F., Lapuschkin, S., Lacourpaille, L., and Hug, F. (2021). Revealing the unique features of each individual's muscle activation signatures. *J. R. Soc. Interface* 18 (174), 20200770. doi:10.1098/RSIF.2020.0770

Albrecht, S., Janssen, D., Quarz, E., Newell, K. M., and Schöllhorn, W. I. (2014). Individuality of movements in music - finger and body movements during playing of the flute. *Hum. Mov. Sci.* 35, 131–144. doi:10.1016/j.humov.2014.03.010

Barth, V., Käsbauer, H., Ferrauti, A., Kellmann, M., Pfeiffer, M., Hecksteden, A., et al. (2019). Individualized monitoring of muscle recovery in elite badminton. *Front. Physiology* 10, 778. doi:10.3389/fphys.2019.00778

Bates, B. T. (1996). Single-subject methodology: An alternative approach. *Med. Sci. Sports Exerc.* 28 (5), 631–638. doi:10.1097/00005768-199605000-00016

Bauer, H. U., and Schöllhorn, W. I. (1997). Self-organizing maps for the analysis of complex movement patterns. *Neural Process. Lett.* 5, 193–199. doi:10.1023/a:1009646811510

Begg, R. K., and Kamruzzaman, J. (2005). A machine learning approach for automated recognition of movement patterns using basic, kinetic and kinematic gait data. *J. Biomechanics* 38 (3), 401–408. doi:10.1016/J.JBIOMECH.2004.05.002

Begg, R. K., Palaniswami, M., and Owen, B. (2005). Support vector machines for automated gait classification. *IEEE Trans. Biomed. Eng.* 52 (5), 828–838. doi:10.1109/TBME.2005.845241

Bicer, M., Phillips, A. T. M., Melis, A., McGregor, A. H., and Modenese, L. (2022). Generative deep learning applied to biomechanics: A new augmentation technique for motion capture datasets. *J. Biomechanics* 144, 111301. doi:10.1016/j.jbiomech.2022.111301

Boser, B. E., Guyon, I. M., and Vapnik, V. N. (1996). "A training algorithm for optimal margin classifier," in Proceedings of the Fifth Annual ACM Workshop on Computational Learning Theory, Pittsburgh, Pennsylvania, July 27-29, 1992. doi:10.1145/130385.130401

Buford, T. W., Roberts, M. D., and Church, T. S. (2013). Toward exercise as personalized medicine. *Sports Med.* 43 (3), 157–165. doi:10.1007/s40279-013-0018-0

Burdack, J., Horst, F., Aragonés, D., Eekhoff, A., and Schöllhorn, W. I. (2020a). Fatigue-related and timescale-dependent changes in individual movement patterns identified using support vector machine. *Front. Psychol.* 11, 551548. doi:10.3389/fpsyg.2020.551548

Burdack, J., Horst, F., Giesselbach, S., Hassan, I., Daffner, S., and Schöllhorn, W. I. (2020b). Systematic comparison of the influence of different data preprocessing methods on the performance of gait classifications using machine learning. *Front. Bioeng. Biotechnol.* 8, 260. doi:10.3389/fbioe.2020.00260

Buss, A. H., and Plomin, R. (1975). *A temperament theory of personality development*. New Jersey, United States: Wiley-Interscience.

Button, C., Davids, K., Bennett, S. ., and Taylor, M. (2000). Mechanical perturbation of the wrist during one-handed catching. *Acta Psychol.* 105 (1), 9–30. doi:10.1016/S0001-6918(00)00044-5

Chan, I. S., and Ginsburg, G. S. (2011). Personalized medicine: Progress and promise. *Annu. Rev. Genomics Hum. Genet.* 12 (1), 217–244. doi:10.1146/annurev-genom-082410-101446

Chau, T. (2001a). A review of analytical techniques for gait data. Part 1: Fuzzy, statistical and fractal methods. *Gait Posture* 13 (1), 49–66. doi:10.1016/S0966-6362(00)00094-1

Chau, T. (2001b). A review of analytical techniques for gait data. Part 2: Neural network and wavelet methods. *Gait Posture* 13 (2), 102–120. doi:10.1016/S0966-6362(00)00095-3

Cortes, C., and Vapnik, V. N. (1995). Support-vector networks. *Mach. Learn.* 20(3), 273–297. doi:10.1023/A:1022627411411

Cutting, J. E., and Kozlowski, L. T. (1977). Recognizing friends by their walk: Gait perception without familiarity cues. *Bull. Psychonomic Soc.* 9 (5), 353–356. doi:10.3758/BF03337021

Dal, U., Erdogan, T., Resitoglu, B., and Beydagi, H. (2010). Determination of preferred walking speed on treadmill may lead to high oxygen cost on treadmill walking. *Gait Posture* 31 (3), 366–369. doi:10.1016/j.gaitpost.2010.01.006

Davids, K., Button, C., and Bennett, S. (1999). Modeling human motor systems in nonlinear dynamics: Intentionality and discrete movement behaviors. *Nonlinear Dyn. Psychol. Life Sci.* 3 (1), 3–30. doi:10.1023/A:1022429522099

Funder, D. C., and Colvin, C. R. (1991). Explorations in behavioral consistency: Properties of persons, situations, and behaviors. *J. Personality Soc. Psychol.* 60 (5), 773–794. doi:10.1037/0022-3514.60.5.773

Ginsburg, G. S., and Willard, H. F. (2009). Genomic and personalized medicine: Foundations and applications. *Transl. Res.* 154 (6), 277–287. doi:10.1016/j.trsl.2009.09.005

Goodfellow, I., Pouget-Abadie, J., Mirza, M., Xu, B., Warde-Farley, D., Ozair, S., et al. (2014). "Generative adversarial nets," in *Advances in neural information processing systems*. Editors Z. Ghahramani, M. Welling, C. Cortes, N. D. Lawrence, and K. Q. Weinberger (New York: Curran Associates, Inc), 2672–2680.

Goodfellow, I., Pouget-Abadie, J., Mirza, M., Xu, B., Warde-Farley, D., Ozair, S., et al. (2020). Generative adversarial networks. *Commun. ACM* 63 (11), 139–144. doi:10.1145/3422622

Grunz, A., Memmert, D., and Perl, J. (2012). Tactical pattern recognition in soccer games by means of special self-organizing maps. *Hum. Mov. Sci.* 31 (2), 334–343. doi:10.1016/j.humov.2011.02.008

Hammad, I., and El-Sankary, K. (2020). "Using machine learning for person identification through physical activities," in Proceedings - IEEE International Symposium on Circuits and Systems, Sevilla, Spain, October 10-21, 2020. doi:10.1109/ISCAS45731.2020.9181231/VIDEO

Hecksteden, A., Kraushaar, J., Scharhag-Rosenberger, F., Theisen, D., Senn, S., and Meyer, T. (2015). Individual response to exercise training - a statistical perspective. *J. Appl. Physiology* 118 (12), 1450–1459. doi:10.1152/japplphysiol.00714.2014

Hoerzer, S., von Tscharner, V., Jacob, C., and Nigg, B. M. (2015). Defining functional groups based on running kinematics using Self-Organizing Maps and Support Vector Machines. *J. Biomechanics* 48 (10), 2072–2079. doi:10.1016/J.JBIOMECH.2015.03.017

Hoitz, F., von Tscharner, V., Baltich, J., and Nigg, B. M. (2021). Individuality decoded by running patterns: Movement characteristics that determine the uniqueness of human running. *Plos One* 16 (4), e0249657. doi:10.1371/JOURNAL.PONE.0249657

Horst, F., Eekhoff, A., Newell, K. M., and Schöllhorn, W. I. (2017a). Intra-individual gait patterns across different time-scales as revealed by means of a supervised learning model using kernel-based discriminant regression. *PLoS ONE* 12 (6), e0179738. doi:10.1371/journal.pone.0179738

Horst, F., Mildner, M., and Schöllhorn, W. I. (2017b). One-year persistence of individual gait patterns identified in a follow-up study – a call for individualised diagnose and therapy. *Gait Posture* 58, 476–480. doi:10.1016/j.gaitpost.2017.09.003

Horst, F., Janssen, D., Beckmann, H., and Schöllhorn, W. I. (2020). Can individual movement characteristics across different throwing disciplines Be identified in high-performance decathletes? *Front. Psychol.* 11, 2262. doi:10.3389/fpsyg.2020.02262

Horst, F., Kramer, F., Schäfer, B., Eekhoff, A., Hegen, P., Nigg, B. M., et al. (2016). Daily changes of individual gait patterns identified by means of support vector machines. *Gait Posture* 49, 309–314. doi:10.1016/j.gaitpost.2016.07.073

Horst, F., Lapuschkin, S., Samek, W., Müller, K. R., and Schöllhorn, W. I. (2019). Explaining the unique nature of individual gait patterns with deep learning. *Sci. Rep.* 9 (1), 2391. doi:10.1038/s41598-019-38748-8

Horst, F., Slijepcevic, D., Simak, M., Horsak, B., Schöllhorn, W. I., and Zeppelzauer, M. (2023). Modeling biological individuality using machine learning: A study on human gait. *Comput. Struct. Biotechnol. J.* 21, 3414–3423. doi:10.1016/J.CSBJ.2023.06.009

Hsu, C., Chang, C., and Lin, C. (2003). *A practical guide to support vector classification*. Available at: http://www.csie.ntu.edu.tw/~cjlin.

Isola, P., Zhu, J.-Y., Zhou, T., Efros, A. A., and Research, B. A. (2017). "Image-to-image translation with conditional adversarial networks," in Proceedings of the IEEE Conference on Computer Vision and Pattern Recognition (CVPR), Honolulu, Hawaii, USA, 21-26 July 2017.

Jacques, T., Bini, R., and Arndt, A. (2022). Inter-limb differences in *in-vivo* tendon behavior, kinematics, kinetics and muscle activation during running. *J. Biomechanics* 141, 111209. doi:10.1016/j.jbiomech.2022.111209

Jäger, J. M., and Schöllhorn, W. I. (2007). Situation-orientated recognition of tactical patterns in volleyball. *J. Sports Sci.* 25(12), 1345–1353. doi:10.1080/02640410701287230

Jain, A. K., Bolle, R. M., and Pankani, S. (2006). *Biometrics: Personal identification in network society*. Berlin, Germany: Springer.

Jaitner, T., Mendoza, L., and Schöllhorn, W. I. (2001). Analysis of the long jump technique in the transition from approach to takeoff based on time-continuous kinematic data. *Eur. J. Sport Sci.* 1 (5), 1–12. doi:10.1080/17461390100071506

Janssen, D., Schöllhorn, W. I., Lubienetzki, J., Fölling, K., Kokenge, H., and Davids, K. (2008). Recognition of emotions in gait patterns by means of artificial neural nets. *J. Nonverbal Behav.* 32 (2), 79–92. doi:10.1007/s10919-007-0045-3

Janssen, D., Schöllhorn, W. I., Newell, K. M., Jäger, J. M., Rost, F., and Vehof, K. (2011). Diagnosing fatigue in gait patterns by support vector machines and self-organizing maps. *Hum. Mov. Sci.* 30 (5), 966–975. doi:10.1016/j.humov.2010.08.010

Johansson, G. (1973). Visual perception of biological motion and a model for its analysis. *Percept. Psychophys.* 14 (2), 201–211. doi:10.3758/bf03212378

John, A. T., Barthel, A., Wind, J., Rizzi, N., and Schöllhorn, W. I. (2022). Acute effects of various movement noise in differential learning of rope skipping on brain and heart recovery analyzed by means of multiscale fuzzy measure entropy. *Front. Behav. Neurosci.* 16, 816334. doi:10.3389/fnbeh.2022.816334

Johnson, J., Alahi, A., and Fei-Fei, L. (2016). "Perceptual losses for real-time style transfer and super-resolution," in 14th European Conference, Amsterdam, The Netherlands, October 11-14, 2016, 694–711. doi:10.1007/978-3-319-46475-6_43

Kaur, R., Motl, R. W., Sowers, R., and Hernandez, M. E. (2023). A vision-based framework for predicting multiple sclerosis and Parkinson's disease gait dysfunctions—a deep learning approach. *IEEE J. Biomed. Health Inf.* 27 (1), 190–201. doi:10.1109/JBHI.2022.3208077

Kaye, D. H. (2010). Probability, individualization, and uniqueness in forensic science evidence. *Brooklyn Law Rev.* 75 (4), 1163–1185.

Kempe, M., Grunz, A., and Memmert, D. (2014). Detecting tactical patterns in basketball: Comparison of merge self-organising maps and dynamic controlled neural networks. *Eur. J. Sport Sci.* 15 (4), 249–255. doi:10.1080/17461391.2014.933882

Ledig, C., Theis, L., Huszar, F., Caballero, J., Cunningham, A., Acosta, A., et al. (2017). "Photo-realistic single image super-resolution using a generative adversarial network," in Computer Vision and Pattern Recognition Conference, Honolulu, HI, USA, July 21 2017 to July 26 2017.

Lee, H. S., Schreiner, L., Jo, S.-H., Sieghartsleitner, S., Jordan, M., Pretl, H., et al. (2022). Individual finger movement decoding using a novel ultra-high-density electroencephalography-based brain-computer interface system. *Front. Neurosci.* 16, 1009878. doi:10.3389/fnins.2022.1009878

Li, C., and Wand, M. (2016). "Precomputed real-time texture synthesis with markovian generative adversarial networks," in *Computer vision – ECCV 2016. ECCV 2016*. Editors B. Leibe, J. Matas, N. Sebe, and M. Welling (Cham: Springer), 702–716. doi:10.1007/978-3-319-46487-9_43

Liao, K., Xiao, R., Gonzalez, J., and Ding, L. (2014). Decoding individual finger movements from one hand using human EEG signals. *PLoS ONE* 9 (1), e85192. doi:10.1371/journal.pone.0085192

Marcus, J., and Roy, J. (2017). Values, personality, and sustainability behaviour: An integrative analysis. *Acad. Manag. Proc.* 2017 (1), 13105. doi:10.5465/AMBPP.2017.13105abstract

Maurer, C., Federolf, P., von Tscharner, V., Stirling, L., and Nigg, B. M. (2012). Discrimination of gender-speed-and shoe-dependent movement patterns in runners using full-body kinematics. *Gait Posture* 36 (1), 40–45. doi:10.1016/J.GAITPOST.2011.12.023

Müller, K. R., Mika, S., Rätsch, G., Tsuda, K., and Schölkopf, B. (2001). An introduction to kernel-based learning algorithms. *Handb. Neural Netw. Signal Process.* 12 (2), 181–201. doi:10.1109/72.914517

Ng, P. C., Murray, S. S., Levy, S., and Venter, J. C. (2009). An agenda for personalized medicine. *Nature* 461 (7265), 724–726. doi:10.1038/461724a

Nuzzo, R. (2014). Scientific method: Statistical errors. *Nature* 506 (7487), 150–152. doi:10.1038/506150a

Pedregosa, F., Varoquaux, G., Gramfort, A., Michel, V., Thirion, B., Grisel, O., et al. (2011). Scikit-learn: Machine learning in python. *J. Mach. Learn. Res.* 12, 2825–2830.

Rein, R., and Memmert, D. (2016). Big data and tactical analysis in elite soccer: Future challenges and opportunities for sports science. *SpringerPlus* 5 (1), 1410. doi:10.1186/S40064-016-3108-2

Savitzky, A., and Golay, M. J. E. (1964). Smoothing and differentiation of data by simplified least squares procedures. *Anal. Chem.* 36 (8), 1627–1639. doi:10.1021/AC60214A047/ASSET/AC60214A047.FP.PNG_V03

Saxena, D., and Cao, J. (2022). Generative adversarial networks (GANs). *ACM Comput. Surv.* 54 (3), 1–42. doi:10.1145/3446374

Schafer, R. W. (2011). What is a savitzky-golay filter? *IEEE Signal Process. Mag.* 28 (4), 111–117. doi:10.1109/MSP.2011.941097

Schmidt, A. (2012). Movement pattern recognition in basketball free-throw shooting. *Hum. Mov. Sci.* 31 (2), 360–382. doi:10.1016/j.humov.2011.01.003

Scholkopf, B., and Smola, A. J. (2002). *Learning with kernels: Support vector machines, regularization, optimization, and beyond*. United States: MIT Press.

Schöllhorn, W. I., and Bauer, H. U. (1998a). "Assessment of running patterns using neural networks," in *Sport und Informatik*. Editors J. Mester and J. Perl (Germany: Sport and Buch Strauss), 208.

Schöllhorn, W. I., and Bauer, H. U. (1998b). "Identifying individual movement styles in high performance sports by means of self-organizing Kohonen maps," in *XVI annual conference of the international society for biomechanics in sport*. Editors H. J. Riehle and M. Vieten (USA: International Society for Biomechanics in Sport), 574–577.

Schöllhorn, W. I. (1993). Biomechanische einzelfallanalyse im diskuswurf: Prozess und produktorientierte technikanalyse mechanischer energieformen [biomechanical single case analysis in discus throwing: Process and product oriented technique analysis of mechanical energy forms]. *Harri Dtsch.* 19.

Schöllhorn, W. I., Nigg, B. M., Stefanyshyn, D. J., and Liu, W. (2002a). Identification of individual walking patterns using time discrete and time continuous data sets. *Gait Posture* 15 (2), 180–186. doi:10.1016/S0966-6362(01)00193-X

Schöllhorn, W. I., Schaper, H., Kimmeskamp, S., and Milani, T. (2002b). Inter- and intra-individual differentiation of dynamic foot pressure patterns by means of artificial neural nets. *Gait Posture* 16 (1), 172–173.

Schöllhorn, W. I., Peham, C., Licka, T., and Scheidl, M. (2006). A pattern recognition approach for the quantification of horse and rider interactions. *Equine Veterinary J.* 38 (36), 400–405. doi:10.1111/j.2042-3306.2006.tb05576.x

Schöllhorn, W. I., Röber, F., Jaitner, T., Hellstern, W., and Käubler, W. (2001). "Discrete and continuous effects of traditional and differential training in sprint running," in *Perspectives and profiles 6th European college on sports science congress*. Editors J. Mester, G. King, H. K. Strüder, E. Tsolakidis, and A. Osterburg (Germany: Sport and Buch Strauß), 331.

Schöllhorn, W. I., Stefanysbyn, D. J., Nigg, B. M., and Liu, W. (1999). Recognition of individual walking patterns by means of artificial neural nets. *Gait Posture* 10 (1), 85–86. doi:10.1016/S0966-6362(99)90454-X

Schöner, G., Zanone, P. G., and Kelso, J. A. S. (1992). Learning as change of coordination dynamics: Theory and experiment. *J. Mot. Behav.* 24 (1), 29–48. doi:10.1080/00222895.1992.9941599

Sherman, R. A., Nave, C. S., and Funder, D. C. (2010). Situational similarity and personality predict behavioral consistency. *J. Personality Soc. Psychol.* 99 (2), 330–343. doi:10.1037/A0019796

Taigman, Y., Polyak, A., and Wolf, L. (2017). "Unsupervised cross-domain image generation," in 2017 International Conference on Learning Representations, Toulon, France, April 24-26, 2017.

Troje, N. F. (2002). Decomposing biological motion: A framework for analysis and synthesis of human gait patterns. *J. Vis.* 2 (5), 2. doi:10.1167/2.5.2

Westphal, N., and Schöllhorn, W. I. (2001). "Identifying Volleyballteams by their tactical moves," in 6th annual congress of the European College of Sport Science, Cologne 2001 - Germany, 24-28 July, 55.

Windle, C. M., Gregory, S. M., and Dixon, S. J. (1999). The shock attenuation characteristics of four different insoles when worn in a military boot during running and marching. *Gait Posture* 9 (1), 31–37. doi:10.1016/S0966-6362(99)00002-8

Zhu, J.-Y., Park, T., Isola, P., and Efros, A. A. (2017). "Unpaired image-to-image translation using cycle-consistent adversarial networks," in 2017 IEEE International Conference on Computer Vision (ICCV), Venice, Italy, Oct. 22 2017 to Oct. 29 2017, 2242–2251. doi:10.1109/ICCV.2017.244

Frontiers in
Bioengineering and Biotechnology

Accelerates the development of therapies, devices, and technologies to improve our lives

A multidisciplinary journal that accelerates the development of biological therapies, devices, processes and technologies to improve our lives by bridging the gap between discoveries and their application.

Discover the latest Research Topics

See more →

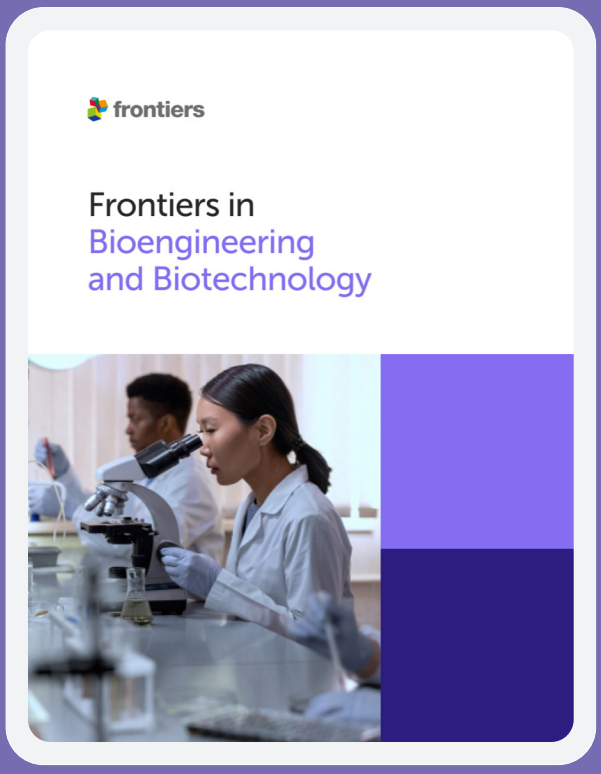

Frontiers

Avenue du Tribunal-Fédéral 34
1005 Lausanne, Switzerland
frontiersin.org

Contact us

+41 (0)21 510 17 00
frontiersin.org/about/contact